Development of new structural systems using novel and eco-efficient construction materials

A Thesis Submitted for the Degree of Doctor of Philosophy

School of Civil, Environmental and Mining Engineering, the University of Adelaide

By:

Ali Fallah Pour

December 2020

Abstract

Development of new structural system using novel and eco-efficient construction materials

A Thesis Submitted for the Degree of Doctor of Philosophy

Ali Fallah Pour

School of Civil, Environmental and Mining Engineering, the University of Adelaide

The University of Adelaide, December 2020

Fibre-reinforced polymer (FRP)-confined high strength concrete (HSC) as a structural system, has received significant attention recently due to higher engineering profits compared to normal strength concrete (NSC). To use widely any new construction material or structural element in the construction industry, its mechanical behavior under different loading type should be accurately determined. Although numerous research was performed to predict the mechanical behavior of FRP-confined concrete, most of the models had a poor prediction for the ultimate axial strain which is a key reference parameter in designing procedure. This inaccuracy can be dependent or on experimental data which were used to develop/validate models, either on the understanding of mechanical response of FRP-confined concrete.

Examination of existing experimental data needed for developing or validating a model in this study shows that the type of measurement method is one important factor affecting the obtained experimental axial stress-strain curve for FRP-confined HSC specimens. This indicates that a better measurement method should be used to obtain both local and overall deformation of specimens during the test procedure. Investigation on the performance of existing models showed that compressive strength of concrete and hoop rupture strain are two influential parameters in existing models which govern the accuracy of models compared to other parameters. However, hoop rupture strain had a large variability of recorded data in existing experiments, partly due to the use of contact measurement methods, i.e. strain gauges that measure local lateral deformation. In addition, this variability can be dependent on the

understanding of mechanical behavior, confinement mechanism and localization characteristics of FRP-confined concrete.

The confinement mechanism was examined in this study by investigation of FRP-confined HSC behavior under concentric and eccentric loading condition. A total of 31 specimens with circular and square cross-section were tested under different eccentricity ranging between 0 to 50 mm. The outcome showed that the load-displacement-curves are influenced significantly by eccentricity. The results also illustrated that the ultimate axial stress decreased by increasing eccentricity opposite to ultimate axial strain. The results also indicate the influence of eccentricity on the confinement mechanism.

The mechanical behavior and localised failure of unconfined and FRP-confined concrete circular specimens for three structural systems, i.e. plain, ultra-high-strength steel and polyvinyl alcohol fibre-reinforced concrete-filled FRP tubes (CFFT), was investigated using Digital Image Correlation (DIC). A new approach also was developed to correlate the mechanical behavior of FRP-confined concrete with its localization characteristics. This approach is able to determine the onset of localization accurately and quantify the localization evolution. Furthermore, probability density function (PDF) was used in this approach to correlate localization characteristics to the mechanical response of FRP-confined concrete. The localization onset of FRP-confined NSC specimens was found to be earlier than in FRP-confined HSC specimens. Furthermore, the outcome indicated the existence of two types of localization evolution in tested specimens. The results showed that the unconfined and insufficiently confined specimens showed abrupt expansion of shear zone opposite to well-confined specimens by more gradual expansion. The results also indicated that the mechanical behavior of FRP-confined HSC is governed by naturally brittle behavior of HSC and the distribution of strain over specimens' surface had similar behavior to probability density function. The analysis and quantification of strain evolution showed that Beta PDF function

can be used to capture the distribution and evolution of Von Mises strain over specimens' surface and to correlate localization characteristics to mechanical response of specimens under compression.

The intrinsically brittle behavior of HSC influences negatively the mechanical performance of unconfined HSC and FRP-confined HSC. An abrupt behavior in the evolution of localization of HSC specimens and FRP-confined HSC compared to NSC was observed in this study, although FRP jackets limited this brittle behavior. In previous reports it has been found that adding fibers such as steel in concrete wet mix improves the performance of HSC and shows more ductile behavior compared to plain HSC. In this study, ultra-high-strength steel and polyvinyl alcohol fibers were used to improve brittle behavior of FRP-confined HSC. The results showed that these fibers improve the ductility of this structural element by disappearance of temporary lose of strength after transition zone in axial stress-strain curve and higher obtained ultimate axial strain. However, it was observed that ultimate axial stress had a marginal increase by adding used fibers in wet mix of concrete at same normalized lateral stiffness. Additionally, as shown in this study, the lateral behavior of these systems was not altered significantly by adding fibers and approximately similar lateral trend as FRP-confined plain concrete can be obtained. Although the more homogenous crack distribution and localization evolution were observed in these structural elements due to the bridging phenomenon, the characteristics of localization did not change intensively. Finally, to establish better engineering characteristics of studied systems, a correlation between bridging and mechanical performance of specimens was made which shows the detail of bridging occurrence under compressive loading.

Declaration

I, Ali Fallah Pour, certify that this work contains no material which has been accepted for the award of any other degree or diploma in my name, in any university or other tertiary institution and, to the best of my knowledge and belief, contains no material previously published or written by another person, except where due reference has been made in the text. In addition, I certify that no part of this work will, in the future, be used in a submission in my name, for any other degree or diploma in any university or other tertiary institution without the prior approval of the University of Adelaide and where applicable, any partner institution responsible for the joint-award of this degree.

I also give permission for the digital version of my thesis to be made available on the web, via the University's digital research repository, the Library Search and also through web search engines, unless permission has been granted by the University to restrict access for a period of time.

I acknowledge that copyright of published works contained within this thesis resides with the copyright holder(s) of those works.

December 2020

Ali Fallah Pour

Acknowledgements

Firstly, I like to thank Dr Togay Ozbakkaloglu for his support and advice. I like to say that I worked more than two years with Dr Togay Ozbakkaloglu and many of my papers could not be published without his help. I also want to express my sincere gratitude to Dr Tom Vincent (Flinders University) for his significant contributions in terms of ideas and technical review towards my research. Finally, I want to thank my principal advisor Associate Professor Giang D. Nguyen, for his wholehearted support and encouragement for technical support and writing of my thesis. His guidance, in both academic and personal life, helped me overcome all the ups and downs in my long journey over the past three years. I would also like to thank the University of Adelaide for providing me with all the necessary facilities and final support during my PhD. At the end, I like to thank the lab technician who helped me a lot during performance of test, i.e. Jon Ayoub, Simon Golding, Ian Ogier, Scott Letton and Dale Hodson.

List of publications

- Published: Fallah Pour A, Gholampour A, Ozbakkaloglu T. Influence of the measurement method on axial strains of FRP-confined concrete under compression. Composite Structures. 2018;188:415-24.
- Published: Fallah Pour A, Ozbakkaloglu T, Vincent T. Simplified design-oriented axial stress-strain model for FRP-confined normal- and high-strength concrete. Engineering Structures. 2018;175:501-16.
- Published: Fallah Pour A, Gholampour A, Zheng J, Ozbakkaloglu T. Behavior of FRP-confined high-strength concrete under eccentric compression: Tests on concrete-filled FRP tube columns. Composite Structures. 2019;220:261-72.
- Published: Fallah Pour A, Nguyen GD, Vincent T, Ozbakkaloglu T. Investigation of the compressive behavior and failure modes of unconfined and FRP-confined concrete using digital image correlation. Composite Structures. 2020:112642.
- Drafted :Analysis of mechanical behavior and localization of deformation in rock and concrete using DIC.
- Drafted: Examination of deformation in FRP-confined high-strength concrete using digital image correlation
- Submited: Axial compressive behavior of ultra-high-strength steel fiber-reinforced concrete-filled FRP tube columns.
- Drafted: Axial compressive behavior of POLYVINYL ALCOHOL fiber-reinforced concrete-filled FRP tube columns.
- Drafted: Evaluation of ultra-high-strength steel fiber-reinforced concrete-filled FRP tubes and unconfined concrete columns under compression: an analysis using Digital Image Correlation

Table of Contents

List of figures

List of tables

Chapter 1: Introduction

By developing urbanism and construction, the influence of human activities on environment attract a great deal of attention. Many of these research studies focused on the use of more eco-efficient materials in construction. These studies investigated the influence of building materials on environment in details then developed a new eco-efficient building materials and/or improved existing structural element to behave more environmental friendly construction materials. One method to minimize the human effect on environment is lowering the depletion of natural resources which are used in the construction of building and infrastructure. This can be performed by replacement of natural sources with other possibilities such as by-products of other industries (e.g. slag or waste rubber) either by reduction of structural members dimension by keeping strength and performance which leads, in turn, lowering the use of natural resources.

It is well understood that high strength concrete (HSC) has higher compressive strength compared to normal strength concrete (NSC) and this indicates to lowering dimension of structural element, i.e. columns, prepared by this type of concrete compared to NSC. It is previously said that lowering dimension of structural element helps to lower the use of natural resources which in turn results in lowering impact on environment. Due to these superior structural engineering properties and environmental issue, the use of high-strength concrete (HSC) in construction has received a great deal of attention because of the benefits offered by high strength concrete (HSC) over normal-strength concrete (NSC) [1-10]. However, HSC shows intrinsically brittle response to compression. This brittle behavior can be improved by using FRP fibers as lateral confinement to obtain more ductile behavior. The previous studies revealed that FRP-confined HSC exhibits a ductile behavior under both concentric and simulated seismic loading conditions. It is well known that FRP-confined HSC showed

numerous advantages: (i) reduction to carbon footprint, (ii) improved durability that prolongs the design life, thereby reducing the cost of structural maintenance and urban renewal, (iii) improvements to the ease of construction that results in reduced construction costs, (iv) improved structural performance. Nonetheless, FRP-confined HSC showed some disadvantages under different loading type which indicated the need for more in-depth study to determine their accurate mechanical behavior. For example, the inherently brittle nature of HSC often showed a temporary post-peak axial strength softening behavior under compression, which unfavourably influenced the concrete columns performance [11-15]. This indicates that the FRP-confined HSC should be studied in detail under different loading types to understand their advantages, disadvantages and precise mechanical behavior to be used widely in construction industry.

1.1 FRP-confined concrete columns

It is well established that the stress-strain curves is a strong instrument to illustrate the mechanical behavior of materials under different loading conditions. These curves are highly influential in designing procedure and an accurate stress-strain curve is able to profit intensely the designing procedure of a building or infrastructure. Over the last two decades, a great number of experimental and analytical studies have been conducted to understand and model the compressive behavior of FRP-confined concrete for both NSC and HSC. Previously developed models included design-oriented models given in closed-forms and analysis-oriented models that predict stress-strain behavior through an incremental process [16]. Design-oriented models are based on the direct interpretation and regression analysis of experimental results as explained by different Refs (e.g. [2, 17-22]). Analysis-oriented models consider the interaction between the concrete and the FRP jacket, in an explicit manner whereas these models can be extended to predict the behavior of concrete confined with other materials [23-26]. Same as design-oriented models, the existing developed analysis –oriented models to

predict the behavior of the FRP-confined concrete were developed and/or validated using experimental datasets.

1.2 Existing models for prediction of FRP-confined concrete behavior and influential parameters on prediction

Design-oriented models use explicit and often simple expression forms to predict the key reference points on stress-strain curves which make them attractive for use in design applications. One of these key points is the transition point, where there is a change in trend of the stress-strain curve after the termination of the initial ascending branch. The other key point on the stress-strain curve is the point corresponding to the ultimate condition, which represent the axial stress and strain of confined concrete at the time of failure. Even the most accurate of the available design-oriented models are relatively poor at predicting the ultimate strain of FRP-confined concrete [27-29]. This poor predictive capability is partly a consequence of the large variability recorded in experiments measuring lateral strains in FRP wraps and tubes at failure [27].

To predict ultimate axial strain (ε_{cu}) and stress (f'_{cc}) of FRP-confined concrete, the models that make use of the hoop rupture strain are significantly more accurate than those that make use of the ultimate tensile strain of fibers (ε_{fu}). Available experimental data for hoop rupture strain ($\varepsilon_{h,rup}$) reported by different studies showed large variations for specimens with similar characteristics such as unconfined concrete strength (f'_{co}) and lateral stiffness (K_l). Bisby and Take [27] and Tabbara and Karam [30] discussed that these variation in recorded data for hoop rupture strain is dependent partly on local shear plane in FRP-confined specimens. Additionally, the accuracy of experimental datasets which are used to develop a design-oriented models is another vital parameters in accuracy of models. It is obvious that the reported datasets depends strongly to recorded data by different measurement instruments and this indicates that the accuracy of measurement is one of the influential parameter on prediction of

FRP-confined concrete behavior. Consequently, an in-depth study of confinement mechanism, failure mechanism of FRP-confined HSC (strain localization evolution), the lateral deformation of FRP jackets over the surface and accuracy of experimental datasets, should be performed.

Analysis-oriented models predict stress-strain behavior through an incremental process [16] by using the interaction mechanism between the concrete core and the FRP jacket in an explicit manner. These models can be extended to predict the behavior of concrete confined with other materials [23-26] and these models are able to create whole stress-strain curve. The analysis oriented models were built based on assumption of equal axial stress and strain of FRP-confined concrete and actively confined concrete at given lateral strain for similar lateral pressure. Therefore, prediction of lateral behavior and the relationship between axial strain and lateral strain are vital importance in developing an analysis-oriented model [14, 31]. The most of existing analysis-oriented models used implicit expression to predict the relationship between axial strain and lateral strain [24, 32-36]. These expressions were developed by modifying original expression which was developed for actively confined concrete. However, Jiang and Teng [31] discussed that this modification is not able to present the real dilation behavior of FRP-confined concrete. Conversely, there are few explicitly developed axial strain –lateral strain relationship which were provided based on obtained results on FRP-confined tests [8, 31, 37-39]. It should be noted that these developed expression were provided by using limited experimental data which were often obtained by the tests that the originators were performed. It can be seen in the Jiang and Teng [31] and Ozbakkaloglu and Lim [14] that using large test database caused the unsatisfactory performance by applying these expressions to wider parametric range compared to initial used databased. Therefore, to develop a more accurate analysis-oriented models, having comprehensive understanding of confinement mechanism and lateral deformation of FRP-confined concrete, is vital importance. Moreover,

same as design-oriented models, the accuracy of any models should be validated by experimental data. These again indicate the need of an investigation on precision of existing experimental results.

1.3 FRP-confined concrete column under eccentric loading

It is well known that the majority of concrete columns are subjected to eccentric loading in real condition. A number of studies have examined the effect of load eccentricity on the behavior of FRP-confined concrete columns with circular [40-46] and non-circular [47-54] cross-sections. However, these studies were concerned with FRP-confined reinforced concrete columns that contained internal steel reinforcement. A few studies have been reported on the behavior of eccentrically loaded FRP-confined concrete columns not having internal steel reinforcement [55-58]. Among them, only two studies experimentally investigated the axial stress-strain behavior of FRP-confined plain concrete under eccentric compression [57, 58]. As explained before, the stress-strain curves of FRP-confined concrete is dependent strongly on confinement mechanism and this mechanism varied in concentric and eccentric compressive axial loading. Consequently, a detailed study on variation in mechanical behavior of FRP-confined concrete leads to better understanding of confinement mechanism of FRP-confined HSC.

1.4 High strength concrete and its intrinsically brittle behavior

The inherently brittle nature of HSC often caused a temporary post-peak axial strength softening behavior, which unfavourably influenced the FRP-confined concrete columns performance [11-15]. The influence of adding fibers in concrete wet mix has been extensively investigated by different research programs [59-76]. The results of these studies showed that the fibers create bridges across the cracks and the crack propagation can be controlled or delayed by these bridges which leads to improving the strength and ductility of concrete [59,

60, 65-70, 72, 73, 75]. These mentioned advantages in the case of using fibers in wet concrete mix of FRP-confined concrete, leads to the reduction of stress concentration on FRP jackets which results in turn the higher hoop rupture strain and ductility [77] and introduction of an ultra-high-performance system which offers an attractive alternative to conventional FRP-confined concrete with better mechanical performance [78]. Although there are some researches on behavior of using different fibers in wet concrete mix of FRP-confined concrete, more detailed studies are needed to focus on lateral behavior and strain localization of this type of elements. It is discussed previously that the lateral behavior is strongly influential to develop an analysis-oriented model which predicts whole stress-strain curves.

1.5 Outline of the thesis

This thesis is organised into 11 chapters; including the current chapter, which serves as an introduction to the aims and scope of this study while outlining the structure of the thesis.

The contents of the successive chapters are as follow:

Chapters 2 discusses about accuracy of experimental data and illustrates the influence of measurement methods on obtained experimental stress-strain curves. In this section, it is exhibited that the variation in measurement methods is able to change the obtained results for brittle material such as HSC. In this section, a database of specimens which their deformations were recorded by two different measurement methods are collected and the obtained results of these two type of measurement were compared. Following this, a discussion on the possible reason for the different results with different measurement methods is provided.

Hoop rupture strain as key parameters which governs the accuracy of existing models is examined in Chapter 3. In this chapter, the performance of existing models to predict the key parameters in axial stress-strain curves, is investigated. As expected, the models which use the hoop rupture strain in their expressions have higher accuracy compared to other models. Consequently, it is investigated if the use of other input data instead of experimental hoop

rupture strain can offer same accuracy. Moreover, the influential parameters on behavior of hoop rupture strain including mechanical characteristics of specimens is examined.

As explained before, analysis-oriented models are significantly dependent on lateral behavior and confinement mechanism of FRP-confined HSC specimens. To investigate the confinement mechanism of FRP-confined specimens, this mechanism should be examined under different types of loading types. As explained previously, most of axial stress-strain curves are obtained by concentric compression whereas the dependency of axial stress-strain curves to confinement mechanism is reported previously. Chapter 4 illustrates the influence of compressive loading types on mechanical behavior of FRP-confined HSC specimens and the change of confinement behavior by variation of loading types, is illustrated.

Chapters 5 introduces a new method to examine the mechanical response, confinement mechanism, hoop rupture strain and lateral deformation of FRP-confined concrete specimens. This new method is developed for better understanding of mechanical response of FRP-confined HSC specimens due to its influence on accuracy of existing models. In this chapter, the developed approach is firstly used on FRP-confined NSC due to obtained results in chapter 2. This approach needs the use of sophisticated measurement methods which shows both local and overall deformation over specimens' surface. Strain localization characteristics is examined in this chapter and the influence of strain localization on confinement mechanism and hoop rupture strain is discussed.

To determine accurately mechanical behavior of FRP-confined HSC, the behavior of HSC should be investigated initially. The developed method in chapter 5 was used in chapter 6 to assess the brittle behavior of HSC and its deformation localization. The developed technique in previous chapter is completed further in this chapter to accurately verify the localization characteristics, i.e. initiation of localization and localization evolution. Additionally, a new way

is suggested in this chapter to use whole obtained data by DIC in validation/developing a constitutive model. This method also is able to quantify localization evolution characteristics.

Chapter 7 displays the results of using developed models in chapter 5 in FRP-confined HSC specimens. This chapter firstly survey the obtained results in chapter 2 for NSC and HSC where different measurement methods showed a consistent results for NSC opposite to HSC. Afterward, the developed technique was used to determine the deformation localization of FRP-confined HSC specimens including localization initiation and evolution. The distribution of Von Mises strain over specimens' surface was examined using the suggested approach introduced in previous chapter.

As explained previously in chapters 2, 6 and 7, HSC showed more brittle behavior compared to NSC and this behavior sometime leads to some unfavourable performances in FRP-confined HSC columns. Adding fiber in concrete matrix was suggested by different studies to improve brittle behavior of HSC. In this study, ultra-high strength steel fiber (UHSSF) and poly vinyl alcohol (PVA) fiber are used to improve mechanical performance of FRP-confined HSC columns. Chapters 8 and 9 show the influence of adding the mentioned fibers in concrete wet mix of FRP-confined NSC and HSC. The mechanical response including lateral behavior of these system are illustrated in these chapters. Additionally, a detailed study on hoop rupture strain for ultra-high strength steel fiber reinforced concrete-filled FRP tubes (UHSSFR-CFFT) and poly vinyl alcohol fiber reinforced concrete-filled FRP tubes (PVAFR-CFFT), was performed. Due to higher engineering profits of UHSSFR-CFFT compared to PVAFR-CFFT, UHSSFR-CFFT is selected to more in-depth study.

Chapter 10 focuses on confinement mechanism, lateral behavior and localization evolution of UHSSFR-CFFT. In this chapter, the developed technique in chapters 6 and 7 is used to evaluate the mechanical response of UHSSFR-CFFT. In this chapter, the influence of adding fiber in

concrete and the change of behavior due to this additives are examine in-depth in this chapter. Moreover, the bridging occurrence due to existence of steel fibers in concrete wet mix, is studied and a correlation between occurrence of bridging and mechanical behavior of UHSSFR-CFFT is made.

Chapter 11 summarises and concludes this study and provides discussions and proposes possible research directions for the future studies.

Chapter 2: Influence of the measurement method on axial strains of FRP-confined concrete under compression

(A paper is published based on this section: Fallah Pour A, Gholampour A, Ozbakkaloglu T. Influence of the measurement method on axial strains of frp-confined concrete under compression. Compos Struct. 2018;188:415-24.(DOI:10.1016/j.compstruct.2018.01.017))

2.1 Introduction

Over the last two decades, several models have been developed to predict the mechanical behavior of fiber reinforced polymer (FRP)-confined concrete [16, 79-83]. Experimental test results were used to establish practical models and to validate proposed analytical and numerical models. Among the mechanical properties of FRP-confined concrete columns, axial compressive behavior has received significant attention. A large number of experimental test results exist in the literature on the axial stress-strain behavior of FRP-confined normal- and high strength concrete (NSC and HSC) [6, 8, 17, 84-92]. However, as was shown previously [14, 16, 17, 93-95], the consistency and reliability of the test database significantly affect the overall performance of the developed model.

A review of the literature shows that axial strains of FRP-confined concrete specimens have been typically measured using two different methods: 1) unidirectional strain gauges placed on the surface of the specimen [96-98]; 2) linear variable displacement transformers (LVDTs) [99-103]. As was discussed previously [104, 105], among these two measurement methods, LVDTs provide more reliable measurements for the axial strain of FRP-confined concretes, as the strain gauges are only able to capture the local strains, which can vary significantly from the overall strains especially along the inelastic portion of the axial stress-strain behavior. Two different LVDT measurement methods, namely full-height and mid-height LVDT (FLVDT and MLVDT) methods, have been used extensively to measure the axial strains of FRP-confined

concrete. FLVDTs are mounted at the corners between loading and supporting steel plates of the testing machine to determine the average axial strain along the entire height of the specimen, whereas MLVDTs are mounted on the surface of the specimen through the use of a cage along the mid-height region to measure the axial strains along this region.

A number of previous studies that used both MLVDT and FLVDT measurement methods [92, 104, 106, 107] have shown that, axial strains obtained from these measurement methods were similar to each other in the case of NSC (i.e. compressive strength below 50 MPa) specimens. However, significant differences were observed in the axial strain of HSC specimens obtained from these two measurement methods and the differences became more pronounced with an increase in unconfined concrete strength (f'_{co}). These observations suggest that the axial strains of HSC specimens can be sensitive to the instrumentation arrangement used in their measurement. Therefore, development of models by the direct use of existing axial strain databases that were obtained from different measurement methods could lead to unreliable results for HSC specimens. Therefore, it is crucial that the influence of instrumentation method should be considered in the modeling to establish an accurate and reliable model, especially in the case of specimens with f'_{co} over 50 MPa. A targeted study is also required to understand the reasons behind the differences in the axial strains obtained from different measurement methods.

As the first systematic study to date, the study presented in this paper was aimed at investigating the relationship between the axial strains of FRP-confined concrete obtained from the two most widely used measurement methods, namely FLVDT and MLVDT methods. A complete database of FRP-confined NSC and HSC cylinders containing both FLVDT and MLVDT axial strain data was assembled. The influential parameters affecting the relationship between axial strains obtained by the two measurement methods are evaluated. An expression is also developed to describe the relationship between the axial strains of FRP-confined HSC obtained

by the two measurement methods with the aim of providing a unified framework for future design and modeling efforts.

Although many design-oriented and analysis-oriented models were developed for FRP-confined concrete, some key reference points on stress-strain curve still need improvement for more accurate prediction [14, 17]. As explained before, experimental data sets are significantly influential in developing or validating a model. As experimental data sets obtain using different measurement methods (e.g. LVDTs and SGs), it is evident that the used measurement method affects intensively the recorded data during test procedure. In this section, a study was performed to illustrate how a measurement method can influence the recorded stress-strain curve using two different methods.

The study presented in this section was aimed at investigating the relationship between the axial strains of FRP-confined concrete obtained from the two most widely used measurement methods, namely FLVDT and MLVDT methods. A complete database of FRP-confined NSC and HSC cylinders containing both FLVDT and MLVDT axial strain data was assembled. The influential parameters affecting the relationship between axial strains obtained by the two measurement methods are evaluated. An expression is also developed to describe the relationship between the axial strains of FRP-confined HSC obtained by the two measurement methods with the aim of providing a unified framework for future design and modeling efforts. This study results in the need of new mythology using more complicated measurement method to investigate the mechanical response of FRP-HSC.

2.2 EXPERIMENTAL DATABASE

Figure 1 shows the test setup and instrumentation arrangement for the FLVDT and MLVDT measurement methods. The test database was compiled with the results from circular FRP-confined concrete specimens with unidirectional fibers in the hoop direction and a height-to-

diameter ratio of 2, for which the axial strains were measured by both FLVDT and MLVDT methods [12, 29, 104-109]. In the database, only the specimens that were confined continuously and experienced FRP rupture failure were included. In addition, six specimens that experienced problems during testing as noted in the source document (marked with "*" in Table 1) together with two specimens that had problems with the displacements recorded by MLVDTs (marked with "**" in Table 1) were excluded from the analysis.

Table 1 in appendix A shows the summary of test results, including the unconfined concrete strength (f'_{co}), the elastic modulus of fibers used in FRP jackets (E_f), the total fiber thickness of FRP jackets (t_f), lateral stiffness (K_l) (where $K_l = \frac{2E_f t_f}{D}$, D is the diameter of the specimen measured at concrete core), the ratio between lateral stiffness over unconfined concrete strength (K_l/f'_{co}), the ultimate axial strain of confined concrete measured by FLVDT ($\varepsilon_{cu,FH}$) and MLVDT ($\varepsilon_{cu,MH}$) methods, and ratio between these two ultimate axial strain ($\varepsilon_{cu,FH}/\varepsilon_{cu,MH}$). The database contained specimens with a nominal diameter (D) of 150 mm and height (H) of 300 mm. 24 of the specimens were confined by carbon FRP (CFRP), 18 by glass FRP (GFRP), and 66 by aramid FRP (AFRP). The f'_{co}, t_f, and E_f varied from 29.6 to 119.3 MPa, 0.167 to 1.2 mm, and 86.9 to 240 GPa, respectively. The coefficient of variation of f'_{co} and K_l were 0.38 and 0.37, respectively. Figure 2 shows the distribution frequency of the datasets in the database with respect to f'_{co} and K_l.

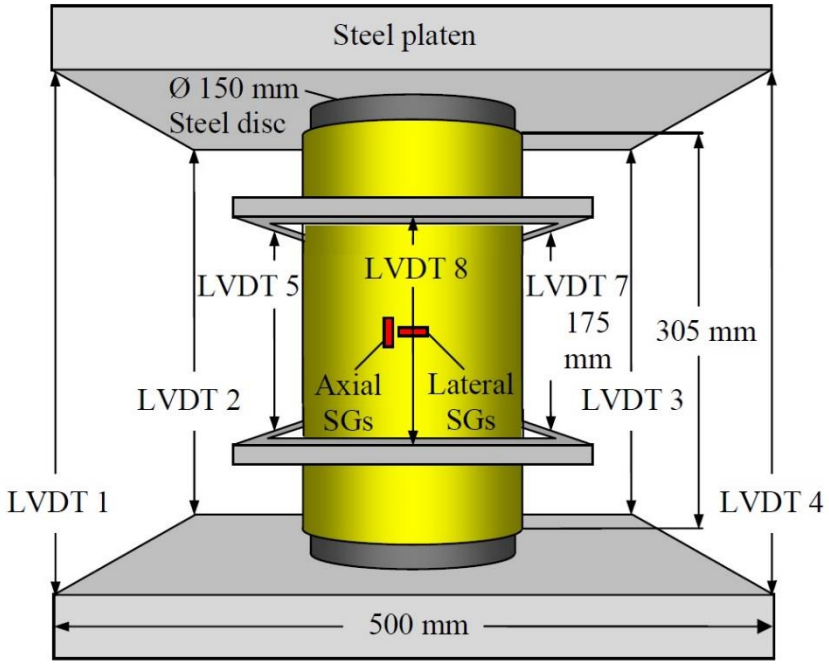

Figure 1- Instrumentation and test setup for FLVDT and MLVDT measurements. LVDT 1–4 and LVDT 5–8 are FLVDTs and MLVDTs, respectively

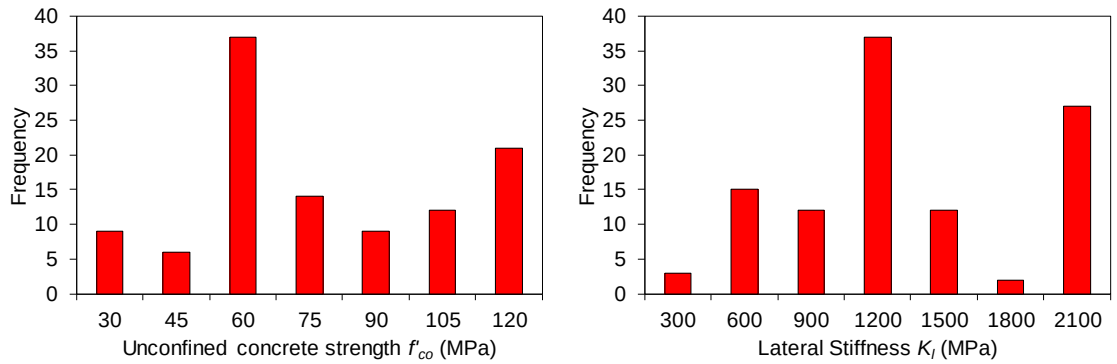

a) b)

Figure 2- Frequency distribution of datasets based on (a) f'_{co} and (b) K_l

2.3 INVESTIGATION OF THE INFLUENCE OF LVDT MEASUREMENT METHODS ON AXIAL COMPRESSIVE BEHAVIOR OF FRP-CONFINED CONCRETE

This section presents a discussion on different failure modes of FRP-confined NSC and HSC specimens and their axial stress-strain relationships obtained by FLVDTs and MLVDTs, which is followed by a detailed discussion on the influential parameters affecting the relationship between axial strains obtained by the two measurement methods.

2.3.1 Failure mode of FRP-confined NSC and HSC

Typical failure modes of FRP-confined NSC and HSC specimens with f'_{co} of 39 MPa and 102 MPa are shown in Figs. 3(a) and 2(b), respectively. It is evident from the figures that the failure resulted from the rupture of the FRP tube in all specimens; however, the failure mode of NSC and HSC specimens are different to each other. As can be seen in Fig. 3(a), NSC specimens experienced gradual concrete crushing as evident from the concrete rubbles exposed after the failure of the FRP tubes [106]. In HSC specimens with strengths over 100 MPa, on the other hand, the crushing of concrete was localized around a few major macrocracks, as shown in Fig. 3(b). Different failure modes of FRP-confined NSC and HSC are attributed to the fact that an increase in the f'_{co} of the concrete results in an increase in the concrete brittleness, which alters the concrete crack patterns from a large number of microcracks to a few localized macrocracks [15, 106, 110]. This in turn affects the axial stress-strain behavior of FRP-confined concrete obtained by the two axial strain measurement methods (i.e. FLVDT and MLVDT), which is discussed in the following section.

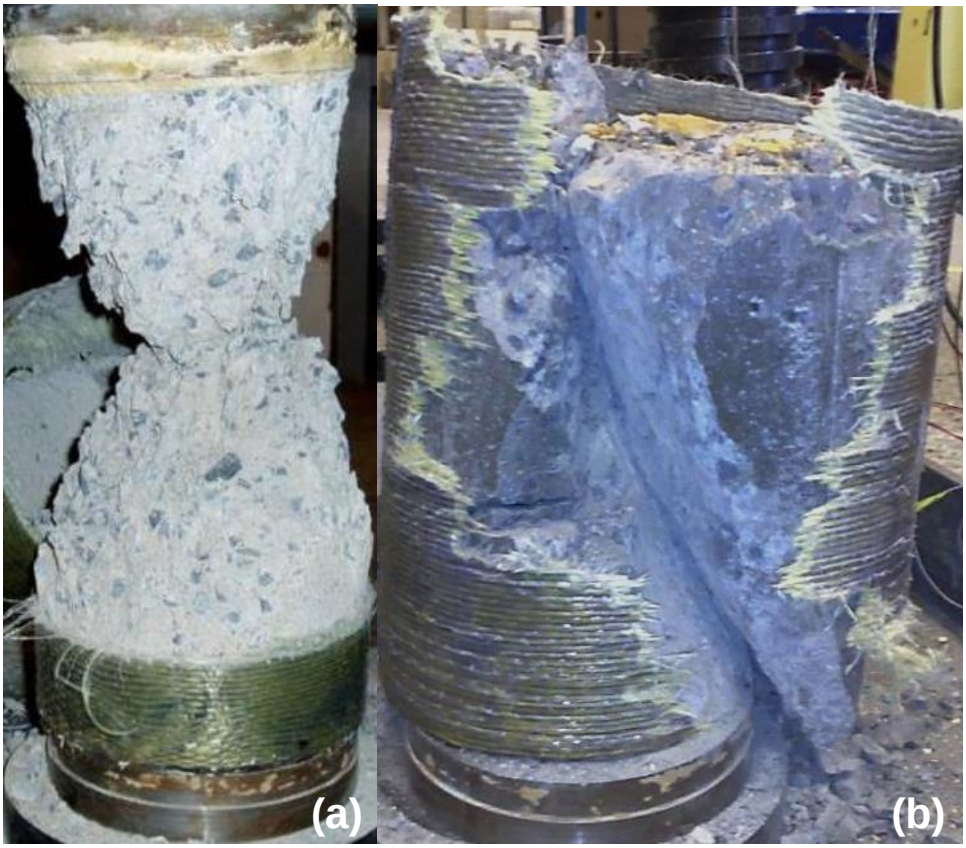

Figure 3- Typical failure mode of FRP-confined (a) NSC (f'_{co}=39 MPa); (b) HSC (f'_{co}=102 MPa)

2.3.2 Axial stress-strain behavior

Figure 4 shows the axial stress-strain relationships of FRP-confined concretes. Axial strains were recorded by FLVDT and MLVDT measurement methods. In the figure, ε_{ct} is the axial strain corresponding to the transition point (obtained from FLVDT) where the axial stress-strain curve transitions from an initial ascending branch to a second branch that can be of ascending or descending type depending on the level of confinement. It can be seen in Fig. 4(a) that FLVDT and MLVDT readings are nearly identical along the axial stress-strain curve of a specimen with f'_{co} of 50 MPa. Conversely, as can be seen in Figs. 4(b) and 4(c), FLVDT and MLVDT readings differ significantly along the curves of specimens with $f'_{co} \geq 70$ MPa. A comparison of the results in Figs. 4(b) and 4(c) reveals that the difference in the axial strains obtained by FLVDT and MLVDT methods becomes more significant with an increase in f'_{co}, this observation is also supported by the rest of the database. The observed difference between

axial stress-strain curves of HSC specimens obtained by FLVDT and MLVDT is attributed to different cracking patterns from heterogenic microcracks in NSC specimens to localized macrocrack in HSC specimens as discussed in Section 3.1 and previous studies [14, 17, 104, 111, 112]. The major localized macrocrack in HSC specimens extended from the top of the specimen to its bottom of (refer to Fig. 3(b)) that formed a sliding plane that separated the discrete segments of the concrete. The presence of such a sliding plane, which was not observed in NSC specimens (refer to Fig.3(a)) created a failure mechanism in which the axial strains were not always captured by MLVDTs, as parts of the axial deformations took the form of rigid body displacements that were only recorded by FLVDTs. The above explains the variation of the observed differences in axial strains obtained by FLVDT and MLVDT (Fig. 4) with concrete strength. This influence is discussed in detail in the following sections.

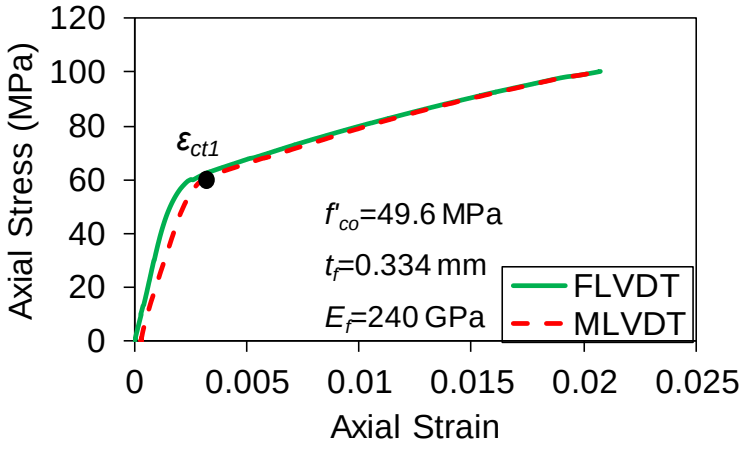

(a)

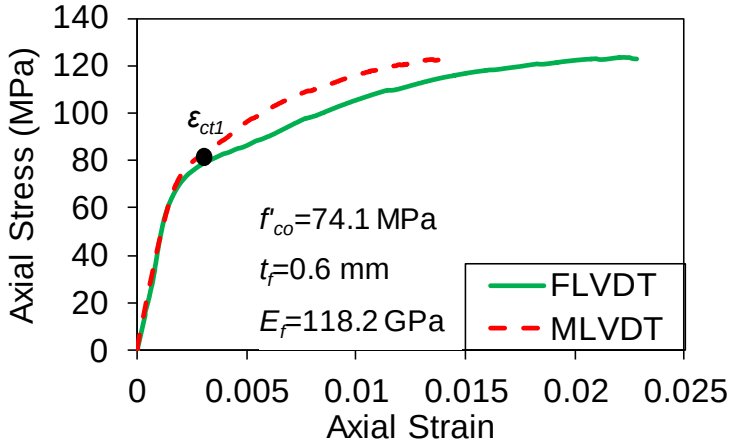

(b)

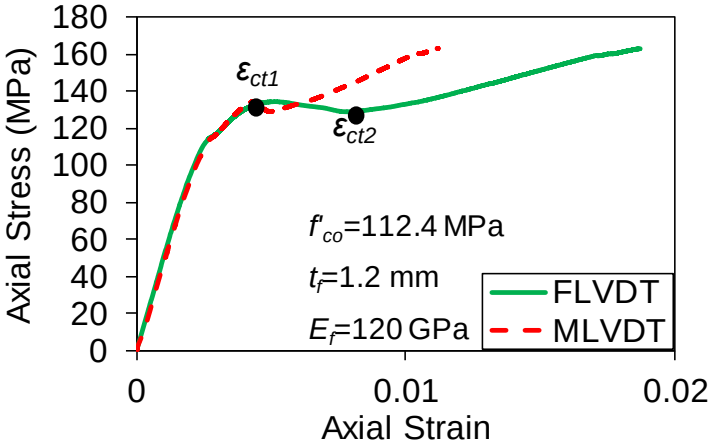

(c)

Figure 4-Axial stress-axial strain relationship obtained by FLVDT and MLVDT: (a) CFRP-confined NSC [35]; (b) CFRP-confined HSC [35]; (c) AFRP-confined HSC [36]. ε_{ct1} and ε_{ct2} are first and second stress-strain curve transition strains obtained from FLVDTs, respectively.

Figures 5-7 present the relationship between the axial strains obtained by MLVDT ($\varepsilon_{c,MLVDT}$) and FLVDT ($\varepsilon_{c,FLVDT}$) methods for specimens with different f'_{co} (i.e. f'_{co} < 50 MPa as group I, 50 MPa ≤ f'_{co} < 100 MPa as group II, and f'_{co} ≥ 100 MPa as group III). As can be seen in Fig. 5, the relationship between $\varepsilon_{c,MLVDT}$ and $\varepsilon_{c,FLVDT}$ in group I was linear, which can be expressed by the following expression:

$$\varepsilon_{c,MLVDT} = \varphi\ \varepsilon_{c,FLVDT} \tag{2.1}$$

in which φ is a coefficient describing the slope of the line in Fig. 5, which varied between 0.85 and 1 in group I specimens. The analysis of test results in database revealed that group I specimens with a normalized lateral stiffness (K_l/f'_{co}) of higher than 13 exhibited 0.95 ≤ φ ≤ 1, whereas φ was lower and ranged between 0.85 and 0.90 for the specimens with K_l/f'_{co} < 13. This observation suggests that the relationship between $\varepsilon_{c,MLVDT}$ and $\varepsilon_{c,FLVDT}$ depends on the FRP confinement, which is discussed in detail in Section 3.2.

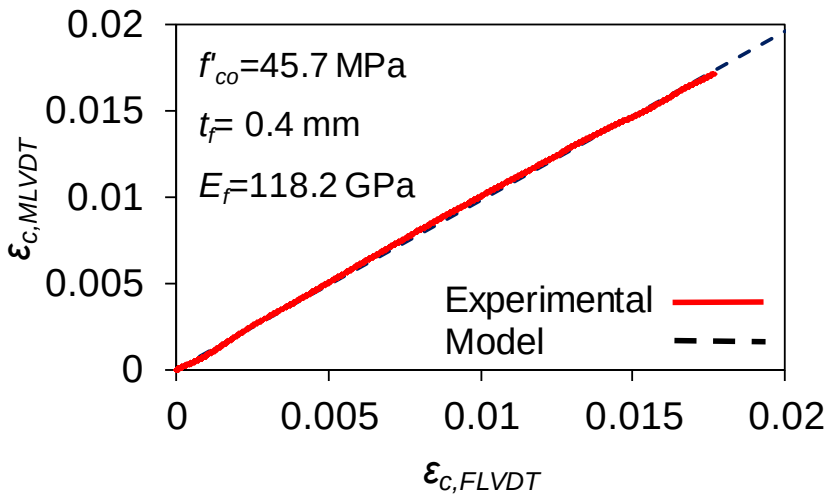

Figure 5- Relationship between FLVDT and MLVDT axial strain for specimen with f'_{co} < 50 MPa

As can be seen in Fig. 6, there three different relationships between $\varepsilon_{c,MLVDT}$ and $\varepsilon_{c,FLVDT}$ were evident in group II; namely, one-, two-, and three-segment relationships. The analysis of test results in the database revealed that specimens with 50 MPa < f'_{co} < 84 MPa and K_l/f'_{co} > 15

and 84 MPa $\leq f'_{co} <$ 100 MPa and 6 $< K_l/f'_{co} <$ 24 typically developed one- and two-segment relationship, respectively. Furthermore, those specimens with 70 MPa $< f'_{co} <$ 100 MPa and axial stress-strain curves showing a softening behavior after the initial peak exhibited three-segment relationship. The almost linear relationship (Fig. 6(a)) between $\varepsilon_{c,MLVDT}$ and $\varepsilon_{c,FLVDT}$ of specimens in group II with a one-segment curve can be expressed by Eq. 1, in which φ varied between 0.5 and 0.85.

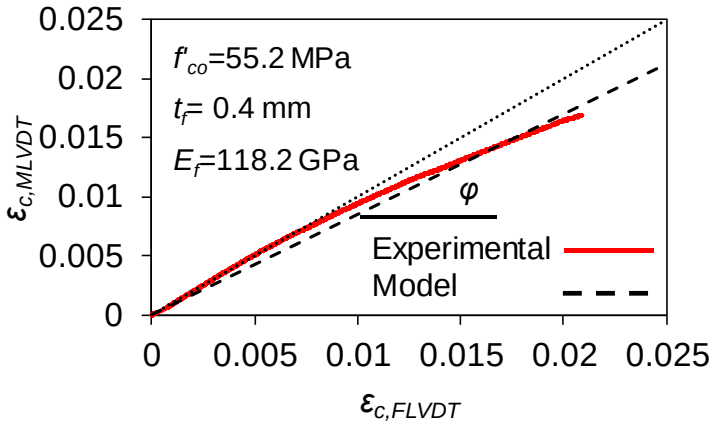

(a)

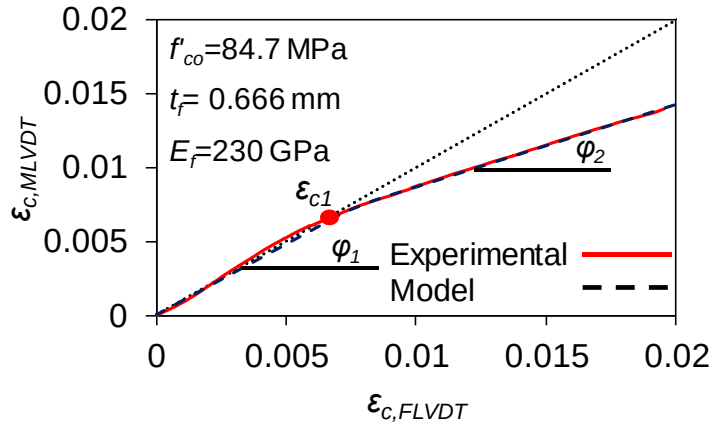

(b)

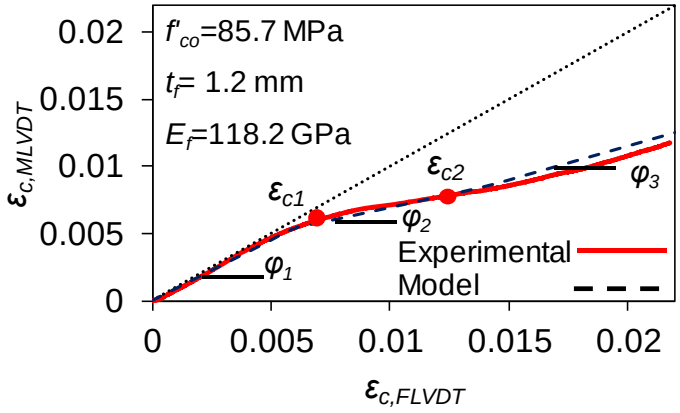

(c)

Figure 6- Relationship between FLVDT and MLVDT axial strain for specimens with 50 MPa $\leq f'_{co} <$ 100 MPa: a) one-segment, b) two-segment, c) three-segment relationship. ε_{c1} and ε_{c2} are first and second LVDT curve transition strains, respectively (Dotted line is the 45-degree line)

The nonlinear two-segment relationship between $\varepsilon_{c,MLVDT}$ and $\varepsilon_{c,FLVDT}$ (Fig. 6(b)) can be expressed by the following bilinear function:

$$\begin{cases} \varepsilon_{c,MLVDT} = \varepsilon_{c1} + \varphi_1\, \varepsilon_{c,FLVDT} & if \quad \varepsilon_{c,FLVDT} < \varepsilon_{c1} \\ \varepsilon_{c,MLVDT} = \varphi_2\, \varepsilon_{c,FLVDT} & if \quad \varepsilon_{c,FLVDT} \geq \varepsilon_{c1} \end{cases} \tag{2.2}$$

where φ_1 and φ_2 are the slopes of the lines describing the relationship between $\varepsilon_{c,MLVDT}$ and $\varepsilon_{c,FLVDT}$ at segments 1 and 2, respectively. As can be seen in Fig. 6(b), in group II specimens with a two-segment relationship, the axial strains measured by MLVDT were nearly identical ($0.9 \leq \varphi_1 \leq 1$) to those by FLVDT along the segment before the transition strain of the LVDT curve (ε_{c1}). After ε_{c1} (i.e. in segment 2), axial strains obtained from MLVDTs were lower ($0.5 \leq \varphi_2 \leq 0.8$) than those from FLVDTs.

Figure 6(c) shows the three-segment relationship between $\varepsilon_{c,MLVDT}$ and $\varepsilon_{c,FLVDT}$, which can be expressed by the following trilinear function:

$$\begin{cases} \varepsilon_{c,MLVDT} = \varphi_1\, \varepsilon_{c,FLVDT} & \text{if} \quad \varepsilon_{c,FLVDT} < \varepsilon_{c1} \\ \varepsilon_{c,MLVDT} = \varepsilon_{c1} + \varphi_2 \varepsilon_{c,FLVDT} & \text{if} \quad \varepsilon_{c,FLVDT} \geq \varepsilon_{c1} \text{ and } \varepsilon_{c,FLVDT} < \varepsilon_{c2} \\ \varepsilon_{c,MLVDT} = \varepsilon_{c2} + \varphi_3 \varepsilon_{c,FLVDT} & \text{if} \quad \varepsilon_{c,FLVDT} \geq \varepsilon_{c2} \end{cases} \tag{2.3}$$

where φ_1, φ_2, and φ_3 are the slopes of the lines describing the relationship between $\varepsilon_{c,MLVDT}$ and $\varepsilon_{c,FLVDT}$ at segments 1 to 3, respectively. As can be seen in Fig. 6(c), in group II specimens with a three-segment relationship, similar to the specimens with a two-segment relationship, the axial strains measured by MLVDT were nearly identical ($0.9 \leq \varphi_1 \leq 1$) to those by FLVDT before the first transition strain of the LVDT curve (ε_{c1}) (i.e. segment 1). In segment 2, the slope line of the relationship between $\varepsilon_{c,MLVDT}$ and $\varepsilon_{c,FLVDT}$ reduced significantly ($0.2 \leq \varphi_2 \leq 0.4$), which subsequently increased after the second transition strain of the LVDT curve (ε_{c2}) in segment 3 to a value that was still lower than that in segment 1 ($0.5 \leq \varphi_3 \leq 0.8$).

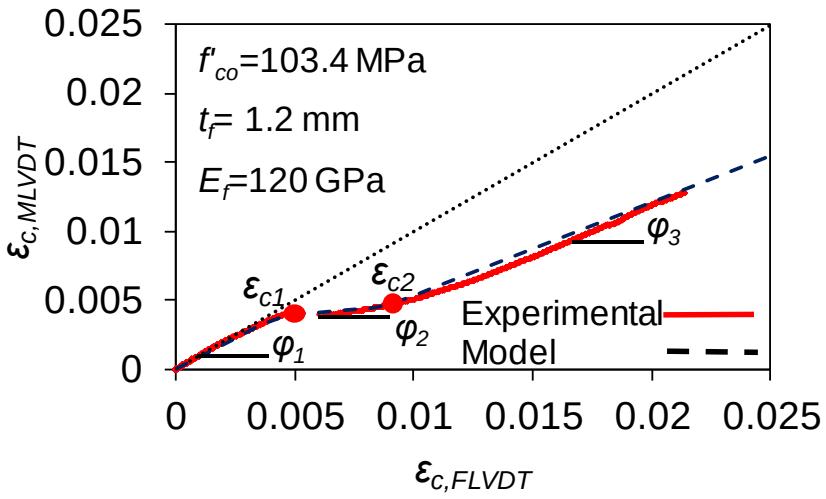

Figure 7- Variation of axial strains measured by MLVDT and FLVDT for specimens with $f'_{co} \geq 100$ MPa. (Dotted line is the 45-degree line)

Figure 7 shows the relationship between the axial strains measured by FLVDT and MLVDT for specimens in group III (i.e. $f'_{co} \geq 100$ MPa). As can be seen in the figure, the specimens in group III exhibited a very similar relationship between $\varepsilon_{c,MLVDT}$ and $\varepsilon_{c,FLVDT}$ compared to the group II with a three-segment relationship. Therefore, the nonlinear relationship between $\varepsilon_{c,MLVDT}$ and $\varepsilon_{c,FLVDT}$ for group III specimens can be expressed by the trilinear function given in Eq. 3. As can be seen in Fig. 7, similar to the group II with a three-segment relationship, the axial strains measured by MLVDT were nearly identical ($0.9 \leq \varphi_1 \leq 1$) to those by FLVDT before ε_{c1}. However, after ε_{c1}, group III specimens developed lower slope lines ($0.1 \leq \varphi_2 < 0.3$ and $0.3 \leq \varphi_3 \leq 0.6$) compared to the group II with a three-segment relationship.

Figure 8 shows the comparison of the axial stress-strain curve and corresponding relationship between $\varepsilon_{c,MLVDT}$ and $\varepsilon_{c,FLVDT}$ in group II with a two- and three-segment relationship and group III specimens. As can be seen in the figure, in group II specimens with a two-segment relationship and 50 MPa $< f'_{co} \leq 70$ MPa, the transition strain of the axial stress-strain curve (ε_{ct1}) does not coincide with the transition strain of the LVDT curve (ε_{c1}) and ε_{ct1} is approximately half of ε_{c1}. On the other hand, the first and second transition strain of the axial

stress-strain curve (ε_{ct1} and ε_{ct2}, respectively) in i) group II specimens with a two-segment relationship and 70 MPa < f'_{co} < 100 MPa, ii) group II specimens with a three-segment relationship, and iii) group III specimens correspond (with < 20% difference) to the first and second transition strain of the corresponding LVDT curve (ε_{c1} and ε_{c2}, respectively) of these specimens.

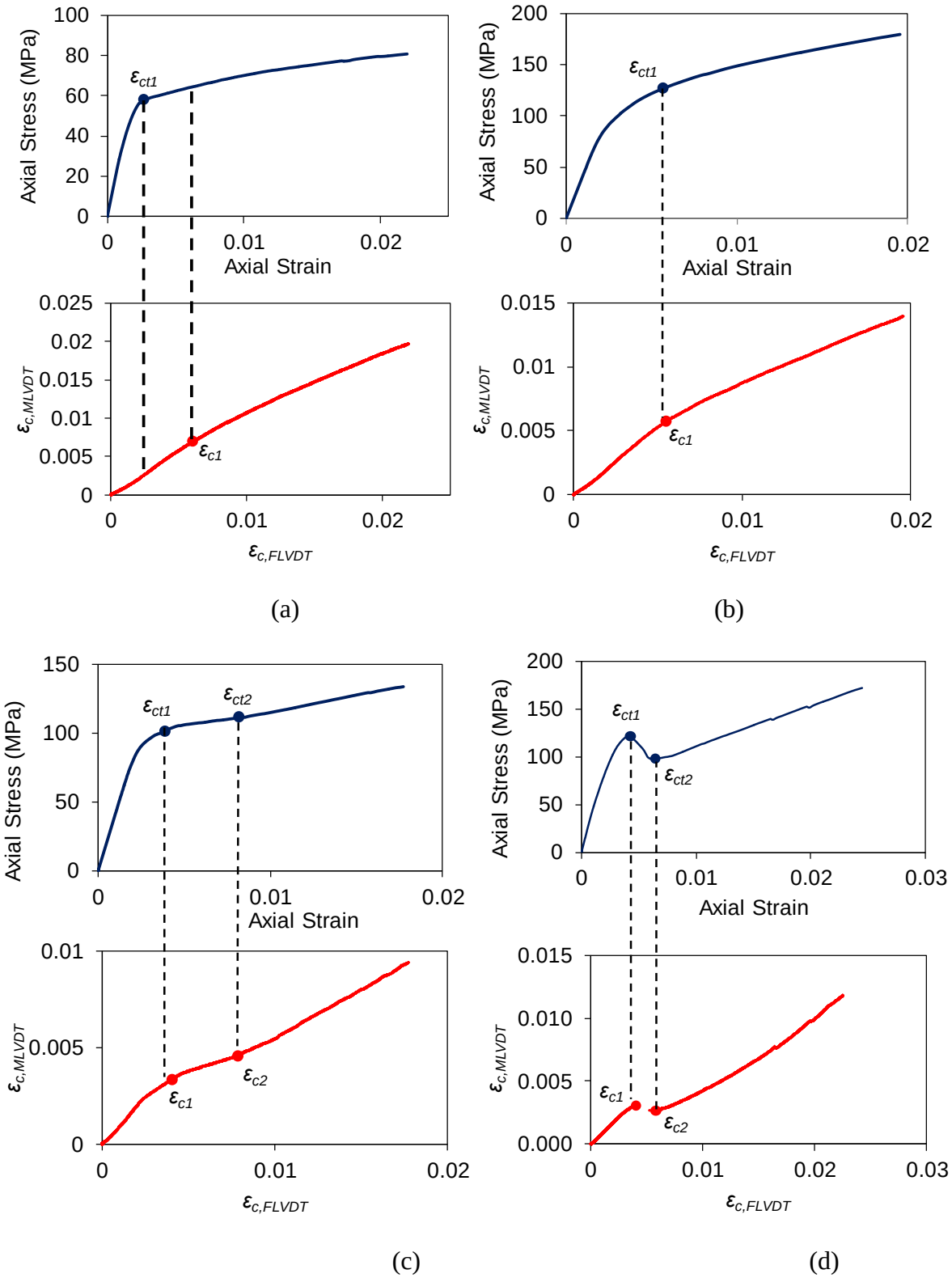

Figure 8-Comparison of the axial stress-strain curve and corresponding relationship between $\varepsilon_{c,MLVDT}$ and $\varepsilon_{c,FLVDT}$: (a) group II with a two-segment relationship with 50 MPa < f'_{co} ≤ 70 MPa, (b) group II with a two-segment relationship with 70 MPa < f'_{co} < 100 MPa, (c) group II with a three-segment relationship, (d) group III specimens

In order to investigate the influence of the confinement method on the MLVDT and FLVDT measurements, the relationship between $\varepsilon_{c,MLVDT}$ and $\varepsilon_{c,FLVDT}$ of the specimens with $f'_{co} > 100$ MPa confined by FRP wrapping and tube encasement techniques is shown in Fig. 9. As can be seen in the figure, the specimens behaved similarly under both confinement methods in term of trend in $\varepsilon_{c,MLVDT}$–$\varepsilon_{c,FLVDT}$ relationship. The analysis of test results revealed that the average third segment slope of the tube-encased and wrapped specimens was very close to each other with $\varphi_3 \approx 0.46$.

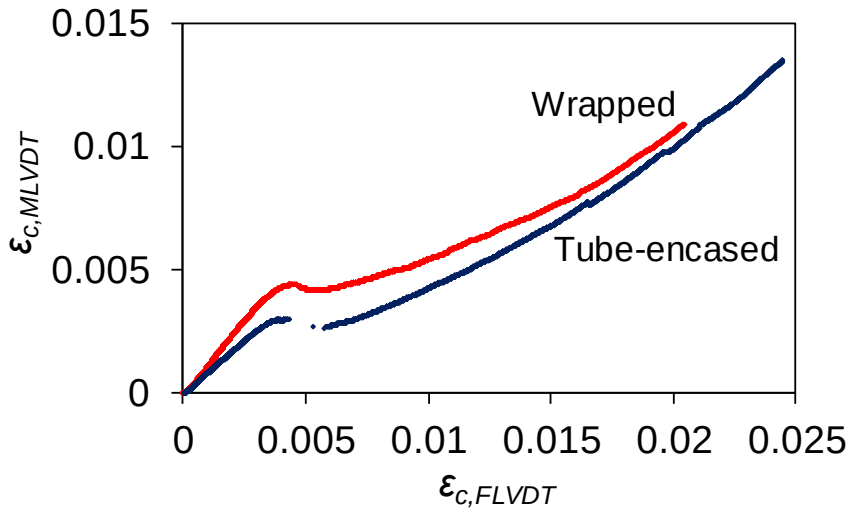

Figure 9- Variation of axial strains measured by MLVDT and FLVDT for specimens with $f'_{co} > 100$ MPa under FRP wrapping and tube-encased confinement

2.3.3 Ultimate axial strains obtained by MLVDT and FLVDT

This section presents a detailed discussion of the effect of f'_{co} and K_l on the relationship between the ultimate axial strains obtained by FLVDT and MLVDT methods. It is important to note that the expressions given in this section are not intended as model expressions that can be applied under any condition. Instead, they should be treated as best fit line expressions for the identified key parameters, which are meaningful only within the parametric space of the geometric and material properties considered in this study.

2.3.3.1 Effect of unconfined concrete compressive strength (f'_{co})

Figure 10 shows the variation of the ultimate axial strain ratio ($\varepsilon_{cu,MH}/\varepsilon_{cu,FH}$, where $\varepsilon_{cu,MH}$ and $\varepsilon_{cu,FH}$ are the ultimate axial strain measured by MLVDT and FLVDT method, respectively) with f'_{co}. As can be seen in the figure, an increase in f'_{co} resulted in a decrease in $\varepsilon_{cu,MH}/\varepsilon_{cu,FH}$. Figure 11 shows the variation of $\varepsilon_{cu,MH}/\varepsilon_{cu,FH}$ with f'_{co} for specimens confined with different types of FRP. As can be seen in the figure, an increase in f'_{co} led to a decrease in $\varepsilon_{cu,MH}/\varepsilon_{cu,FH}$ in all groups; however, the decrease was higher for GFRP-confined specimens compared to that seen in CFRP- and AFRP-confined specimens. It can also be seen in Figs. 10 and 11 that $\varepsilon_{cu,MH}/\varepsilon_{cu,FH}$ ratio of specimens with $f'_{co} \leq 30$ MPa is approximately 1, indicating that in NSC specimens with $f'_{co} \leq 30$ MPa similar axial strains are obtained from FLVDT and MLVDT. The ratio is reduced to approximately 0.4 for f'_{co} of 120 MPa. This change is attributed to the different failure conditions of NSC and HSC specimens as was discussed in Section 3.1.1. Figure 12 shows and Eq. 1.4 describes the proposed relationship between $\varepsilon_{cu,MH}/\varepsilon_{cu,FH}$ and f'_{co}, where $\varepsilon_{cu,MH}/\varepsilon_{cu,FH}$ is kept constant with a value equal to 1 for $f'_{co} \leq 30$ MPa.

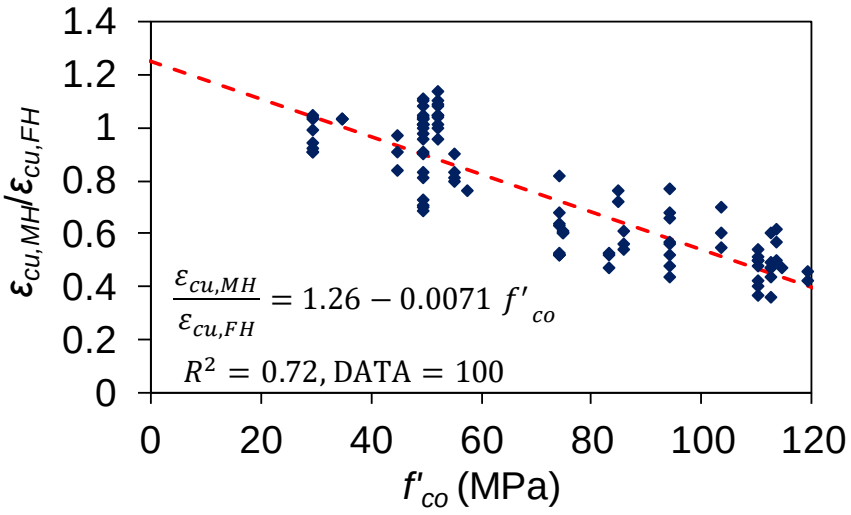

Figure 10- Variation of the ultimate axial strain ratio ($\varepsilon_{cu,MH}/\varepsilon_{cu,FH}$) with f'_{co}

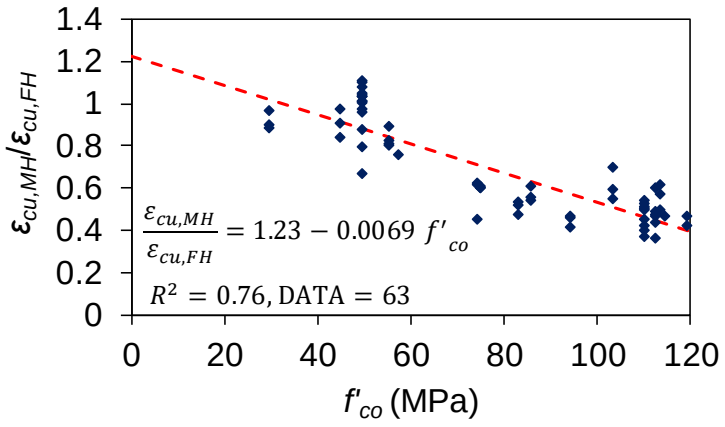

(a)

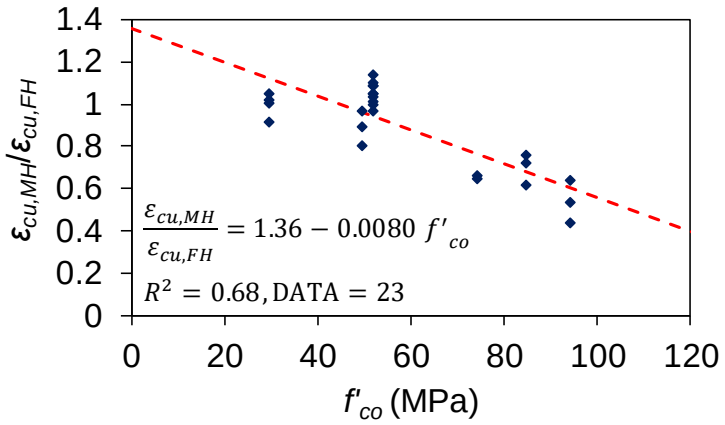

(b)

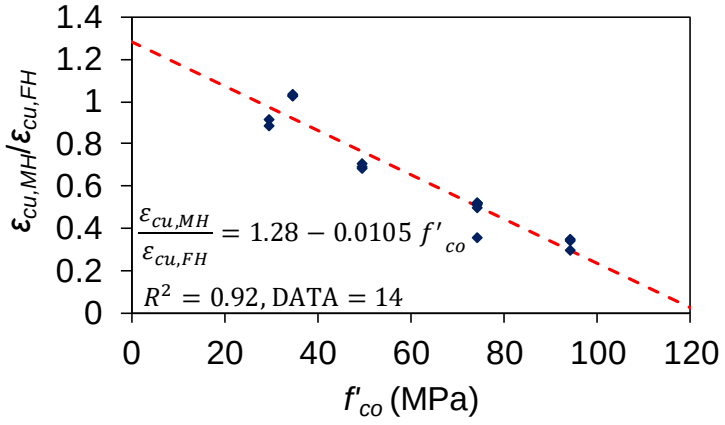

(c)

Figure 11- Variation of the ultimate axial strain ratio ($\varepsilon_{cu,MH}/\varepsilon_{cu,FH}$) with f'_{co} for different FRP types: (a) AFRP, (b) CFRP, (c) GFRP

$$\left(\frac{\varepsilon_{cu,MH}}{\varepsilon_{cu,FH}}\right)_{Pro} = \begin{cases} 1 & if\ f'_{co} \leq 30 \\ 1 - a\ (f'_{co} - 30) & if\ f'_{co} > 30 \end{cases} \quad (2.4)$$

where $(\varepsilon_{cu,MH}/\varepsilon_{cu,FH})_{Pro}$ is the proposed ultimate axial strain ratio and a is the slope line for the second part of the relationship between $(\varepsilon_{cu,MH}/\varepsilon_{cu,FH})_{Pro}$ and f'_{co}.

2.3.3.2 Effect of lateral stiffness of FRP jacket (K_l)

In order to evaluate the effect of FRP confinement on the relationship between the ultimate axial strains measured by FLVDT and MLVDT methods, the relationship between the normalized ultimate axial strain ratio $((\varepsilon_{cu,MH}/\varepsilon_{cu,FH})_{Exp}/(\varepsilon_{cu,MH}/\varepsilon_{cu,FH})_{Pro}$, where $(\varepsilon_{cu,MH}/\varepsilon_{cu,FH})_{Exp}$ is experimental ultimate axial strain ratio) and K_l/f'_{co} was studied. Figure 13 shows the variation of the normalized ultimate axial strain ratio with K_l/f'_{co}. As can be seen in the figure, an increase in the K_l/f'_{co} led to an increase in the normalized ultimate axial strain ratio, indicating that the lateral stiffness is an influential parameter on the relationship between the axial strains measured by FLVDT and MLVDT methods. Eq. 2.5 presents the expression obtained from the database to describe this relationship.

$$\frac{\left(\frac{\varepsilon_{cu,MH}}{\varepsilon_{cu,FH}}\right)_{Exp}}{\left(\frac{\varepsilon_{cu,MH}}{\varepsilon_{cu,FH}}\right)_{Pro}} = 0.019\ \frac{K_l}{f'_{co}} + 0.74 \quad (2.5)$$

2.3.3.3 Prediction of the ultimate axial strain ratio ($\varepsilon_{cu,MH}/\varepsilon_{cu,FH}$)

To develop a unified framework for design and modeling purposes, an expression is developed to describe the relationship between the axial strains of FRP-confined HSC obtained by the two measurement methods. Eq. 2.6 is proposed to incorporate the influence of f'_{co} and K_l/f'_{co} on the $\varepsilon_{cu,MH}/\varepsilon_{cu,FH}$ of FRP-confined HSC specimens.

$$\left(\frac{\varepsilon_{cu,MH}}{\varepsilon_{cu,FH}}\right)_{Mod} = A \times B \quad (2.6)$$

where *A* and *B* are the functions defined by Eqs. 4 and 5, respectively. The average absolute error (AAE), mean (M), standard deviation (SD), and root-mean-square deviation (RMSE) were used to assess the agreement between the predictions of Eq. 6 and experimental results. Figure 14 shows the comparison of the predictions of ultimate axial strain ratio by Eq. 6 ($(\varepsilon_{cu,MH}/\varepsilon_{cu,FH})_{Mod}$) with respect to the experimental values ($(\varepsilon_{cu,MH}/\varepsilon_{cu,FH})_{Exp}$). As can be seen in the figure, the predictions are in good agreement with the experimental results.

It should be noted that the specific expression presented in Eq. 6 was obtained based on specimens with a dimension of 150 × 300 mm and are instrumented along their mid-height within a region that covered approximately 60% of their total heights. The relationship between the axial strains measured by FLVDT and MLVDT methods might be affected by the size and aspect ratio of the specimens and the relative height of the MLVDT region with respect to the total specimen height.

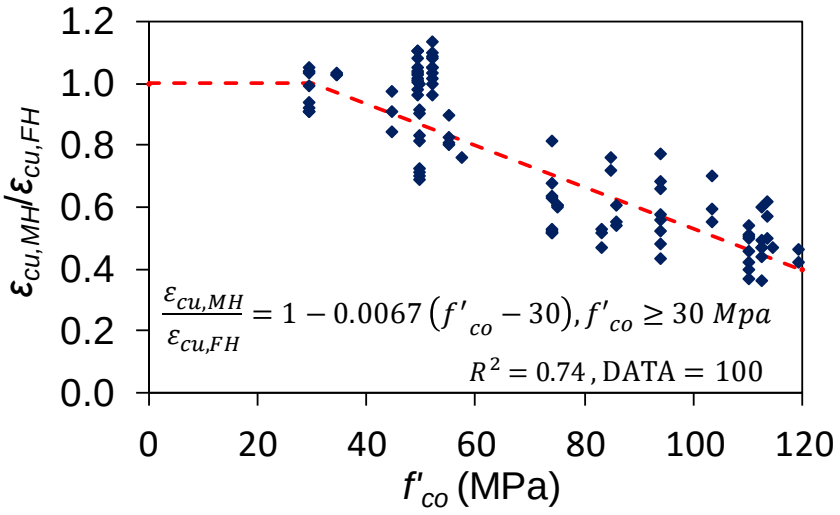

Figure 12- The proposed relationship between the ultimate axial strain ratio ($\varepsilon_{cu,MH}/\varepsilon_{cu,FH}$) and f'_{co}

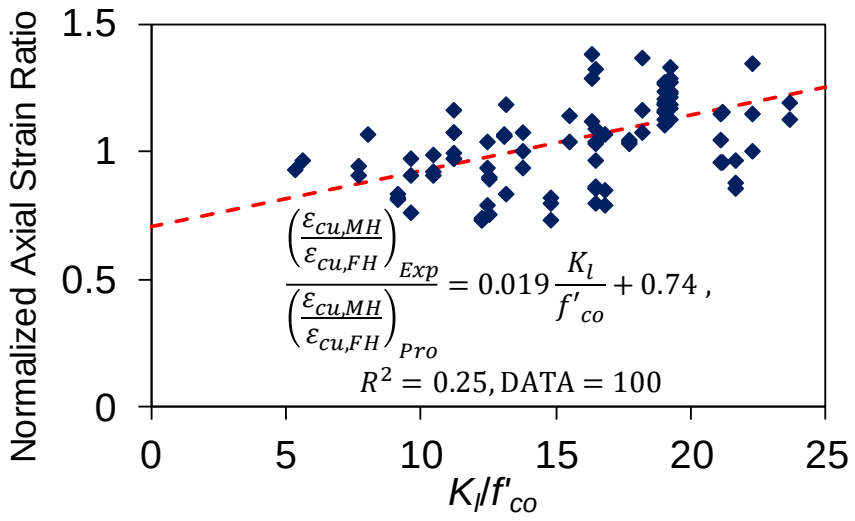

Figure 13- Variation of normalized ultimate axial strain ratio with normalized lateral confinement stiffness (K_l/f'_{co})

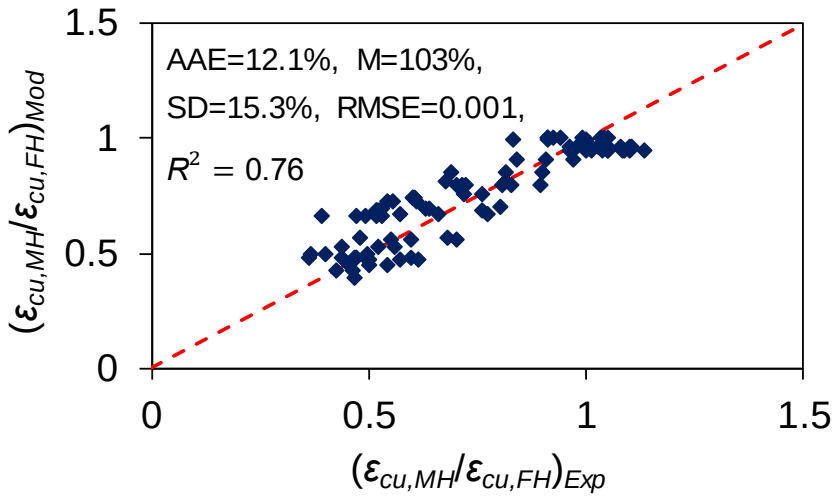

Figure 14- Comparison of the model predictions with experimental results

2.4 Conclusion

As it was discussed in this section, the measurement method is influential in analysing the experimental data and their use in developing/validating a model. This indicates the need of a comprehensive measurement methods and a new approach to analyse the experimental datasets. Based on the analysis results, the following conclusions can be drawn:

1) Failure mode of FRP-confined NSC and HSC specimens are different to each other. FRP-confined NSC specimens (f'_{co} < 50 MPa) exhibits gradual concrete crushing through the formation of large number of microcracks, whereas in HSC specimens with strengths over 100 MPa crushing of concrete is localized around a few major macrocracks.
2) Axial strains obtained from FLVDT and MLVDT methods remain close to each other in the case of FRP-confined NSC, whereas significant differences exist in axial strains of HSC specimens obtained from the two measurement methods, and this difference increases with an increase in f'_{co} (e.g. for f'_{co} = 120 MPa the ultimate strain obtained from MLVDT is only around 40% of that by FLVDT). This indicates that the axial strains of HSC are highly sensitive to the instrumentation arrangement used in their measurement.
3) The transition strains of the axial stress-strain curve do not coincide with the transition strains of the LVDT curve for specimens with 50 MPa < $f'_{co} \leq$ 70 MPa and a two-segment relationship. On the other hand, axial stress-strain curve transition strains nearly correspond to the LVDT curve transition strains for specimens with f'_{co} > 70 MPa and a two- or three-segment relationship.
4) An increase in f'_{co} results in a decrease in the ratio between the ultimate axial strains measured by MLVDT and FLVDT methods. This is caused by the change in the failure mode of concrete with an increase in $f'_{co.}$ On the other hand, an increase in K_l/f'_{co} leads to an increase in the ratio between the ultimate axial strains measured by MLVDT and FLVDT methods.
5) The results of the assessment study show that the proposed expression provide close predictions of the ultimate axial strain ratio ($\varepsilon_{cu,MH}/\varepsilon_{cu,FH}$) of FRP-confined HSC, making it suitable for use in establishing relationships between the strains obtained

from the FLVDT and MLVDT measurement methods for specimens sharing similar geometric properties to the specimens considered in this study.

The findings of this study on the dependence of axial strains of FRP-confined HSC on the measurement method is significant and should inform future analysis and modeling efforts as well as additional targeted experimental studies into this area.

Chapter 3: Simplified design-oriented axial stress-strain model for FRP-confined normal- and high-strength concrete

(A paper is published based on this section: Fallah Pour A, Ozbakkaloglu T, Vincent T. Simplified design-oriented axial stress-strain model for frp-confined normal- and high-strength concrete. Eng Struct. 2018;175:501-16. (DOI: 10.1016/j.engstruct.2018.07.099))

3.1 Introduction

For the design of fiber reinforced polymer (FRP)-confined concrete members, a model to accurately predict the axial stress-strain behavior of FRP-confined concrete is essential. Previously developed models included design-oriented models given in closed-forms and analysis-oriented models that predict stress-strain behavior through an incremental process [16]. Design-oriented models are based on the direct interpretation and regression analysis of experimental results, with examples of this type of model [2, 17-22] presented and assessed in Section 5 of this study. Analysis-oriented models consider the interaction between the concrete and the FRP jacket, in an explicit manner. These models [23-26] can be extended to predict the behavior of concrete confined with other materials.

Although they are shown to be versatile and capable of predicting the entire stress-strain curves, the analysis-oriented models use a time-intensive iterative approach and their accuracy depend greatly on their prediction of the lateral strain-to-axial strain relationship. In the majority of these models this relationship is based on the modification of an implicit expression originally proposed for actively confined concrete, which is unable to accurately capture the dilation behavior of FRP-confined concrete [86, 113]. Furthermore, as was shown recently [23, 114], the use of the path independency assumption for the application of the confining pressure can result in modeling inaccuracies. A notable example of these inaccuracies is the predictions of the stress-strain curves of FRP-confined high-strength concrete (HSC) based on the approach

adopted by conventional analysis-oriented models. To overcome this shortcoming a new approach was proposed in Lim and Ozbakkaloglu [23] that resulted in accurate models for FRP-confined normal and high-strength concrete. However, because of the iterative nature of the model, its application requires a significant computational effort.

Conversely, design-oriented models use explicit and often simple expression forms that make them attractive for use in design applications. Recognizing these advantages, in this study a design-oriented model was adopted for further development to provide a complete axial stress-strain curve of FRP-confined concrete in circular sections. In such models the prediction of key stress and strain values is essential because these points define the stress-strain curve. One of these key points is the transition point, where there is a change in trend of the stress-strain curve after the termination of the initial ascending branch. The other key point on the stress-strain curve is the point corresponding to the ultimate condition, which represent the axial stress and strain of confined concrete at the time of failure.

As discussed in Ozbakkaloglu, Lim [16], many models for prediction of the ultimate condition (f'_{cc}, ε_{cu}) have been proposed in the last three decades. However, only a few models have been developed to predict the transition point (f'_{c1}, ε_{c1}) of the stress-strain curve [93, 115-117], as discussed in detail in Sections 4.2 and 5.2, whose accurate determination is important to obtain an accurate curve. The expressions proposed for the transition point were developed based on limited experimental data, and hence in the presence of a larger database it should be possible to improve their accuracy.

The use of high-strength concrete (HSC) in column construction has received a great deal of attention because of the benefits offered by higher strength concretes over normal-strength concrete (NSC) in these applications [17]. Until 2014, the availability of models applicable to FRP-confined HSC was extremely limited [2, 5, 8, 118, 119] both in number and in accuracy.

Since then, new and accurate design-oriented models have been proposed for FRP-confined HSC [17, 85]. Although these models are capable of accurately predicting the ultimate condition of FRP-confined HSC they do not provide to predict the complete axial stress-strain curve. Therefore, there is need for a design-oriented model that can accurately predict the complete axial stress-strain curve of FRP-confined HSC.

It is now well-known that the hoop strain measured on the FRP jacket at the time of FRP rupture ($\varepsilon_{h,rup}$) is often lower than the ultimate tensile strain of the fibers (ε_{fu}) or FRP material (ε_{FRP}) used in the jacket as discussed in detail in many previous studies (e.g. [21, 29, 38, 93, 111, 120-122]). As discussed in Ozbakkaloglu and Lim [14], models that make use of the hoop rupture strain ($\varepsilon_{h,rup}$) predict the ultimate axial strain (ε_{cu}) and stress (f'_{cc}) of FRP-confined concrete significantly more accurately than those that make use of the ultimate tensile strain of fibers (ε_{fu}). Although using the hoop rupture strain ($\varepsilon_{h,rup}$) provides increased accuracy for models, it comes at the cost of increased complexity, because these data are often not readily available to design engineers. As a result, the development of a stress-strain model that does not require hoop rupture strain ($\varepsilon_{h,rup}$) as input data, and that performs with comparable accuracy to most accurate existing models based on $\varepsilon_{h,rup}$, will be of vital importance for practical design applications.

This paper presents a model to accurately predict the complete axial stress-strain curve of FRP-confined concrete using simple expressions. To achieve this goal, the format of the expressions to predict the ultimate point and transition point was borrowed from existing research but new coefficients were created. These coefficients (k_1, k_2, k_3 and k_4) were developed by closely investigating the influential parameters and monitoring the accuracy of the proposed expressions to maintain comparable accuracy with expressions of the best performing existing models, without the need for parameters that are not always readily available (e.g. $\varepsilon_{h,rup}$).

For the prediction of the ultimate point (f'_{cc}, ε_{cu}), this study proposes two new expressions for coefficients which were a result of investigating influential parameters as mentioned above. A similar procedure was performed for stress at transition point (f'_{c1}) where an existing expression format for predicting this stress for HSC [3] was modified for the expression to be applicable to both NSC and HSC. This new model has a simpler expression format and produces better accuracy than existing models. Furthermore, an existing expression that was proposed to predict the lateral strain (ε_{l1}) at transition point [3] was modified based on dilation data to predict the axial strain at transition point (ε_{c1}). This expression for ε_{c1} has a simpler equation format and provides higher accuracy than existing models. Finally, through the use of these newly developed expressions a new model is proposed to predict the full axial stress-strain curve for FRP-confined NSC and HSC. The model is applicable to a wide range of concrete compressive strengths (f'_{co}) ranging from 10 to 120 MPa and it uses readily available input data. In the development of the model expressions, the comprehensive experimental database presented in Ozbakkaloglu and Lim [14] and Lim and Ozbakkaloglu [17] were used to obtain the expressions for the ultimate point (f'_{cc}, ε_{cu}). In addition, a new database with 266 datasets was compiled for the prediction of the axial stress and strain at the transition point (f'_{c1}, ε_{c1}).

3.2 Mechanism of confinement

In FRP-confined concrete circular columns under concentric compression, FRP shell provides a uniform lateral confining pressure around the column circumference (Figure. 15). This confining pressure at column failure (referred to as the ultimate) (f_{lu}) can be theoretically calculated using Eq. (3.1).

$$f_{lu} = \frac{2E_f t_f \varepsilon_{fu}}{D} \tag{3.1}$$

where E_f, t_f, and ε_{fu} are the elastic modulus, total nominal thickness, and ultimate tensile strain of fibers and D is the diameter of the column.

Figure 16 shows the typical axial stress-axial strain curves for unconfined and confined concrete. As can be seen in the figure, the axial stress-strain curves of confined concrete consist of an ascending portion that is followed by a second branch. Depending on the confinement parameters, the stress-strain curve may demonstrate a full ascending second branch or it may consist of a second branch with a descending trend. This study is concerned with FRP-confined concrete exhibiting an ascending second branch. In describing such a curve, four parameters have a significant meaning. These parameters are the compressive strength (f'_{cc}), ultimate axial strain (ε_{cu}), axial stress at the transition point (f'_{c1}), and axial strain at the transition point (ε_{c1}). A simple and accurate stress-strain model that is developed using these parameters is presented in the following sections.

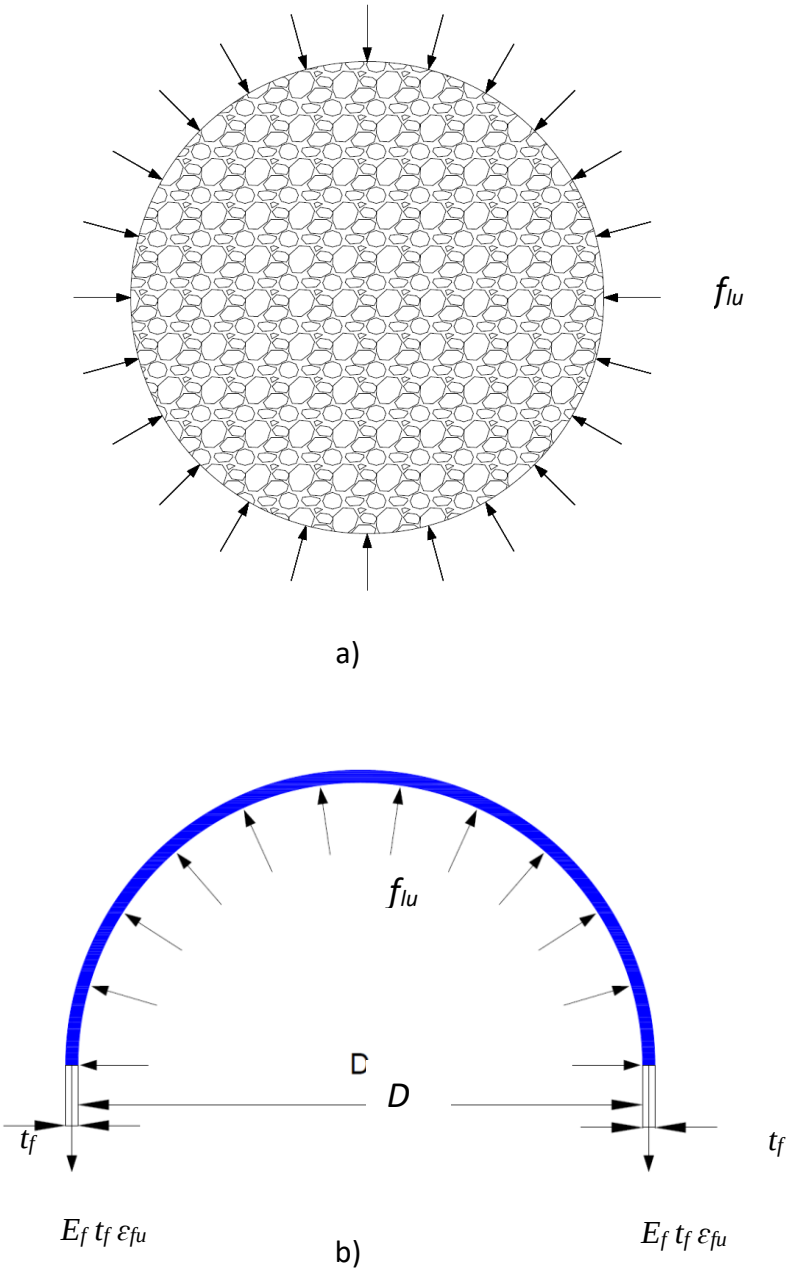

Figure 15- Confining action of FRP jacket to concrete: a) concrete, b) FRP jacket. E_f, t_f, ε_{fu} and f_{lu} are the elastic modulus, total nominal thickness, ultimate tensile strain of fibers and ultimate lateral confining pressure, respectively.

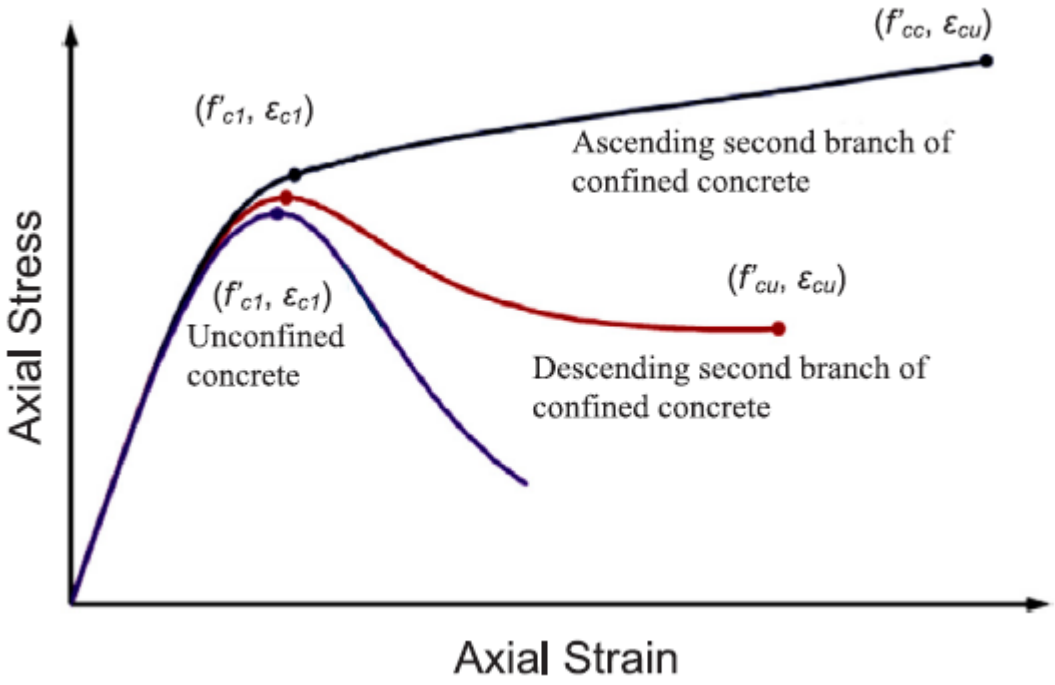

Figure 16- Typical axial stress-axial strain curves for confined and unconfined concrete

3.3 Experimental test database

Table 1 shows the details of the database that was used for the prediction of the axial strain and stress at the ultimate point. The actual database can be found in Ozbakkaloglu and Lim [14] and Lim and Ozbakkaloglu [17]. Table 1 in Appendix B shows the new database prepared for the prediction of the transition point (f'_{c1} and ε_{c1}) based on previous studies [5, 15, 92, 93, 103-105, 107-109, 115, 118, 123, 124]. In this table the diameter of specimens (D), height of specimens (H), elastic modulus of fibers used in FRP jackets (E_f), tensile strength of FRP (f_f), total fiber thickness of FRP jackets (t_f), and unconfined concrete strength (f'_{co}) are presented.

As discussed previously [17, 125], in order to develop an accurate design-oriented model, a reliable and consistent test database is required. To this end, using a similar process adopted in Lim and Ozbakkaloglu [17] and Lim and Ozbakkaloglu [85] a carefully determined selection criteria was applied in the dataset selection. The results included in the database were obtained from specimens that were confined with FRP continuously and had a height-to-diameter ratio less than three. By applying the selection criteria, 836, 571, and 266 datasets were included in

the development of the models to predict the compressive strength, ultimate axial strain, and axial stress and strain at the transition point, respectively.

Table 1- Summary of test results in the database

Number of datasets	Unconfined concrete strength range, f'_{co} (MPa)	Strength enhancement ratio (f'_{cc}/f'_{co}) range	Strain enhancement ratio range, $\varepsilon_{cu}/\varepsilon_{co}$	Confinement ratio range, f_{lu}/f_{co}
1063	6.2-125	0.75-3.4	1.01-15.77	0.037-2.05

3.4 New design-oriented model to predict key points on the stress-strain curve

3.4.1 Prediction of the ultimate condition of FRP-confined concrete

The existing ultimate condition models that typically provide higher levels of accuracy make use of experimental input data, such as hoop rupture strains ($\varepsilon_{h,rup}$), which are typically not readily available in design applications. To address this practical challenge, the expressions developed in this study to predict the ultimate condition of FRP-confined made use of readily available material properties, such as the ultimate tensile strain (ε_{fu}) and elastic modulus of fibers (E_f). Additionally, to determine the ultimate axial strain (ε_{cu}), the axial strain corresponding to the compressive strength of unconfined concrete (ε_{co}) is typically used in most existing models. It should be noted that the assumed values of ε_{co} (usually 0.002) were often not accurate especially for higher strength concretes, which negatively affected model accuracy. This study adopted an accurate expression for ε_{co}, which was proposed by Lim and Ozbakkaloglu [23], and showed good predictive outcomes.

3.4.1.1 Compressive strength

A simple linear expression form that was originally proposed by Richart, Brandtzaeg [126] was used to determine the compressive strength (f'_{cc}) due to its simplicity and accuracy as demonstrated in previous studies:

$$f'_{cc} = f'_{co} + k_1 K_l \varepsilon_{fu} \tag{3.2}$$

where $K_l = \frac{2\,E_f t_f}{D}$ is the lateral stiffness of the FRP jacket. Although other expression forms were considered, such as those that use a logarithmic or exponential function, the improvement in accuracy was not sufficient in predicting the compressive strength (f'_{cc}) to justify the increased complexity. To determine the compressive strength (f'_{cc}), the variations of the strength enhancement coefficient (k_1) with different key confinement parameters (i.e. f'_{co}, K_l, and K_l/f'_{co}) was studied. Based on regression analysis, a new expression was proposed for the strength enhancement coefficient (k_1):

$$k_1 = 2.5 - 0.01\, f'_{co} \tag{3.3}$$

In the modeling of k_1 expression a number of different expression forms were considered. Figure 17 shows the two best performing forms, namely a linear and logarithmic function. To analyze the performance of different expression forms the average absolute error (AAE) was used to assess the overall model accuracy. As can be seen in the figure the use of a linear expression resulted in a similar AAE compared to that obtained by the use of a logarithmic expression, and hence considering its simplicity the linear from was adopted.

Exclusion of data that deviated from the main trend-lines was studied through the application of error lines (Figure. 17). As can be seen in the figure, the exclusion of data based on different error lines (EL), did not result in a major change in the form or accuracy of the expression. As a result, no data exclusion was made in the development of expression presented in Eq. (3.3) on the grounds of significant deviation from the major trend-line.

Figure 18 shows the comparisons of the experimental compressive strength results with those predicted using Eqs. (2.2) and (2.3). In the figure, 45° line corresponds to a perfect agreement between the predictions and test results. A trend that spans above the 45° reference line represents overestimation of the experimental results by model predictions, whereas a trend

that spans below the reference line indicates an underestimation of the test results. In addition to AAE, the standard deviation (SD) was used to determine the magnitude of the scatter associated with model predictions, the mean (M) was used to describe the associated average overestimation or underestimation of the model.

Figures 19a and 19b show the model predictions of the compressive strength (f_{cc}) separately for NSC and HSC respectively, where HSC has been defined as f'_{co} greater than 50 MPa. As it is evident from these figures, the model predictions are in good agreement with test results.

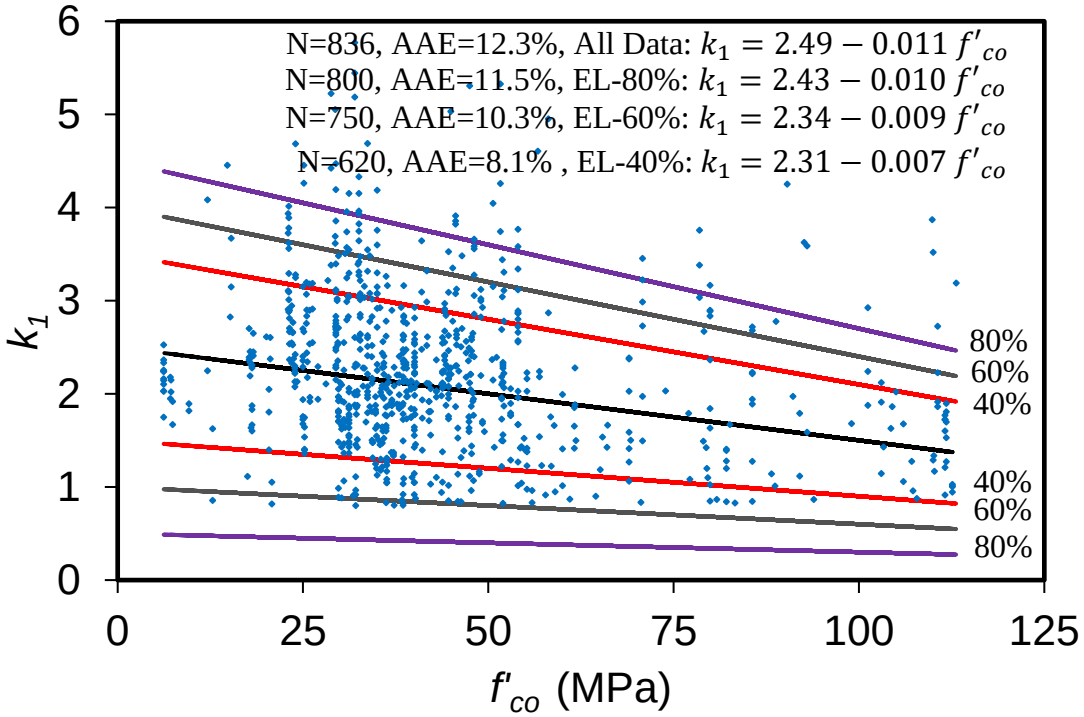

a)

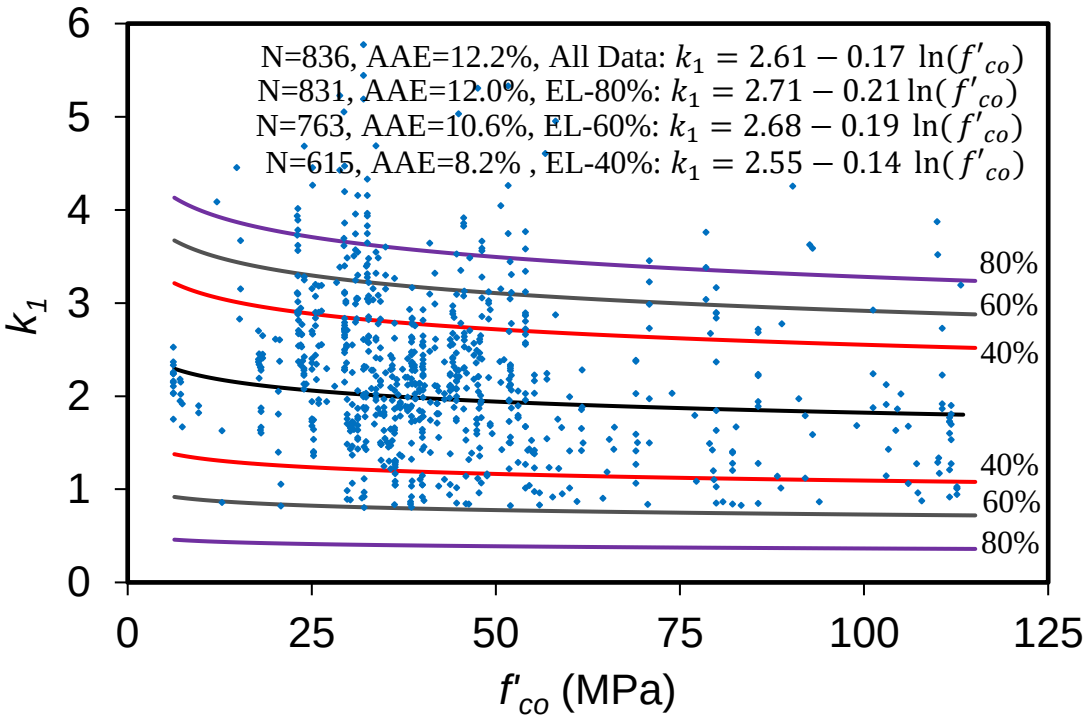

b)

Figure 17- Variation of the strength enhancement coefficient, k_1, with f'_{co}: a) linear expression; b) logarithmic expression

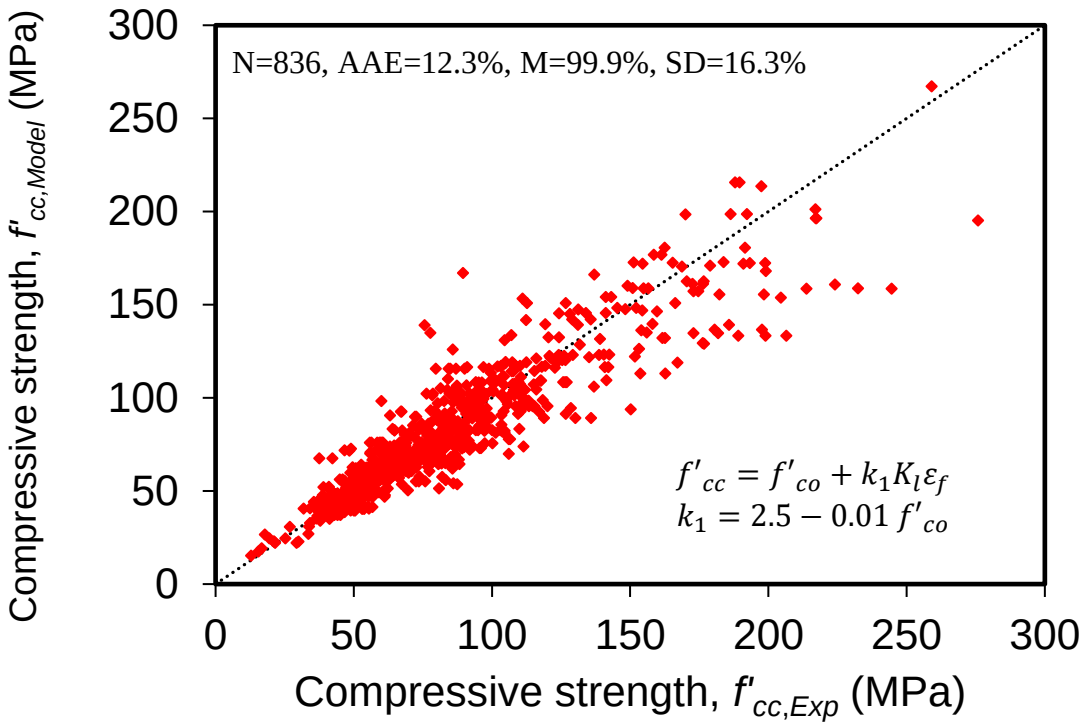

Figure 18-Comparison of model predictions of compressive strength with experimental data

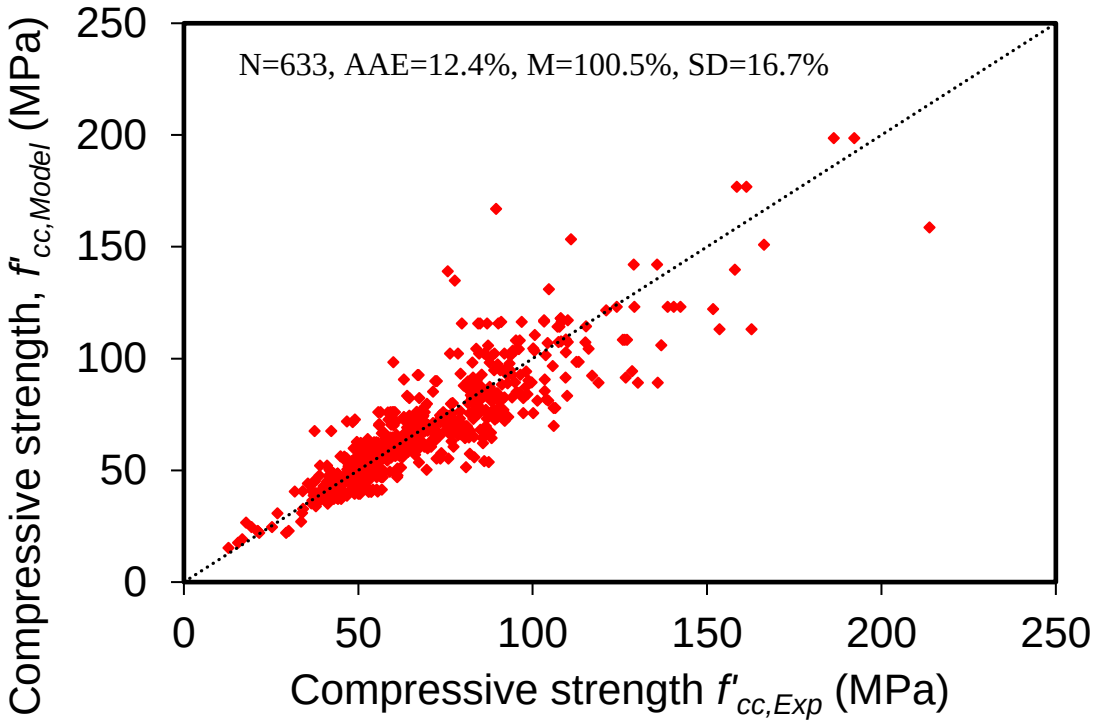

a)

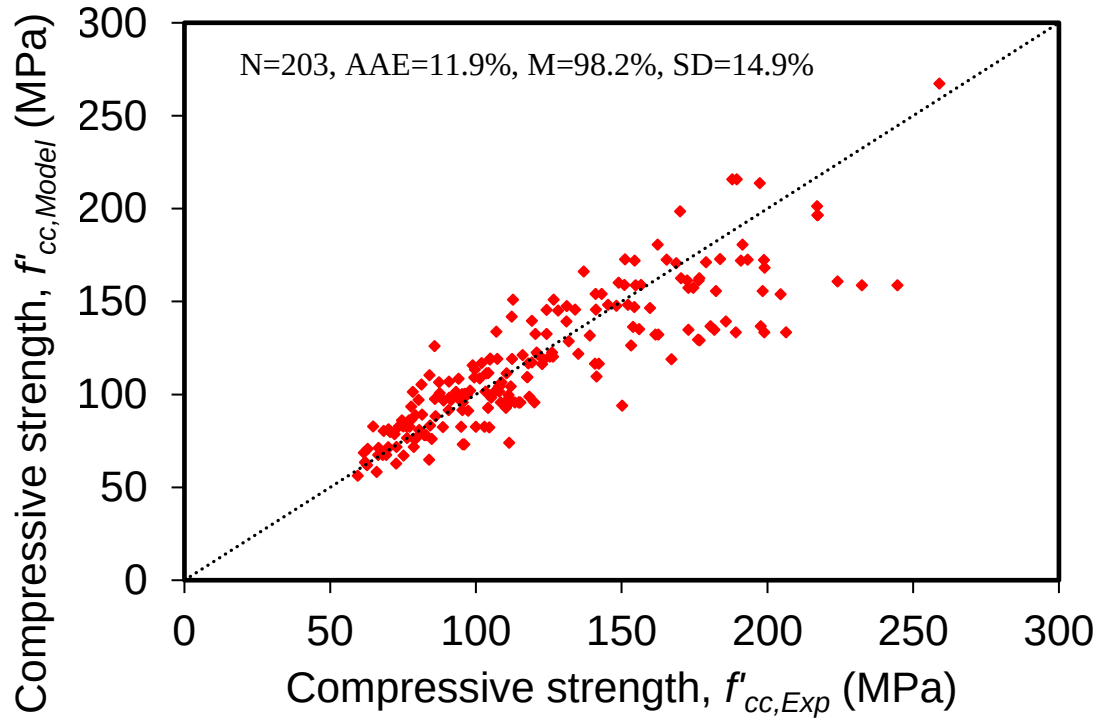

b)

Figure 19- Comparison of model predictions of compressive strength with experimental data based on f'_{co}: a) NSC, b) HSC

3.4.1.2 Ultimate axial strain

A non-linear expression, shown in Eq. (3.4), was adopted to predict the ultimate axial strain of FRP-confined concrete

$$\varepsilon_{cu} = \gamma\, \varepsilon_{co} + k_2 \left(\frac{K_l}{f'_{co}}\right)^{\alpha} \varepsilon_{fu}^{\beta} \tag{3.4}$$

where k_2 is the enhancement coefficient for the ultimate axial strain, ε_{fu} is the ultimate tensile strain of fibers, and γ, α and β are constant values that were used to calibrate the model.

A multivariable regression analysis was performed to determine the constant values in Eq. (2.4) (α, β, γ and k_2) by using 633 datasets with a range of f'_{co} between 10 to 120 MPa. Based on this analysis α, β, γ and k_2 were determined as 0.75, 1.35, 1.5 and 0.20, respectively. To provide an expression with higher accuracy, the database was divided into seven sub-classes based on f'_{co} (e.g., f'_{co} < 30 MPa, 30 MPa < f'_{co} < 45 MPa, 45 MPa < f'_{co} < 60 MPa, 60 MPa < f'_{co} < 75 MPa, 75 MPa < f'_{co} < 90 MPa, 90 MPa < f'_{co} < 105 MPa, 105 MPa < f'_{co} < 120 MPa) after recognizing the significant influence of f'_{co} on ε_{cu}. The regression analysis was performed individually for each sub-class, and the results indicated that α, β and γ varied only slightly across different sub-classes whereas, k_2 varied significantly with the variation of f'_{co}.

During the regression analysis it was found that ε_{cu} of the very lightly-confined specimens with ultimate axial strains lower than 0.006 exhibited significant scatter and they deviated by a large margin from the overall trends of the database. For example, the SD of the best fit expression changed from 45% to 29% when 62 datasets with ε_{cu} < 0.006 were excluded. The same analysis showed that the inclusion of all datasets resulted in a k_2 value of 0.2, whereas for datasets with ε_{cu} >0.006 the value of k_2 was 0.26. This noticeable variation is due to fact that the datasets with ε_{cu} < 0.006 produced a significantly lower k_2 value of 0.08 than the rest of the database. Based on these observations, specimens with ultimate axial strains (ε_{cu}) lower than 0.006 were

excluded from the analysis, which resulted in a database of 571 datasets that were used in the modeling of ε_{cu}.

The variation of k_2 with f'_{co} is shown in Fig. 20, which also shows that the trendlines were not particularly sensitive to data selection. After obtaining k_2 values for each f'_{co} sub-class an expression was proposed for k_2 as a function of f'_{co}. The proposed expression to predict the strain enhancement coefficient (k_2) is shown in Eq. (3.5).

$$k_2 = 0.3 - 0.001\, f'_{co} \tag{3.5}$$

The process summarized above resulted in the expression shown as Eq. (2.6) that was proposed to predict the ultimate axial strain. In this expression ε_{co} is determined by the expression $\varepsilon_{co} = \frac{f'^{0.225}_{c0}}{1000}\left(\frac{152}{D}\right)^{0.1}\left(\frac{2\,D}{H}\right)^{0.13}$, which was originally proposed by Lim and Ozbakkaloglu [23].

$$\varepsilon_{cu} = 1.5\,\varepsilon_{co} + k_2\left(\frac{K_l}{f'_{co}}\right)^{0.75}\varepsilon_{fu}^{1.35} \tag{3.6}$$

Figure 21 shows the comparisons of the experimental ultimate axial strain results with those predicted using Eq. (3.6). In the figure, 45° line corresponds to perfect agreement between the predictions and test results, and the comparison shows that the model predictions and experimental results are in good agreement. As can be seen in Figures 22a and 22b, showing the comparisons for NSC and HSC, respectively, the model predictions are in good agreement with the experimental test results for both concrete types.

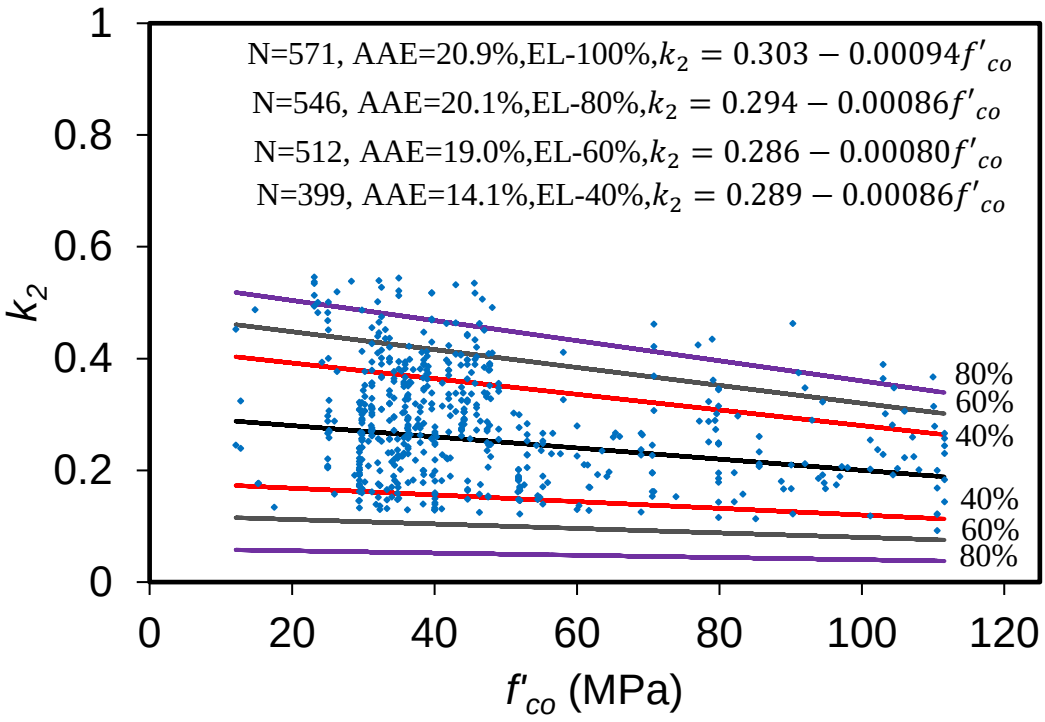

Figure 20-Variation of strain enhancement coefficient, k_2, with f'_{co}

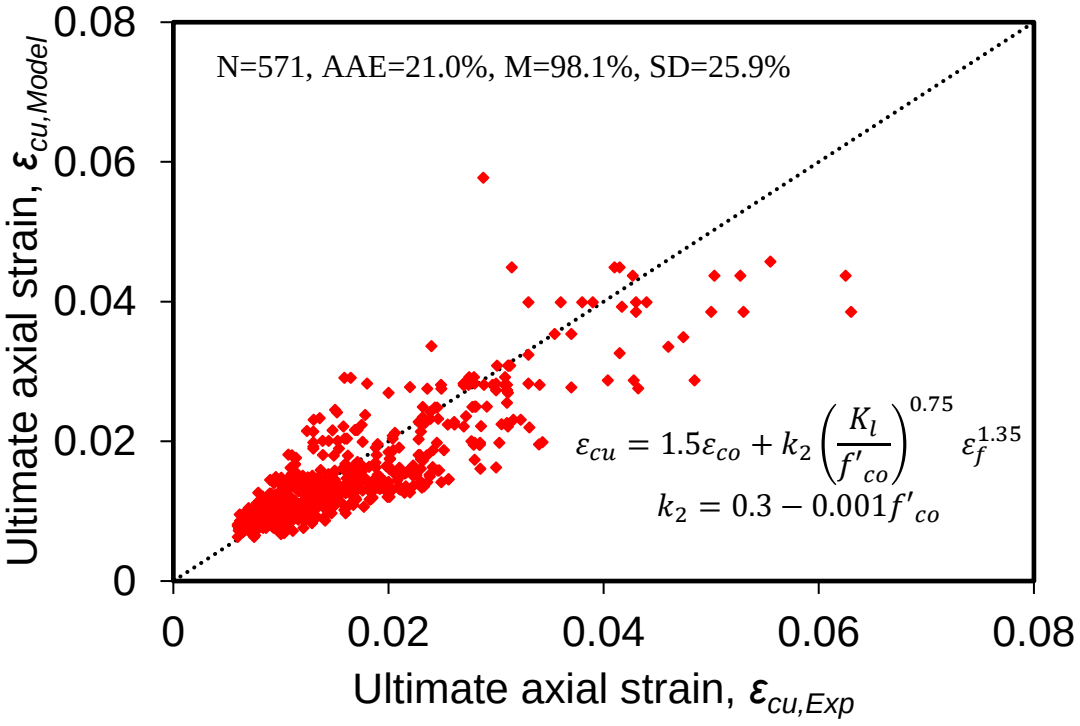

Figure 21-Comparison of model predictions of ultimate axial strain with experimental data

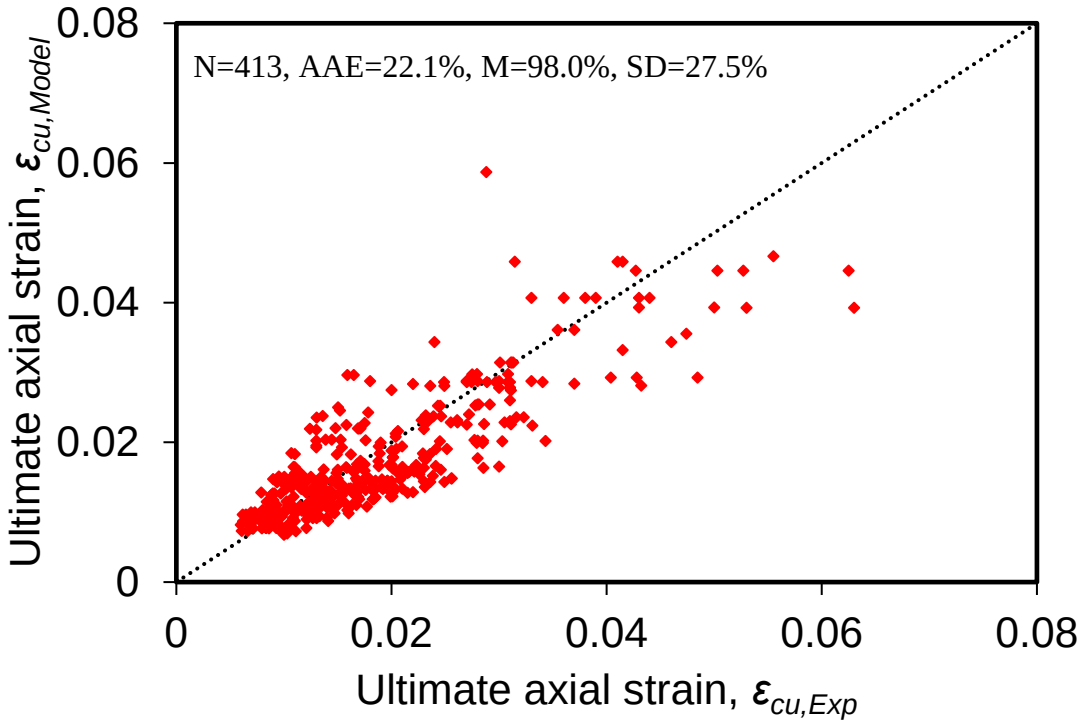

a)

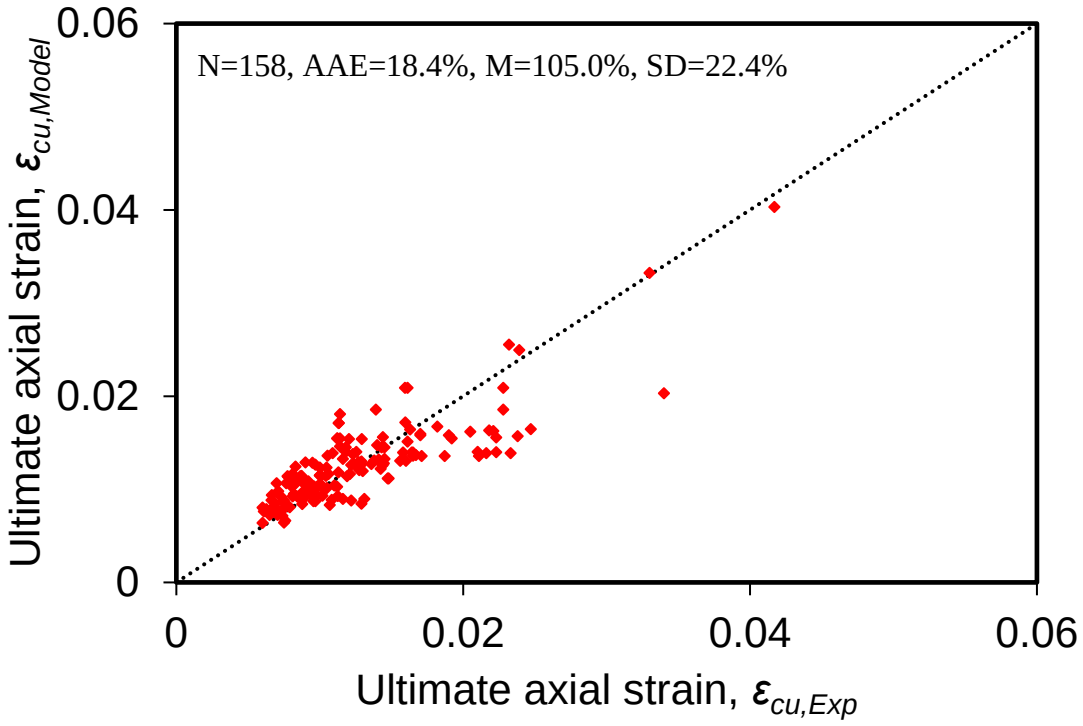

b)

Figure 22-Comparison of model predictions of ultimate axial strain with experimental data based on f'_{co} : a) NSC, b) HSC

3.4.2 Prediction of the transition point in the axial stress-strain curve of FRP-confined concrete

To model the complete axial stress-strain curve, the transition point where the axial stress-strain curve transitions from an initial ascending branch to a second branch (only the curves with an ascending type second branch are considered in this study) is a key point to determine to accurately capture the full axial stress-strain response. To predict this point, a new database for axial stress at the transition point (f'_{c1}) and the axial strain at the transition point (ε_{c1}) was prepared. Although few models for predicting the transition point exist, these models did not cover all FRP fiber types, such as high-modulus carbon fiber-reinforced polymer (HM CFRP) and the number of datasets used in their development were limited [17, 93, 115-117] . In addition, the better performing expressions from the existing models exhibit complex forms (e.g. [115, 116]), and as such, a new expression for the transition point (f'_{c1}, ε_{c1}) was developed to provide improved simplicity and accuracy.

The transition point was determined by studying the experimental datasets at axial stress-strain curve especially after unconfined compressive strength (f'_{co}). Carefully inspection of the axial stress-strain behavior at this region has revealed two different types of behavior: i) the specimens that exhibited monotonically ascending type of curves (typically seen in FRP-confined NSC), ii) the specimens that exhibited initial strength softening right after the transition point (typically seen in FRP-confined HSC, especially with f'_{co} > 75 MPa, as discussed in detail in Lim and Ozbakkaloglu [3]). The axial transition stress (f'_{c1}) and axial strain (ε_{c1}) of the first type of curves were defined by identifying where the second branch of the axial stress-strain curve transitioned to the near linear second branch, whereas the transition point of the second type of curves corresponded to the point on the stress-strain curve that marked the beginning of the softening behavior.

By finding the point at which the change of behavior in axial stress-strain curve for two mentioned cases were observed.

3.4.2.1 Axial stress at transition point

As opposed to the nonlinear forms adopted previously [115, 116], in this study a simple linear form was adopted to predict f'_{c1}:

$$f'_{c1} = f'_{co} + k_3 K_l \tag{3.7}$$

where k_3 is the strength enhancement coefficient for the prediction of f'_{c1}.

In the prediction of f'_{c1} the variations of k_3 with different key confinement parameters (i.e. f'_{co}, K_l, and K_l/f'_{co}) was closely studied. The regression analysis revealed that the coefficient k_3 can be considered constant with a value equal to 0.007, as shown in Figure 23. Consequently, the expression proposed by this study for prediction of f'_{c1} is presented in Eq. (3.8).

$$f'_{c1} = f'_{co} + 0.007\, K_l \tag{3.8}$$

Figure 24 illustrates the performance of the proposed model in the prediction of the axial stress at transition point (f'_{c1}) by comparing model predictions to experimental values. This comparison shows that the model predictions are in close agreement with the experimental results. Figures 25a and 25b show a comparison of modelled values of f'_{c1} against experimental data for NSC and HSC respectively, which shows good agreement.

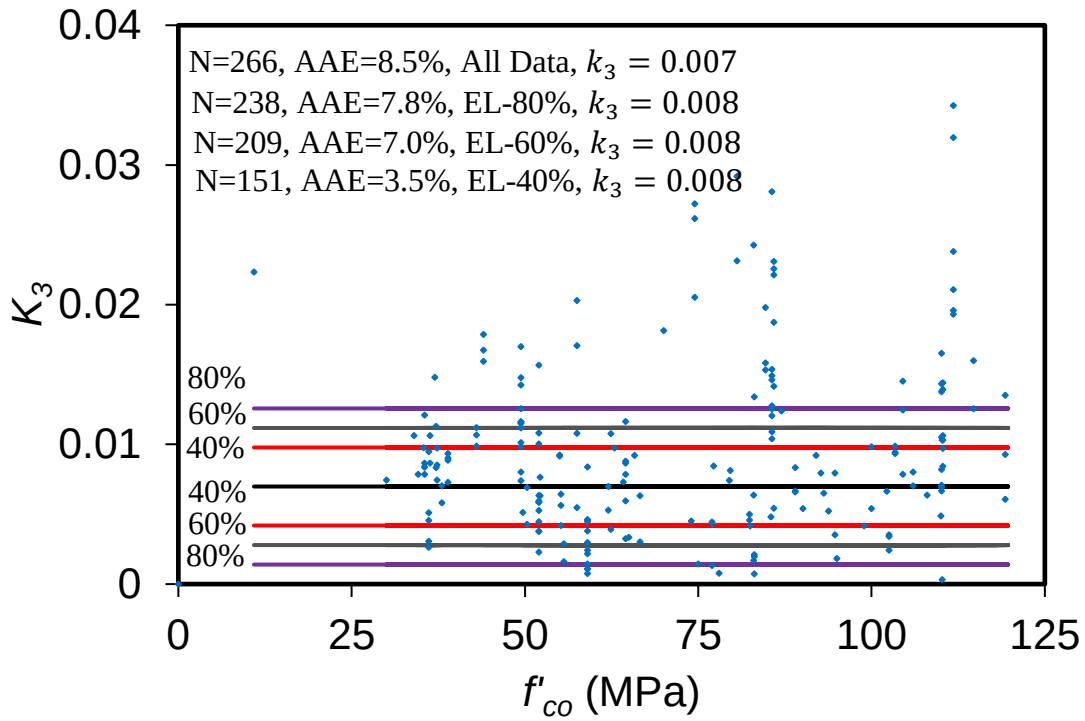

Figure 23-Variation of strength enhancement coefficient, k_3, at transition point with f'_{co}

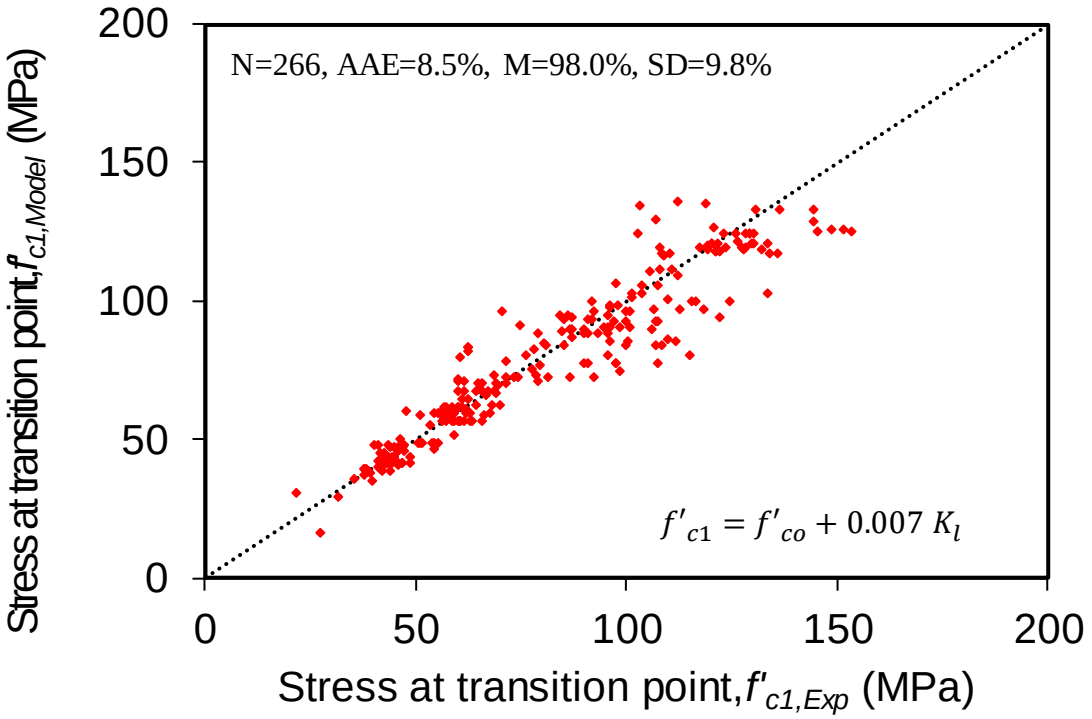

Figure 24- Comparison of model predictions of axial stress at transition point, f'_{c1}, with experimental data

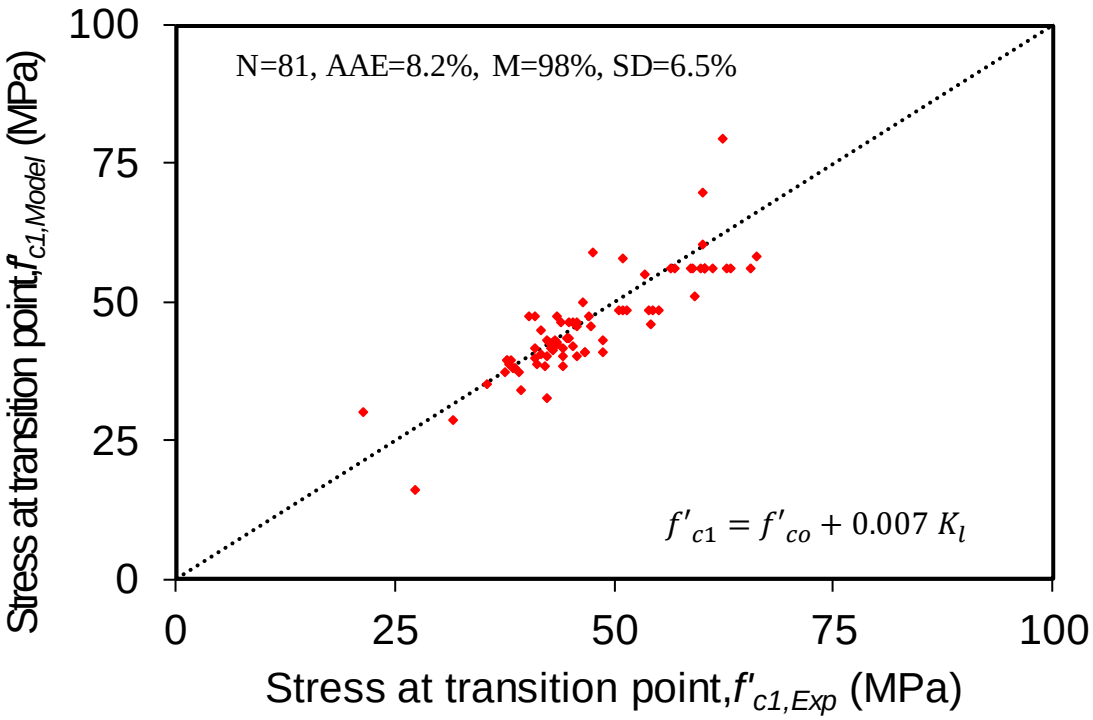

a)

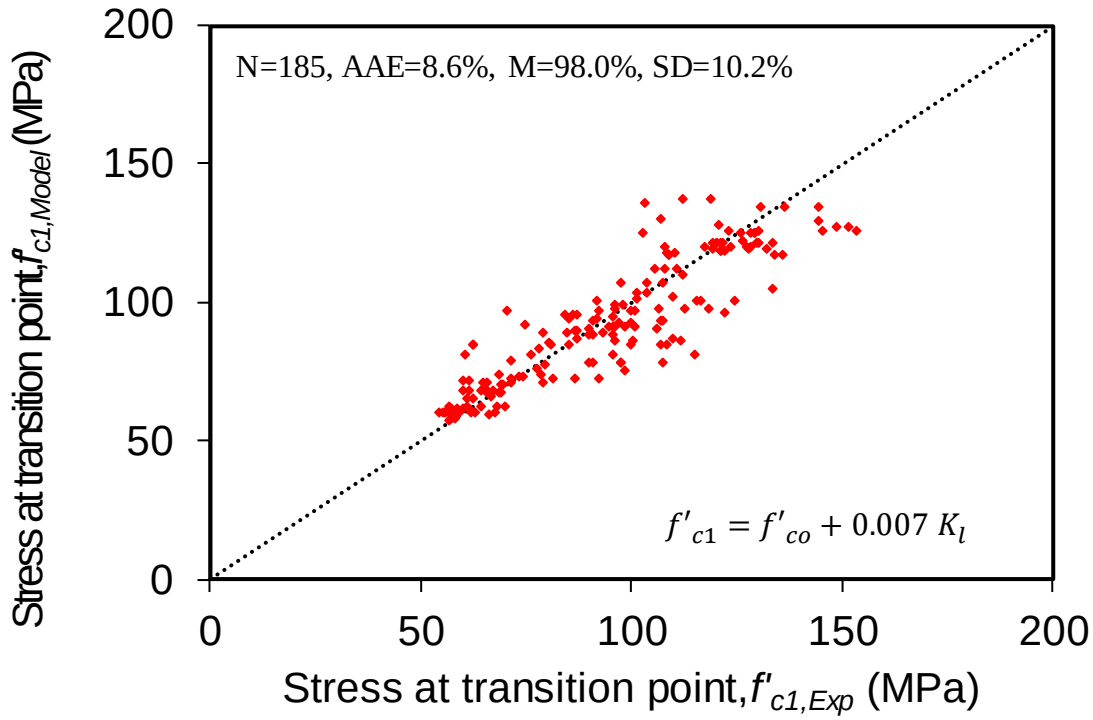

b)

Figure 25- Comparison of model predictions of axial stress at transition point with experimental data based on f'_{co}: a) NSC, b) HSC

3.4.2.2 Axial strain at transition point

An expression proposed by Lim and Ozbakkaloglu [17] to predict the lateral strain (ε_{l1}) at transition point [3] was modified based on dilation data to predict the axial strain at transition point (ε_{c1}). The new expression, shown in Eq. (3.9) has a simpler equation format.

$$\varepsilon_{c1} = \varepsilon_{co}\left(1 + k_4 \frac{\mathrm{K}_l}{f'_{co}}\right) \tag{3.9}$$

where k_4 is the strain enhancement coefficient for the prediction of ε_{c1}.

To predict ε_{c1}, a regression analysis on the key parameters influencing the strain enhancement coefficient (k_4) was performed. This analysis resulted in a constant value of k_4 equal to 0.024, as shown in the analysis summary presented in Figure 26. Based on this analysis, Eq. (3.10) is proposed to predict the axial strain at transition point (ε_{c1}).

$$\varepsilon_{c1} = \varepsilon_{co}\left(1 + 0.024 \frac{\mathrm{K}_l}{f'_{co}}\right) \tag{3.10}$$

Figure 27 shows the performance of the proposed model for the prediction of the axial strain at transition point (ε_{c1}). As can be seen in the figure, the model predictions are in close agreement with experimental results. Figures 28a and 28b present a comparison of ε_{c1} predicted by proposed model against test results for NSC and HSC respectively, where a good agreement is observed for both concrete types.

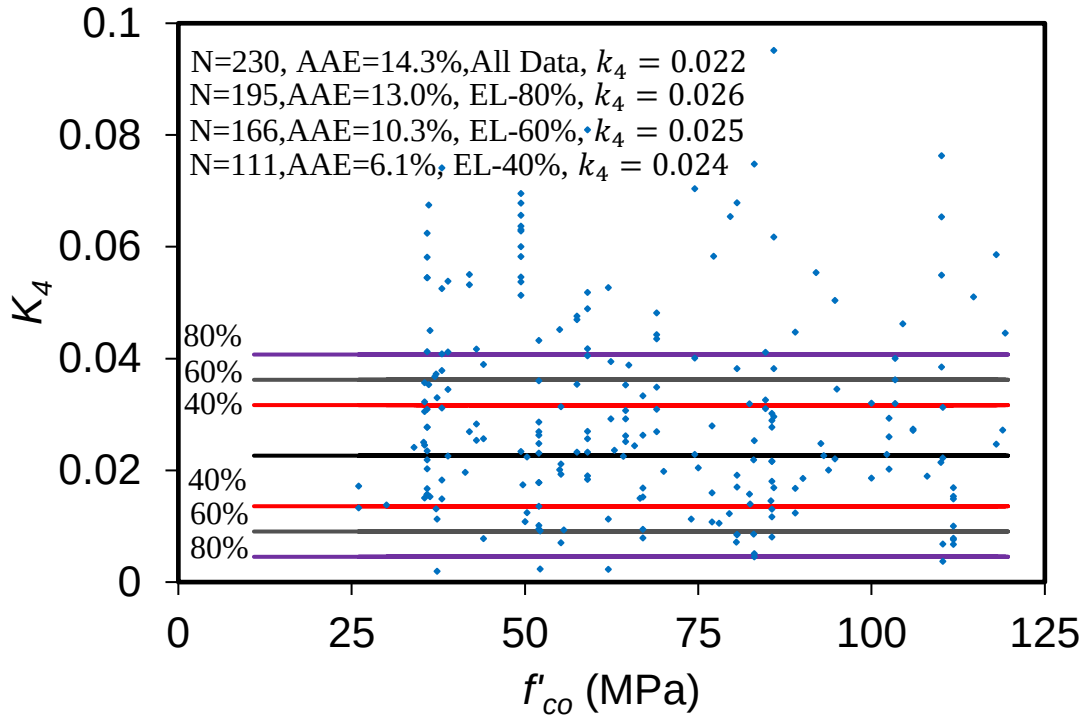

Figure 26- Variation of strain enhancement coefficient, k_4, at transition point

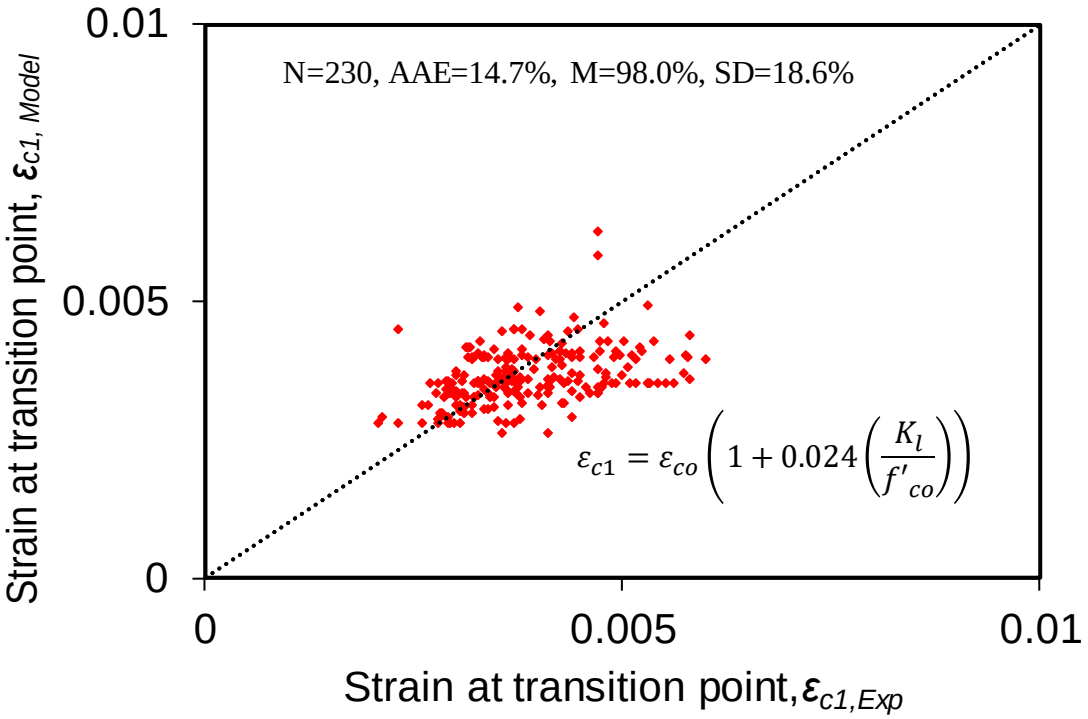

Figure 27- Comparison of model predictions of transition strain, ε_{c1}, with experimental data

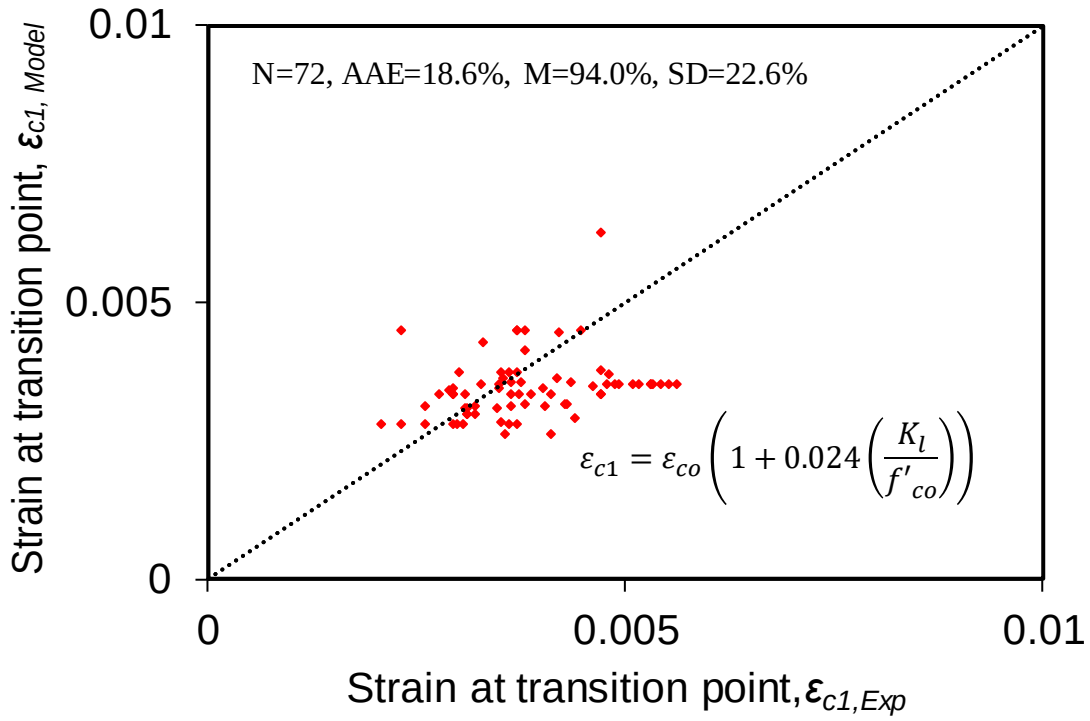

a)

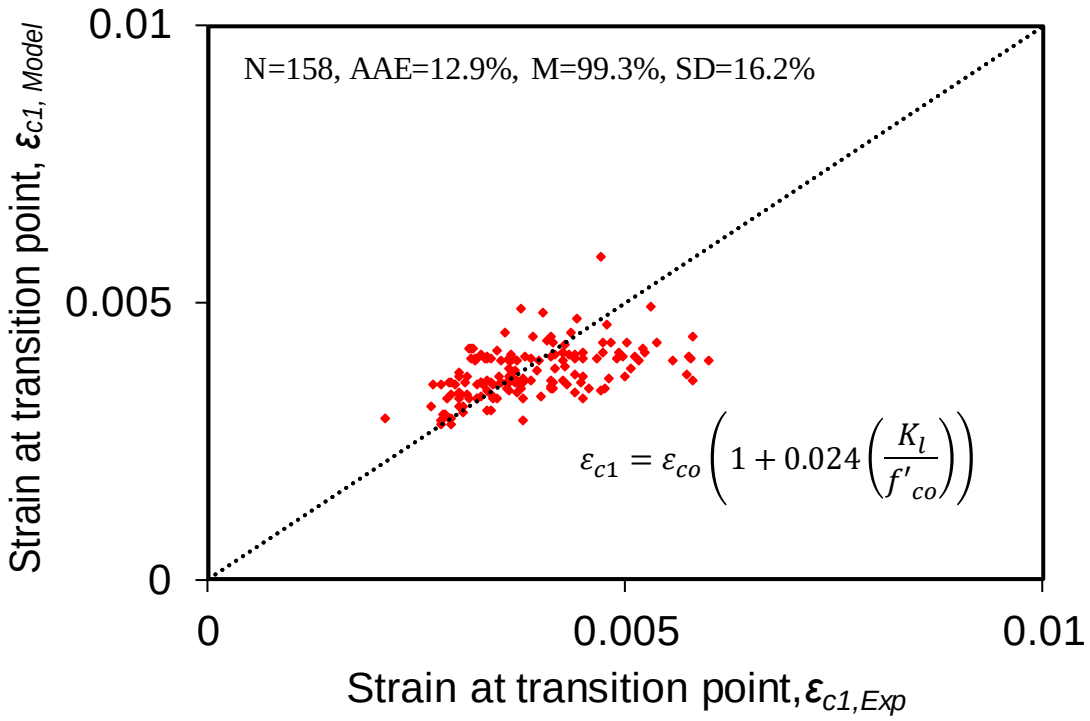

b)

Figure 28- Comparison of model predictions of transition strain with experimental data based on f'_{co}: a) NSC, b) HSC)

3.5 Comparison of the proposed design-oriented model with existing models

To evaluate the performance of the proposed expressions, their prediction statistics were compared with those of the best performing models proposed to date. This comparison included quantifying the accuracy and consistency of best performing models and proposed expressions through the use of the previously mentioned statistical indicators (i.e. AAE, SD, M) in addition to the root mean square error (RMSE).

3.5.1 Performance of the proposed expressions to predict the ultimate condition

To compare the proposed model with existing models for ultimate condition, all models were evaluated by the same database. For models that require hoop rupture strain ($\varepsilon_{h,rup}$) as an input parameter for their prediction, experimental values for $\varepsilon_{h,rup}$ were used.

3.5.1.1 Compressive strength

Table 2 shows a comparison of the statistical indicators obtained for predictions of f'_{cc} by the proposed model against the best existing models, with Figure 29 summarizing this data graphically. It can be seen in Table 2 that the prediction of f'_{cc} by the proposed model has the best AAE, M and SD for all datasets and a comparable RMSE to the next best model. In addition, Tables 3 and 4 present separate comparisons for NSC and HSC specimens, respectively, where a similar trend can be seen.

Table 2- Prediction statistics of the best performing compressive strength models

Model	Prediction of f'_{cc}				
	Test Data	AAE (%)	M (%)	SD (%)	RMSE (MPa)
Proposed Model	836	12.3	99.9	16.3	14.9
Lim and Ozbakkaloglu [3]	836	12.6	102.9	16.8	14.6
Berthet et al. [2]	836	13.0	104.1	18.6	17.9
Wu and Zhou [48]	836	13.3	107.2	18.9	17.6
Pham and Hadi [44]	836	14.0	118.2	18.2	17.3
Al-Salloum [49]	836	14.1	108.7	21.0	22.0
Wei and Wu [45]	836	14.3	108.6	20.6	21.1
Wu and Wang [47]	836	14.3	108.6	20.6	21.1
Teng et al. [6]	836	14.6	95.1	17.1	17.4
Youssef et al. [19]	836	15.7	118.2	21.4	22.7

Table 3-Prediction statistics of the best performing compressive strength models for NSC

Model	Prediction of f'_{cc} for NSC				
	Test Data	AAE (%)	M (%)	SD (%)	RMSE (MPa)
Proposed Model	633	12.4	100.5	16.7	12.0
Lim and Ozbakkaloglu [3]	633	12.5	102.8	16.4	11.7
Wu and Zhou [48]	633	12.6	105.2	17.9	12.9
Berthet et al. [2]	633	12.7	102.9	17.7	12.9
Al-Salloum [49]	633	12.9	104.8	18.5	13.6
Wei and Wu [45]	633	12.9	104.5	18.1	13.1
Wu and Wang [47]	633	12.9	104.5	18.1	13.1
Teng et al. [6]	633	15.0	92.6	15.5	13.2
Youssef et al. [19]	633	16.1	96.1	19.0	15.4
Pham and Hadi [44]	633	16.1	96.1	19.0	15.4

Table 4-Prediction statistics of the best performing compressive strength models for HSC

Model	Prediction of f'_{cc} for HSC				
	Test Data	AAE (%)	M (%)	SD (%)	RMSE (MPa)
Proposed Model	203	11.9	98.2	14.9	22.1
Lim and Ozbakkaloglu [3]	203	12.8	103.3	15.2	21.5
Teng et al. [6]	203	13.6	101.8	19.1	25.3
Berthet et al. [2]	203	13.9	107.4	20.4	26.8
Pham and Hadi [44]	203	14.3	100.0	18.8	24.4
Youssef et al. [19]	203	14.6	107.3	25.0	35.3
Wu and Zhou [48]	203	15.2	112.5	20.5	26.2
Al-Salloum [49]	203	17.5	118.9	23.6	35.7
Wei and Wu [45]	203	17.9	119.5	22.8	34.3
Wu and Wang [46]	203	17.9	119.5	22.8	34.3

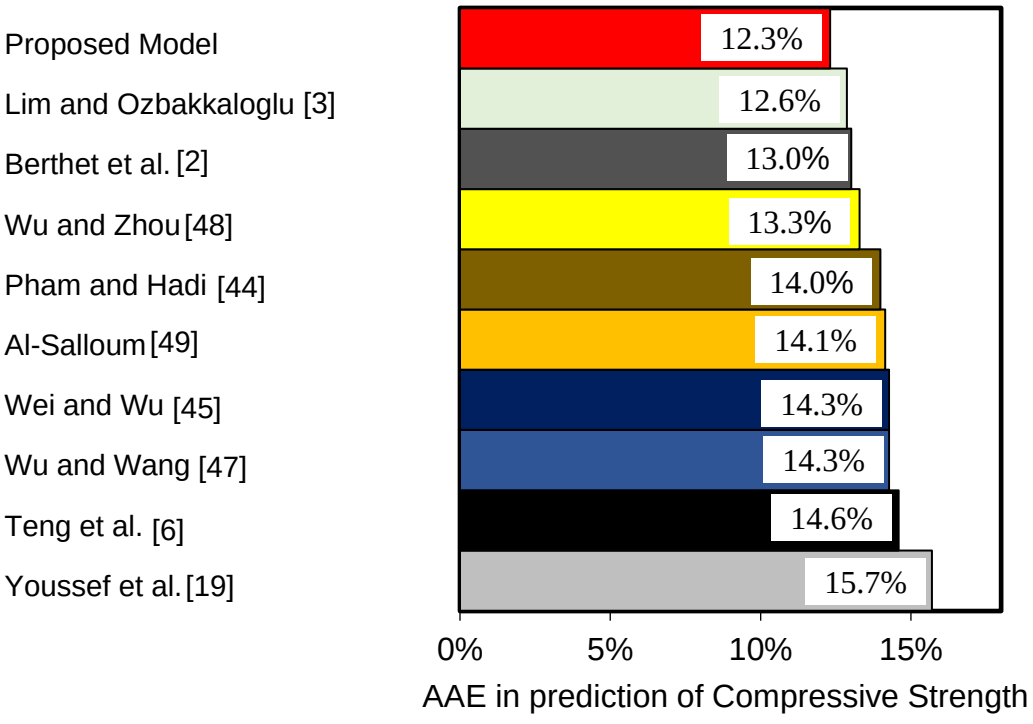

Figure 29-Average absolute error in model predictions of compressive strength

3.5.1.2 Ultimate axial strain

Table 5 and Figure 30 presents the statistical indicators for the prediction of ultimate strain (ε_{cu}) for the proposed and best existing models. As can be seen in this table, the AAE for the proposed model is comparable with the best performing models that use hoop rupture strain ($\varepsilon_{h,rup}$) as an input parameter.

To illustrate the performance of different models for different concrete types, the same statistical indicators were studied for NSC and HSC separately as presented in Tables 6 and 7, respectively. It can be seen that the most accurate models for NSC specimens are those that use experimental hoop rupture strains ($\varepsilon_{h,rup}$) [14, 17, 20, 24, 127], whereas the most accurate model for HSC specimens is the proposed model. Although these NSC expressions show a slightly better AAE when compared to the proposed expression, they require $\varepsilon_{h,rup}$ as input, which is not readily available in many cases. Therefore, the proposed model offers an excellent balance between accuracy and simplicity, keeping the expression in its simplest form without compromising the accuracy. It is worth mentioning that in this assessment the hoop rupture strains ($\varepsilon_{h,rup}$) required by the existing models were determined by the model presented in [16], as this approach provided a higher modeling accuracy compared to the use of experimental values or those given by the source model.

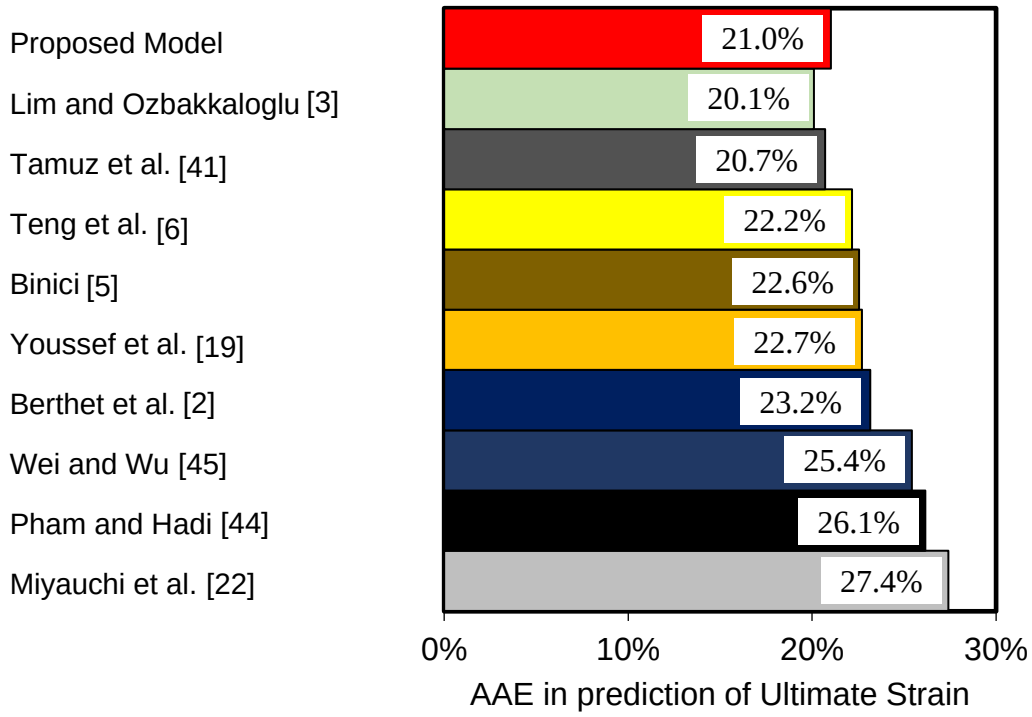

Figure 30-Average absolute error in model predictions of ultimate strain

Table 5-Prediction statistics of the best performing ultimate axial strain models

Model	Prediction of ε_{cu}				
	Test Data	AAE (%)	M (%)	SD (%)	RMSE (%)
Proposed Model	571	21.0	98.1	25.9	0.50
Lim and Ozbakkaloglu [3]	571	20.1	97.5	23.9	0.50
Tamuzs et al. [41]	571	20.7	106.5	28.7	0.50
Teng et al. [6]	571	22.2	122.1	34.1	0.66
Binici [5]	571	22.6	124.1	37.7	0.85
Youssef et al. [19]	571	22.7	112.8	34.8	0.71
Berthet et al. [2]	571	23.2	121.5	41.9	0.75
Wei and Wu [45]	571	25.4	103.9	31.3	0.62
Pham and Hadi [44]	571	26.1	129.8	40.5	0.85
Miyauchi et al. [22]	571	27.4	122.1	40.9	0.65

Table 6-Prediction statistics of the best performing ultimate axial strain models for NSC

Model	Prediction of ε_{cu} for NSC				
	Test Data	AAE (%)	M (%)	SD (%)	RMSE (%)
Proposed Model	413	22.1	98.0	27.5	0.53
Lim and Ozbakkaloglu [3]	413	20.5	96.0	23.5	0.53
Tamuzs et al. [41]	413	20.5	104.7	28.6	0.54
Teng et al. [6]	413	21.2	119.2	33.3	0.66
Binici [5]	413	21.7	121.2	37.2	0.84
Berthet et al. [2]	413	23.0	128.9	44.1	0.85
Youssef et al. [19]	413	23.8	110.6	36.9	0.77
Miyauchi et al. [22]	413	25.7	126.2	40.6	0.69
Pham and Hadi [44]	413	25.8	129.8	41.9	0.93
Wei and Wu [45]	413	26.9	102.1	32.8	0.69

Table 7-Prediction statistics of the best performing ultimate axial strain models for HSC

Model	Prediction of ε_{cu}				
	Test Data	AAE (%)	M (%)	SD (%)	RMSE (%)
Proposed Model	158	18.4	105.0	22.4	0.32
Lim and Ozbakkaloglu [3]	158	19.0	101.4	24.9	0.42
Youssef et al. [19]	158	20.0	118.3	27.9	0.50
Tamuzs et al. [41]	158	21.2	111.4	28.2	0.38
Wei and Wu [45]	158	21.6	108.6	26.5	0.37
Berthet et al. [2]	158	23.5	102.2	27.6	0.40
Teng et al. [6]	158	24.7	129.5	35.2	0.63
Binici [5]	158	24.7	131.9	38.2	0.89
Pham and Hadi [44]	158	27.0	129.8	36.7	0.57
Miyauchi et al. [22]	158	31.8	111.4	39.7	0.52

3.5.2 Performance of the proposed expressions in predicting transition point

The same database and statistical indicators were used to examine the performance of the proposed model against the existing models for the prediction of the transition point ($\varepsilon_{c1}, f'_{c1}$).

3.5.2.1 Axial stress at transition point

Table 8 and Figure 31 present the statistical indicators of different models for predicting the axial stress at the transition point (f'_{c1}). From this comparison it can be seen that the proposed model for f'_{c1} shows the best performance across all statistical indicators.

3.5.2.2 Axial strain at transition point

As can be seen in Table 9 and Figure 32, the proposed simplified model for ε_{c1} exhibited improved performance against the existing more complex models with improvements in all statistical indicators.

Table 8-Prediction statistics of the best performing transition strength models

Model	Prediction of f'_{c1}				
	Test Data	AAE (%)	M (%)	SD (%)	RMSE (MPa)
Proposed Model	266	8.5	98.0	9.8	8.5
Saafi et al. [17]	266	8.5	97.5	11.6	10.2
Lim and Ozbakkaloglu [3]	266	8.8	95.1	10.1	9.0
Youssef et al. [19]	266	9.2	96.7	12.8	11.5
Toutanji [18]	266	9.8	103.0	13.1	10.5

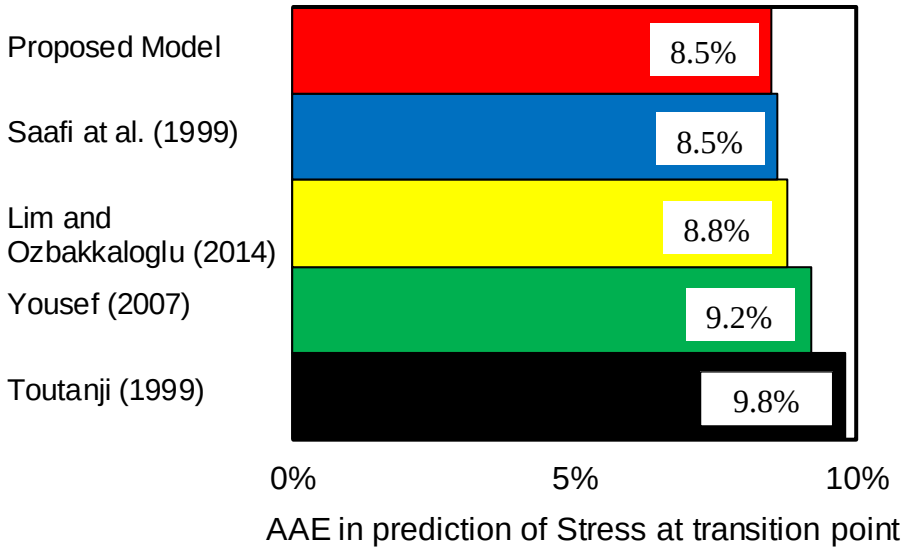

Figure 31-Average absolute error in model predictions of the transition point of axial stress

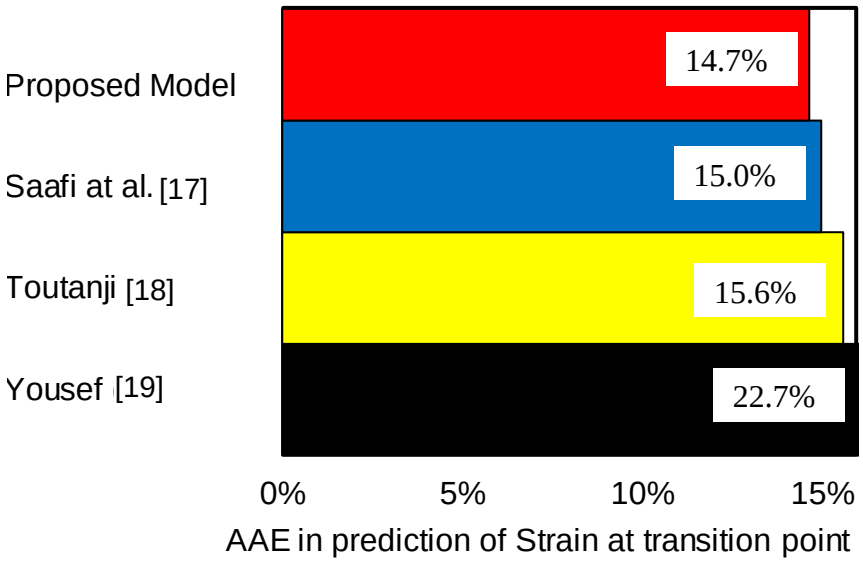

Figure 32-Average absolute error in model predictions of the transition point of axial strain

Table 9-Prediction statistics of the best performing transition strain models

Model	Prediction of ε_{c1}				
	Test Data	AAE (%)	M (%)	SD (%)	RMSE (%)
Proposed Model	230	14.7	98.0	18.6	0.08
Saafi et al. [17]	230	15.0	101.0	18.8	0.08
Toutanji [18]	230	15.6	103.0	19.3	0.08
Youssef [19]	230	22.7	118.0	22.4	0.10

3.6 New stress-strain model and its validation against experimental data

A new axial stress-strain model was developed by applying the proposed design-oriented models for the ultimate and transition points. The new stress-strain model uses the expression given by Popovics [128] for the first portion of the stress-strain curve (see Eq.3.11) and a linear expression was used to model the second portion of stress-strain curve (see Eq.3.13). These selections were made due to good performance of these proposed shapes for the first and second ascending portions of the stress-strain curve as demonstrated previously [16, 23]. Therefore, to construct the whole stress-strain curve only four parameters (i.e. ε_{cu}, f'_{cc}, f'_{c1} and ε_{c1}) are required.

$$f_{cc} = f'_{c1}\left(\frac{\varepsilon_c}{\varepsilon_{c1}}\left(n/\left(\mathrm{n} - 1 + \left(\frac{\varepsilon_c}{\varepsilon_{c1}}\right)^{n}\right)\right)\right) \qquad if\ 0 \le \varepsilon_c \le \varepsilon_{c1} \tag{3.11}$$

where f_{cc} and ε_c are the axial stress and axial strain, respectively, and n is a term introduced by Carreira and Chu [129] to define concrete brittleness:

$$n = E_c/\left(E_c - \frac{f'_{c1}}{\varepsilon_{c1}}\right) \tag{3.12}$$

where $E_c = 4400\sqrt{f'_{co}}$ (in MPa) and f'_{co} is the compressive strength of unconfined concrete in MPa.

Following the first branch, the second branch is presented by a linear expression:

$$f_{cc} = f'_{c1} + E_2\left(\varepsilon_c - \varepsilon_{c1}\right) \qquad if\ \varepsilon_{c1} < \varepsilon_c \le \varepsilon_{cu} \tag{3.13}$$

where $E_2 = \frac{f'_{cc} - f'_{c1}}{\varepsilon_{cu} - \varepsilon_{c1}}$ is the slope of the second branch of the stress-strain curve.

As a final step, the full axial stress-strain curves were created based on proposed expressions using f'_{cc}, f'_{c1}, ε_{cu} and ε_{c1}, and the resulting curves were compared with experimental stress-strain curves. The results from several groups of specimens are shown in figure 33 to illustrate

the performance of the model in predicting the behavior of specimens with different unconfined concrete strengths that were confined by different types of FRP (i.e. carbon, aramid, glass, and high-modulus carbon fiber-reinforced polymer (CFRP, AFRP, GFRP, and HM CFRP, respectively)) under different levels of confinement pressure. As it is evident from these comparisons, the predictions of the proposed model are in good agreement with the experimental results.

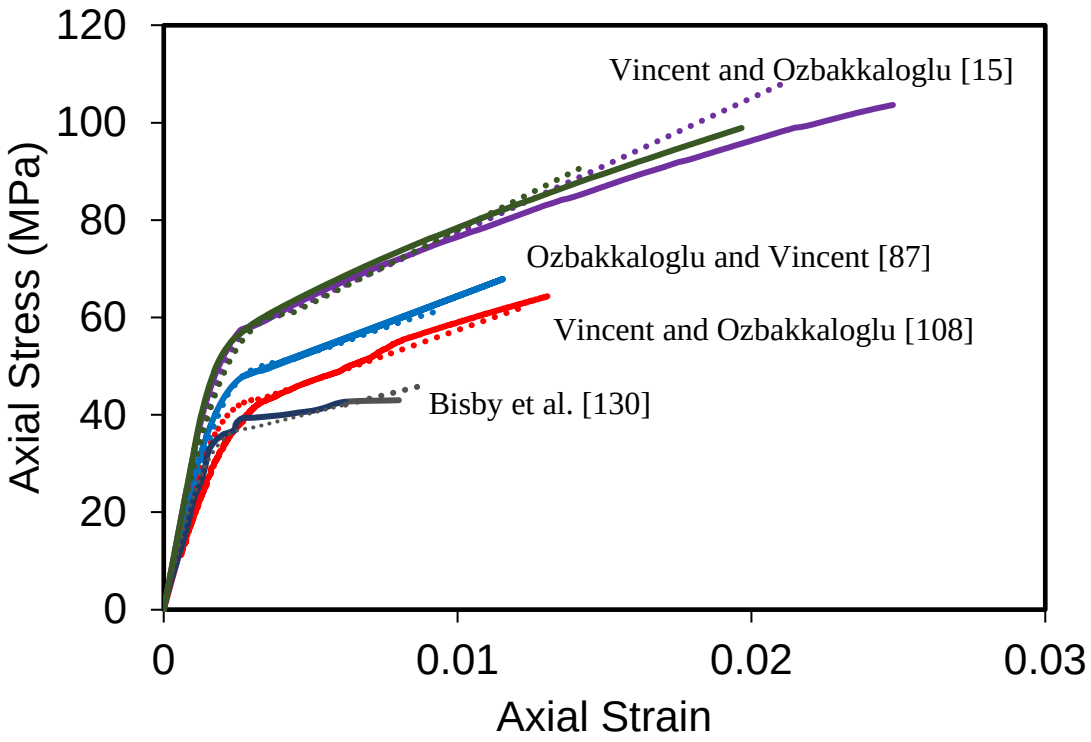

a)

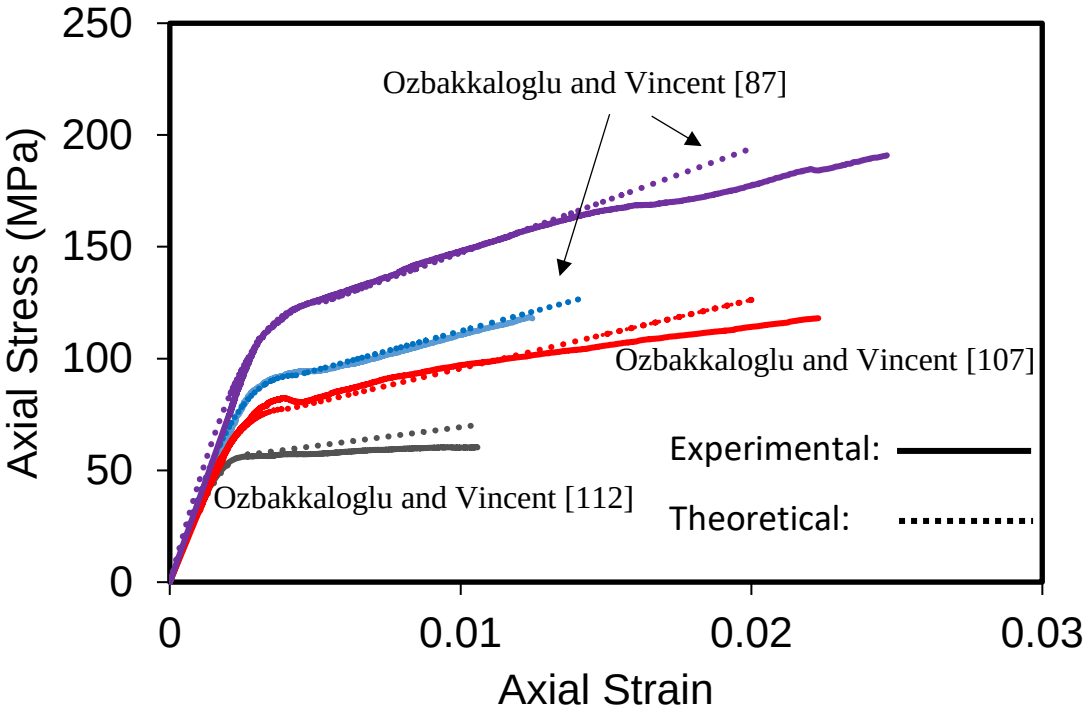
Ozbakkaloglu and Vincent [87]
Ozbakkaloglu and Vincent [107]
Ozbakkaloglu and Vincent [112]
Experimental:
Theoretical:
Axial Stress (MPa)
Axial Strain
0
50
100
150
200
250
0
0.01
0.02
0.03

b)

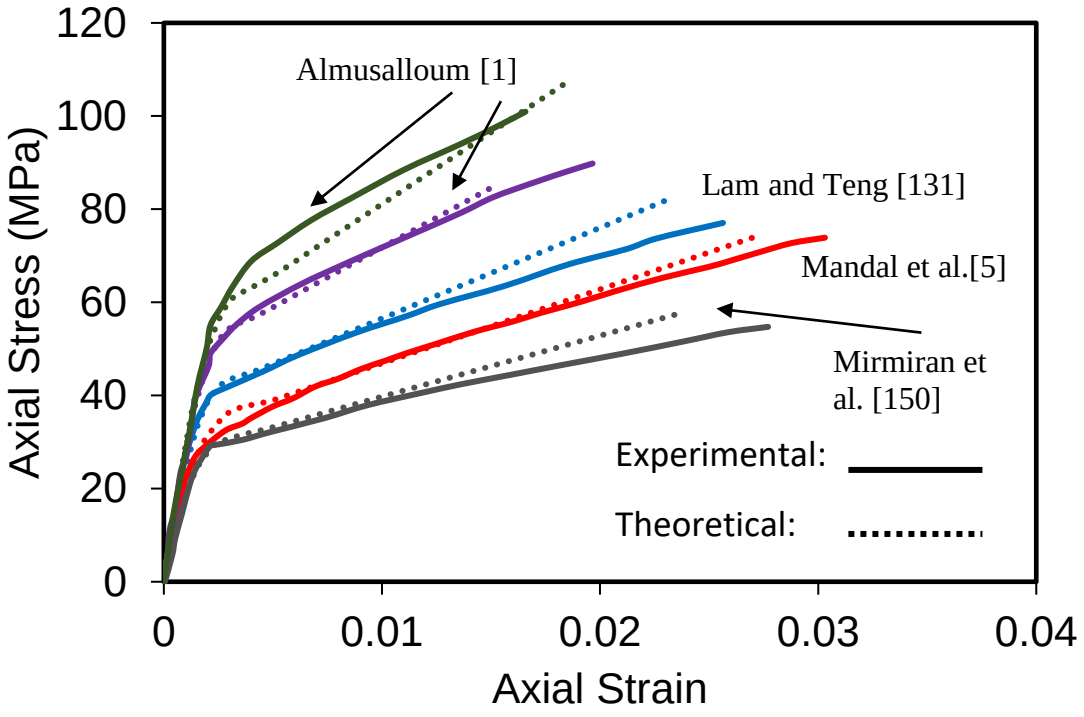
Almusalloum [1]
Lam and Teng [131]
Mandal et al.[5]
Mirmiran et al. [150]
Experimental:
Theoretical:
Axial Stress (MPa)
Axial Strain
0
20
40
60
80
100
120
0
0.01
0.02
0.03
0.04

c)

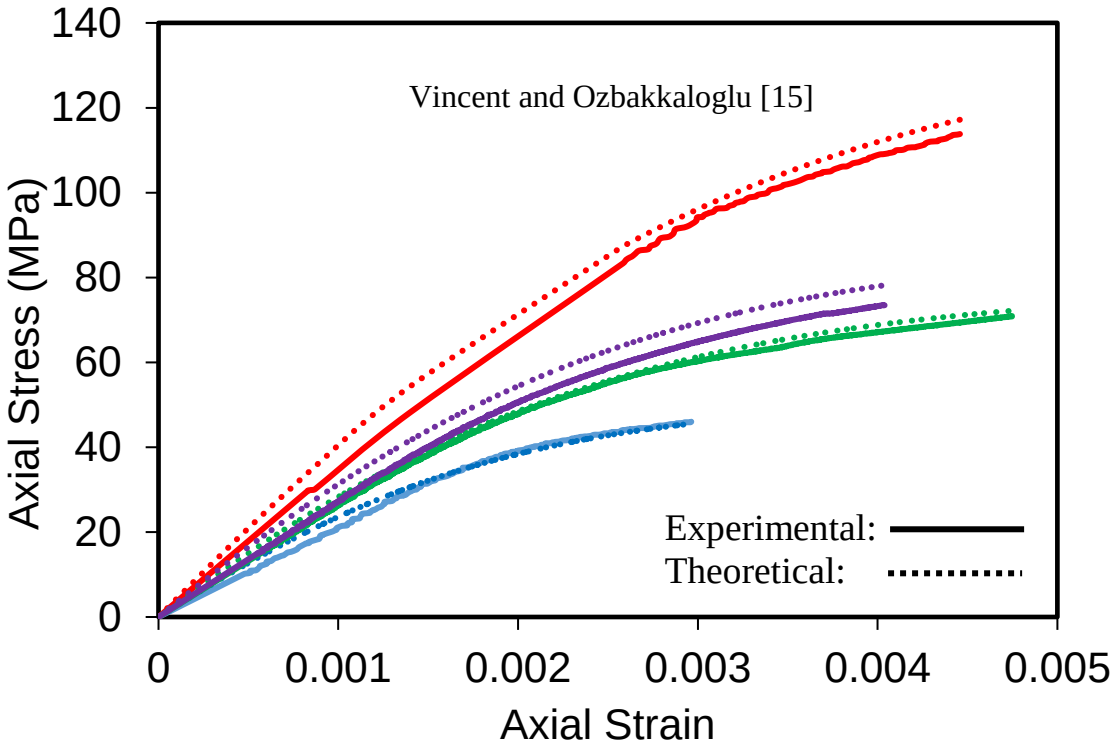

d)

Figure 33-Comparison of predicted and experimental stress-strain curves for FRP-confined concrete: a) CFRP; b) AFRP; c) GFRP; d) HM-CFRP

3.7 Conclusion

This section again illustrates the significance of measurement methods in validating or developing a model and the dependency of existing models on experimental hoop rupture strain which is used as input data. Although more complicated analysis was made to increase the accuracy of models using available input data instead of experimental data, the outcome showed that the existing models predicts more accurate when they are using appropriate experimental data. The following points summarize the main findings and contributions of this study:

1- The importance of using hoop rupture strain ($\varepsilon_{h,rup}$), especially for prediction of ultimate axial strain (ε_{cu}), is well established. Nonetheless, in this study a simple model for predicting ε_{cu} was proposed that uses readily available input data, namely the ultimate tensile strain (ε_{fu})

in place of $\varepsilon_{h,rup}$, and it performs with comparable accuracy to its best performing counterparts adopting $\varepsilon_{h,rup}$.

2- Using readily available input parameters, such as those provided by FRP material suppliers, the transition point (ε_{c1}, f'_{c1}) and ultimate point (f'_{cc}, ε_{cu}) can be predicted by the proposed models with an accuracy that is similar to the best performing existing models with more complex forms or specific input parameters.

3- The importance of using hoop rupture strain ($\varepsilon_{h,rup}$), especially for prediction of ultimate axial strain (ε_{cu}), is well established. Nonetheless, in this study a simple model for predicting ε_{cu} was proposed that uses readily available input data, namely the ultimate tensile strain (ε_{fu}) in place of $\varepsilon_{h,rup}$, and it performs with comparable accuracy to its best performing counterparts adopting $\varepsilon_{h,rup}$.

4- The assessment undertaken in this study has revealed f'_{co} as a most influential parameter on the compressive behavior of FRP-confined concrete. This agrees with the authors previous studies on the effect of unconfined concrete strength and additional experimental studies targeting this influence are recommended.

5- Enhancement coefficients of compressive strength (f'_{cc}) and ultimate strain (ε_{cu}), k_1 and k_2 respectively, decrease with an increase in f'_{co} and this influence can be modelled accurately with a linear relationship. Alternative non-linear relationships that were considered did not lead to significant improvements in the statistical performance indicators.

6- The proposed model for the prediction of the axial stress and strain at transition point (f'_{c1} and ε_{c1}) exhibit improved performance when compared with the existing model with more complex forms. It is found that, the enhancement coefficients (k_3 and k_4) in the proposed forms of the expressions remain mostly constant across a range of f'_{co} between 10 and 120 MPa.

Chapter 4: Behavior of FRP-confined high-strength concrete under eccentric compression

(A paper is published based on this section: Fallah Pour A, Gholampour A, Zheng J, Ozbakkaloglu T. Behavior of frp-confined high-strength concrete under eccentric compression: Tests on concrete-filled frp tube columns. Compos Struct. 2019;220:261-72 (DOI: 10.1016/j.compstruct.2019.03.031))

4.1 Introduction

It is now well understood that lateral confinement of concrete columns with fiber-reinforced polymer (FRP) sheets can significantly enhance their compressive strength and axial strain capacity. During the past two decades, extensive researches have been conducted on the use of FRP composite as confinement reinforcement in both retrofitting existing concrete columns [88, 89, 102, 111, 131] and in the development of new high-performance composite columns [77, 107, 109, 132-134]. A recent comprehensive review of the literature undertaken by Ozbakkaloglu et al. [16] revealed that over 500 studies have been undertaken during the last two decades on the behavior of FRP-confined concrete columns under concentric axial compression loading. These studies have resulted in the development of over 110 axial stress-strain models.

In real structures, the majority of concrete columns are subject to eccentric loading. A number of studies have examined the effect of load eccentricity on the behavior of FRP-confined concrete columns with circular [40-46] and non-circular [47-54] cross-sections. However, these studies were concerned with FRP-confined reinforced concrete columns that contained internal steel reinforcement. A few studies have been reported on the behavior of eccentrically loaded FRP-confined concrete columns not having internal steel reinforcement [55-58]. Among them, only two studies experimentally investigated the axial stress-strain behavior of FRP-confined plain concrete under eccentric compression [57, 58]. These studies have shown that concrete columns under eccentric compression behave differently than those under

concentric compression because of the way confinement actions are affected by the presence of load eccentricity. However, they reached differing conclusions as to the effect of the load eccentricity on the axial stress-strain behavior of FRP-confined concrete. Fam, Flisak [57] reported that an increase in the load eccentricity led to a decrease in the second branch slope of the stress-strain curve, whereas Wu and Jiang [58] concluded the opposite. One thing is clear, however, that the existing concentric axial stress-strain models of FRP-confined concrete are not able to accurately capture the behavior of concrete under eccentric compression [56-58] and specific models are needed to accurately model the behavior of concrete under the latter condition. Therefore, it is crucial to have additional experimental studies to clearly understand the effect of load eccentricity on the behavior of FRP-confined plain concrete. Furthermore, the existing studies on FRP-confined concrete without internal reinforcement investigated the behavior of only the normal-strength concrete (NSC) columns. As previously discussed in detail [87, 135, 136], owing to the advantages it offers over NSC, high-strength concrete (HSC) is now being used in large quantities in a wide range of structural applications, including in concrete-filled FRP tubes (CFFTs) that are designed as high-performance composite structural members [16, 40, 107, 109, 112, 135-138]. Therefore, it is timely to study the behavior of FRP-confined HSC under eccentric compression through experimental studies.

This paper presents the first experimental study on the behavior of FRP-confined HSC columns having no internal steel reinforcement under eccentric loading. The paper initially provides a summary of the experimental program, which is followed by the results of the experimental tests. The axial stress-strain curves are subsequently obtained through sectional analysis conducted using the experimental measurements. Finally, a detailed discussion on the results is presented to discuss the effect of eccentricity on the axial stress-strain behavior of concrete.

As it was explained and well understood, the columns are not ideally subjected to concentric load in real condition and a study of FRP-confined HSC behavior as columns in real condition can help to develop a better prediction of mentioned structural element behavior. In this section, the behavior of FRP-confined HSC under concentric and eccentric load is studied and the influence of combination of compression and bending on FRP-confined HSC is presented. This helps to better comprehension of the FRP-confined HSC mechanical behavior under real condition of columns in building.

This section presents the first experimental study on the behavior of FRP-confined HSC columns having no internal steel reinforcement under eccentric loading. The section initially provides a summary of the experimental program, which is followed by the results of the experimental tests. The axial stress-strain curves are subsequently obtained through sectional analysis conducted using the experimental measurements. Finally, a detailed discussion on the results is presented to discuss the effect of eccentricity on the axial stress-strain behavior of concrete.

4.2 EXPERIMENTAL PROGRAM

4.2.1 Test specimens and materials

A total of 31 CFFTs, including 16 circular and 15 square cross-section specimens were manufactured and tested under compression. Table 10 shows the details of the test specimens. Five target load eccentricities, including 10, 20, 30, 40, and 50 mm were considered. The specimens had a cross-section of 152 mm, measured at the concrete core, and a height of 300 mm. Square specimens were designed with rounded corners with a radius of 30 mm to maintain relatively high confinement efficiency [85, 112, 132, 133, 135].

The properties of unidirectional fiber sheets used in the fabrication of the FRP tubes are shown in Table 11. Carbon FRP tubes were used in this study, where the fibers were oriented in the hoop direction (perpendicular to column axis). The flat coupon tests were conducted (Fig. 34)

to obtain the material properties in accordance with ASTM standard D3039M-08 [139]. The number of FRP layers was selected based on the expressions proposed previously in Lim and Ozbakkaloglu [17] and Lim and Ozbakkaloglu [85] in order to obtain an axial stress-strain curve with a slightly ascending second branch. For square specimens, a shape factor was used to consider the effectiveness of FRP confinement in non-uniform confinement, as proposed in Ref. [85]. This resulted in a thicker FRP tube in square CFFTs (i.e. 1.32 mm total fiber thickness) than in circular CFFTs (i.e. 0.666 mm total fiber thickness). Similar tube designs were used in a large number of previous studies investigating the behavior of CFFTs under concentric compression (e.g. [15, 87, 105, 107]).

Table 10-Details of test specimens

Specimen ID	Number of FRP layers	Fiber Thickness per Layer (mm)	Cross-Section	Target Eccentricity (mm)
C1	6	0.111	Circular	0
C2	6	0.111	Circular	0
C3*	6	0.111	Circular	10
C4	6	0.111	Circular	10
C5*	6	0.111	Circular	10
C6*	6	0.111	Circular	20
C7	6	0.111	Circular	20
C8	6	0.111	Circular	30
C9	6	0.111	Circular	30
C10	6	0.111	Circular	30
C11	6	0.111	Circular	40
C12*	6	0.111	Circular	40
C13	6	0.111	Circular	40
C14	6	0.111	Circular	50
C15	6	0.111	Circular	50
C16*	6	0.111	Circular	50
S1	8	0.165	Square	0
S2	8	0.165	Square	0
S3	8	0.165	Square	10
S4	8	0.165	Square	10
S5	8	0.165	Square	20
S6	8	0.165	Square	20
S7	8	0.165	Square	30
S8	8	0.165	Square	30
S9	8	0.165	Square	30
S10	8	0.165	Square	40
S11	8	0.165	Square	40
S12	8	0.165	Square	40
S13	8	0.165	Square	50
S14	8	0.165	Square	50
S15*	8	0.165	Square	50

* Marked samples have been excluded due to problems in se

The specimens were prepared using a HSC mix with a 105 MPa unconfined compressive strength (f'_{co}). The details of the concrete mix are shown in Table 3. The mix consisted of crushed basalt as the coarse aggregate with a nominal maximum size of 10 mm. Polycarboxylic ether polymer-based superplasticizer and silica fume were added to the mix in order to achieve both a high compressive strength and sufficient workability.

Table 11-Material properties of fibers and FRP composites

Type	Nominal dry fiber thickness t_f (mm/ply)	Fiber/FRP properties					
		Provided by manufacturers			Obtained from coupon tests*		
		Ultimate tensile stress f_f (MPa)	Ultimate tensile strain ε_f (%)	Elastic modulus E_f (GPa)	Ultimate tensile stress f_{FRP} (MPa)	Ultimate tensile strain ε_{FRP} (%)	Elastic modulus E_{FRP} (GPa)
CFRP	0.111/0.165	4830	2.10	230.0	4598	1.95	236.0

* Calculated based on nominal dry fiber thickness

Figure 34- FRP tension coupon specimens

4.2.2 Specimens preparation

Carbon FRP tubes were manufactured using a manual wet lay-up process by wrapping epoxy resin impregnated fiber sheets around precision-cut high-density polystyrene foam templates in the hoop direction. The epoxy resin was allowed to cure at room temperature for at least 24 hours before the FRP tubes were removed from their molds. The tubes were prepared with an overlap length of 150 mm to prevent premature debonding failure. Additional 30 mm wide FRP strips were applied to the specimens in the hoop direction at both ends to ensure their failure occurred near the mid-height region, where lateral strain gauges were placed. The six-layer tubes for circular specimens were continuously wrapped with a single FRP sheet,

whereas the eight-layer tubes for square specimens were prepared by using two FRP sheets, resulting in two overlap zones at the same location.

To support the tubes and ensure that they remained stable during the process of concrete pouring, a wooden formwork was developed. The CFFTs were removed from the formwork and placed in a curing room one day after the concrete casting, and kept at a constant temperature of 23±2℃ until test day. 12 cylinders with 100 mm in diameter and 200 mm in height were prepared for each batch of concrete and were cured in the same room to monitor the development of concrete strength at different ages. On the testing day, the CFFTs were removed from the curing room and ground by a surface-grinding machine to ensure a smooth surface at their ends.

4.2.3 Instrumentation and testing

The specimens were tested using a 5000-kN capacity universal testing machine. The loading was initially applied with load control at a rate of 3 kN/sec and subsequently with displacement control at a rate of 10 microstrain/sec beyond initial softening until specimen failure. Figures 35(a) and (b) show the instrumentation and test setup used in this study. As can be seen in Fig. 35(a), the load eccentricity (e) was applied by two pin supports placed at top and bottom of the specimens. The bearing plates were 50 mm thick and 100 mm wide, and the cylinder roller had a diameter of 40 mm. This setup allowed the free rotation at the top and bottom surfaces of specimens, which was caused by eccentric loading. Two additional square flat plates (20 mm thick and 200 mm wide) were placed at top and bottom surface of specimens in order to evenly distribute load to the specimen. As can be seen in Fig. 35, pin supports were located at the centerline of the loading machine, which transfer the load along the middle of pin supports. The load eccentricity was achieved by adjusting the location of the specimen between the two pin supports.

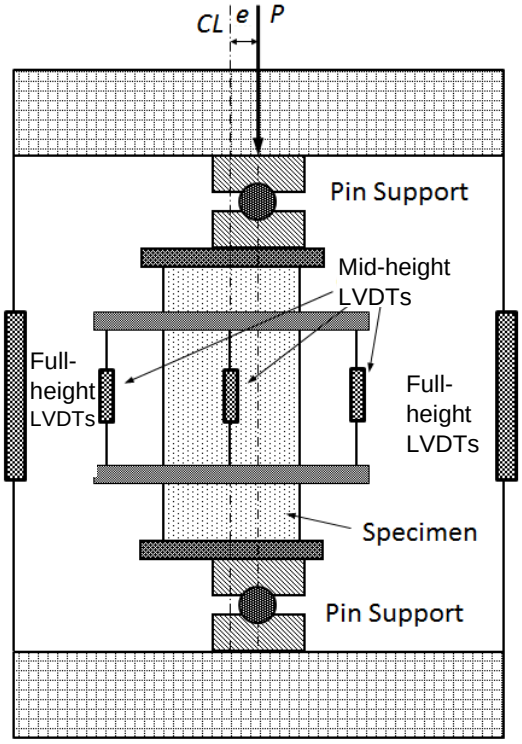
CL
e
P
Pin Support
Mid-height
LVDTs
Full-
height
LVDTs
Full-
height
LVDTs
Specimen
Pin Support

(a)

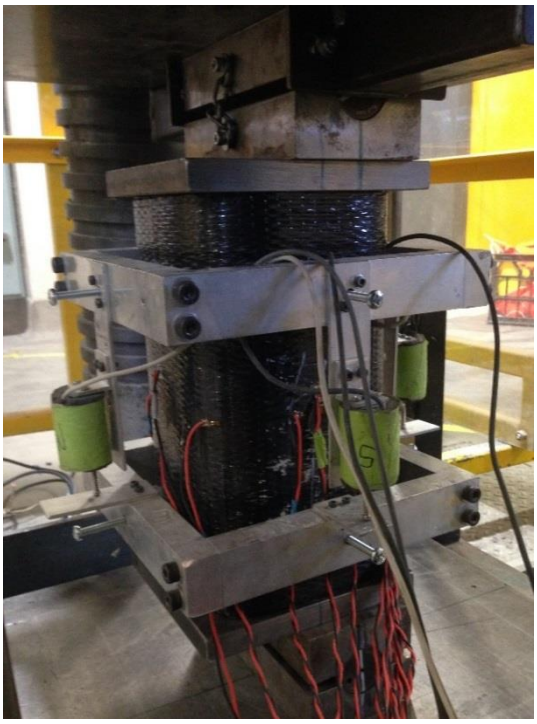

(b)

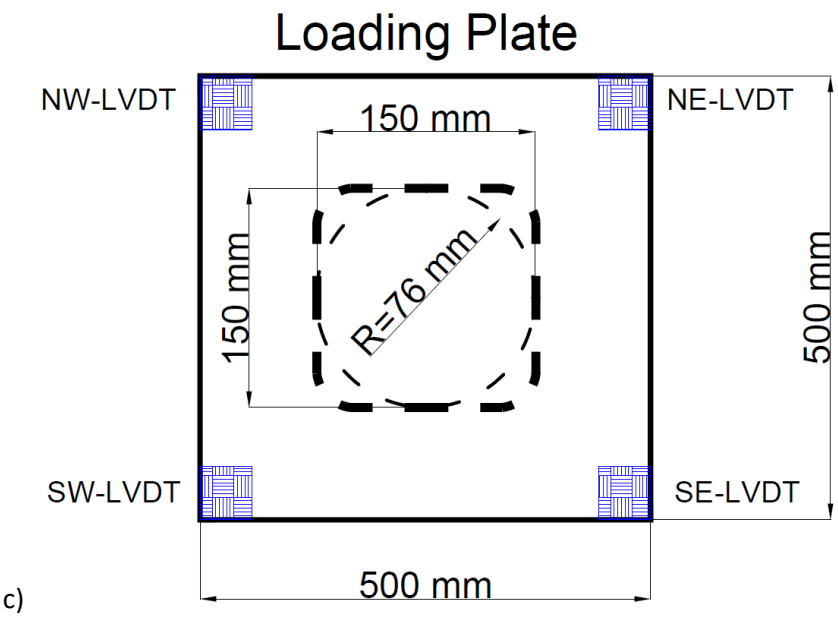
Loading Plate
NW-LVDT
NE-LVDT
150 mm
150 mm
R=76 mm
500 mm
SW-LVDT
SE-LVDT
500 mm

c)

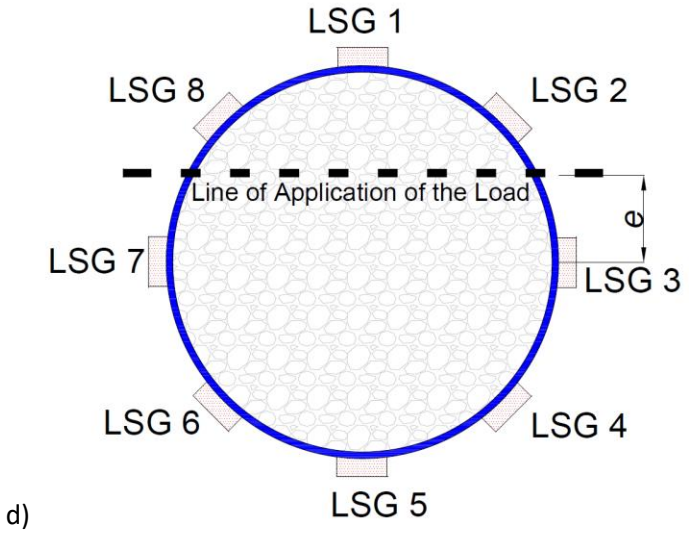

d)

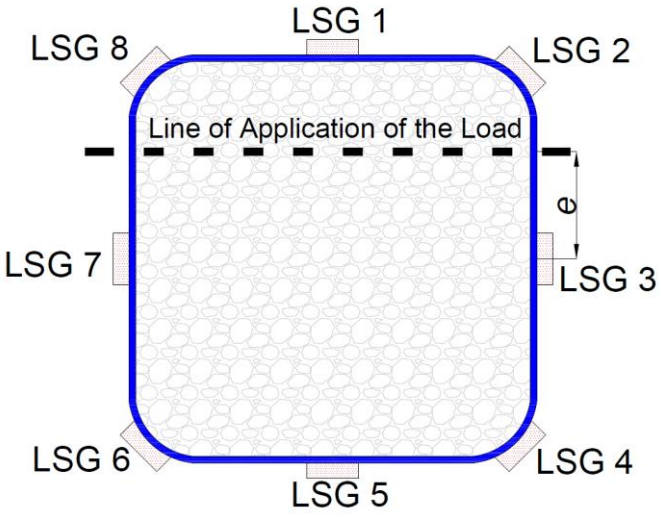

e)

Figure 35-Test setup for eccentrically loaded specimens: a) test setup; b) photo of actual test setup; c) location of full-height LVDTs in cross-section d) location of lateral strain gauges for circular specimens; e) location of lateral strain gauges for square specimens

The axial deformations of the specimens were measured by four linear variable displacement transformers (LVDTs) mounted at the corners of each specimen, between the loading and supporting steel plates of the compression testing machine (referred to as full-height LVDTs) as shown in Fig. 35(c). Additional four LVDTs were placed at mid-height of specimens within a gauge length of 175 mm (referred to as mid-height LVDTs). They were placed between two aluminium frames to measure the axial deformation of the middle portion of the specimens. The top and bottom aluminium frames were fixed to the specimen by tightening the screws to

make sure that the four mid-height LVDTs were symmetrically placed at the center of the specimen. Furthermore, four unidirectional strain gauges were placed at the mid-height of the specimen in the axial direction to validate LVDT measurements at the early stages of loading. Lateral strains were measured by eight unidirectional strain gauges placed at the mid-height of the specimens as shown in Fig. 35(d).

4.3 Test Results

4.3.1 Failure mode

Figure 36 shows typical failure modes of circular and square specimens under a lower (i.e. e ≤ 20 mm) and higher (e > 20 mm) eccentricity. The failure of the specimens occurred as a result of FRP rupture initiating at the compression side. Similar failure modes were evident for circular and square CFFTs under a given eccentricity. Concentrically loaded specimens failed suddenly and explosively by FRP rupture in the hoop direction around the mid-height of the specimen as discussed in detail in Ref. [140]. In square specimens the FRP rupture occurred near one of the column corners. As can be seen in Fig. 36(a), in the case of lower eccentricity, the specimens failed abruptly by the rupture of FRP tube in the hoop direction but with a less violent explosive sound compared to the failure of the concentric loaded specimen. On the other hand, the specimens with a higher eccentricity failed by the rupture of FRP tube at the compression side, while separations have been observed on the FRP tube among the horizontal FRP layers around the mid-height region of the specimen on the tension side (Fig. 36(b)). The failure occurred abruptly with a sudden loss of applied load recorded on the system, but without an explosive sound.

(a) (b)

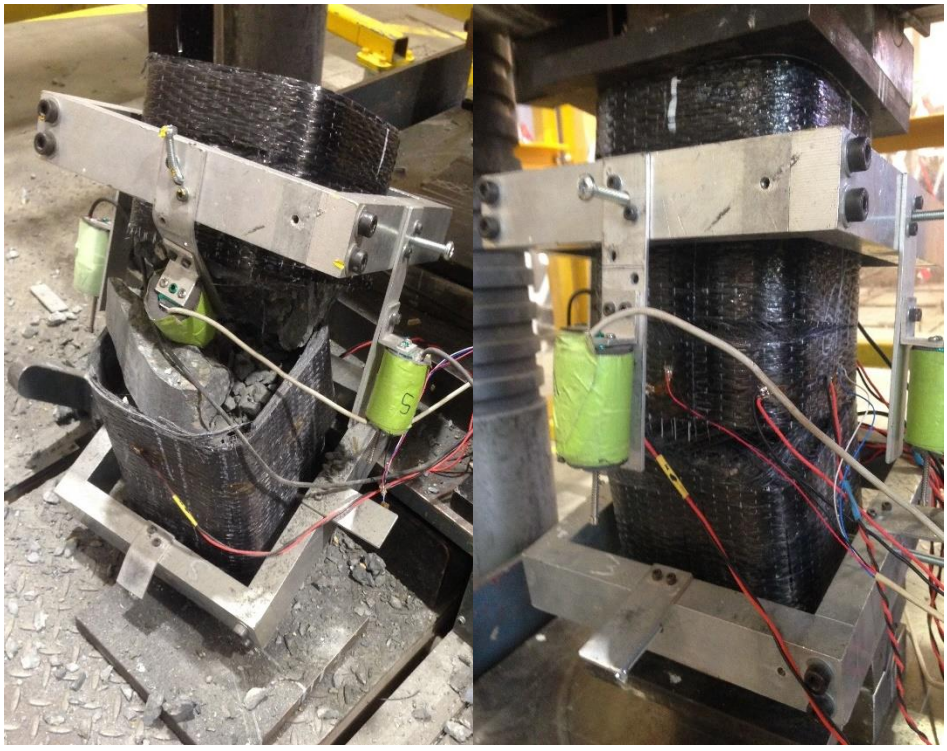

(c) (d)

Figure 36-Failure modes FRP-confined HSC with (a) circular cross-section under lower eccentricity, (b) circular cross-section under higher eccentricity, (c) square cross-section under lower eccentricity, (d) square cross-section under higher eccentricity square

4.3.2 Axial load-displacement curves

Figures 37(a) and 37(b) show the axial load-displacement curves of specimens with a circular and square cross-section under different target load eccentricities, respectively. Axial displacements were obtained at the point of loading along the height of the specimen from the average values of four full-height LVDTs. The measurements of load eccentricity applied to the specimens obtained during the tests showed that there were slight differences between the actual applied eccentricity (e) and the target eccentricity (e_t). Table 12 shows the measured eccentricity (e) (i.e. actual eccentricity) together with the recorded ultimate axial load and corresponding axial displacement for each test specimen configuration. It should be noted that test results for Specimens C3, C5, C6, C12, C16, and S15 were missed because of the problems experienced during their tests. It is evident from Figs. 37(a) and 37(b) that the load eccentricity had a significant influence on the behavior of FRP-confined HSC columns. Figure 38 shows the variation of the ultimate axial load and displacement of FRP-confined concrete with measured load eccentricity. It can be seen from the figure that the ultimate axial load and corresponding axial displacement at the point of loading decreased almost linearly with an increase in the load eccentricity. These reductions are as expected and attributed to the presence of bending loads and their increase with an increase in the eccentricity. In addition, although the rate of ultimate axial load reduction was similar for both circular and square specimens, the reduction of the ultimate axial displacement was higher in square specimens than that in circular specimens.

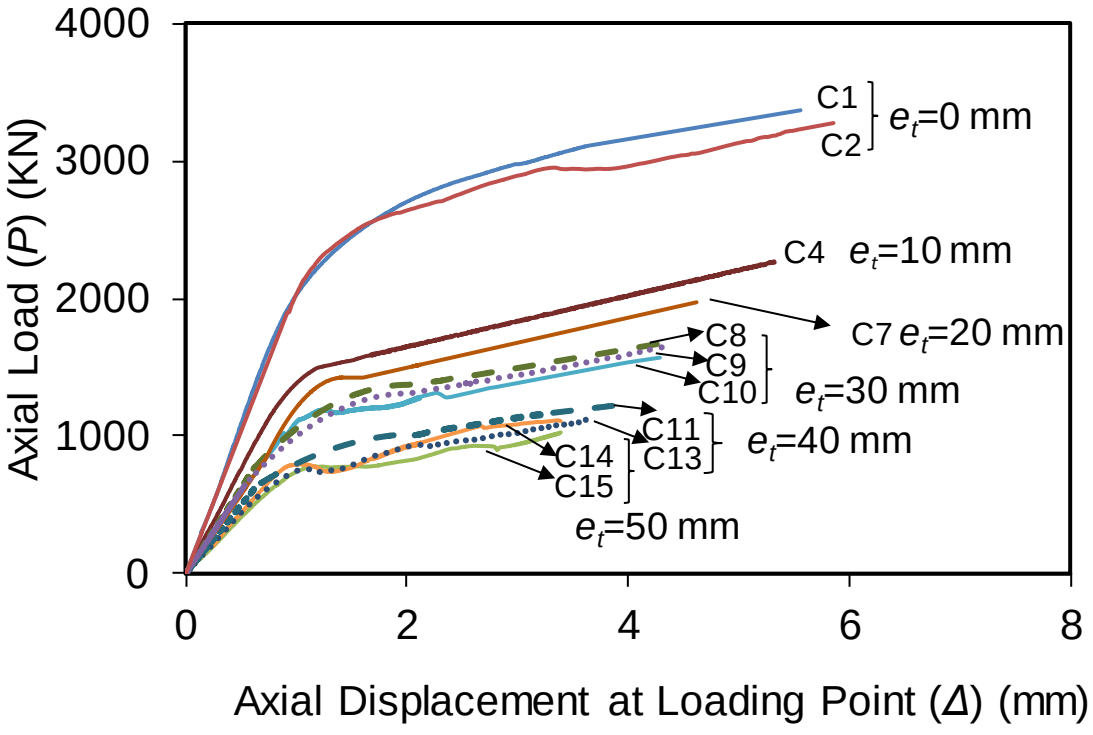

(a)

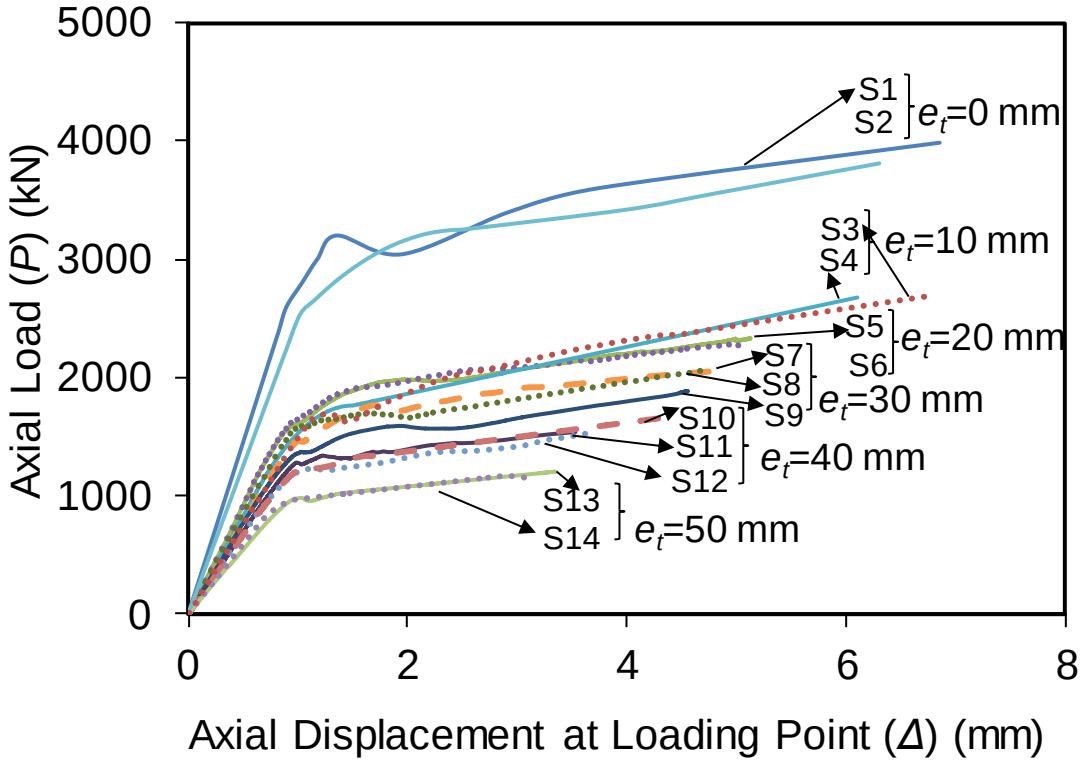

(b)

Figure 37- Experimental axial load-displacement curves of FRP-confined HSC with a) circular and b) square cross-section

Table 12-Results of compression tests

Specimen ID	Measured Eccentricity (mm)	Ultimate Axial Load (kN)	Axial Displacement* (mm)
C1	0	3370	5.5
C2	0	3266	5.9
C4	15	2411	5.3
C7	23	1972	4.7
C8	33	1650	4.3
C9	34	1570	4.3
C10	33	1545	4.3
C11	38	1218	3.9
C13	45	1127	3.7
C14	45	1113	3.4
C15	48	1025	3.4
S1	0	3989	6.7
S2	0	3810	6.3
S3	15	2677	6.1
S4	16	2699	6.8
S5	21	2283	5.1
S6	22	2332	5.0
S7	28	2074	5.0
S8	30	2058	4.7
S9	35	1885	4.6
S10	39	1656	4.3
S11	44	1534	3.6
S12	44	1537	3.5
S13	49	1191	3.3
S14	51	1152	3.1

* Measured by full-height LVDTs at the point of loading

Figures 39(a) and 39(b) show the axial load-displacement curves of two representative eccentrically-loaded specimens, one with a circular and one with a square cross-section, measured by full-height LVDTs installed at different positions. As can be seen in the figures, displacements measured by the two sets of LVDTs varied significantly along the direction perpendicular to the line of application of the load, which naturally resulted in a change in the lateral confinement effectiveness along the cross-section.

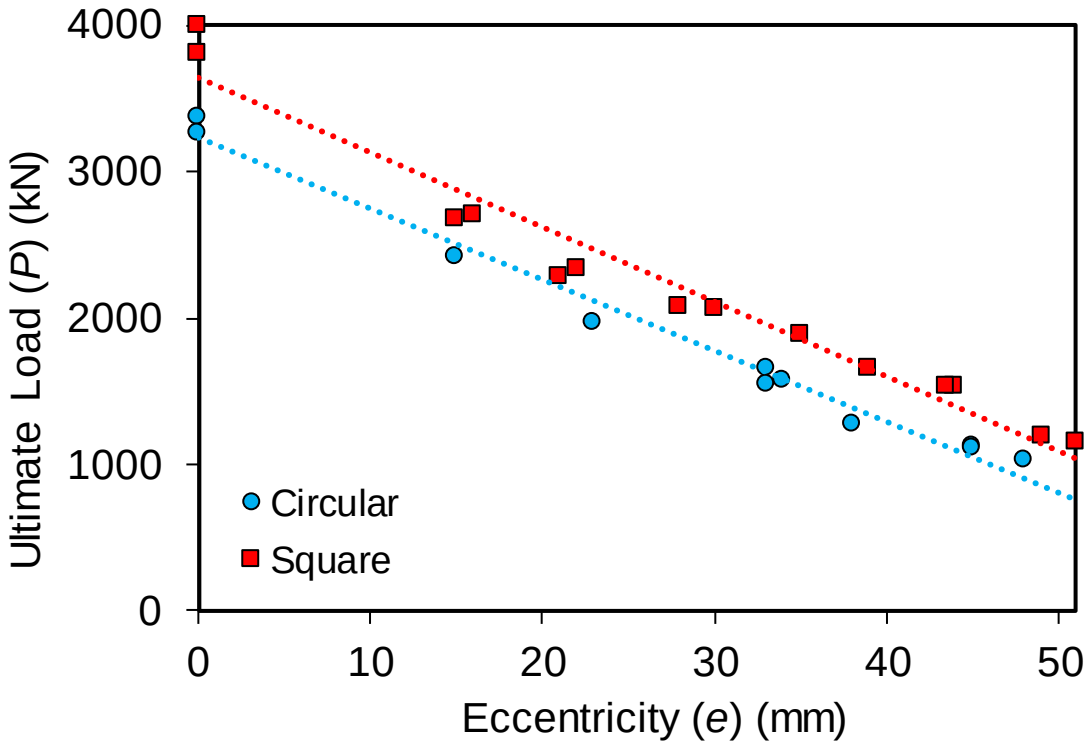

(a)

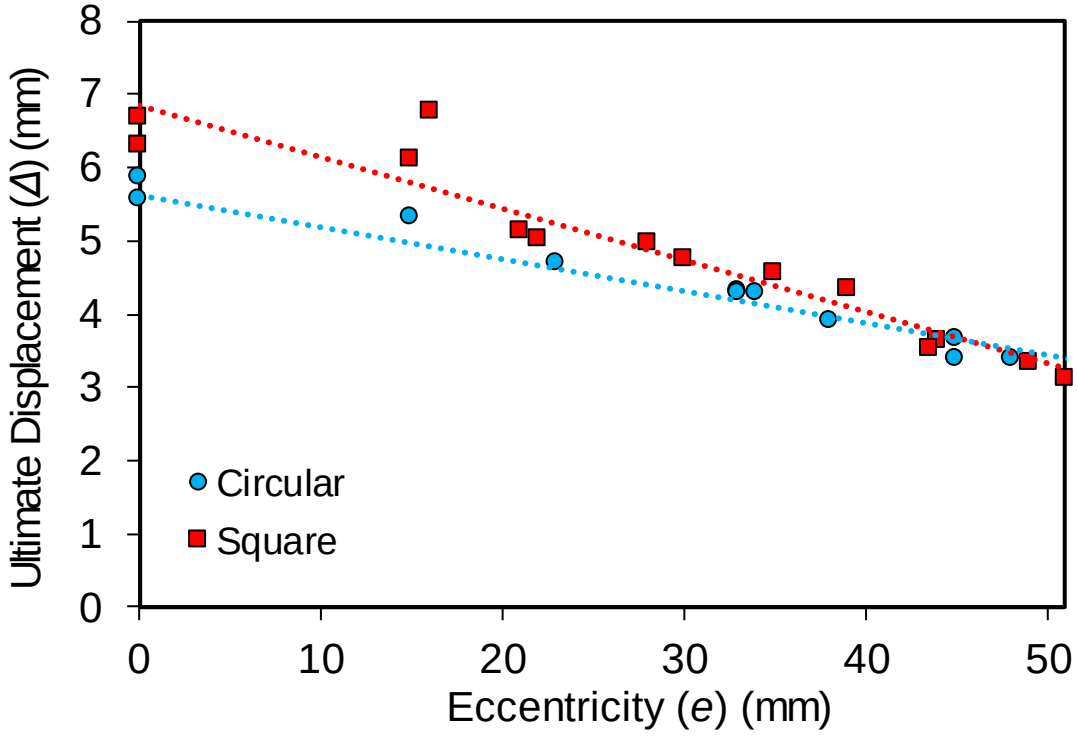

(b)

Figure 38- Variation of ultimate axial (a) load and (b) displacement at the point of loading with load eccentricity

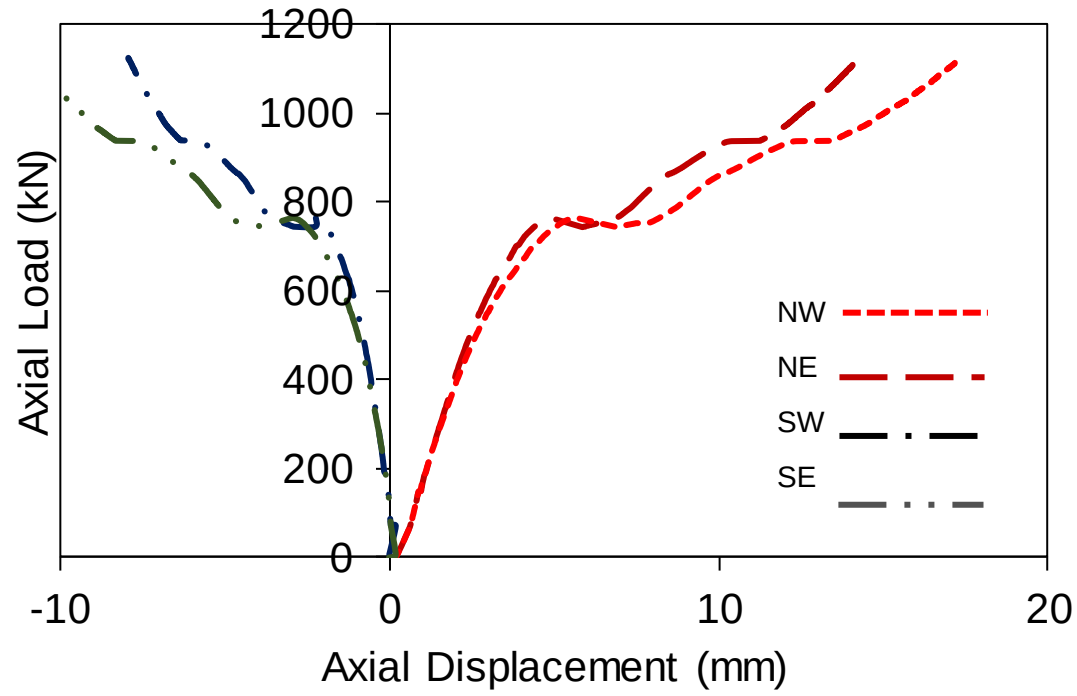

(a)

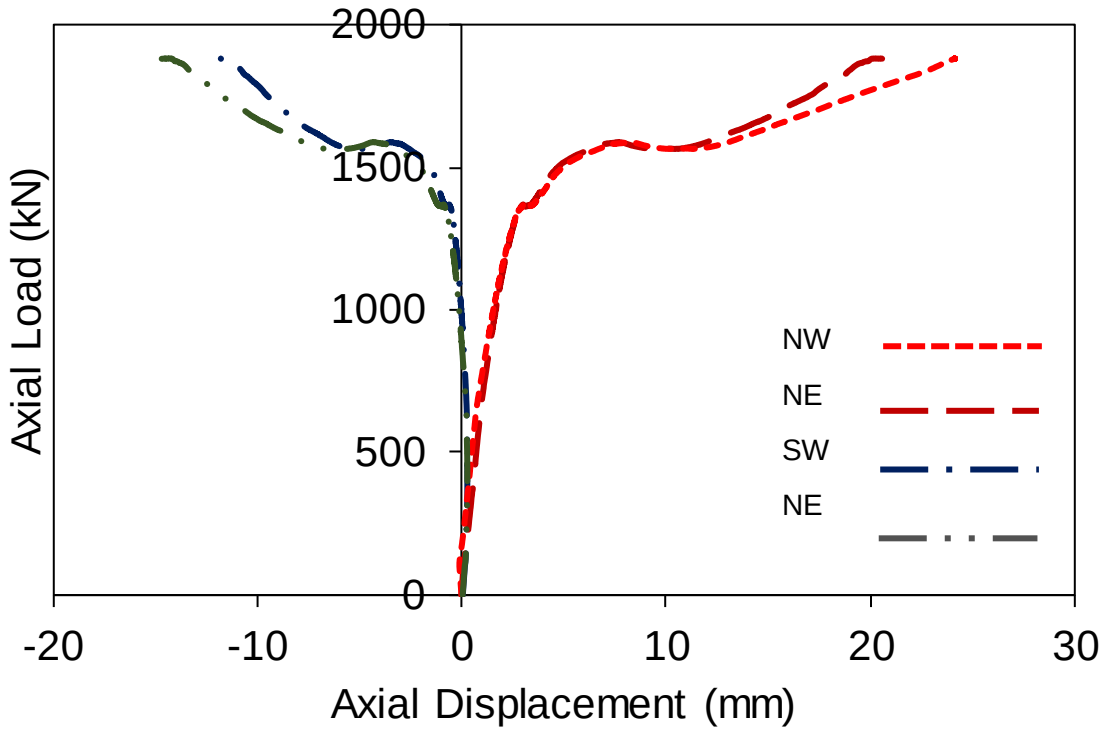

(b)

Figure 39- Axial load-displacement relationships measured by different full-height LVDTs: (a) circular (C13, *e* = 45 mm), (b) square (S9, *e* = 35 mm)

4.3.3 Axial load-lateral displacement and axial load-curvature curves

Figure 40 shows the axial load-lateral strain relationships of representative specimens (i.e. C9 and S6) at different strain gauge locations shown in Fig. 35(d). As can be seen in the figure, under eccentric loading, the maximum lateral strains were recorded at the extreme compression face and they decreased as the strain gauge location moved away from this section toward the extreme tension face.

In order to investigate the sectional bending behavior of FRP-confined concrete under eccentricity the variation of axial load with curvature is studied. Figures 41(a) and 41(b) show the axial load-curvature (determined from mid-height LVDTs) relationships of specimens with circular and square cross-section, respectively. It can be seen in the figures that, as expected, the ultimate curvature increased with an increase in the eccentricity, which translated to an increase in the bending moment.

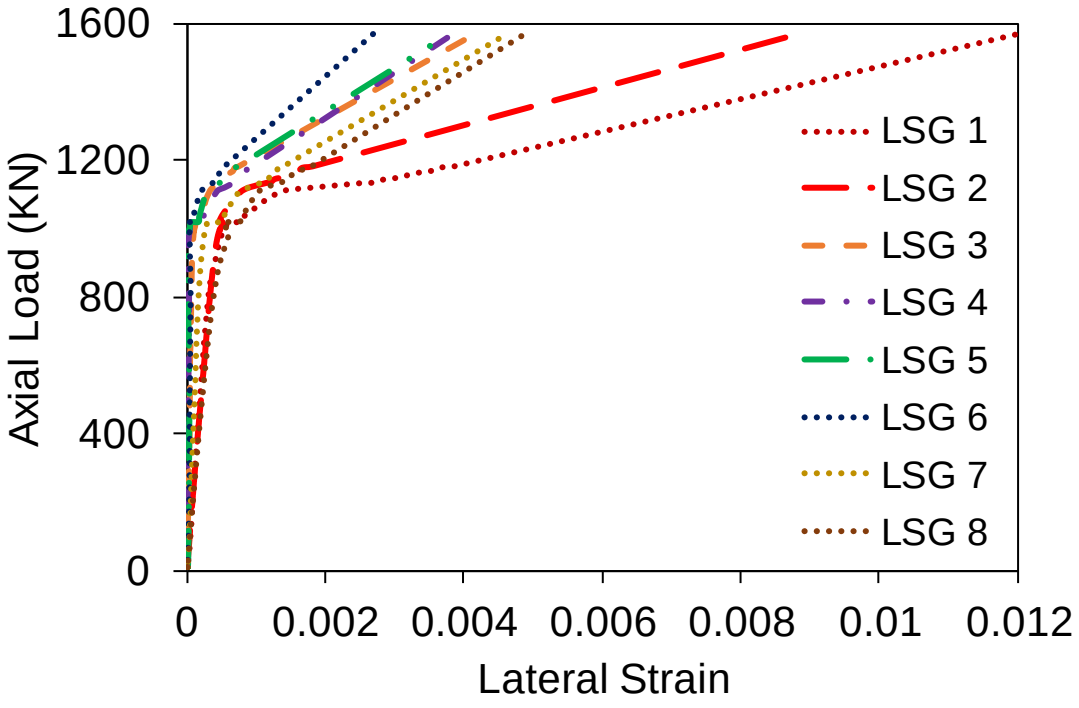

(a)

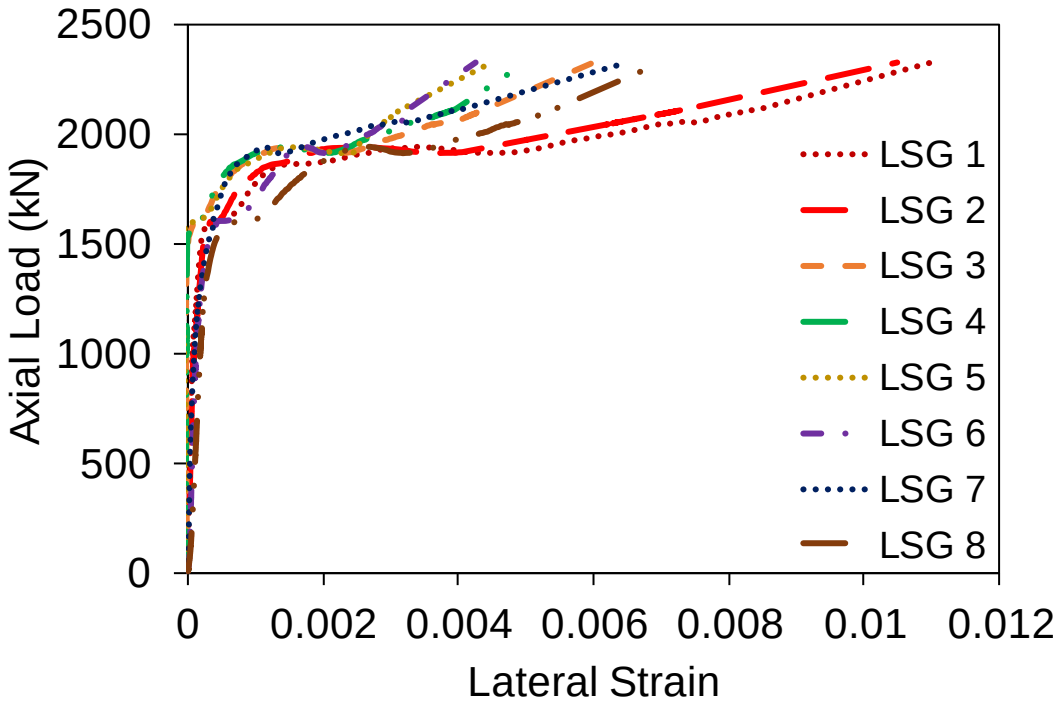

(b)

Figure 40- Axial load-lateral strain relationship of FRP-confined specimens at different positions of full-height LVDT: (a) circular (C9, *e* = 34 mm), (b) square (S6, *e* = 22 mm)

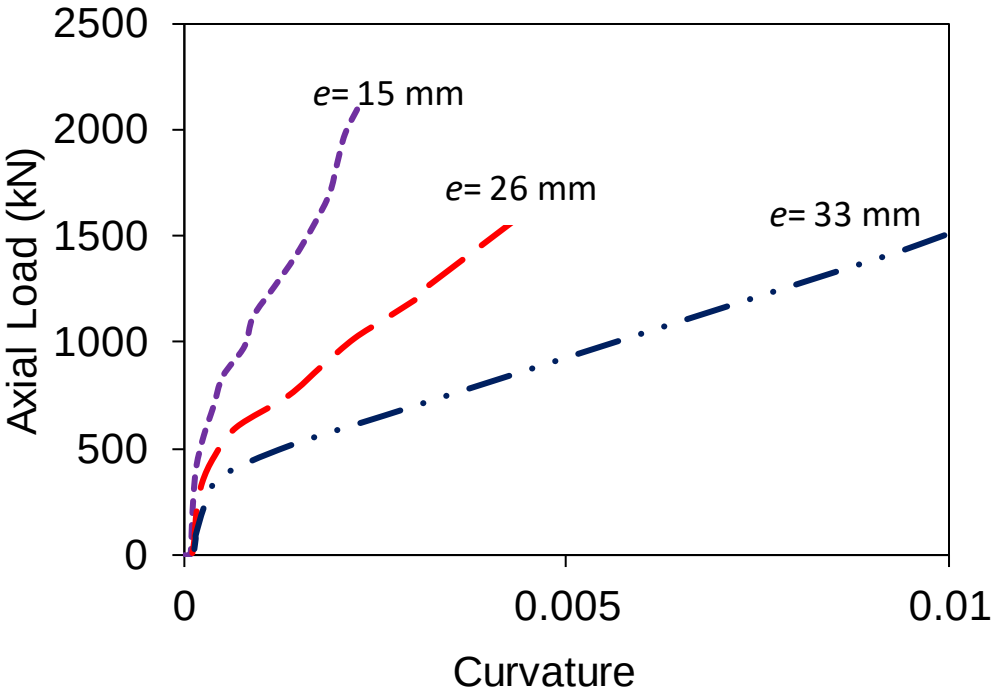

(a)

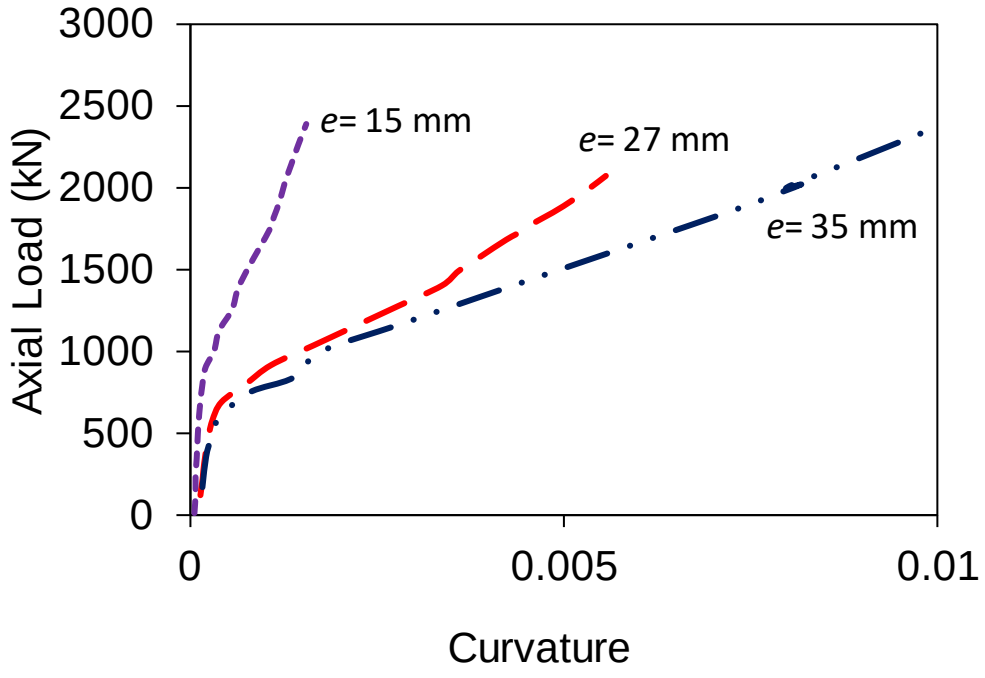

(b)

Figure 41- Axial load-curvature relationship of FRP-confined specimens with (a) circular and (b) square cross-sections

4.3.4 THEORETICAL LOAD-DISPLACEMENT CURVE AND EQUIVALENT AXIAL STRESS-STRAIN RELATIONSHIP

The use of axial stress-strain curves obtained by concentric loading leads to inaccurate predictions of the axial load-displacement of specimens in eccentric loading. As the stress-strain relationship of concrete changes along the depth of the cross-section, an equivalent axial stress-strain relationship that is representative of the entire cross-section of the concrete can be obtained to accurately predict the axial load-displacement curve. Figure 42 shows the typical cross-sectional stress and strain distributions of a circular and square concrete column under eccentric compression. It is well understood that axial stress-strain relationship of FRP-confined concrete columns highly depends on the uniformity of lateral confinement pressure [85, 86, 141]. As can be seen in Fig. 42, the stress and strain over the cross-section of FRP-confined concretes under eccentric loading are not distributed uniformly due to the load eccentricity. This strain gradient on the specimen cross-section results in a non-uniform dilation rate and confining pressure for confined concretes. This is the reason why the axial stress-strain models proposed for columns under concentric loading would not be able to accurately capture the behavior of those under eccentric compression.

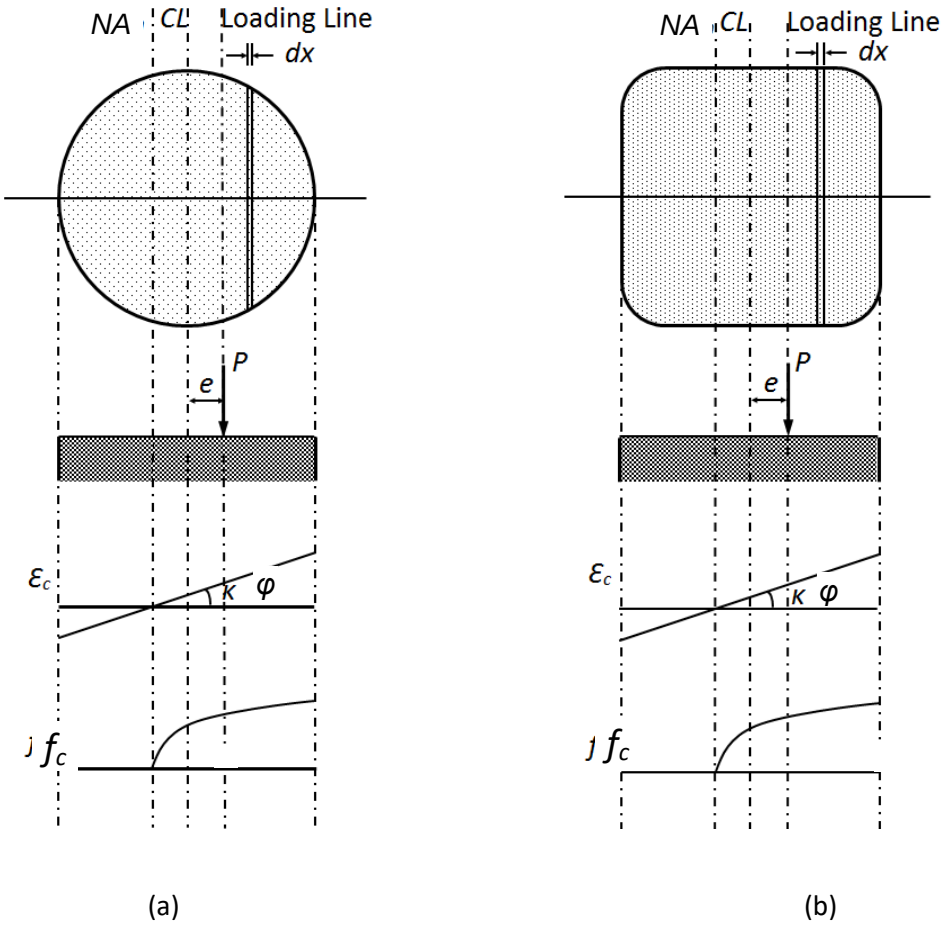

Figure 42-Sectional analysis: a) circular cross-section, b) square cross-section. ε_c, φ, P, e, *NA*, and *CL* are axial stress, axial strain, curvature, applied axial load, eccentricity, neutral axis, and center line of the cross-section, respectively

Figure 43 shows typical axial stress-strain relationships for unconfined and FRP-confined concrete to introduce the key properties on these curves. In this study, sectional analysis with an iterative procedure (Fig. 44) was conducted to obtain the axial stress-strain curves of FRP-confined HSC under eccentric loading based on the experimental data. An axial stress-strain relationship with an ascending branch and a linear second branch (with a slope of E_2), that transitioned at a point referred to as the transition point (defined by the axial strain ε_{ct} and the corresponding axial stress f'_{ct}) was first assumed. The theoretical load-displacement curves were subsequently obtained using the algorithm shown in Fig. 44.

As can be seen in Fig.44, the sectional analysis was adopted in this study to obtain the axial stress-strain curves (see Figs. 42 and 43). Concrete surface was assumed to remain plane and

the tensile strength of the concrete was ignored. Compressive stresses and strains were considered to be positive. Full-height LVDT readings averaged at both the compression and tension sides were used to determine the axial displacement at point of loading. Curvatures and locations of neutral axis of the cross-section were calculated using mid-height LVDT readings. It became evident from the careful study of the load eccentricities applied to the specimens in the tests that there were slight differences in measured and target eccentricities (e and e_t). The measured eccentricities (e) reported in Table 12 were determined from the test results along the initial elastic part of the load-displacement curve.

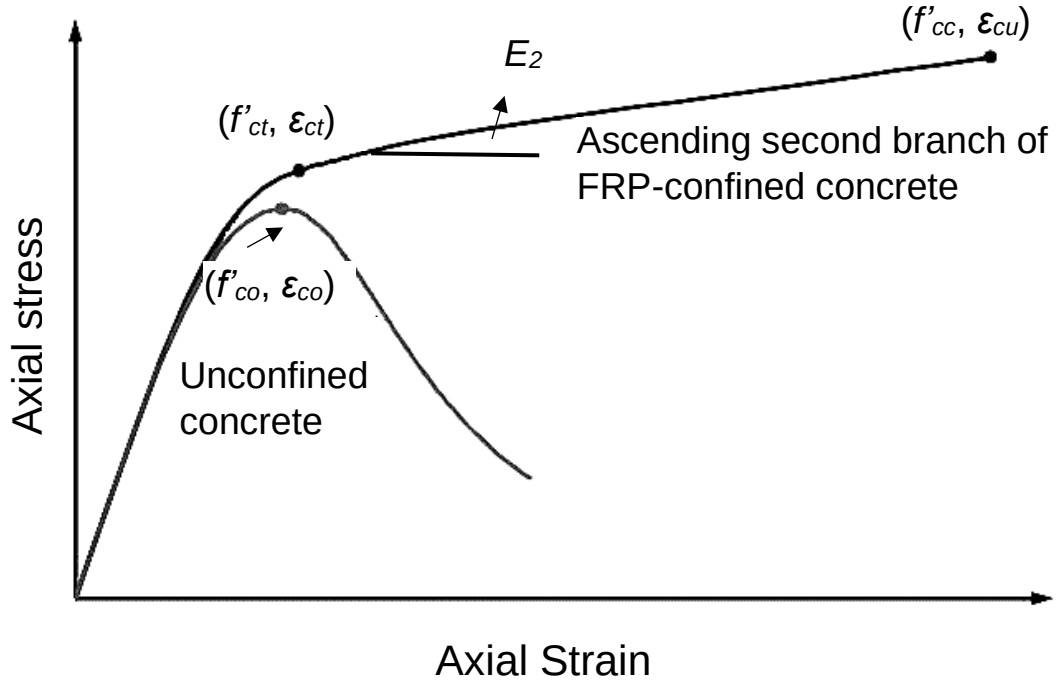

Figure 43- A typical axial stress-strain curve for unconfined and confined concrete

In the determination of axial stress-strain curves, cross-sections were divided into a large number of small layers (dx), as shown in Fig. 42. Second branch slope (E_2), transition stress (f'_{ct}), and corresponding strain (ε_{ct}) were first assumed using the values obtained under the concentric loading as the starting point. To obtain each point in the axial stress-strain curve, curvature (φ) and axial strain (ε_c) were calculated based on the axial displacement measured

by mid- and full-height LVDTs (Δ), respectively. The location of the neutral axis (*NA*) was then determined based on the obtained curvature and axial strain. Theoretical axial load (P_{th}) and moment (M_{th}) were calculated by Eqs. 4.1 and 4.2.

$$P_{th} = \int_{-D/2}^{D/2} f_{cj} dA \tag{4.1}$$

$$M_{th} = \int_{-D/2}^{D/2} f_{cj} y dA \tag{4.2}$$

where D is specimen cross-sectional dimension, f_{cj} is axial stress at the given layer of j, and y is the distance between the given layer and the centroid. The process was repeated until the specimen failure as a result of FRP rupture initiating at the compression side to produce the complete theoretical load-displacement curve. In cases where theoretical and experimental load-displacement curves were not in agreement, by adjusting E_2, f'_{ct}, or ε_{ct} the process was repeated until a close agreement between theoretical and experimental load-displacement curves is obtained.

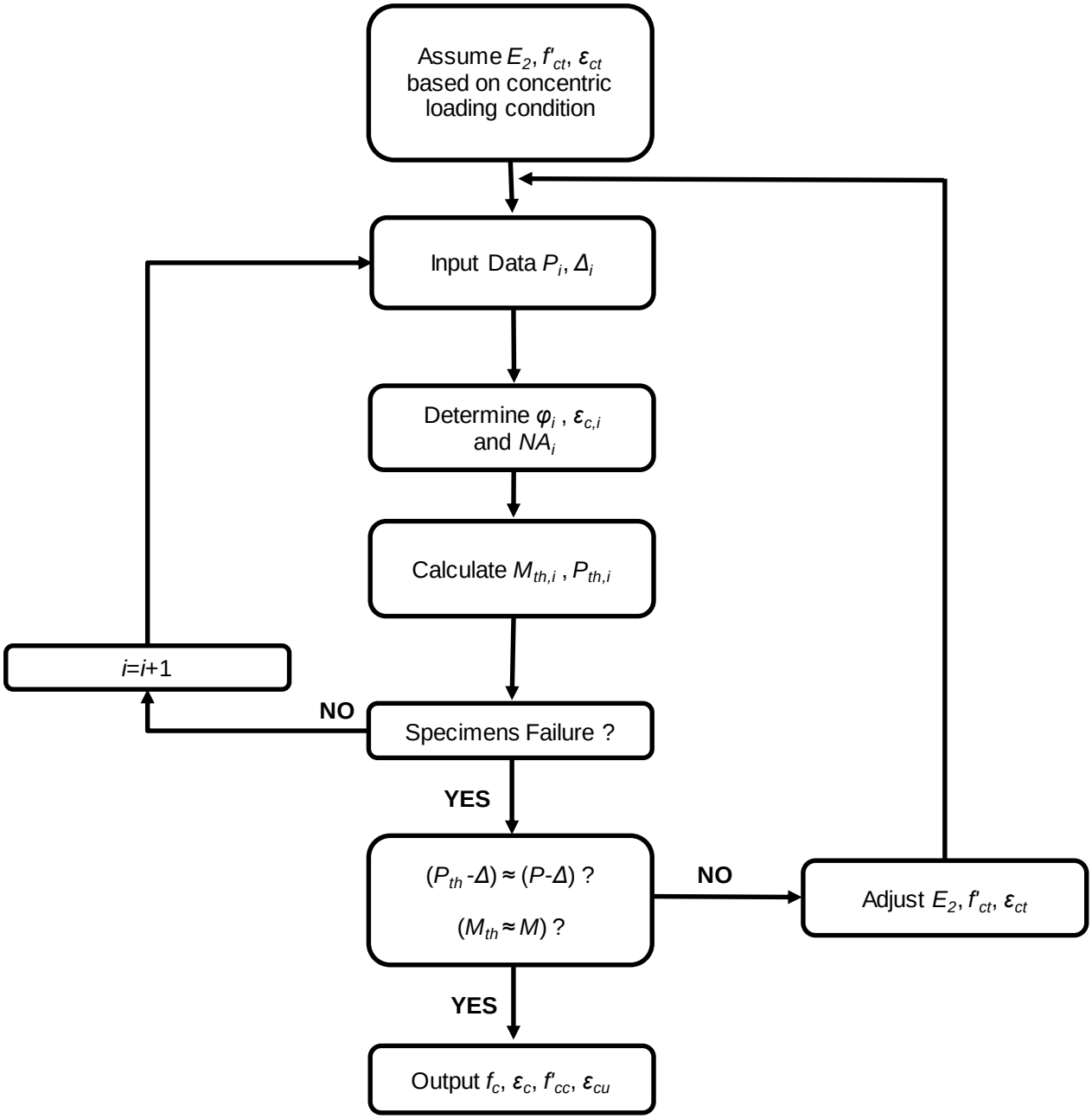

Figure 44- Flowchart for the determination of axial stress-strain curves. P, M, Δ, φ, NA, E_2, ε_{ct}, f'_{ct}, P_{th}, M_{th}, f_c, ε_c, f'_{cc}, and ε_{cu} are experimental axial load, experimental moment, axial displacement at loading point, curvature, location of neutral axis, second branch slope, axial strain at transition point, corresponding axial stress, theoretical axial load, theoretical moment, axial stress, corresponding axial strain, ultimate axial stress, and corresponding axial strain, respectively.

The parameters in the axial stress-strain curve (E_2, f'_{ct}, ε_{ct}) were finally adjusted by matching the theoretical and experimental load-displacement curve through regression analysis (see Appendix for more details). The Popovic's curve [128] was used for the initial ascending portion of the axial stress-strain curve. The second branch of the curve was obtained by

connecting the point of transition to the ultimate point (defined by the ultimate axial strain ε_{cu} and the corresponding axial stress f'_{cc}) through a straight line. Eq. 4.3 presents the adopted axial stress-strain relationship of FRP-confined concrete.

$$f_c = \begin{cases} f'_{ct}\frac{\varepsilon_c}{\varepsilon_{ct}}\left(\frac{n}{n-1+\left(\frac{\varepsilon_c}{\varepsilon_{ct}}\right)^n}\right) & \varepsilon_c \le \varepsilon_{ct} \\ f'_{ct} + E_2(\varepsilon_c - \varepsilon_{ct}) & \varepsilon_{ct} < \varepsilon_c < \varepsilon_{cu} \end{cases} \quad (4.3)$$

where ε_c and f_c represent the axial strain and stress, respectively, and n is defined by Eq. 4.4 [129]:

$$n = \frac{E_c}{E_c - \frac{f'_{ct}}{\varepsilon_{ct}}} \quad (4.4)$$

$$E_c = 4400\sqrt{f'_{co}} \quad (4.5)$$

where E_c and f'_{co} are the elastic modulus and unconfined concrete strength in MPa, respectively.

Figures 45(a) and 45(b) show the axial stress-strain curves obtained from the experimental axial load-displacement curves of specimens with circular and square cross-section tested under different load eccentricities, respectively. It should be noted that the ultimate axial strain is the axial strain obtained at specimen failure as a result of FRP tube rupture. As can be seen in Figs. 45(a) and 45(b), an increase in the load eccentricity led to an increase in ε_{cu} but a decrease in E_2, which translated to a reduced ultimate axial stress (f'_{cc}) for the specimens of this study. It can also be seen from the figures that f'_{ct} of circular specimen decreased slightly in the presence of load eccentricity, whereas f'_{ct} of square specimen remained mostly unchanged.

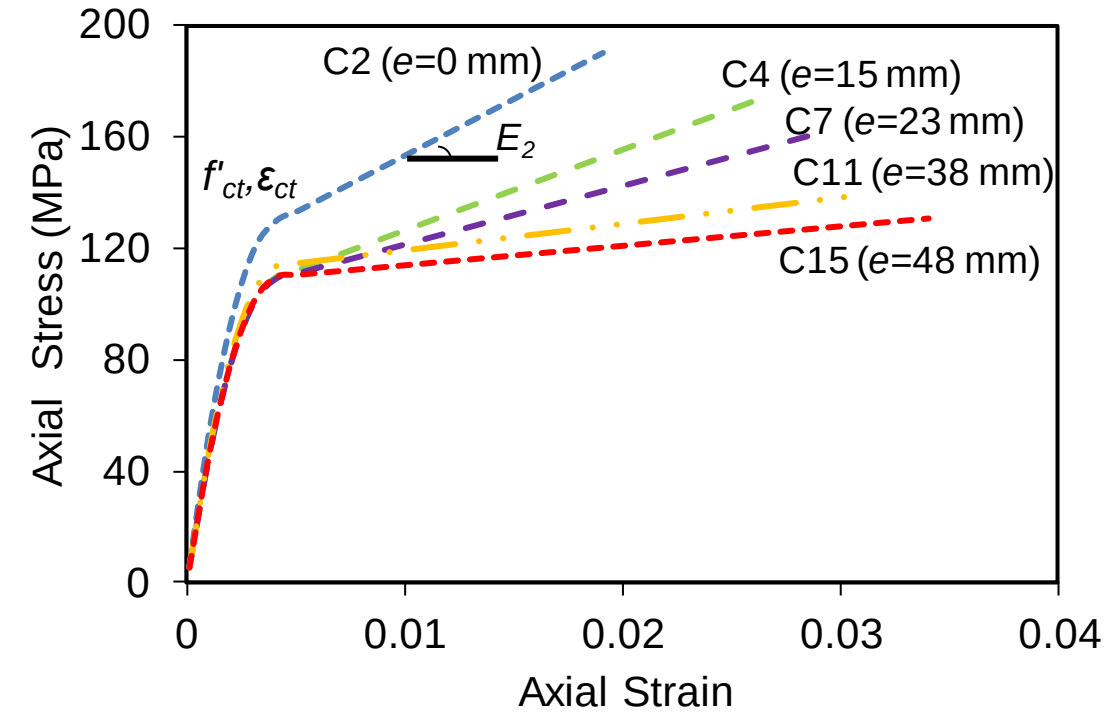

(a)

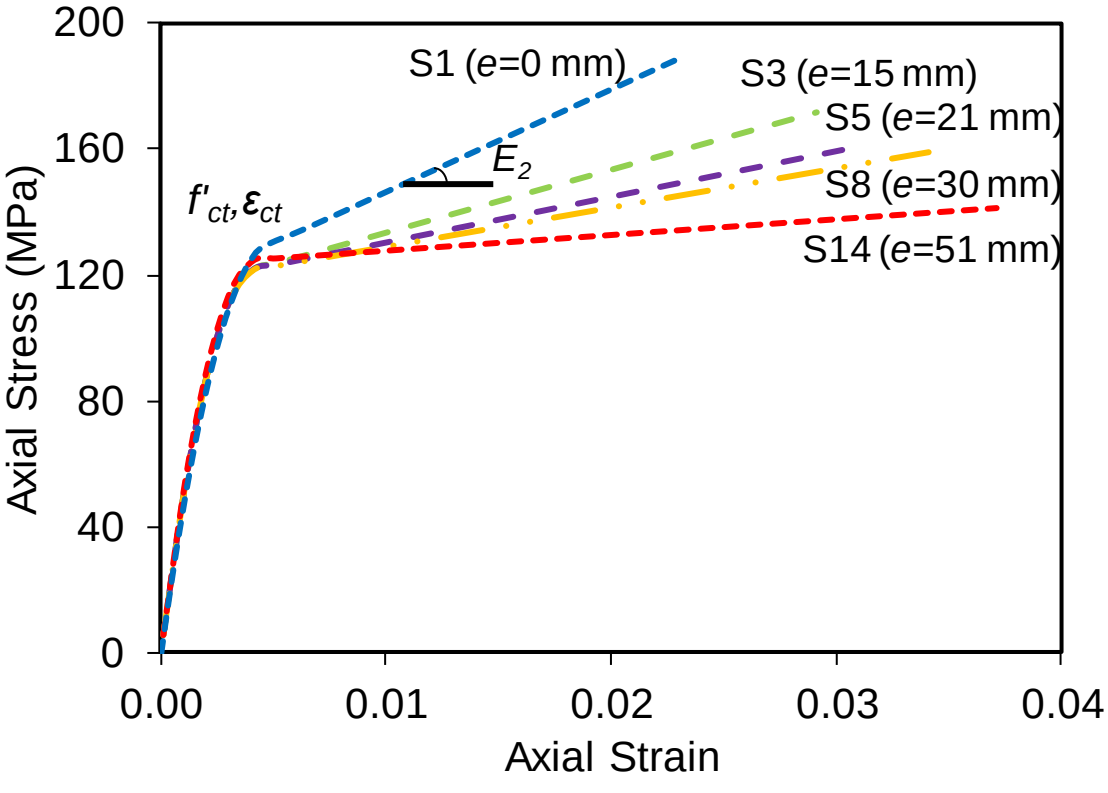

(b)

Figure 45- Axial stress-strain relationships of concretes under eccentricity: a) circular, b) square cross-section

Table 13 shows the variation of the ultimate axial stress and strain and the second branch slope with load eccentricity. As can be seen in the table, in the case of concentric loading (i.e. e = 0), the strength enhancement ratio (f'_{cc}/f'_{co}) of the FRP-confined concrete columns was approximately 1.80. It can also be seen in the table that for both circular and square specimens, f'_{cc}/f'_{co} decreased to approximately 1.30 with increasing e to 50 mm. Table 1 3 also shows that the axial strain enhancement ratio ($\varepsilon_{cu}/\varepsilon_{co}$) of concrete increased with an increase in e. These observations are discussed in detail in the following section.

Figure 46 illustrates the theoretical axial load-displacement curves obtained through the process outlined in Fig. 44 together with the experimental curves. As can be seen in the figure, the application of the proposed equivalent axial stress-strain curves resulted in accurate representations of the axial load-displacement curves of specimens under eccentric loading.

Table 13- Variation of key axial stress-strain curve parameters with eccentricity

Specimen ID	Measured Eccentricity (e) (mm)	2nd Branch Slope (E_2) (MPa)	Ultimate Axial Stress (f'_{cc}) (MPa)	Ultimate Axial Strain (ε_{cu})	Normalized 2nd Branch Slope ($E_2/E_{2,0}$)*	Normalized ultimate axial strain ($\varepsilon_{cu}/\varepsilon_{cu,0}$)**	Normalized ultimate axial stress ($f'_{cc}/f'_{cc,0}$) ***	Axial strain enhancement ratio ($\varepsilon_{cu}/\varepsilon_{co}$)	Strength enhancement ratio (f'_{cc}/f'_{co})
C1	0	4120	190.7	0.018	1.03	0.95	1.01	6.32	1.81
C2	0	3900	185.8	0.020	0.97	1.05	0.99	7.02	1.80
C4	15	2900	173.4	0.026	0.72	1.40	0.92	9.12	1.65
C7	23	2100	159.4	0.028	0.52	1.51	0.85	9.83	1.51
C8	33	1500	148.9	0.029	0.37	1.54	0.79	10.18	1.41
C9	34	1100	143.3	0.030	0.27	1.60	0.76	10.53	1.36
C10	33	1250	142.1	0.030	0.31	1.60	0.75	10.53	1.35
C11	38	950	138.7	0.030	0.24	1.62	0.74	10.53	1.32
C13	45	900	135.2	0.032	0.22	1.72	0.72	11.23	1.28
C14	45	750	138.3	0.031	0.19	1.67	0.73	10.88	1.31
C15	48	700	130.2	0.033	0.17	1.77	0.69	11.58	1.23
S1	0	3750	183.4	0.023	1.07	1.04	1.02	8.07	1.75
S2	0	3250	175.1	0.021	0.93	0.96	0.98	7.37	1.67
S3	15	2250	164.4	0.029	0.64	1.30	0.92	10.18	1.54
S4	16	2000	170.2	0.028	0.57	1.30	0.95	9.83	1.60
S5	21	1450	162.3	0.032	0.41	1.46	0.91	11.23	1.53
S6	22	1450	158.2	0.029	0.41	1.34	0.88	10.18	1.49
S7	28	1350	156.3	0.033	0.39	1.49	0.87	11.58	1.47
S8	30	1250	158.6	0.034	0.36	1.53	0.88	11.93	1.50
S9	35	1150	151.6	0.034	0.33	1.53	0.85	11.93	1.43
S10	39	1110	147.2	0.033	0.32	1.52	0.82	11.58	1.39
S11	44	650	144.5	0.034	0.19	1.57	0.81	11.93	1.37
S12	44	600	140.3	0.035	0.17	1.58	0.78	12.28	1.33
S13	49	550	141.1	0.037	0.16	1.70	0.79	12.98	1.34
S14	51	500	141.2	0.037	0.14	1.67	0.79	12.98	1.34

* $E_{2,0}$ is the second branch slope of the specimen under concentric loading

** $\varepsilon_{cu,0}$ is the ultimate axial strain of the specimen under concentric loading

*** $f'_{cc,0}$ is the ultimate axial stress of the specimen under concentric load

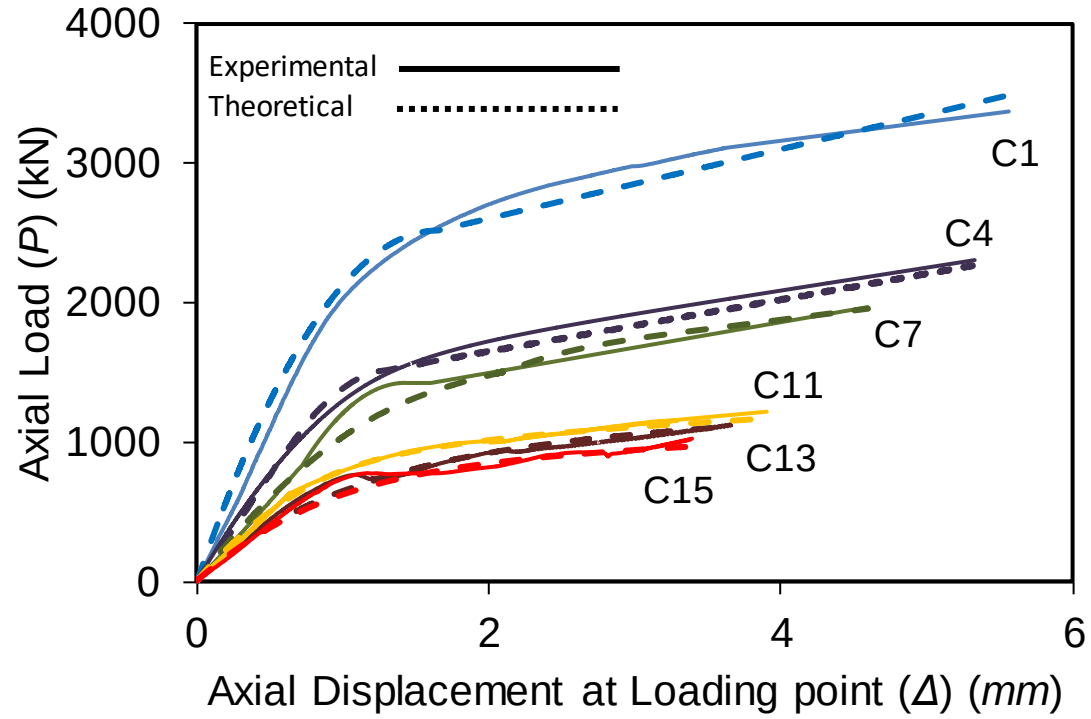

(a)

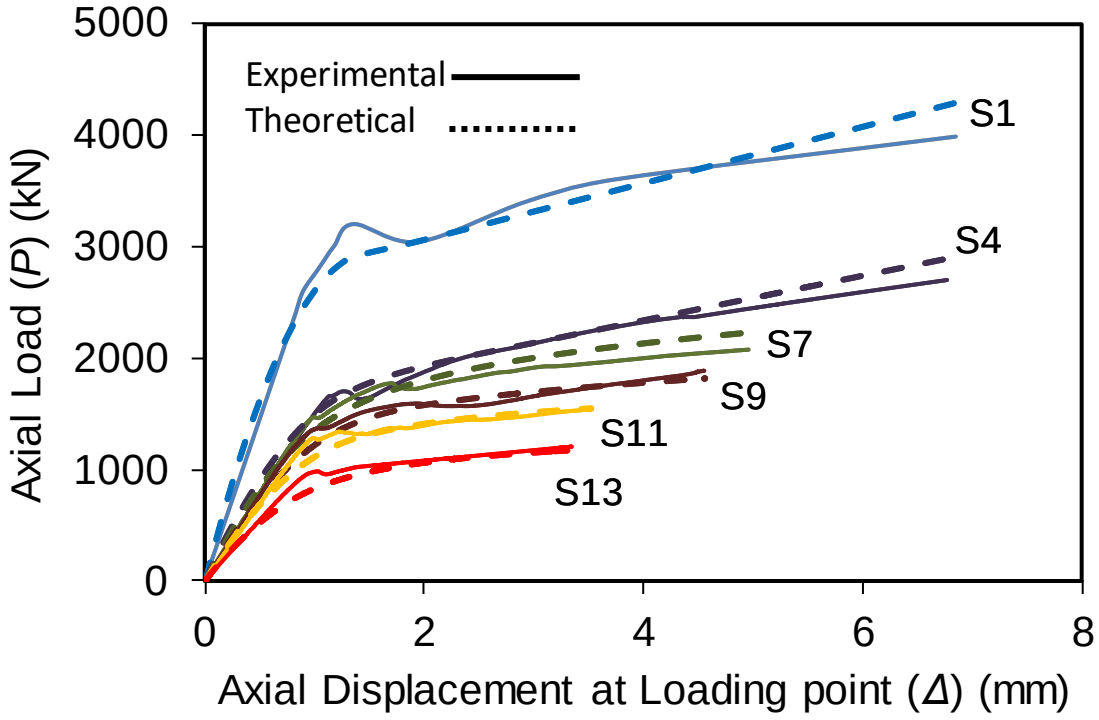

(b)

Figure 46- Comparison of experimental and theoretical axial load-displacement curves: a) circular, b) square cross-section

4.4 Discussion

4.4.1 Relationship between the second branch slope and load eccentricity

Figure 47 shows the variation of normalized second branch slope ($E_2/E_{2,0}$, where $E_{2,0}$ is the second branch slope of the specimen under concentric loading) of FRP-confined concrete with normalized eccentricity (e/R, where R is the cross-sectional radius). As can be seen in the figure, $E_2/E_{2,0}$ of FRP-confined concrete decreased almost linearly with an increase in e/R. Based on the regression analysis, it was found that the relationship between $E_2/E_{2,0}$ and e/R can be expressed by Eq. 4.6.

$$\frac{E_2}{E_{2,0}} = 1 - k_{e,E}\left(\frac{e}{R}\right) \tag{4.6}$$

where $k_{e,E}$ is eccentricity coefficient for the second branch slope of axial stress-strain relationship. As can be seen from Fig. 47, $k_{e,E}$ of the circular and square specimens is approximately the same, indicating that the second branch slope of axial stress-strain relationship is geometry independent within the parametric ranges investigated in the current study. The specific expressions shown in Fig. 47 are not intended as general model expressions, but they are trend-line equations that describe the behaviors of the specimens tested in the current study.

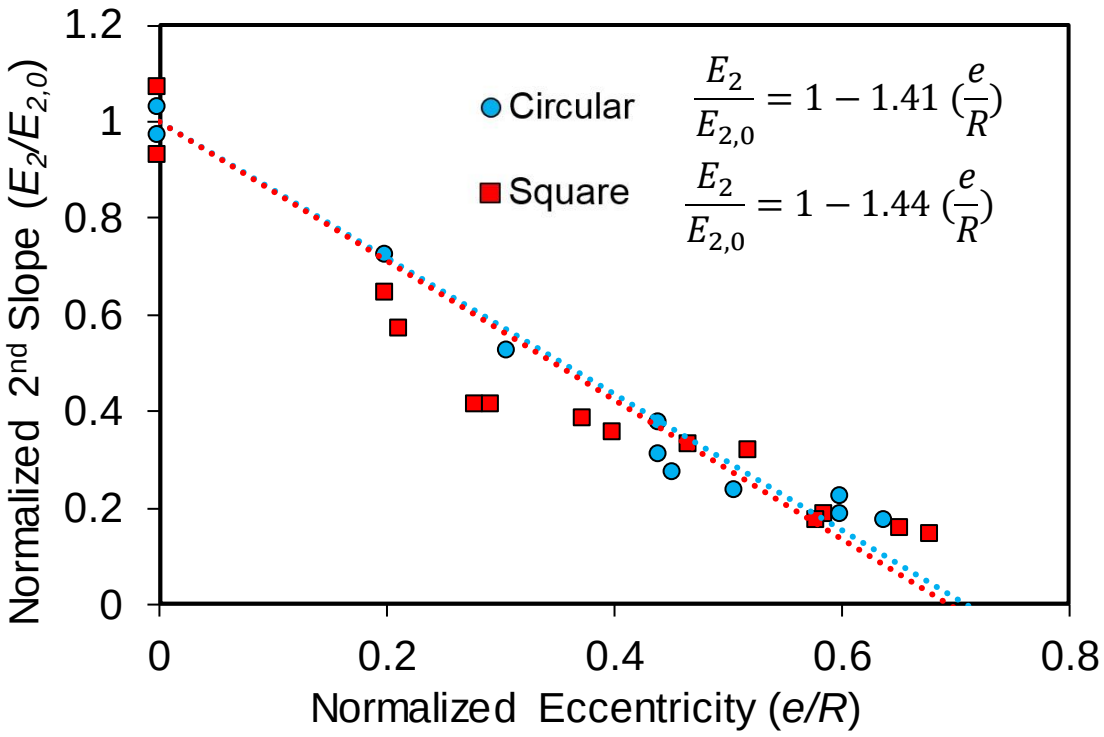

Figure 47- Variation of normalized second branch slope with normalized eccentricity

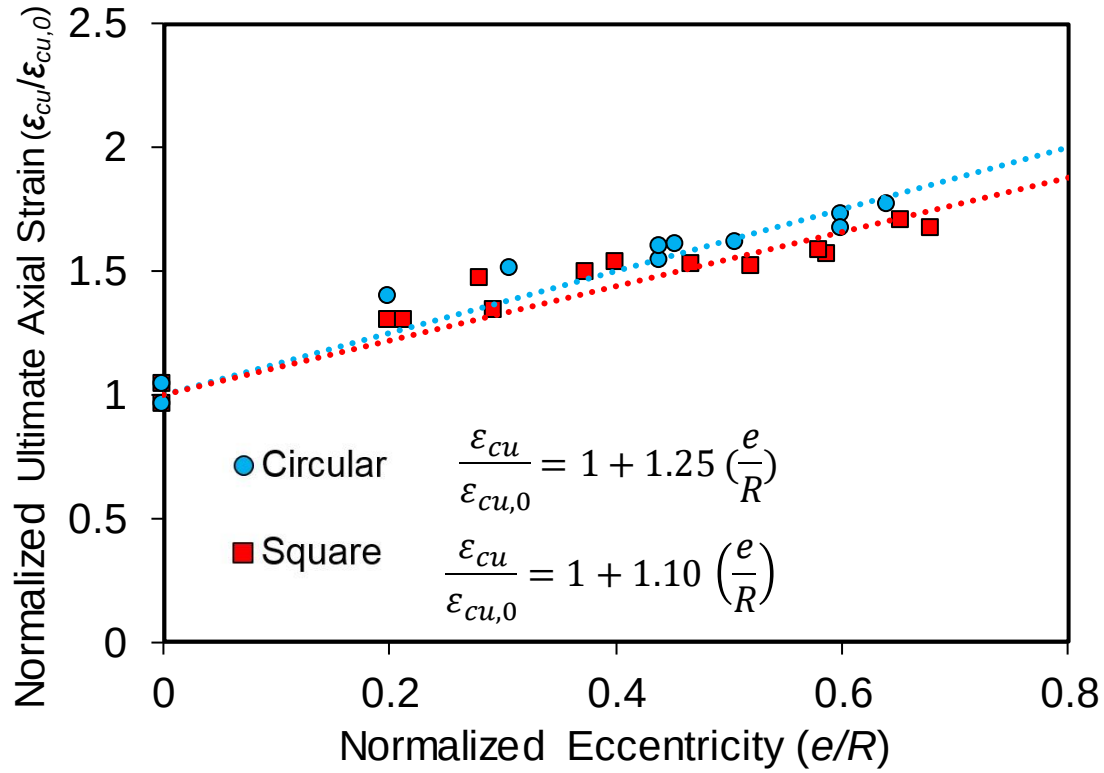

Figure 48- Variation of normalized ultimate axial strain with normalized eccentricity

4.4.2 Relationship between the ultimate axial strain and stress and load eccentricity

Figure 48 illustrates the relationship between normalized ultimate axial strain ($\varepsilon_{cu}/\varepsilon_{cu,0}$, in which $\varepsilon_{cu,0}$ is the ultimate axial strain of the specimens under concentric loading) and e/R of specimens with circular and square cross-sections. It can be seen from the figure that $\varepsilon_{cu}/\varepsilon_{cu,0}$ increased almost linearly with an increase in e/R, and the shape of the cross-section had only a marginal effect on the trend. The relationship between $\varepsilon_{cu}/\varepsilon_{cu,0}$ and e/R can be expressed by Eq. 4.7.

$$\frac{\varepsilon_{cu}}{\varepsilon_{cu,0}} = 1 + k_{e,\varepsilon}\left(\frac{e}{R}\right) \tag{4.7}$$

where $k_{e,\varepsilon}$ is the eccentricity coefficient for the ultimate axial strain.

Figure 49 shows the variation of the normalized ultimate axial stress ($f'_{cc}/f'_{cc,0}$, where $f'_{cc,0}$ is the ultimate axial stress of the specimens under concentric loading) with e/R. Eq. 6 presents the linearly decreasing trend of the ultimate axial stress with increasing eccentricity as seen in the figure.

$$\frac{f'_{cc}}{f'_{cc,0}} = 1 - k_{e,f}\left(\frac{e}{R}\right) \tag{4.8}$$

where $k_{e,f}$ is eccentricity coefficient for the ultimate axial stress. As can be seen in Fig. 49, circular and square specimens showed a similar trend. It can also be seen in the figure that f'_{cc} of circular specimens decreased more significantly than those of square specimens with an increase in the eccentricity. Once again, the equations given in Figs. 48 and 49 should not be treated as general model expressions, as these relationships are expected to be influenced by the confinement parameters such as the normalized confinement ratio (f_{lu}/f'_{co}, where f_{lu} is the ultimate confining pressure).

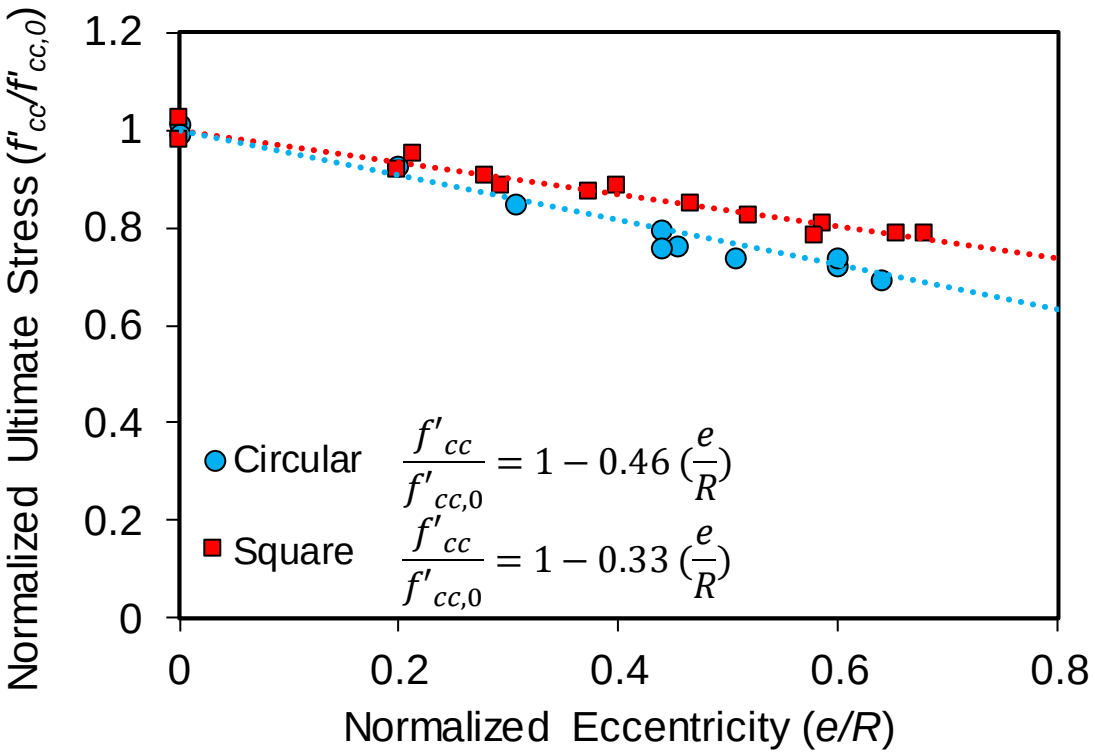

Figure 49-Variation of normalized ultimate axial stress with normalized eccentricity

4.4.3 Relationship between the transition stress and strain and load eccentricity

Figure 50 shows the variation of normalized stress at transition point ($f'_{ct}/f'_{ct,0}$, in which $f'_{ct,0}$ is the transition stress of the specimens under concentric loading) with e/R. As can be seen from the figure, $f'_{ct}/f'_{ct,0}$ of the circular specimens decreased slightly in the presence of load eccentricity, but the ratio remained mostly unchanged (i.e. 0.87) under different load eccentricities. It can also be seen in the figure that $f'_{ct}/f'_{ct,0}$ of FRP-confined specimens with square cross-sections remained nearly constant (i.e. 0.97) under different load eccentricities. Figure 51 shows the variation of normalized strain at transition point ($\varepsilon_{ct}/\varepsilon_{ct,0}$, in which $\varepsilon_{ct,0}$ is the transition strain of the specimens under concentric loading) with e/R. It can be seen from the figure that $\varepsilon_{ct}/\varepsilon_{ct,0}$ of the circular specimens increased slightly in the presence of load eccentricity, but it remained mostly unchanged (i.e. 1.09) under different load eccentricities. It can also be seen in the figure that $\varepsilon_{ct}/\varepsilon_{ct,0}$ of FRP-confined square specimens remained nearly constant (i.e. 1.02) under different load eccentricities. These observations indicate that the

load eccentricity had only a limited influence on the axial stress and strain of FRP-confined HSC at the transition point.

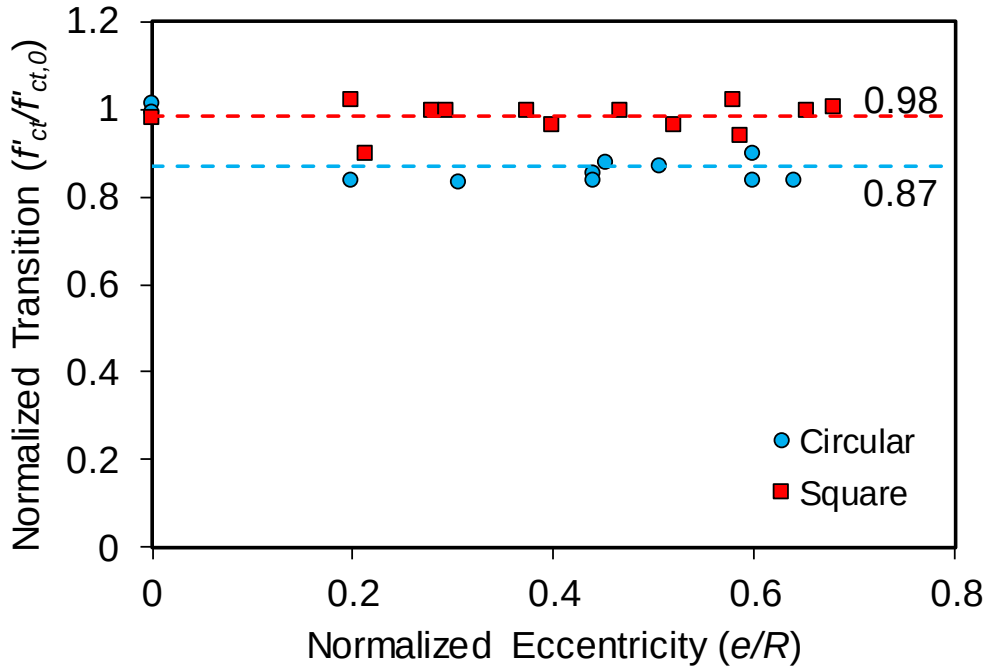

Figure 50- Variation of normalized ultimate axial stress with normalized eccentricity

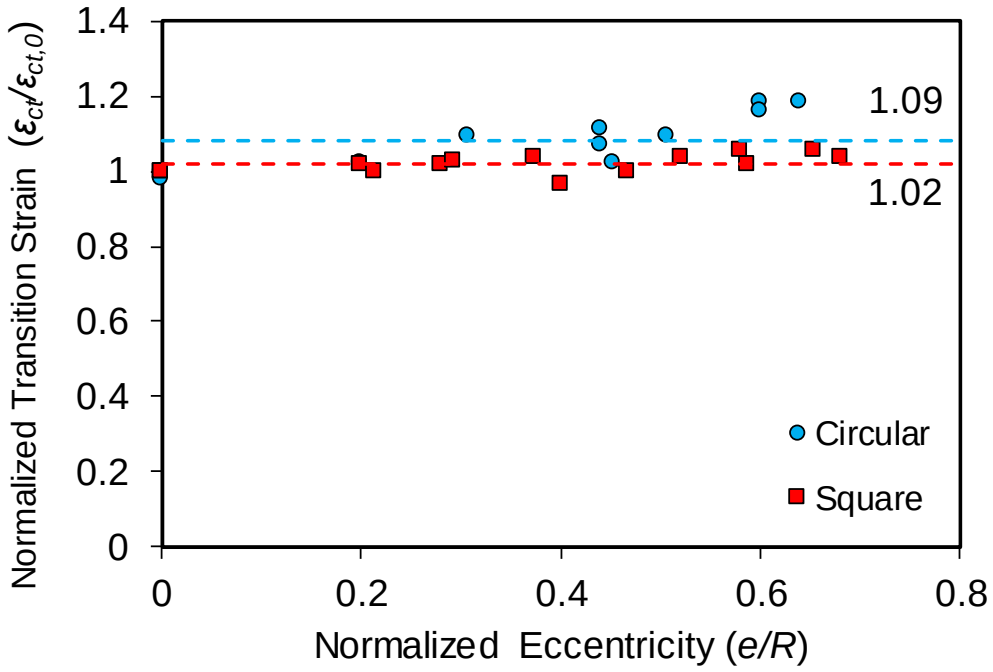

Figure 51- Variation of normalized transition strain with normalized eccentricity

4.5 Conclusion

Based on the results presented in this section, the following conclusions can be drawn：

1. Load eccentricity significantly affects the behavior of FRP-confined HSC columns under axial compression. An increase in load eccentricity leads to a decrease in the ultimate axial load and displacement at the point of loading.
2. An increase in the load eccentricity results in an increase in the ultimate axial strain but a decrease in the second branch slope of the axial stress-strain curve, which resulted in a reduced ultimate axial stress in the specimens of the current study.
3. The ultimate axial strain increases and ultimate axial stress and second branch slope of the axial stress-strain curves decrease almost linearly with an increasing eccentricity.
4. The transition stress and strain of axial stress-strain curves of FRP-confined HSC specimens with square cross-section remain mostly unchanged under load eccentricity. In specimens with circular cross-section these values slightly decrease and increase, respectively, in the presence of load eccentricity, and they remain mostly unchanged under different load eccentricities.

Because of the relatively significant influence of the load eccentricity on the axial stress-strain behavior of FRP-confined concrete, caution is required when applying the concentric axial stress-strain models of FRP-confined concrete to predict the behavior of members under load eccentricity. Additional focused studies are recommended on eccentrically loaded FRP-confined concrete columns to expand the currently limited test database, so that reliable stress-strain models incorporating the effect of eccentricity can be developed.

Chapter 5: Investigation of the compressive behavior and failure mode of unconfined and FRP-confined concrete using digital image correlation

(A paper is published based on this section: Fallah Pour A, Nguyen GD, Vincent T, Ozbakkaloglu T. Investigation of the compressive behavior and failure modes of unconfined and frp-confined concrete using digital image correlation. Compos Struct. 2020:112642 (DOI: 10.1016/j.compstruct.2020.112642))

5.1 Introduction

The lateral confinement of concrete columns with fiber-reinforced polymer (FRP) sheets significantly enhance their compressive strength and axial strain capacity. During the past two decades, the use of FRP composite as confinement reinforcement in retrofitting existing concrete columns has been studied extensively in parallel with the development of new high-performance composite columns [15, 88, 89, 92, 102, 111, 131]. Over 500 studies have been performed on the behavior of FRP-confined concrete columns under concentric axial compression loading as is shown in a recent comprehensive review of literature undertaken by Ozbakkaloglu, Lim [16]. These studies have resulted in the development of over 110 stress-strain models to predict the axial compressive behavior.

However, even the most accurate models are relatively poor at predicting the ultimate strain of FRP-confined concrete [27-29]. This poor predictive capability is partly a consequence of the large variability recorded in experiments measuring lateral strains in FRP wraps and tubes at failure [27]. To predict ultimate axial strain (ε_{cu}) and stress (f'_{cc}) of FRP-confined concrete, the models that make use of the hoop rupture strain are significantly more accurate than those that make use of the ultimate tensile strain of fibers (ε_{fu}) [17]. It should be noted that the lateral strain measured on the FRP jacket at the time of FRP rupture ($\varepsilon_{h,rup}$) does not equal to the ultimate tensile strain of the fibers (ε_{fu}) and is significantly lower than that [28, 29, 38, 89]. In addition, by studying the large database of reported hoop rupture strain ($\varepsilon_{h,rup}$), there exists a

notable lack of consistency and with some data deviating from general trends [16, 29]. Available experimental data for hoop rupture strain ($\varepsilon_{h,rup}$) reported by different studies showed large variations for specimens with similar characteristics such as unconfined concrete strength (f'_{co}) and lateral stiffness (K_l). Many researchers studied the reduction of $\varepsilon_{h,rup}$ with respect to ε_{fu} and they proposed a reduction factor (k_ε) to determine $\varepsilon_{h,rup}$ [28, 29]. However, the use of these reduction factors did not results in accurate prediction of ε_{cu} [17, 93]. DIC method was used by different studies for FRP-confined concrete [27, 142, 143]. As it was shown in previous studies [27, 29, 96, 142] by using different methods (strain gauges and DIC) that strain gauges is inadequate to capture the actual values of $\varepsilon_{h,rup}$ due to strong variation of strains over the specimen surface. It is explained by Bisby and Take [27] and Tabbara and Karam [30] that this variation is due to local shear failure that facilitated the movement of concrete wedge along the activated failure planes.

It is well established in existing studies that cracked concrete dilates rapidly during the transition zone and the lateral expansion triggers the passive confinement mechanism of the FRP shell (e.g. [15, 17, 92, 97, 99, 103, 111, 144]). This transition zone separates the two typically quasi-linear stages on the axial stress-strain curve during development of passive confinement. The lateral confining pressure (f_l) generated by the FRP shell counteracts degradation of the axial stiffness of the concrete core and prevents the core from losing its integrity. This confinement mechanism often leads to a ductile plateau in the axial stress–strain curve after the initial ascending branch, which is often referred to as the second branch. Numerous previous studies (e.g. [15, 17, 92, 96, 97, 99, 103, 111]) have shown that FRP-confined concrete specimens typically fail due to rupture of the FRP confining shell. After failure of the FRP tubes, inspection of the exposed concrete rubble reveals a large number of microcracks were created during failure which indicates gradual concrete crushing during failure [106]. A few DIC-based studies on localization and concentration of strain for

unconfined and FRP-confined concrete specimens under bending (e.g. [145-147]) and unconfined concrete specimens under compressive loading (e.g. [148-151]) have shown the benefits and potentials of the technique in furthering the understanding of failure. However, to the best of our knowledge the strain development and shear failure zone expansion of FRP-confined concrete at different stages of compressive loading has not been investigated in detail in the literature.

It is well understood that the level of confinement provided by the FRP shell influences the behavior of FRP-confined specimens under compression. If this level is greater than the threshold confinement level, the second branch of the stress–strain curve will display strain hardening behavior [16]. In addition, the confinement level is able to change the transition point (f'_{c1}, ε_{c1}) and slope of second branch of axial stress-strain curve [10, 17, 21, 22, 24, 93, 99, 103, 115, 116, 152, 153]. As discussed previously [154], the measurement methods used in experimental testing can influence the recorded axial stress-strain curve, and the use of DIC to measure the axial and lateral strain development and variation of hoop rupture strains can lead to a better understanding of the mechanical behavior compared to that can be derived through the use of contact methods [27, 142, 155]. The DIC based studies showed the variation of hoop strain at rupture ($\varepsilon_{h,rup}$) over specimens' surface. In addition, Li, Wu [142] showed the effect of f'_{co} on carbon fiber reinforced polymer specimens under monotonic and cyclic compressive loading. This study showed the significance of unconfined concrete strength (f'_{co}) on behavior of FRP-confined specimens and they obtained a higher strain reduction factor (k_ε) for CFRP-confined concrete specimens with f'_{co} lower than 60 MPa compared to higher values of f'_{co}. This existing study was limited to carbon and glass FRP with no detailed discussion on the effect of confinement characteristics such as elastic modulus (E_f), ultimate tensile strain and strength (ε_{fu} and f_f) on progression of failure resulting in FRP rupture.

This paper presents a study about the variation of strain development and confinement mechanism for unconfined and FRP-confined concrete columns. The effect of FRP characteristics on specimens' behavior under compression were studied and it is illustrated how different E_f and ε_f are able to change the localization and concentration of strain. In addition, the development of shear failure planes in unconfined specimens and FRP-confined concrete was investigated. This research helps to determine how the proposed expressions to predict the mechanical behavior of FRP-confined concrete specimens are influenced by variation of FRP elastic modulus (E_f) and strain measurement methods. To perform this aim, DIC was used as the non-contact measurement to illustrate and analyze the three-dimensional surface deformation and to obtain the hoop and axial strains.

Initially, the experimental results are presented and a comparison between two measurement methods using DIC and contact measurement is provided. Following this, an analysis is performed on DIC images and strain localization and concentration was investigated closely for both unconfined and FRP-confined concrete specimens. A discussion on strain evolution and the influence of key confinement parameters on strain development is provided. In addition, a detailed study on shear zone expansion during axial compression is discussed. Finally, an analysis of hoop rupture strain ($\varepsilon_{h,rup}$) variation over the surface of FRP-confined concrete specimens is presented.

5.2 Experimental program

5.2.1 Details of specimens

A total of 10 unconfined and FRP-confined concrete cylindrical specimens, all with 100 mm diameter (D) and 200 mm height (H), were manufactured and tested. The concrete mix used had a target compressive strength of 30 MPa with control cylinders tested at selected time intervals to determine the in-place unconfined concrete strength gain. 8 specimens were

manufactured as FRP tube-encased specimens, where the tubes were prepared using a manual wet lay-up process by wrapping epoxy resin impregnated carbon fiber sheets around precision-cut high-density Styrafoam templates in the hoop direction; the summary of these test specimens is presented in Table 14.

The specimens were manufactured with either carbon, glass or basalt fiber-reinforced polymer (CFRP, GFRP or BFRP) confinement. The number of FRP layers was selected dependent on material properties with lower grade FRPs receiving more layers to ensure adequate confinement. Accordingly, 1 layer of confinement was allocated to CFRP and GFRP specimens, whereas BFRP specimens received 2 or 3 layers due to low elastic modulus. Two nominally identical specimens were manufactured and tested for each confinement parameter as marked in Table 14.

Table 14-Details of test specimens

Specimen	Concrete Type	FRP-Type	Number of Layers	$t_{f\text{-total}}$ (mm)
N-G1	NSC	GFRP	1	0.2
H1-G2	HSC1	GFRP	2	0.4
H2-G3	HSC2	GFRP	3	0.6
N-C1	NSC	CFRP	1	0.167
H1-C2	HSC1	CFRP	2	0.334
H2-C3	HSC2	CFRP	3	0.501
N-B2	NSC	BFRP	2	0.150
N-B3	NSC	BFRP	3	0.225
H1-B4	HSC1	BFRP	4	0.300
H1-B6	HSC1	BFRP	6	0.450
H2-B6	HSC2	BFRP	6	0.450
H2-B9	HSC2	BFRP	9	0.675

5.3 Material properties

5.3.1 Concrete

The ingredients for concrete used in this research were sourced from a local concrete supplier and were batched and mixed in the laboratory. The mixes consisted of crushed limestone as the coarse aggregate, with a 10 mm nominal maximum diameter. The resulting slump for all batches of concrete was over 100 mm. Control cylinders with 100 by 200 mm dimensions were cast and tested in parallel to the FRP-confined specimens to determine compressive strength (f'_{co}), as was mentioned previously. The details of the concrete mix are shown in Table 15.

Table 15-Concrete mix proportions

Ingredient	NSC	HSC1	HSC2
Cement (kg/m^3)	360	437	506
Silica fume (kg/m^3)	-	38	44
Sand (kg/m^3)	700	710	700
Gravel (kg/m^3)	1050	1065	1050
Water (kg/m^3)	230	164	148
Superplasticizer* (kg/m^3)	-	10	20
w/c	0.64	0.36	0.30
Total (kg/ m^3)	2340	2424	2468

* Superplasticizer contained 70% water by weight

5.3.2 FRP

The material properties of the fiber unidirectional sheets used to manufacture the FRP tubes and jackets are shown in Table 16. The FRP epoxy adhesive used consisted of two parts, epoxy resin binder (MBrace Saturant) and thixotropic epoxy adhesive (MBrace Laminate Adhesive), which were mixed in the ratio of 3:1. All fiber sheets were positioned with fibers aligned in the hoop direction with a 150 mm overlap; the specimens were wrapped with 1 continuous sheet.

Table 16-Material properties of fibers and FRP composites

Type	Nominal dry fiber thickness t_f (mm/ply)	Fiber/FRP properties					
		Provided by manufacturers			Obtained from coupon tests*		
		Ultimate tensile stress f_f (MPa)	Ultimate tensile strain ε_f (%)	Elastic modulus E_f (GPa)	Ultimate tensile stress f_{FRP} (MPa)	Ultimate tensile strain ε_{FRP} (%)	Elastic modulus E_{FRP} (GPa)
CFRP	0.167	4830	2.10	230	4598	1.95	236
S-Glass	0.2	3040	3.50	86.9	3055	3.21	95.3
BFRP	0.075	1680	2.30	73.0	1584	2.10	76.0

* Calculated based on nominal dry fiber thickness

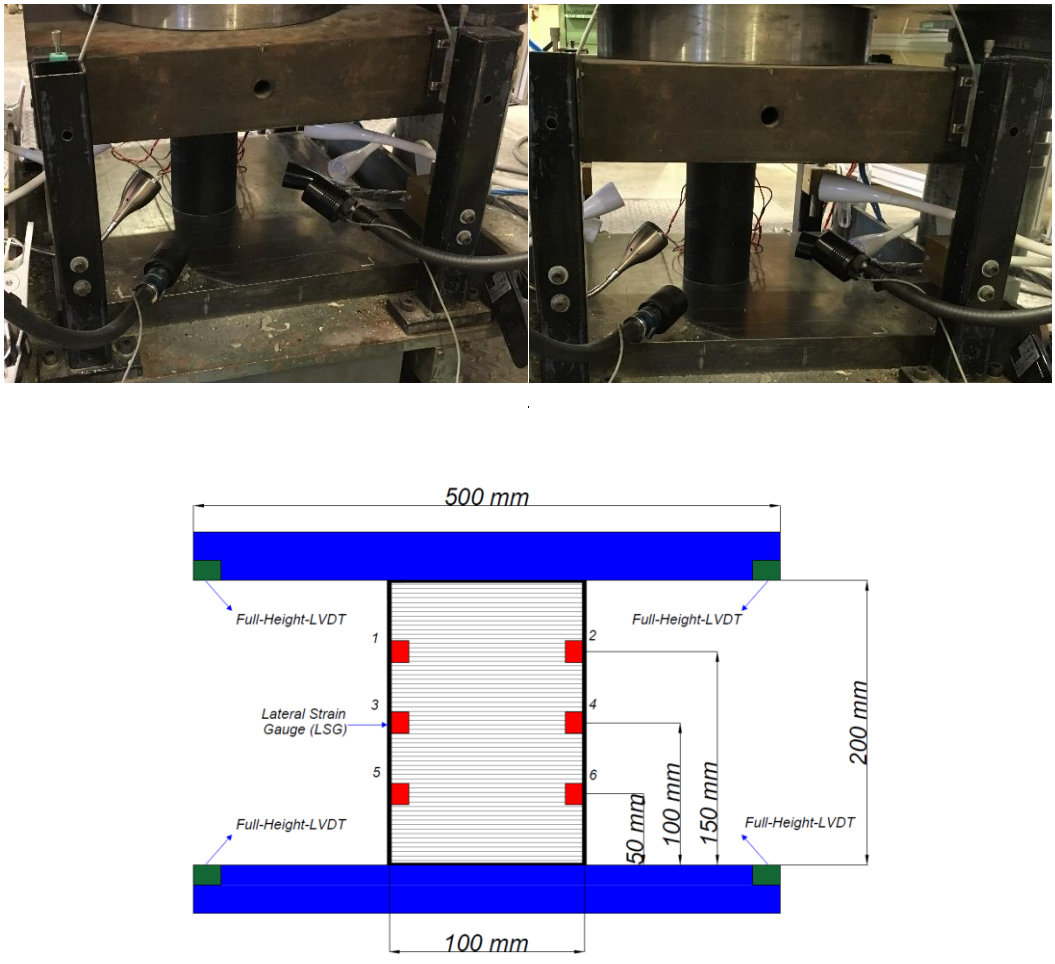

Figure 52- Test setup and instrumentation

5.4 Instrumentation and Testing

Axial deformations of the specimens were recorded with four linear variable differential transformers (LVDT), which were mounted at the corners between the loading and supporting steel plates of the test machine as shown in Fig. 52. The recorded deformations were used in the calculation of the average axial strains along the height of the specimens. Lateral strains were measured by a total of 6 unidirectional lateral strain gauges (SG) having a gauge length of 5 mm that were bonded on the FRP jacket outside the overlap region. These strain gauges were installed in pairs located at heights of 50, 100 or 150 mm with each pair of gauges attached at opposing sides of the specimen.

The specimens were tested under monotonic axial compression using a 5000 kN capacity universal testing machine. During the test, displacement was applied at the rate of approximately 2 microstrain per second until specimen failure. The instrumentation and testing equipment used in this experimental study is shown in Fig. 52.

A DIC analysis was used in this study to obtain values of axial and lateral strain by a contactless method. DIC is principally based on the correlation of the digital images taken during the deformation and failure of the specimens. By using this technique, a speckle pattern with white or black dots is required on the specimen surface. The 3D DIC system used in the experiments consisted of two monochrome 2.8-megapixel, conventional charge-coupled device (CCD) cameras. It had a sensor size of 1/1.8" and a maximum resolution of 1928×1448 pixels. The camera lens was a 75-mm Fujifilm prime lens with an aperture size range of 1/22-1/2.8. This lens has minimal distortion, therefore, no correction for distortion was necessary. The camera body had a Universal Serial Bus (USB) 3 interface for the fast and reliable image transfer; Figure 2 shows the detail of DIC setup. The three-dimensional DIC calibration was performed to provide the geometrical information of the object being imaged. It should be noted that the

recorded strains by DIC do not cover the entire FRP surface as the area covered by DIC camera is smaller than the full specimen surface, as shown in Fig. 53.

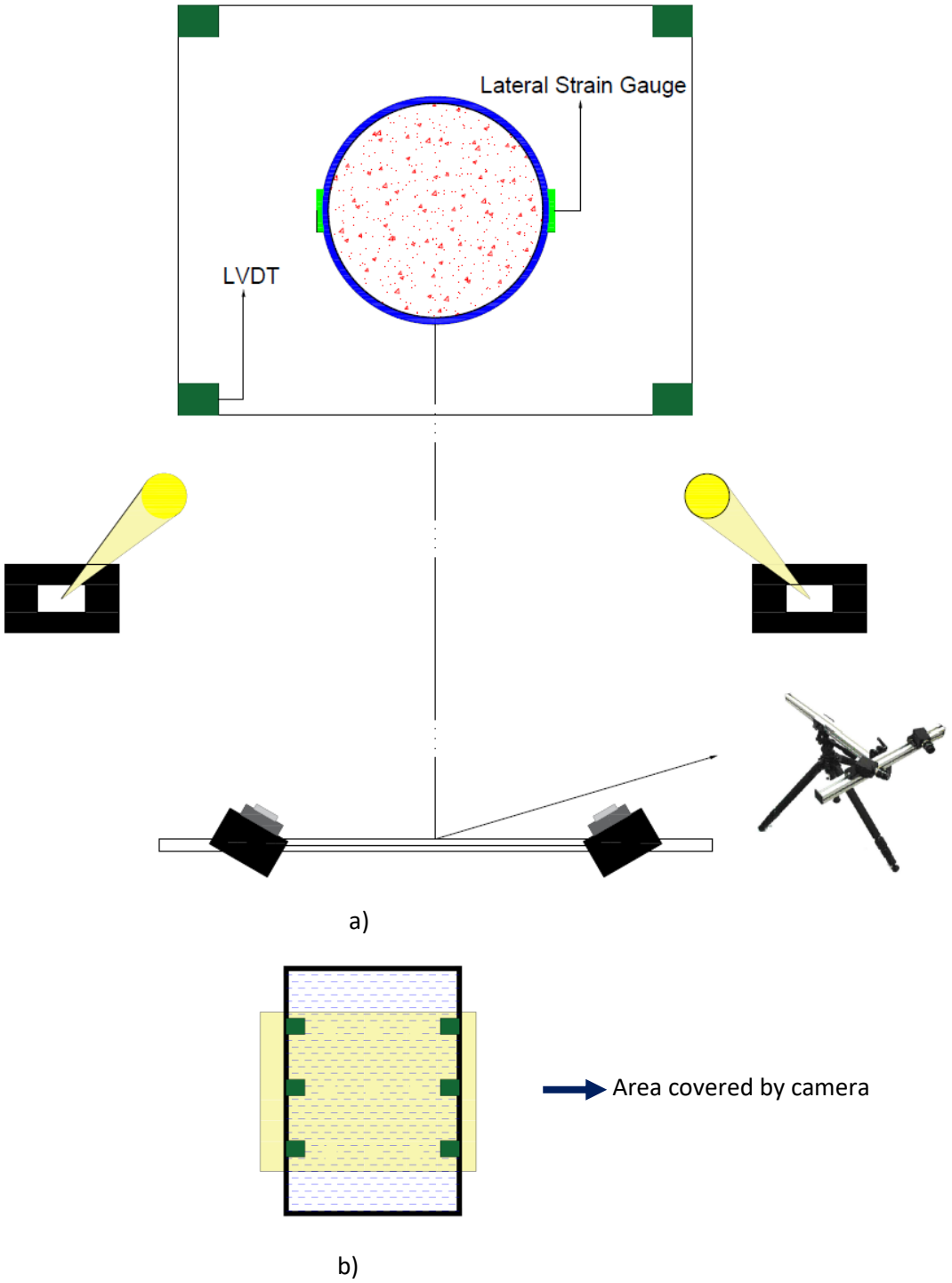

Figure 53- DIC system setup a) camera setup, b) area covered by camera

5.5 Test Results

5.5.1 Axial stress-strain and axial stress-lateral strain

The axial strain and lateral strain recorded by LVDTs and SGs are presented in this section. The softening behavior of specimens after failure (f'_{cc}) was recorded to show the influence of FRP types on failure progression. The axial strain was calculated by averaging of 4 LVDT measurements while lateral strain for each of the three selected heights (Fig. 53) was averaged from two lateral strain gauges at a given height. However, the analysis of images obtained with DIC system provides both local and overall values of axial strain for comparison and analysis as discussed later in this paper.

Figure 54 shows the axial stress-axial and lateral strain response for unconfined concrete specimens. It should be noted that some of SGs ruptured during the tests and the results could not be presented in the figure after their rupture.

Figure 55 presents the axial stress-axial and lateral strain curves for all confined specimens obtained by LVDTs and SGs. It can be seen in the axial stress–strain relationships presented in the figure that all specimens exhibit ascending second branches with ductile behavior. In addition, as expected, the difference in lateral stiffness (K_l) ($K_l = \frac{2E_f t_f}{D}$, where E_f, t_f and D are elastic modulus, thickness and diameter of the FRP, respectively) significantly change the compressive strength and ductility of the specimens as discussed in detail later in the paper. In addition, it can be seen in the figure that companion specimens exhibit similar axial stress-strain behavior but axial stress-lateral strain curves show differences except for CFRP specimens. Also, it can be seen in the figure that the CFRP specimens with high elastic modulus showed a rapid rupture of FRP fibers but the other two FRP fibers types (GFRP and BFRP) presented a gradual failure progression and concrete degradation after f'_{cc}. It is worth mentioning that the CFRP specimens had highest fiber elastic modulus (E_f=230 GPa) and sudden rupture occurred due to sudden release of high strain energy by CFRP confinement.

In addition, the 3 types of FRPs used in this study had noticeably different characteristics; CFRP has high E_f and f_f, GFRP has lower E_f and comparable f_f to CFRP whereas BFRP has low E_f with low f_f. It can be seen in Fig. 4 that the FRP fibers with highest values of E_f and f_f (i.e. CFRP) led to highest stress and strain enhancement with a sudden FRP rupture at failure. Conversely, the FRP with lowest values of E_f and f_f (i.e. BFRP) caused the lowest stress and strain enhancement and a more gradual failure at ultimate.

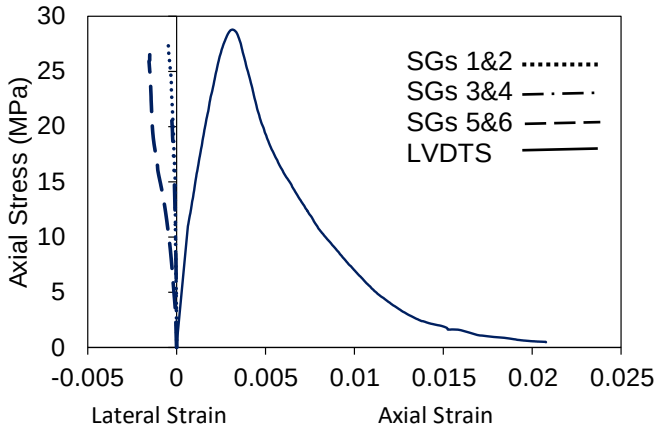

a) U-N-1

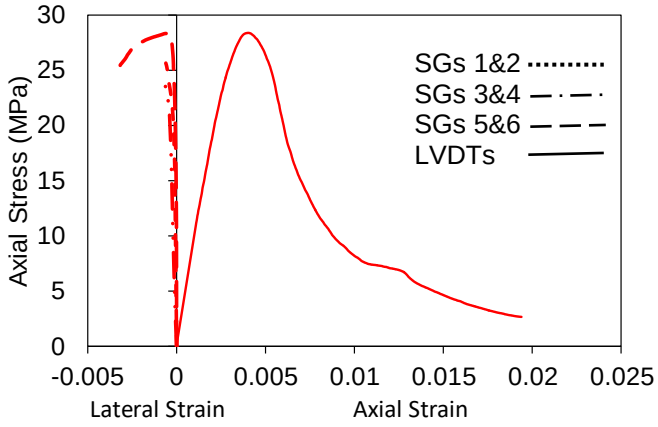

b) U-N-2

Figure 54-Axial stress-axial strain response of unconfined specimens

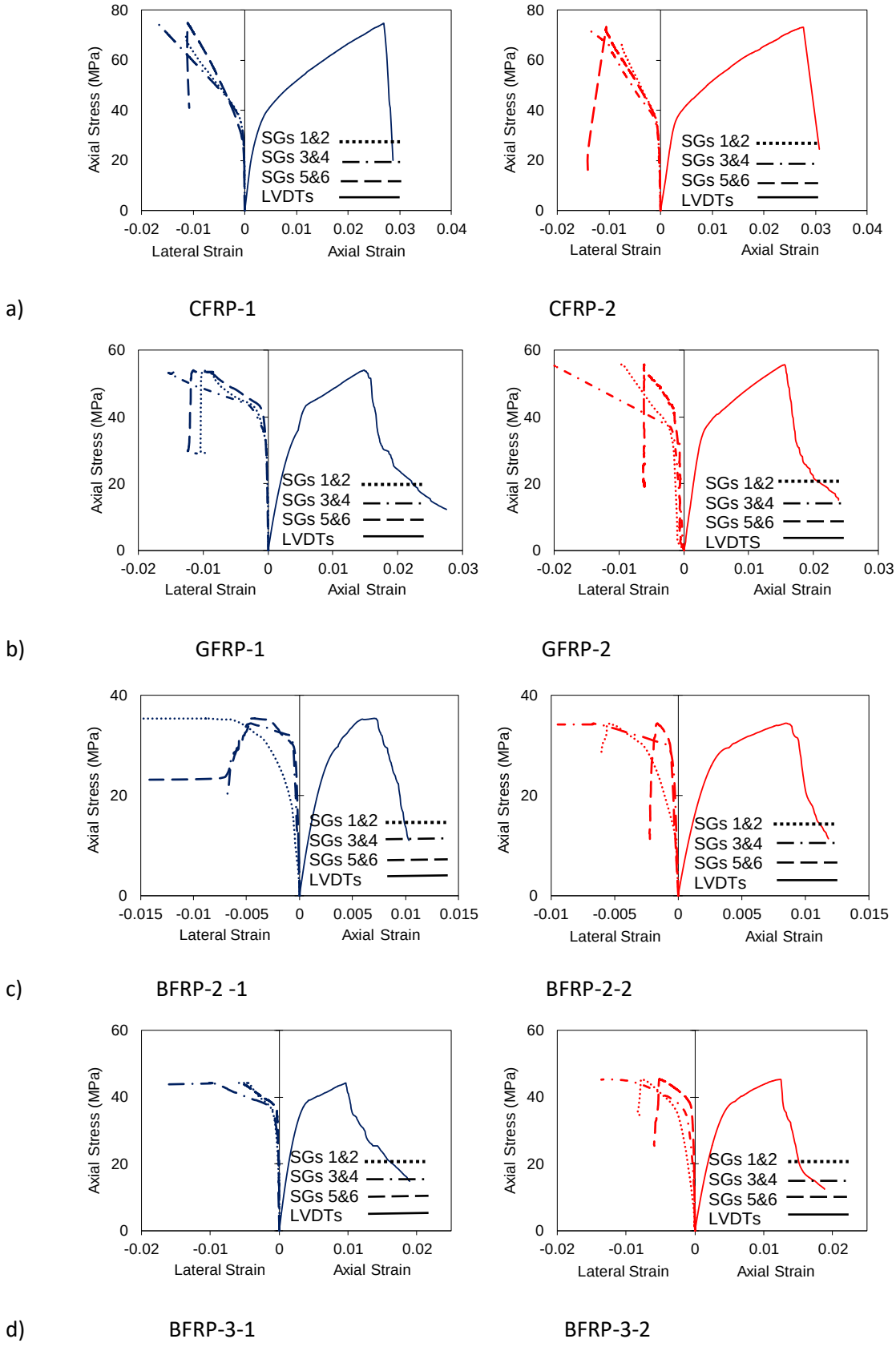

Figure 55- Axial stress-axial and lateral strain response of FRP confined specimens: a) CFRP-1&2, b) GFRP-1&2, c) BFRP-2-1&2, d) BFRP-3-1&2

5.5.2 Comparison of conventional strain measurement methods with DIC

Fig. 56 shows the area that was analyzed by DIC and the vertical and horizontal profiles which are used to compare different measurement methods. To assess and compare the different strain measurement methods applied in this study, a comparison between LVDT, SGs and DIC was performed. This analysis was also used to validate the results obtained from different measurement methods. For lateral strain, 3 profiles were selected to perform the comparison and these profiles are illustrated in the Fig. 38 as h-1, h-2 and h-3 with the same heights selected for the locations of SGs. To show the result of the comparison between different measurement methods for axial strain, the average of axial strain obtained by DIC analysis of longitudinal profiles (v-1, v-2 and v-3) was compared to LVDT results.

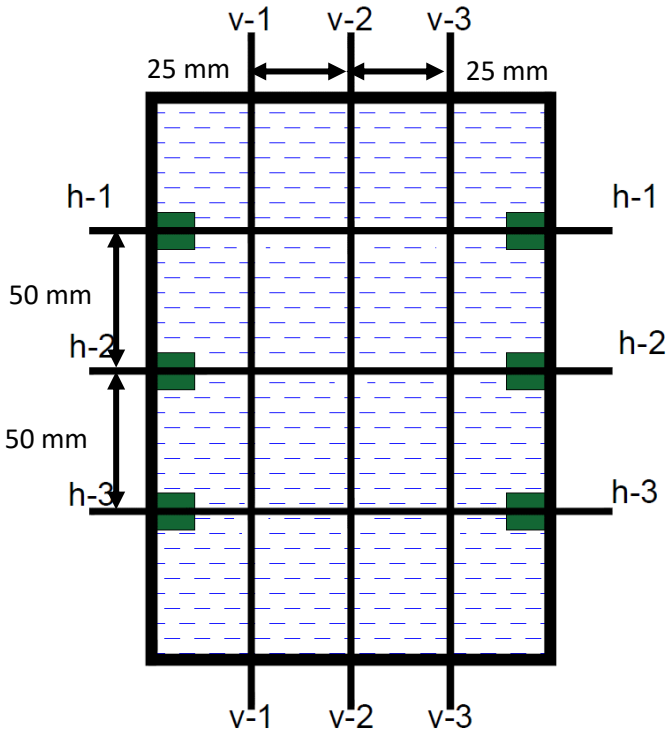

Figure 56-Vertical and horizontal profiles used to compare strain distributions obtained from DIC and conventional measurement methods

5.5.2.1 Lateral Strain

A comparative analysis was performed to examine the consistency or inconsistency of overall and local lateral behavior of specimens recorded by SG and DIC. This comparison was performed by using virtual strain option presented in DIC and the recorded data from two SGs

at the same height were averaged (Fig. 56). It can be seen in Fig. 57 that, the lateral strain development measured by DIC and SG are noticeably different, however the general trend of recorded data by both methods is similar. As can be seen in the figure, the obtained results for profile h-1 corresponding to the same height as SGs 1 and 2, showed maximum difference between DIC and strain gauges. In addition, the results obtained for profile h-3 by DIC and SGs were consistent except for in GFRP specimens. Finally, a comparison of the results obtained by DIC and SGs 3 and 4 for profile h-2 had smaller differences compared to profile h-1. This difference increased after initiation of plastic behavior, which indicates that the localized shear plane effect influences lateral strain behavior differently at different specimen heights. Figure 57 also shows that lateral strains obtained by DIC were higher than those obtained by SGs. This can be attributed to the local nature of the SG measurements as opposed to DIC results showing the overall displacement across horizontal profiles as obtained by applying the virtual strain option in VIC-3D software. Finally, it should be noted that the lateral strain started to increase rapidly at a load corresponding to 60-70 percent of f'_{co}, which is the sign of inelastic behavior initiation.

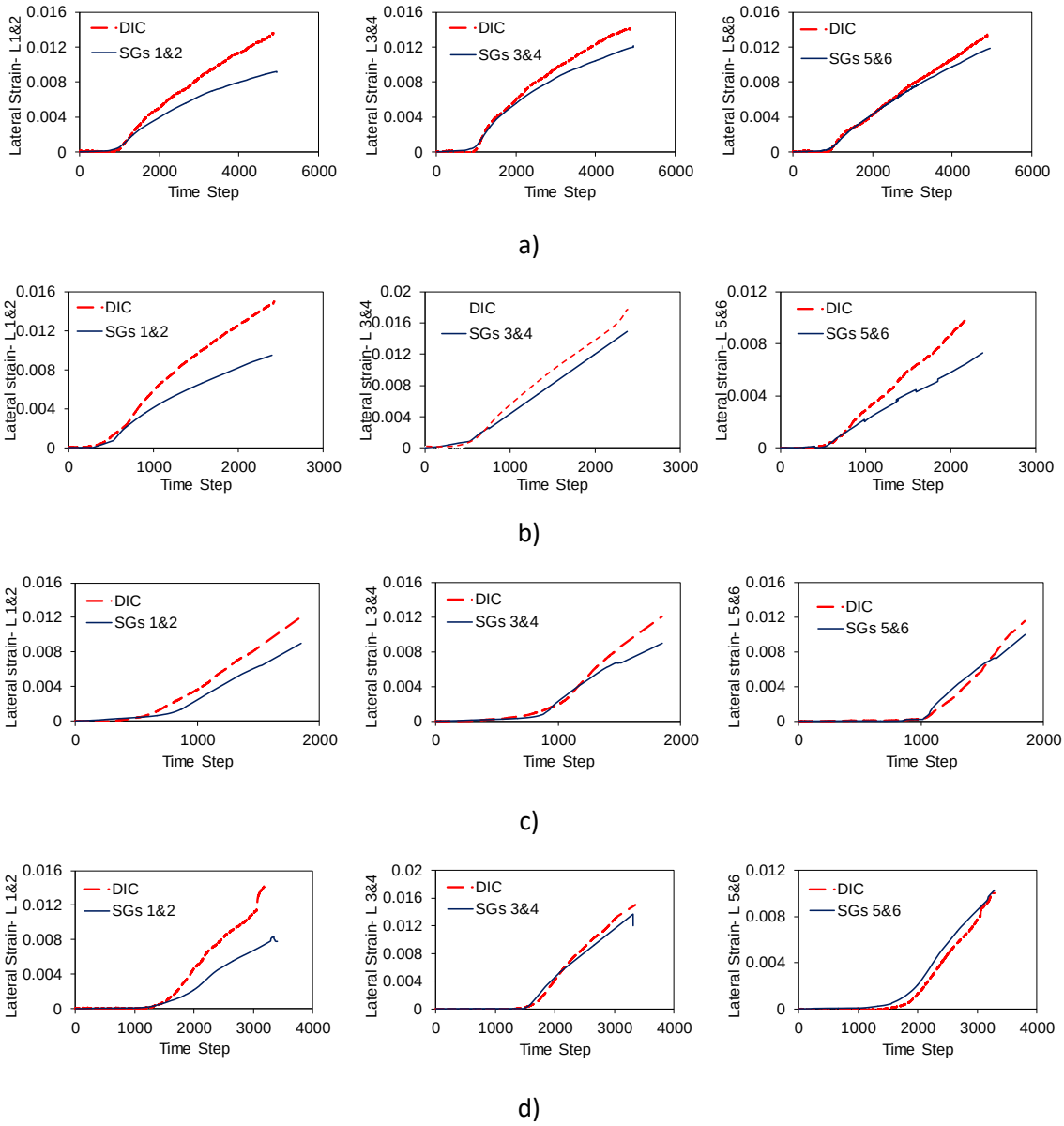

Figure 57- Comparison between lateral strain obtained by SGs and DIC: a) CFRP, b) GFRP, c) BFRP-2; d) BFRP-3

5.5.2.2 Axial strain

Fig. 58 presents the comparison between axial strain obtained by LVDTs and DIC system. Once again the axial strain obtained by DIC analysis was calculated by using virtual strain option in the post-processing software used (VIC 3D). The virtual strain uses the change of distance between two points on the surface of specimens. It can be seen in the figures that the overall axial strain obtained by LVDTs and DIC results are consistent for CFRP, which has high elastic modulus.

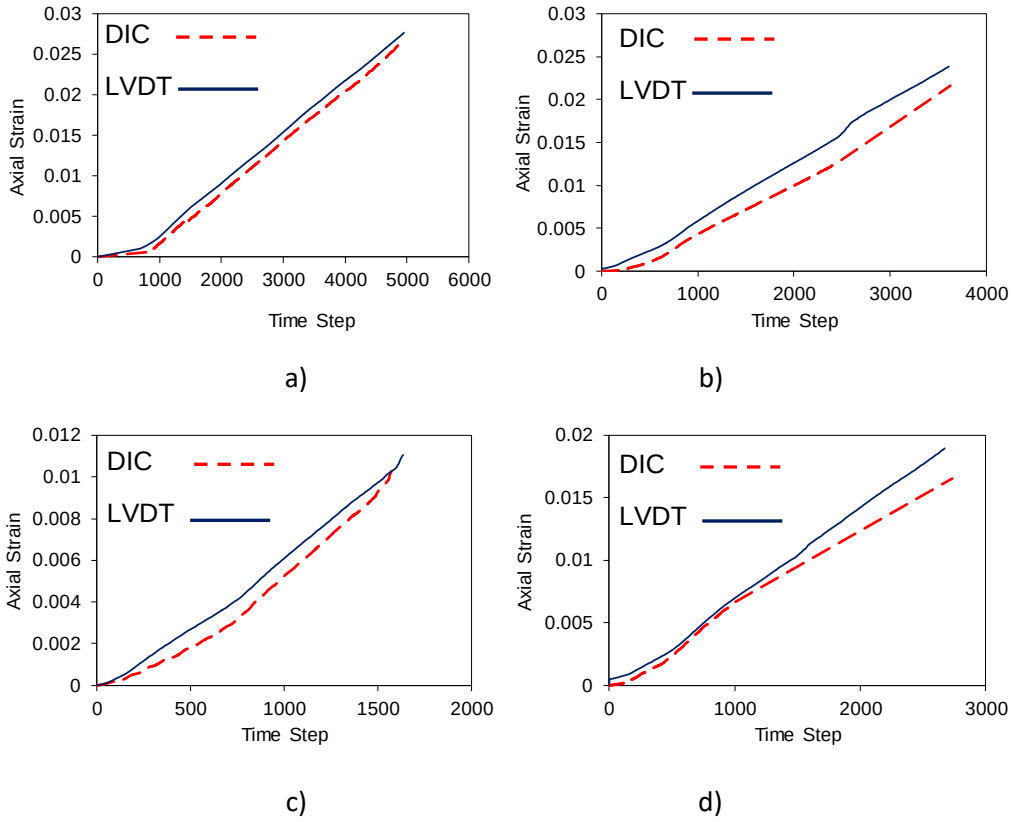

Figure 58- Comparison between axial strain obtained by LVDTs and DIC: a) CFRP, b) GFRP, c) BFRP-2, d) BFRP-3

Furthermore, comparison of Figs. 58 a and b shows that confinement stiffness affects the behavior of specimens. It can be seen in the Figs.57 and 58 that the plastic behavior initiates around the 60-70 percent of the unconfined concrete strength (f'_{co}) by rapid increase of lateral strain, and before this point minimal lateral strain development can be seen. As can be seen in Fig. 40, the GFRP and BFRP specimens showed larger differences between DIC and LVDT results compared to the CFRP specimens. This difference in behavior can be attributed to the difference in K_l with GFRP and BFRP having noticeably lower values of K_l compared to CFRP. The difference in K_l results in differences in localization patterns of strain and shear plane, which were measured by LVDTs but not recorded by DIC. It should also be noted that GFRP and BFRP-3 specimens with similar lateral stiffness exhibited a similar behavior for whole time steps and both types of specimens showed similar differences between LVDTs and DIC results.

5.5.2.3 Strain developments on the surface of specimens

DIC was used in this study to understand the difference between various strain measurement methods and to examine the reasons for inconsistencies in obtained strain results in existing literature, as discussed previously. In addition, this measurement method helps to better understand and illustrate the large variability of $\varepsilon_{h,rup}$ over FRP confinement surface. This method also shows the details of the failure mechanism and propagation of the shear failure plane and localization of strains under axial compression. All these help link the macro stress-strain behavior with the effects of FRP confinement on the strain distribution in the specimens.

Fig. 59 shows the DIC results for unconfined specimens and Figs. 60 and 61 for GFRP, CFRP and BFRP-confined specimens. These figures illustrate the influence of confinement in distribution of cracks and localization of strains during the performed test. From the recorded Von Mises strain contours at different stages of deformation, it can be seen that the localization of deformation is much stronger in unconfined specimen and strains are distributed more homogenously in confined concrete than in unconfined concrete. The effects of FRP confinement in changing the failure mode from very localized to more homogeneous, in association with increasing strength, can be clearly seen.

To analyze the influence of lateral stiffness (K_l) on localization of strain, BFRP-2 and CFRP confined specimens were compared (Fig. 60). This selection was made as CFRP-confined specimens had the highest lateral stiffness (K_l) of 768.2 MPa, whereas BFRP-2 specimens had the lowest at 219 MPa. As it can be seen in Fig. 60, the size of the localization zone for CFRP specimen is larger than that of BFRP-2 specimens. The large lateral stiffness of CFRP specimens caused a more homogenous distribution of strain and cracks in the specimen; conversely, BFRP-2 specimens under weaker confinement exhibited much more localized deformations.

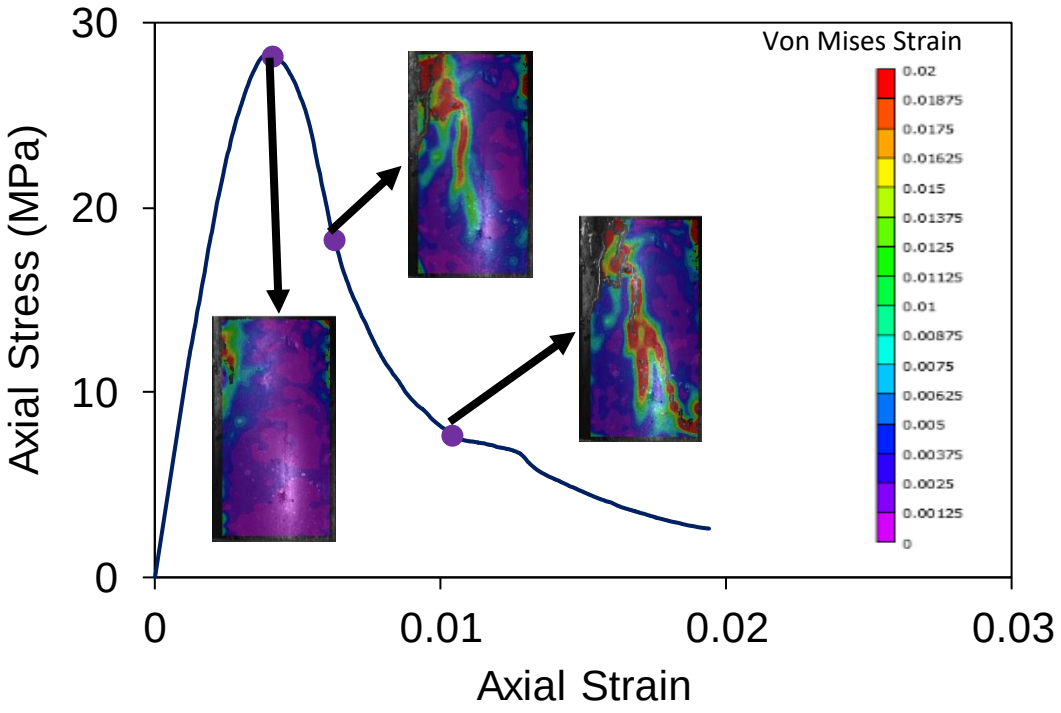

Figure 59- Von Mises strain evolution of unconfined specimens obtained by DIC

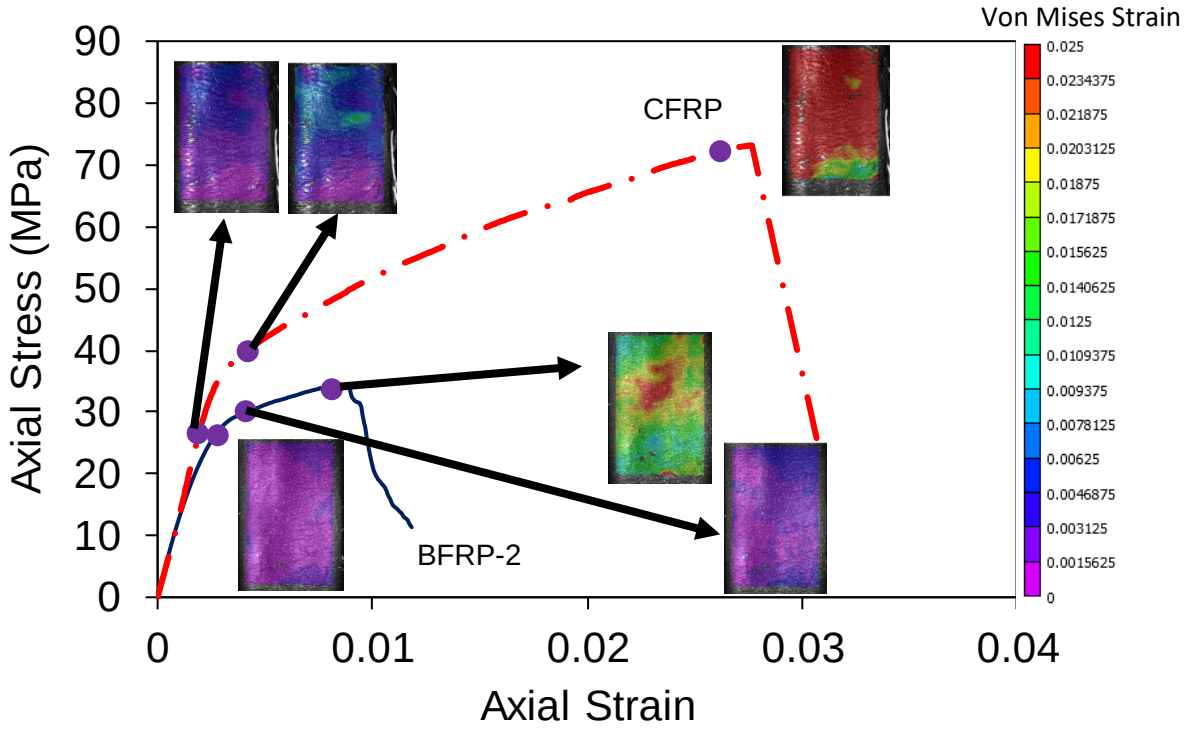

Figure 60- Von Mises strain evolution of BFRP-2 and CFRP confined specimens obtained by DIC

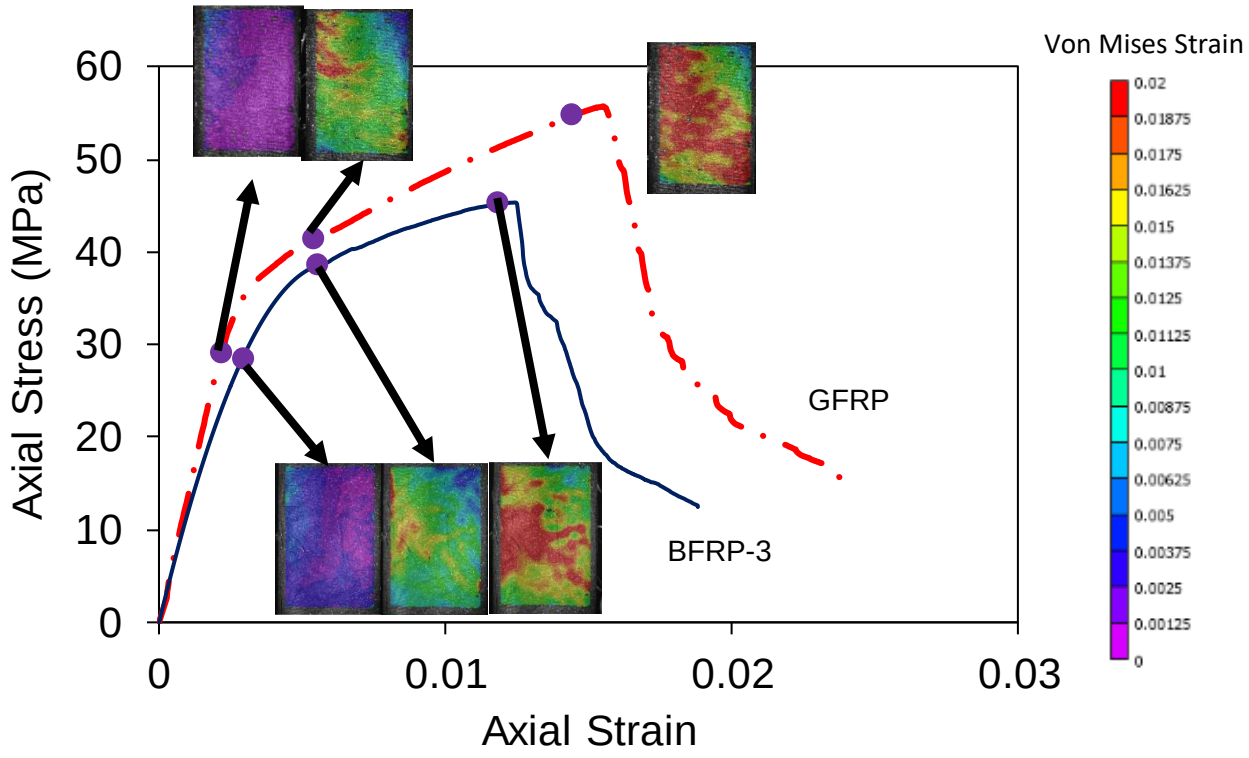

Figure 61- Von Mises strain evolution of BFRP-3 and GFRP specimens obtained by DIC

An analysis of the FRP type on the behavior was performed by comparing DIC recorded strains of GFRP and BFRP-3 specimens with similar K_l (i.e. 347.6 MPa for GFRP specimens and 328.5 MPa for BFRP-3 specimens). Fig. 61 illustrates this comparison. As it can be seen in the figure, these two specimens showed a similar behavior and the deformation in the GFRP with higher ultimate strength was slightly more homogeneous.

The results presented in this section qualitatively show the strong link between macro behavior and distribution of strains. Higher strength resulting from higher lateral confinement stiffness is accompanied with more homogeneous deformations, owing to the confinement provided by the FRP.

5.6 Analysis and discussion

As discussed in Section 5.5, the DIC results showed differences in homogeneity of deformation in specimens with different confinement parameters. To perform a more detailed and quantitative analysis, the evolution of Von Mises strain for different vertical and horizontal profiles shown in Fig. 56 is investigated in this section. In addition, the effect of lateral stiffness on the behavior and variation of hoop rupture strains are also discussed in this section.

5.6.1 Development of strains along specimen height

Von Mises strain evolution along specimen height for unconfined and FRP-confined specimens is presented in Figs 62 and 63. In these figures the vertical profile selected was profile V-2 shown previously in Figure 56. The specimens presented in these figures were selected based on providing varying ranges of lateral stiffness and f'_{co}. Figure 62 presents the behavior of an unconfined specimen, whereas Figs. 63a and 63b present comparisons of specimens with noticeably different and similar values of lateral stiffness, respectively. The Von Mises strain evolution for different specimens was obtained by synchronizing the DIC camera results with stress and strain recorded by data acquisition system. To observe the localization of strain during axial loading, the evolution of strain field (Von Mises strain) was correlated with the axial stress-axial strain curve. As can be seen in Fig. 62, the maximum Von Mises strain for unconfined concrete occurred in the upper region, with little to no strain development elsewhere along the specimen height. A comparison of all specimens presented in Figs 62-63 reveals that Von Mises strain development along the V-2 profile is significantly higher in FRP-confined specimens compared to unconfined specimens. It can also be seen that the height corresponding to maximum Von Mises strain is typically located towards the mid-region for all FRP-confined specimens rather than upper region for unconfined specimens. Ignoring the statistical aspect (e.g. inhomogeneity of an intact material) that may affect where localization takes place, the clear difference between localized behavior in Figs. 62 and 63 can be observed and linked with the macro responses of the specimens. Confinement provided by the FRP in

this case prevented the localization of deformation and as a consequence significantly altered the specimen's behavior.

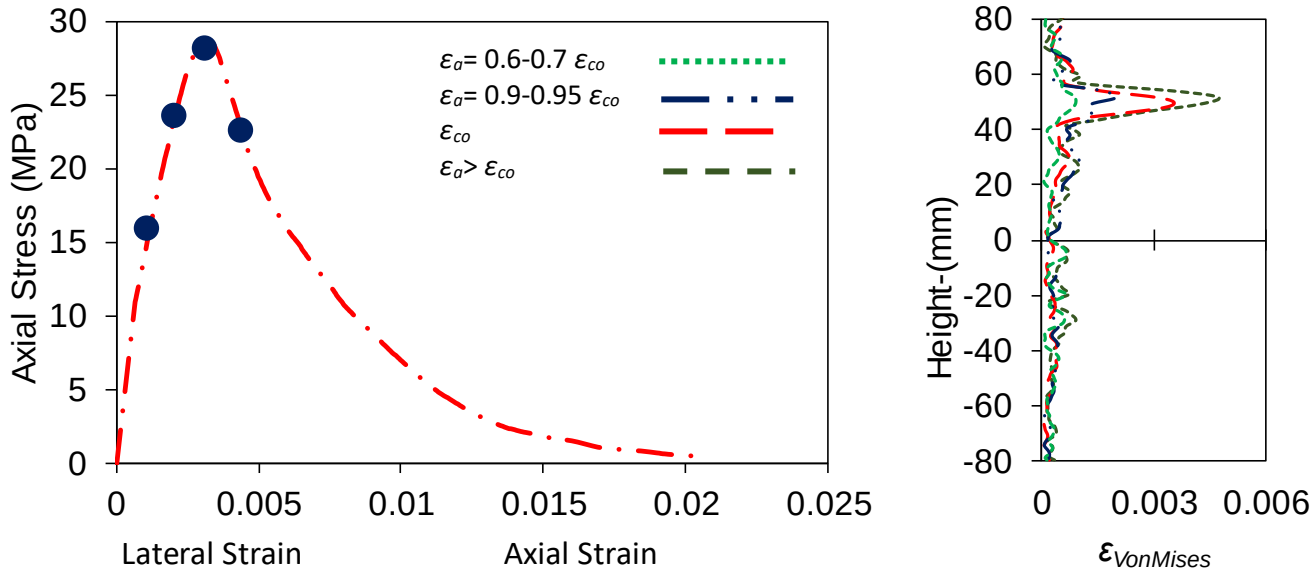

Figure 62- Comparison of Von Mises strain development for unconfined specimens

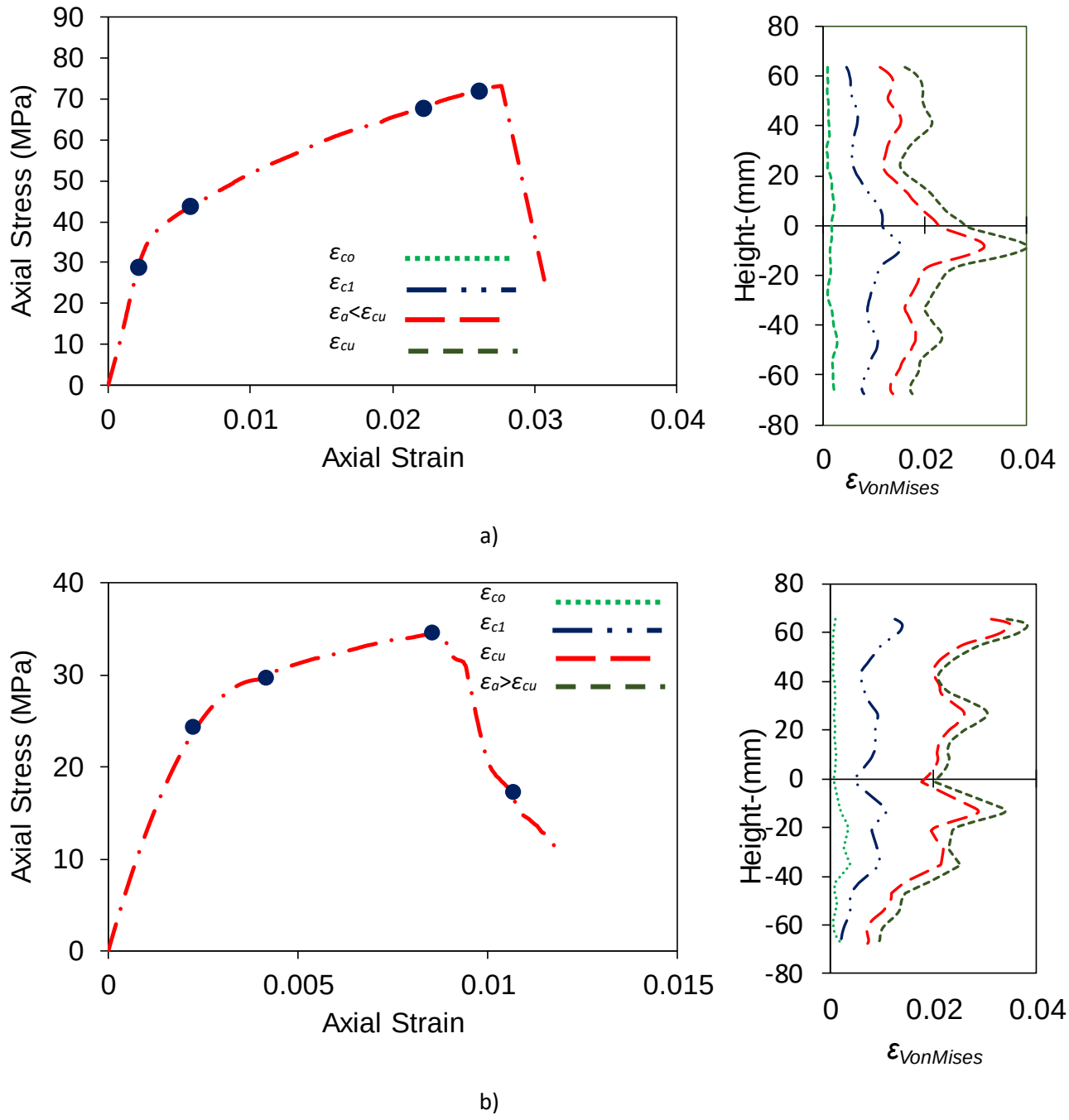

Figure 63-Comparison of Von Mises strain development for: a) CFRP and b) BFRP-2 confined specimens

Figs. 63a and b present a comparison of Von Mises strain evolution along the height of specimens for CFRP & BFRP-2 and GFRP & BFRP-3, respectively. These two comparisons were selected as CFRP and BFRP-2 specimens respectively have the highest and lowest lateral stiffness, and GFRP and BFRP-3 have approximately the same lateral stiffness. As can be seen in Figs. 63a and b, the lateral stiffness directly affects the lateral strain behavior of specimens.

The location of maximum Von Mises strain varied with a change in lateral stiffness and this location moved closer to the mid-height of the specimen with increasing lateral stiffness. In addition, BFRP-2 specimens with lower lateral stiffness displayed a more inhomogeneous behavior compared to GFRP and CFRP specimens. This is due to the fact that lower lateral stiffness allowed local deformations as its magnitude was not adequate to limit localization of strains.

As was discussed previously, inelastic behavior in the unconfined specimens initiated when the stress reached approximately 60-70% of f'_{co} and this was followed by strain localization. The confined specimens showed rapid increase of lateral strain after approximately 60-70% f'_{co} (refer to Fig. 54), which indicates the activation of confinement. In the segment between 60-70% of f'_{co} and f'_{c1}, lateral strains remained relatively low. As expected, the confinement actions became more pronounced beyond f'_{c1} which is evident from a noticeable increase in lateral strains in Figs. 63a and 63b. As it can be seen in Figs 62 and 63, the localization of strain over the specimen surface were limited to small area of unconfined and confined specimens at f'_{co}. This behavior that begins after 60-70% of f'_{co} (e.g. Fig. 62) is attributed to the strain concentration, which results in higher lateral strains. However, the confinement change the lateral behavior of specimens and the approximately similar lateral response was observed after f'_{c1} until specimen failure as can be seen in Figs. 63a and b.

Table 17 shows the maximum, minimum, average and standard deviation (SD) of Von Mises strains obtained at f'_{co}, f'_{c1} and f'_{cc} along profile v-2. It can be seen in the table that the differences between the maximum and minimum Von Mises strains along the studied profile was similar for unconfined and FRP-confined specimens at f'_{co}. However, this difference for FRP-confined specimens increased beyond this point and it reached to its maximum value at f'_{cc}. In this table the largest differences between maximum and minimum values of f'_{cc} were

seen in the N-C1 specimens which have the highest lateral stiffness (K_l) and ultimate axial strain (ε_{cu}). This observation indicates that an increase in K_l results in an increase in variability between Von Mises strains along the height of FRP-confined specimens. Furthermore, it can be seen that this difference for B2-1 and B2-2 are lower than other specimens at f'_{c1} but GFRP specimens showed lowest differences among specimens at f'_{cc}. As discussed previously, B2 series of specimens had the lowest lateral stiffness and their behavioral characteristics were closer to those of unconfined specimens in terms of both mechanical responses and evolution of strain localization.

Table 17- Statistical result for obtained Von Mises strain ($\varepsilon_{VonMises}$) along profile v-2

Specimen	f'_{co}				f'_{c1}				f'_{cc}			
	$\varepsilon_{Von\ Mises}$(%)				$\varepsilon_{Von\ Mises}$(%)				$\varepsilon_{Von\ Mises}$(%)			
	Max	Min	Average	SD	Max	Min	Average	SD	Max	Min	Average	SD
U-1	0.34	0.01	0.05	0.06	-	-	-	-	-	-	-	-
U -2	0.32	0.01	0.08	0.06	-	-	-	-	-	-	-	-
G1-1	0.29	0.05	0.17	0.06	1.16	0.30	0.66	0.22	2.56	1.10	1.88	0.52
G1-2	0.32	0.09	0.18	0.05	1.23	0.60	0.94	0.16	3.01	1.50	2.03	0.29
C1-1	0.33	0.04	0.15	0.08	1.33	0.13	0.71	0.36	4.98	0.77	2.58	0.95
C1-2	0.27	0.05	0.14	0.14	1.14	0.32	0.67	0.24	4.68	1.69	2.58	2.58
B2-1	0.28	0.04	0.11	0.06	0.59	0.07	0.24	0.12	2.48	0.42	1.44	0.53
B2-2	0.30	0.02	0.11	0.06	0.57	0.32	0.40	0.05	2.84	0.37	1.12	0.59
B3-1	0.32	0.08	0.17	0.06	0.96	0.29	0.70	0.21	3.04	0.71	1.65	0.50
B3-2	0.31	0.04	0.09	0.04	1.02	0.34	0.69	0.17	2.92	1.10	1.70	0.53

5.6.2 Strain developments around specimen perimeter

Figs. 64-66 show the evolution of Von Mises strains at three different horizontal profiles (h-1, h-2 and h-3) for specimens with three different levels of confinement. The three specimens selected for this comparison are unconfined, lowest level of confinement (BFRP-2) and highest level of confinement (CFRP), shown in each of the figures respectively.

A comparison of Fig. 64 with Figs. 65 and 65 reveals that the presence of FRP-confinement results in a reduced localization of strain along the three studied horizontal profiles. The unconfined specimen displays brittle behavior associated with strong non-homogenous strain along the horizontal profiles after nonlinearity starts. In addition, the amount of confinement stiffness (K_l) can be seen to influence this behavior, which can be observed by comparing the CFRP and BFRP-2 specimens. A comparison of these specimens reveals that an increase in confinement stiffness amount increased the uniform development of Von Mises strains.

It is worth noting that, as it can be seen in the Figs 62-66 and Table 17, it is difficult to assess the evolution of shear zone using raw DIC data. In particular, the raw DIC data as seen in Figs. 62-63 involve the effects of statistical inhomogeneity of the material, making it harder to see how localization of strain evolved in unconfined and FRP-confined specimens. A way to remove this statistical effect to facilitate the analysis of rich microstructural data was proposed in Nguyen, Nguyen [156] and applied in this paper to the DIC data in all specimens.

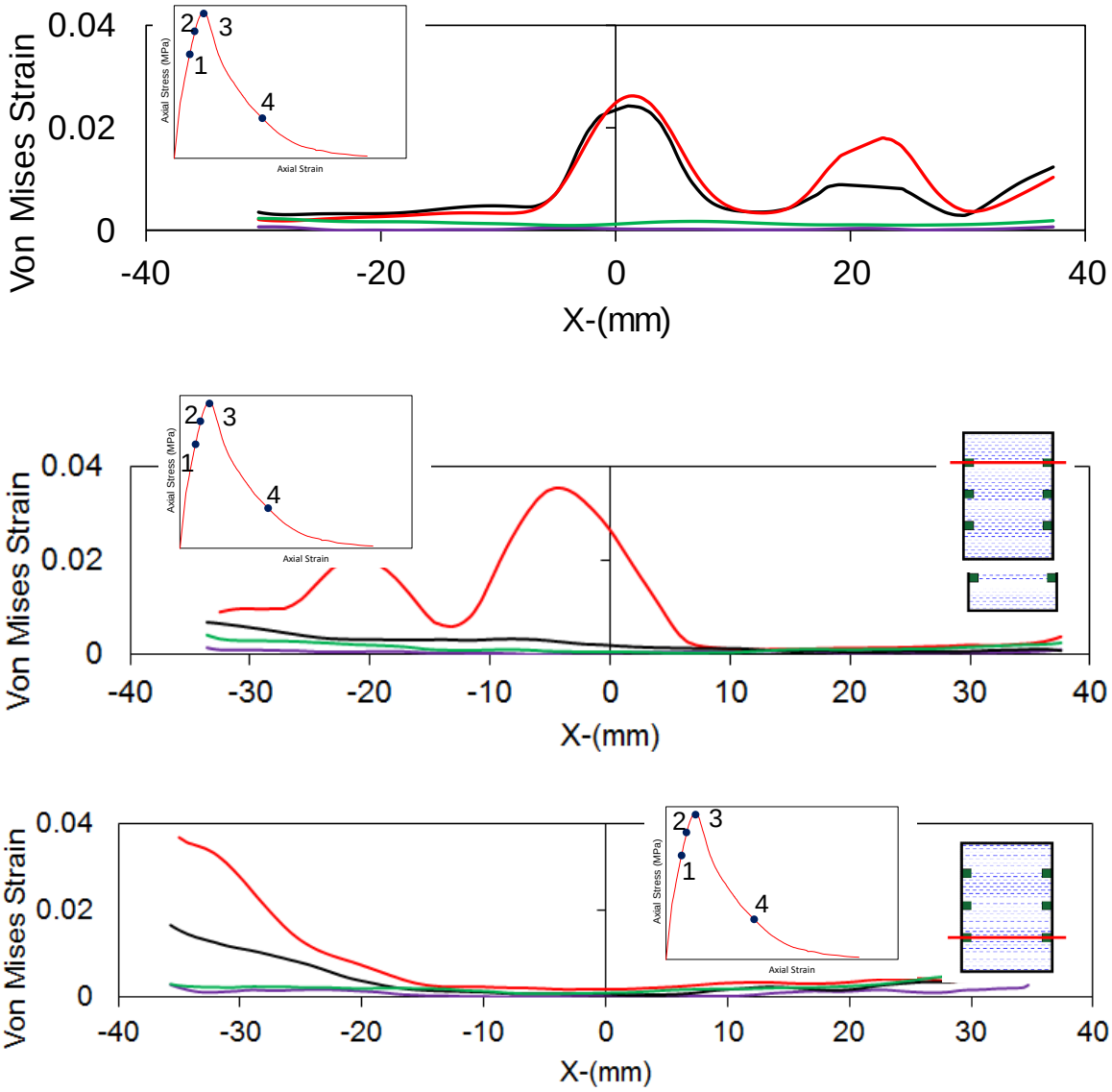

Figure 64-Lateral Evolution of Von Mises strain for unconfined specimen

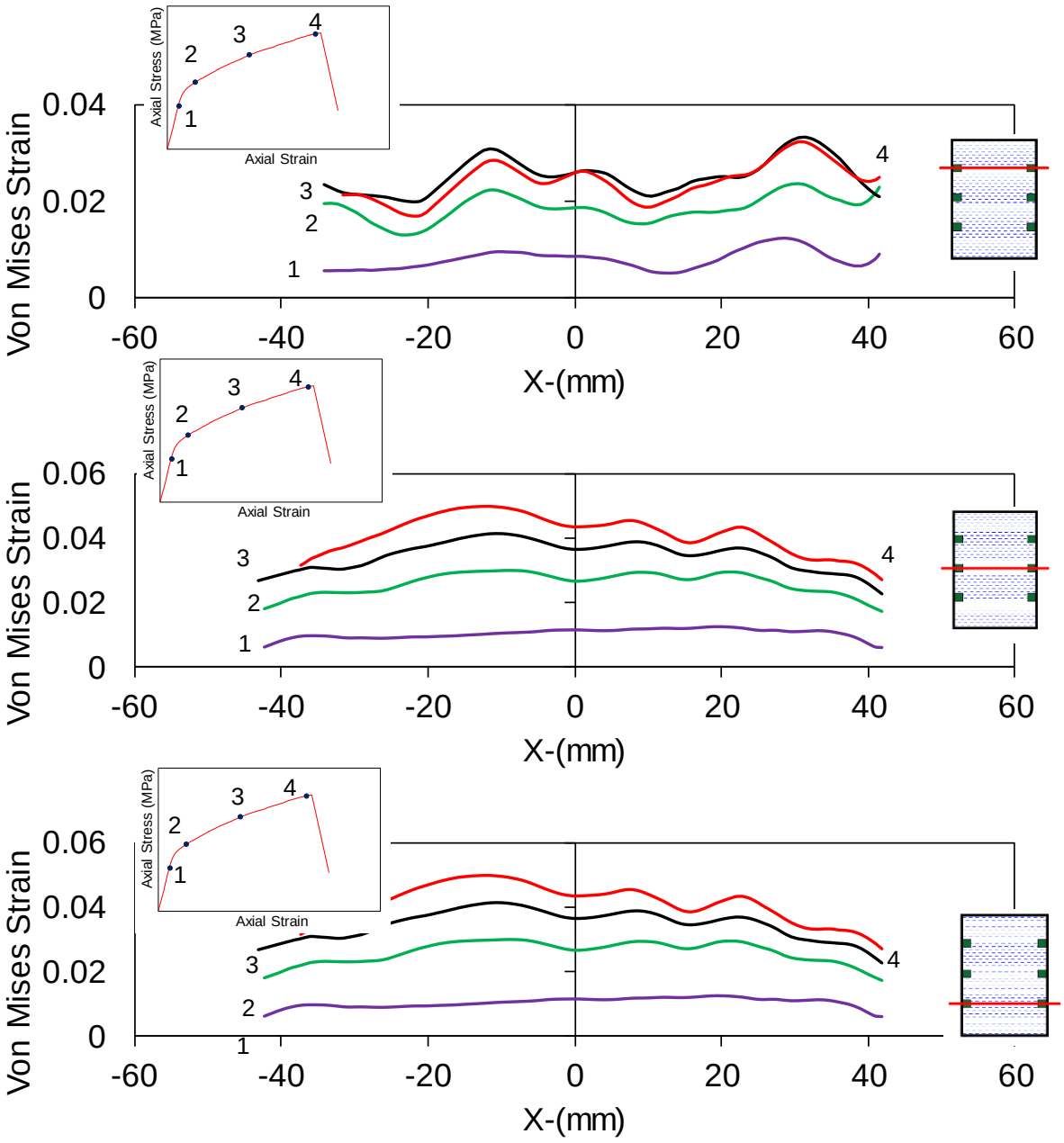

Figure 65- Lateral Evolution of Von Mises strain for CFRP confined specimen

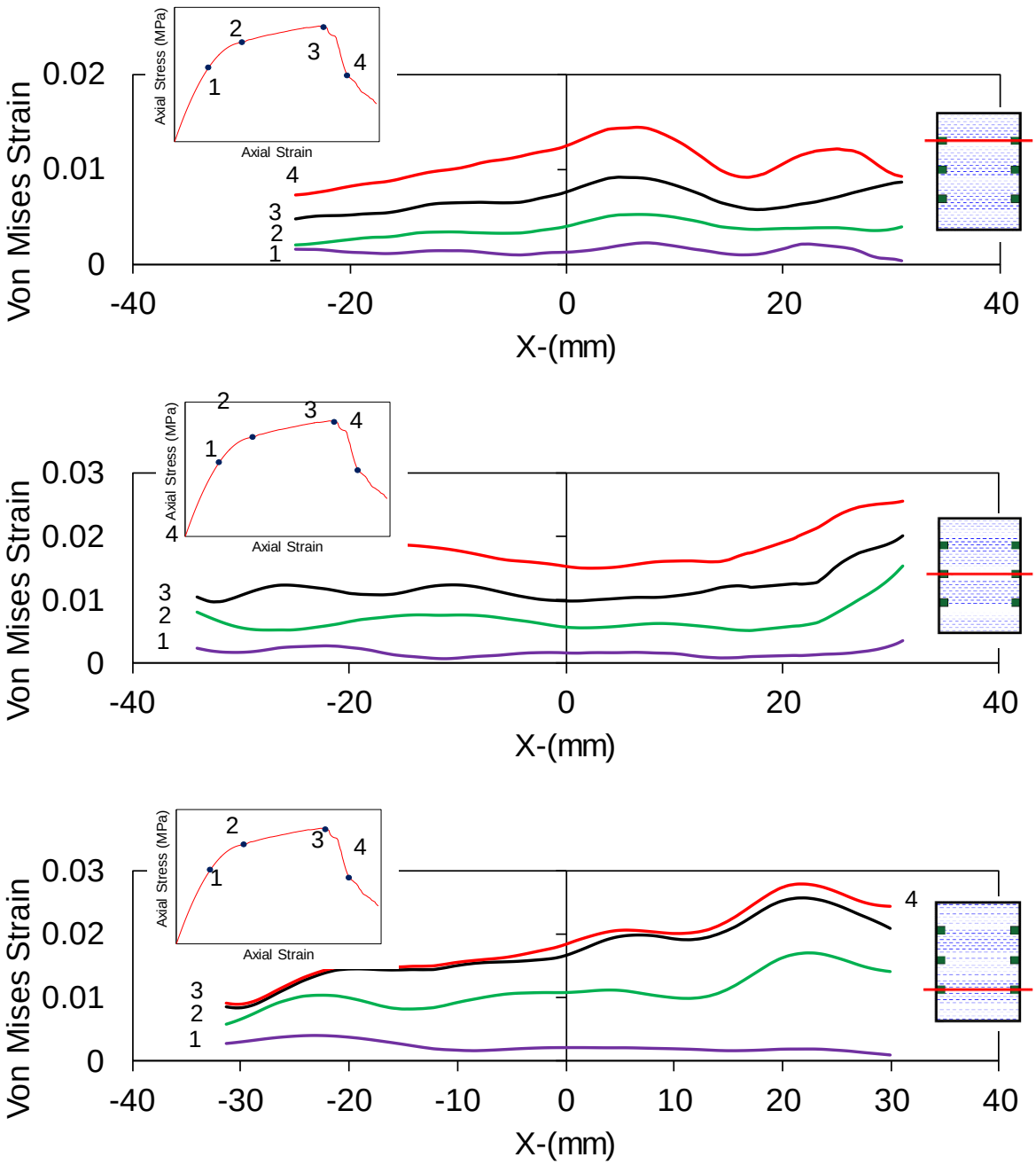

Figure 66- Lateral Evolution of Von Mises strain for BFRP-2 confined specimen

5.6.3 Influence of confinement on shear zone expansion

Figure 67 shows the expansion of the shear zone during axial compression for unconfined and confined specimens. To investigate the expansion of shear zone during the compression testing, the average DIC obtained Von Mises strain over the specimen surface was calculated along specimen height then these average strains were sorted in descending order from top to bottom of specimens, as shown in Fig. 67. This process removes the correlation between strain and

position and hence can give a clearer view on the development of strain during deformation. It can be seen in the figure that the evolution of Von Mises strain during the test procedure for both unconfined and confined can be categorized into two groups. The first group represents steady development of $\varepsilon_{vonmises}$ during axial compression prior to pre-peak stage along the height of specimens, which can be seen in well-confined specimens (i.e. CFRP, GFRP and BFRP-3 series). Conversely, there is a second group of specimens (unconfined and BFRP-2 specimens), which displayed more localized behavior after yielding followed by a strong increase of non-homogeneity during and after specimen failure. As can be seen in the figure, the shear failure zone for well-confined specimens expanded gradually during testing, whereas the unconfined specimens showed a rapid transition from homogenous to localized behavior. These observations indicate that localization of strain and crack patterns develop gradually in well-confined specimens but are very abrupt for unconfined specimens. In addition, as discussed previously, lightly-confined BFRP-2 specimens displayed a behavior closer to that of unconfined specimens due to their low lateral confinement stiffness (K_l).

It can be also seen in Fig. 67 that, although the evolution of Von Mises strain for specimens are similar up to f'_{co}, this evolution changed after the transition point for FRP-confined specimens depending on their amount of lateral stiffness (K_l). It can be observed in the figure that the CFRP specimen with highest lateral stiffness (K_l=768.2 MPa) showed more gradual behavior compared to BFRP-2 specimen with lowest lateral stiffness (K_l = 219 MPa).

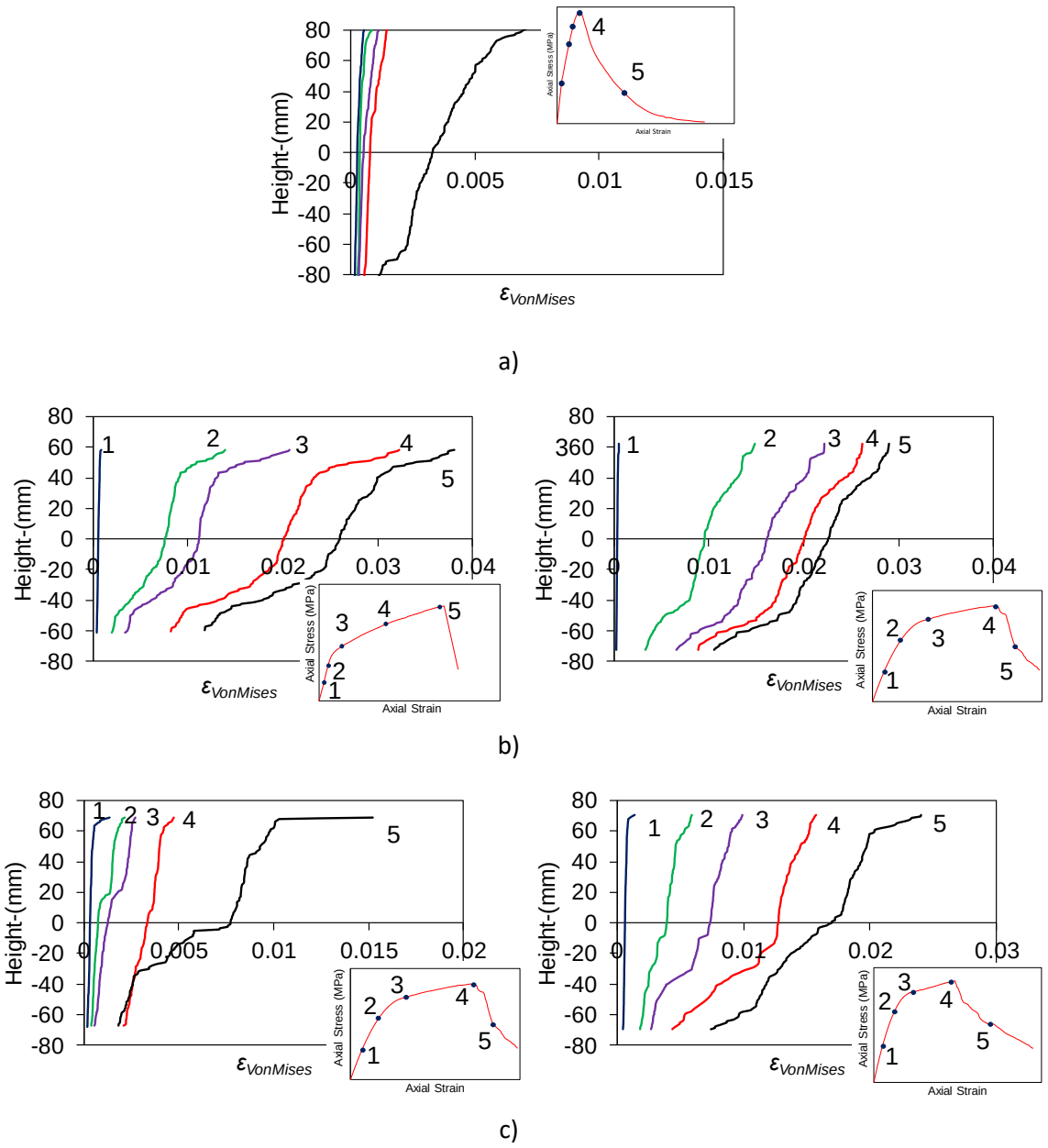

Figure 67- Expansion of shear zone; a) unconfined specimen; b) CFRP and GFRP confined specimen; c) BFRP-2 and BFRP-3 confined specimens

5.6.4 Comparison of hoop rupture strain measurement methods

It is well established that the most accurate prediction of ultimate axial strain (ε_{cu}) can be performed by using hoop rupture strain ($\varepsilon_{h,rup}$) as an input data. However, the determination of $\varepsilon_{h,rup}$ is difficult when using strain gauges which only record localized behavior as explained previously in Section. 1. Using the DIC camera to measure the variation of $\varepsilon_{h,rup}$ on the full surface of the FRP shell gives an opportunity to find the location and magnitude of maximum $\varepsilon_{h,rup}$ and the influence of key confinement parameters such as f'_{co}, E_{frp} and f_{frp}.

Table 16 presents a comparison between hoop rupture strains at failure recorded by DIC camera and SGs. In addition, the strain reduction factors (k_ε) for maximum recorded lateral strain recorded by DIC and SGs are presented in Table 18. It should be noted that the lateral strains obtained by DIC do not cover the entire FRP surface as the area covered by DIC camera is smaller than the full specimen surface, as shown previously in Fig. 53. The large difference observed between maximum and average recorded lateral strain in Table 16 indicates that the hoop rupture strain ($\varepsilon_{h,rup}$) varied significantly along the specimen height. These results suggest that the SGs are not capable of providing the actual hoop rupture strain, and the recorded values depend on the location of the attachment and failure surface. This outcome is in agreement with Bisby and Take [27] who observed a similar variation of hoop rupture strain over surface of specimens. In Table 5 two specimens showed very low lateral strain values recorded by SGs which are marked with *. Upon closer inspection of these results, it was found that SGs experienced premature rupture and they did not record accurate data (Fig. 55). This table shows that the GFRP specimens had larger difference between the reduction factors obtained by SG and DIC, whereas CFRP showed smaller differences between these two measurement types for k_ε. This observation can be attributed to occurrence of local shear plane which influence the hoop rupture strain location. It is significant to say that the different characteristics GFRP and CFRP caused the differences in mechanical behavior of these two types of fiber as explained in Section. 5.5 including the strain localization and local shear plane location.

Table 18- Numerical summary of observed lateral strain variation along the height of specimens

Specimen	$\varepsilon_{h,rup}$ (%)-DIC				MAX- LSG (%)	k_ε (DIC)	k_ε (LSGs)
	Max	SD	Average	Median		-	-
G1-1	3.17	0.42	1.35	1.47	1.23*	0.91	-
G1-2	3.33	0.34	0.70	0.69	2.03	0.95	0.58
C1-1	2.20	0.38	1.40	1.49	1.51	1.05	0.72
C1-2	2.17	0.44	1.23	1.10	1.77	1.03	0.84
B1-1	2.13	0.32	0.66	0.63	0.91*	0.92	-
B1-2	1.63	0.42	0.84	0.85	1.49	0.71	0.65
B2-1	2.03	0.28	0.64	0.64	1.70	0.88	0.74
B2-2	2.11	0.33	0.79	0.84	1.49	0.92	0.65

*Early rupture of LSGs

5.7 Conclusion

This paper presents the results of an experimental study on the localization of strain over the surface of FRP-confined concrete columns with circular cross-sections under compression loading. The axial stress-strain curves are obtained and synchronized with images captured by a DIC system. Based on the results obtained in this study, the following conclusions can be drawn.

1-The image-based DIC strain and deformation measurement method is able to give much richer data in terms of full-field strains and their evolutions on the specimen surface compared to LVDTs and strain gauges, which provide only global or local strain. This provides a better understanding of confinement mechanisms and its effects on the mechanical response of confined specimens. In addition, the outcome indicates that this system provides the same levels of accuracy to LVDTs for axial strain and strain gauges for lateral strain measurements.

2- The DIC data also showed that strain gauges, when used in isolation and in small numbers, are not capable of determining the actual $\varepsilon_{h,rup}$ needed for accurate prediction of ultimate points on the stress-strain curve, because this strain varies significantly over the specimen surface, making it difficult to obtain accurate measurements using strain gauges.

3-The outcomes obtained by DIC show that deformations are more localized in unconfined concrete specimens, and strains are distributed more homogenously in confined specimens.

4- The lateral stiffness of FRP jacket (K_l) influences the dilation behavior of FRP-confined concrete; larger lateral stiffness of CFRP confinement leads to a more homogenous distribution of strain and cracks in the specimen; conversely, BFRP-confined specimens under weaker confinement exhibit much more localized deformations.

5- Maximum Von Mises strains occur at a location corresponding to specimen mid-height region for all FRP-confined specimens and upper region for unconfined specimens. This outcome shows a clear difference between localized strain behavior for unconfined and confined specimens along the height of specimens.

6-An increase in confinement stiffness (K_l) increases the uniformity of Von Mises strains around the specimen perimeter. In addition, Von Mises strain evolution changes from more localized for specimens with low lateral stiffness to more uniformly distributed for higher lateral stiffness.

Given the richness of DIC data, a new way to condense and analyze DIC data is needed to correlate the obtained data by DIC with mechanical behavior. This paper adopted and improved a simple method previously proposed by the authors to correlate the obtained data by DIC and behavior under axial compression to investigate the expansion of shear zone by removing the correlation between strains and position and hence can give a clearer view on the development of strain during deformation.

Chapter 6: Analysis of mechanical behavior of deformation in normal- and high-strength concrete using digital image correlation

(A paper is drafted based on this section "Analysis of mechanical behavior of deformation in rock and concrete using digital image correlation" by Ali Fallah Pour, Rupesh Kumar Verma, Giang Nguyen and Ha Bui)

6.1 Introduction

Most materials fail due to localized deformation leading to shear band formation [157-162] and eventual cracks [147, 161, 163]. In such cases, very high deformation tends to localize in a narrow band across the specimens. For example, unconfined concrete specimens under compressive loading exhibit brittle behavior in association with the fast transition from homogenous to localized failure [164-167]. However, under confining conditions with lateral pressure, this transition is often observed less abrupt [160]. Its correlation with mechanical behavior can be seen in the following reported experiments [160, 164-167]. Under such scenario, the evolution of localized band thickness characterizes the above transition which further could be linked with the material behavior characteristics; for example, brittle behavior shows a more abrupt transition from homogenous to localization indicating the significance of thickness and orientation of localization band in concrete and other geo-materials [156, 168-174]. Therefore, it becomes essential to develop a reliable approach for analyzing the localized band thickness evolution. It may not be possible via contact measurement techniques like a linear variable differential transformer (LVDT) and strain gauges due to their ability to record displacement of/over isolated points. In this view, X-ray computed tomography [7, 21-25] and digital image correlation (DIC) (e.g. [1, 26-32]) provide efficient alternatives, especially in the case of geo-materials and concrete.

The localized behavior of geo-materials and concrete has been extensively investigated using X-ray computed tomography [160, 175-179] and digital image correlation (DIC) (e.g. [27, 96, 98, 142, 147, 155, 180, 181]). It should be noted that this is an impossible task using contact measurement techniques like a linear variable differential transformer (LVDT) and strain gauges due to their ability to record only or overall displacement either isolated points. The X-ray computed tomography method enables to the record of the full-field 3D strain and localization evolution of different materials in detail. It offers a high-resolution observation of full-field strain using significant density variation occurrence, which changes the X-ray absorption [182]. However, as discussed by Landis et al. [183], [184] and [185], the use of X-ray computed tomography is limited due to the need of a small size of specimens, typically 5-10 mm, to obtain the expected advantages. Moreover, Landis and Keane [183] and Ando, Hall [160] explained the use of the X-ray instrumentation technique in the determination of micromechanical behavior of specimens under different types of loading including compression. They indicated that the loading should be stopped to perform the X-ray scan at different stages of the test in order to determine the evolution of the cracking and crack network in the specimen. This leads to a long and expensive test procedure if the continuous outcome is needed in the test plan.

On the other hand, the digital image correlation (DIC) technique provides a cheap and affordable alternative to measure the continuous deformation over specimen surfaces throughout the test. This method uses non-contact full-field kinematics measurement of planar or non-planar surfaces deformation [186, 187]. It has been used extensively to study the localization mechanism in different geo-materials and concrete (e.g. [142, 145, 147, 188-193]). DIC applications in the uniaxial compression test of unconfined reinforced and confined concrete (e.g. [27, 142, 148-151, 191]) and rock (e.g. [194-198]) demonstrated the competency of this approach to measure full-field strain evolution to understand the localization

mechanism. This can be further illustrated from Choi and Shah [148] who discussed that DIC is a powerful method to measure the non-uniform deformations on the surface of concrete specimens. In their paper, the non-uniform displacements over concrete specimen surfaces were shown by using displacement contour maps at various stages of the test. How cracks circumvented the aggregates and propagated parallel to the loading direction in the matrix, can be seen in their research. Li, Xiao [151] used DIC to investigate the failure processes of recycled aggregate concrete under uniaxial compression and observed that the main cracks developed along the loading direction in cement-based materials.

Bisby and Take [27] used the DIC method to evaluate the hoop rupture strain measurement due to its influence on the precise prediction of ultimate axial stress and strain of FRP-confined concrete. They showed that about 50% variation of hoop strains compared to the coupon failure strain could be seen over the surface of FRP confined circular concrete cylinders at failure. They explained that the localization of shear failure planes within the concrete is among the prime reasons for hoop strain variation over specimen surface, which followed by the movement of solid concrete wedges along those failure planes. They suggested that more researches are needed to improve further understanding of the true mechanism of confinement and the factors influencing hoop strain efficiency, thus subsequent model predictions. On the other hand, the effect of unconfined concrete compressive strength (f'_{co}) on carbon fiber reinforced polymer specimens under monotonic and cyclic compressive loading was studied in [142]. This DIC based experiment obtained a higher strain reduction factor (k_ε) for CFRP-confined concrete specimens with f'_{co} lower than 60 MPa compared to higher values of f'_{co}.

Similarly, Bobet, Fakhimi [194] and [197] demonstrated the reliability of a non-contact full-field strain measurement (DIC) compared to conventional methods for geo-materials specimens such as cemented rock specimens. Fracture initiation and propagation in sandstone

specimens using DIC were studied by He and Hayatdavoudi [195], and they found that the cracks are more likely to initiate from the centre or near the loading ends. Whereas the crack propagation is along diametrical loading plane independent of crack initiation. The influence of aspect ratios on sandstone rock behavior using DIC is investigated in the study [198], which found that shear zone localization did not occur in specimens with smaller aspect ratio but in the specimen with aspect ratio 2.4 and 3.5. Axial macro cracks were also observed to be extended parallel to applied axial load at the end of the compression tests. Moreover, it was found in this study that the evolution of localization around the future failure plane favourable to shear zone localization took place for specimens typically with aspect ratios of 2.4 and 3.5.

Although the above-mentioned studies on concrete and rock performed a detailed study on strain localization and its evolution or transition from homogenous to localized deformation, the correlation of the strain localization with the mechanical behavior of specimens still requires further attention. This correlation can bring more insights into the mechanical behavior of concrete or rock specimens under confined or unconfined compression [168]. As shown in Nguyen and Bui [168], the raw micro-mechanical data should be analyzed and condensed to make them useful in developing and/or validating constitutive models. They can also help improve the prediction of mechanical behavior of the material under consideration, using findings on the links between mechanical behavior and evolution of localization. Similarly, several studies were aimed to study the rock behavior using DIC technique but majorities of them lack in-depth correlation analysis [196, 198-201]. This issue has been addressed partly in Fallah Pour, Nguyen [202] in which a few different ways to analyse DIC data and the links between localization of deformation with the macro responses have been explored. The results are promising, opening a new way to correlate DIC data on deformation and localization with the macro behaviour for more insights into localized failure of geo-materials. Nevertheless, there are still several challenges due to very different localization patterns that do not show

clear shape of shear localization bands in different materials. The onset of localized failure and transition from diffuse to localization have also not been addressed in our previous study (Pour et al, 2020). As pointed out in our recent theoretical approach (Nguyen & Bui, 2020), this onset and transition are behind the observed macro behaviour of a material.

This section focuses on the correlation between evolution of localisation and the mechanical responses of concrete and the analysis of data for the proposal of useful relationships for constitutive modelling. The analysis of rich DIC data is used for the determination of onset of localization and transition from diffuse to localized failure, in conjunction with the proposal of a new statistical approach to predict the evolution of localization and transition of failure modes. DIC data on concrete and sandstone in conjunction with their mechanical responses under uniaxial compression are used. This approach results in the condensation of obtained data by DIC and leads to a potential method which can be applied in validation and/or development of constitutive models. The experiments are briefly presented in Section 2, followed by the descriptions of a new approach to determine the onset and evolution of localization from DIC data in Section 3. Sections 4 and 5 present a new way to condense rich DIC data for findings that can be useful for the validation and development of constitutive models.

6.2 Experimental program

6.2.1 Concrete

This study used the experimental data from the previous section performed on NSC and FRP-confined concrete behavior [202] . Additionally, new specimens prepared from HSC with two different targets compressive strength (f'_{co}). Three types of concrete specimens were prepared from one normal strength concrete (NSC) batch and two high strength concrete (HSC) batches. A total of 6 unconfined concrete cylindrical specimens, all with 100 mm diameter (D) and 200 mm height (H), were manufactured and tested. The concrete mix used had a target compressive

strength of 30, 70, and 100 MPa with control cylinders tested at selected time intervals to determine the in-place unconfined concrete strength gain. The ingredients for concrete used in this research were sourced from a local concrete supplier and were batched and mixed in the laboratory. The mixes comprises of crushed basalt as the coarse aggregate, with a 10 mm nominal maximum diameter. The resulting slump for all batches of concrete was over 100 mm. Control cylinders with 100 mm diameter and 200 mm height were cast and tested in parallel to unconfined specimens to determine compressive strength (f'_{co}). Table 19 present the detail of HSC mixes.

Table 19-Concrete mix proportions

HSC-1		HSC-2	
Ingredient	Amount	Ingredient	Amount
Cement (kg/m^3)	437	Cement (kg/m^3)	506
Silica fume (kg/m^3)	38	Silica fume (kg/m^3)	44
Sand (kg/m^3)	710	Sand (kg/m^3)	700
Gravel (kg/m^3)	1065	Gravel (kg/m^3)	1050
Water (kg/m^3)	164	Water (kg/m^3)	148
Superplasticizer* (kg/m^3)	10	Superplasticizer* (kg/m^3)	20
w/c	0.36	w/c	0.30
Total (kg/ m^3)	2424	Total (kg/ m^3)	2468

* Superplasticizer contained 70% water by weight

6.3 Instrumentation

The brief experimental set-up is presented in figure 68 where axial deformations of the concrete specimens were recorded with four linear variable differential transformers (LVDT), mounted at the corners between the loading and supporting steel plates. The recorded deformations were used in the calculation of the average axial strains along with the height of the specimens. The lateral strain was measured by a total of 6 unidirectional lateral strain gauges (SG) having a gauge length of 5 mm that were bonded on the surface of the specimen. These strain gauges were installed in pairs located at heights of 50, 100, or 150 mm, with each pair of gauges

attached at opposing sides of the specimen. The specimens were tested under monotonic axial compression using a 5000 kN capacity universal testing machine. During the test, displacement was applied at the rate of approximately two micro-strains per second until specimen failure. It should be said that the detail of configuration can be found in previous sections, i.e. Figs. 52, 53 and 56.

The 3D DIC instrumentation utilized two monochrome 2.8-megapixel conventional charge-coupled device (CCD) cameras at an inclination of more than 25^0 but smaller than 60^0. These cameras have a sensor size of 1/1.8" with a maximum resolution of 1928×1448 pixels. The camera lens is a 75-mm Fujifilm prime lens with an aperture size range of 1/22-1/2.8 with minimal distortion, i.e., no correction for distortion required. The camera body has a Universal Serial Bus (USB) 3 interface for the fast and reliable image transfer. This instrumentation includes three-dimensional DIC calibration. Figure 68 presents a brief outline of the overall experimental setup and DIC arrangement.

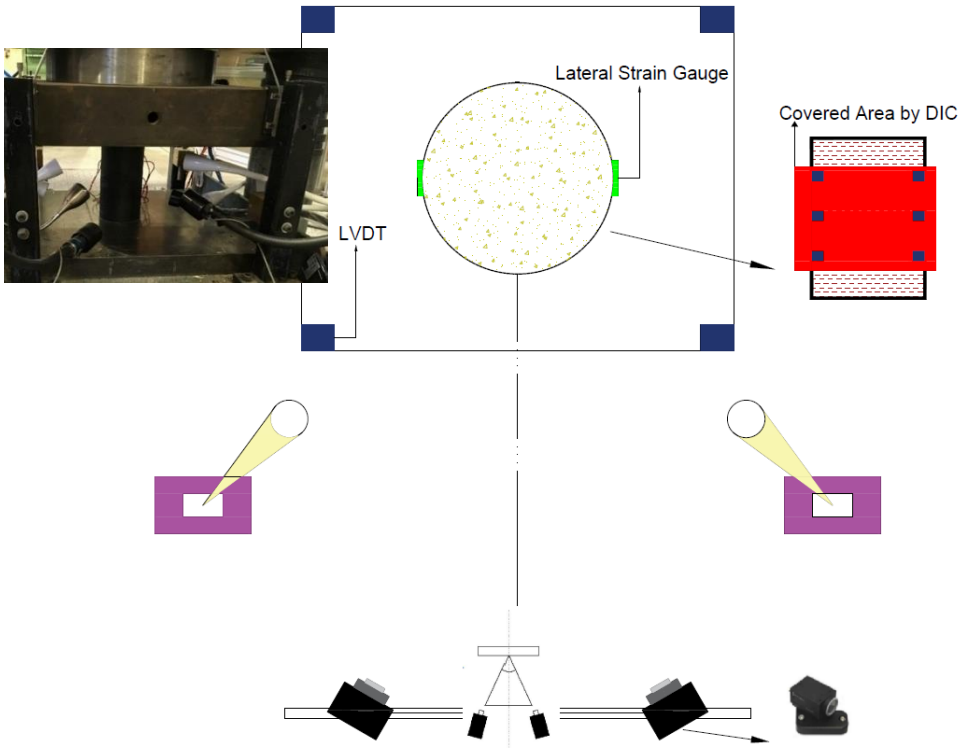

Figure 68-Test setup and instrumentation

6.4 Correlation between mechanical behavior and evolution of localization

6.4.1 NSC

The correlation of mechanical behavior and localization evolution for NSC specimens under uniaxial compression are shown in Fig. 69. As shown in that figure, the localization behavior varied slightly in NSC specimens compared to obtained results for Geo-materials (sandstone). The slightly different behavior in NSC compared to sandstone can be explained by different friction conditions between the specimen and loading platens, promoting splitting like a failure instead of a localization band across the width of the specimen like in sandstone. Despite this slight difference, the other characteristics of the localization evolution for NSC is similar to the case of sandstone. Fig. 69a can be used to determine the initiation of localization while Fig. 69b illustrates the evolution of localization for NSC specimens. As shown in Fig. 69b, a noticeable increase of Von Mises strain along the profile at middle of specimens after point 3 can be observed. This figure also illustrates the increasing of strain localization inside the shear zone after point 4 while other part of specimens experienced an unloading behavior. It should

be said that the measured Von Mises strain along the height of specimens illustrate relatively homogenous behavior before point 3. As can be seen in Fig. 69a, the localization initiated before compressive strength of concrete (f'_{co}) in NSC. This indicates a more accurate approach is needed to investigate the localization onset. The transition from diffuse to localized failure was illustrated in Fig. 69c. By removing the correlation of obtained Von Mises strain to location, a method to condense the DIC rich data can be developed which helps to determine quantitatively the trend of the mentioned transition, as explained in section 5.

Fig. 70 shows the onset of localization for NSC specimens. In this figure, the Von Mises strain evolution is illustrated for two separate points placed inside and outside of localization zone. As can be seen in the Fig. 70, the shear band in NSC specimens initiated (i.e. bifurcation of Von Mises strain curves) at about 55%-65% of f'_{co}. This result indicates to earlier occurrence of the bifurcation phenomenon in NSC than sandstone as observed before in Fig. 69a. It is noted that the speckle pattern in concrete specimen were lost a few steps after maximum obtained axial stress (i.e. f'_{co}) and hence strain could not be calculated after this point (point 5).

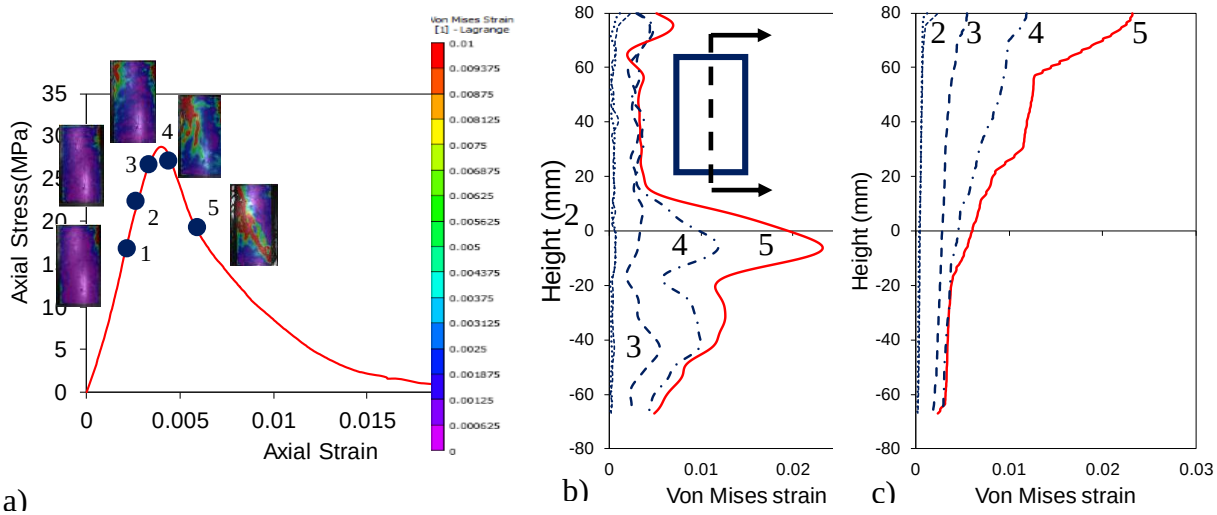

Figure 69-NSC specimens- Correlation between mechanical behaviour and evolution of localisation: (a) stress-strain response and contours of Von Mises strain at 5 stages indicated by 5 points; (b) evolution of strain profiles (centre line indicated in the inset); (c) Removing link between strain and position and sorting strains in ascending order.

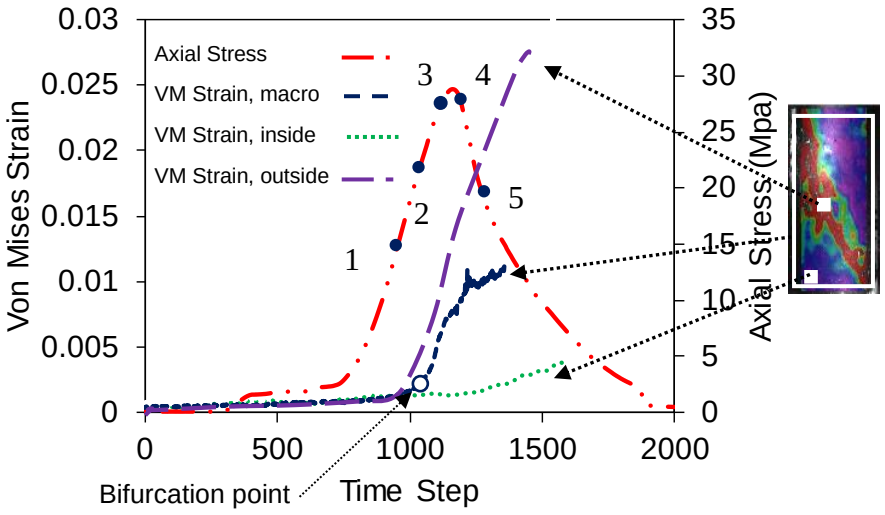

Figure 70-Onset of localisation observed by plotting macro axial strain, and local strains inside and outside the localisation zone, NSC.

6.4.2 HSC

Same as NSC, the used methodology in previous section is applied on obtained DIC data for HSC specimens and results are shown in Figs. 71 and 72. As can be seen in Figs. 71 and 72, both studied batches of HSC showed unclear localization patterns compared to previous tested

specimens, i.e. NSC specimens. The figures illustrate that the localization pattern varied from clear shear band in sandstone and NSC to diffuse cracks in HSC. Comparing Figs. 69a with 71a and 72a (points 3 and 4) shows clearly the difference of localization onset and evolution in HSC compared to NSC. As shown in Figs 71a and 72a, the onset of localization can be observed later compared to NSC specimens but approximately similar to sandstone specimens. However, despite of different observed pattern for NSC and HSC1 in Figs 69a and 71a, Figs 69b and 71b illustrate the similar pattern of localization evolution for these two different types of concrete. As can be seen in Fig. 71b for HSC1, an evident increase of Von Mises strain can be seen along the middle profile of tested specimens after points 3 same as NSC. This strain localization increase occurred inside the shear zone beyond point 4 (as can be seen in Figs. 71b) and other part of specimens after this point encounter a unloading behavior except few points. However, this pattern changes for HSC2 and the increase in Von Mises strain along height of specimens occurs later, i.e. after point 4. It should be noted that HSC2 has highest value of f'_{co} among all prepared concrete batches which translates to more brittle behavior in this type of concrete. Figs. 71c and 72c are prepared by detaching the correlation of obtained Von Mises strain from location to condense the obtained DIC data for both types of HSC specimens. This was performed to determine the trend of transition from diffuse to localized failure quantitatively. Similar to sandstone and NSC, the characteristics of localized failure remain the same for HSC and strain intensification (i.e., loading) inside the localization zone can be seen while unloading can be obtained outside the localization zone, as can be seen in Figs 71c and 72c.

Figs. 73 and 74 illustrate more evidently and accurately the initiation of localization for HSC specimens. The figures' preparation details were explained earlier for NSC specimens. As can be observed in Figs. 73 and 74, although HSC specimens showed approximately similar behavior in bifurcating of three types of studied strain curves to NSC, both types of HSC had

slightly later bifurcation occurrence whereas the bifurcation happened at approximately 80-90% of f'_{co}. This can be attributed to more brittle behavior of HSC specimens compared to NSC. This more brittle behavior enhances its similarity with rock in contrast to NSC. As it was shown in these figures, the bifurcation phenomenon occurred approximately at maximum axial strength more similar to HSC. In addition, the HSC specimens showed a sudden jump in the obtained Von Mises strain inside of shear zone after bifurcation point. However, this abrupt jump was not seen in NSC and a more gradual increase of Von Mises strain inside of localization band was seen, shown in Figs, 70, 73 and 74. It is well understood that the brittleness of concrete increased by an increase in f'_{co}. This leads to more abrupt behavior of HSC compared to NSC, which is in agreement with obtained results.

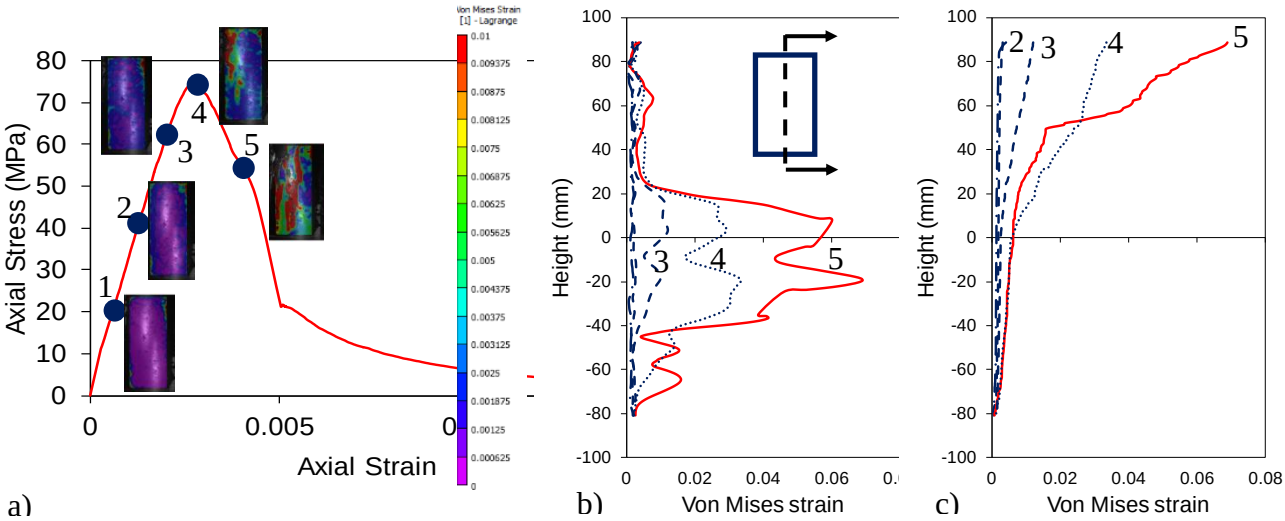

Figure 71-HSC1 specimens- Correlation between mechanical behaviour and evolution of localisation: (a) stress-strain response and contours of Von Mises strain at 5 stages indicated by 5 points; (b) evolution of strain profiles (centre line indicated in the inset); (c) Removing link between strain and position and sorting strains in ascending order.

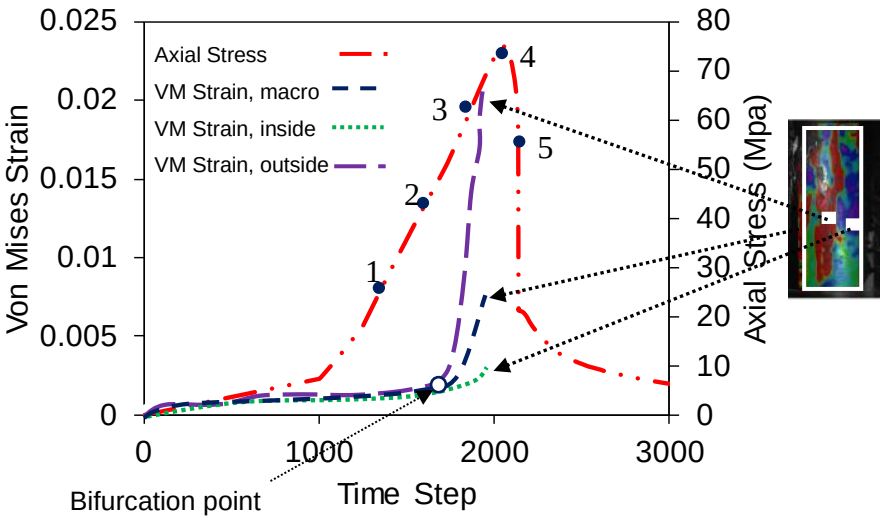

Figure 72-Onset of localisation observed by plotting macro axial strain, and local strains inside and outside the localisation zone, HSC1.

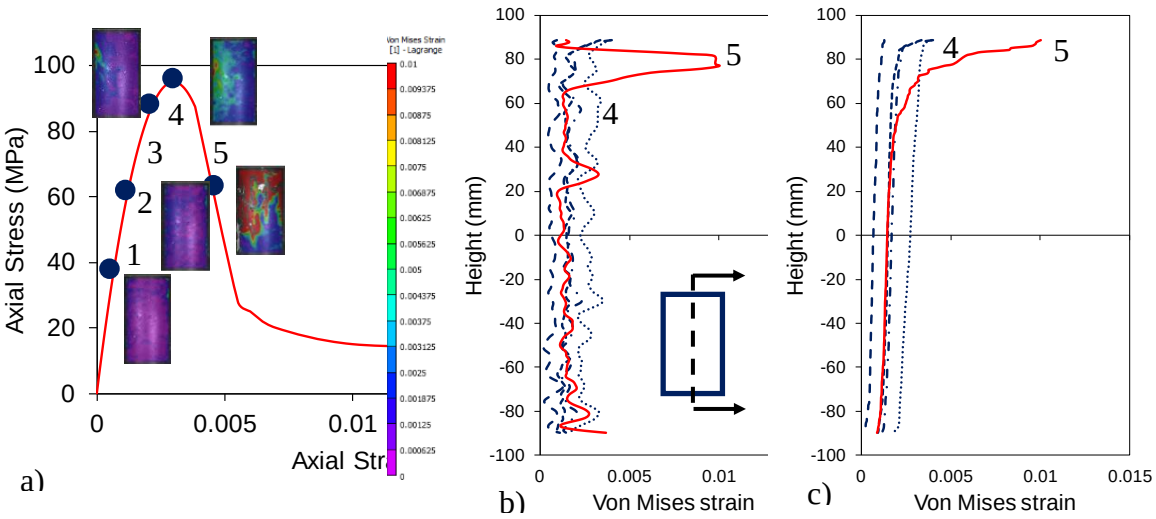

Figure 73-HSC2 specimens- Correlation between mechanical behaviour and evolution of localisation: (a) stress-strain response and contours of Von Mises strain at 5 stages indicated by 5 points; (b) evolution of strain profiles (centre line indicated in the inset); (c) Removing link between strain and position and sorting strains in ascending order.

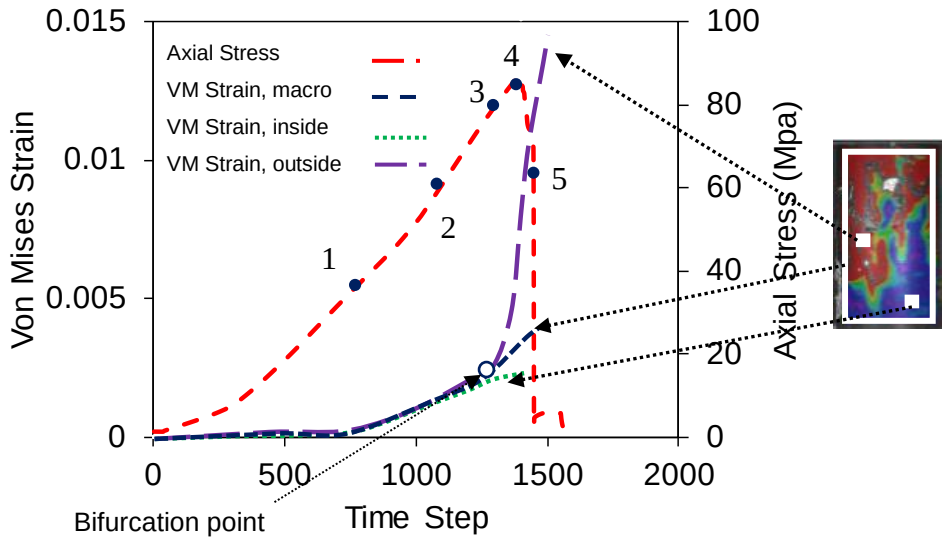

Figure 74-Onset of localisation observed by plotting macro axial strain, and local strains inside and outside the localisation zone, HSC2.

6.4.3 Discussion

The obtained outcome from NSC and HSC in previous sections showed a diffused crack patterns in HSC. This dissimilar observed behavior in HSC compared to NSC makes the determination of transition from diffused to localized failure difficult which signifies the need of more comprehensive method to analyse and quantify the mentioned transition. Moreover, the obtained results for both concrete types, i.e. Figs. 69-74, show the evolution of full-field strain along only one profile (unsorted and sorted) and do not include all measured full-field strains obtained by DIC over specimens surface. As can be seen in the figures, changing the profile from one location to another across the specimen's perimeter, the different shapes for unsorted and sorted Von Mises strain profiles can be observed. This indicates the need of more profiles for determining accurately the transition pattern from diffused to localized failure. It is evident that using more profiles to investigate the mentioned transition is hard to be practiced in developing/validating a constitutive model due to high number of datasets obtained by DIC. Consequently, a new approach should be developed which uses all obtained data by DIC but in condense format. Section 4 will illustrate a possible method to perform the data contraction by using a new approach.

6.5 A statistical approach to analysing localised failure

6.5.1 Correlation between macro mechanical behavior and evolution of localization

As discussed in previous section, a new approach needs to be developed which offers a powerful instrument to capture all localization characteristics including initiation and evolution. It is significant to be noted that the use of measurement method which is able to provide both local and global deformation data sets is essential to develop such a method, e.g. DIC. This approach should be capable to evaluate and quantify the overall and local mechanical behavior of tested specimens and correlate them to localization characteristics. In this sense, determining distributions of full-field strains over specimen surface and linking obtained distribution at each step to other steps could be a potential option for such a type of approach. Using this method offers a robust instrument to link the macro mechanical behavior of specimens with localization characteristics and provides a lower scale of information compared to continuum mechanics.

To model and determine the full-field strain distribution over specimen surface, probability density function (PDF) and its accumulation form for each step of the test could be one of the possible techniques. To develop this approach, the obtained Von Mises strain over whole front surface of the specimens were used while the connections to their locations were ignored. Afterward, the range between maximum obtained Von Mises strain at failure and zero was divided into 50 intervals. Following this, the number of obtained Von Mises strains that fall into these intervals were counted at each step. The frequency number of data in each bin was divided by a total number of analyzed data obtained by DIC over specimens' front surface. A histogram was provided based on obtained frequency numbers and related intervals then the top of all bars of the histogram was connected together. It should be noted that approximately similar maximum Von Mises strain was used for all specimens to make easier comparing different specimens' behavior to each other.

Figures 75-77 present the obtained Von Mises strain distribution and their accumulative form at different steps of tests for NSC and HSC specimens. It can be seen in the figures that the shape of Von Mises strain distribution at each step is very similar to statistical PDF and this shape remained similar up to maximum axial stress for sandstone and concrete specimens.

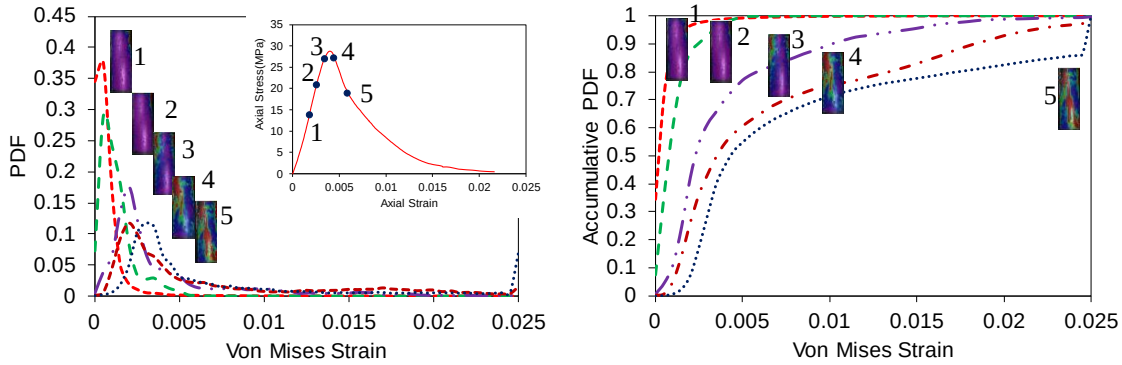

Figure 75- Von Mises strain distribution evolution of NSC specimen obtained results by DIC

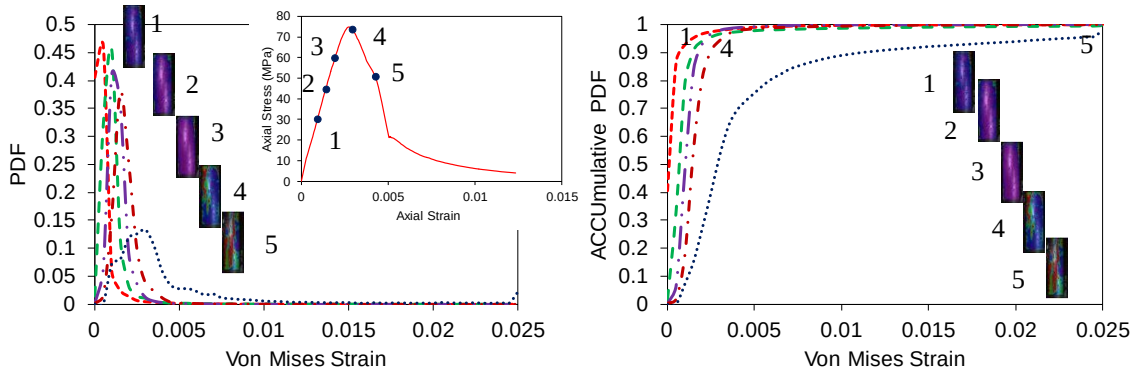

Figure 76-Von Mises strain distribution evolution of HSC1 specimen obtained results by DIC

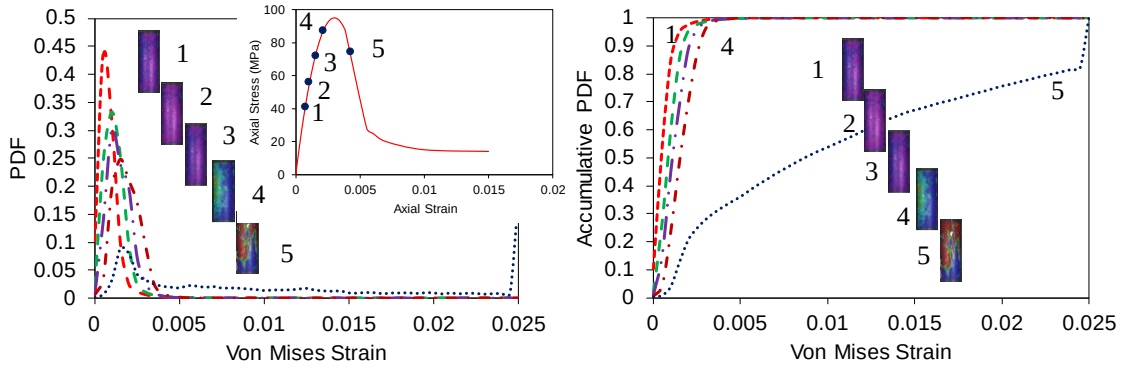

Figure 77- Von Mises strain distribution evolution of HSC2 specimen obtained results by DIC

6.5.2 Statistical distribution function and parameters

The Beta distribution was selected in this study to model the Von Mises strain distribution over the specimens' surface at each step of the test procedure in this study. This selection was made due to the existence of three parameters which govern the shape of the distribution and these parameters help to recreate the experimental distribution curves at different stages of the test. The details related to the Beta distribution and three mentioned parameters are presented in Appendix C. To create the theoretical Beta distribution curves and compare them to experimental curves, three parameters (ξ, p, q) should be determined. To determine these parameters, two conditions were considered. Firstly, the obtained theoretical curves should have a similar shape as experimental Von Mises strain distribution shape; secondly, they should have approximately similar area under both types of curves. Fig. 78 shows the both obtained PDF curves, i.e. experimental and theoretical curves, for NSC specimen. This specimen is selected as representative of whole specimens due to similarity of obtained results including both types of studied concrete types. This figure demonstrates a good agreement between experimental and theoretical curves for NSC. It should be noted that the similarity of shapes was lost after creation of a shear band. Additionally, as can be seen in Figs. 78 and same as obtained p for whole concrete specimens, p are constant it equals 3. However, ξ and q vary at different steps of test procedure and different values at different axial strain are obtained.

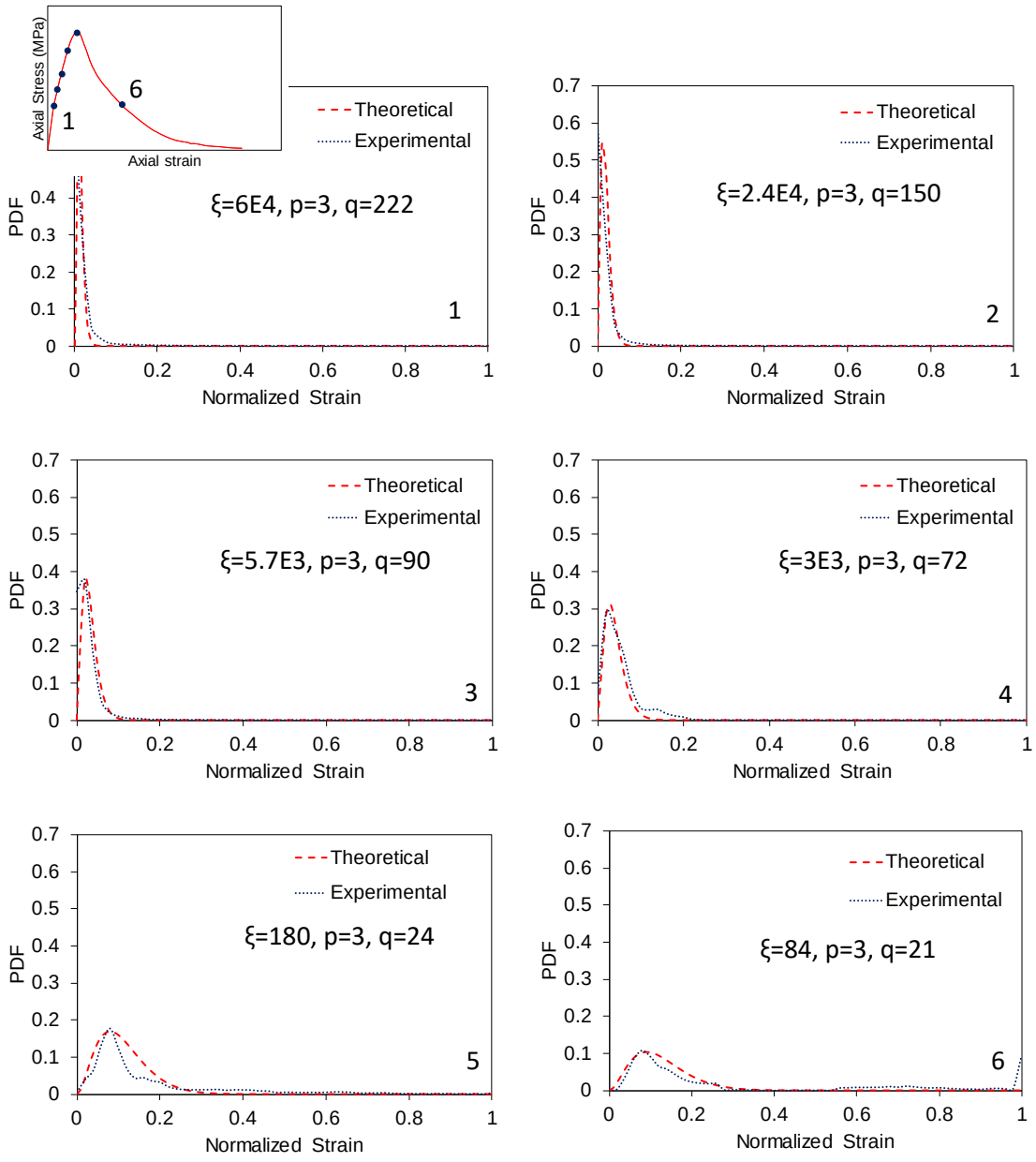

Figure 78- Beta Distribution of Von Mises strain for NSC specimen

To investigate the relationship between the obtained coefficients, i.e. ξ and q, and mechanical response of sandstone and concrete specimens, the variation of these coefficients with axial strain is investigated in this study. Fig. 79 shows the relationship between ξ and q and recorded axial strain for NSC and HSC specimens. It should be said that 6 points over axial stress-strain curves are selected and obtained ξ and q for each point are plotted in Fig. 79. It also should be said that the 6 selected points in axial stress-strain curves are similar points which were used in Figs. 75-77. As can be seen in the Fig. 79, ξ and q for concrete specimens decrease by an increase in the axial strain and this relationship can be expressed by a power function. Eq. 6.1

shows a general form of a expression which describes the relationship between ξ and q and axial strain (ε_a).

$$\xi \ or \ q = \theta \varepsilon_a^{\varphi} \tag{6.1}$$

where ε_a is an axial strain, φ and θ are coefficients that vary in sandstone and concrete specimens. Due to existence of more experimental data for concrete compare to sandstone, the sandstone was not investigated in this part of study and the main concern is on the concrete specimens. By studying the obtained experimental coefficients (φ and θ) for NSC and HSC specimens, it can be observed that θ can be expressed as a function of compressive strength of concrete (f'_{co}) and corresponding axial strain (ε_{co}) and φ can be considred conctant. Using regression analysis, θ in Eq. 6.1 can be expressed by two speperate equations, i.e. Eqs. 6.2 and 6.3, for ξ and q, respectively.

$$\theta_{\xi} = \frac{f'^{0.225}_{co}}{1000} \tag{6.2}$$

$$\theta_q = f'^{0.65}_{co} \varepsilon_{co} \tag{6.3}$$

It should be mentioned again that φ was obtained and considered constant and φ equals to (-3) for ξ and (-1) for q. By substituting the Eqs. 6.2 and 6.3 in the Eq. 1, the following expressions are proposed to predict the ξ and q for both studied types of concrete (i.e. NSC and HSC).

$$\xi = \frac{f'^{0.225}_{co}}{1000} \frac{\varepsilon_a^{-3}}{100} \tag{6.4}$$

$$q = f'^{0.65}_{co} \varepsilon_{co} \frac{3}{\varepsilon_a} \tag{6.5}$$

It should be noted that, $\frac{f'^{0.225}_{co}}{1000} \left(\frac{152}{D}\right)^{0.1} \left(\frac{2D}{H}\right)^{0.13}$ is approximation of ε_{co} (see Ref. [23]) and θ is proportion of this approximation, i.e. $\frac{f'^{0.225}_{co}}{1000}$, as can be seen in Eq. 6.4. This indicates the

dependency of θ to both unconfined concrete compressive strength (f'_{co}) and corresponding strain (ε_{co}). Fig. 81 shows the comparison between experimental and predicted values for ξ and q by using Eqs. 6.4 and 6.5. As can be seen in the figures, there is approximately a good agreement between predicted and experimental obtained ξ and q. However, it should be noted again that these results were obtained in this study and a more detailed study is needed to develop a general statement.

Fig. 82 shows the obtained Von Mises strain distribution curves using Eqs. 6.4 and 6.5 and comparing these curves with obtaine experimental distribution for NSC, HSC1 and HSC2. As can be seen in the figure, although there are differences between predicted distribution curves by Eqs. 6.4 and 6.5 compared to experimental curves, it can be said that the shape of experimental curves are in good agreement with modelled curves. However, it should be again said that this outcome needs more detailed studies and more experimental data to generalize these results.

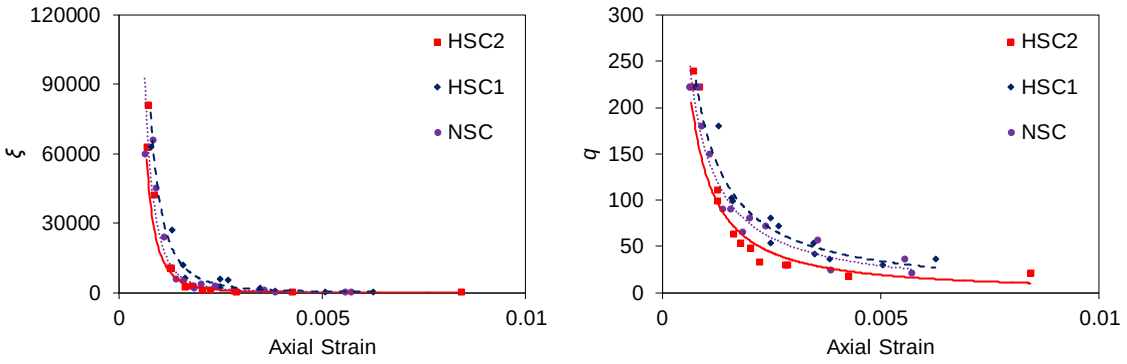

b) Concrete

Figure 79- Obtained ξ and q for concrete and sandstone specimens

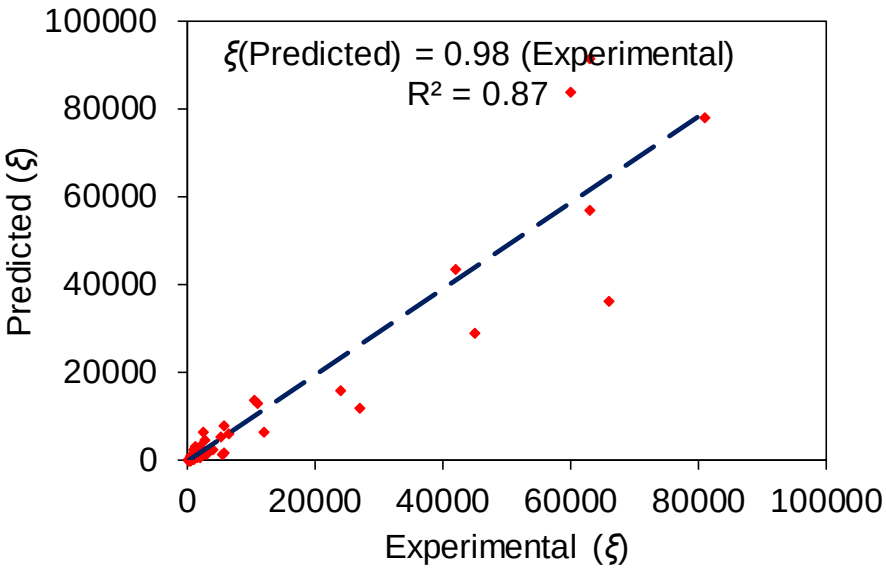

a) ξ

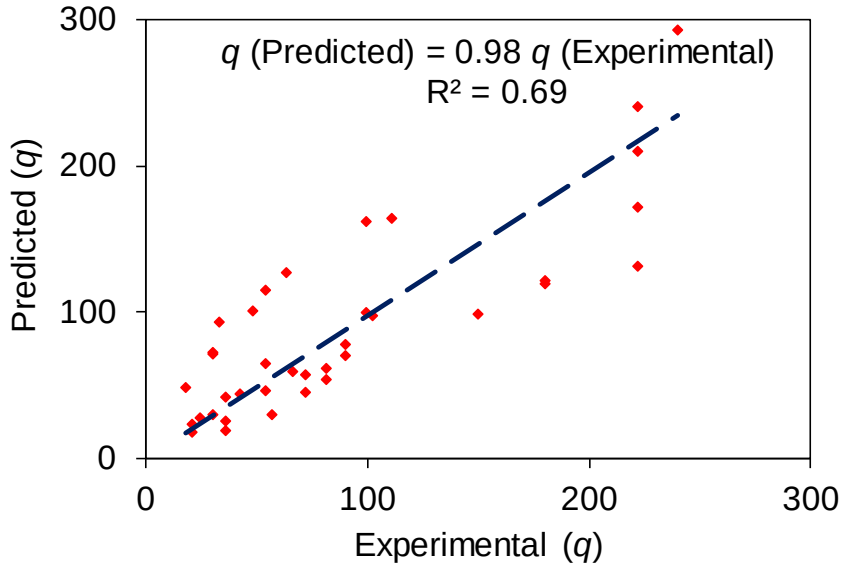

b) q

Figure 80-Comparison between experimental and predicted values for ξ/p and q/p for concrete specimens

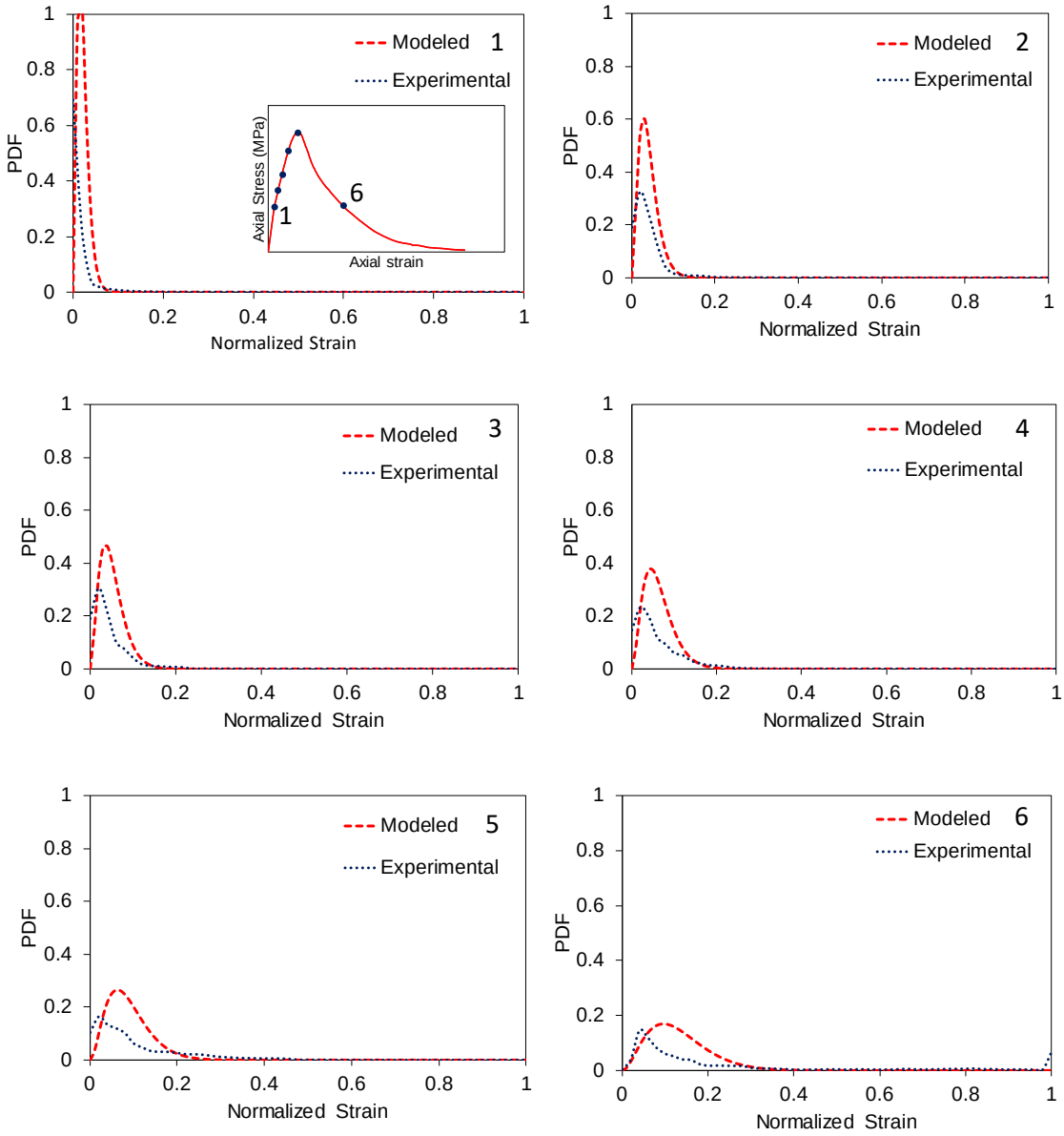
Modeled 1
Experimental
PDF
Normalized Strain
Axial Stress (MPa)
Axial strain
1
6
Modeled 2
Experimental
PDF
Normalized Strain
Modeled 3
Experimental
PDF
Normalized Strain
Modeled 4
Experimental
PDF
Normalized Strain
Modeled 5
Experimental
PDF
Normalized Strain
Modeled 6
Experimental
PDF
Normalized Strain

a) NSC

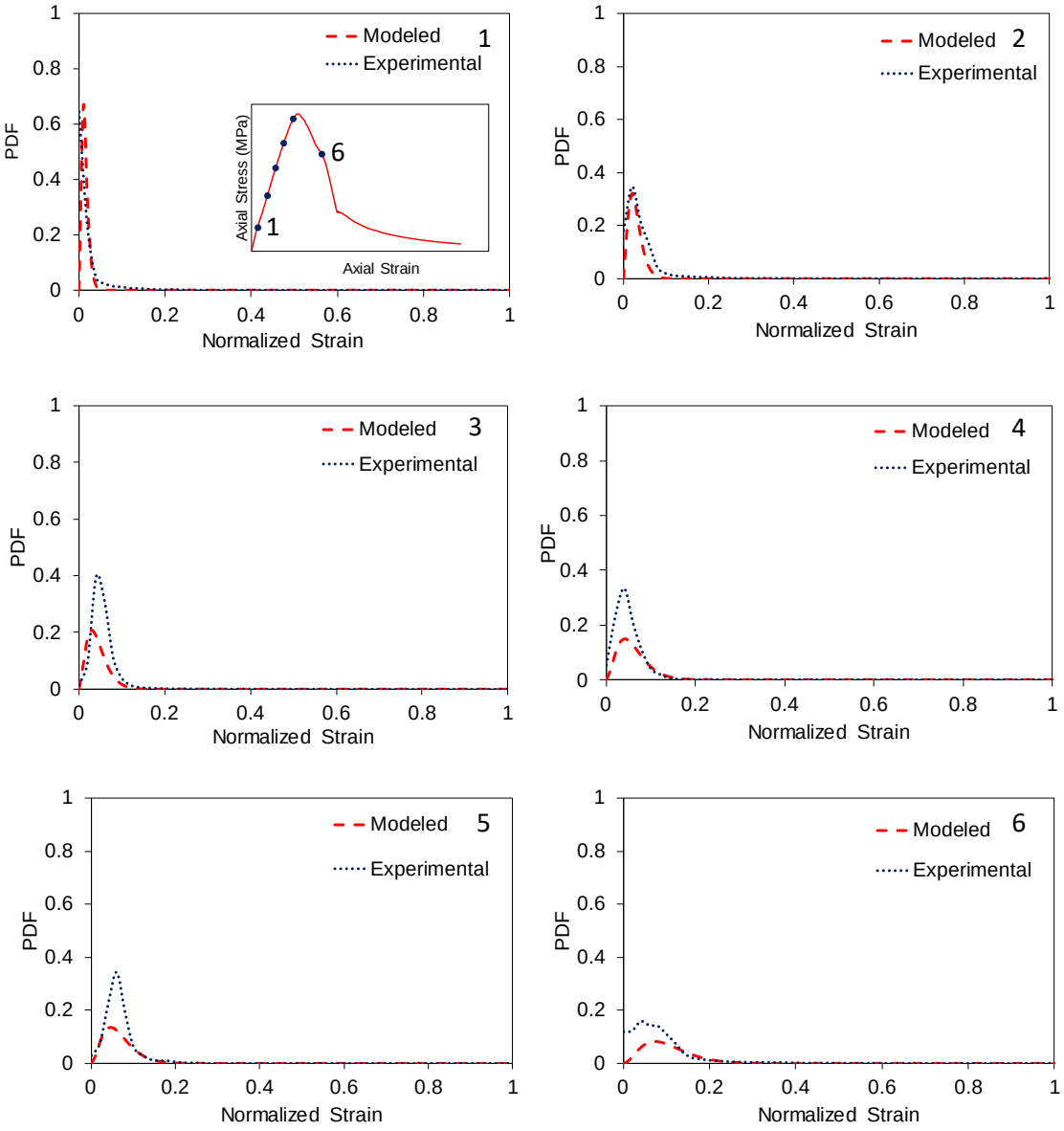
Modeled
Experimental
1
2
3
4
5
6
PDF
Normalized Strain
Axial Stress (MPa)
Axial Strain

b) HSC

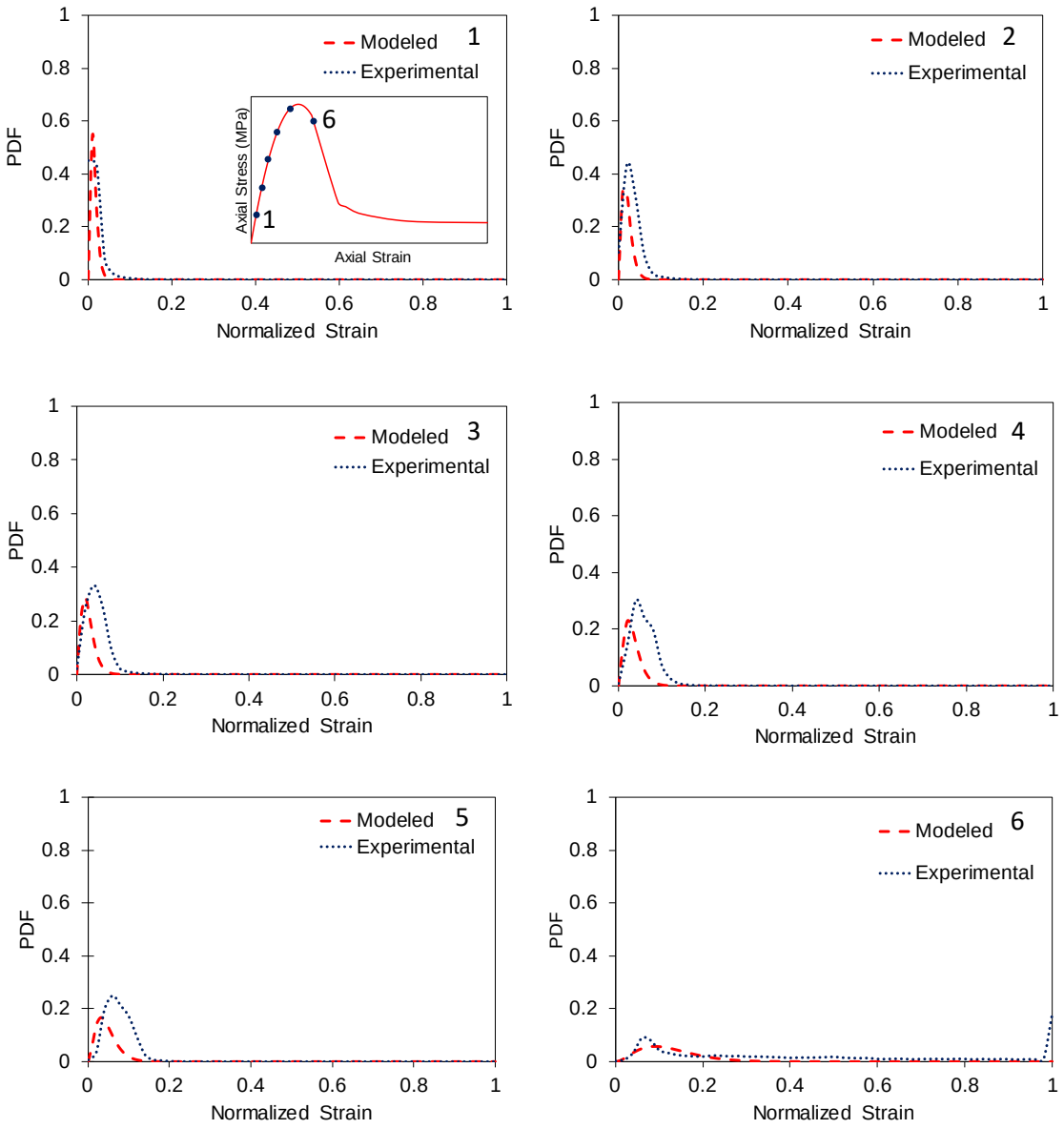

c) VHSC

Figure 81-Comparison between experimental and predicted Von Mises strain distribution over concrete specimens surface: a) NSC; b) HSC; c) VHSC

6.6 Conclusion

This paper presents the results of an experimental study on the localization of strain for sandstone, NSC, and HSC columns with circular cross-sections under compression loading. The axial stress-strain curves were obtained and synchronized with images that are captured by the DIC system. The following points summarize the main findings and contributions to this study:

1-Given the richness of DIC data, a new way to condense and analyze DIC data is needed to correlate the obtained data by DIC with mechanical responses of specimens. This paper proposes a simple method to correlate the obtained data by DIC and confined specimen mechanical response under compression.

2-The Von Mises strain evolution shows relatively homogeneous behavior during the pre-peak regime. The Von Mises strain profile in the middle of the front surface also of specimens indicates this homogeneous deformation before the peak. The localization of strain gets stronger at the peak, and very localized deformation happens during the post-peak regime: the Von Mises strain inside the localization band keeps increasing while the strain outside the band decreases, indicating elastic unloading.

3- The shear band in NSC specimens initiates to penetrate at about 60-70% of f'co, and both inside and outside of shear band average Von Mises strain showed approximately similar behavior before this point (occurrence of bifurcation). Although HSC specimens showed approximately similar to NSC, both types of HSC show slightly later initiation of bifurcation occurrence and it happens at approximately 80-90% of f'co.

5- A new method is developed in this study to condense the obtained data by DIC and keep the accuracy of localization characteristics. Using this method leads to determine distributions

of strain over the specimen surface and link the strain distribution to a statistical expression. Moreover, this method is capable of quantifying the strain distribution evolution during the test procedure by using the same function and existing coefficients in this function. This offers a robust approach to correlate the macro mechanical behavior of specimens with localization characteristics, whereas this offers a lower scale of information compared to continuum mechanics.

7- In this study, Beta distribution is used to model the Von Mises strain distribution at each step of the test procedure. This selection is made due to the existence of three parameters that govern the shape of the distribution and these parameters help to recreate the experimental distribution shape. The outcome shows that the experimental distribution of Von Mises strain over specimens surface can be modelled approximately accurately using Beta Distribution.

Chapter 7: Examination of deformation in FRP-confined high-strength concrete using digital image correlation

(A paper is drafted based on this section "Deformation behavior investigation in FRP-confined high-strength concrete using digital image correlation" by Ali Fallah Pour and Giang Nguyen.)

7.1 Introduction

The mechanical behavior of concrete columns enhances by using fiber-reinforced polymer (FRP) sheets as lateral confinement. Over last two decades, many researches were performed on application of FRP composite as confinement of concrete columns (e.g. [15, 88, 89, 92, 102, 111, 131]) and many of them examined the mechanical behavior of FRP-confined concrete columns under concentric axial compression loading (e.g. [15, 16, 88, 89, 92, 102, 111, 131]). Due to the better structural performance offered by FRP-confined HSC compared to NSC and improving intrinsically brittle behavior of HSC due to FRP-confinement, the use of this structural system in construction industry , e.g. bridges and multi-storey building, has recently received a great deal of attention [14, 15, 17, 92, 106, 111]. However, vast application of any structural system including FRP-confined HSC is possible when an accurate model to predict the mechanical response of this structural system (i.e. stress-strain curve) under different type of loading is available.

It is reported previously that the obtained experimental axial and lateral stress-strain curves of FRP-confined HSC can be influenced by many parameters such as measurement methods [27, 142, 154, 155]. Most of existing available models for FRP-confined HSC are relatively poor at predicting the key references strain in their axial stress-strain curves, e.g. ultimate axial strain (ε_{cu}) [27-29, 142, 154]. It should be noted that the most accurate models to predict ultimate axial strain (ε_{cu}) use hoop rupture strain ($\varepsilon_{h,rup}$) as input data [17]. This poor predictive ability of various models is partly consequence of the large variability recorded in experiments

measuring strains in FRP wraps and tubes at failure [27]. The most popular existing measurement methods, i.e. linear variable differential transformer (LVDTs) and strain gauges (SGs), are sometimes unable to capture the key references point on the stress-strain curves such as $\varepsilon_{h,rup}$. For example, the large variability recorded data of $\varepsilon_{h,rup}$ by different studies is partly due to ability of SGs to show the behavior of one point over specimen surface where they are attached. To illustrate the accurately behavior of FRP-confined concrete, a new measurement method recently was applied which offers both local and overall engineering strain evolution by correlation of digital images (DIC). This method was used recently by different researches to study the inconsistency of reported results for hoop rupture strain ($\varepsilon_{h,rup}$) of FRP-confined specimens, e.g. [27, 142]. As it was shown by previous studies [27, 29, 142, 144], localized strain gauges cannot capture the actual behavior of hoop strain including hoop rupture strain ($\varepsilon_{h,rup}$). It is explained by Bisby and Take [27] and Tabbara and Karam [30] that variation of lateral strain in FRP-confined concrete including $\varepsilon_{h,rup}$ is due to variation of localization of shear failure planes within concrete which followed by movement of solid concrete wedge along failure planes. Revising the existing literature focused on hoop rupture strain ($\varepsilon_{h,rup}$) showed that although few researches on strain localization of FRP-confined NSC was performed (e.g. [27, 191, 202]), FRP-confined HSC needs more detailed study on lateral behavior of FRP-confined HSC due to different behavior of HSC compared NSC.

Existing studies on failure procedure of concrete and FRP-confined concrete showed that the appearance of crack in concrete caused fast lateral expansion during the transition zone and this dilation triggers the passive confinement mechanism of the FRP shell (e.g. [15, 17, 92, 97, 99, 103, 111, 144]). As a result, the first ascending portion of axial stress-strain curves transitioned to typically ascending quasi-linear stages on the axial stress-strain curve during development of passive confinement, i.e. triggering confinement mechanism. This indicates that the degradation of the axial stiffness of the concrete column contracts by lateral pressure

(f_l) which made by FRP jacket. The lateral pressure helps the concrete columns to avoid losing its integrity and to show more ductile behavior compared to unconfined concrete. As previously studies reported, i.e. [15, 17, 92, 96, 97, 99, 103, 111], the FRP-confined concrete specimens typically fail due to rupture of the FRP confining shell. The observed concrete rubble after the failure of the FRP tubes and a large number of microcracks created during failure progression indicates the gradual concrete crushing during failure progression [106]. A few studies used DIC method to describe better the failure procedure of unconfined and FRP-confined concrete specimens under bending (e.g. [145-147]) and compression (e.g. [148-151]). These studied reported the benefits and potentials of this technique for better explanation of failure procedure and mode for tested specimens. The literature review performed by this group showed that no researchers at present examined FRP-confined HSC strain localization to describe more accurate the influence of more brittle behavior of HSC on FRP-confined HSC failure procedure.

The mechanical response of FRP-confined concrete under compression was examined by various studies (e.g. [142, 202]). These studies monitored the influence of key parameters such as f'_{co} and K_l on FRP-confined concrete behavior. Li, Wu [142] with applying DIC investigated the effect of f'_{co} on carbon fiber reinforced polymer specimens under monotonic and cyclic compressive loading. This study showed the significance of unconfined concrete strength (f'_{co}) on behavior of FRP-confined specimens and they obtained the higher reduction factor (k_ε) for CFRP-confined concrete specimens with f'_{co} lower than 60 MPa compared to higher value of f'_{co}. It should be noted that the reduction factor shows the reduction of $\varepsilon_{h,rup}$ compared to ultimate tensile strain of FRP (ε_{fu}) (e.g.[28, 29]). Fallah Pour et al. [202] discussed the influence of FRP types and lateral stiffness (K_l) on FRP-confined NSC mechanical response under axial compression. They showed that FRP tubes caused more homogenized crack distribution over specimens' surface and they create bigger shear zone compared to unconfined specimens. They

also illustrated that the expansion of shear zone is more gradual compared to unconfined specimens which have abrupt behavior. However, the accomplished literature review by authors indicates the absence of any study on mechanical response of FRP-confined HSC accompanied with correlation of strain localization to mechanical response of FRP-confined HSC. This is evident that the mentioned study helps to develop a more accurate prediction of the mechanical behavior of FRP-confined HSC.

This section presents a detail study on the Von Mises strain evolution, strain localization and confinement mechanism of FRP-confined HSC columns and influence of f'_{co} variation and FRP tube characteristics on FRP-confined HSC behavior. The section initially provides a brief of the experimental program which is followed by the test results illustration. The evolution of engineering strains were provided and discussed in details. Afterward, the effect of f'_{co}, lateral stiffness (K_l) and FRP types on localization evolution was studied. In the end, a method which was developed in last sections (i.e. sections 5 and 6) to quantify the localization characteristics, was used. This section was completed by modelling the Von Mises strain distribution over specimens surface which helps to correlate the localization characteristics with mechanical response of FRP-confined HSC.

7.2 Experimental program

7.2.1 Details of specimens

A total of 16 FRP-confined concrete cylindrical specimens, all with 100 mm diameter (D) and 200 mm height (H), were manufactured and tested. The used concrete mixes had a targets compressive strength of 70 and 100 MPa. The control cylinders prepared and tested at selected time intervals to determine the in-place unconfined concrete strength gain. These 16 specimens were manufactured as FRP tube-encased specimens, where the tubes were prepared using a manual wet lay-up process by wrapping epoxy resin impregnated carbon fiber sheets around precision-cut high-density Styrofoam templates in the hoop direction; the summary of these

specimens is presented in Table 20. The FRP tubes were manufactured with either carbon, glass or basalt fiber-reinforced polymer (CFRP, GFRP or BFRP) fibers. The number of FRP layers for different specimens was selected dependent on material properties where lower grade FRPs receiving more layers to ensure adequate confinement. Accordingly, 2 and 3 layers of confinement was allocated to CFRP and GFRP specimens (HSC and VHSC), whereas BFRP specimens received 4, 6 and 9 layers due to low elastic modulus and thickness. Two nominally identical specimens were manufactured and tested for each confinement parameter as marked in Table 20.

Table 20-Details of test specimens

Specimen	Concrete Type	FRP-Type	Number of Layers	$t_{f\text{-total}}$ (mm)
N-G1	NSC	GFRP	1	0.2
H-G2	HSC1	GFRP	2	0.4
VH-G3	HSC2	GFRP	3	0.6
N-C1	NSC	CFRP	1	0.167
H-C2	HSC1	CFRP	2	0.334
VH-C3	HSC2	CFRP	3	0.501
N-B2	NSC	BFRP	2	0.150
N-B3	NSC	BFRP	3	0.225
H-B4	HSC1	BFRP	4	0.300
H-B6	HSC1	BFRP	6	0.450
VH-B6	HSC2	BFRP	6	0.450
VH-B9	HSC2	BFRP	9	0.675

7.2.2 Materials

7.2.2.1 Concrete

The ingredients for concrete used in this research were sourced from a local concrete supplier and were batched and mixed in the laboratory. The mixes consisted of crushed basalt as the coarse aggregate, with a 10 mm nominal maximum diameter. The resulting slump for all batches of concrete was over 200 mm. Control cylinders with 100 by 200 mm dimensions were cast and tested in parallel to the FRP-confined specimens to determine compressive strength (f'_{co}), as was mentioned previously. The details of the HSC mixes are shown in Table 21.

Table 21-Concrete mix proportions

Ingredient	HSC	VHSC
Cement (kg/m^3)	437	506
Silica fume (kg/m^3)	38	44
Sand (kg/m^3)	710	700
Gravel (kg/m^3)	1065	1050
Water (kg/m^3)	164	148
Superplasticizer* (kg/m^3)	10	20
w/c	0.36	0.30
Total (kg/ m^3)	2424	2468

* Superplasticizer contained 70% water by weight

7.2.2.2 FRP

The material properties of the fiber unidirectional sheets used to manufacture the FRP tubes are shown in Table 22. The FRP epoxy adhesive used consisted of two parts, epoxy resin binder (MBrace Saturant) and thixotropic epoxy adhesive (MBrace Laminate Adhesive), which were mixed in the ratio of 3:1. All fiber sheets were positioned with fibers aligned in the hoop direction with a 150 mm overlap; the specimens were wrapped with 1 continuous sheet.

Table 22-Material properties of fibers and FRP composites

Type	Nominal dry fiber thickness t_f (mm/ply)	Fiber/FRP properties					
		Provided by manufacturers			Obtained from coupon tests*		
		Ultimate tensile stress f_f (MPa)	Ultimate tensile strain ε_f (%)	Elastic modulus E_f (GPa)	Ultimate tensile stress f_{FRP} (MPa)	Ultimate tensile strain ε_{FRP} (%)	Elastic modulus E_{FRP} (GPa)
CFRP	0.167	4830	2.10	230	4598	1.95	236
S-Glass	0.2	3040	3.50	86.9	3055	3.21	95.3
BFRP	0.075	1680	2.30	73.0	1584	2.10	76.0

* Calculated based on nominal dry fiber thickness

7.2.3 Instrumentation and Testing

Axial deformations of the specimens were recorded with four linear variable differential transformers (LVDT), which were mounted at the corners between the loading and supporting steel plates of the test machine as shown in Figs. 52 and 53 in previous section (i.e. section 5).

The recorded deformations were used in the calculation of the average axial strains along the height of the specimens. Lateral strains were measured by a total of 6 unidirectional lateral strain gauges (SG) having a gauge length of 5 mm that were bonded on the FRP jacket outside the overlap region. These strain gauges were installed in pairs located at heights of 50, 100 or 150 mm with each pair of gauges attached at opposing sides of the specimen. Additionally, a DIC system was used to study the strain localization and its evolution. This method was used due to its ability to record both local and overall deformation. The detail of this method was presented in previous work by authors and more detail about this method can be find in [202]. Figures 52 and 53 shows the detail of DIC setup. It should be noted that the three-dimensional DIC calibration was performed to provide the geometrical information of the object being imaged [202].

The specimens were tested under monotonic axial compression using a 5000 kN capacity universal testing machine. During the test, the load was applied at approximately 2 microstrain per second until specimen failure. The instrumentation and testing equipment used in this experimental study is shown in Figs. 52 and 53.

7.3 Test Results

7.3.1 Axial stress-strain and axial stress-lateral strain

The axial strain and lateral strain recorded by LDVTs and SGs are presented in this section whereas the behavior of specimens after failure (i.e. after f'_{cc}), namely post-peak behavior, was added in these figures. The axial strain was calculated by averaging of 4 LVDTs measurement while lateral strain for each of the three selected heights (Figs. 52 and 53) was calculated by averaging of two lateral strain gauges attached at the same height.

Fig. 82 presents the axial stress-axial strain curves for BFRP-, CFRP- and GFRP-confined HSC and VHSC specimens. It can be seen in the figure that CFRP and GFRP specimens exhibit or ascending second branches either recovering strength after temporary softening behavior after

transition point (f'_{c1}, ε_{c1}). Transition region signifies a change in the trend of the stress-strain curve after the termination of the initial ascending branch (f'_{c1}, ε_{c1}) [17]. Conversely, the BFRP specimens showed various behaviors after transition point (f'_{c1}, ε_{c1}). H-B4-1, H-B6-2 and VH-B6 showed a descending behavior after transition zone without recovering the transition strength (f'_{c1}), i.e. f'_{c1} was the highest obtained axial compressive strength. However, H-B6-1 and VH-B9 showed an ascending behavior after transition zone or they recovered their strength after temporary strength loose. These observations, as expected, indicate that lateral stiffness (K_l) ($K_l = \frac{2E_f t_f}{D}$, where E_f, t_f and D are elastic modulus, thickness and diameter of the FRP) can significantly change the compressive strength and ductility behavior of the specimens. Moreover, it can be seen in the figure that companion specimens illustrate approximately similar axial stress-strain curves especially for specimens with higher K_l such as CFRP-confined HSC and VHSC specimens. Fig. 82 also illustrates that the GFRP and BFRP specimens had a more gradual softening behavior after f'_{cc} while CFRP specimens had a sudden FRP rupture at failure in their axial stress-strain curves. It should be again noted that CFRP have highest elastic modulus (E_f), tensile strength (f_f) and lateral stiffness (K_l) among all used FRP jackets.

Fig. 83 displays the axial stress-lateral strain for BFRP, CFRP and GFRP-confined concrete specimens. As it was said previously, the SGs present a local lateral behavior where the strain gauges were attached. As can be seen in the figure, the obtained lateral strain at middle of specimens (SGs 3&4) is either biggest recorded lateral strain or one of the biggest which accompanied with another height recorded data (e.g. Fig. 83f). In addition, it can be seen in the figures that the GFRP specimens showed highest lateral strain compared to other specimen, it should be noted that glass fibers (GFRP) have highest ultimate tensile strain (ε_{fu}) compared to CFRP and BFRP.

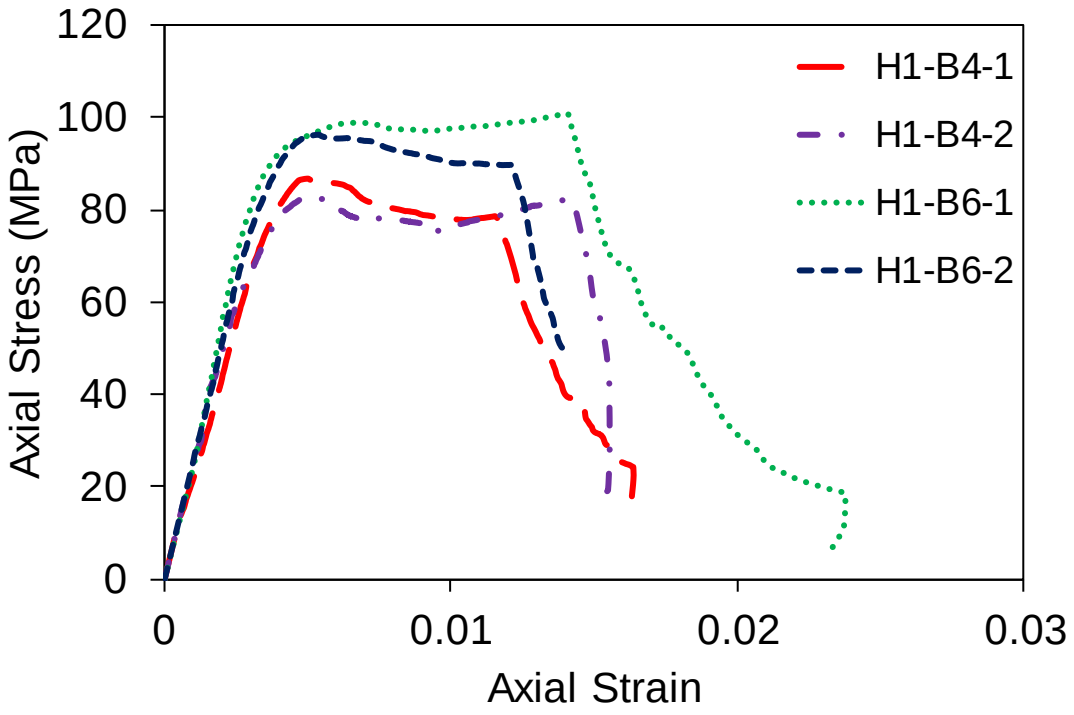
120
100
80
60
40
20
0
Axial Stress (MPa)
0
0.01
0.02
0.03
Axial Strain
H1-B4-1
H1-B4-2
H1-B6-1
H1-B6-2

a)

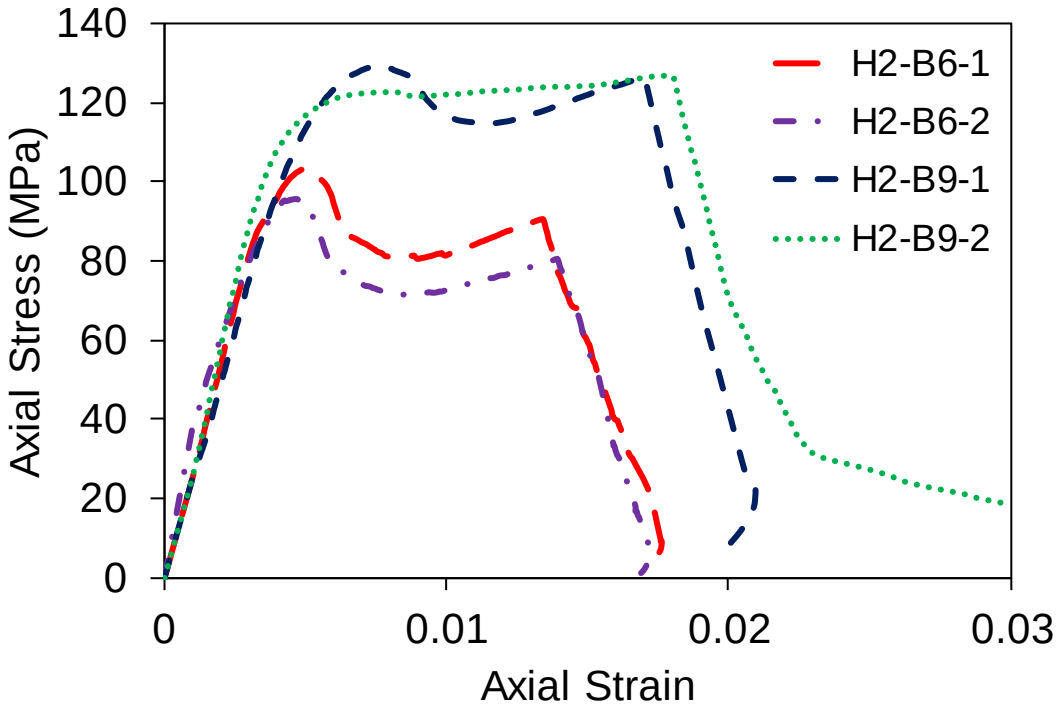
140
120
100
80
60
40
20
0
Axial Stress (MPa)
0
0.01
0.02
0.03
Axial Strain
H2-B6-1
H2-B6-2
H2-B9-1
H2-B9-2

b)

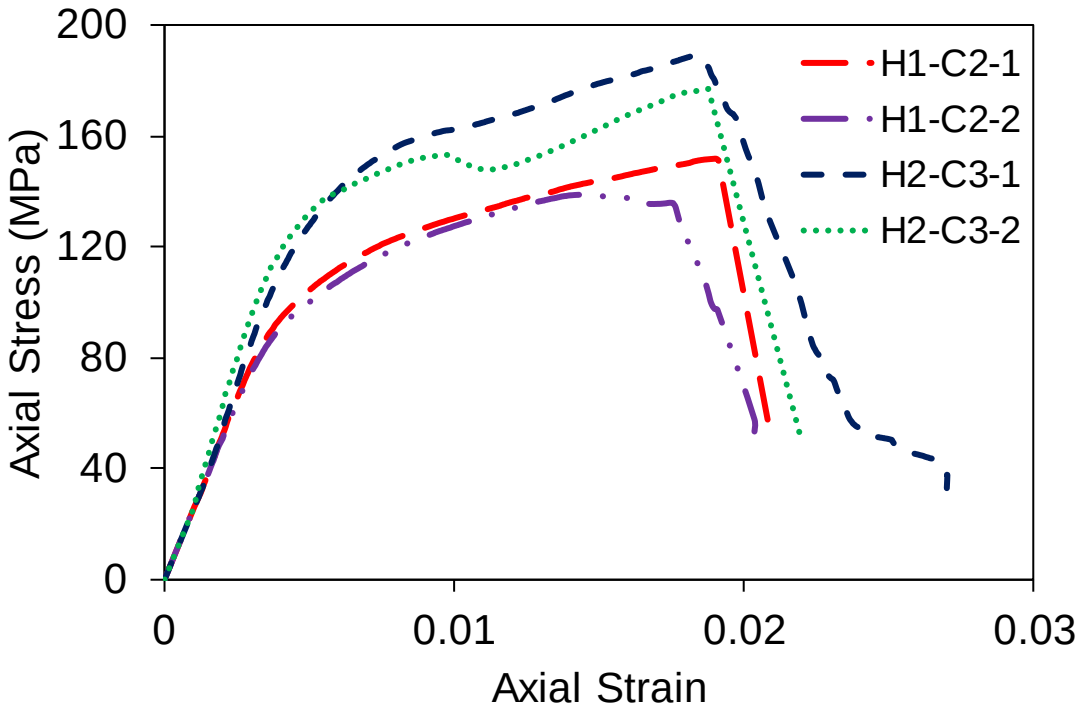

c)

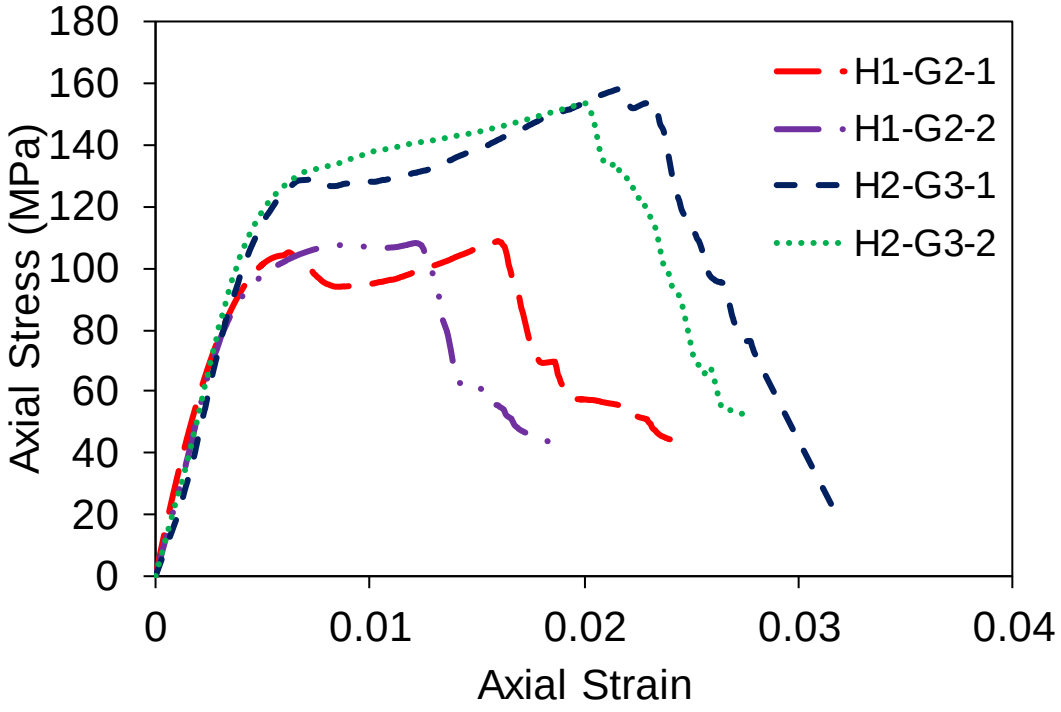

d)

Figure 82- Axial stress-axial strain response of FRP confined specimens: a) BFRP-4&6 layers (HSC-1), b) BFRP-6&9 layers (HSC-2), c) CFRP-2&3 layers (HSC-1), d) GFRP-2&3 layers (HSC-2)

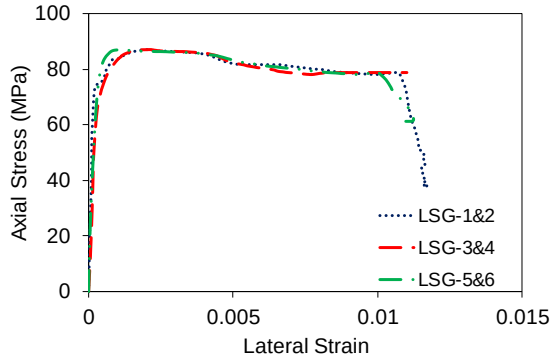

a) BFRP-4 layers (HSC-1)

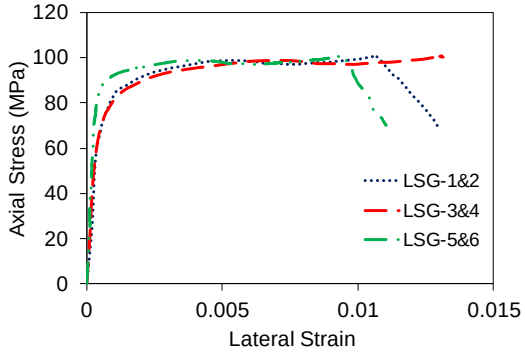

b) BFRP-6 layers (HSC-1)

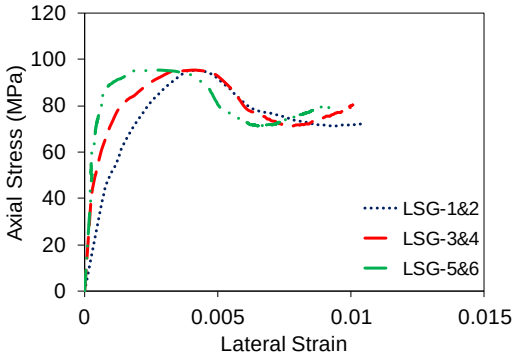

c) BFRP-6 layers (HSC-2)

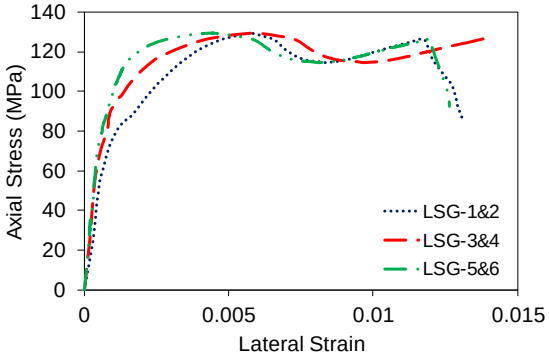

d) BFRP-9 layers (HSC-2)

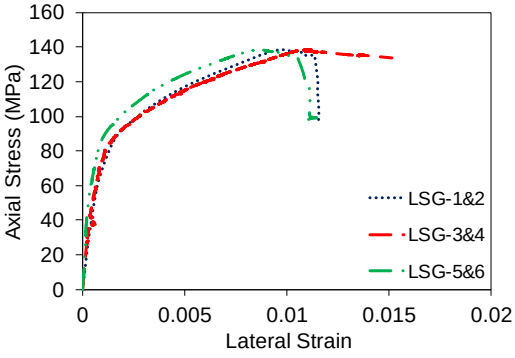

e) CFRP-2 layers (HSC-1)

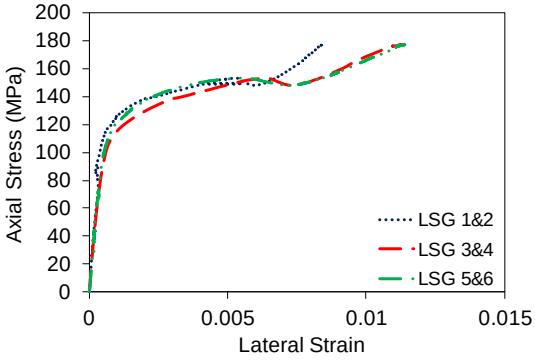

f) CFRP-3 layers (HSC-2)

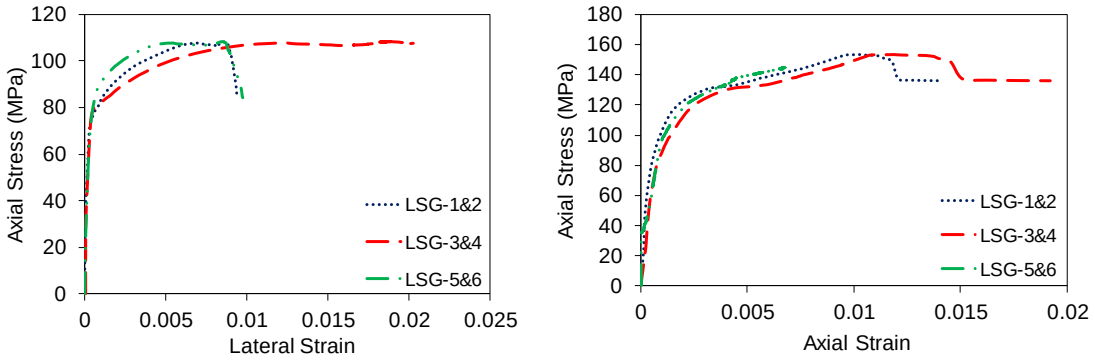

g) GFRP-2 layers (HSC-1) h) GFRP-3 layers (HSC-2)

Figure 83- Axial stress-Lateral strain response of FRP confined specimens: a) BFRP-4layers, b) BFRP-6 layers (HSC-1), c) BFRP-6 layers (HSC-2), d) BFRP-9 layers, e) CFRP-2 layers, f) CFRP-3 layers, g) GFRP-2 layers, h) GFRP-3 layers

7.3.2 Comparison of various strain measurement methods

Fig. 56 in section 5 shows the covered area by DIC and the different vertical and horizontal profiles which used in this study to evaluate behavior of specimens. To assess and compare the different strain measurement methods applied in this study, a comparison between LVDT, SGs and DIC obtained data was performed. For lateral strain, 3 profiles were selected to perform the comparison and these profiles are illustrated in the Fig. 56 as h-1, h-2 and h-3 with the same heights of SGs. Same as lateral strain, three longitudinal profiles (i.e. v-1, v-2 and v-3) were selected and the axial strain was calculated by averaging the obtained results by DIC along these profiles. It should be noted that the lateral and axial strain obtained by DIC analysis was calculated by using virtual strain option in the post-processing software (VIC 3D). The virtual strain uses the change of distance between two points on the surface of specimens.

7.3.2.1 Lateral Strain

A comparative analysis was performed to examine the consistency or inconsistency of obtained lateral behavior of specimens recorded by SGs and DIC. As can be seen in Fig.84, BFRP-4 layers and BFRP-6 layers (VHSC) specimens showed noticeable different between obtained results by DIC and SGs at some heights, e.g. SGs 1-2. These two specimens had lowest K_l/f'_{co} among all specimens and equal K_l to K_{lo} (K_{lo} is minimum threshold to have second ascending

branch) and their weaker normalized lateral stiffness allowed more non-homogenous lateral behavior along the height of specimens. The results for other specimens showed that the results are consistent for two studied heights, although there is a height which the obtained outcome by these two methods showed slightly inconsistency. For example, CFRP-2 layers and GFRP-2 layers and GFRP-3 layers specimens showed consistent results for h-1 and h-3 profiles but the obtained results for h-2 showed small differences between recorded data by DIC and SGs. In addition, the specimens with highest K_l among BFRP specimens (BFRP-9 layers) showed a consistent outcome between obtained data by DIC and SGs for all over studied area, as shown in Fig. 84d. It should also be said that BFRP-9 layers have highest t_f among all tested specimens.

7.3.2.2 Axial strain

Fig. 85 presents the comparison between axial strain obtained by LVDTs and DIC system. As it was explained in previous study performed with this research group [154], the curve of axial stress-axial strain measured by full-height and mid-height LVDTs of FRP-confined HSC specimens shows different results. It is mention worthy that using virtual strain over covered area by DIC offers the measurement of axial strain similar to the mid-height LVDT measurements for front face of specimens. Comparing obtained data by LVDTs as full-height measurement and DIC as mid-height measurement indicates that the deformation due to few local shear planes in tested specimens cannot be captured by mid-height measurements opposite to LVDTs as full-height measurement. The Figs. 85c and 85d show clearly that some displacement due to local shear plane which occurred at top and bottom of specimens cannot be recorded by DIC. However, LVDTs measure overall axial displacement and they are not able to show the occurrence of local shear plane.

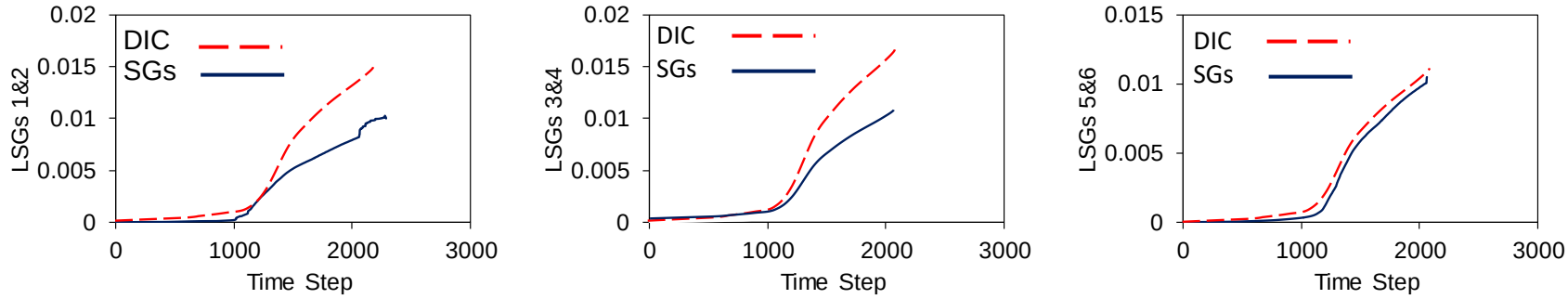

a) BFRP-4 layers

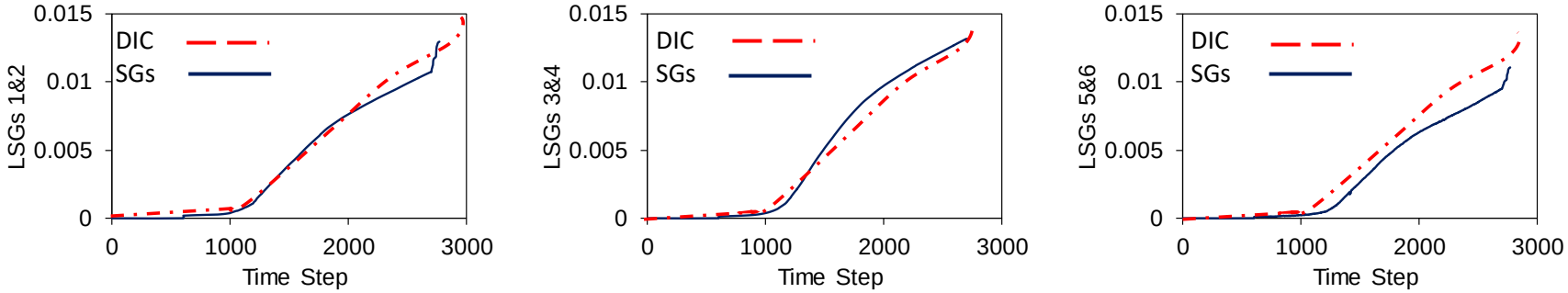

b) BFRP-6 layers (HSC-1)

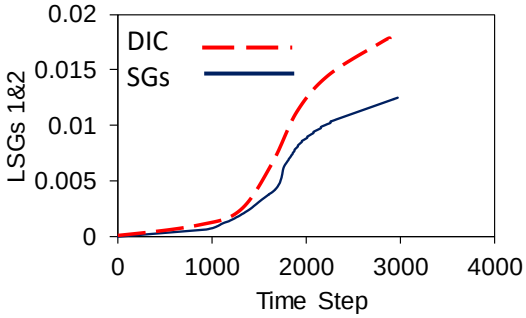

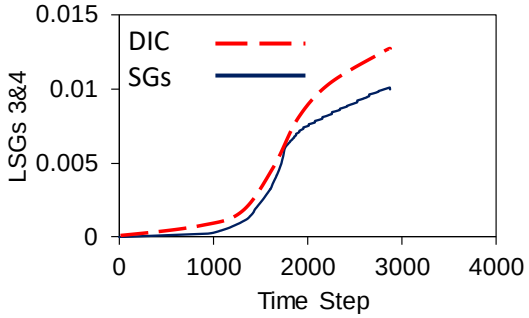

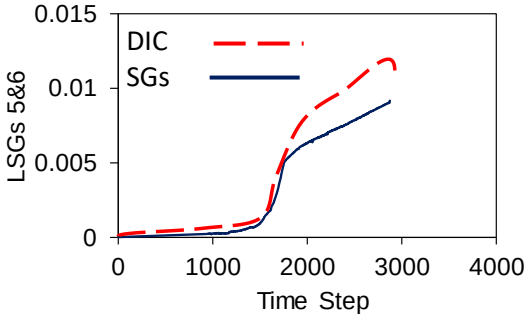

c) BFRP-6 layers (HSC-2)

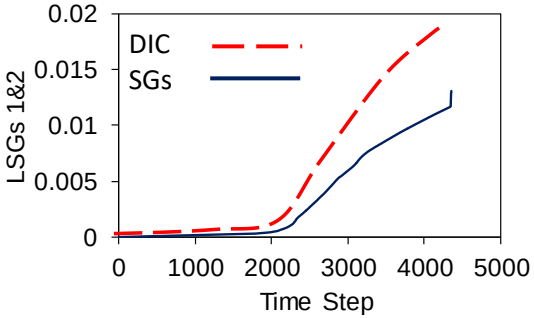

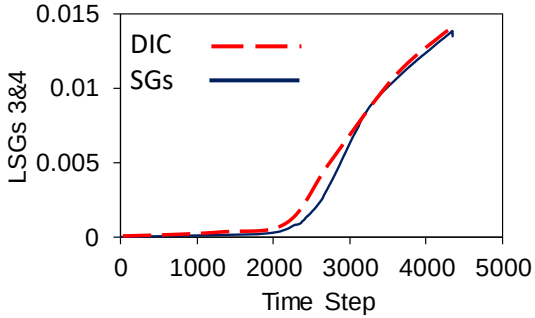

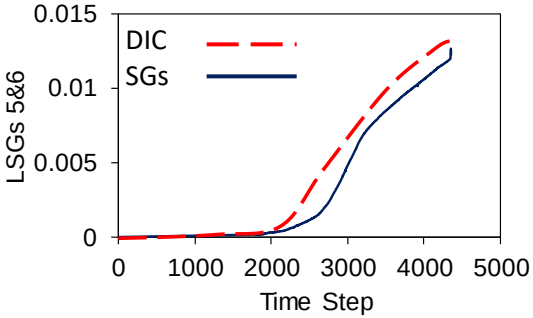

d) BFRP-9 layers

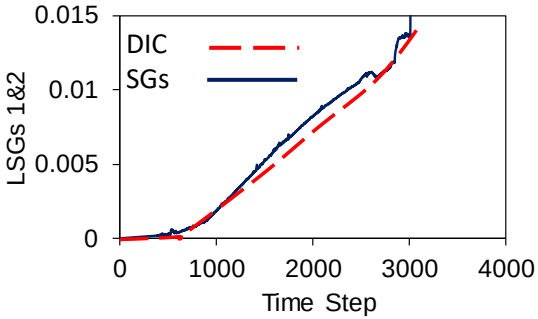

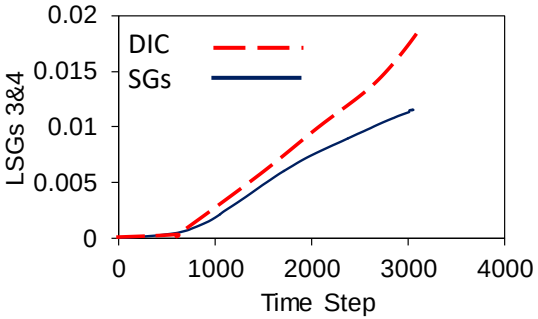

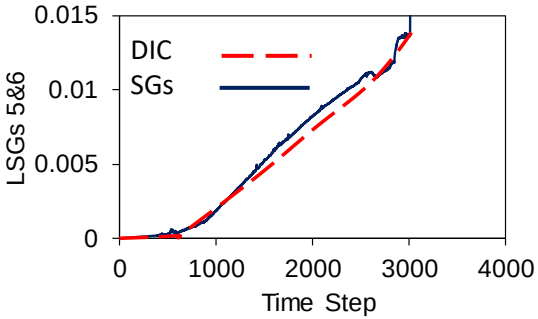

e) CFRP-2 layers

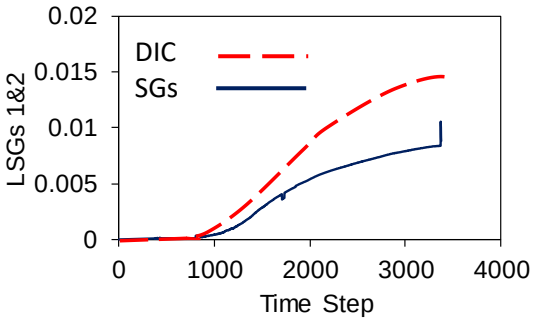

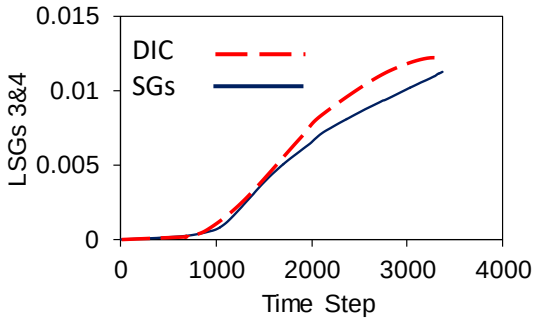

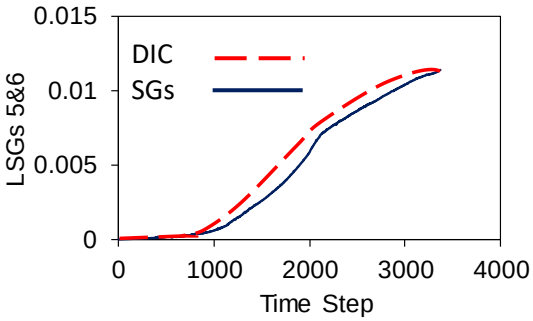

f) CFRP-3 layers

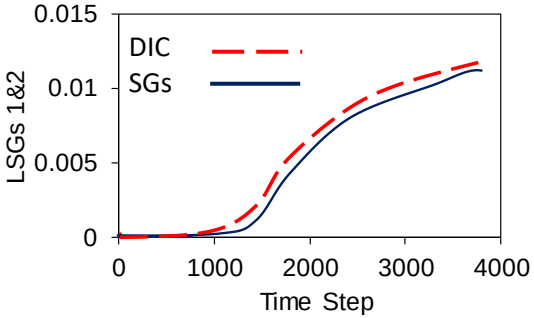

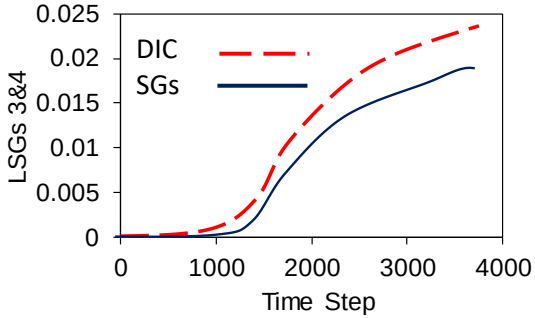

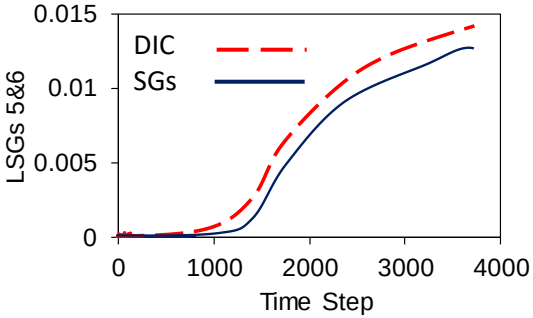

g) GFRP-2 layers

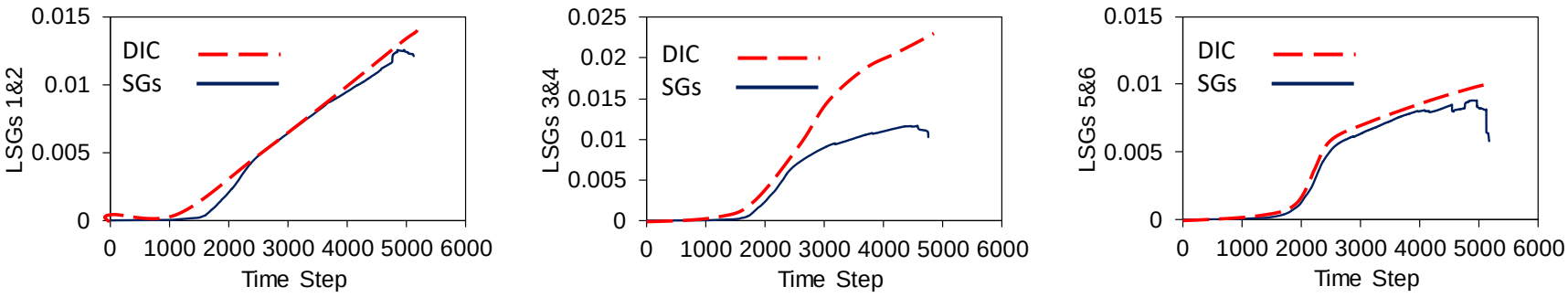

h) GFRP-3 layers

Figure 84- Comparison between lateral strain obtained by LVDTs and DIC (local strain) for a) BFRP-4 layers specimen; b) BFRP-6 layers specimen (HSC-1); c) BFRP-6 layers specimen (HSC-2); d) BFRP-9 layers specimen; e) CFRP-2 layers; f) CFRP-3 layers; g) GFRP-2 layers; h) GFRP-3 layers

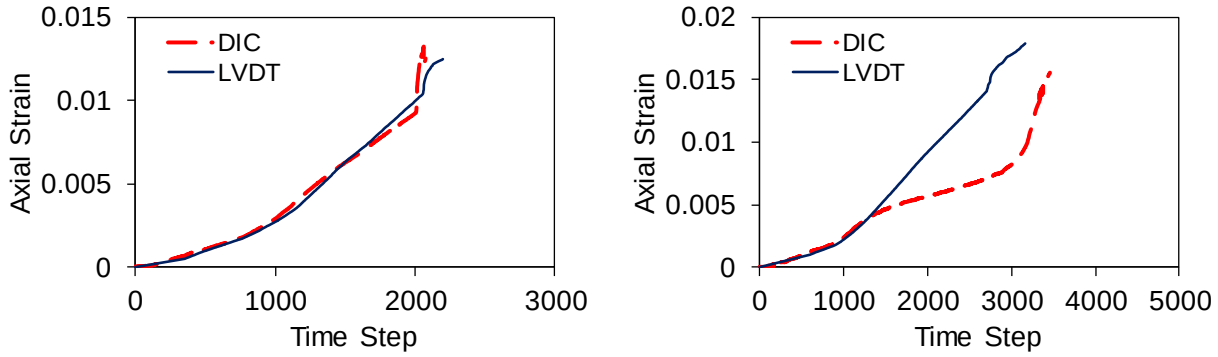

a) BFRP 4&6 layers (HSC-1)

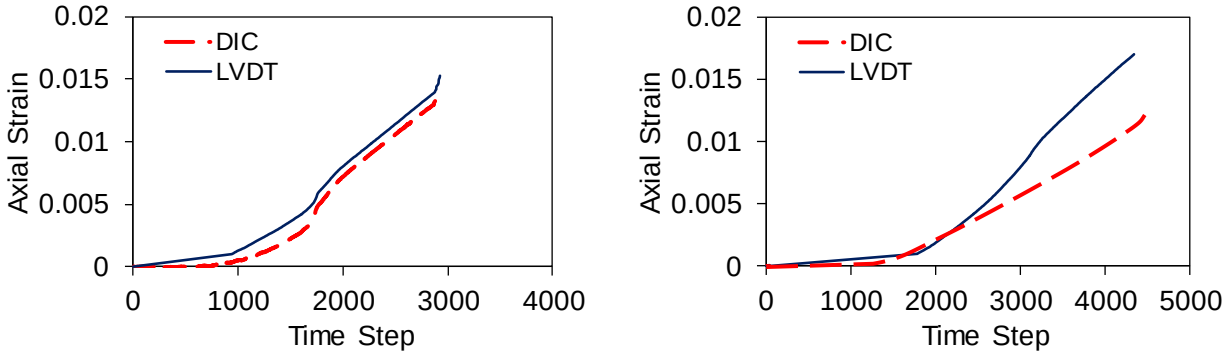

b) BFRP 6&9 layers (HSC-2)

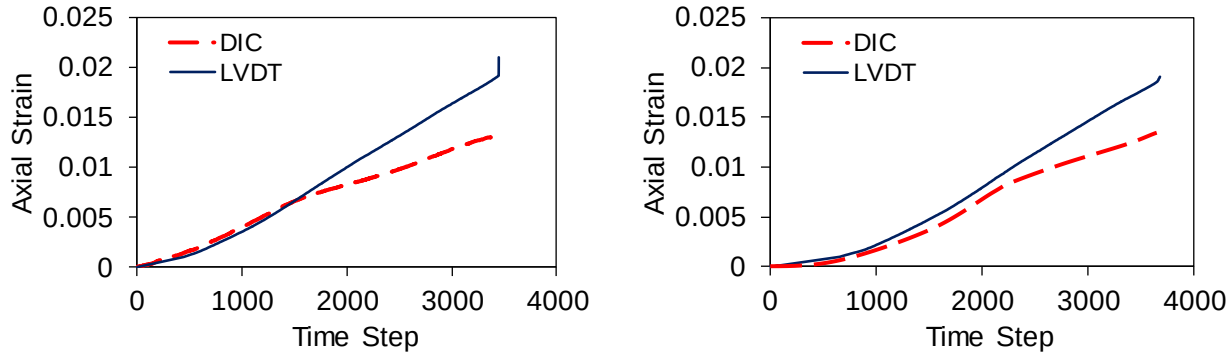

c) CFRP 2&3 layers

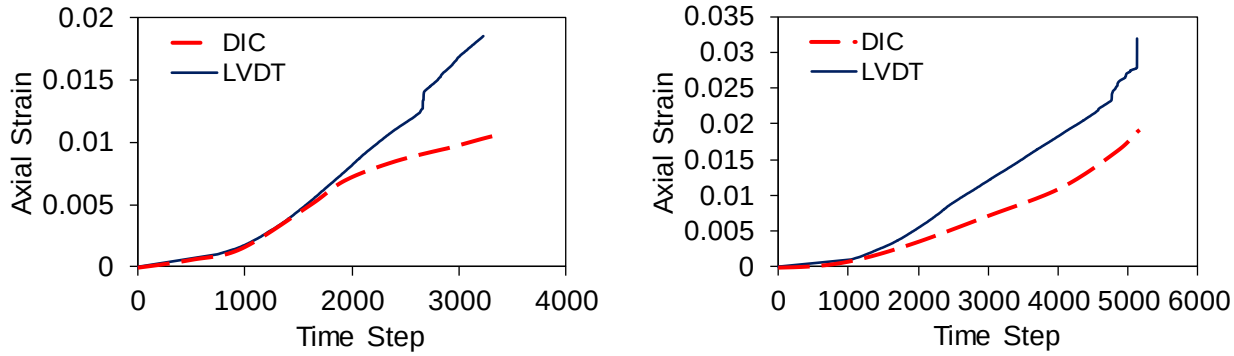

d) GFRP 2&3 layers

Figure 85- Comparison between axial strain obtained by LVDTs and DIC (virtual strain): a) BFRP-4 layers specimen and BFRP-6 layers specimen (HSC-1); b) BFRP-6 layers specimen (HSC-2) and BFRP-9 layers specimen; c) CFRP-2 layers and CFRP-3 layers; d) GFRP-2 layers and GFRP-3 layers

7.4 Analysis and discussion

As discussed previously, the DIC data is able to show the evolution of Von Mises strain, strain localization and shear band expansion during test procedure. In this section, the results of a detailed study on distribution of Von Mises strains over specimens' surface and evolution of localization to failure is exhibited. Afterward, the Von Mises strain ($\varepsilon_{Von\ Mises}$) evolution was plotted along the height of specimens and around the specimens' perimeter. This helps to determine accurately the localization characteristics namely initiation and evolution of localization.

7.4.1 Strain developments on specimens surface

Figs. 86, 87 and 88 show the Von Mises strain evolution of BFRP, CFRP and GFRP-confined concrete specimens. The obtained images by DIC were analysed to the end of existence of speckle pattern over specimen surface. These figures exhibit the detail of Von Mises strain evolution from f'_{co} to failure point. Comparing Figs. 86-88 with previous studies of this group on FRP-confined NSC specimens in section 5 illustrates an approximately same pattern of strain localization and evolution for FRP-confined NSC, HSC and VHSC [202]. As it was explained previously, the localization of deformation is much stronger and abrupt in unconfined specimen while strains are distributed more homogenously over FRP-confined concrete. Comparing Figs 86-88 with Figs 72-73 confirms mentioned observation where strain localization pattern varied significantly due to existence of FRP jackets.

It is well established that to investigate and quantify a failure procedure to be develope a constitutive model, two parameters should be precisely determined. These two parameters are the onset of localization and localization evolution trend. As can be seen in Figs. 86-88, the initiation of localization as one of the significant key parameter in failure development in specimens cannot be verified accurately. This is due to dependency of colour map on input data for analysis. These parameters are minimum and maximum Von Mises strain and number of

intervals in colour map. It is evident that changing one parameters among these parameters leads to different results. This leads to need a new approach to determine the onset of localization. Additionally, although the evolution of localization and cracks can be observed in Figs 86-88, it is very difficult to quantify this evolution and it needs again a more sophisticated methods to overcome this problem.

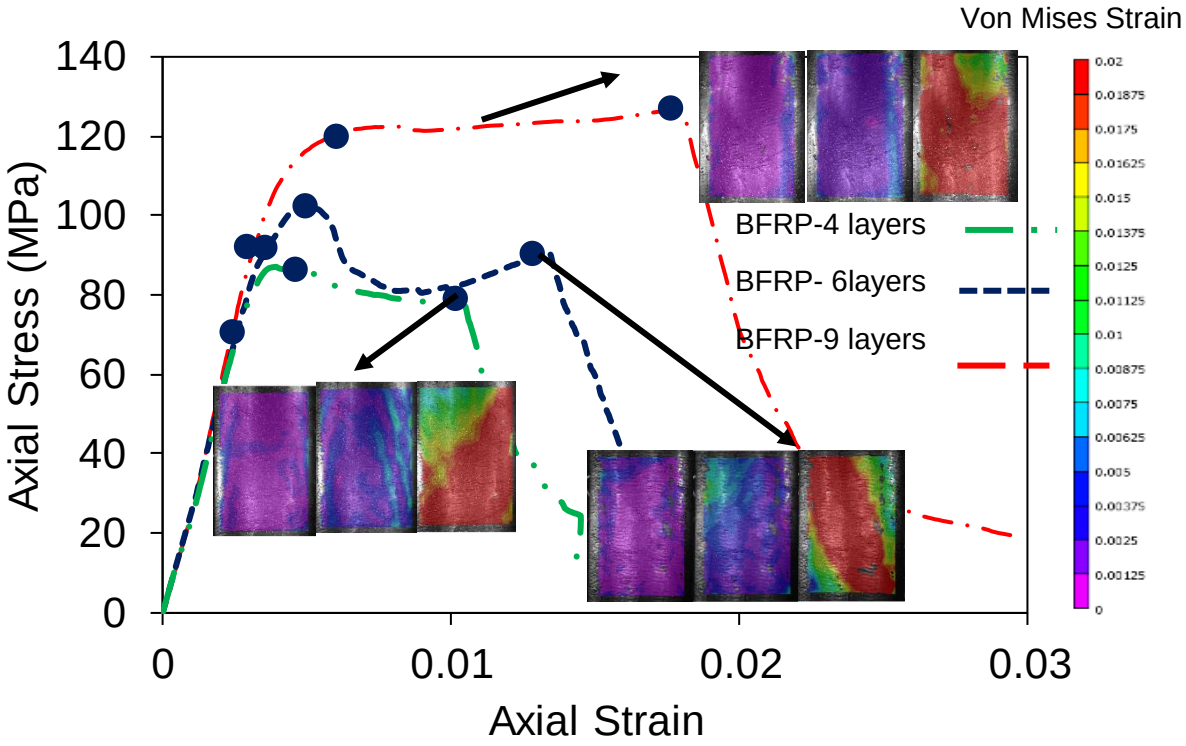

Figure 86-Von Mises strain evolution of BFRP-confined specimen (4, 6 and 9 layers-HSC1) Obtained results by DIC

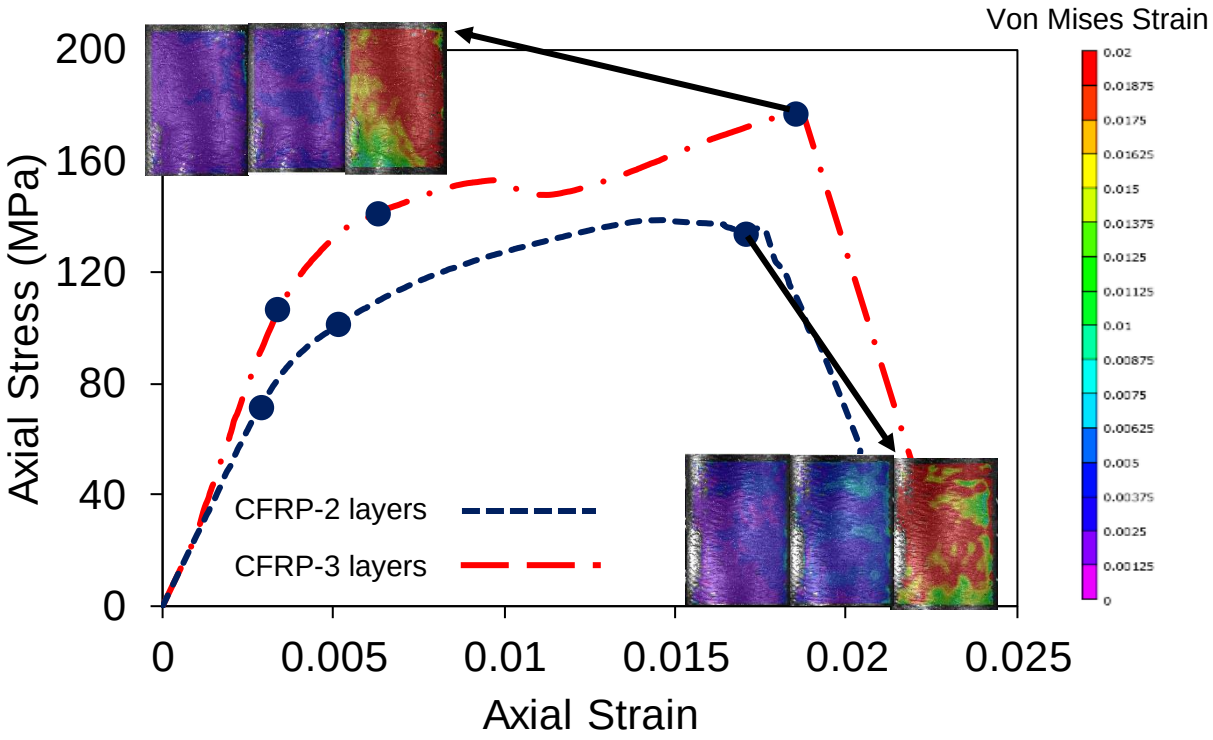

Figure 87- Von Mises strain evolution of CFRP-confined specimen (2 and 3 layers) Obtained results by DIC

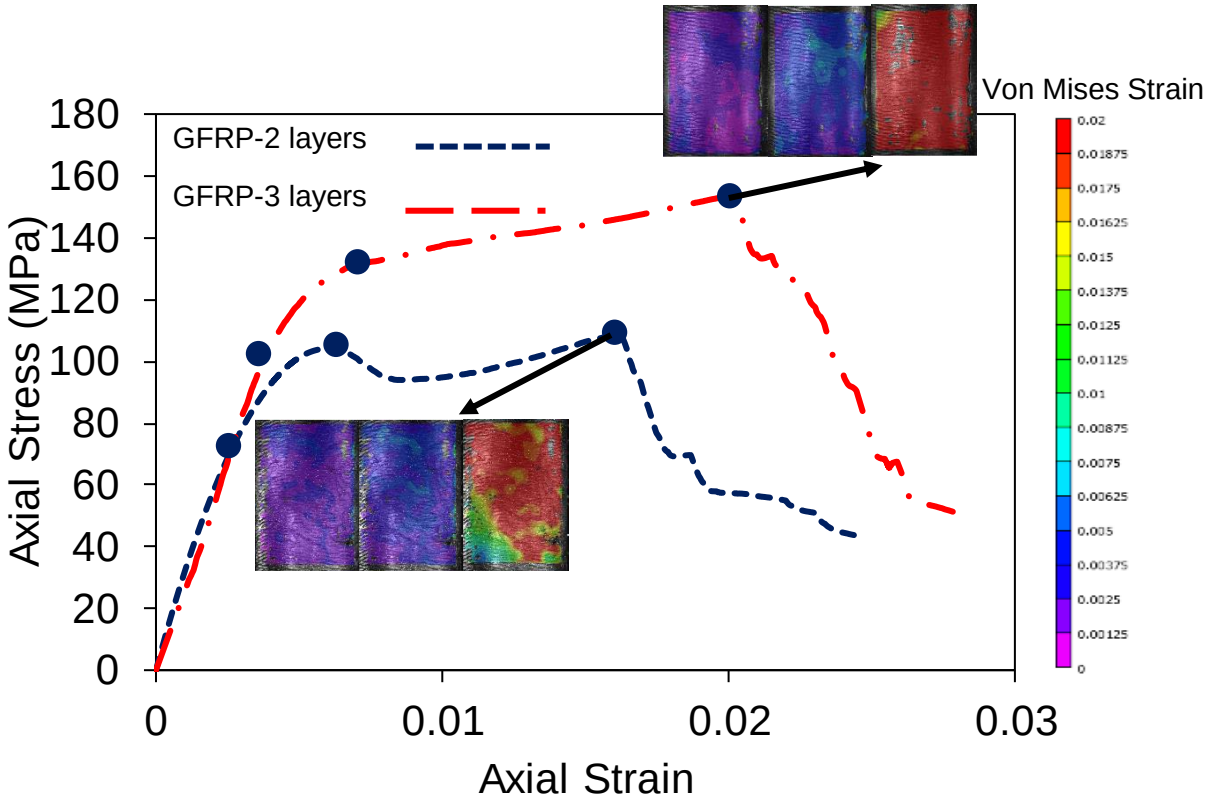

Figure 88-Von Mises strain evolution of GFRP-confined specimen (2 and 3 layers) Obtained results by DIC

7.4.2 Strain evolution

7.4.2.1 Along specimens height

Figs. 89-92 show the evolution of Von Mises strain along the vertical profile at the middle of studied area (shown in Fig. 56) for BFRP-4, 6 & 9 layers, CFRP-2 & 3 layers and GFRP-2 & 3 layer. A synchronization was made between the DIC results and stress-strain curves recorded by data acquisition system and a correlation was provided between the evolutions of full-field strain (e.g. Von Mises strain) and the axial stress-axial strain curves. As can be seen in Figs. 89-92, the specimens with lower value of lateral stiffness (i.e. BFRP- 4 layers and BFRP-6 layers (VHSC)) displayed more localized behavior. However, the specimens with stronger lateral stiffness showed more homogenous behavior along the height of specimens (CFRP and GFRP specimens). Comparing the obtained FRP-confined HSC and VHSC results in this study with NSC outcome obtained in last work performed with this research group, i.e. [202], exhibits approximately similar influence of K_l on specimens behavior, although more localization zone can be observed in FRP-confined HSC and VHSC along specimen height, e.g. Figs. 90a and

91a. This slightly differences of behavior between NSC compared to HSC and VHSC can be attributed to more brittle nature of HSC.

Investigating the vertical Von Mises strain profile along specimens' height offer accurate determination of localization onset. As can be seen in Figs. 89-92, the onset of localization and location of localization initiation can be marked along the profiles of specimens. However, as it can be seen in the Figs 86-92, it is hard to quantify the evolution of shear zone and measure the dimension of localized zone using raw data. This is due to change of profile shape by variation of profile location. This indicates the need of more profiles to analyse localization characteristics. Moreover, using raw data cannot put a figure easily on the difference of localization pattern for unconfined and FRP-confined specimens. Therefore, a more detailed analysis and an improved method to process DIC strain data is required which is discussed in following section (Section 5).

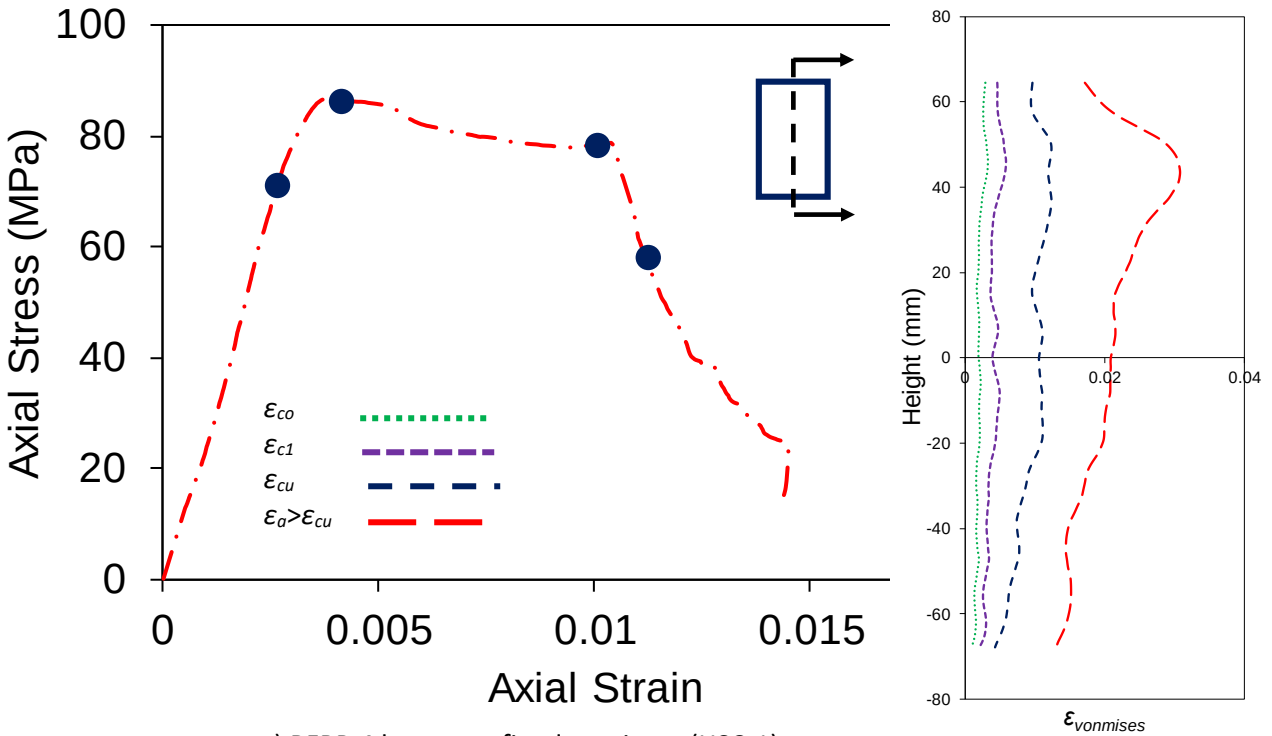

a) BFRP-4 layers confined specimen (HSC-1)

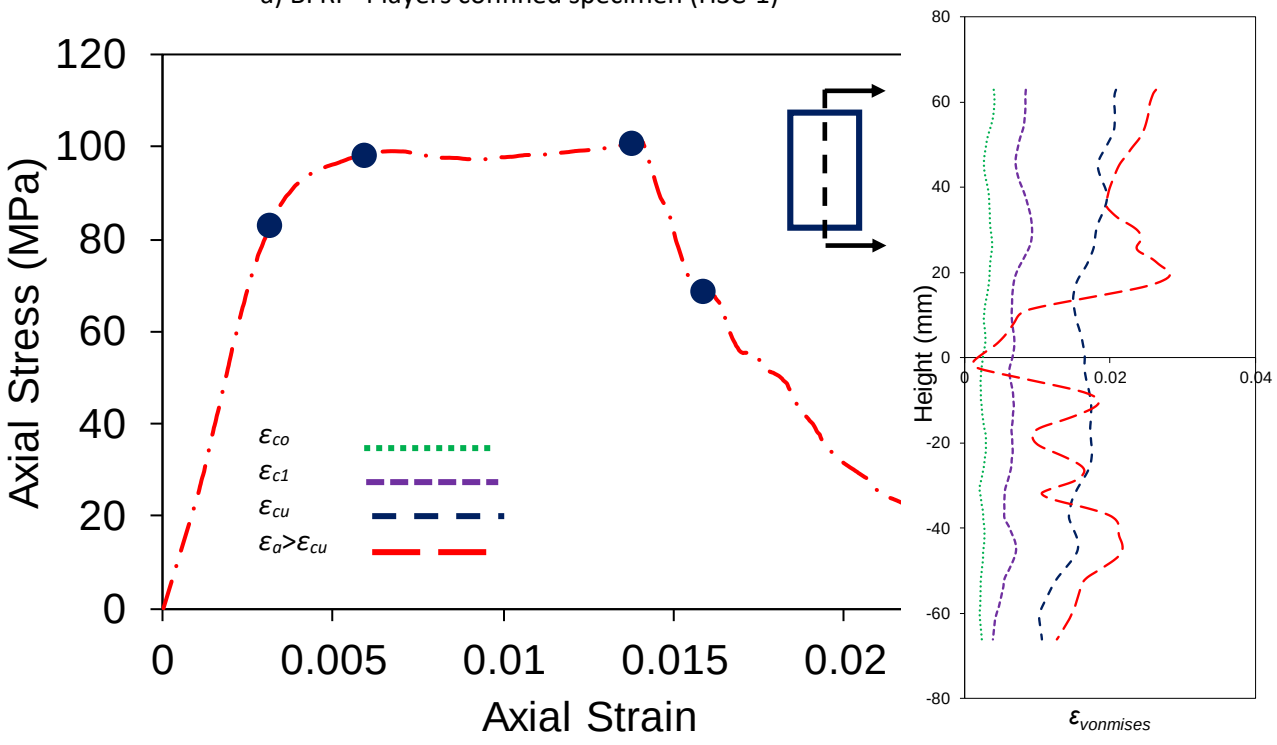

b) BFRP-6 layers confined specimen (HSC-1)

Figure 89- Comparison of Von Mises strain development for BFRP-4 layers FRP and BFRP-6 layers confined specimens

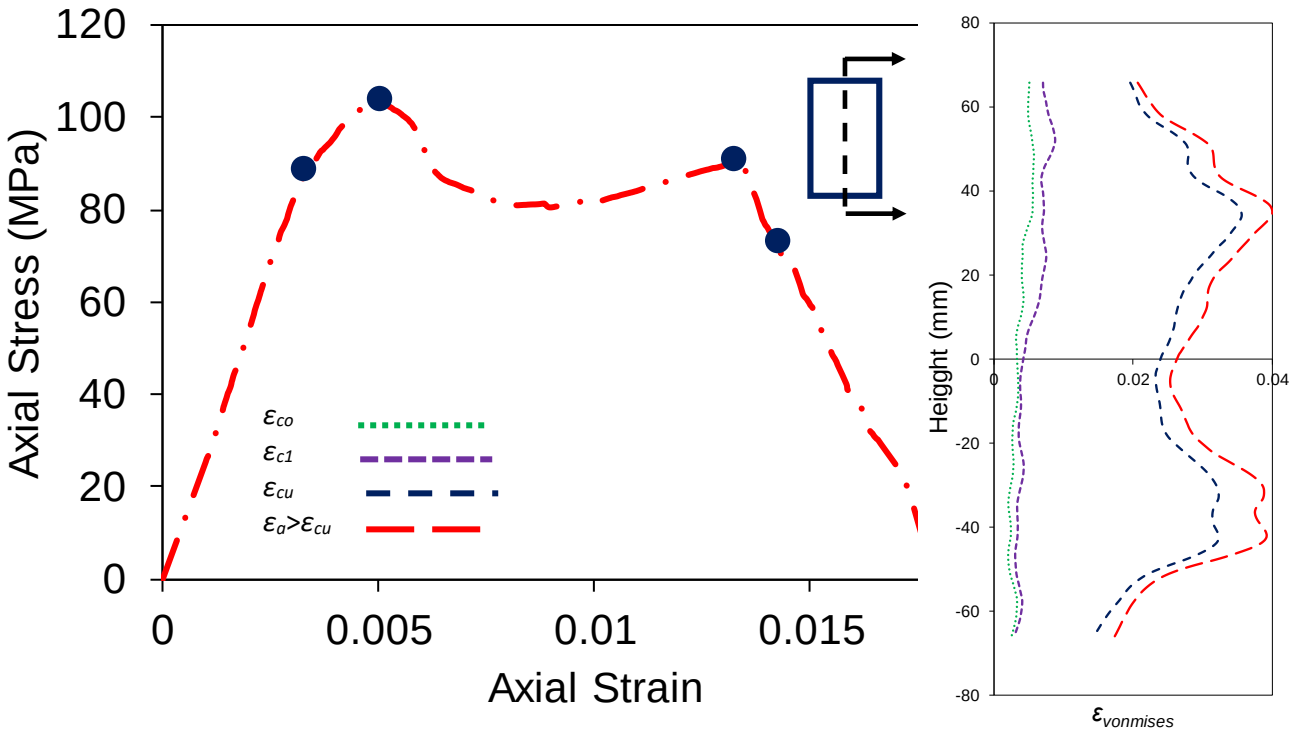

a) BFRP-6 layers confined specimen (HSC-2)

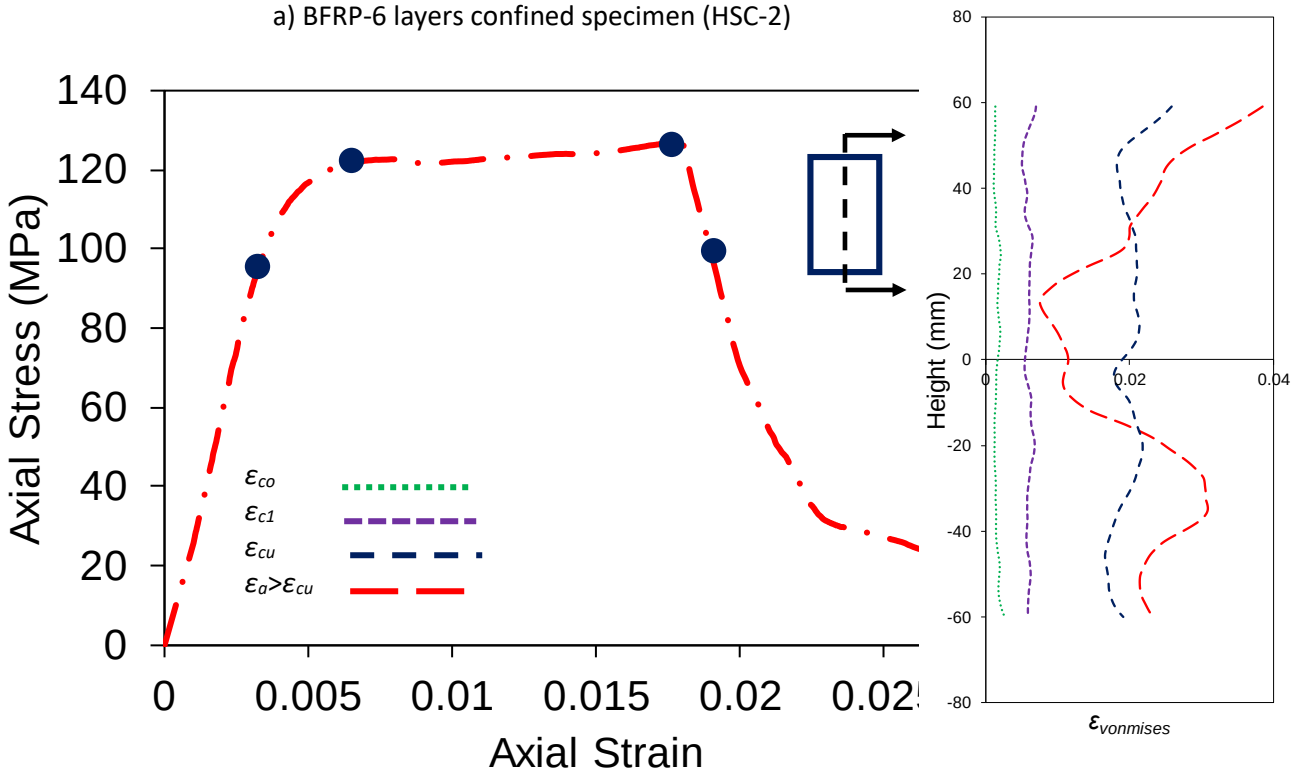

b) BFRP-9 layers confined specimen (HSC-2)

Figure 90- Comparison of Von Mises strain development for BFRP-6 layers FRP and BFRP-9 layers confined specimens

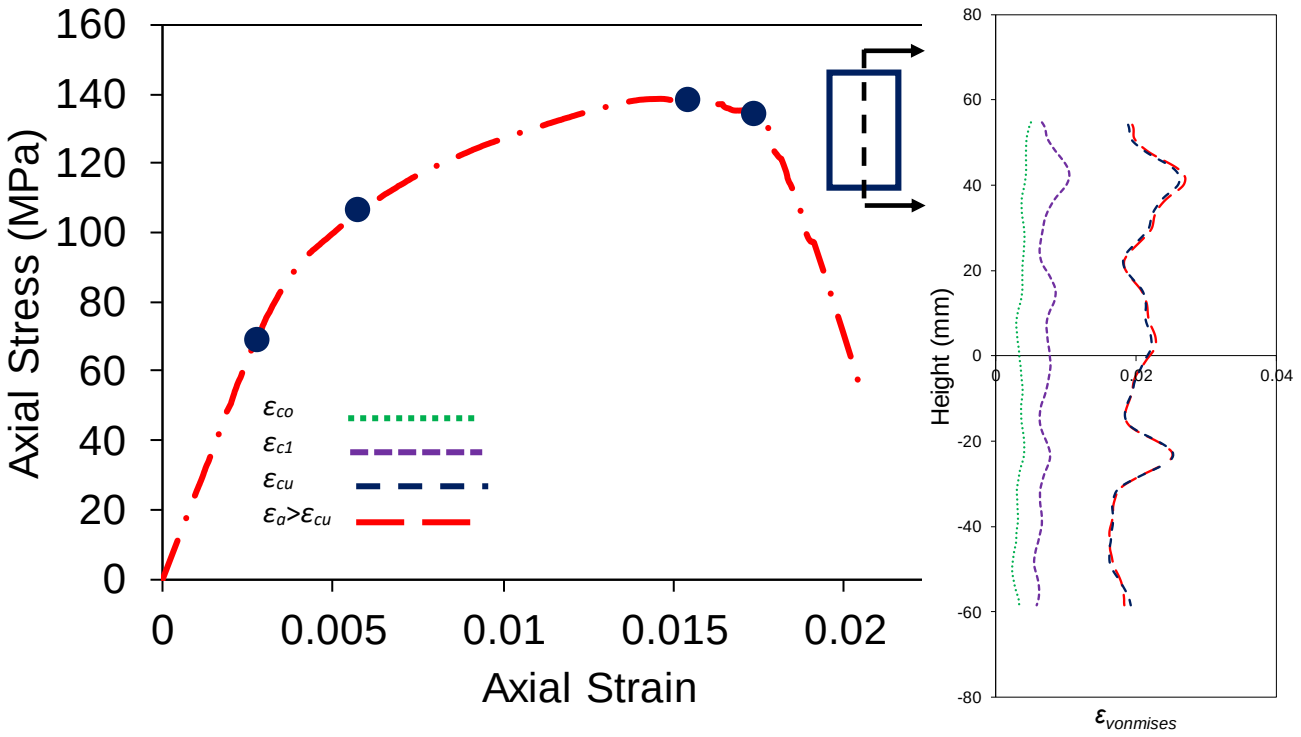

a) CFRP-2 layers confined specimen (HSC-1)

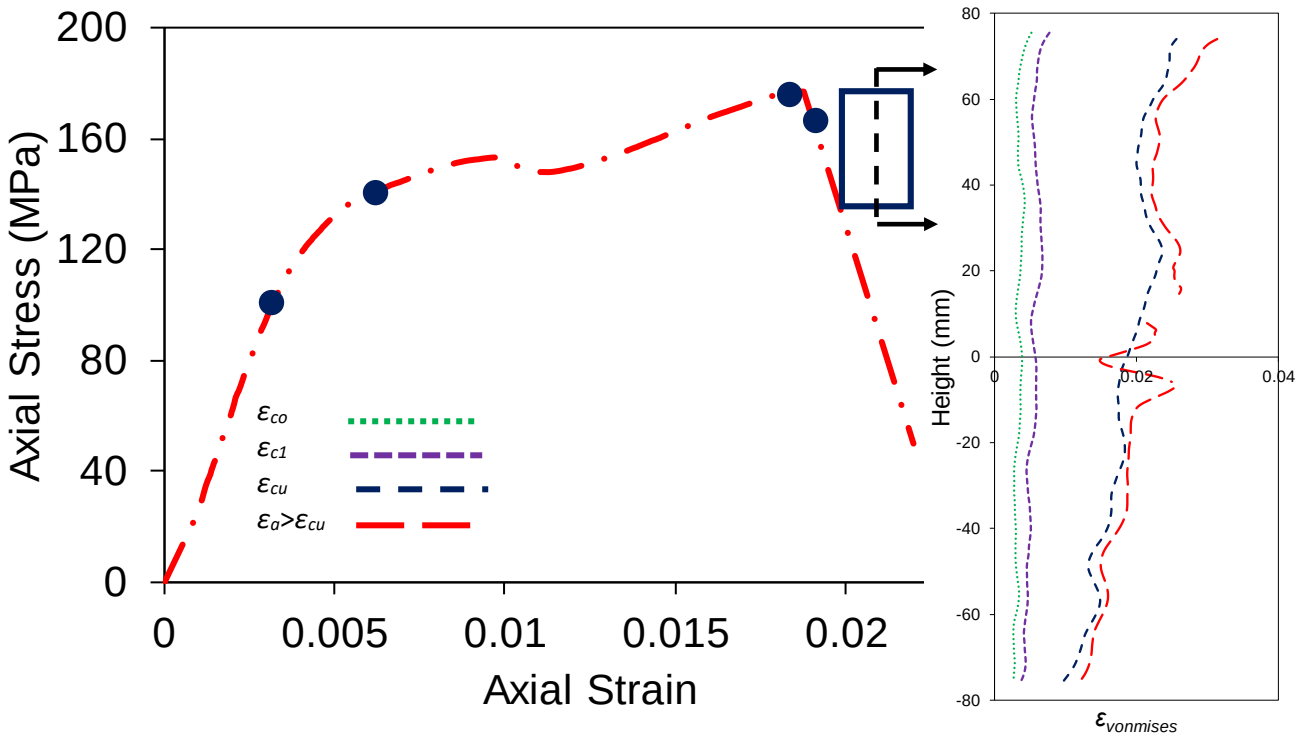

b) CFRP-3 layers confined specimen (HSC-2)

Figure 91- Comparison of Von Mises strain development for CFRP-2 layers FRP and CFRP-3 layers confined specimens

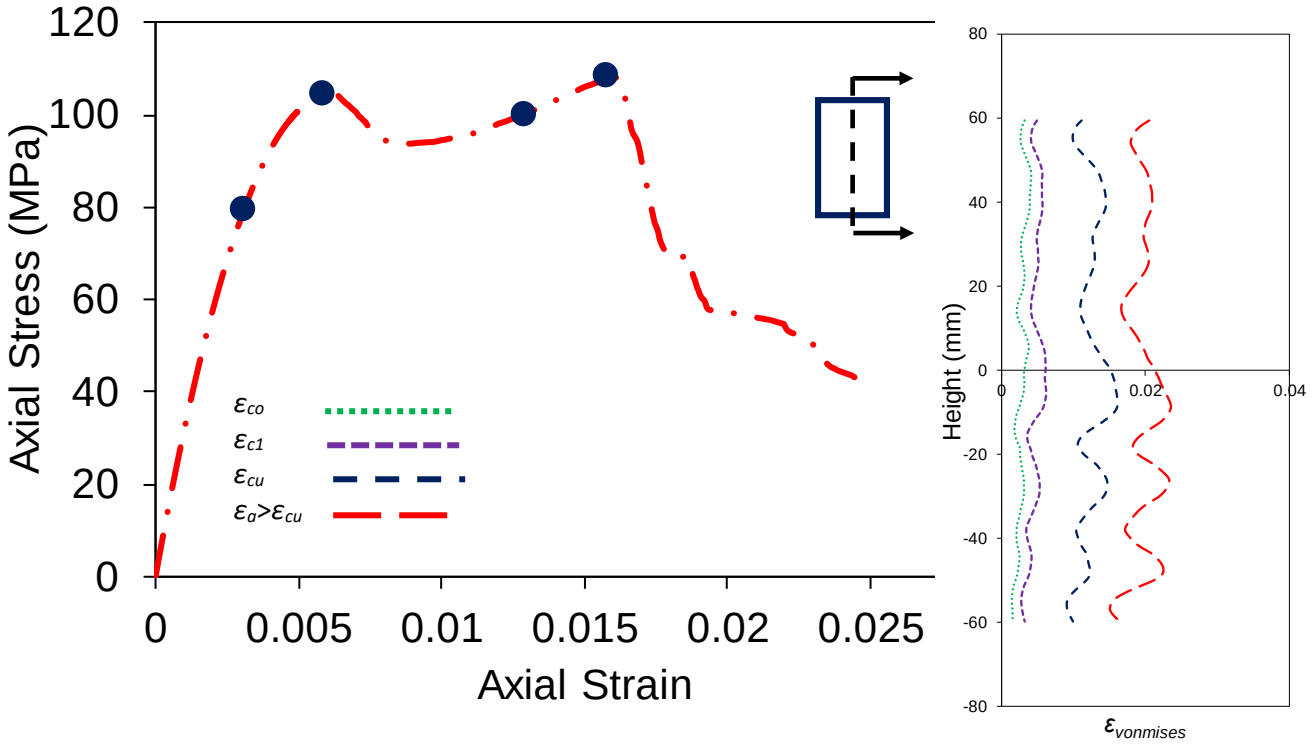

a) GFRP-2 layers confined specimen (HSC-1)

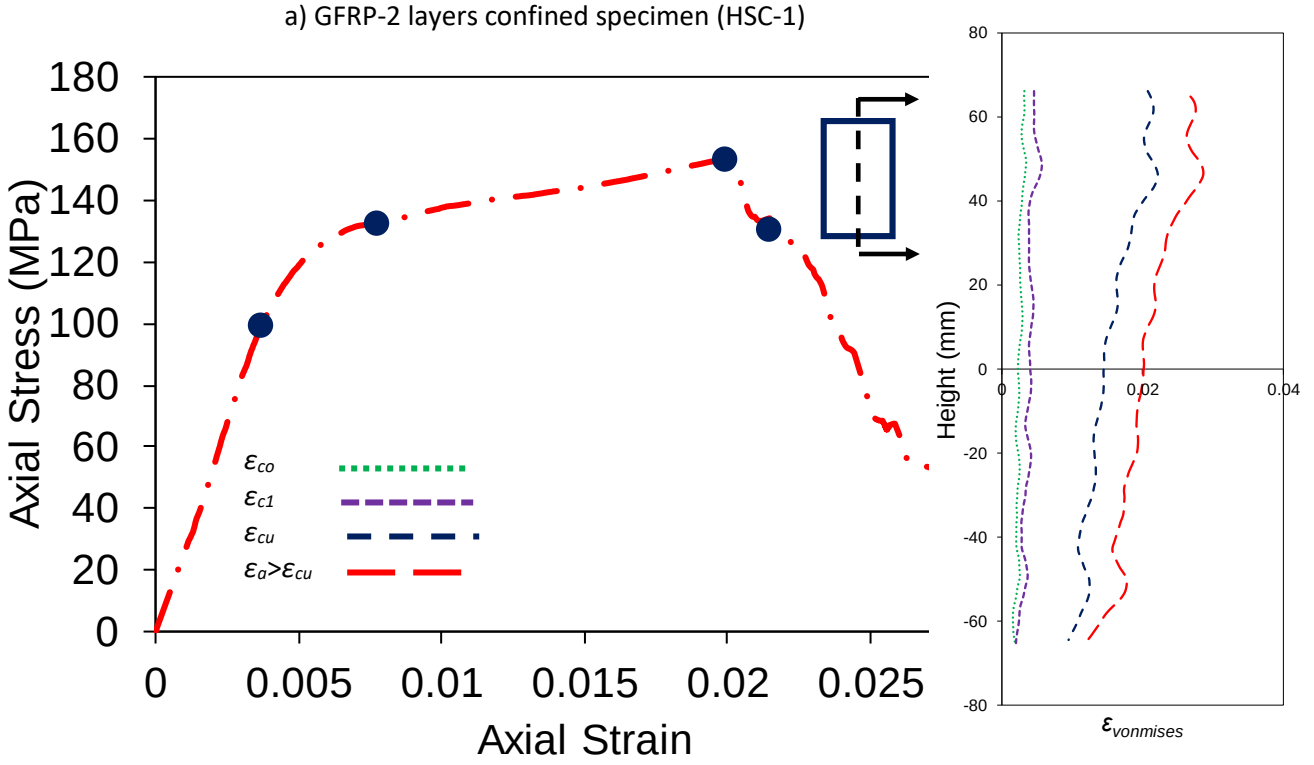

b) GFRP-3 layers confined specimen (HSC-2)

Figure 92- Comparison of Von Mises strain development for GFRP-2 layers FRP and GFRP-3 layers confined specimens

7.4.2.2 Around specimen perimeter

Figs. 93-95 illustrate the evolution of $\varepsilon_{Von\ Mises}$ around the specimen perimeter at different height of CFRP-2 layers, BFRP-6 layers (HSC) and GFRP-3 layers. Due to similar results obtained by whole specimens, these three specimens were selected and studied to show the lateral behavior around the specimen perimeter by variation of heights. As can be seen in the figures, the confinement influences the behavior of specimens compared to unconfined specimens (Section 6). As can be seen in the figures, the FRP jacket distributed the localization all over specimens' surface and more homogenized behavior was observed. Comparing FRP-confined HSC, VHSC Von Mises strain evolution with NSC, illustrates approximately similar trend of lateral behavior, although a more localized behavior in FRP-confined HSC and VHSC was observed by approaching to f'_{cc}. This again can be attributed to more brittle behavior of HSC which cause more abrupt and localized behavior compared to more ductile NSC behavior. It should be noted that the unconfined and FRP-confined NSC outcome was displayed in previous work performed by authors [202]. However, it should be again said that the quantification of shear zone evolution and measurement of the localization zone dimension is very challenging by using obtained raw data without further processing same as obtained results for vertical profiles. Therefore, as explained previously, a more detailed analysis to process DIC data is essential.

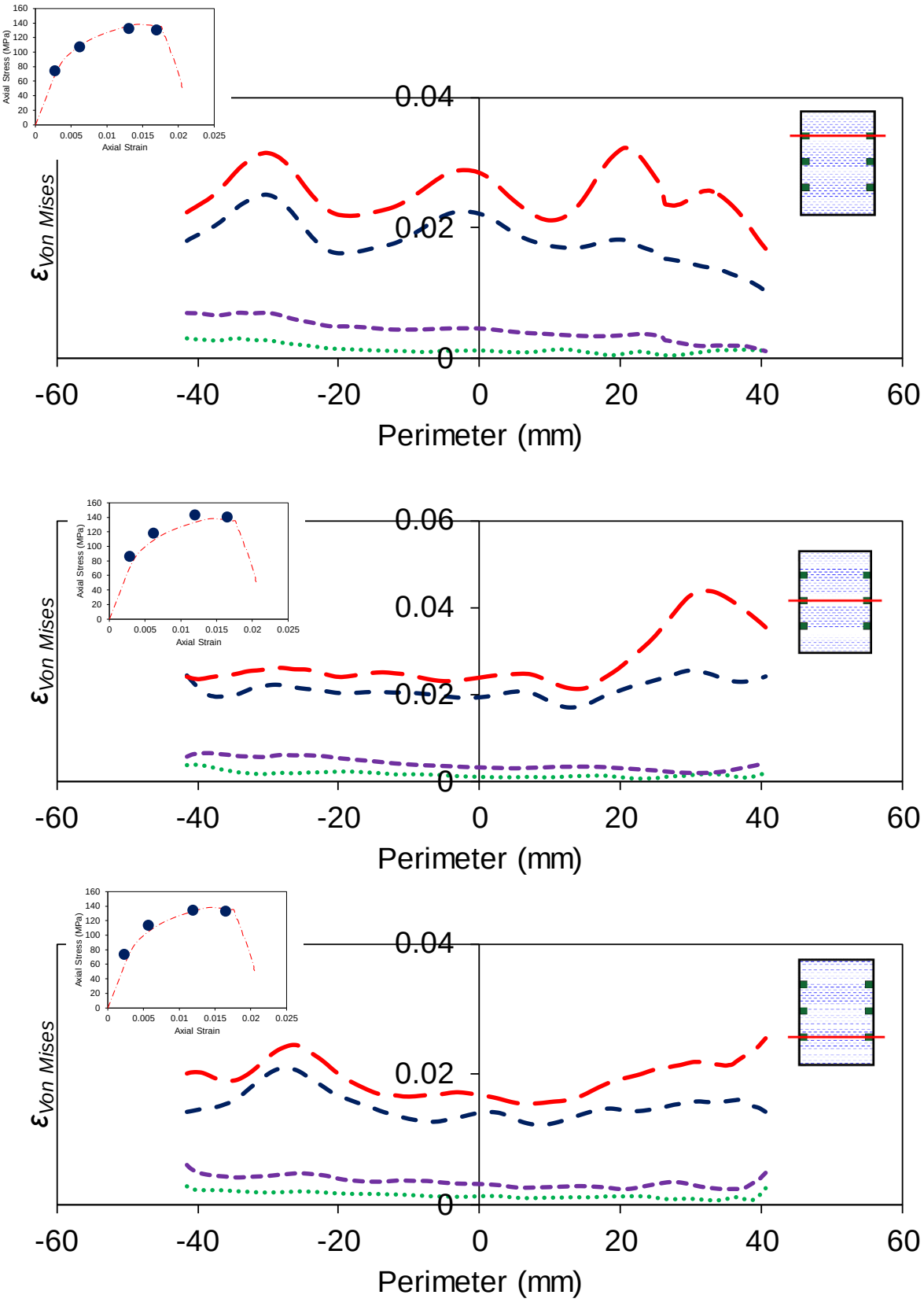

Figure 93- Lateral evolution of Von Mises strain for CFRP-2 layers (HSC-1)

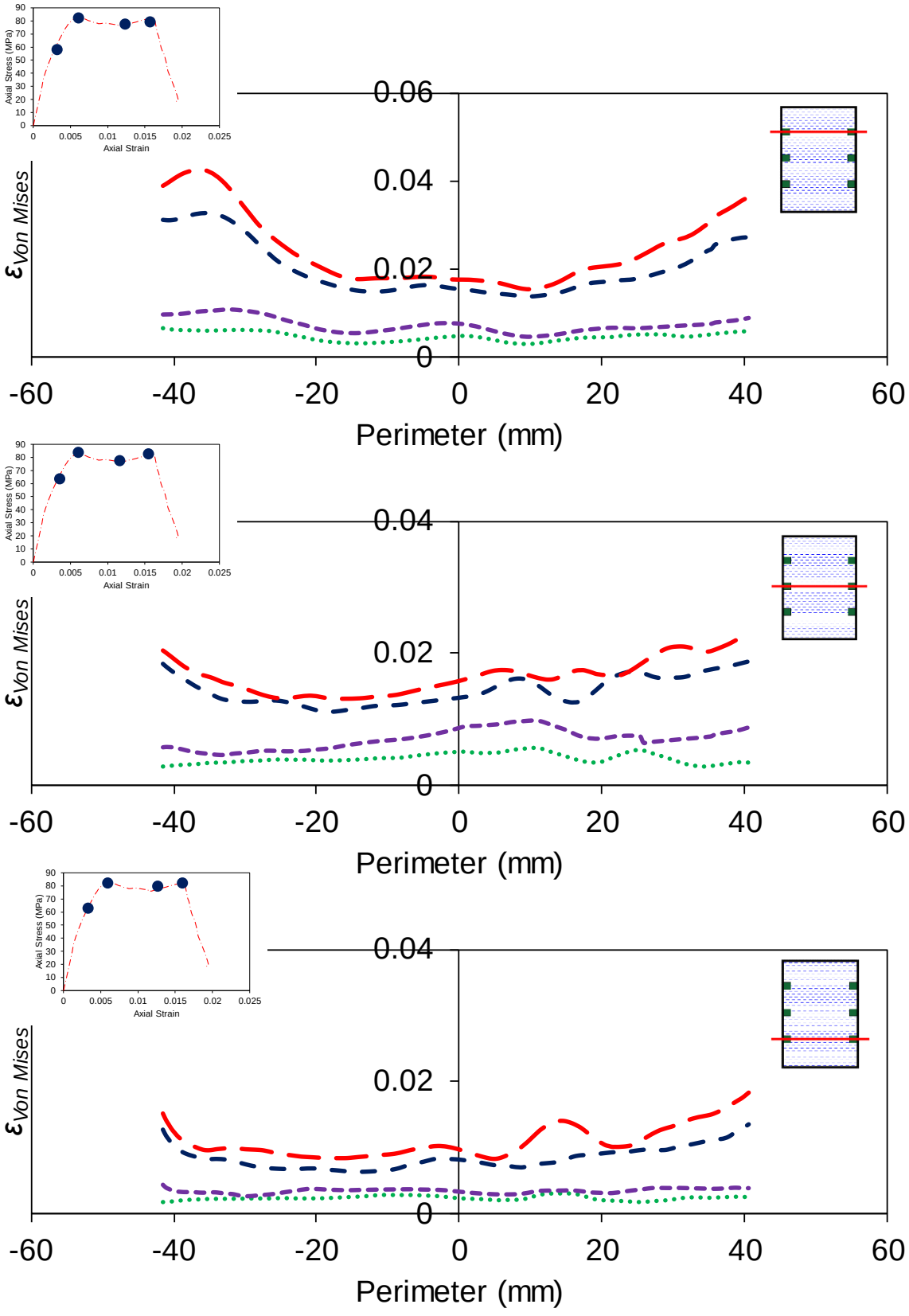

Figure 94- Lateral evolution of Von Mises strain for BFRP-6 layers (HSC-1)

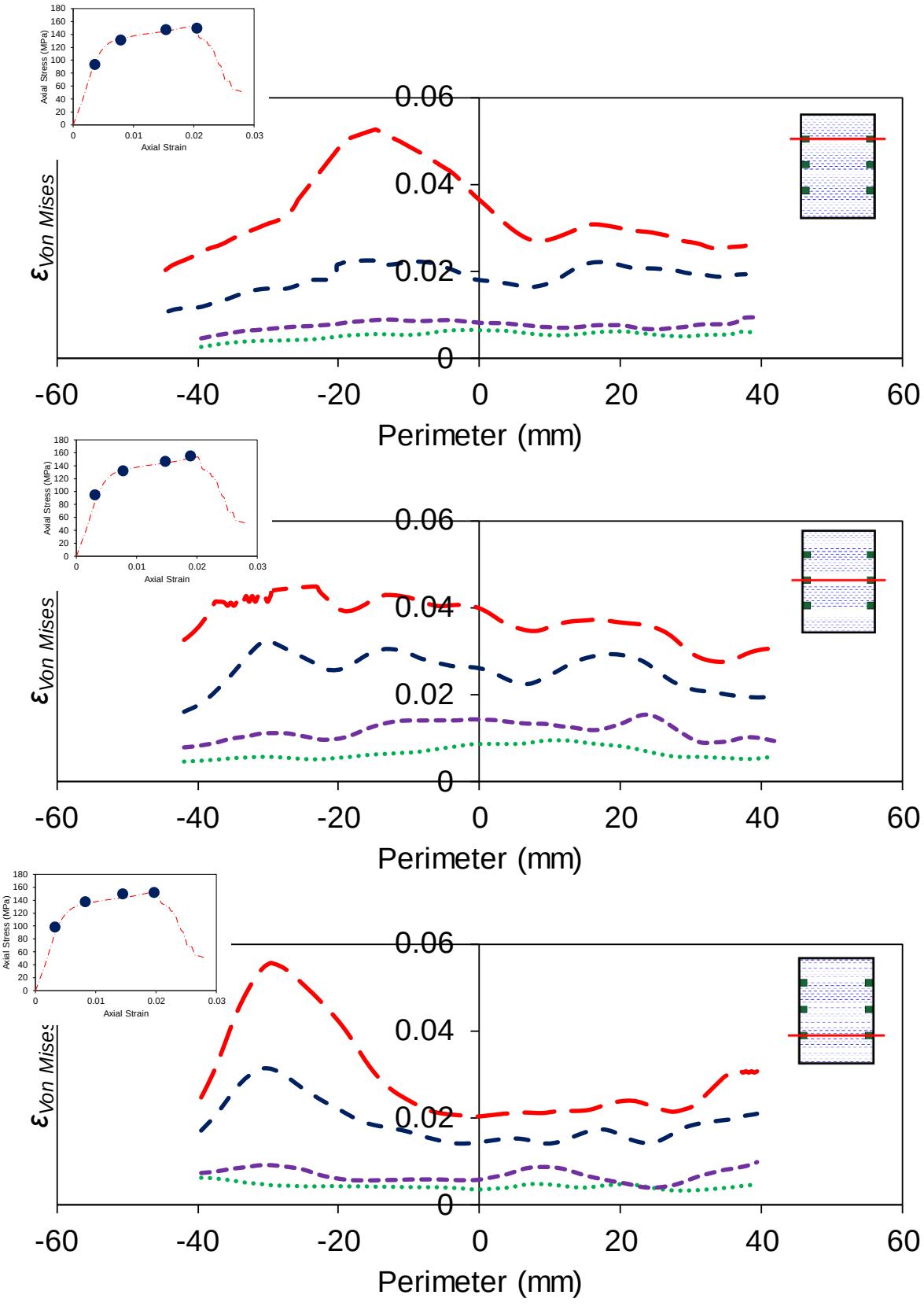

Figure 95- Lateral evolution of Von Mises strain for GFRP-3 layers (HSC-2)

7.5 Correlation between mechanical behavior and evolution of localization

As discussed in section 4, using existing methods to analyze DIC data do not offer accurately localization characteristics, i.e. localization initiation and characteristics of localization evolution. To mark initiation of localization, the bifurcation phenomenon was used which compares the behavior of material inside and outside of shear zone. Afterward, a new approach which was developed in previous section was used to assess and determine localization evolution characteristic of FRP-confined HSC and VHSC.

7.5.1 Localization initiation

The onset of localization can be more precisely determined by plotting the evolution of two local strains, i.e. inside and outside of the localization zone, against time steps. To verify this initiation, three specimens with different characteristics were selected. These three specimens are H-b4, H-G2 and VH-C3 specimens. These three specimens are representative of whole FRP-confined HSC and VHSC specimens whereas the H-B4 had lowest lateral stiffness and VH-C3 had highest K_l among all tested specimens. Figs. 96- 98 present the obtained results for selected specimens, i.e. H-B4, H-G2 and VH-C3. Additionally, one vertically inspection profile along the specimen centre (V2) and obtained Von Mises strain by DIC over specimen' surface are illustrated in these figures. This helps to correlate the mechanism of localization to mechanical behavior of FRP-confined HSC and VHSC which leads to better understanding of cracking, shear band formation and triggering of confinement mechanism.

As can be seen in the Fig. 96, the origination of localization starts at about 80%-90% of f'_{co}. It is well known and previously discussed in section 6 that the material outside of shear zone for unconfined specimen display unloading behavior after formation of shear band, i.e after bifurcation point. However, the FRP tubes changed this behavior and the FRP-confined HSC and VHSC specimens did not show this unloading behavior. As can be seen in these figures, the localization of strain outside of shear zone of specimens illustrates the ascending trend to

failure, although this ascending trend had lower rate of Von Mises strain-time steps compared to material inside of shear zone. After failure, the unloading behavior can be seen but this unloading behavior can be observed in both inside and outside of shear zones. This relaxation of strain concentration was abrupt in CFRP-3 layers specimens opposite to other two selected specimens which showed more gradual behavior. In addition, both inside and outside of shear band Von Mises strains displayed approximately similar behavior before bifurcation point. At the end, it should be noted that marking initiation of localization can be seen easily by investigation the bifurcation phenomenon but sorted and unsorted vertical Von Mises strain profile are not able to find initiation easily.

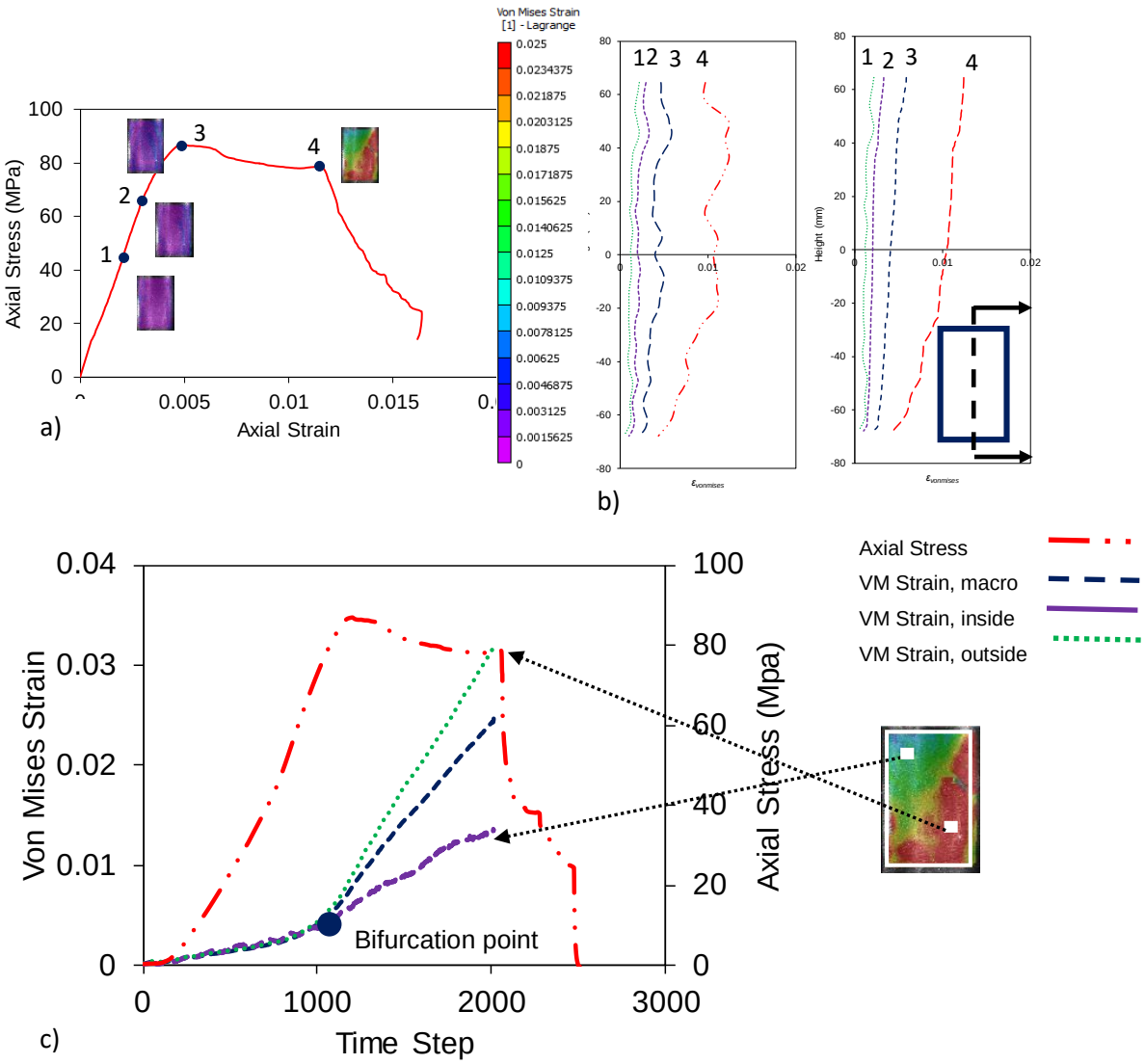

Figure 96- Von Mises strain distribution evolution of BFRP-4 layers (HSC1) specimen obtained results by DIC

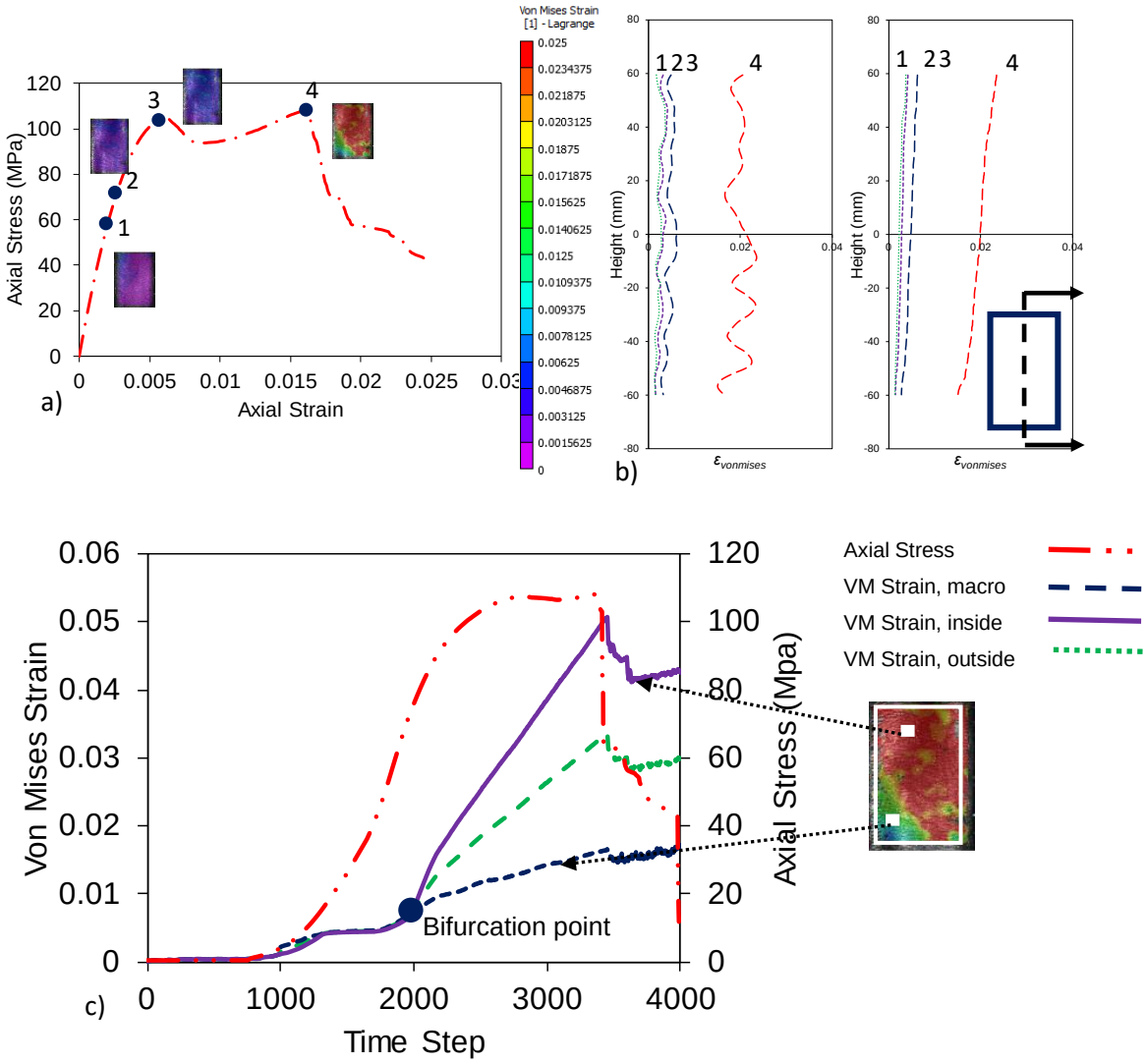

Figure 97- Von Mises strain distribution evolution of GFRP-2 layers (HSC) specimen obtained results by DIC

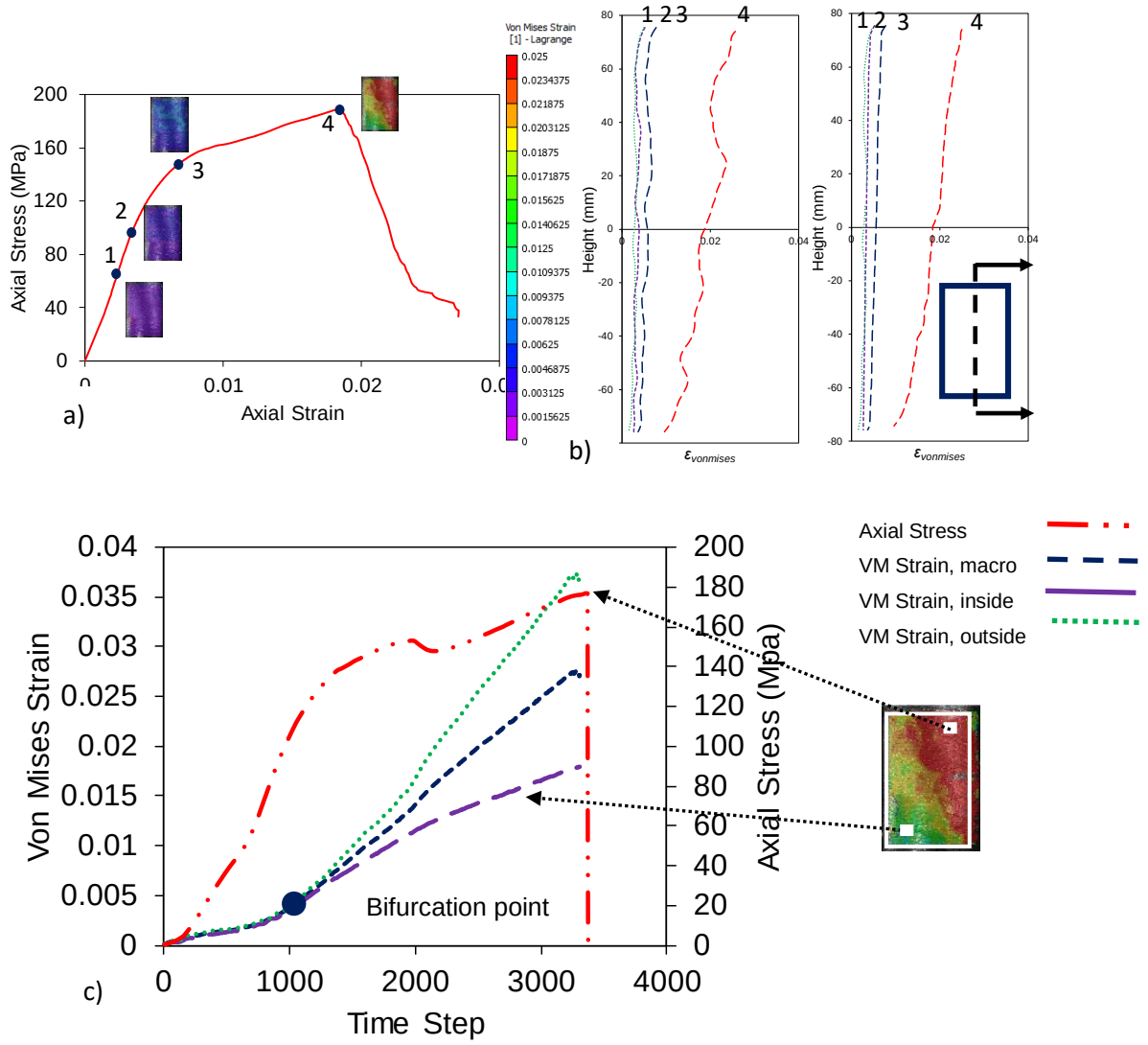

Figure 98- Von Mises strain distribution evolution of CFRP-3 layers (VHSC) specimen obtained results by DIC

7.5.2 Expansion of shear zone

7.5.2.1 Along specimen height

Figure 99 shows the expansion of the shear zone during axial compression for FRP-confined HSC along the height of specimens. As discussed in previous study, to evaluate the shear zone expansion, a method was developed and improved by Authors [202] where the average of obtained Von Mises strain by DIC over specimen surface was calculated at each height then these average Von Mises strains were sorted in descending order from top to bottom of specimens as shown in Fig. 99. Similar to previous study, two groups of $\varepsilon_{Von\ Mises}$ evolution can be observed. The first group represents steady development of $\varepsilon_{von\ Mises}$ during axial compression prior to pre-peak, which can be seen in well-confined specimens (e.g. CFRP, GFRP and BFRP-9 series). Conversely, there was a second group of specimens (e.g. BFRP-4

layers, BFRP-6 layers (VHSC)), which displayed more localized behavior after yielding followed by a strong increase of non-homogeneity during and after specimen failure. As can be seen in the figure, the shear failure zone for well-confined specimens expanded gradually during testing, whereas the insufficiently confined specimens showed a rapid transition from homogenous to localized behavior. Moreover, as can be seen in the Fig. 99, the evolution of Von Mises strain for whole specimens are approximately similar to f'_{c1} but the expansion of shear zone showed different pattern after transition zone dependent on different confinement level.

7.5.2.2 Around specimen perimeter

Fig. 100 presents the evolution of the shear zone for FRP-confined HSC and VHSC specimens around the perimeter. Similar to investigation of shear zone evolution along specimen height, the average of Von Mises strain along height of specimens for every point of perimeter was calculated and sorted from left to right. It can be seen in the figure that the evolution of Von Mises strain from f'_{co} to f'_{c1} changed by variation of FRP types. As can be seen in the figures, the insignificant differences between recorded Von Mises strain at f'_{co} and f'_{c1} were observed for BFRP specimens while the CFRP and GFRP specimens showed evident differences. As can be seen in the Table 3, basalt fibers have lowest E_f and f_f compared to other fibers. In addition, considering BFRP specimens to investigate the influence of K_l on shear zone expansion due to existence of two series of specimens at given f'_{co}, a more localized behavior by increasing K_l can be observed.

As can be seen in Figs 99 and 100, although the localization characteristics of specimens can be determined by using the new used approach, the quantification of this evolution is not still possible. Moreover, this method is not able to correlate the localization expansion to mechanical response of FRP-confined HSC specimens.

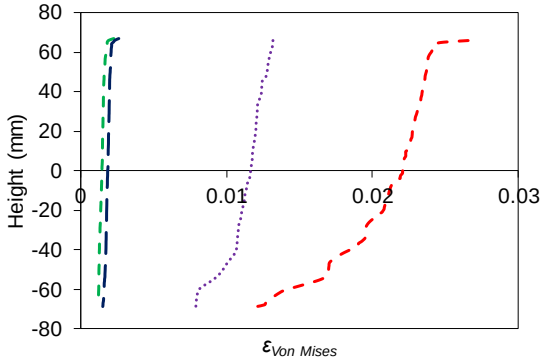

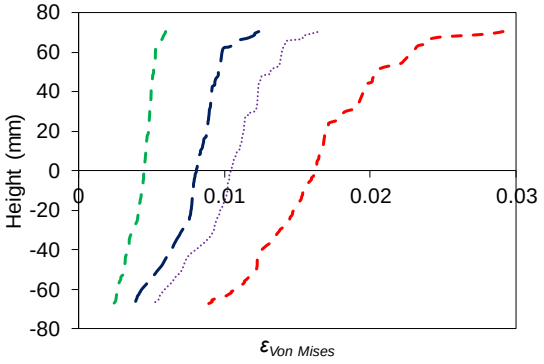

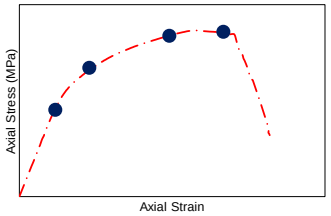

a) Confined specimen BFRP-4 layers HSC-1 BFRP-6 layers HSC-1

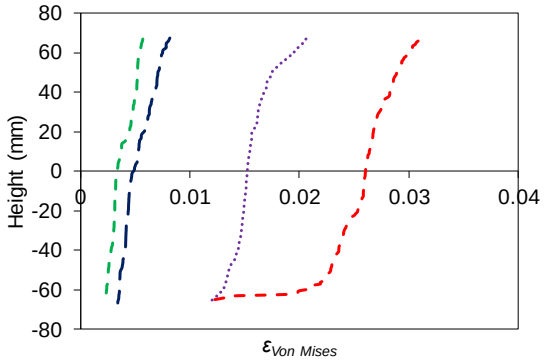

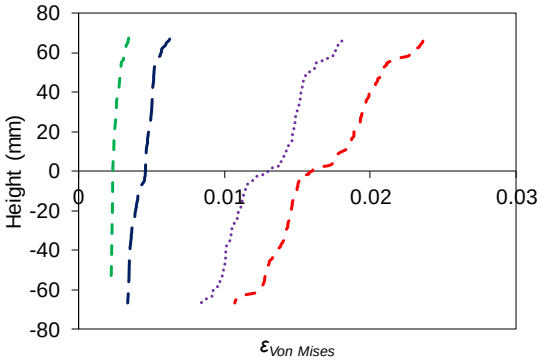

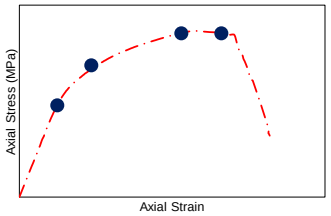

b) Confined specimen BFRP-6 layers HSC-2 BFRP-9 layers HSC-2

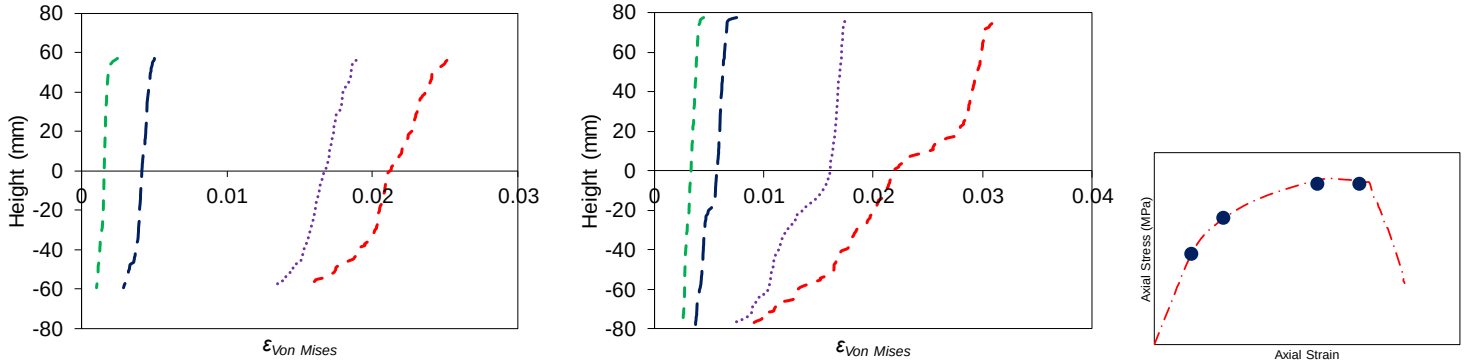

c) Confined specimen CFRP-2 layers HSC-1 CFRP-3 layers HSC-2

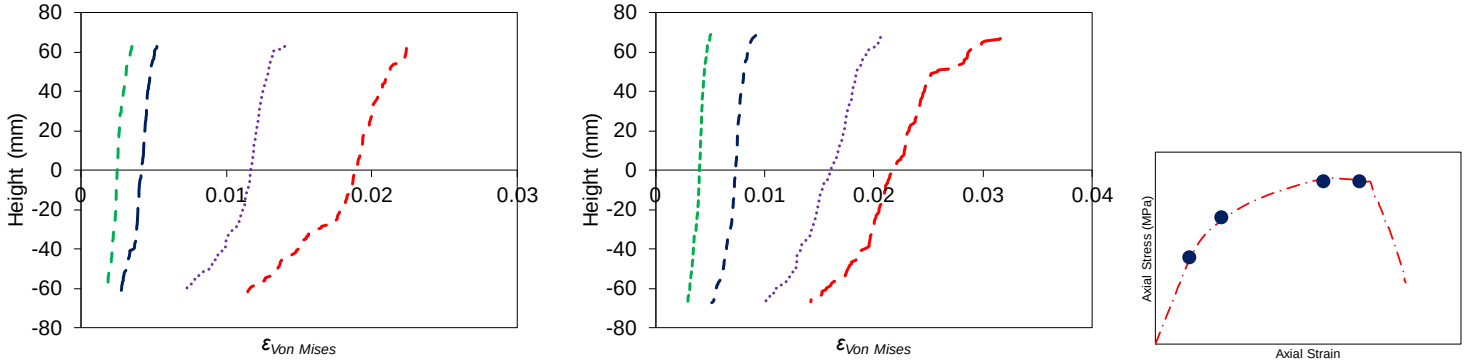

d) Confined specimen GFRP-2 layers HSC-1 GFRP-3 layers HSC-2

Figure 99- Expansion of shear zone along specimen height; a) BFRP confined specimens (HSC-1); b) BFRP confined specimens (HSC-2); c) CFRP confined specimens; d) GFRP confined specimens

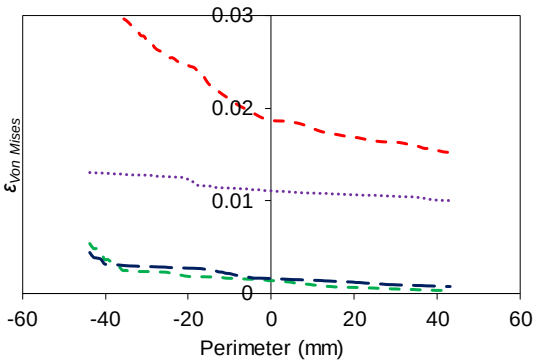

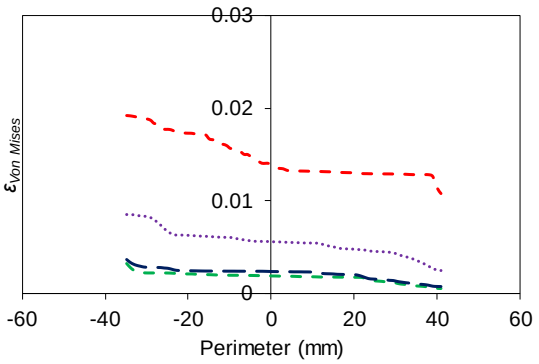

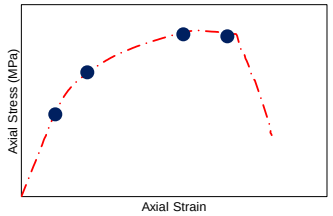

a) Confined specimen BFRP-4 layers HSC-1 BFRP-6 layers HSC-1

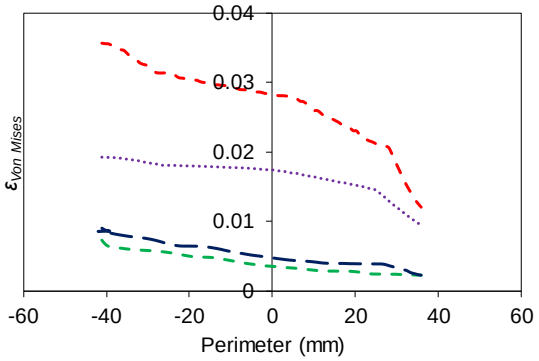

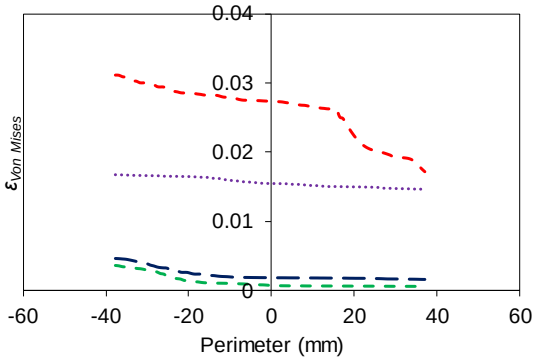

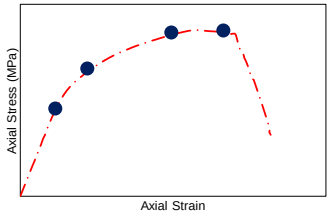

b) Confined specimen BFRP-6 layers HSC-2 BFRP-9 layers HSC-2

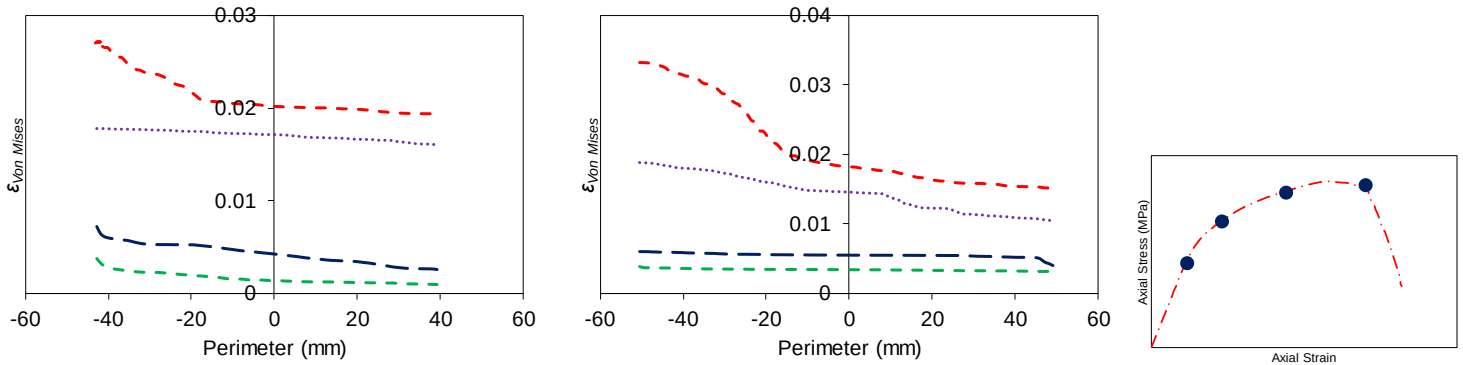

c) Confined specimen CFRP-2 layers HSC-1 CFRP-3 layers HSC-2

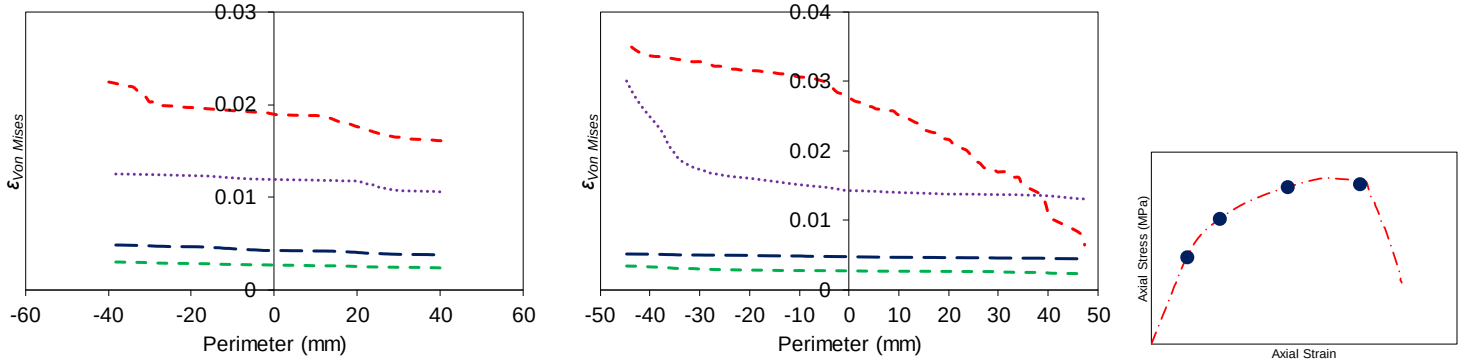

d) Confined specimen GFRP-2 layers HSC-1 GFRP-3 layers HSC-2

Figure 100- Expansion of shear zone around specimen perimeter; a) BFRP confined specimens (HSC-1); b) BFRP confined specimens (HSC-2); c) CFRP confined specimens; d) GFRP confined specimens

7.6 Correlation between macro mechanical behavior of FRP-confined HSC and evolution of localization

As discussed previously, developing a new approach to analyze the strain localization locally and globally and correlating the evolution of localization to mechanical behavior of specimens, is a robust potential instrument to develop/validate a constitutive model [168, 186]. As DIC is able to record both local and overall strain evolution, DIC was used in this study to record both overall and local strain over specimens' surface. However, this method, i.e. DIC, creates a huge amount of data which makes use of these data very difficult or impossible to study or quantify the strain localization in detail. It is discussed previously [168, 186] that the existing methods to evaluate DIC data, namely maps, counters and profiles, are not able to correlate accurately the strain localization to mechanical response of specimens. Therefore, an approach should be developed to condense whole obtained data by DIC to make use of these data practical. This approach also should be able to correlate obtained data to mechanical response of specimens which is one of the main aim in this research. For these reasons, determination of the full-field strain distributions over specimen surface and linking obtained distribution at different steps to each other and to mechanical behavior of specimens, could be a possible way to develop this type of approach. This methodology should be capable to quantify the strain distribution over specimen's surface and its evolution during test procedure. Additionally, this methodology should offer an approach to correlate the macro and micro mechanical behaviour of specimens with localization characteristics and provide a lower scale of information compared to continuum mechanics. Obtaining these advantages leads to an easy incorporation of this approach in developing a constitutive models in order to predict the accurate overall and local mechanical behaviour of materials.

In this study, the Von Mises strain distribution over specimen surface was used as explained in section 6. To perform this, the dependency of the obtained Von Mises strain to coordinate was released. The range between maximum obtained Von Mises strain few steps after failure

(considering the loss of speckle pattern) and zero was divided into 50 intervals. Following this, the number of obtained Von Mises strains that fall into each intervals were counted. Afterward, the frequency number of data in each bin was divided to a total number of the data obtained by DIC over specimens' surface; this referred as normalized frequency. A histogram was provided based on normalized frequency values and related intervals; then the top of each bar of the histogram was connected together. It should be noted that although maximum obtained Von Mises strains were different for different specimens, the approximately similar maximum Von Mises strain was selected for all specimens in this study. The mentioned procedure was repeated for each selected image where the selection was made at key points in the stress-strain curve.

Figures 101 illustrates the obtained experimental accumulative Von Mises distribution curves for BFRP, CFRP and GFRP specimens. As can be seen in this figure, the distribution curves are similar to accumulative PDF curves as discussed previously in details in section 6. However, the shape of Von Mises distribution curves changed after f'_{cc}. It should be noted that the speckle patterns over some area of FRP jacket were lost after f'_{cc} for H-B4 and VH-B9 which caused loss of data for analysis. However, the other specimens (H-B6, VH-B6, H-C2, VH-C3, H-G2 and VH-G3) showed evidently an unloading behavior after f'_{cc}. Additionally, it can be seen in Fig. 101 that VH-B9, VH-C3 and VH-G3 had sudden jump in their distribution curves after point 3 opposite to specimens which cast by HSC including H-B6, H-C2 and H-G2. This can be attributed to more intrinsically brittle behavior of VHSC compared to HSC where VHSC had higher f'_{co}. Nonetheless, H-B4 was only specimens which was prepared by HSC and it showed a sudden jump in its distribution curves. It was previously explained that two sets of BFRP specimens exist and one of these sets had lower K_l compared to the second set. This lower lateral stiffness (K_l) leads to more none-homogenous behavior of this set and

the existing sudden jump in H-B4 curves can be explained by this lower lateral stiffness of H-B4.

In this study, the experimental Von Mises strain distribution curves were modelled by using Beta probability density function (PDF) with using three existing coefficients inside this function, see section 6. These three coefficients offer firstly an instrument to govern the shape of distribution curve and secondly correlate the mechanical characteristics of various steps of test together. The detail of the use of Beta PDF and modeling Von Mises strain distribution over surface of specimens was presented in previous section. Figures 102 presents the obtained experimental and predicted none-accumulative histograms for BFRP, CFRP and GFRP-confined HSC specimens. It can be seen in the figures that the shape of Von Mises strain distribution at each step is very similar to a PDF curve, and this shape remained approximately similar up to maximum axial stress (f'_{cc}) for whole specimens. This observation indicates that the Von Mises strain distribution over surface of specimens can be modelled nearly accurate using Beta PDF. Nevertheless, it should be noted that more detail study is essential to generalize the obtained outcome by this research. Additionally, due to existing the various influential parameters such as FRP types, FRP tube thickness, K_l, f'_{co} and specimen geometry, more experimental study is essential to generalize the obtained outcome by this research. This indicates the need of more experimental data to correlate of the obtained p, q and ξ to mechanical response of FRP-confined concrete specimens. As a result, a detailed study on obtained coefficients and correlate them to characteristics of FRP-confined concrete such as f'_{co}, ε_{co}, K_l and FRP types, was not performed in this section. Correlating p, q and ξ to mechanical characteristics of specimens offers a robust approach to associate the localization characteristics to mechanical response of specimens and helps to quantify these localization characteristics, as performed in section 6.

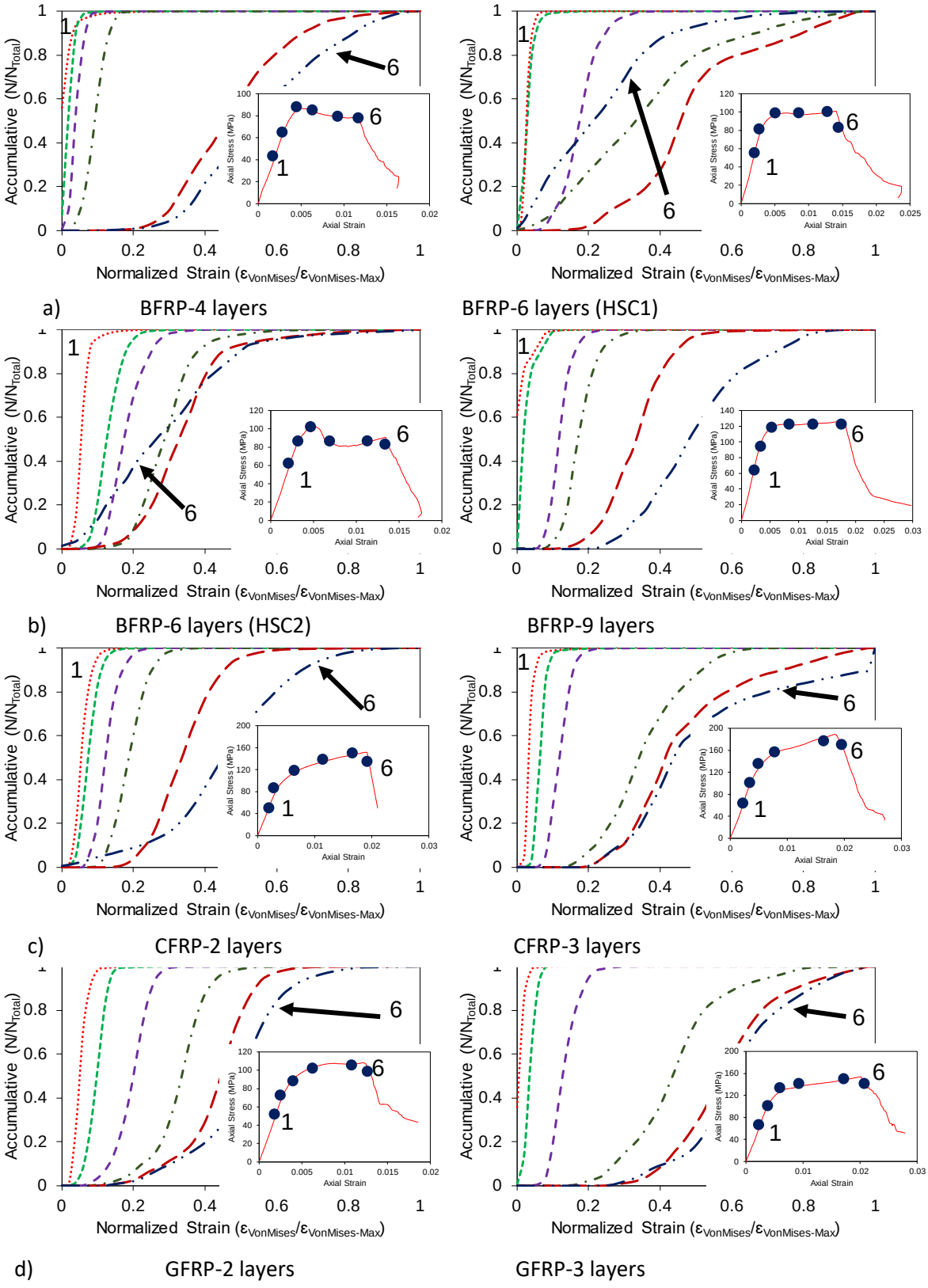

Figure 101- Experimental Von Mises strain accumulative distribution evolution of BFRP specimens obtained results by DIC; a) BFRP-4 layers and BFRP-6 layers (HSC1), b) BFRP-6 layers (HSC2) and BFRP-9 layers, c) CFRP-2 layers and CFRP-3 layers**,** d) GFRP-2 layers and GFRP-3 layers

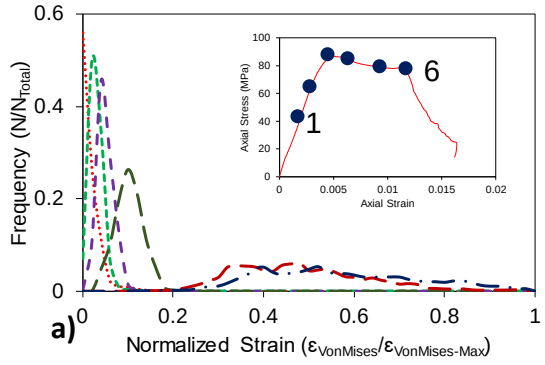

a)

	ξ	p	q
1	66000	3	240
2	5100	3	90
3	15000	3	150
4	2400	6	12
5	54	6	6
6	940	12	6

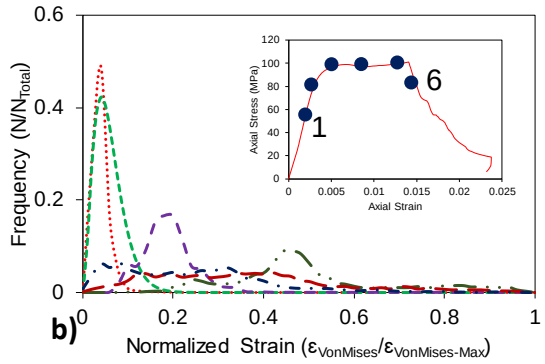

b)

	ξ	p	q
1	21000	3	148
2	12000	3	102
3	5700	3	81
4	5400	3	75
5	36000000	6	72
6	210	3	30

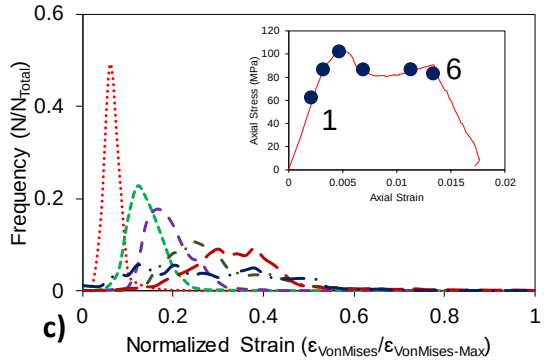

c)

	ξ	p	q
1	48000000	6	72
2	4.8E+09	9	54
3	9E+11	12	54
4	6E+11	15	36
5	1.5E+13	18	36
6	4.5E+08	18	18

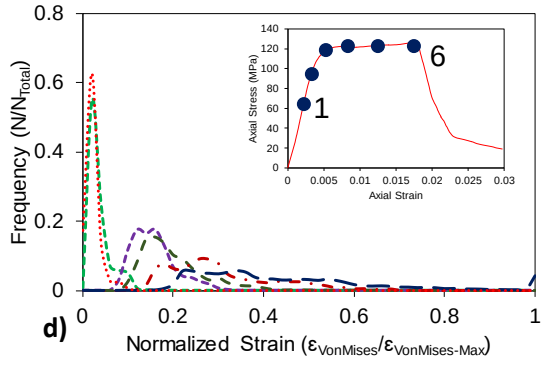

d)

	ξ	p	q
1	87000	3	240
2	2700	3	72
3	360	3	30
4	39000	6	21
5	6000	6	15
6	2100	6	12

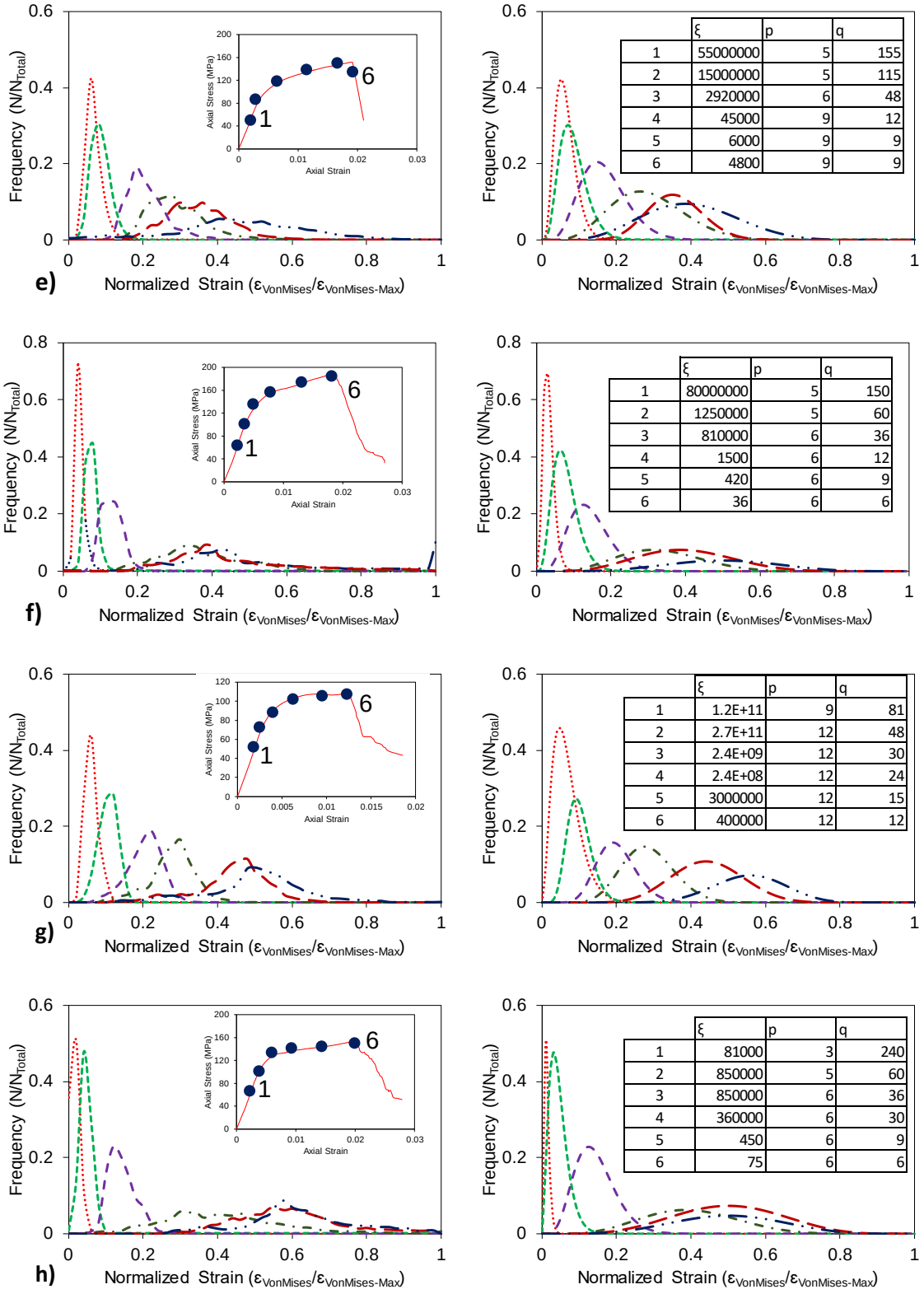

h) GFRP-3 layers

Figure 102- Von Mises strain distribution evolution of BFRP specimens obtained results by DIC; a) BFRP-4 layers, b) BFRP-6 layers (HSC1), c) BFRP-6 layers (HSC2), d) BFRP-9 layers, e) CFRP-2 layers, f) CFRP-3 layers**,** g) GFRP-2 layers, h) GFRP-3 layers

7.7 Conclusions

This section presents the results of an experimental study on the localization of deformation of FRP-confined HSC columns with circular cross-sections under compression. The axial stress-strain curves were obtained and synchronized with captured images by DIC system. Based on the results presented in this study, the following conclusions can be drawn :

1-The specimens with weaker lateral stiffness (BFRP- 4 layers and BFRP-6 layers (HSC-2)) suffered more localized behavior due to local shear plane in the specimens. Conversely, the stronger lateral stiffness make the specimens to display more homogenous behavior along the height of specimens.

2-The initiation of bifurcation starts at about 80%-90% of f'_{co} for FRP-confined HSC. Although it is well known that the material outside of shear zone for unconfined specimens initiate to show unloading behavior after formation of shear band, the FRP tubes changed this behavior and the HSC confined specimens do not show this unloading behavior outside of shear zone. After failure, the unloading behavior can be seen but this unloading behavior locates in both zones, namely inside and outside of shear zone.

3-Two groups of $\varepsilon_{VonMises}$ evolution can be observed during the test procedure in FRP-confined HSC specimens. The first group shows a homogenous evolution of $\varepsilon_{VonMises}$ during the test procedure and corresponding to pre-peak stage (before f'_{cc}). The second group which showed a sudden jump during their $\varepsilon_{VonMises}$ evolution corresponds to more localized behavior after yielding.

4-The shape of Von Mises strain distribution at each step is very similar to statistical PDF, and this shape of curve remained approximately similar up to maximum axial stress for whole specimens.

5-The experimental Von Mises strain distribution curves are recreated using Beta distribution function (β) and three various coefficients inside this function. The comparison between the experimental and theoretical distribution curves indicate that the strain distribution over surface of specimens can be modelled nearly accurate by using Beta distribution function (β).

It should be noted that more detail study is highly essential to generalize the obtained outcome by this research. This is due to various number of influential parameters, e.g. FRP types, FRP tube thickness, K_l, f'_{co} and specimen geometry.

Chapter 8: Axial compressive behavior of ultra-high-strength steel fiber-reinforced concrete-filled FRP tube columns

(A paper is submitted based on this section to Composite structures Journal (Elsevier) at 14/12/2020, "Axial compressive behavior of ultra-high-strength steel fiber-reinforced concrete-filled FRP tube columns" by Ali Fallah Pour, Togay Ozbakkaloglu and Tom Vincent)

8.1 Introduction

By adding steel fibers to wet concrete mix of FRP-confined concrete, an ultra-high-performance structural system can be developed, which offers better mechanical performance compared to conventional FRP-confined concrete [78]. This improvement is due to simultaneous use of FRP, which provides lateral confinement to the concrete enhancing the compressive strength and ductility [14, 16, 17], and steel fibers, which improve the intrinsically brittle response of plain concrete [59-63, 203-206]. The superior structural engineering properties of high-strength concrete (HSC) over normal strength concrete (NSC) make this material attractive for use in an ultra-high-performance structural systems [1-10]. However, it was previously shown that FRP-confined HSC experiences a temporary post-peak axial strength softening behavior due to brittle mechanical behavior of higher strength concretes [16]. The new structural system proposed in this research has the potential to amend this temporary softening behavior for FRP-confined HSC specimens, due to the addition of internal steel fibers.

The influence of internal steel fibers on concrete behavior has been extensively investigated by different research programs [62-64, 72-76, 203-206]. The formation of isolated major cracks in the concrete can be decreased by adding steel fibers to the concrete mix which results in improved control over concrete crack growth. The steel fibers create bridges across the cracks and the crack propagation can be controlled or delayed by these bridges, consequently

improving the ductility of concrete [59, 60, 65-70, 72, 73, 75]. In the case of steel fiber reinforced concrete-filled FRP tubes (SFR-CFFT) this leads to the reduction of stress concentration on FRP jackets which results in improved hoop rupture strain and higher ductility [77].

It has been shown previously that steel fiber reinforced concretes (SFRCs) offer better mechanical behavior compared to plain concrete under bending, tension and compression (e.g. [61, 63, 205, 207-212]). A number of experimental studies on SFR-CFFTs have been performed to determine the mechanical behavior of this confinement system under different type of loading such as concentric and eccentric compression [9, 77, 91, 213, 214]. The studies focused on concentric compressive loading [9, 77, 214] reported that the axial stress-strain relationship of the FRP-CFFT specimens were influenced by volume fraction (V_f) and aspect ratio (A_R). Xie and Ozbakkaloglu [77] reported that ultimate axial stress (f'_{cc}), ultimate axial strain (ε_{cu}) and hoop rupture strain ($\varepsilon_{h,rup}$) decrease due to an increase in A_R for a given V_f. Conversely, they showed that f'_{cc}, ε_{cu}, and $\varepsilon_{h,rup}$ increased with an increase in V_f for a given A_R. However, although the existing studies have examined different steel fiber types, such as hooked end, crimped and straight, in FRP-confined concrete and the effect of V_f on their mechanical behavior, no study to date has examined the compressive behavior of FRP-confined ultra-high strength steel (UHSS) fiber-reinforced concrete as affected by the variation of f'_{co} and lateral stiffness (K_l).

To address the current research gap, this paper presents the results of the first reported study on the axial compressive behavior of UHSSFR-CFFTs that examined the influence of f'_{co} and FRP type. In the following section, the test program is first presented explaining specimen properties and testing procedures, followed by the presentation of experimental outcomes. Following this is an in-depth discussion on the experimental results where the influence of key

experimental parameters such as concrete type and lateral FRP jacket stiffness (K_l) are discussed.

8.2 Test Program

8.2.1 Test Specimens

24 circular CFFTs were manufactured and tested under axial compression. The specimens were 100 mm in diameter, measured at the concrete core, and 200 mm in height. Three types of concrete were used including one batch of NSC and two batches of HSC. The volume fraction of steel fiber was selected as 1.5% based on a previous study performed by this research group [77]. The FRP tubes were manufactured by using a manual wet lay-up procedure with unidirectional fiber sheets. Three different FRP fiber types were used in this study, which were glass, carbon and basalt fiber reinforced polymer (GFRP, CFRP and BFRP). Two nominally identical specimens were tested for each unique specimen configuration. The details of the specimens are presented in Table 23.

8.2.2 Materials

8.2.2.1 Concrete

NSC and HSC used in this research were batched and mixed in the laboratory with mix details provided in Table 24. As can be seen in Table 2, two different HSC batches were prepared with different f'_{co} and the target f'_{co} for the three prepared batches (namely, NSC, HSC and VHSC) were 35, 75 and 100 MPa, respectively. These mixes consisted of crushed basalt as the coarse aggregate, with a 10 mm nominal maximum size. The resulting slump for each batch was over 100 mm for NSC and over 200 mm for both HSC mixes. Control cylinders with the same 100 by 200 mm dimensions were cast from each concrete mix and tested in parallel to the FRP confined specimens to determine the concrete compressive strength (f'_{co}). The confined specimens include 6 GFRP, 6 CFRP and 12 BFRP confined specimens.

Table 23-Details of test specimens

Specimen	V_f (%)	Concrete Type	FRP-Type	Number of Layers	$t_{f\text{-total}}$ (mm)
N-G1	1.5	NSC	GFRP	1	0.2
H1-G2	1.5	HSC1	GFRP	2	0.4
H2-G3	1.5	HSC2	GFRP	3	0.6
N-C1	1.5	NSC	CFRP	1	0.167
H1-C2	1.5	HSC1	CFRP	2	0.334
H2-C3	1.5	HSC2	CFRP	3	0.501
N-B2	1.5	NSC	BFRP	2	0.150
N-B3	1.5	NSC	BFRP	3	0.225
H1-B4	1.5	HSC1	BFRP	4	0.300
H1-B6	1.5	HSC1	BFRP	6	0.450
H2-B6	1.5	HSC2	BFRP	6	0.450
H2-B9	1.5	HSC2	BFRP	9	0.675

Table 24-Concrete mix proportions

Ingredient	NSC	HSC1	HSC2
Cement (kg/m^3)	360	437	506
Silica fume (kg/m^3)	-	38	44
Sand (kg/m^3)	700	710	700
Gravel (kg/m^3)	1010	1025	1015
Fiber (kg/m^3)	117	117	117
Water (kg/m^3)	228	157	155
Superplasticizer* (kg/m^3)	3	20	30
w/c	0.64	0.36	0.32
Total (kg/ m^3)	2418	2504	2562

* Superplasticizer contained 70% water by weight

8.2.2.2 Steel fibers

UHSS fibers used in this study are shown in Fig. 103 and their details are presented in Table 25. The reinforcing index (*RI*) for the selected volume fraction was 0.975, as was determined from Eq. 8.1.

$$RI = (V_f \times A_s) \tag{8.1}$$

where V_f is the fiber volume fraction (i.e. volume of fiber per unit of volume of concrete) and A_s is the fiber aspect ratio ($A_s = \frac{l_f}{d_f}$, where l_f is the fiber length and d_f is the equivalent fiber diameter).

Figure 103-Ultra-high-strength steel fibers

Table 25-Details of ultra-high-strength steel fibers

Name	WSF 0213*
Diameter	2 mm
Length	13 mm
Ultimate tensile stress	>2850 MPa

*copper coated micro steel fiber

8.2.2.3 FRP tubes

The FRP tubes were prepared using three different fiber types (GFRP, CFRP and BFRP) through a manual wet lay-up process by wrapping epoxy resin impregnated fiber sheets around precision-cut high-density Styrofoam templates in the hoop direction. A summary of the FRP material properties used in this study is presented in Table 26.

The number of FRP layers was selected by considering the required lateral stiffness to ensure an ascending second branch on the axial stress-strain curve. The lateral stiffness can be

calculated by $K_l = \frac{2E_{FRP}t_f}{D}$, where E_f is the elastic modulus of FRP fiber, t_f is total fiber thickness of FRP jacket and D is diameter of concrete core. As previously proposed by Lim and Ozbakkaloglu [17], the minimum lateral stiffness required to ensure an ascending second branch (K_{lo}) in MPa can be expressed by $K_{lo} = f'^{1.65}_{co}$ where f'_{co} is unconfined compressive strength of concrete in MPa [17].

A larger number specimens were prepared for BFRP-confined concrete than GFRP and CFRP-confined concrete due to having fewer previous experimental studies on this type of FRP. Consequently, two different K_l values were selected for BFRP confined specimens, the first corresponded to K_{lo}, whereas a higher second value was selected to ensure an ascending-type second branch of axial stress-axial strain curve Throughout this paper, the BFRP confined specimens prepared with low and high values of K_l are referred to as lightly- and adequately-confined, respectively.

Table 26-Material properties of fibers and FRP composites

Type	Nominal dry fiber thickness t_f (mm/ply)	Fiber/FRP properties					
		Provided by manufacturers			Obtained from coupon tests*		
		Ultimate tensile stress f_f (MPa)	Ultimate tensile strain ε_f (%)	Elastic modulus E_f (GPa)	Ultimate tensile stress f_{FRP} (MPa)	Ultimate tensile strain ε_{FRP} (%)	Elastic modulus E_{FRP} (GPa)
S-Glass	0.2	3040	3.50	86.9	3055	3.21	95.3
CFRP	0.167	4830	2.10	230	4598	1.95	236
BFRP	0.075	1680	2.30	73.0	1584	2.10	76.0

* Calculated based on nominal dry fiber thickness

8.2.2.4 Specimen designation

The specimens presented in Table 23 were labelled according to unconfined concrete strength (35.2, 78.7 and 105.2 MPa), FRP fiber type (GFRP, CFRP and BFRP) and number of FRP layers (again). For example, the specimen label of H2-C3 relates to a specimen manufactured with the VHSC concrete mix and confined by 3-layer CFRP sheets.

8.2.2.5 Instrumentation and testing

Axial deformations of the specimens were measured with four linear variable differential transformers (LVDTs), which were mounted at the corners between the loading and supporting steel plates of the test machine as shown in Figs. 52 and 53. The calculation of the average axial strains was performed with recorded deformations along the height of the specimens. Lateral strains were measured by a total of 6 unidirectional lateral strain gauges (LSG) having a gauge length of 5 mm that were bonded on the FRP jacket outside the overlap region. These strain gauges were installed in pairs located at heights of 50, 100 or 150 mm with each pair of gauges attached at opposing sides of the specimen.

The specimens were tested under monotonic axial compression using a 5000 kN capacity universal testing machine. During the test, the loading was applied at approximately 2 microstrain per second until specimen failure. The instrumentation and testing equipment used in this experimental study are shown in Fig. 52 and 53.

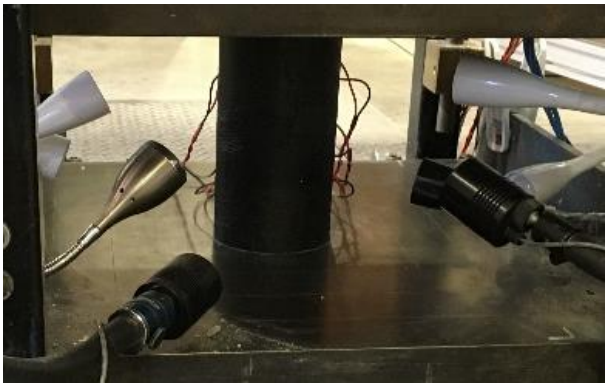

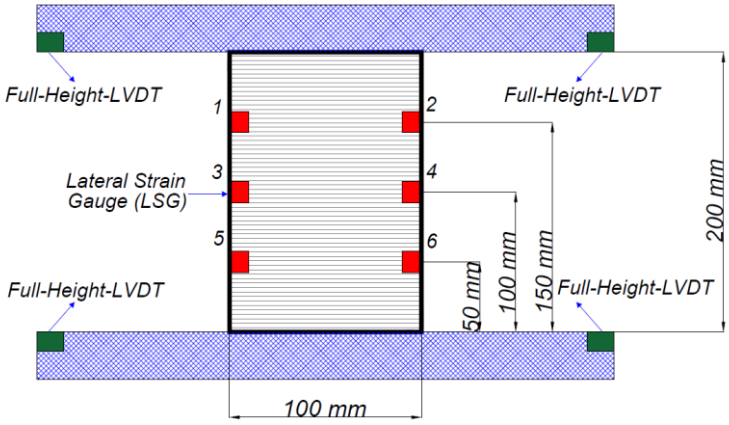

Figure 104-Test setup and instrumentation

8.3 Test Results and discussion

8.3.1 Unconfined specimens

8.3.1.1 Failure mode

Figs. 105 (a-c) shows typical failure modes for UHSSFR unconfined concrete specimens. It should be noted that the surface of these specimens was painted a dark colour for easier identification and monitoring of crack development. As can be seen in these figures, the unconfined UHSSFRC specimens exhibited different failure modes to those typically seen in plain unconfined concrete specimens. Figs. 105 (a-c) show more homogenous crack distribution patterns in UHSSFR specimens compared to plain concrete specimens. It can be seen in Figs. 105 (a-c) that the addition of steel fibers results in bridging of cracks and this effect reduces the localization of cracks, which increases the integrity and residual strength of specimens during post-peak behavior.

a) NSC b) HSC c) VHSC

Figure 105-Failure modes for unconfined test specimens

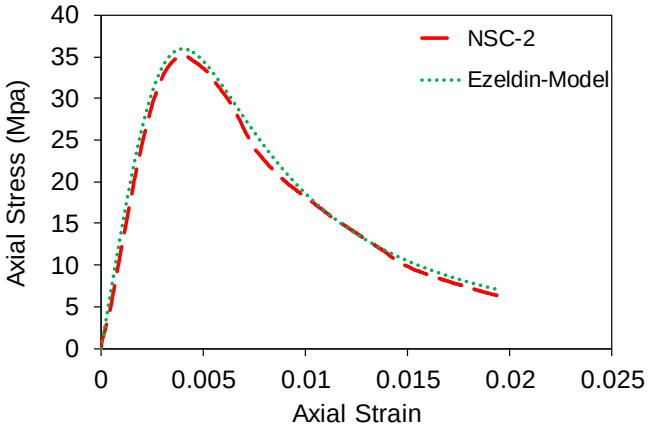

a)

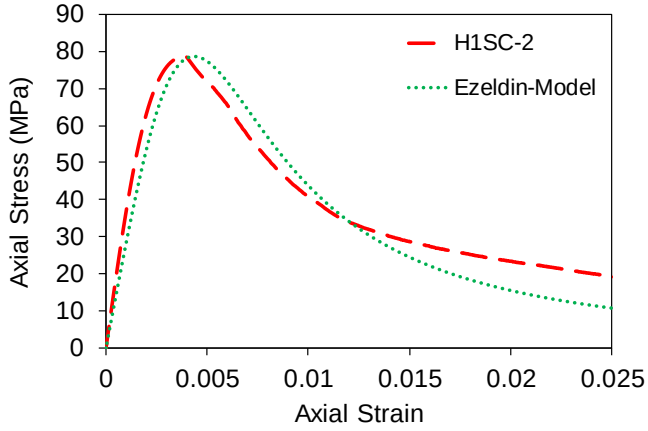

b)

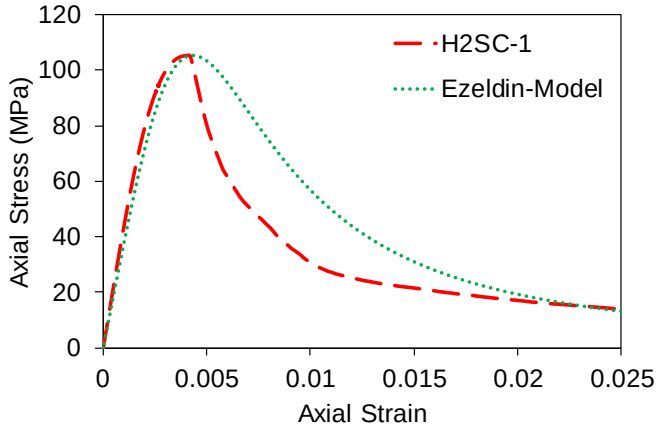

c)

Figure 106- Experimental and theoretical axial stress-strain curves of unconfined concrete: a) NSC, b) HSC1, c) HSC2

8.3.1.2 Axial stress-strain behavior

Table 27 presents the recorded compressive strengths (f'_{co}) and corresponding axial strains (ε_{co}) for the unconfined SFRC specimens. Additional SFRC mechanical performance can be seen in Fig. 106, which shows the axial stress-strain curve for the three different concrete mixes.

Table 27-Properties of unconfined concrete at test day of CFFTs

Concrete Type	Fiber Volume fraction V_f (%)	f'_{co} (Mpa)	ε_{co} (%)
NSC	1.5	35.2	0.33
HSC1	1.5	78.7	0.39
HSC2	1.5	105.2	0.40

It is well established that accurate prediction of the axial stress-strain behavior is a vital step in the design of concrete members. Many studies have been performed to predict the axial stress-strain curve for unconfined NSC and HSC, but these models are not intended to be used for SFRC specimens due to a change in behavior as a result of adding steel fibers to the concrete mix. A few stress-strain models specifically applicable to SFRC have been developed (e.g. [64, 65, 67]) based on different fiber type, such as hooked end, straight or crimped. Of these models, only the one developed by Ezeldin and Balaguru [64] was designed for use with high strength straight steel fibers, however this model did not consider UHSS fibers. The model by Ezeldin and Balaguru [64] was compared to the experimentally recorded stress-strain curves presented in Fig 3. In this figure it can be seen that the model accurately predicts NSC-UHSSFRC specimens; however, the obtained results for two HSC-UHSSFRC specimens showed small differences between experimental axial stress-strain curves and predicted curves by Ezeldin and Balaguru [24] model. It can be seen in the figure that the difference between experimentally recorded and predicted axial stress-strain curves increased with an increase in f'_{co} particularly for the post-peak behavior, which can be attributed to the model's underestimation of the brittleness of very high strength concrete (VHSC).

8.3.2 Confined specimens

8.3.2.1 Failure mode

Figs. 107 (a-l) show typical failure modes for UHSSFR FRP-confined concrete specimens. The failure mode of FRP-confined specimens was a consequence of FRP jacket rupture associated with a loss of applied load. The mentioned rupture mode occurred for all specimens except for two specimen that suffered an early FRP debonding failure (i.e. H1-C2-2 and N-B3-2, which are marked in Table 28 with *). All CFRP-confined specimens and GFRP-confined HSC specimens displayed a sudden rupture of jacket immediately at specimen failure, whereas the BFRP- and GFRP-confined NSC and HSC specimens showed a more progressive FRP jacket rupture. As shown in Fig. 107 (a-l), the FRP jacket rupture was observed to occur at the mid-height region of each specimen.

a) N-G1-1 b) H1-G2-1 c) H2-G3-2

d) N-C1-1 e) H1-C2-1 f) H2-C3-1

g) N-B2-1 h) H1-B4-1 i) H2-B6-1

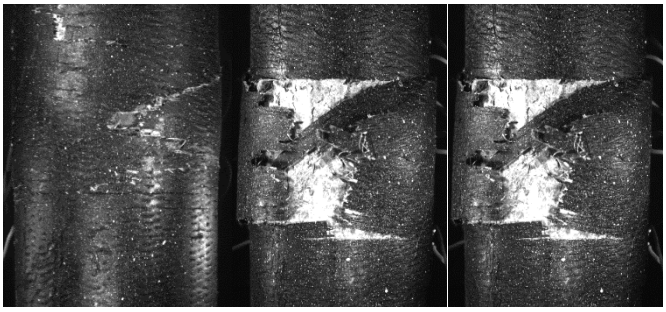

j) N-B3-1 k) H1-B6-1 l) H2-B9-1

Figure 107- Failure modes for test specimens (a), (b) and (c) GFRP-confined, (d), (e) and (f) CFRP-confined, (g), (h), (i), (j), (k) and (l) BFRP-confined

8.3.2.2 Axial Stress-strain behavior

8.3.2.2.1 General observations

Figs. 108-110 illustrate the axial stress-strain curves of GFRP-, CFRP- and BFRP-confined specimens, respectively. It is well understood that sufficiently confined concrete exhibits a monotonically ascending curve, which consists of a parabolic first ascending portion and a nearly linear second branch [14, 16, 17]. However, the inherently brittle nature of higher strength concretes causes FRP-confined HSC to experience a sudden drop in axial stress immediately after the initial peak stress (f'_{c1}) and corresponding axial strain (ε_{c1}) on the axial stress-strain curve. Moreover, this brittle behavior of HSC compared to NSC influences the ultimate compressive strength (f'_{cc}) and axial strain (ε_{cu}) of FRP-confined concrete. This influence can be investigated using the strength enhancement (k_1) and strain enhancement (k_2) coefficients. As can be seen in Figs. 108 and 109, all GFRP- and CFRP-confined specimens showed ascending-type axial stress-strain curves, without suffering any loss of strength along the transition zone, which is a region that signifies a change in the trend of the stress-strain curve after the termination of the initial ascending branch (f'_{c1}, ε_{c1}) [17]. This observation indicates that the addition of UHSS fibers can limit or eliminate the sudden drop typically observed in the axial stress of concrete at the transition zone associated with the brittle nature of HSC [17].

As can be seen in the Fig. 110, all BFRP-confined NSC specimens displayed axial stress-strain curves with ascending behavior. However, BFRP-confined specimens prepared with HSC showed axial stress-strain curves with both ascending and descending types of second branches. The lightly-confined VH-B6 series with a lower confinement level (f_{lu}/f'_{co}) showed slightly descending behavior starting at the transition zone (Fig. 110.a). The nominal lateral confining pressure at ultimate of FRP jacket (f_{lu}/f'_{co}) was determined by $f_{lu} = K_l \times \varepsilon_{fu}$ where K_l and ε_{fu} are the lateral stiffness of the FRP jacket and ultimate tensile strain of fibers, respectively. Conversely, the adequately-confined H-B6 and VH-B9 series with a higher f_{lu}/f'_{co}

exhibited a monotonically ascending axial stress-strain curve similar to GFRP- and CFRP-confined specimens (Fig. 110b). It can be seen in Fig. 110b that VH-B9-1 showed a gradual drop in strength after the transition point; however, this strength was eventually recovered. This can be attributed to subtle imperfections in the manufacturing of this specimens, as the companion specimen VH-B9-2 did not display this behavior.

Table 28 presents the test results, including the unconfined compressive strength (f'_{co}) and corresponding strain (ε_{co}), compressive strength (f'_{cc}), ultimate axial strain (ε_{cu}) and axial stress and strain enhancement ratio (f'_{cc}/f'_{co} and $\varepsilon_{cu}/\varepsilon_{co}$). As expected, f_{lu}/f'_{co} influences the recorded ultimate axial strain (ε_{cu}) with low values of f_{lu}/f'_{co} leading to low values of ε_{cu}. Additionally, it is previously shown for FRP-confined plain concrete that ε_{cu} decreases with an increase in f'_{co} at a given f_{lu}/f'_{co} [10]. However, similar values of ε_{cu} for FRP-confined NSC and VHSC UHSSFR-CFFT specimens' points to a possible change in the behavior of FRP-confined concrete through the addition of steel fibers. A comparison of all BFRP specimens in Table 28 indicates that BFRP- VHSC specimens exhibited some of the highest values of ε_{cu} compared to the companion NSC and HSC series of specimens with similar values of f_{lu}/f'_{co}, which again indicates the positive influence of UHSS fibers on the axial deformation capacity of HSC and VHSC.

The influence of adding steel fiber in the concrete mix on f'_{cc}/f'_{co} can also be observed in Table. 28. The results show that, for a given f_{lu}/f'_{co}, f'_{cc}/f'_{co} decreased with an increase in f'_{co} consistent with previous research on FRP-confined plain concrete. It can also be seen in Table 28 that, as expected, BFRP specimens with the lowest values of K_l/f'_{co} (i.e. N-B2, H-B4 and VH-6) had the lowest f'_{cc}/f'_{co}, whereas CFRP specimens with the highest values of K_l/f'_{co} (i.e. N-C1, H-C2 and VH-C3) recorded the highest f'_{cc}/f'_{co}.

As mentioned previously and can be seen in Figs 108-110, two specimens (H-C2-2 and N-B3-2) experienced premature failure with their axial stress-strain curves showing lower values for the ultimate stress and strain, and consequently, these datasets should be avoided when making comparisons.

Table 28- Variation of key axial stress-strain curve parameters with eccentricity

Specimen ID	Measured Eccentricity (e) (mm)	2nd Branch Slope (E_2) (MPa)	Ultimate Axial Stress (f'_{cc}) (MPa)	Ultimate Axial Strain (ε_{cu})	Normalized 2nd Branch Slope ($E_2/E_{2,0}$)*	Normalized ultimate axial strain ($\varepsilon_{cu}/\varepsilon_{cu,0}$)**	Normalized ultimate axial stress ($f'_{cc}/f'_{cc,0}$) ***	Axial strain enhancement ratio ($\varepsilon_{cu}/\varepsilon_{co}$)	Strength enhancement ratio (f'_{cc}/f'_{co})
C1	0	4120	190.7	0.018	1.03	0.95	1.01	6.32	1.81
C2	0	3900	185.8	0.020	0.97	1.05	0.99	7.02	1.80
C4	15	2900	173.4	0.026	0.72	1.40	0.92	9.12	1.65
C7	23	2100	159.4	0.028	0.52	1.51	0.85	9.83	1.51
C8	33	1500	148.9	0.029	0.37	1.54	0.79	10.18	1.41
C9	34	1100	143.3	0.030	0.27	1.60	0.76	10.53	1.36
C10	33	1250	142.1	0.030	0.31	1.60	0.75	10.53	1.35
C11	38	950	138.7	0.030	0.24	1.62	0.74	10.53	1.32
C13	45	900	135.2	0.032	0.22	1.72	0.72	11.23	1.28
C14	45	750	138.3	0.031	0.19	1.67	0.73	10.88	1.31
C15	48	700	130.2	0.033	0.17	1.77	0.69	11.58	1.23
S1	0	3750	183.4	0.023	1.07	1.04	1.02	8.07	1.75
S2	0	3250	175.1	0.021	0.93	0.96	0.98	7.37	1.67
S3	15	2250	164.4	0.029	0.64	1.30	0.92	10.18	1.54
S4	16	2000	170.2	0.028	0.57	1.30	0.95	9.83	1.60
S5	21	1450	162.3	0.032	0.41	1.46	0.91	11.23	1.53
S6	22	1450	158.2	0.029	0.41	1.34	0.88	10.18	1.49
S7	28	1350	156.3	0.033	0.39	1.49	0.87	11.58	1.47
S8	30	1250	158.6	0.034	0.36	1.53	0.88	11.93	1.50
S9	35	1150	151.6	0.034	0.33	1.53	0.85	11.93	1.43
S10	39	1110	147.2	0.033	0.32	1.52	0.82	11.58	1.39
S11	44	650	144.5	0.034	0.19	1.57	0.81	11.93	1.37
S12	44	600	140.3	0.035	0.17	1.58	0.78	12.28	1.33
S13	49	550	141.1	0.037	0.16	1.70	0.79	12.98	1.34
S14	51	500	141.2	0.037	0.14	1.67	0.79	12.98	1.34

* $E_{2,0}$ is the second branch slope of the specimen under concentric loading

** $\varepsilon_{cu,0}$ is the ultimate axial strain of the specimen under concentric loading

*** $f'_{cc,0}$ is the ultimate axial stress of the specimen under concentric loading

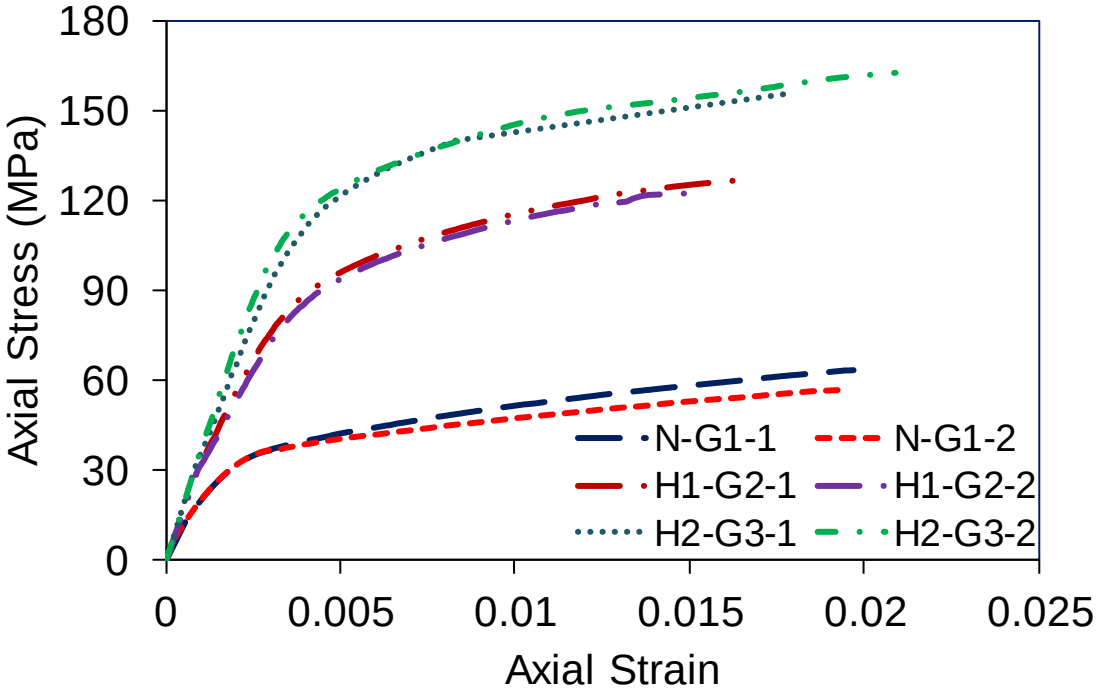

Figure 108- Axial stress-strain response of GFRP-confined concrete specimens

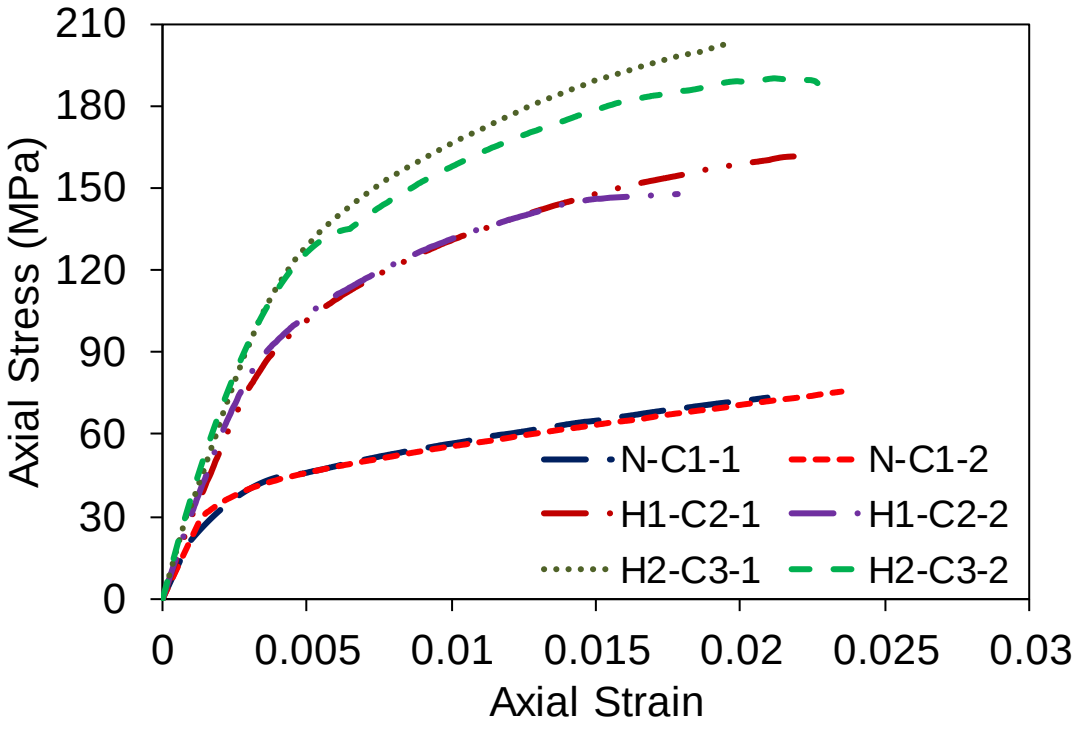

Figure 109- Axial stress-strain response of CFRP-confined concrete specimens

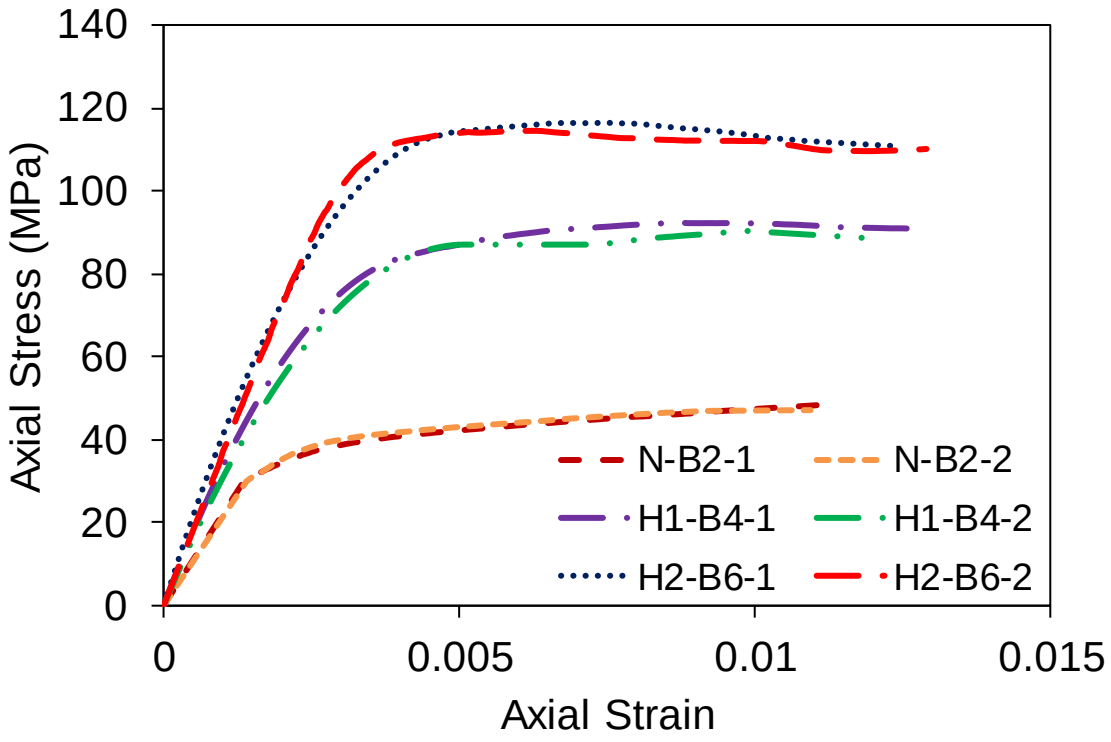

a)

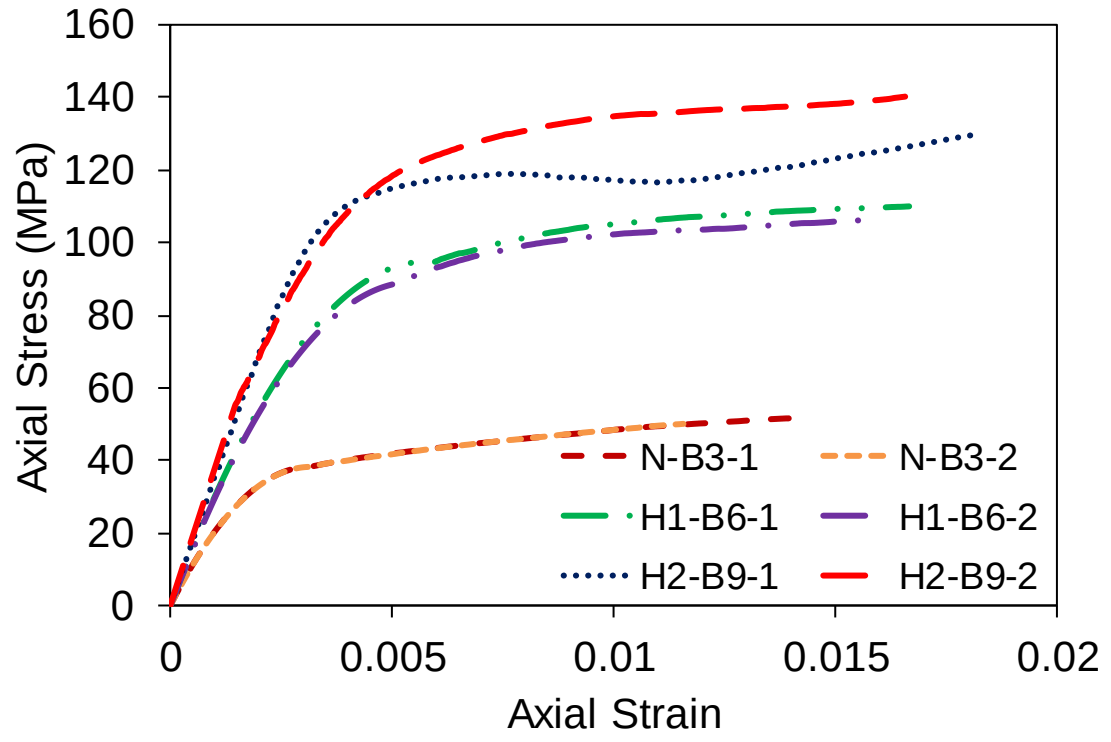

b)

Figure 110- Axial stress-strain response of BFRP-confined concrete specimens, (a) 2, 4 and 6 layers, (b) 3, 6, 9 layers

8.3.2.2.2 Influence of amount of confinement

Table 28 presents the nominal confinement ratio (f_{lu}/f'_{co}), strength enhancement coefficient (k_1) and axial strain enhancement ratio (k_2) of the specimens. A comparison of the nominal confinement ratios (f_{lu}/f'_{co}) in Table 28 reveals that the values are comparable within groups of a given fiber type, with BFRP having both a lightly- and adequately-confined group. It can also be seen in Table 28 that f'_{cc}/f'_{co} and $\varepsilon_{cu}/\varepsilon_{co}$ both increase with an increase in f_{lu}/f'_{co} for all types of FRP-confined SFRC specimens, which is as expected and consistent with the behavior of FRP-confined plain concrete.

f_{lu}/f'_{co} can be used to examine the influence of amount of confinement on UHSSFR-CFFT behavior. Due to the existence of two sets of BFRP specimens with different f_{lu}/f'_{co} at a given f'_{co}, the variation of k_1 and k_2 with f_{lu}/f'_{co} were investigated in these two sets. As can be seen in Table 28, at a given f'_{co}, an increase in f_{lu}/f'_{co} leads to an increase in the obtained k_1 and k_2 values. As can be observed in Fig. 8, the lightly- confined specimens, i.e. N-B2, H-B4 and VH-B6, exhibited a nearly horizontal second branch in their axial stress-axial strain curves. The lower k_1 values of lightly-confined. Specimens than those of adequately-confined specimens is attributed to this behavior, which also led to slightly lower k_2 values in the former series.

8.3.2.2.3 Influence of f'_{co}

The influence of concrete compressive strength (f'_{co}) on the axial stress-strain response of UHSSFR-CFFT was examined by comparing strength enhancement coefficient (k_1) and axial strain enhancement ratio (k_2) with varying amounts of f'_{co}. For this investigation, it should be noted that comparable specimens with similar values of f_{lu}/f'_{co} were selected for each type of FRP. As can be seen in Table 28, most of the comparable specimen groups showed similar behavior with values of k_1 decreasing with an increase in f'_{co}.

A comparison of k_1 within groups of specimens with the same fiber type and similar values of f_{lu}/f'_{co} , reveals f'_{co} has a similar influence on UHSSFR-CFFTs independent of fiber type. The

obtained k_1 for GFRP specimens and adequately-confined BFRP specimens (i.e. N-B3, H-B6 and VH-B9) decreased with an increase in f'_{co}. A similar trend can be seen in insufficiently confined BFRP specimens (i.e. N-B2, H-B4 and VH-B6), which showed a higher rate of decrease in k_1 when increasing f'_{co}. Although CFRP-confined NSC and VHSC specimens showed similar trends of k_1 to GFRP- and BFRP-confined specimens where k_1 decreased by an increase in f'_{co}, the CFRP-confined HSC specimens exhibited the opposite behavior where k_1 increased with an increase in f'_{co}.

Similar to the above comparisons for k_1, the variation of k_2 with f'_{co} was investigated in this study to present the influence of f'_{co} on axial strain enhancement ratio. It can be seen in Table 28 that k_2 of GFRP and insufficiently-confined BFRP specimens did not show a specific trend by the variation of f'_{co}. On the other hand, the k_2 for CFRP specimens showed a decrease with an increase in f'_{co}. Additionally, adequately-confined BFRP specimens displayed an opposite behavior to CFRP-confined specimens, with k_2 increasing with an increase in f'_{co}. These observations suggest that k_2 of UHSSFR-CFFTs was not significantly influenced by f'_{co} and that influence varied with the FRP type.

8.3.2.2.4 Influence of FRP type

To investigate the influence of FRP type on the mechanical behavior of UHSSFR-CFFT specimens, k_1 and k_2 values were examined for comparable specimens manufactured with different FRP confinement materials. As shown in Table 28, the highest values for axial enhancement ratio (k_1) for a given f'_{co} were obtained for CFRP-confined specimens, with GFRP- and BFRP-confined specimens showing lower values of k_1 of similar magnitudes. As can be viewed in Table 286, the CFRP and BFRP specimens displayed similar values of k_2 whereas the GFRP specimens had lower values of k_2 compared to these companion specimens.

8.3.2.3 Axial strain-lateral strain behavior

It is well established that the prediction of axial strain-lateral strain relationship is of vital importance in developing or validating analysis oriented models [113]. The analysis oriented models are robust instruments to predict the mechanical response of FRP-confined concrete under compression as previously discussed by Lim and Ozbakkaloglu [113]. Therefore, a detailed study on lateral mechanical behavior of UHSSFR-CFFT is influential to prepare an accurate analysis-oriented model for SFRC FRP-confined specimens. In this study, the lateral behavior of UHSSFR-CFFT at different heights, namely 50, 100 and 150 mm from top of specimens, was studied to determine the lateral behavior along specimen height.

Figs. 111-113 show the axial strain-lateral strain curves for GFRP, CFRP and BFRP-confined specimens, respectively. As demonstrated in these figures, the lateral strain development at mid-height of all specimens was higher when compared to the measured lateral strains at other heights. It can also be seen in Fig. 111 that lateral strain development of the top (SGs 1&2) and bottom (SGs 5&6) regions for GFRP specimens showed similar strain development. However, this trend was not seen in the BFRP and CFRP specimens which showed a noticeable difference in recorded lateral behavior at the top and bottom regions. This can be attributed to the differences in the local shear plane formations for different tested FRP-types.

Fig. 114 presents the variation of lateral strain-axial strain recorded at mid-height of specimens by increasing f'_{co} for GFRP, CFRP and BFRP specimens. Fig. 114a shows the obtained results for GFRP specimens and can be used to compare NSC specimen behavior with f'_{co} of 35.2 MPa to HSC specimen behavior with f'_{co} of 78.7 MPa. As can be seen in this figure, the shape of lateral strain-to-axial strain curves for the mid-height region (i.e. SGs 3 and 4) of N-G1 and H-G2 after the inflection points changed noticeably. The same figure shows that HSC specimens with f'_{co} of 78.7 MPa and VHSC specimens with 105.2 MPa had approximately similar lateral behavior. As illustrated in the figure, H1-G2 and VH-G3 had approximately

similar shape of lateral-axial strain curve after inflection point and the increase in f'_{co} was not influential for HSC specimens. Conversely, the results of CFRP and BFRP specimens showed that increasing f'_{co} did not change the shape of lateral strain-to-axial strain curve significantly, as shown in Fig. 114b, c and d. These observations indicate that the lateral behavior of GFRP specimens by variation of f'_{co} was not similar to GFRP-confined plain concrete [113]. Conversely, the CFRP and BFRP specimens showed approximately similar behavior when compared to FRP-confined plain concrete.

Fig. 115 illustrates the variation of lateral strain-axial strain curves for different FRP types at given f'_{co}. As can be seen in Fig. 13a, the obtained results at mid-height of specimens showed the various lateral strain-to-axial strain curves for different FRP types after inflection point at given f'_{co}. The same results can be seen for HSC and VHSC specimens in Figs. 115 b and c. This results is not in agreement with previous obtained study on FRP-confined plain concrete, i.e. Lim and Ozbakkaloglu [113], where they reported identical lateral strain-to-axial strain curves for various FRP fiber types. Additionally, the influence of confinement level on lateral strain-axial strain curves of UHSSFR-CFFT can be investigated by studying the BFRP specimens' behavior as explained before in previous section. As can be seen in the Fig. 115, increasing f_{lu}/f'_{co} at given f'_{co} changed the shape of lateral strain-axial strain curves after inflection point. This outcome is similar to FRP-confined plain concrete lateral behavior as previously discussed in detail by Lim and Ozbakkaloglu [113].

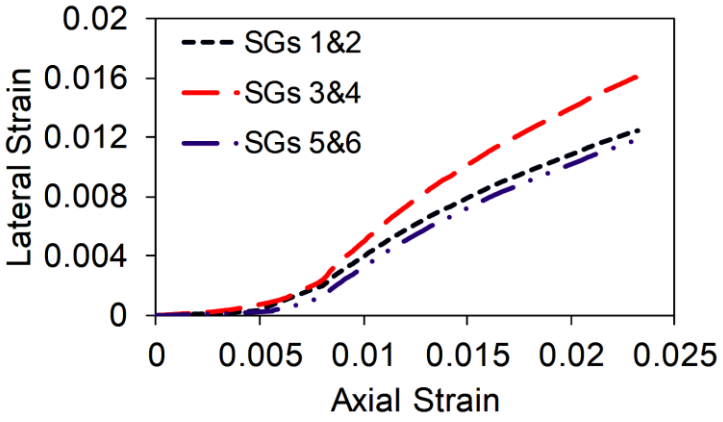

a) NSC

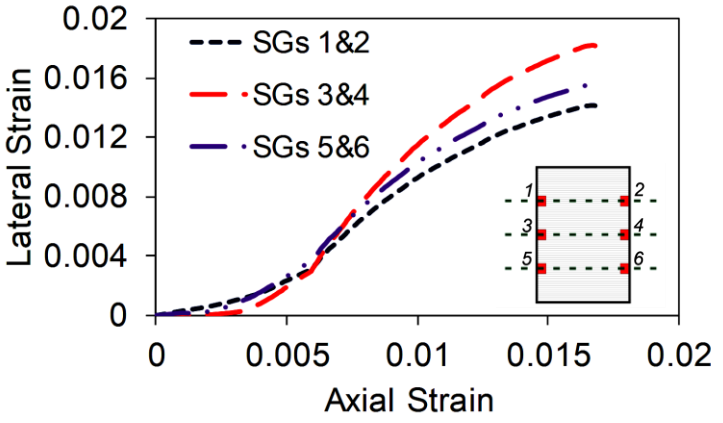

b) HSC1

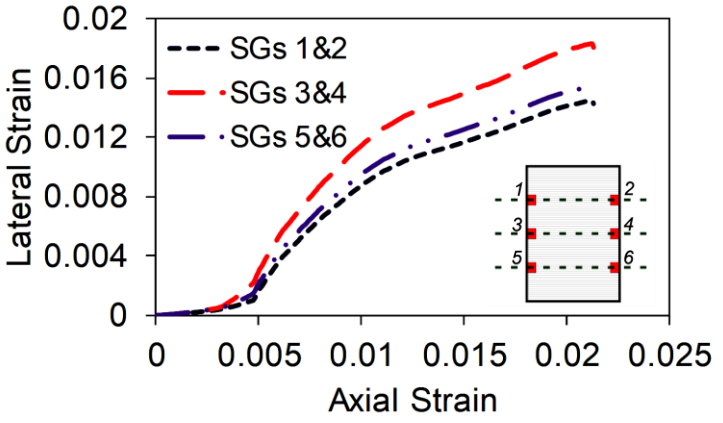

c) HSC2

Figure 111- Axial Strain-lateral strain relationship of GFRP-confined specimens at different strain gauge locations

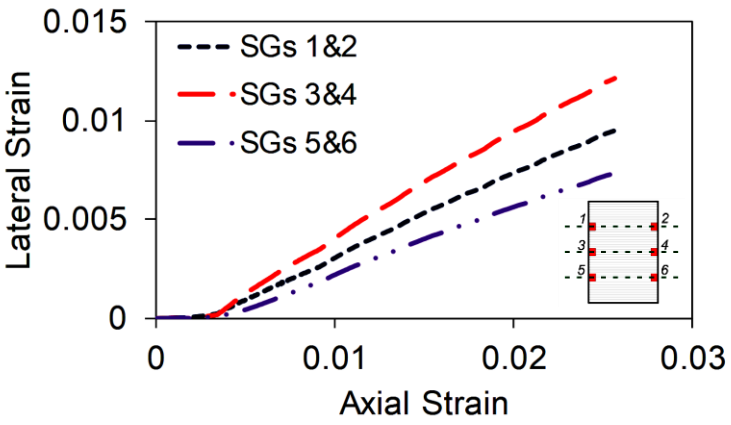

a) NSC

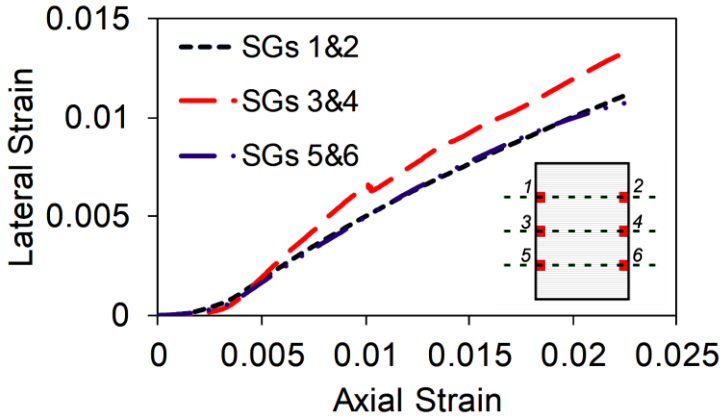

b) HSC1

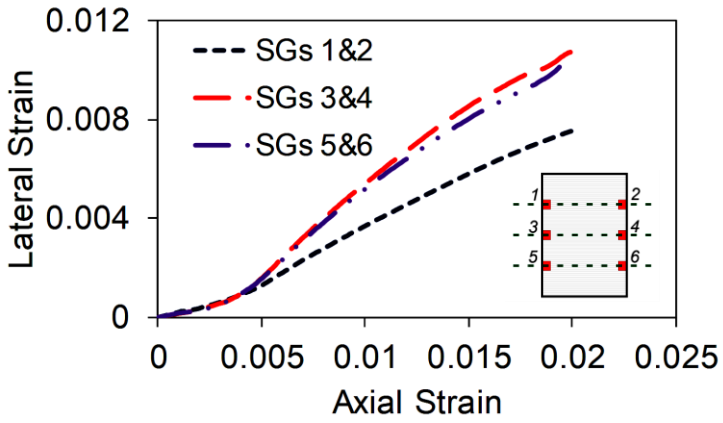

b) HSC2

Figure 112- Axial Strain-lateral strain relationship of CFRP-confined specimens at different positions of Strain Gauges

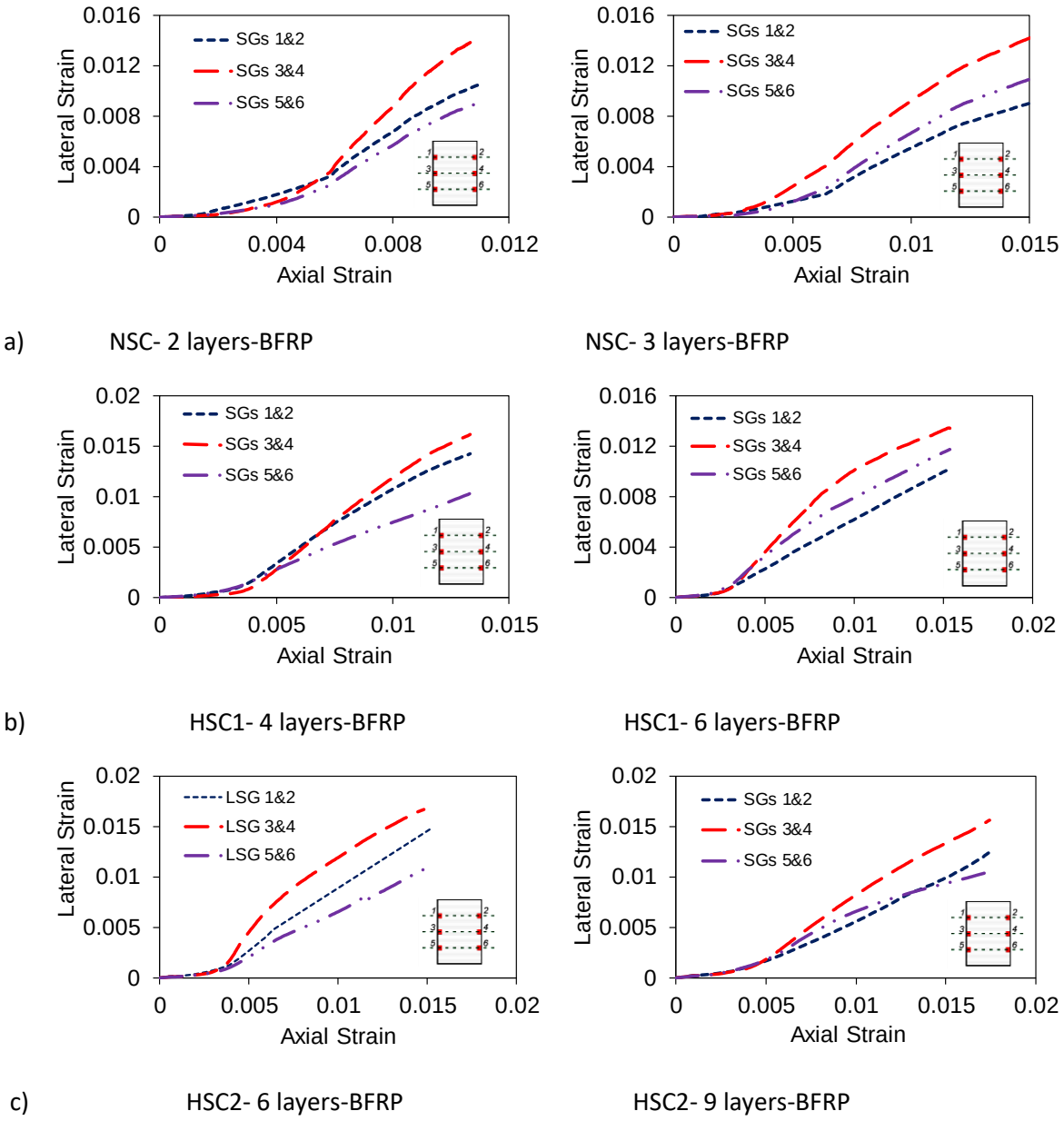

Figure 113- Axial Strain-lateral strain relationship of BFRP-confined specimens at different positions of Strain Gauges

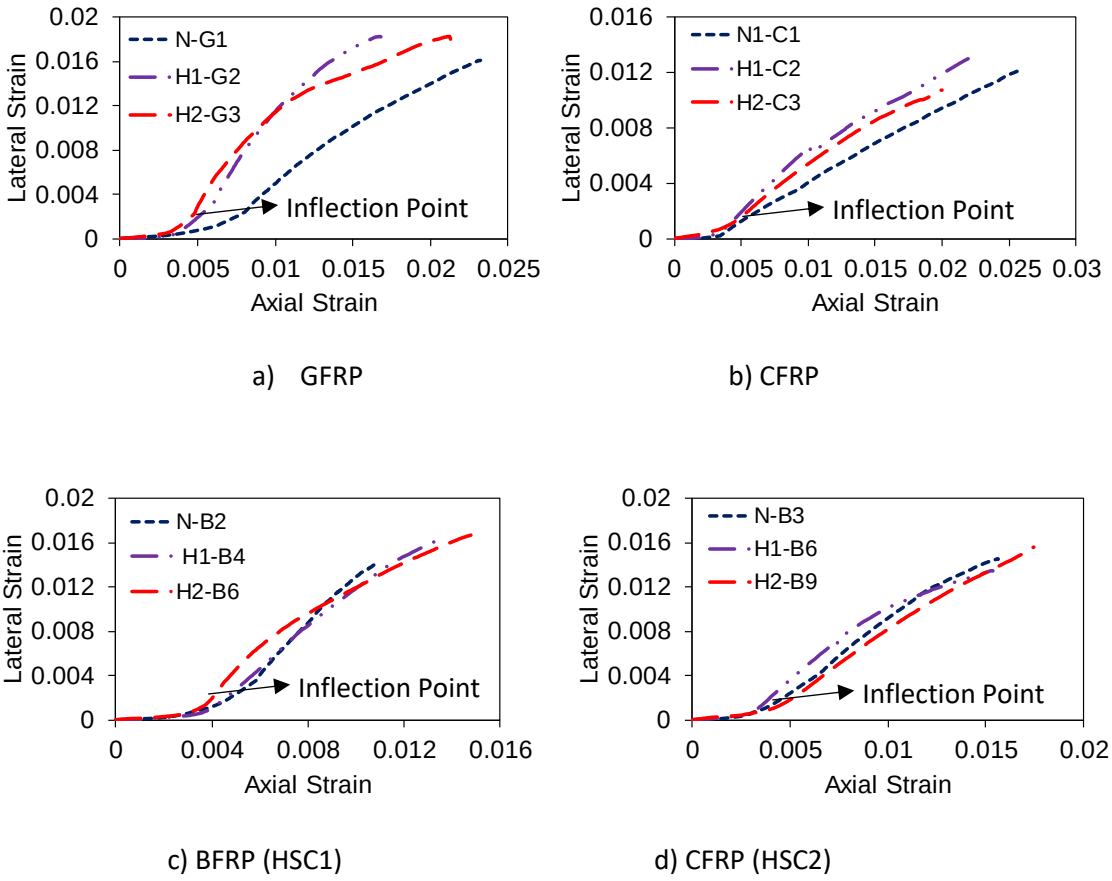

Figure 114-Lateral strain-to-axial strain relationships of FRP-confined concrete specimens having comparable confinement stiffness ratios and different unconfined concrete strengths

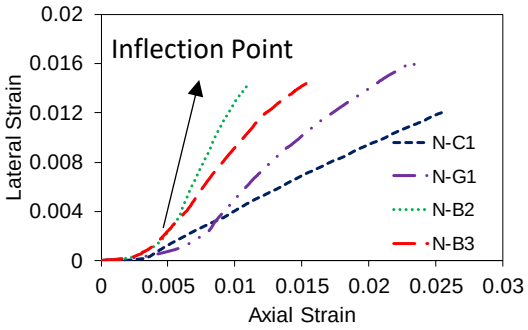

a) NSC

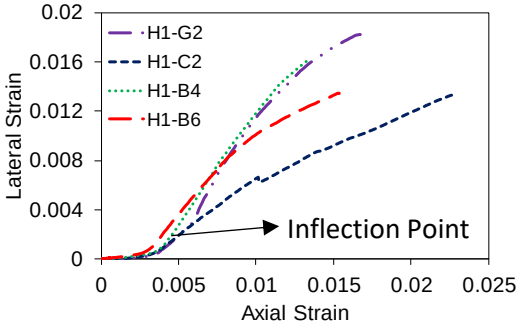

b) HSC1

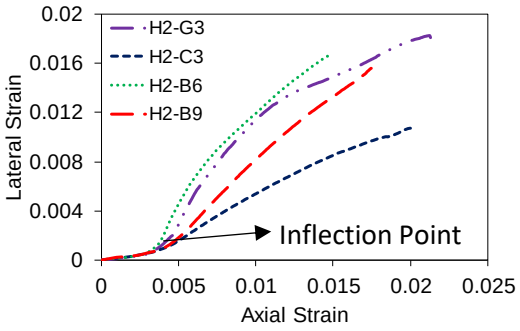

c) HSC2

Figure 115-Lateral strain-to-axial strain relationships of FRP-confined concrete specimens having comparable confinement stiffness ratios and different FRP types

Table 29- Results of lateral strain at failure for confined specimens

Specimen	Lateral strain (%) SG 1&2	Lateral strain (%) SG 3&4	Lateral strain (%) SG 5&6	$\varepsilon_{h,rup\ (Max)}$ %	$k_{\varepsilon\ 1\&2}$ SG 1&2	$k_{\varepsilon\ 3\&4}$ SG 3&4	$k_{\varepsilon\ 5\&6}$ SG 5&6	k_{ε} L&O (2014)
N-G1-1	1.21	1.57	1.15	1.45	0.39	0.51	0.37	0.75
N-G1-2	1.18	1.75	1.41	1.75	0.38	0.56	0.45	0.75
H1-G2-1	1.10	1.67	1.25	1.71	0.35	0.54	0.40	0.65
H1-G2-2	1.41	1.82	1.55	1.90	0.45	0.59	0.50	0.65
H2-G3-1	1.18	1.67	1.21	1.74	0.38	0.54	0.39	0.60
H2-G3-2	1.43	1.80	1.52	1.89	0.46	0.58	0.49	0.60
N-C1-1	0.93	1.28	1.03	1.56	0.44	0.61	0.49	0.65
N-C1-2	0.95	1.21	0.73	1.75	0.45	0.58	0.35	0.65
H1-C2-1	1.12	1.33	1.08	1.44	0.53	0.63	0.51	0.55
H2-C3-1	0.75	1.07	1.05	1.21	0.36	0.51	0.50	0.50
H2-C3-2	0.90	1.01	0.97	1.01	0.43	0.48	0.46	0.50
N-B2-1	1.11	1.54	1.14	1.61	0.48	0.67	0.50	0.76
N-B2-2	1.05	1.42	0.90	1.46	0.46	0.62	0.39	0.76
N-B3-1	0.92	1.45	1.12	1.47	0.40	0.63	0.49	0.76
H1-B4-1	1.43	1.62	1.03	2.06	0.62	0.70	0.45	0.66
H1-B4-2	0.95	1.57	1.12	1.87	0.41	0.68	0.49	0.66
H1-B6-1	1.02	1.35	1.18	1.50	0.45	0.59	0.51	0.66
H1-B6-2	0.63	1.52	1.03	1.55	0.27	0.66	0.45	0.66
H2-B6-1	0.90	1.47	1.11	1.48	0.39	0.64	0.48	0.60
H2-B6-2	1.47	1.68	1.11	1.90	0.64	0.73	0.48	0.60
H2-B9-1	1.33	1.56	1.21	1.78	0.58	0.68	0.53	0.60
H2-B9-2	1.25	1.56	1.06	1.67	0.54	0.68	0.46	0.60

8.3.2.3.1 Hoop rupture strain

Table 29 shows the hoop rupture strains at failure. In this table, the average of hoop strain measured by two lateral strain gauges, the maximum lateral strain ($\varepsilon_{h,rup\ (Max)}$) and the reduction factor related to each calculated average (k_ε) are presented. The reduction factor was calculated by $k_\varepsilon = \frac{\varepsilon_{h,rup}}{\varepsilon_f}$, where $\varepsilon_{h,rup}$ and ε_f are maximum hoop strain obtained by SGs and ultimate tensile strain of FRP, respectively [29]. In addition, Lim and Ozbakkaloglu [17] proposed an expression to predict k_ε for FRP-confined plain concrete and this prediction is also presented in Table 7. It should be noted that k_ε expression was developed for FRP-confined plain concrete and shows the general behavior of this type of confined concrete. Consequently, comparing the obtained experimental k_ε values with theoretical values obtained by the expression presents a potential method to compare UHSSF-CFFT behavior with plain concrete.

As can be seen in Table 29, the obtained reduction factor (k_ε) ranged between 0.27 and 0.73. It can be seen in the table that the measured k_ε at mid-height of specimens are consistently higher when compared to the remaining two locations. This indicates that the rupture of FRP jackets and its corresponding strain ($\varepsilon_{h,rup}$) occurred at mid-height of specimens, as also typically observed in FRP-confined plain concrete. Furthermore, the Table 29 shows that the obtained k_ε values by Lim and Ozbakkaloglu [17]'s expression vary noticeably with f'_{co}, however this is not the case for these experimentally recorded steel fiber specimens. The GFRP and BFRP-confined SFR concrete specimens appeared noticeably less influenced by unconfined concrete compressive strength (f'_{co}). Conversely, CFRP-confined SFR concrete specimens revealed a decreasing trend of k_ε for an increase in f'_{co} which is the same trend observed in FRP-confined plain concrete. This indicates the different behavior of GFRP and BFRP-confined SFR concrete specimens in comparison to CFRP-confined SFR concrete and FRP-confined plain concrete. This different behavior of GFRP and BFRP specimens compared to CFRP specimens show the influence of FRP types in mechanical behavior of studied specimens. This different behavior

can be attributed to lower value of f_{lu}/f'_{co} for GFRP and BFRP specimens compared to CFRP specimens. Moreover, a comparison between the predicted values of k_ε at specimen mid-height and the experimentally recorded values in Table 29 displays the good agreement for BFRP and CFRP specimens. However, GFRP specimens showed large difference between predicted and experimentally recorded values of k_ε. This observation can be attributed to the effect of fiber type on development of local shear planes. As strain gauges measure the lateral strain locally, the location of their attachment relative to the development of local shear planes can significantly influence the recorded data.

8.4 Conclusion

The following points summarize the main findings and contributions of this study:

1- GFRP-, CFRP- and BFRP-confined UHSSFR-CFFTs show a decrease in axial stress enhancement ratio (k_1) with an increase in f'_{co}. Conversely, the axial strain enhancement ratio (k_2) is not significantly influenced by f'_{co} and this affect changes with the FRP type.

2- The lateral behavior of CFRP- and BFRP-confined UHSSF-CFFTs reveals that an increase in f'_{co} does not influence the shape of lateral strain-to-axial strain curve significantly. However, this same increase in f'_{co} was observed to influence the GFRP-confined specimens, where a noticeable change in the shape of lateral strain-to-axial strain curves was observed after the inflection point for the mid-height region.

3- An increase in f_{lu}/f'_{co} for the BFRP-confined UHSSFR-CFFTs leads to an increase in both k_1 and k_2. Additionally, an increase in the amount of f_{lu}/f'_{co} reduces the slope of lateral strain-axial strain curves after the inflection point. These observations are in agreement with previous reported results for FRP-confined plain concrete specimens.

4- Axial stress enhancement ratio (k_1) of UHSSFR-CFFT is highly dependent on the fiber type of the FRP confinement. k_1 exhibits an increase by increasing f_{lu}/f'_{co} for GFRP and BFRP specimens while CFRP-confined specimens showed the opposite trend.

5- GFRP- and BFRP-confined UHSSFR-CFFT show an increase in k_2 when increasing f_{lu}/f'_{co}, whereas CFRP-confined specimens show a decrease. This indicates that GFRP and BFRP specimens show a similar behavior to FRP-confined plain concrete when increasing f_{lu}/f'_{co}.

6- The strain reduction factor (k_ϵ) for GFRP and BFRP specimens is more influenced by f_{lu}/f'_{co} than f'_{co}. Conversely, CFRP specimens show a significant influence of f'_{co} on strain reduction factor (k_ϵ), with this behavior similar to that for FRP-confined plain concrete.

Chapter 9: Mechanical response of POLYVINYL ALCOHOL fiber-reinforced concrete-filled FRP tube columns under compression

(A paper is drafted based on this section, "Mechanical response of POLYVINYL ALCOHOL fiber-reinforced concrete-filled FRP tube columns under compression" by Ali Fallah Pour, Togay Ozbakkaloglu and Tom Vincent)

9.1 Introduction

Confining laterally concrete columns with fiber reinforced polymer (FRP) sheets and adding fibers in concrete wet mix leads to formation of a composite structural system with decent mechanical response under compressive axial loading [92]. Review studies by Ozbakkaloglu et.al. [14, 16] have shown numerous studies have established the benefits of FRP-confined concrete under axial compression for both FRP-wrapped concrete [25, 88, 131, 215-218] and concrete-filled FRP tubes (CFFTs) [112, 152, 219-221]. These benefits apply to both normal and high-strength concrete (NSC and HSC), with HSC gaining more attention in recent years due to the higher mechanical performance offered by HSC over NSC [1-10]. However, it is well known that the naturally brittle behavior of HSC results in some unfavourable behavior for both concentric and simulated seismic loading. For example, a temporary post-peak axial strength softening behavior of FRP-confined HSC under compression at transition zone was observed which influences negatively the performance of FRP-confined HSC columns in real loading conditions [11-13, 15].

Addition of fibers to concrete mix which is FRP-confined has proven to result in significant improvements in mechanical performance of composite concrete columns [78]. Existing studies have examined the influence of types of fiber on ductility and toughness of concrete (e.g. [59, 76, 204, 222, 223]). It was found that these fibers are able to increase the dynamic characteristics of concrete owing to improvements in the damping ratio of plain concrete [59,

76, 204, 222-225]. One fiber that has received significant research attention due to its favourable influence on concrete mechanical behavior, is Poly vinyl alcohol (PVA) [222-225]. PVA is adopted from poly vinyl acetate which is hydrolysed by treating an alcoholic solution with aqueous acid or alkali [226]. PVA is a white powder with specific gravity ranging from 1.2 to 1.3 (1200–1300 kg/m^3) and this powder is then formed and extruded to become PVA fibers as commercial production [227]. PVA fibers offer high ultimate tensile strength, relatively high modulus of elasticity, good chemical compatibility with Portland cement, good affinity with water and no health risks [228]. These characteristics make PVA fiber a well-suited ingredient in the concrete wet mixture to improve the mechanical properties of concrete.

As previously reported [229-231], adding PVA fiber to concrete wet mix increases ductility of PVA fiber reinforced concrete in addition to slightly increase of compressive strength and Elastic modulus. Furthermore, Noushini et al. [229] illustrated that longer PVA fibers results in higher concrete compressive strength in fiber reinforced concrete and maximum increase of compressive strength obtained for 0.25% of volume fraction. Hannawi et al. [231] also showed that adding PVA fiber to concrete matrix results in increasing the thresholds of initial and unstable cracking. They discussed that this outcome is consequence of adding PVA fiber to concrete which control the cracking process in concrete under different types of loading [231]. Finally, Shao and Shah [232] showed high tensile strength and exceptional post-peak toughness due to adding PVA fibers to concrete mixture. In addition, they showed that an increase in length of fiber, volume ratio and cement content leads to higher deflection at pick of load when PVA fiber reinforced concrete was under bending [232].

This improvement in fiber reinforced concrete characteristics occurs due to a higher stiffness of PVA fibers when compared to concrete and good interfacial bond with the cement matrix [228]. The higher tensile strength of PVA fibers sustain the crack expansion and resist the pull

out force due to the strong bond between the fiber and the cementitious matrix [228]. Additionally, the PVA fibers are able to elongate and transfer the load to different parts of the concrete matrix and as a result the applied load is distributed more evenly throughout the specimens [227]. Although the beneficial of using PVA fibers in concrete wet mix has been well examined, no study to date has examined the influence of PVA reinforced concrete that is laterally confined by FRP jackets.

To address this research gap, this original study reports on the axial compressive behavior of PVA fiber reinforced CFFTs (PVAR-CFFTs). A range from 15 to 70 MPa of unconfined concrete compressive strengths (f'_{co}) has been examined to illustrate the influence of f'_{co} on PVAR-CFFTs. This was followed by examination of the influence of lateral stiffness (K_l) and FRP types using 3 types of FRP tubes. Initially, this investigation delivers a brief explanation of the test program by considering the specimen properties and testing process. Following this, the obtained experimental outcome was presented for both unconfined and FRP-confined specimens. Next, an in-depth discussion on the experimental results is provided where the influence of key parameters is investigated, namely concrete strength (f'_c), lateral stiffness (K_l) and FRP type. Finally, a detailed study on hoop strain at rupture plus lateral deformation along specimen height is presented.

9.2 Test program

9.2.1 Test specimens

A total of 24 circular CFFTs specimens were manufactured and tested under axial compressive loading. The specimens' dimensions were selected 100 mm as diameter measured at the concrete core, and 200 mm as height. Three types of concrete were prepared for this research with three different f'_{co} including 15, 30 and 70 MPa. These three different concrete batches referred as LSC, NSC and HSC, respectively. The volume fraction of PVA fibers was selected as 0.375% to keep integrity of concrete batches in preparation of the mixes and casting the FRP

tubes. A manual wet lay-up procedure was used to manufacture FRP tubes with unidirectional fiber sheets. Three different FRP fiber types were used in this study which are carbon reinforced polymer fiber (CFRP), glass reinforced polymer fiber (GFRP) and basalt reinforced polymer fiber (BFRP). It should be noted that two nominally identical specimens were tested for each unique specimen configuration; the detail of each prepared specimen in this study is presented in Table 30. As can be seen in Table 1, the confined specimens include 6 GFRP confined specimens, 6 CFRP confined specimens and 12 BFRP confined specimens.

Table 30-Details of test specimens

Specimen	V_f (%)	Concrete Type	FRP-Type	Number of Layers	$t_{f\text{-total}}$ (mm)
L-G1	0.375	N1SC	GFRP	1	0.2
N-G2	0.375	N2SC	GFRP	2	0.4
H-G3	0.375	HSC	GFRP	3	0.6
L-C1	0.375	N1SC	CFRP	1	0.167
N-C2	0.375	N2SC	CFRP	2	0.334
H-C3	0.375	HSC	CFRP	3	0.501
L-B2	0.375	N1SC	BFRP	2	0.150
L-B3	0.375	N1SC	BFRP	3	0.225
N-B4	0.375	N2SC	BFRP	4	0.300
N-B6	0.375	N2SC	BFRP	6	0.450
H-B6	0.375	HSC	BFRP	6	0.450
H-B9	0.375	HSC	BFRP	9	0.675

9.2.2 Materials

9.2.2.1 Concrete

Low, normal and high strength concrete (LSC, NSC and HSC) was prepared and cast in this research where the ingredient were sourced from a local concrete supplier. These mixes were batched in the laboratory where the details of these mixes can be seen in the Table 31. The gravel used for these mixes consistent of crushed basalt with a 10 mm nominal maximum diameter, with a 10 mm nominal maximum diameter. The resulted slump for each batch was of over 100 mm for LSC and NSC mixes and over 200 mm for HSC. Control cylinders with

100 by 200 mm dimensions were cast from the same concrete type mixes and tested in parallel to the FRP confined specimens to determine the compressive strength (f'_{co}).

Table 31- Concrete mix proportions

Ingredient	N1SC	N2SC	HSC
Cement (kg/m^3)	360	437	506
Silica fume (kg/m^3)	-	38	44
Sand (kg/m^3)	700	710	700
Gravel (kg/m^3)	1010	1025	1015
Fiber (kg/m^3)	4.88	4.88	4.88
Water (kg/m^3)	227	164	168
Superplasticizer* (kg/m^3)	10	24	35
w/c	0.65	0.38	0.35
Total (kg/ m^3)	2311	2402	2467

* Superplasticizer contained 70% water by weight

9.2.2.2 PVA fibers

The PVA fiber was used in this study as it is shown in the Fig. 116 and the detail of the fiber was presented in Table 32. It is mentioned before that 0.375% was selected as volume fraction and reinforcing index was 45 by using Eq. 45.

$$\boldsymbol{RI} = (\boldsymbol{V_f} \times \boldsymbol{A_s}) \quad (9.1)$$

where V_f is the fiber volume fraction (i.e. volume of fiber per unit of volume of concrete) and A_s is the fiber aspect ratio ($A_s = \frac{l_f}{d_f}$, where l_f is the fiber length and d_f is the equivalent fiber diameter).

Table 32- Details of PVA fibers

Name	PVA
Diameter (D)	0.1 mm
Length (l)	12 mm
Aspect ratio (l/D)	120
Specific gravity	1.3 t/m^3
Tensile Strength	1230 MPa

Figure 116- Poly-vinyl alcohol (PVA) fibers

9.2.2.3 FRP tubes

A manual wet lay-up process of wrapping epoxy resin impregnated fiber sheets around precision-cut high-density Styrofoam templates in the hoop direction was used to prepare the FRP tubes. A summary of the FRP material properties used in this study is presented in Table 33.

The number of FRP layers was selected by taking into account the unconfined concrete compressive strength (f'_{co}) in order to have ascending second branch on axial load-displacement curve. This indicates that the specimens with higher f'_{co} received proportionally more layers to ensure adequate confinement. However, it should be noted that the presence of PVA fiber in wet concrete mix changes the minimum required number of FRP layers. This leads to a higher number of layers by considering targeted f'_{co} of specimens when compared to plain concrete. It should be said that lateral stiffness (K_l) can be estimated by $K_l = \frac{2E_{FRP}t_f}{D}$, where E_f is the elastic modulus of FRP fiber, t_f is the total fiber thickness of FRP jacket and D is the specimen diameter measured at the concrete core. Lim and Ozbakkaloglu [17] discussed on minimum required K_l for FRP-confined plain concrete, namely K_{lo}, to have ascending second branch in axial stress-strain curves. K_{lo} can be calculated by $K_{lo} = f'^{1.65}_{co}$ where f'_{co} is unconfined compressive strength of concrete in MPa [17]. Two series of BFRP-confined

specimens with different K_l values were cast in this experimental program while only one series of GFRP- and CFRP-confined specimens was studied. This is due to having fewer previous experimental studies on this type of FRP, i.e. basalt fiber reinforced polymer. The second set of BFRP-confined concrete specimens had higher value of K_l compared to first set to guarantee an ascending-type second branch of axial stress-axial strain curve. Throughout this paper, the BFRP-confined specimens prepared with low and high values of K_l are referred to as lightly- and adequately-confined, respectively.

Table 33- Material properties of fibers and FRP composites

Type	Nominal dry fiber thickness t_f (mm/ply)	Fiber/FRP properties					
		Provided by manufacturers			Obtained from coupon tests*		
		Ultimate tensile stress f_f (MPa)	Ultimate tensile strain ε_f (%)	Elastic modulus E_f (GPa)	Ultimate tensile stress f_{FRP} (MPa)	Ultimate tensile strain ε_{FRP} (%)	Elastic modulus E_{FRP} (GPa)
CFRP	0.167	4830	2.10	230	4598	1.95	236
S-Glass	0.2	3040	3.50	86.9	3055	3.21	95.3
BFRP	0.075	1680	2.30	73.0	1584	2.10	76.0

* Calculated based on nominal dry fiber thickness

9.2.2.4 Specimens designation

The higher number of BFRP confined specimen was due to less pervious information about this type of FRP fibers studied by this research group as it can be seen in the [17]. The database used in mention research to predict K_{l0} did not include any dataset for BFRP specimens. Consequently, two different K_l were selected for BFRP specimens, one equal to K_{l0} (minimum threshold to have second ascending branch) and second one slightly higher value needed to satisfy K_{l0} [17]. The detail of specimens are presented in Table 30 and included specimens' name, V_f, concrete type, FRP type, number of layers and nominal thickness (t_f).

9.2.2.5 Instrumentation and testing

Axial deformations of the specimens were measured with four linear variable differential transformers (LVDT), which were mounted at the corners between the loading and supporting steel plates of the test machine as shown in Figs. 52-53. The calculation of the average axial strains was performed with recorded deformations along the height of the specimens. Lateral strains were measured by 6 unidirectional strain gauges having a gauge length of 5 mm that were bonded on the FRP jacket outside the overlap region. The lateral strain gauges (SGs) position was determined to illustrate the lateral behavior of specimens along the height of specimens and every two lateral strain gauges were attached at the same height with 180 degrees interval.

The specimens were tested under monotonic axial compression using a 5000 kN capacity universal testing machine. During the test, the loading was applied with 2 microstrain per second until specimen failure. The instrumentation and testing equipment used in this experimental study are shown in Figs. 52 and 53.

9.3 Test results and discussion

9.3.1 Unconfined specimens

9.3.1.1 Failure mode

Fig. 117a, 117b and 117c shows typical obtained failure mode for PVA unconfined LSC, NSC and HSC, respectively. As it is shown in the Fig. 3a, b and c, the unconfined concrete specimens' failure mode changed from LSC to HSC. As can be seen in the figure, the PVAR-LSC and PVAR-NSC showed approximately similar failure mode. However, the cracks were distributed more homogenously in PVAR-NSC specimens compared to LSC. The obtained crack distribution for the PVAR-LSC and PVAR-NSC was different compared to plain concrete specimens where more localized shear zone can be seen. It is mention worthy that a dark painting was used over specimens surface to easier verification of crack development. This different behavior in PVAR-LSC and PVAR-NSC can be attributed by occurrence of

bridging due to existence of PVA fibers in the matrix of concrete. Conversely, the PVAR-HSC unconfined specimens showed more brittle behavior than other two types of specimens and the major cracks expanded close to load direction.

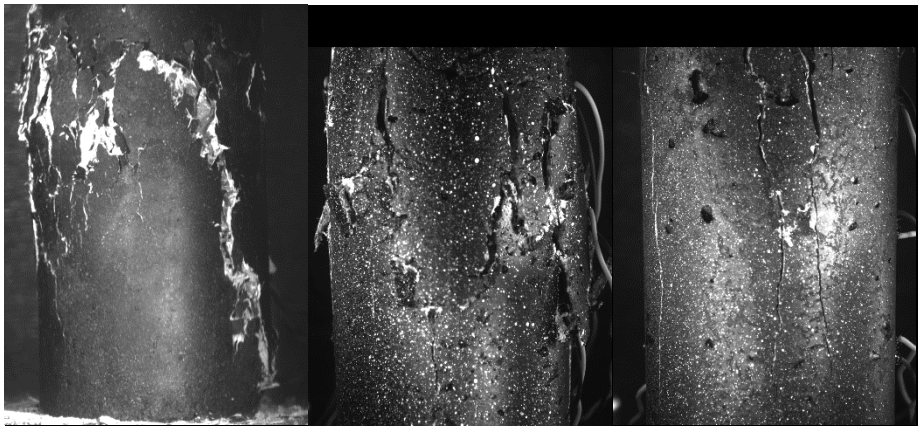

a) LSC b) NSC C) HSC

Figure 117- Failure modes for unconfined specimens

9.3.1.2 Axial stress-strain behavior

Table 34 presents the compressive strength (f'_{co}) and corresponding axial strain (ε_{co}) for tested unconfined specimens. As it can be seen in the table, the related f'_{co} for these three concrete batches are 15.5, 29.1 and 70.5 MPa. In addition, Fig. 4 shows obtained axial stress-strain curve for different concrete types, i.e. PVAR- LSC, NSC and HSC. It can be seen in the figures that the obtained axial stress-strain for identical specimens are in good agreement. However, it should be said that the best obtained agreement in axial stress-strain curve for two identical specimens was observed in PVAR-LSC and PVAR-NSC compared to PVAR-HSC. This can be attributed to more brittle behavior of HSC.

Table 34-Properties of unconfined concrete at test day of CFFTs

Concrete Type	Fiber Volume fraction V_f (%)	f'_{co} (MPa)	ε_{co} (%)
LSC	0.375	15.5	0.24
NSC	0.375	29.1	0.27
HSC	0.375	70.5	0.31

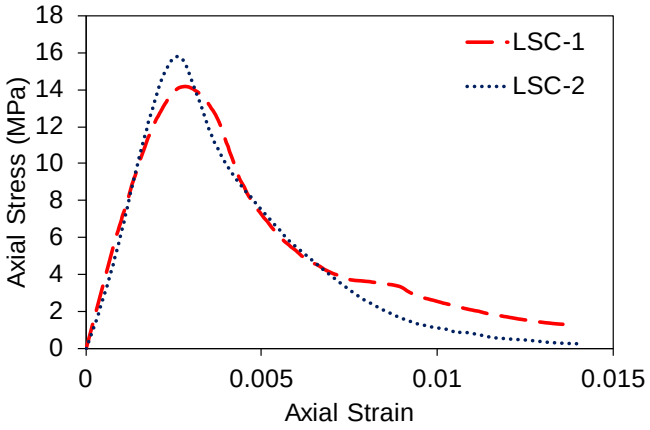

a)

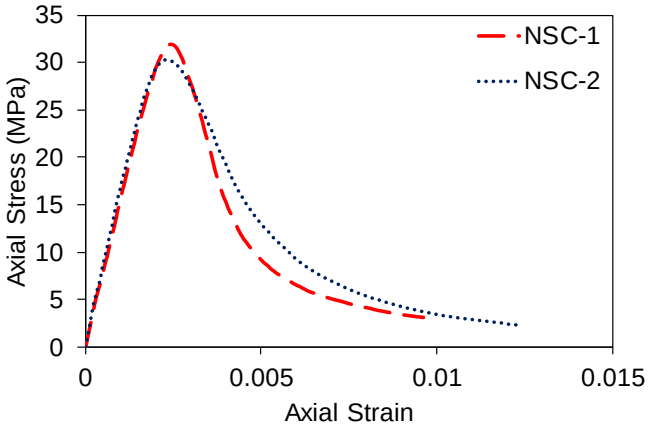

b)

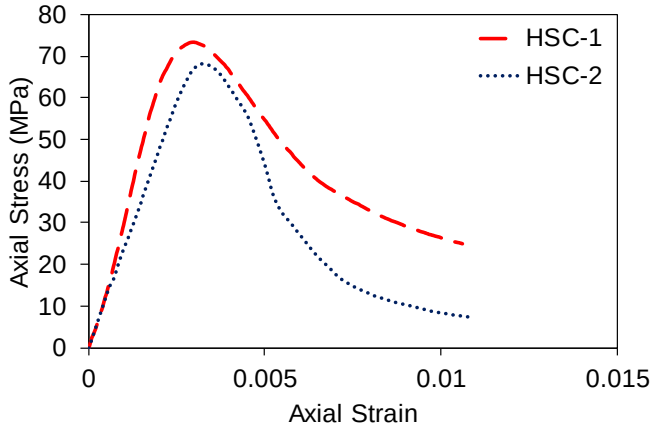

c)

Figure 118- Experimental and theoretical axial stress-strain curves of unconfined concrete: a) LSC, b) NSC, c) HSC

9.3.2 Confined specimens

9.3.2.1 Failure mode

9.3.1 Failure mode

Figs. 119a-119l show the failure mode of FRP-confined concrete with PVA fibers in wet concrete mix. The FRP-confined specimens' failure mode was consequence of FRP jacket rupture associated with a loss of applied axial load. The mentioned rupture mode occurred for all specimens except for one specimen that suffered an early FRP debonding failure (L-B3-2) which is marked in Table 35 with *. The observation showed a sudden loss of applied load for HSC confined specimens (e.g. H-G3, H-C3 and H-B9) after failure, however other specimens namely L-G1, N-G2, L-C1, N-C2, L-B2, L-B3, N-B4 and N-B6 showed a more gradual loosing strength after failure. In addition, as shown in these figures, the FRP jackets rupture happened at the mid-height region of the specimens for all cases even for specimens with premature failure.

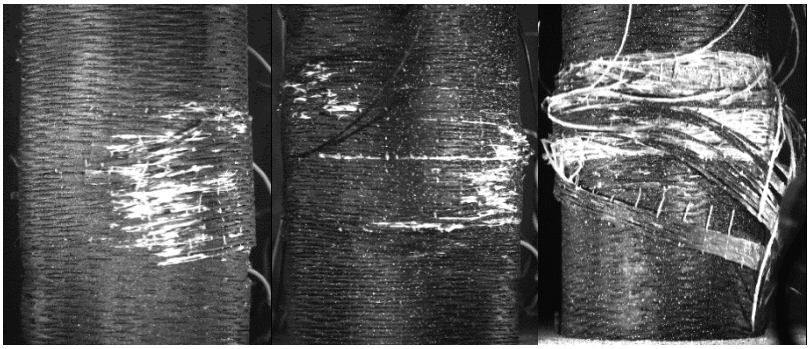

a) L-G1-1 b) N-G2-1 c) H-G3-2

d) L-C1-1 e) N-C2-1 f) H-C3-1

g) L-B2-1 h) N-B4-1 i) H-B6-1

j) L-B3-1 k) N-B6-1 l) H-B9-1

Figure 119- Failure modes for test specimens: (a) L-G1-1, (b) N-G2-1 (c) H-G3-2, L-C1-1, (e) N-C2-1 (f) H-C3-1, L-B2-1, N-B4-1, H-B6-1, L-B3-1, N-B6-1 and H-B9-1

9.3.1.1 Axial stress-strain behavior

9.3.1.1.1 General observations

Figs 120-122 illustrate the experimental axial stress-strain curves for GFRP, CFRP and BFRP specimens, respectively. The axial strains were obtained by averaging of 4 axial displacement recorded by full-height LVDTs. Previously, it was discussed that FRP-confined HSC specimens suffers a sudden drop in their axial stress-strain curves at transition zone (f'_{c1}, ε_{c1}). This sudden drop is opposite to previous understanding where using sufficient confinement for concrete columns results in a nearly linear ascending second branch after first parabolic ascending branch [14, 16, 17]. It should be said that the transition zone is a region that signifies a change in the trend of the stress-strain curve after the termination of the initial ascending branch (f'_{c1}, ε_{c1}) [17]. This drop in axial load is due to brittle behavior of HSC which also influences the ultimate axial stress (f'_{cc}) and strain (ε_{cu}) of FRP-confined HSC specimens. To investigate the influence of brittleness of HSC on FRP-confined HSC behavior and to compare the behavior of HSC confined specimens to NSC and LSC, the strength enhancement (k_1) and strain enhancement (k_2) coefficients were used. It should be noted that the details of definition and calculation of the strength enhancement (k_1) and strain enhancement (k_2) coefficients can be found in Ref. [10].

Figs. 120-122, show the obtained axial stress-strain curves in this experimental program for PVAR FRP-confined specimens. As can be seen in Figs 120, 7121 and 122b, all GFRP-, CFRP- and adequately confined BFRP-confined specimens showed ascending-type axial stress-strain curves, without suffering any loss of strength along the transition zone. This observation indicates that the addition of PVA fibers in HSC wet mix can limit or eliminate the sudden drop typically observed in the axial stress of concrete at the transition zone associated with the brittle nature of HSC [17]. Conversely, the lightly-confined H2-B6 series with a lower confinement level (f_{lu}/f'_{co}) showed slightly descending behavior starting at the transition zone, shown in Fig. 122.a. It is mention worthy that the nominal lateral confining pressure at ultimate

of FRP jacket (f_{lu}/f'_{co}) was determined by $f_{lu} = K_l \times \varepsilon_{fu}$ where K_l and ε_{fu} are the lateral stiffness of the FRP jacket and ultimate tensile strain of fibers, respectively. This results indicates the need of higher level of confinement for lightly confined BFRP specimens compared to other specimens, i.e. GFRP, CFRP and adequately confined BFRP specimens.

Table 35 presents the obtained results from tested specimens including unconfined compressive strength (f'_{co}) and corresponding strain (ε_{co}), compressive strength (f'_{cc}), ultimate axial strain (ε_{cu}), and ultimate axial stress and strain enhancement ratio (f'_{cc}/f'_{co} and $\varepsilon_{cu}/\varepsilon_{co}$). As can be seen in Table 35, the average of f'_{cc}/f'_{co} of identical specimens for CFRP- and adequately BFRP-confined specimens, increased by an increase in f_{lu}/f'_{co}. Conversely, GFRP- and lightly BFRP-confined specimens did not show the same trend and other key parameter such as f'_{co} or FRP types were more influential than f_{lu}/f'_{co}. It can also be seen in Table 35 that BFRP specimens with the lowest values of f_{lu}/f'_{co} (i.e. N-B2, H-B4 and VH-6) had the lowest f'_{cc}/f'_{co}, whereas CFRP specimens with the highest values of f_{lu}/f'_{co} (i.e. N-C1, H-C2 and VH-C3) recorded the highest f'_{cc}/f'_{co}, as expected.

As can be seen in Table 35, although the obtained $\varepsilon_{cu}/\varepsilon_{co}$ showed small differences for each type of FRP by variation of f'_{co}, these difference are not noticeable and increasing f'_{co} or f_{lu}/f'_{co} did not noticeably influenced the obtained average $\varepsilon_{cu}/\varepsilon_{co}$ for each configuration of specimens. Similar values of $\varepsilon_{cu}/\varepsilon_{co}$ for FRP-confined LSC, NSC and HSC specimens' points to a possible change in the behavior of FRP-confined concrete through the addition of PVA fibers. Nonetheless, L-G1-2 and N-C2-showed the highest obtained values for ε_{cu} which this different obtained results can be attributed to distribution, location and orientation of fibers in matrix of these specimens. It is well established that the PVA fibers due to its fine nature, as can be seen in Fig. 116, cannot be distributed ideally uniform in batches in lab scale and available instrument in the lab. It is well known that the smaller fiber leads to more fibers existence for

any given specific weight. This higher number of fibers in mixture increases the possibility of mix choking or flocculation at higher dosage rates of fibers. Although maximum attempt was performed in this study to distribute PVA fibers uniformly in concrete batch, it was not possible to have ideal distribution in concrete mix.

Table 35-Results of compression tests for confined specimens

Specimen	f'_{co} (MPa)	ε_{co} (%)	f_{lu} (MPa)	f_{lu}/f'_{co} -	f'_{cc} (MPa)	ε_{cu} (%)	f'_{cc}/f'_{co}	$\varepsilon_{cu}/\varepsilon_{co}$	k_1	k_2
L-G1-1	10.5	0.24	12.2	1.16	32.3	2.10	3.08	8.76	1.58	0.153
L-G1-2	10.5	0.24	12.2	1.16	27.1	3.19	2.58	13.28		
N-G2-1	29.1	0.27	24.3	0.84	57.5	2.14	1.98	7.92	1.18	0.152
N-G2-2	29.1	0.27	24.3	0.84	58.2	2.23	2.01	8.25		
H-G3-1	70.5	0.31	36.5	0.52	130.2	2.66	1.85	8.58	1.81	0.282
H-G3-2	70.5	0.31	36.5	0.52	143.0	2.88	2.03	9.29		
L-C1-1	10.5	0.24	16.1	1.54	43.7	2.22	4.17	9.23	1.85	0.135
L-C1-2	10.5	0.24	16.1	1.54	36.9	2.16	3.51	9.02		
N-C2-1	29.1	0.27	32.3	1.11	68.4	2.88	2.35	10.65	1.34	0.201
N-C2-2	29.1	0.27	32.3	1.11	76.3	2.23	2.62	8.27		
H-C3-1	70.5	0.31	48.4	0.69	181.5	3.01	2.57	9.71	2.08	0.300
H-C3-2	70.5	0.31	48.4	0.69	160.5	2.37	2.28	7.65		
L-B2-1	10.5	0.24	5.0	0.48	18.8	1.26	1.79	5.26	1.38	0.186
L-B2-2	10.5	0.24	5.0	0.48	16.1	1.69	1.54	7.06		
L-B3-1	10.5	0.24	7.6	0.72	28.3	1.97	2.69	8.19	2.35	0.198
L-B3-2*	10.5	0.24	7.6	0.72	27.6	0.75	2.63	3.14		
N-B4-1	29.1	0.27	10.1	0.35	45.7	1.39	1.57	5.16	1.27	0.193
N-B4-2	29.1	0.27	10.1	0.35	38.0	1.23	1.31	4.56		
N-B6-1	29.1	0.27	15.1	0.52	58.7	1.75	2.02	6.48	1.93	0.196
N-B6-2	29.1	0.27	15.1	0.52	57.7	1.56	1.98	5.76		
H-B6-1	70.5	0.31	15.1	0.21	90.8	1.56	1.29	5.02	0.84	0.330
H-B6-2	70.5	0.31	15.1	0.21	75.8	1.54	1.07	4.96		
H-B9-1	70.5	0.31	22.7	0.32	110.9	1.76	1.57	5.69	1.72	0.307
H-B9-2	70.5	0.31	22.7	0.32	108.1	1.90	1.53	6.11		

* Excluded from calculations due to a problem encountered during testing

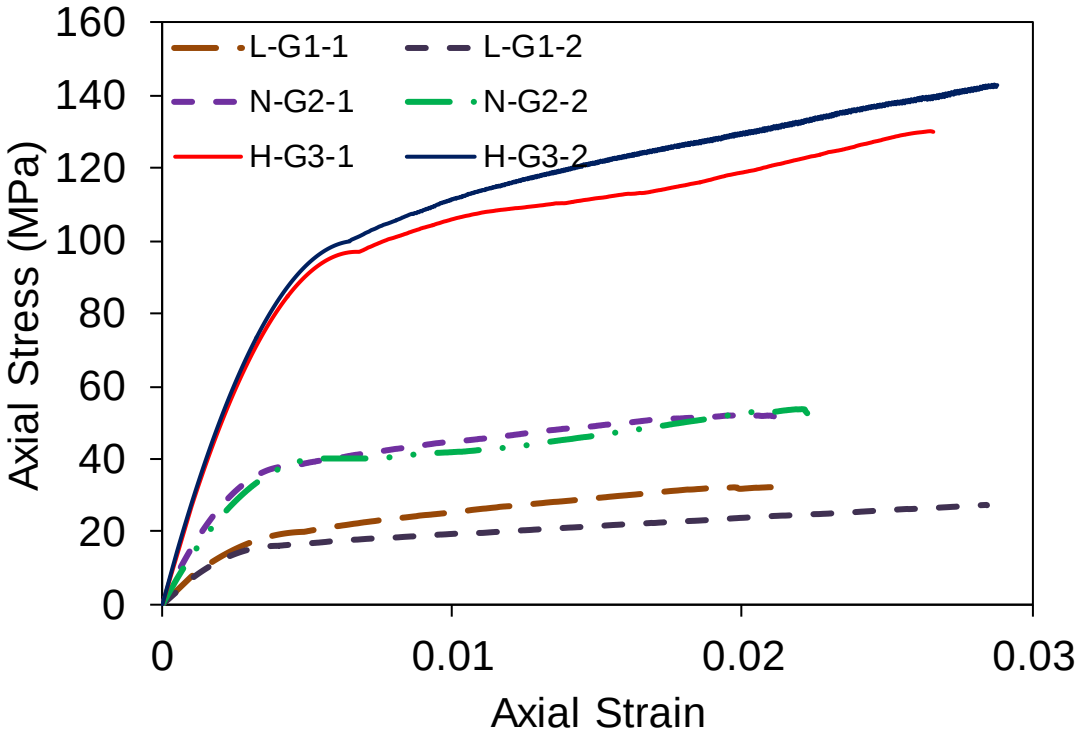

Figure 120- Axial stress-strain response of GFRP-confined concrete specimens

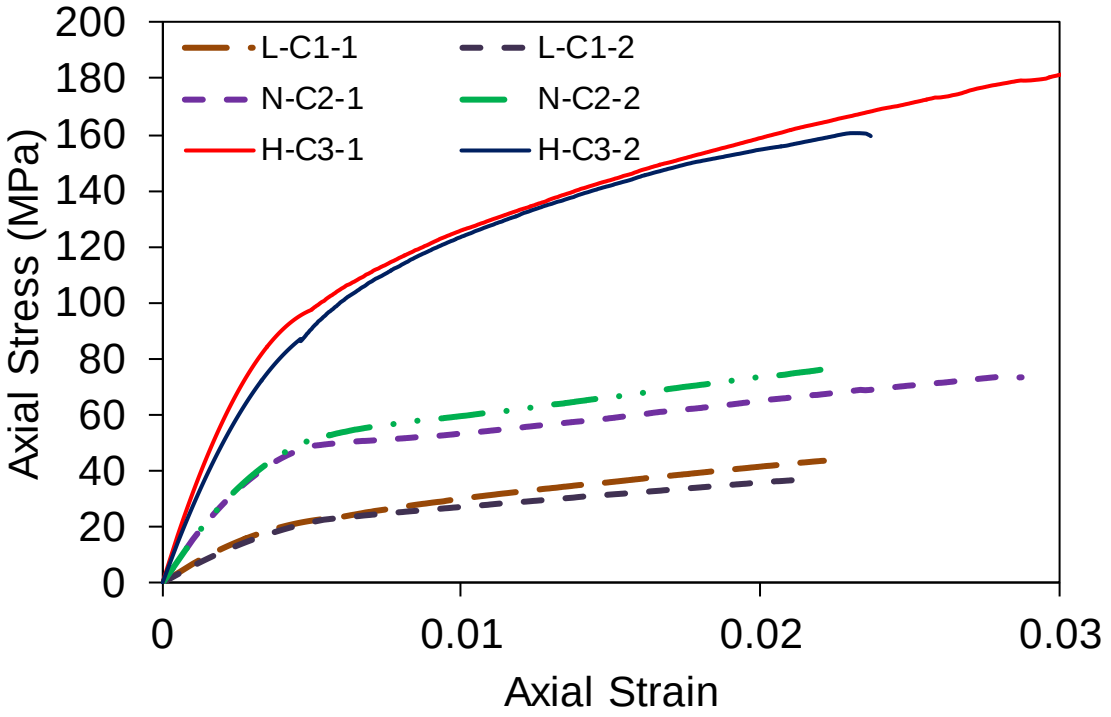

Figure 121- Axial stress-strain response of CFRP-confined concrete specimens

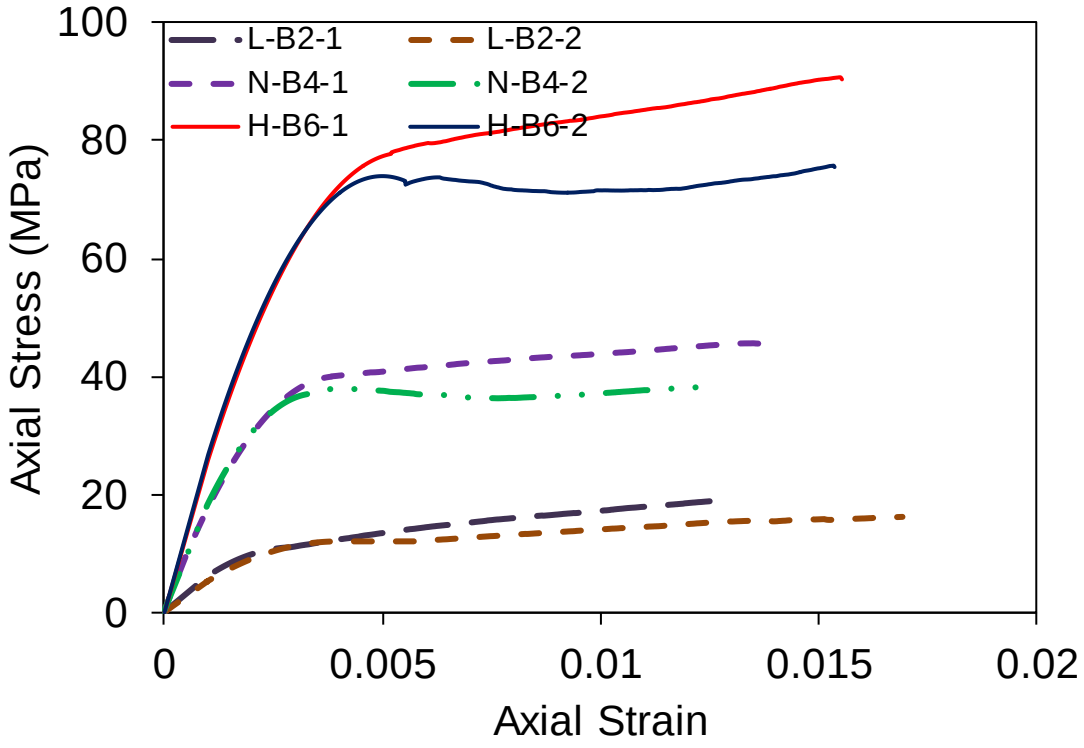

a)

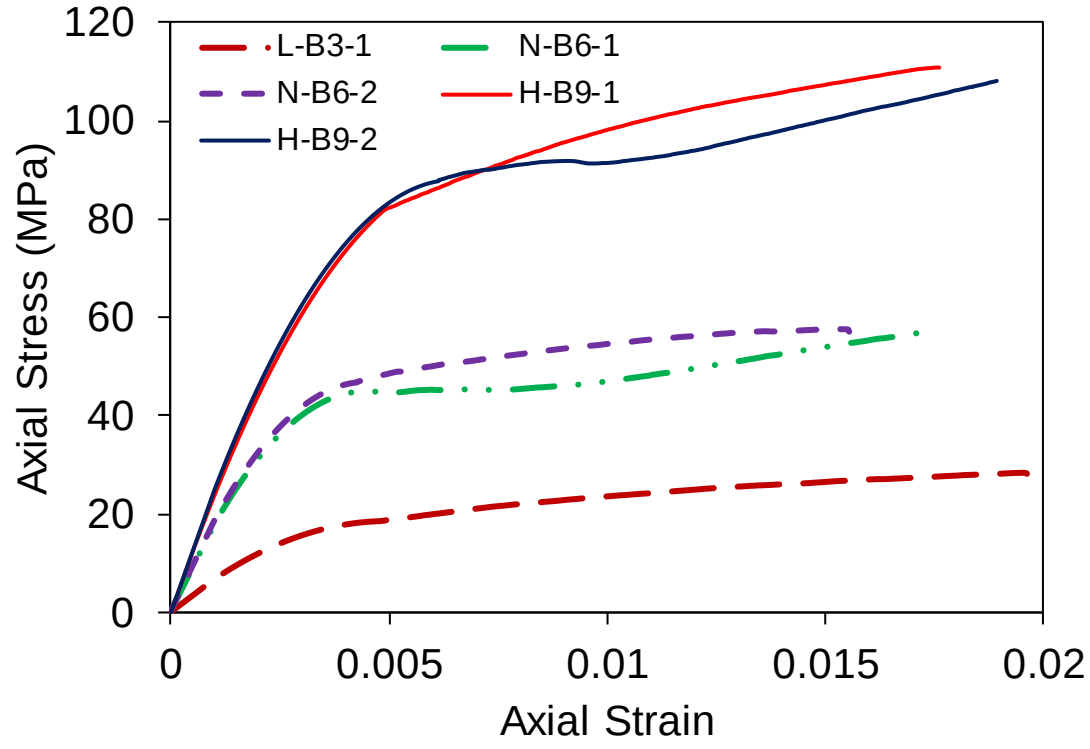

b)

Figure 122- Axial stress-strain response of BFRP-confined concrete specimens, (a) 2, 4 and 6 layers, (b) 3, 6, 9 layers

9.3.1.1.2 Influence of amount of confinement

The nominal confinement ratio (f_{lu}/f'_{co}), strength enhancement coefficient (k_1) and axial strain enhancement ratio (k_2) are presented in Table 35. Owing to existence of two sets of BFRP specimens with different f_{lu}/f'_{co} at a given f'_{co}, the variation of k_1 and k_2 with f_{lu}/f'_{co} were investigated to illustrate the influence of amount of confinement in this study. As can be seen in Table 35, at a given f'_{co}, an increase in f_{lu}/f'_{co} leads to an increase in the obtained k_1 and k_2 values. As can be observed in Fig. 122, the lightly- confined specimens, i.e. N-B2, H1-B4 and H2-B6, exhibited a nearly horizontal second branch in their axial stress-axial strain curves. The lower k_1 values of lightly-confined specimens than those of adequately-confined specimens is attributed to this behavior, which also led to slightly lower k_2 values in the former series.

9.3.1.1.3 Influence of f'_{co}

To investigate the influence of f'_{co} on behavior of PVAR-CFFTS, the change of k_1 and k_2 by variation of f'_{co}, was assessed in this study. For this investigation, the comparable specimens with similar values of f_{lu}/f'_{co} were selected for each type of FRP. As can be seen in the Table 35, FRP-confined LSC and NSC specimens have approximately similar f_{lu}/f'_{co} and these specimens were used in this section to study the influence of f'_{co} on behavior of PVAR-CFFT. As can be seen in the Table 35, the obtained k_1 for GFRP- and CFRP-confined LSC and NSC specimens showed a decrease by increasing f'_{co} at approximately constant f_{lu}/f'_{co} while both series of BFRP specimens displayed opposite behavior. This indicates that GFRP and CFRP specimens had similar behavior as FRP-confined plain concrete but BFRP specimens showed opposite behavior. Additionally, it can be seen in the table that k_2 decreased by an increase in f'_{co} for GFRP- and both series of BFRP-confined LSC and NSC specimens. Conversely, CFRP specimens showed opposite trend and k_2 for these specimens increased by an increase in f'_{co}. This result indicates that the obtained k_2 for GFRP and BFRP specimens had similar pattern as plain concrete but CFRP specimens displayed opposite behavior. Moreover, these results

indicates the significance of FRP types and its influence on mechanical behavior of PVAR-CFFTs.

9.3.1.1.4 Influence of FRP types

The influence of FRP types on the axial stress-strain response of PVAR-CFFT was investigated using k_1 and k_2 same as other studied influential parameters, i.e. amount of confinement level and f'_{co}. As can be seen in Table 35, the obtained k_1 for CFRP and adequately confined BFRP specimens had highest values at given f'_{co} and lightly confined BFRP specimens showed the lowest k_1 among whole specimens. Additionally, the obtained k_2 for BFRP specimens showed a higher values of k_2 compared to GFRP and CFRP specimens.

9.3.1.2 Axial strain-lateral strain behavior

It is well established that the prediction of axial strain-lateral strain relationship is vital importance in developing an analysis-oriented models [113]. It should be noted that the analysis-oriented models are a robust instrument to predict the mechanical response of FRP-confined concrete under compression as previously discussed by Lim and Ozbakkaloglu [113]. Therefore, a detailed study on lateral mechanical behavior of PVA-CFFT is influential to prepare an accurate analysis oriented model for PVA FRP-confined specimens. In this study, the lateral behavior of PVA-CFFT at different heights, namely 50, 100 and 150 mm from top of specimens, was studied to determine the lateral behavior along specimen height.

Figs. 123-125 show the lateral strain-axial strain curves for PVAR GFRP-, CFRP- and BFRP-confined specimens, respectively. As illustrated in Figs. 123-125, the mid-height of all specimens showed higher lateral strain compared to the measured lateral strains at other heights. In addition, the lateral behaviour of specimens at top (SGs 1&2) and bottom (SGs 5&6) of specimens showed different behaviour in different specimens. For example, L-G1, N-C2, L-B2 and N-B3 specimens had higher lateral strain recorded at bottom of specimens compared to top of specimens; other specimens such as N-G2 and L-C1 showed opposite

behaviour and recorded data by SGs 1&2 were higher than SGs 5&6. In addition, few specimens showed similar behaviour for SGs 1&2 and 5&6 such as H-C3 and H-G3. This can be attributed to lateral stiffness, placement of PVA fiber on specimens, occurrence of strain localization and location of local shear plane that governed the local and overall behavior of specimens.

Fig. 126 displays the variation of lateral strain-axial strain recorded at mid-height of specimens by increasing f'_{co} for GFRP, CFRP and BFRP specimens. As illustrated in the figures, the lateral strain-axial strain curves of FRP-confined LSC had different behavior after inflection points compared to other concrete types (NSC and HSC) and the lateral behavior of FRP-confined LSC altered by variation of FRP types. As can be seen in the figure, GFRP and BFRP-confined LSC specimens had the lower slope of lateral strain-to-axial strain compared to CFRP-confined LSC specimens. This obtained outcome for LSC indicates that the lateral behavior of PVAR FRP-confined LSC specimens is more influenced by FRP types by variation of f'_{co}. Conversely, the NSC and HSC specimens did not show a noticeable different behavior after inflection points for all FRP types which this observation is in agreement with previous work performed by Lim and Ozbakkaloglu [113].

The influence of FRP types on lateral strain-axial strain curves at the mid-height of specimens and at given f'_{co} is illustrated in Fig. 127. As exhibited in Fig. 127a, the FRP types is less influential in FRP-confined LSC specimens at constant f'_{co} and all types of FRP fibers showed approximately similar behavior after inflection point. This observation is opposite to previous observation in the last paragraph where FRP types were influential by change in f'_{co}. Conversely, the FRP-confined NSC and HSC specimens showed different trends at given f'_{co} by variation of FRP types. As illustrated in Figs. 127b and c, CFRP-confined NSC and HSC specimens showed lower lateral strain-axial strain slope after inflection points compared to

GFRP and BFRP specimens. However, Fig. 127b and c displays the similar influence of FRP types on lateral strain-axial strain curves for GFRP- and BFRP-confined NSC and HSC specimens compared to plain concrete [113]. This indicates that CFRP-confined PVAR NSC and HSC specimens showed opposite trend to FRP-confined plain concrete. It should be noted that carbon fiber reinforced polymer has highest elastic modulus (E_f) compared to other FRP types. Finally, the BFRP specimens can be used to investigate the influence of f_{lu}/f'_{co} on lateral strain-axial strain curve of tested specimens at given f'_{co}.

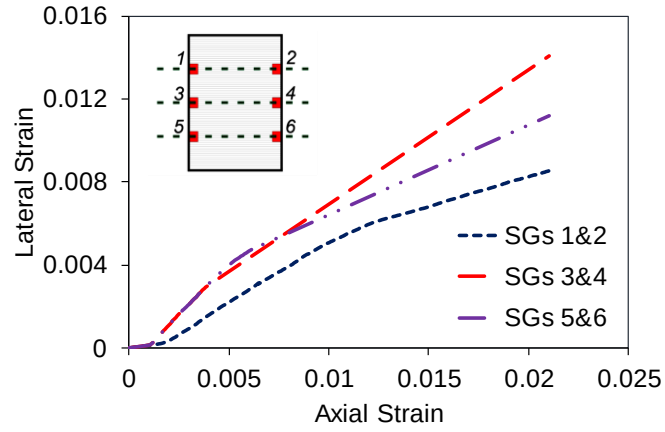

a) LSC

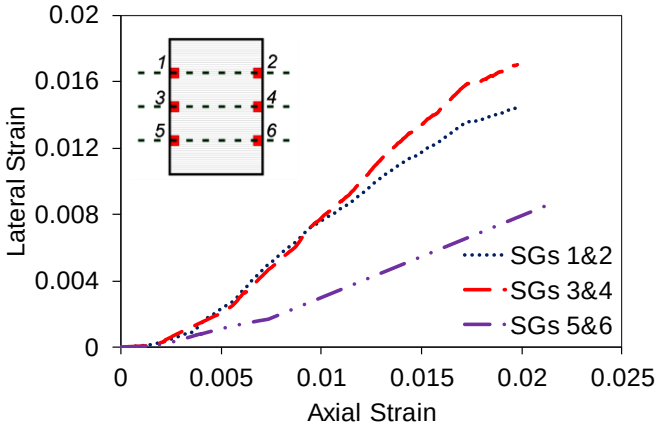

b) NSC

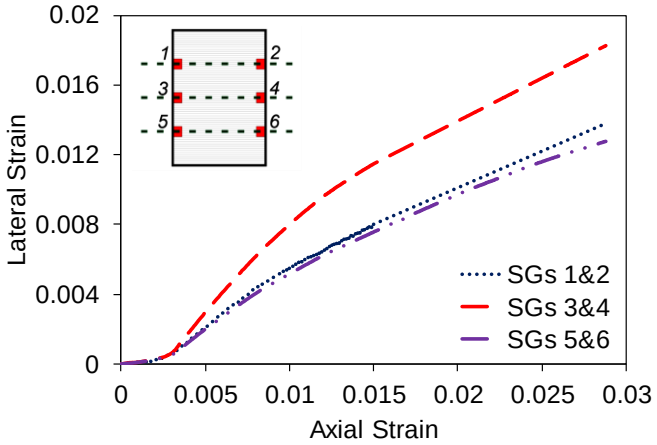

c) HSC

Figure 123- Axial Strain-lateral strain relationship of GFRP-confined specimens at different strain gauge locations

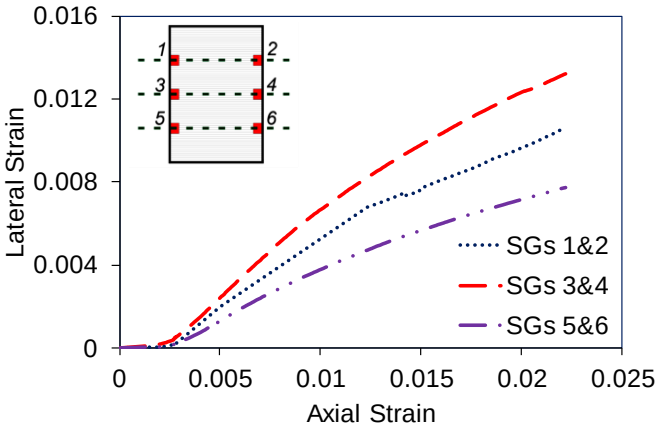

a) LSC

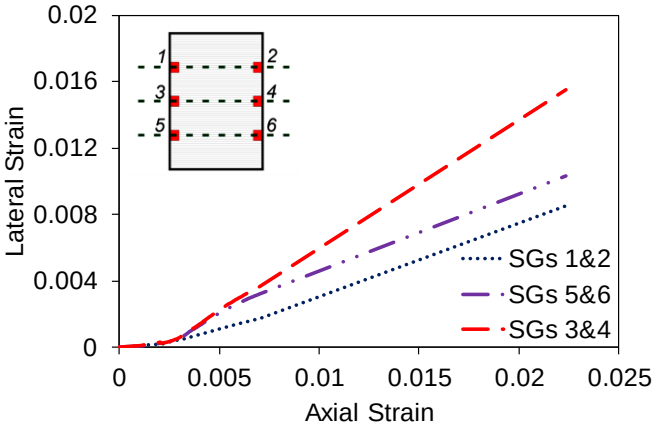

b) NSC

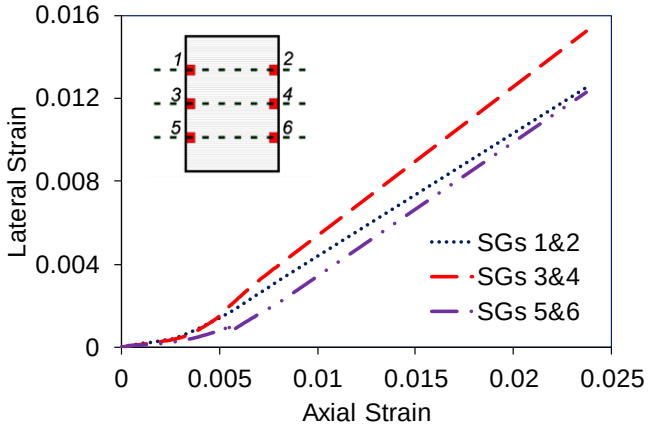

b) HSC

Figure 124- Axial Strain-lateral strain relationship of CFRP-confined specimens at different positions of Strain Gauges

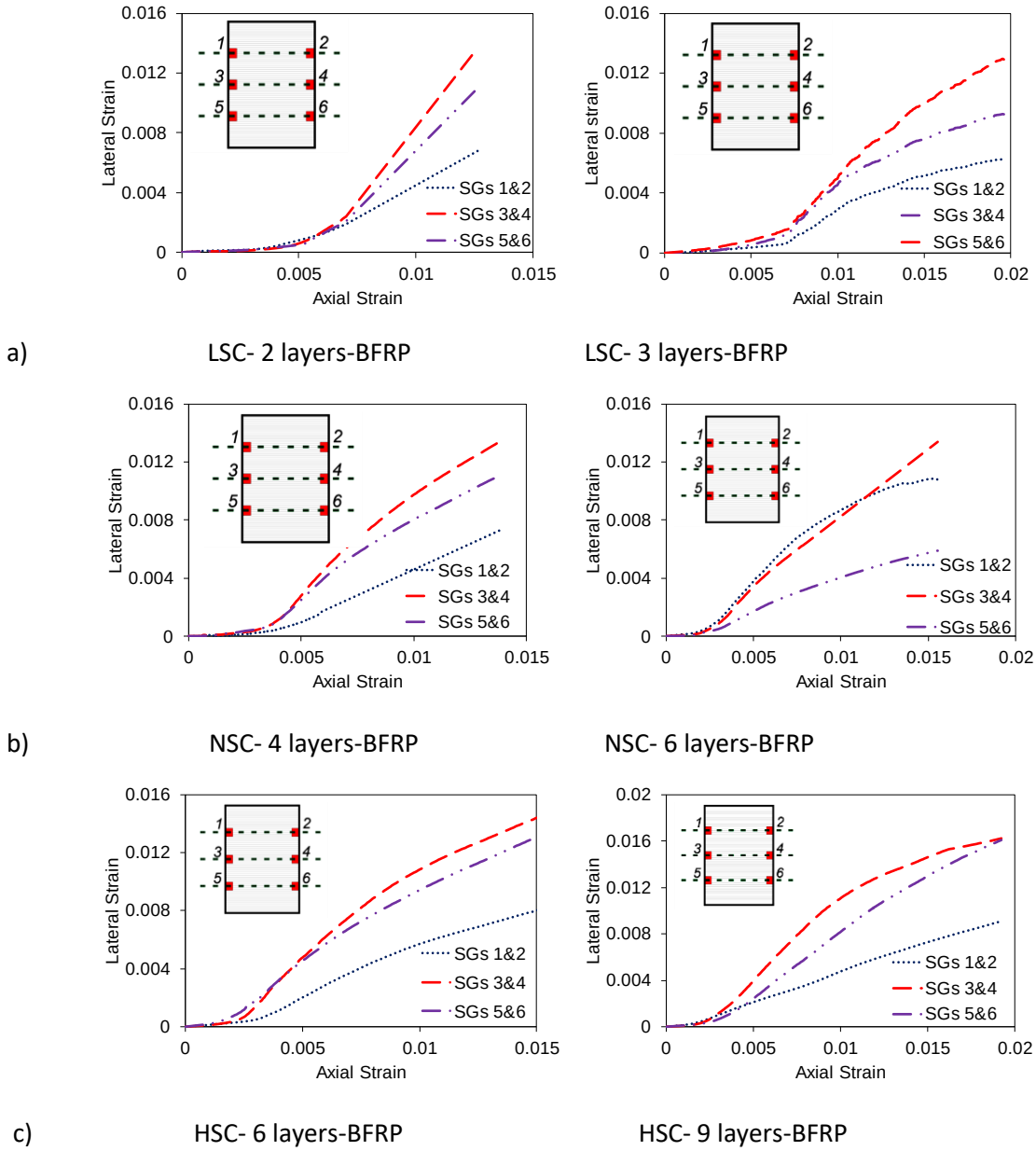

Figure 125- Axial Strain-lateral strain relationship of BFRP-confined specimens at different positions of Strain Gauges

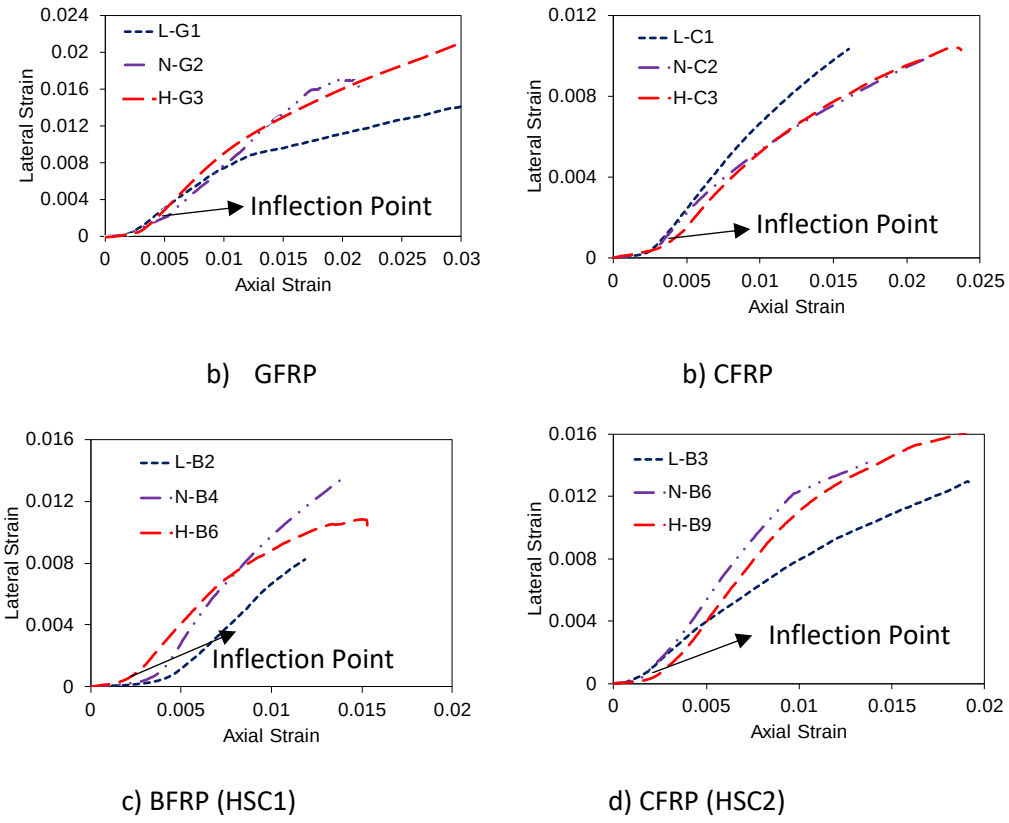

Figure 126-Lateral strain-to-axial strain relationships of FRP-confined concrete specimens having comparable confinement stiffness ratios and different unconfined concrete strengths

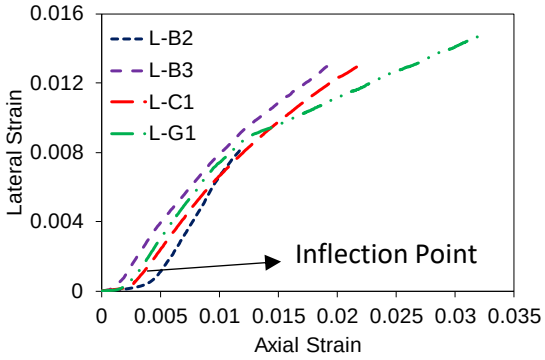

a) LSC

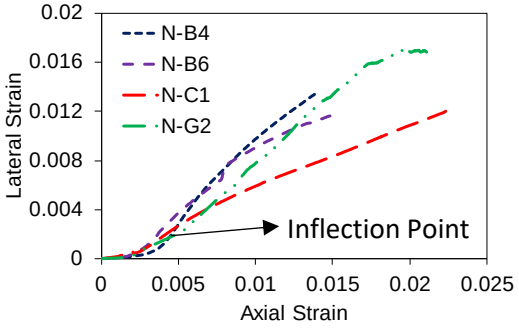

b) NSC

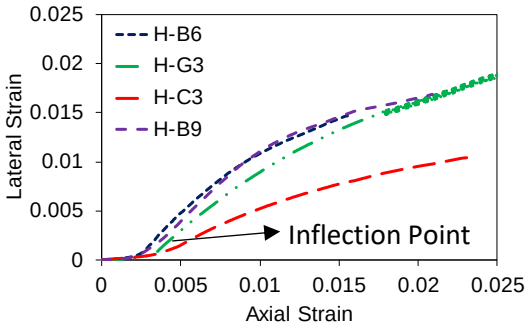

c) HSC

Figure 127-Lateral strain-to-axial strain relationships of FRP-confined concrete specimens having comparable confinement stiffness ratios and different FRP types

9.3.1.2.1 Hoop rupture strain

Table 36 shows the detail of obtained hoop strain at failure over surface of FRP jacket. In this table, the average of hoop strain measured by two lateral strain gauges at same height, the maximum lateral strain measured by SGs and the reduction factor related to each calculated average are presented. The reduction factor was calculated by $k_\varepsilon = \frac{\varepsilon_{h,rup}}{\varepsilon_{fu}}$, where $\varepsilon_{h,rup}$ and ε_{fu} are maximum hoop strain obtained by SGs and ultimate tensile strain of FRP (ε_f), respectively [29]. In addition, Lim and Ozbakkaloglu [17] proposed an expression to predict hoop rupture strain reduction factor (k_ε) and this prediction is presented in the same table. It should be noted that k_ε expression was developed for FRP-confined plain concrete and shows the general behavior of this type of confined concrete. Consequently, comparing the obtained experimental k_ε values with theoretical values obtained by the expression presents a potential method to compare PVA-CFFT behavior with plain concrete.

Table 36 shows that the whole obtained reduction factors (k_ε) are limited between 0.20 and 0.79 and the highest value of k_ε measured at mid-height of specimens compared to other obtained reduction factor (k_ε) recorded at different height of specimens, as typically expected for FRP-confined concrete specimens. Moreover, it can be observed in the table that the reduction factors for SGs 3&4, i.e. hoop rupture strain ($\varepsilon_{h,rup}$), increased by an increase in f_{lu}/f'_{co} at given f'_{co}. Same as previous section, BFRP specimens were used to investigate the influence of f_{lu}/f'_{co} on k_ε behavior due to existence of two series of BFRP specimens at given f'_{co}. Additionally, due to similarity of f_{lu}/f'_{co} for LSC and NSC specimens, the obtained results for these two types of concrete were used to investigate the influence of f'_{co} at approximately constant f_{lu}/f'_{co}. As can be seen in Table 36, k_ε increased by an increase in f'_{co} for all FRP types except for H-B6 specimens which showed a decrease by an increase in f'_{co}. It should be noted that H-B6 specimens had lowest value of f_{lu}/f'_{co} among all specimens. Furthermore, Table 7 shows the prediction of k_ε using Lim and Ozbakkaloglu [17]'s expression where the predicted

values vary noticeably with f'_{co}. These observations indicate the change of PVAR-CFFT k_ε trend compared to FRP-confined plain concrete behavior by variation of f'_{co}. This can be explained by presence of PVA fiber in wet mix of concrete and change of mechanical behavior and ductility of PVAR-CFFT due to existence of these fibers.

Table 36- Results of lateral strain at failure for confined specimens

Specimen	Lateral strain (%) SG 1&2	Lateral strain (%) SG 3&4	Lateral strain (%) SG 5&6	$\varepsilon_{h,rup\ (Max)}$ %	$k_{\varepsilon\ 1\&2}$ SG 1&2	$k_{\varepsilon\ 3\&4}$ SG 3&4	$k_{\varepsilon\ 5\&6}$ SG 5&6	k_{ε} L&O (2014)
L-G1-1	0.85	1.80	0.70	2.10	0.24	0.51	0.20	0.81
L-G1-2	0.84	1.41	1.12	2.02	0.24	0.40	0.32	0.81
N-G2-1	1.02	1.78	0.86	2.07	0.29	0.51	0.25	0.77
N-G2-2	0.80	1.70	0.94	1.90	0.23	0.49	0.27	0.77
H-G3-1	1.05	2.21	0.90	2.31	0.30	0.63	0.26	0.70
H-G3-2	1.37	1.96	1.27	2.54	0.39	0.56	0.36	0.70
L-C1-1	1.15	1.35	0.60	1.40	0.55	0.64	0.29	0.70
L-C1-2	0.81	1.51	1.12	1.61	0.39	0.72	0.53	0.70
N-C2-1	1.08	1.58	0.89	1.71	0.51	0.75	0.42	0.66
N-C2-2	0.85	1.55	1.03	1.58	0.40	0.74	0.49	0.66
H-C3-1	1.51	1.65	1.34	1.71	0.72	0.79	0.64	0.57
H-C3-2	1.32	1.52	1.23	1.55	0.63	0.72	0.59	0.57
L-B2-1	0.68	1.37	1.10	1.49	0.30	0.60	0.48	0.82
L-B2-2	0.61	1.21	1.14	1.23	0.27	0.53	0.50	0.82
L-B3-1	1.12	1.34	0.82	1.33	0.58	0.36	0.58	0.82
L-B3-2*	1.07	1.46	0.69	1.65	0.63	0.30	0.72	0.82
N-B4-1	0.80	1.55	1.24	1.75	0.35	0.67	0.54	0.78
N-B4-2	0.74	1.41	1.13	1.53	0.32	0.61	0.49	0.78
N-B6-1	0.55	1.57	1.36	1.61	0.24	0.68	0.59	0.78
N-B6-2	1.12	1.34	0.61	1.75	0.49	0.58	0.27	0.78
H-B6-1	0.82	1.46	1.35	1.81	0.36	0.63	0.59	0.71
H-B6-2	1.12	1.54	1.01	1.54	0.49	0.67	0.44	0.71
H-B9-1	1.42	1.60	1.19	1.61	0.62	0.70	0.52	0.71
H-B9-2	0.90	1.62	1.60	1.70	0.39	0.70	0.70	0.71

9.4 Conclusion

The following points summarize the main findings and contributions of this study:

1- Similar values of $\varepsilon_{cu}/\varepsilon_{co}$ are observed for each FRP type specimens and increasing f'_{co} or f_{lu}/f'_{co} does not intensively influence these values. Similar values of $\varepsilon_{cu}/\varepsilon_{co}$ for FRP-confined LSC, NSC and HSC specimens' by variation of f'_{co} points to a possible change in the behavior of FRP-confined concrete through the addition of PVA fibers.

2- f_{lu}/f'_{co} influences the axial stress enhancement ratio (k_1) and axial strain enhancement ratio (k_2) of PVAR-CFFTS and these coefficients increases by an increase in f_{lu}/f'_{co}.

3- k_1 for GFRP and CFRP-confined LSC and NSC specimens show a decrease by increasing f'_{co} at approximately constant f_{lu}/f'_{co} while both series of BFRP specimens display opposite behavior.

4- k_2 decreases by an increase in f'_{co} at approximately constant for GFRP and both series of BFRP-confined LSC and NSC specimens. Conversely, CFRP specimens show opposite trend and k_2 for these specimens increases by an increase in f'_{co}.

5-The lateral strain-axial strain curves of FRP-confined LSC shows the noticeable influence of f'_{co} on lateral strain-axial strain curves after inflection points. This observation is opposite to other two types of concrete which were investigated in this study and to FRP-confined plain concrete.

6-The FRP types is less influential in FRP-confined LSC specimens at constant f'_{co} and all types of FRP fibers showed approximately similar behavior after inflection point in lateral strain-axial strain curves. Conversely, the FRP-confined NSC and HSC specimens showed different trends at given f'_{co} and the shape of lateral strain-axial strain curves changed by variation of FRP types.

7- k_ϵ increases by increasing f'_{co} which indicated the different behavior of obtained k_ϵ for PVAR-CFFT compared to FRP-confined plain concrete.

Chapter 10: Evaluation of ultra-high-strength steel fiber-reinforced concrete-filled FRP tubes columns compressive behavior: an analysis using Digital Image Correlation

(A paper is drafted based on this section, "Evaluation of ultra-high-strength steel fiber-reinforced concrete-filled FRP tubes and unconfined concrete columns under compression: an analysis using Digital Image Correlation" by Ali Fallah Pour and Giang Nguyen)

10.1 Introduction

Due to superior mechanical performance of HSC, namely higher compressive strength (f'_{co}), this type of concrete recently received a great deal of attention in the construction industry [1-10]. However, the more brittle behavior of HSC compared to NSC causes some disadvantages in mechanical response of FRP-confined HSC under different type of loading such as compression [16]. It is well established that adding fibers into the wet concrete mix leads to create a more ductile structural system [78]. Steel fiber used widely in concrete wet mix to improve the brittle behavior of concrete and steel fiber reinforced concrete (SFRC) examined by numerous researches previously (e.g. [59, 60, 65-70, 72, 73, 75]),

Adding steel fiber to wet mix of concrete improves intrinsically brittle response of concrete and changes the mechanical response of steel fiber reinforced concrete (SFRC) (i.e. ductility, compressive and tensile strength) compared to plain concrete [59-63, 203-205]. The influence of steel fibers on concrete behavior has been extensively investigated by different research programs [59-76, 203-205]. The results of these studies showed that the steel fibers create bridges across the cracks and the crack propagation can be controlled or delayed by these bridges which improve the ductility of concrete [59, 60, 65-70, 72, 73, 75]. In addition, adding steel fibers in concrete mix offers better compressive and tensile strength compared to plain concrete which is results of bridging phenomenon [61, 63, 205, 207-212]. It was previously

discussed that this improvement is under influence of many parameters such as volume fraction and aspect ratio. It is well understood that the strength and toughness of SFRC under compressive loading increased by increasing the volume fraction (or weight fraction) and decreased slightly by increasing the aspect ratio of the fibers [59-61, 63, 64, 208, 210, 233-237]. The existing studies showed that the compressive strength improved at maximum up to 15% by adding steel fibers [208, 209]. In addition, it was reported that the pre-peak ascending branch of the compressive stress-strain relationship was marginally improved with increasing fiber content [207]. Rangan et al. [210] reported that increasing fiber content leads to the higher load absorption capacity of concrete in compression. However, the revision of literature performed by this research group exhibited that a detailed study on performance of fibers in concrete matrix and the correlation of bridging phenomenon with mechanical behavior of SFRC does not exist.

As mentioned previously in section 8, an ultra-high-performance system can be built by adding steel fiber to wet concrete mix of FRP-confined concrete [78]. Simultaneous use of FRP tube as lateral confinement of concrete columns which enhances the compressive strength and ductility [14, 16, 17] and steel fiber which amends the intrinsically brittle response of plain concrete [59-63, 203-206], leads to developing a mega-performance structural system. A number of experimental studies on SFR-CFFT have been performed to determine the mechanical behavior of this system under a different type of loading such as concentric and eccentric compression [9, 77, 91, 213, 214]. Previously discussed, this new system can amend temporary softening behavior of FRP-confined HSC specimens after transition point (f'_{c1} and ε_{c1}) [11-15]. It should be noted that the point where the axial stress-strain curve transitions from an initial ascending branch to a second branch, is referred as transition point (f'_{c1} and ε_{c1}) and it is discussed in details in Ref. [17]. It is well known that the temporary loss of strength after transition point (f'_{c1} and ε_{c1}) of FRP-confined HSC specimens is due to brittle nature of HSC

[12, 15, 85, 108]. Additionally, the studies focused on concentric compressive loading of SFR-CFFTs [9, 77, 214] reported that the axial stress-strain relationship of the SFR-CFFT specimens can be influenced by volume fraction (V_f) and aspect ratio (A_R) similar to SFRC. Xie and Ozbakkaloglu [77] discussed that the compressive strength of SFR-CFFTs decreased by an increase in A_R at given V_f. The same results were obtained for ultimate axial strain (ε_{cu}) and hoop rupture strain ($\varepsilon_{h,rup}$) of SFR-CFFTs in this study. Conversely, They showed that f'_{cc}, ε_{cu}, and $\varepsilon_{h,rup}$ increased by an increase in V_f at a given A_R. Additionally, section 8 showed the influence of concrete compressive strength (f'_{co}) and FRP types on axial compressive behavior of ultra-high strength steel fiber reinforced (UHSSFR)-CFFTs. It is shown in section 8 that the axial stress enhancement ratios (k_1) decreased with an increase in f'_{co} for different fiber types with similar values of the nominal confinement ratio (f_{lu}/f'_{co}). Conversely, the obtained results for axial strain enhancement ratios (k_2) in section 8 indicated that k_2 is not significantly influenced by f'_{co} and FRP type can change the behavior of k_2 by variation of f'_{co}. Furthermore, the obtained results in section 8 displayed that the lateral deformation of UHSSFR-CFFTs was approximately similar to FRP-confined plain concrete, although a few differences were observed.

To design and construct a building using SFRC or SFR-CFFT, existence of a model to accurately predict the axial stress-strain behavior of SFRC and SFR-CFFTs is of vital importance. Although some stress-strain curve models were developed to determine the SFRC behavior under compression for specific types of steel fiber [59, 64, 65, 67, 72, 238], an in-depth study to interpret the influence of steel fiber on concrete behavior and strain localization, e.g. axial stress-strain curve, is essential. As Bencardino et al. [59] discussed, the comprehensive definition of a stress-strain relationship which includes all types of SF, e.g. hooked-ends, corrugated, flat-ends and ultra-high strength concrete (UHSSF), does not yet

exist. This indicates the need of more detailed study on mechanical behavior of each type of SFRC to determine the influence of different fiber types on SFRC mechanical response.

It is well established that the prediction of lateral behavior of FRP-confined concrete is a vital importance in developing or validating an analysis oriented model for FRP-confined columns under compression [113]. The understanding of confinement mechanism and its influence on lateral behavior of this type of confined concrete are the key parameters to determine the mechanical behavior of FRP-confined concrete accurately, i,e, develop a stress-strain model. Although confinement mechanism of FRP-confined plain concrete was investigated in details by different studies (e.g. [2, 15, 16, 92, 97, 103, 111, 144]), the influence of adding steel fiber on FRP confinement mechanism did not yet examined. Additionally, Fallah Pour et al.[202] discussed the influence of strain localization and evolution of strain localization on lateral deformation of FRP-confined concrete which in turn activate the confinement mechanism. Although the literature review performed by this research group showed the existence of some researches on strain localization and its evolution in FRP-confined plain concrete (e.g. [27, 202]), no study still discuss on SFR-CFFTs strain localization and its evolution.

This section is a first detailed study on the deformation localization and localization evolution of ultra-high strength steel fiber reinforced concrete (UHSSFRC) and UHSSFR-CFFTs under compression. In this study, the strain localization and its evolution over specimen surface were monitored using digital image analysis (DIC). The mechanical response of UHSSFRC and UHSSFR-CFFT under compression were correlated to localization evolution and a detailed study on initiation of localization was performed. This followed by an in-depth investigation on occurrence of bridging and variation of this phenomenon by increasing f'_{co}. Later, a detailed discussion on the influential parameters in strain localization including f'_{co} and lateral stiffness (K_l) was performed. At the end, a statistical approach which had been developed by this

research group to condense DIC data for accurate correlation between localization and mechanical response of specimens, was performed.

10.2 Experimental program

Same as FRP-plain concrete, this study used DIC to determine better the mechanical response of UHSSF-CFFT specimens. This study is an extension of previous section, i.e. Section 8; this indicates that the same specimens were examined by new measurement method (DIC). The detail of specimens are presented in Section 8.1and Table 37; furthermore, DIC method was explained in Section 5.1 in detail in detail.

Table 37- Details of test specimens

Specimen	V_f (%)	Concrete Type	FRP-Type	Number of Layers	$t_{f\text{-total}}$ (mm)
N-G1	1.5	NSC	GFRP	1	0.2
H-G2	1.5	HSC	GFRP	2	0.4
VH-G3	1.5	VHSC	GFRP	3	0.6
N-C1	1.5	NSC	CFRP	1	0.167
H-C2	1.5	HSC	CFRP	2	0.334
VH-C3	1.5	VHSC	CFRP	3	0.501
N-B2	1.5	NSC	BFRP	2	0.150
N-B3	1.5	NSC	BFRP	3	0.225
H-B4	1.5	HSC	BFRP	4	0.300
H-B6	1.5	HSC	BFRP	6	0.450
VH-B6	1.5	VHSC	BFRP	6	0.450
VH-B9	1.5	VHSC	BFRP	9	0.675

10.3 Test Results

The DIC method was applied in this study to display and describe the details of the failure mechanism and expansion of the shear zone under axial compression for UHSSFRC and UHSSFR-CFFT. A synchronization between obtained results by DIC and the obtained experimental stress-strain curves was provided to have a better understanding of the evolution of strain localization during test procedure. This synchronization helps to correlate the strain localization to mechanical response of specimens which results in better determination and

quantification of localization characteristics. It should be said again that the details of experimental axial stress-axial and lateral strain curves can be found in section 8.

10.3.1 Strain developments on specimens surface

Figs. 128-131 show the recorded Von Mises strain ($\varepsilon_{Von\ Mises}$) and its evolution over specimens' surface obtained by DIC for unconfined, BFRP, CFRP and GFRP-confined specimens. It should be noted that 3 different points in axial stress-strain curves as representative of whole curves, were selected. As can be seen in Fig. 128 for UHSSFRC and by comparing this figure with obtained results for plain concrete [202], a different crack distribution pattern for UHSSFRC can be observed. This different crack pattern as discussed previously, can be hinged to occurrence of bridging which changed the natural brittle behavior of plain concrete and more homogenous crack distribution were observed. It should be added that the influence of steel fibers in variation of the failure mode from very localized to more homogeneous was associated with increasing marginally compressive strength of UHSSFRC (f'_{co}). This influence is similar for all concrete types including NSC, HSC and VHSC. The influence of steel fiber in concrete column behavior will be discussed in details later in this study. Additionally, Fig. 128 shows approximately the onset of localization using colour map, although the accurate determination using this method is very difficult. This is due to dependency of the obtained results using colour map on selection of maximum value, minimum value and number of interval in VIC-3D software. VIC-3D software provides the colour map using the mentioned values which should be decided by user. This is evident that change one of the mentioned values to analyze DIC data using colour map, can influence the obtained results and lead to wrong evaluation of the obtained data by DIC.

Figs. 129-131 show the evolution of Von Mises strain at three key references points in the stress-strain relationship of BFRP, CFRP and GFRP specimens. These points are compressive strength of concrete (f'_{co}), transition stress (f'_{c1}) and ultimate axial stress (f'_{cc}). Comparing the

obtained results for UHSSFR-CFFT with plain CFFT specimens [202] illustrates a significant increase in thickness of the shear zone and more homogenous distribution of cracks over specimens' surface. This can be attributed to the creation of bridges by steel fibers across the cracks and changing behavior of specimens to more ductile behavior compared to plain CFFT. Nevertheless, as can be seen in Fig. 5a, BFRP specimens with 2, 4 and 6 (VHSC) layers and lower values of K_l/f'_{co} compared to their peer BFRP specimens, showed a slightly different pattern where more similar behavior to FRP-confined plain concrete can be observed. This can be expressed due to the lower value of K_l/f'_{co} and its influence on FRP-confined concrete behavior. As explained previously for UHSSFRC, marking the onset of localization is very difficult using colour map and a better way to spot the localization initiation should be used.

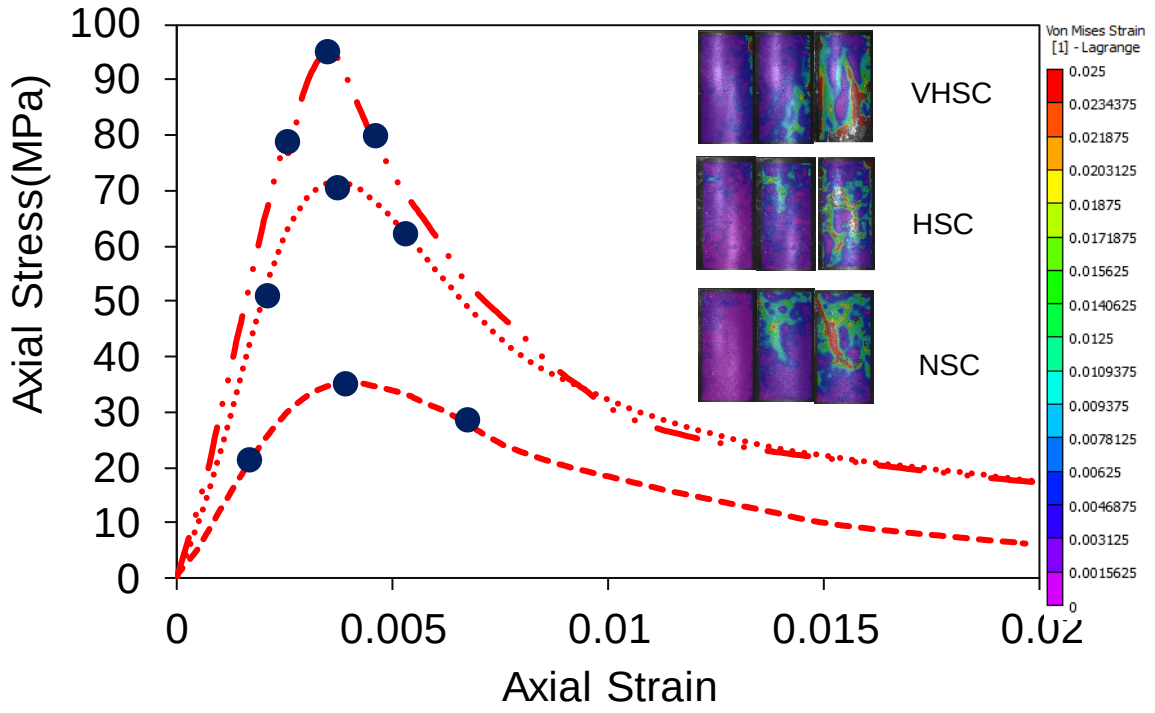

Figure 128- Von Mises strain evolution of unconfined specimen (NSC, HSC and VHSC) Obtained results by DIC

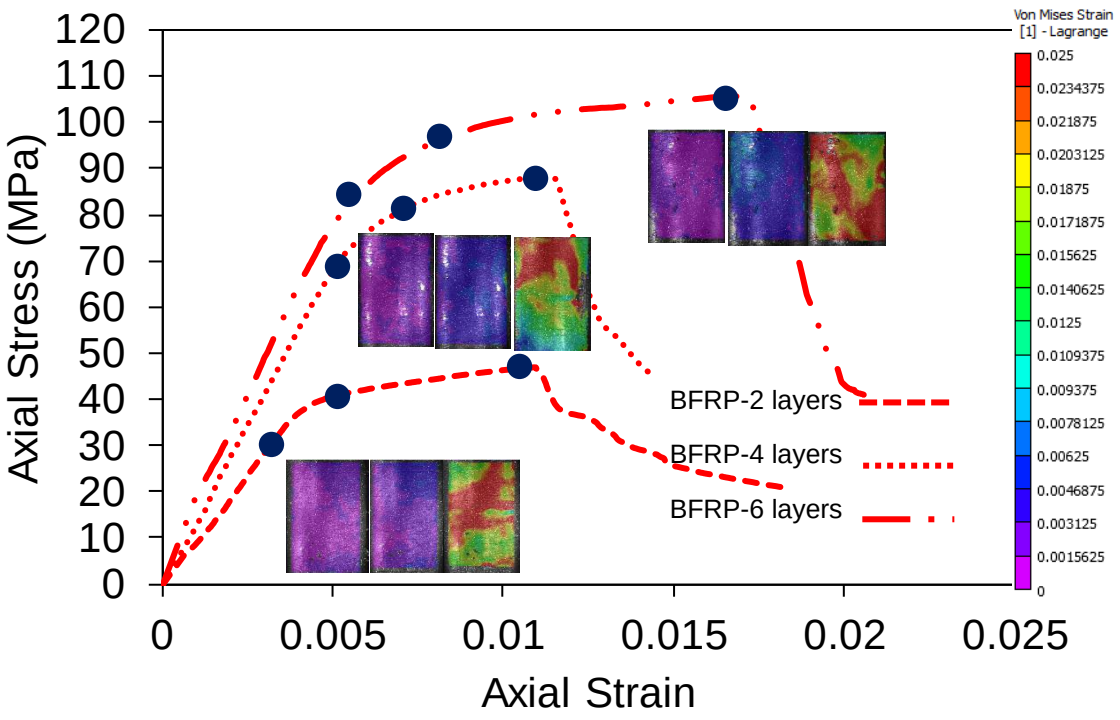

a) BFRP-2, 4 and 6 (HSC) layers

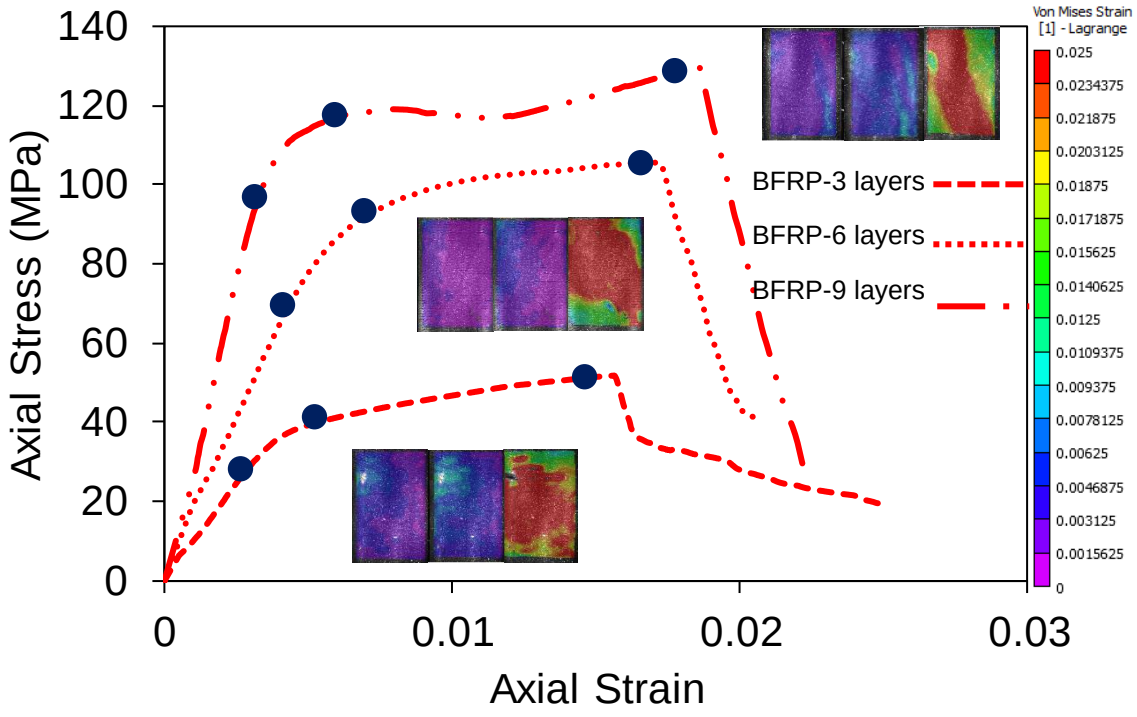

b) BFRP-3, 6 (VHSC) and 9 layers

Figure 129- Von Mises strain evolution of BFRP-confined specimen (2, 3, 4, 6 and 9 layers) Obtained results by DIC

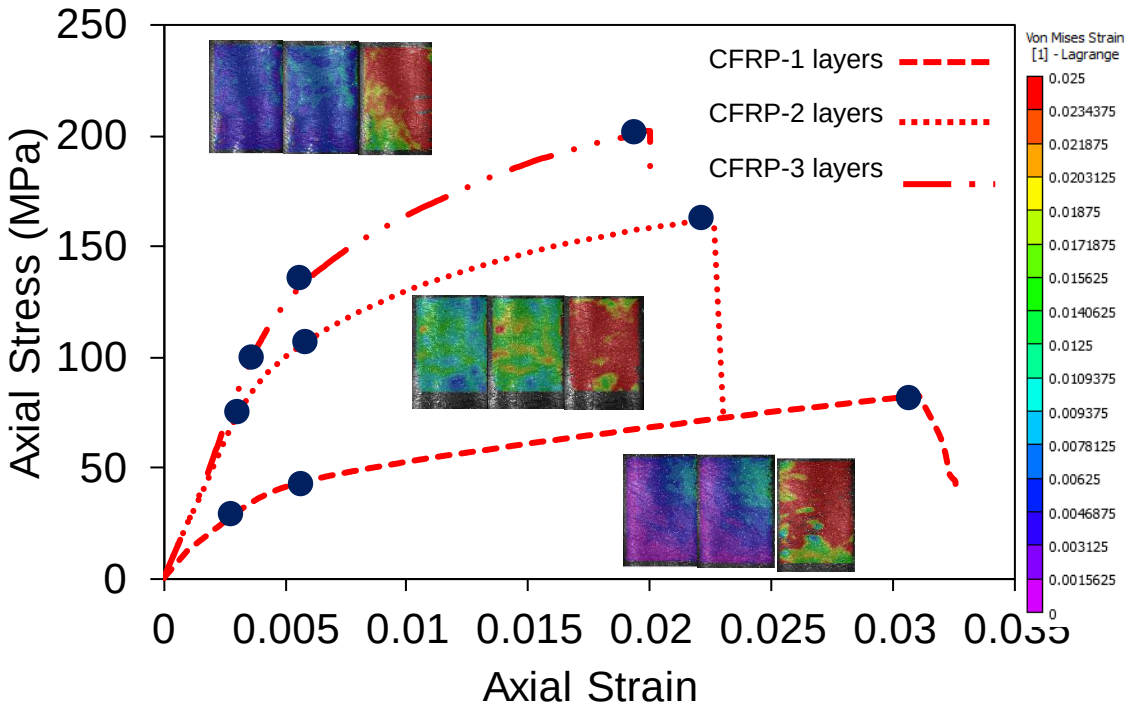

Figure 130- Von Mises strain evolution of CFRP-confined specimen (1, 2 and 3 layers) Obtained results by DIC

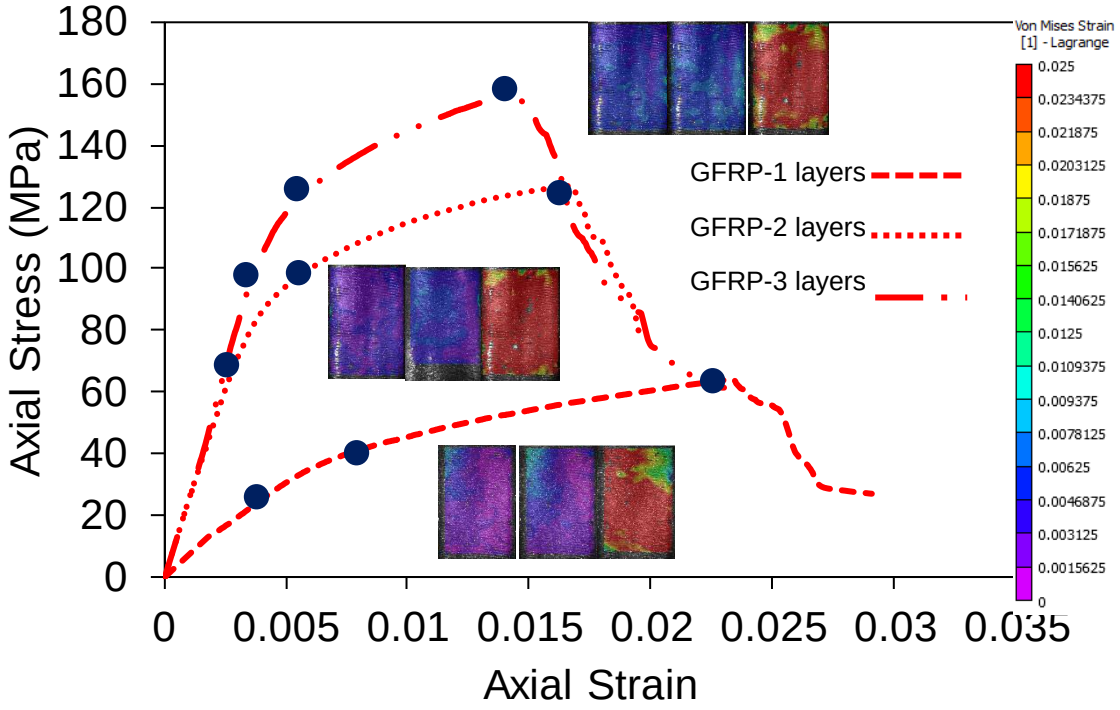

Figure 131-Von Mises strain evolution of GFRP-confined specimen (1, 2 and 3 layers) Obtained results by DIC

10.3.2 Correlation between bridging and axial stress-strain

As explained previously, the pattern of crack distribution of fiber reinforced concrete including UHSSFRC specimens change by formation of bridges by fibers across the cracks compared to plain concrete. This leads to higher unconfined compressive strength, better post-peak behavior and more ductile behavior of fiber reinforced concrete specimens. Better understanding of this phenomenon in fiber reinforced concrete helps to have more accurate prediction of structural element mechanical behavior which is a significant step of a practical designing procedure. Figs. 132-134 display the correlation between axial stress-strain curves, full-field strains (axial and Von Mises strain) evolution and the influence of steel fiber on specimens' behavior. As can be seen in these figures and it is discussed previously, the strain localization started at approximately 50-60% and 70-80% of f'_{co} for NSC and HSC, respectively. It can be seen in the Figs. 132-134 that the bridging phenomenon did not initiate before this point. By onset of strain localization, the steel fibers initiated to form a bridge across the localized zone. The formation of bridge impeded the expansion of localization along first orientation and this followed by creating a new strain localized zone approximately perpendicular to the direction of the first localized region. It should be said that the direction of strain localized zone related to bridging occurrence depends strongly to the orientation of steel fibers at that part of specimens. By appearance the second localization region, new fibers were triggered and these fibers in turn obstructed the progression of second localization zone. This leads to formation of a new localization zone which is approximately parallel to the first localization zone. This procedure leads to two sets of localized strain bands which are approximately perpendicular together and they distributed all over the surface of specimens. It should be said that the steel fibers lose their influence by progression in the test when the activated fiber being pulled out from the matrix and the localized zone started again to develop again along their primary orientation. This later expansion again in turn triggered the other steel fiber at a different portion of specimens and this procedure continued to the failure of specimens. It is evident that

this bridging procedure results in higher unconfined strength (f'_{co}) and more ductile post-peak behavior.

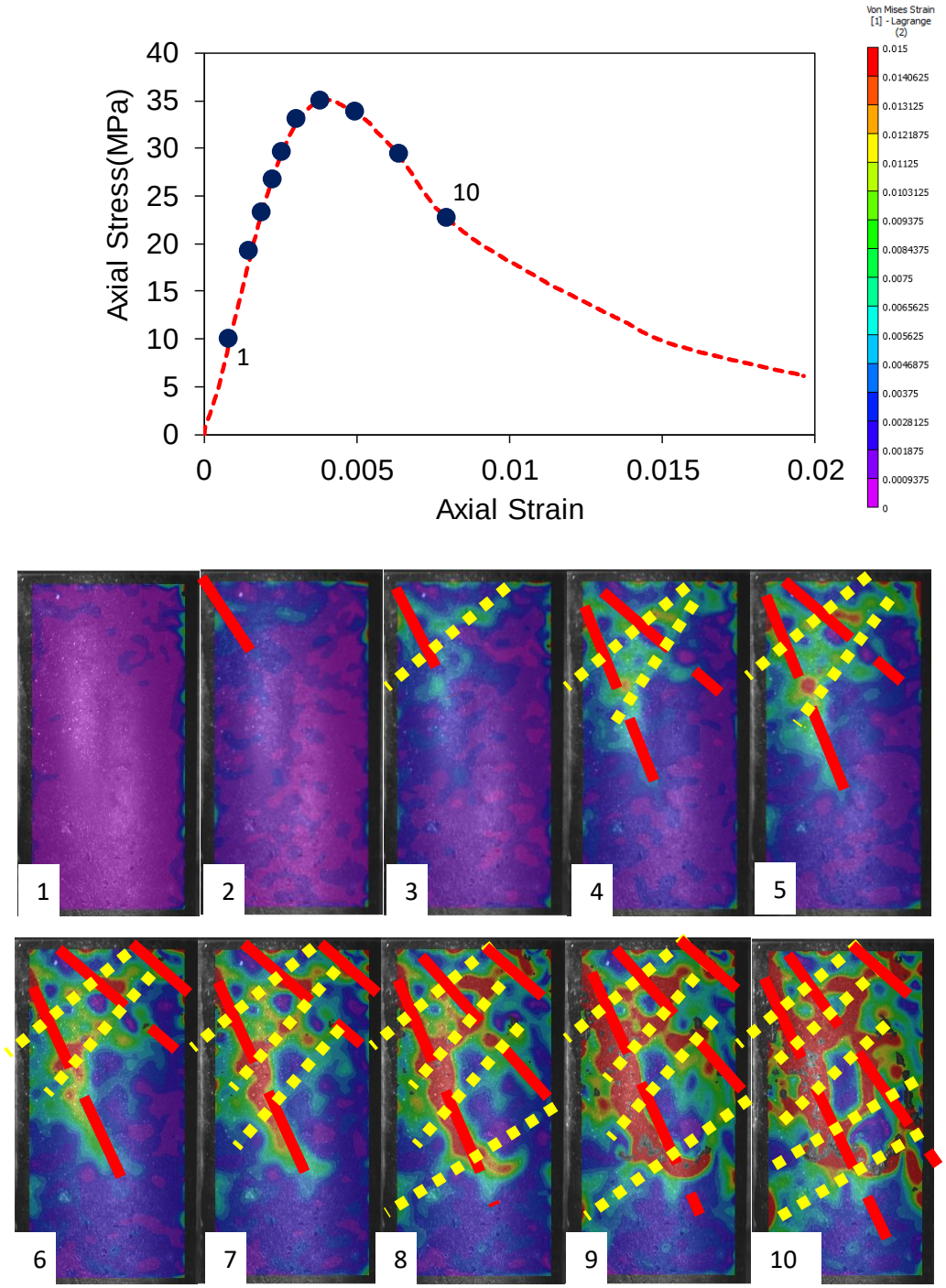

Figure 132- Bridging procedure in NCS

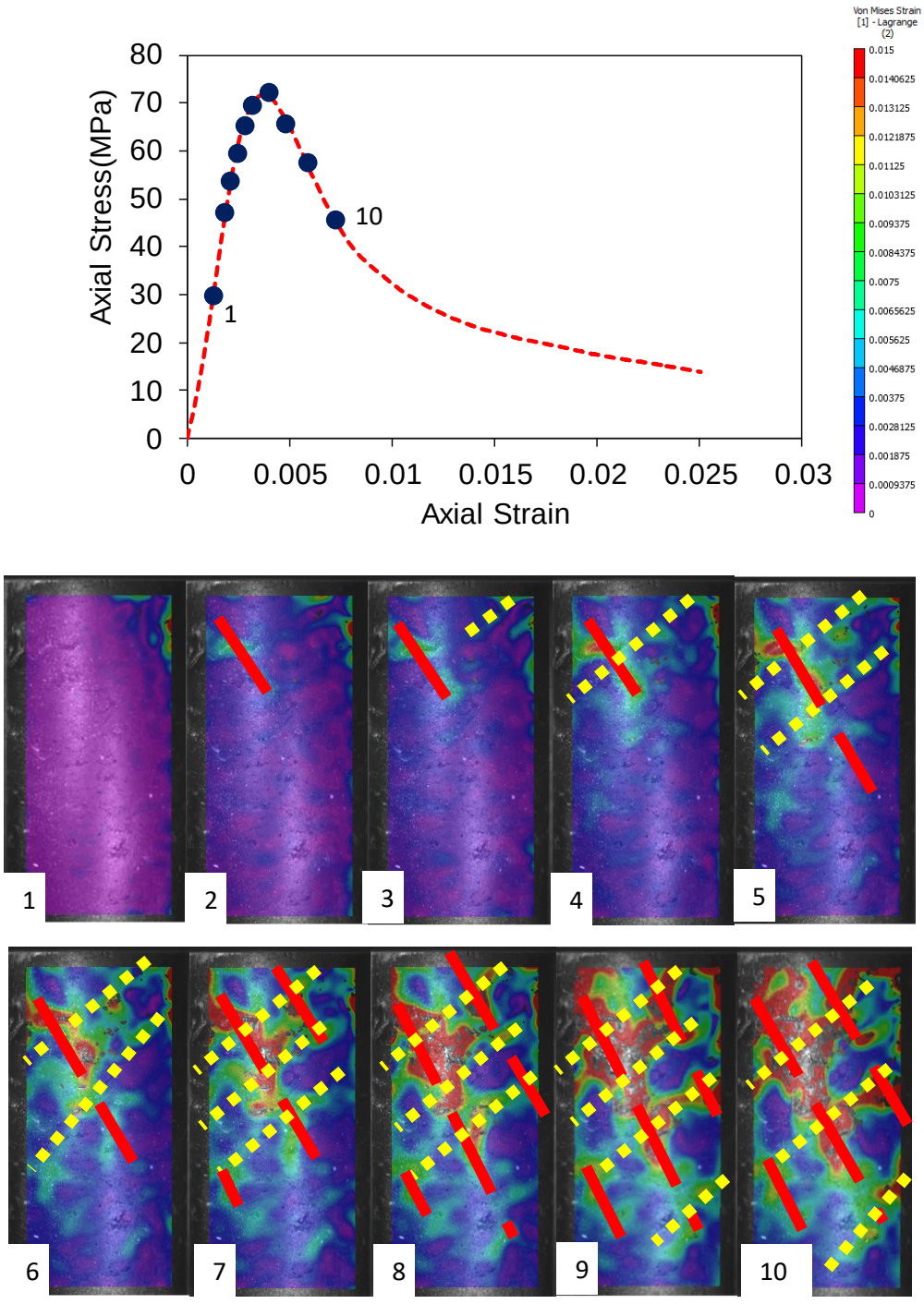

Figure 133- Bridging procedure in HCS

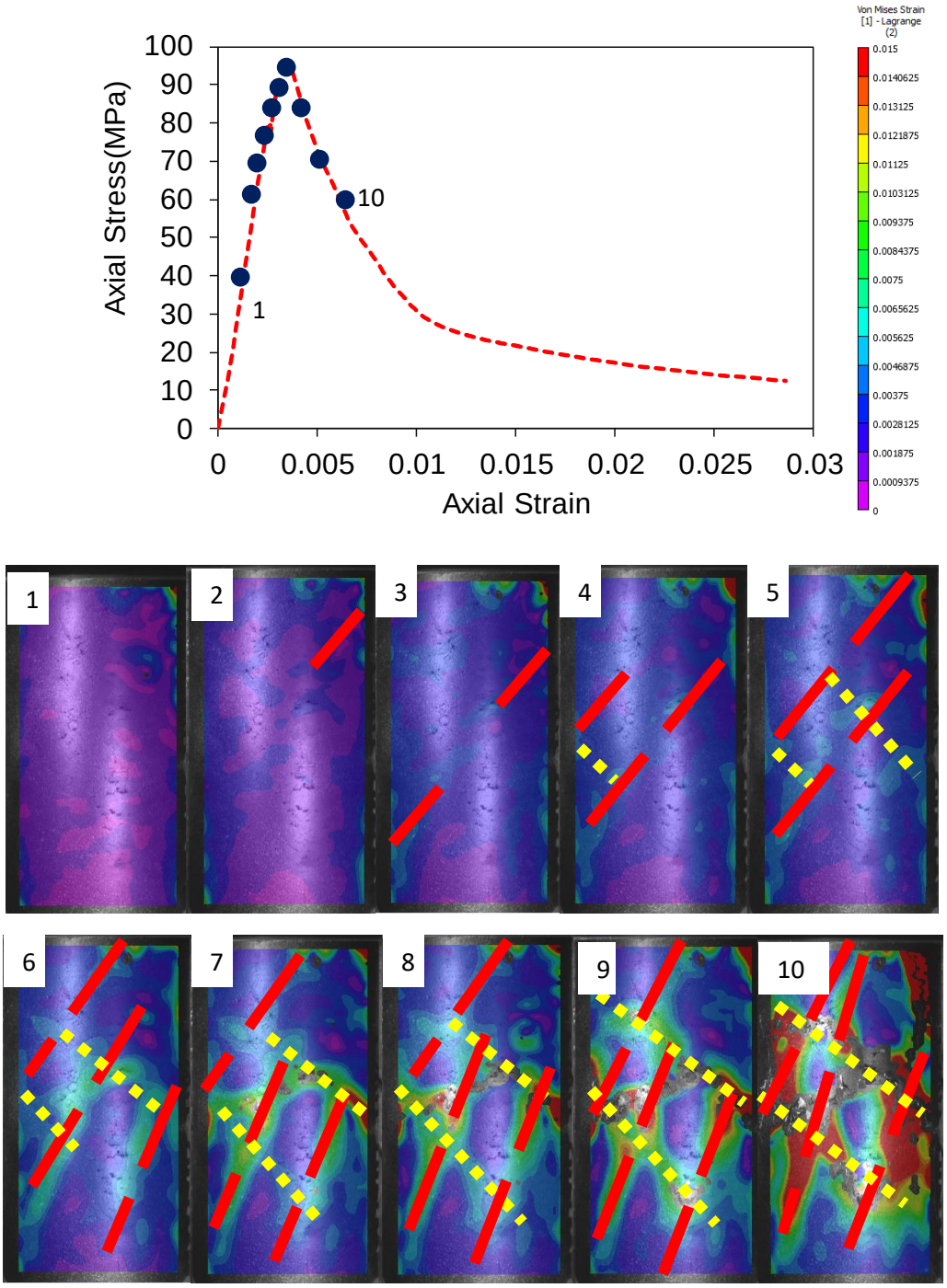

Figure 134- Bridging procedure in VHCS

10.3.3 Development of strains along specimen height

The evolution of Von Mises strain along the specimen height is presented in Figs. 135-138 for unconfined and BFRP, CFRP and GFRP-confined concrete specimens. The selected profile located at middle of specimens' front surface as can be seen in Fig. 53 and referred as v-2 in this figures. Additionally and same as previous section, the synchronization between the

obtained Von Mises strain by DIC along the profile and axial stress-strain curves are provided. As can be seen in Fig. 135, the maximum Von Mises strain for UHSSFRC occurred in the upper region, with little to no strain development elsewhere along the specimen height. Furthermore, it can be seen in Fig. 135 that the initiation of localization occurred at point two for NSC opposite to HSC and VHSC which showed later initiation, i.e. between points 2-3. It is mention worthy to indicate again that although this figure is able to mark the initiation of localization accurately for one profile, using this method still is difficult due to change profiles' shape from one profile to another one. This indicates that the accurate determination of localization onset needs to study more than one profiles over specimens' surface which makes this investigation time consuming. Same as localization initiation study, although the evolution of localization from initiation to failure can be investigated in details using one profile over specimens' surface as shown in Fig. 9, this examination is very difficult due to change of results from one profile to another, as can be seen in Fig. 128. It should be said that this different obtained behavior from one profile to another one is due to existence of different local shear planes in specimens which govern the overall specimens' behavior as explained before [27, 191].

Comparing Fig.135 with Figs. 136-138 illustrates the different Von Mises strain development along the height of FRP-confined concrete specimens compared to unconfined specimens. As can be seen in Figs 136-138, the maximum Von Mises strain was observed approximately at the middle height of FRP-confined specimens except for BFRP 2, 4 and 6 layers which have lower K_l/f'_{co} compared to other FRP-confined specimens. Ignoring the statistical aspect (e.g. inhomogeneity of an intact material) that may influence where localization takes place, the obvious difference between localized behaviors in Figs. 136-138 compared to Fig. 135 can be seen which can be connected to the macro responses of the specimens under compression. Confinement provided by the FRP jacket altered the deformation localization trend and this

significantly changed the specimen's behavior as an evident consequence. Finally, it should be said that CFRP specimens showed a sudden rupture of FRP-confinement opposite to other specimens with more gradual loss of strength. Same as obtained results for unconfined specimens, the initiation and evolution of localization can be examined in-depth by using different types of profiles such as horizontal and vertical; however, this examination is difficult due to need of many profiles to have accurate outcome.

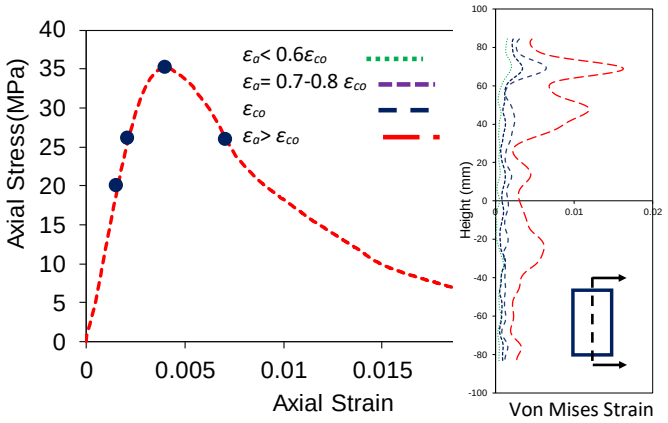

a) NSC

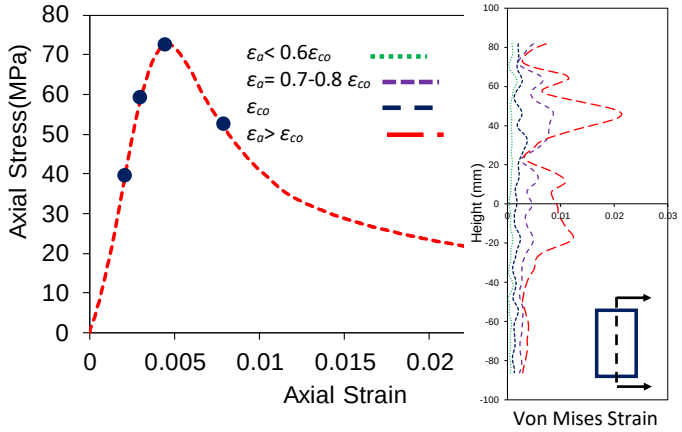

b) HSC

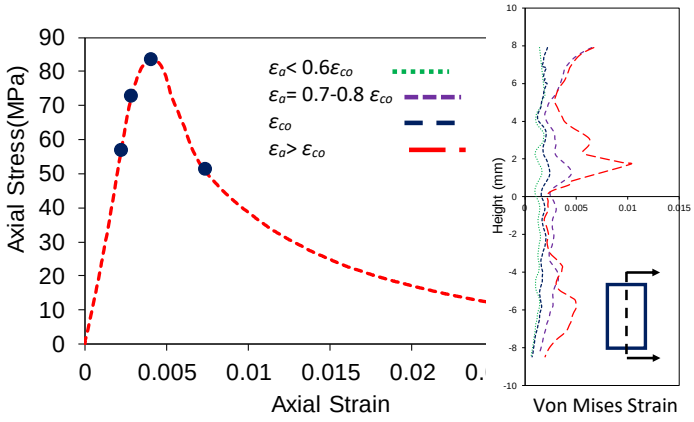

c) VHSC

Figure 135- Comparison of Von Mises strain development for unconfined specimens

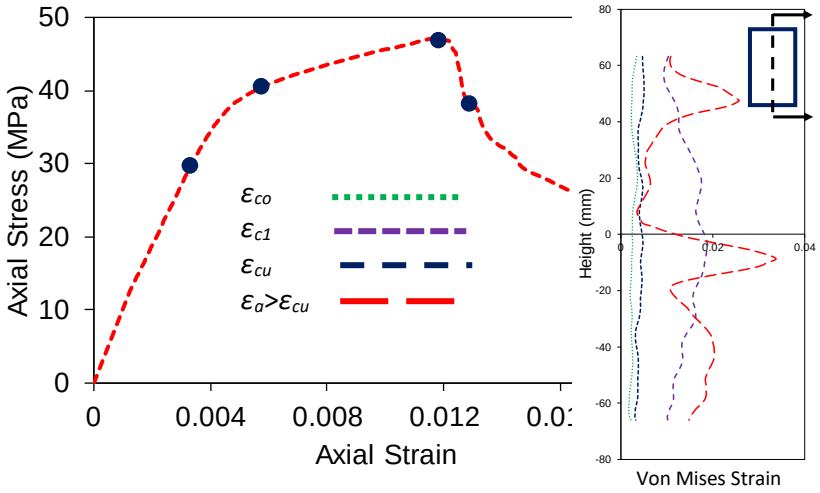

a) BFRP-2 layers confined specimen (NSC)

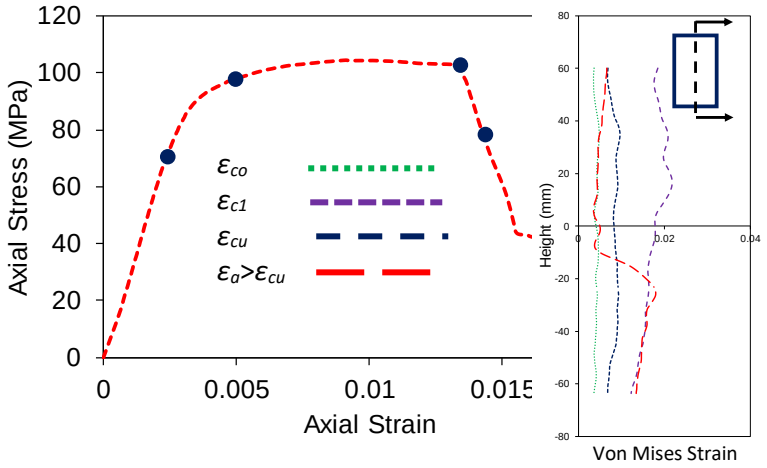

b) BFRP-4 layers confined specimen (HSC)

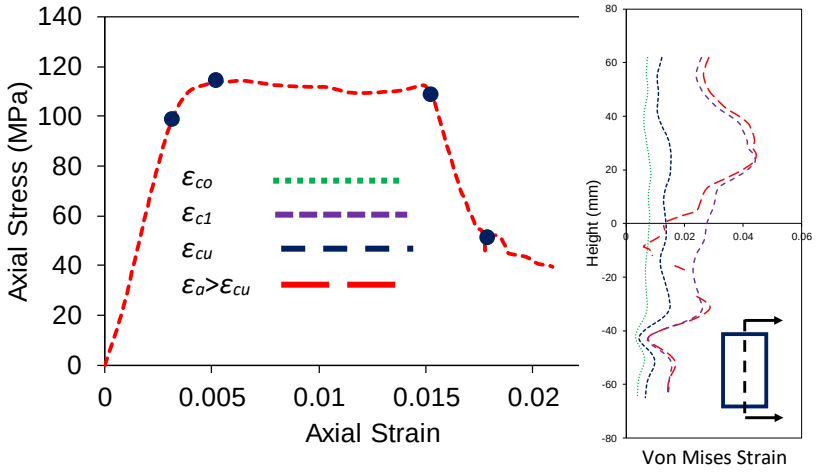

c) BFRP-6 layers confined specimen (VHSC)

Figure 136- Comparison of Von Mises strain development for BFRP-2 layers, BFRP-4 layers FRP and BFRP-6 layers confined specimens

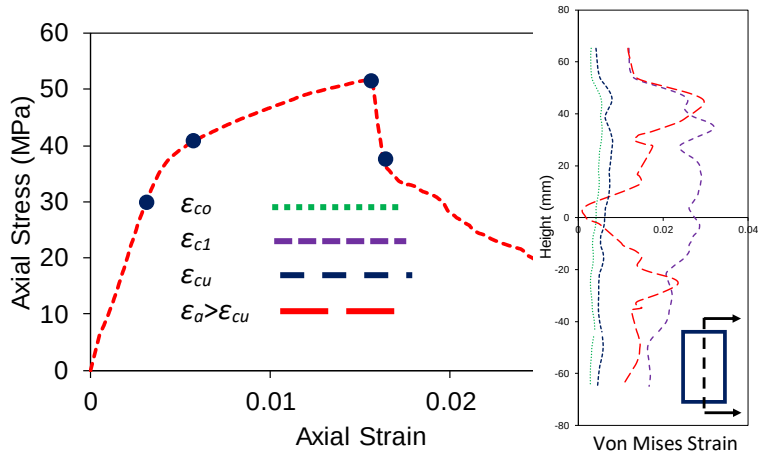

a) BFRP-3 layers confined specimen (NSC)

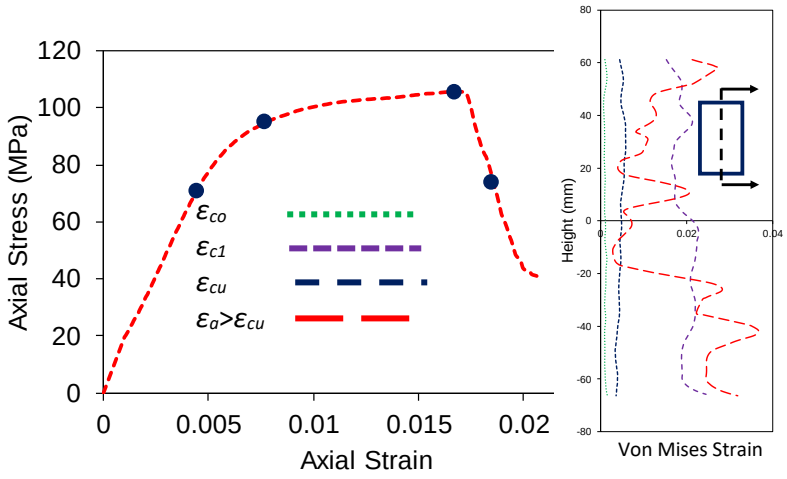

b) BFRP-6 layers confined specimen (HSC)

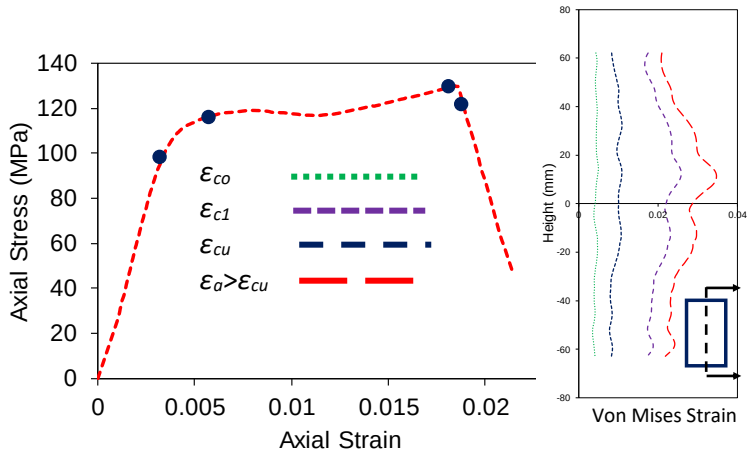

c) BFRP-9 layers confined specimen (VHSC)

Figure 137-Comparison of Von Mises strain development for BFRP-3 layers, BFRP-6 layers FRP and BFRP-9 layers confined specimens

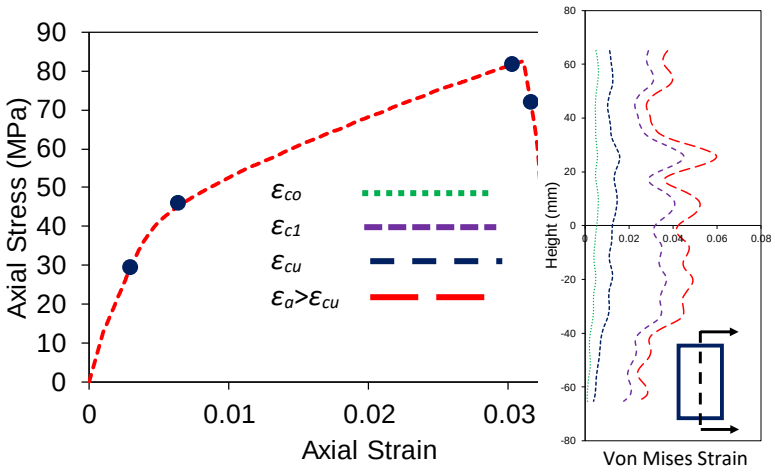

a) CFRP-1 layers confined specimen (NSC)

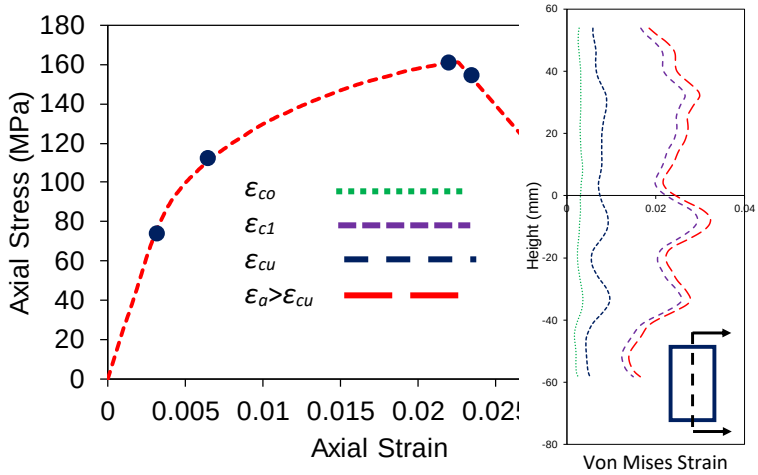

b) CFRP-21 layers confined specimen (HSC)

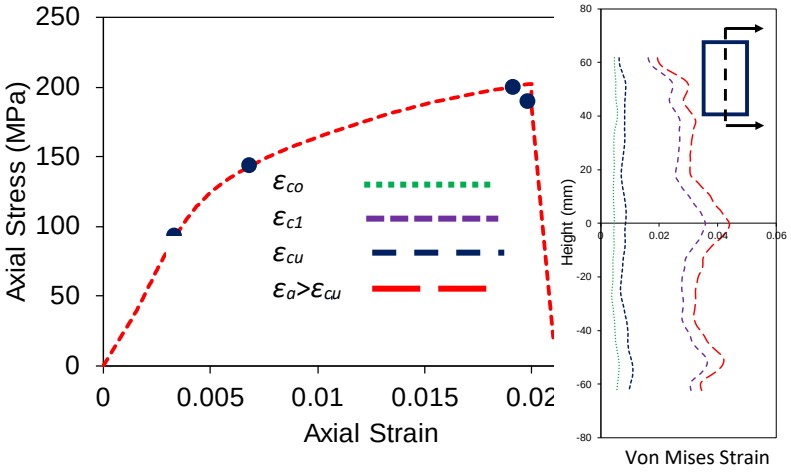

c) CFRP-3 layers confined specimen (VHSC)

Figure 138-Comparison of Von Mises strain development for CFRP-1 layer, CFRP-2 layers FRP and CFRP-3 layers confined specimens

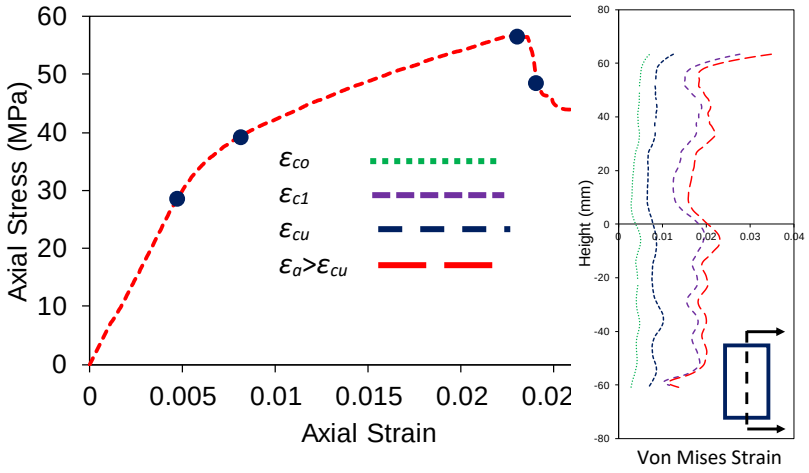

a) GFRP-1 layers confined specimen (NSC)

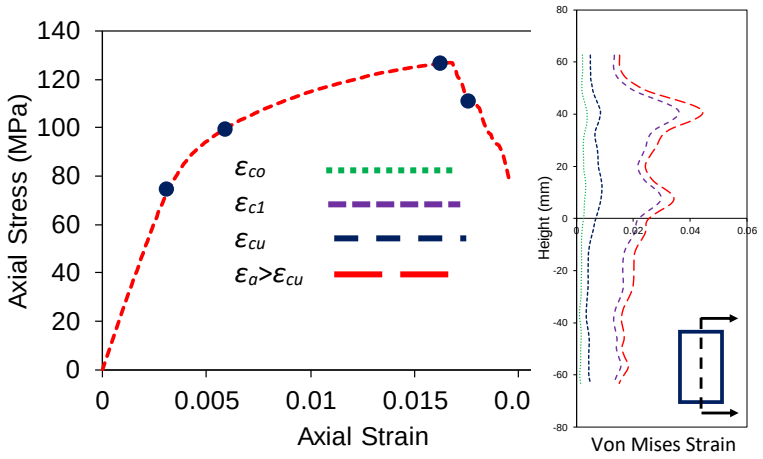

b) GFRP-2 layers confined specimen (HSC)

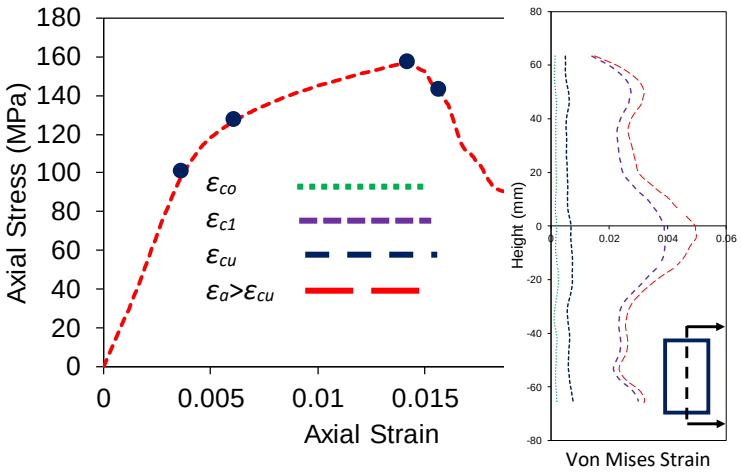

c) GFRP-3 layers confined specimen (VHSC)

Figure 139- Comparison of Von Mises strain development for GFRP- 1 layer, GFRP-2 layers FRP and GFRP-3 layers confined specimens

10.4 Correlation between mechanical response of UHSSF-FRP-confined concrete and strain localization

It is well established that to interpret the deformation localization, localization characteristics should be accurately described and quantified. These parameters are the onset of localization, characteristics of localization evolution to failure and correlation of these characteristics to mechanical response of materials. Determination of these parameters helps significantly in developing/validating a constitutive model which predict the mechanical behavior of materials or structural system. The following sections present a potential method to describe and enumerate the characteristics of localization for UHSSFRC and UHSSFR-CFFTs.

10.4.1 Localization onset

It was presented in section 10.3 that using existing method to analyze DIC data is not able to spot accurately the initiation of localization. As discussed previously [239], the behavior of materials inside and outside of localization zone bifurcate by onset of localization and this phenomenon can be used to mark accurately the onset of localization. To illustrate and quantify this phenomenon, i.e. bifurcation, the applied measurement method in experimental program should be able to capture both local and overall deformation of specimens. DIC due to its ability to measure the strain at each point over specimens' surface and the virtual strain option in post processing software which shows overall strain, could be a powerful method to show the bifurcation occurrence [239]. It should be said that the bifurcation shows the behavior of materials inside and outside of the localization zone and it provides material's local-scale response to applied load. The detail of bifurcation analysis by DIC was presented in previous section, i.e. section 6.

Figs. 140-147 illustrate the initiation of localization for UHSSFRC and UHSSFR-CFFTs specimens. In these figures, macro axial stress development, evolution of Von Mises strain of two small zone inside and outside of localization zone (i.e. micro scale)and overall all growth of Von Mises strain (i.e. macro scale) are shown against the time steps. In addition, the recorded

Von Mises strains along the middle profile of specimens' surface in 4 key reference points in axial stress-strain curves, i.e. Figs. 135-139, are added in these figures. It should be said that both sorted and unsorted measured Von Mises strain along the profile are displayed. These additional figures are added to show how bifurcation is able to mark the initiation of localization accurately while the other standard methods of DIC data analysis are not capable. It should be note that the sorting Von Mises strain along the height of specimens as discussed previously in section 6, is the first step to condense the obtained data by DIC.

Fig. 140 shows the obtained results for determination of localization onset of UHSSFR-NSC, HSC and VHSC, respectively. Comparing Figs 140a, c and e with Figs. 140 b, d and f shows evidently the initiation of localization by studying the behavior of material inside and outside of localization zone. It also can be seen in Figs. 140a, c and e that the NSC, HSC and VHSC specimens showed similar Von Mises strain behavior for inside and outside of the shear zone before separation point where this bifurcation occurred between 50-80% of f'_{co} dependent on types of concrete. It should be noted that the bifurcation point for VHSC appeared later compared to NSC and HSC whereas the VHSC separation was seen at about 70-80 per cent of f'_{co}. In addition, the VHSC specimens showed rapid expansion of Von Mises strain evolution after bifurcation point compared to the other two types of concrete, i.e. NSC, HSC. Furthermore, it can be seen in these figures that the unloading behavior after bifurcation point cannot be seen clearly in UHSSFRC behavior and this can be assigned to existence of fibers and bridging phenomenon where bridging transfer load to all part of specimens. It should be said that the behavior of material inside of shear zone could not be captured after losing of speckle pattern over specimens' surface. In addition, the sorted and unsorted vertical Von Mises strain profiles are presented in this figure to show that initiation of localization can be marked easier by study bifurcation occurrence compared to using profiles.

Figs 141-147 illustrate the bifurcation phenomenon for Von Mises strain evolution in BFRP, CFRP and GFRP specimens. Due to similarity of results few representative specimens were selected to show how different behavior can be observed inside and outside of localization. These selected specimens are BFRP-2&9 layers, CFRP-2&3layers, GFRP-1 layer and GFRP-2 layers. As can be seen Figs. 140-147, the separation point for all FRP-confined specimens was occurred at about 50-80% of f'_{co} in agreement with unconfined specimens and previous sections, i.e section 6 and 7. However, it can be seen in these figures that the unloading behavior did not occurred to failure point (ultimate axial strength (f'_{cc})) where both zones and overall behavior showed an unloading behavior. It should be said again that the speckle pattern which is essential to analyze DIC data, was lost after failure and this can be seen in the figures and the analysis gave the unstable and unreliable results.

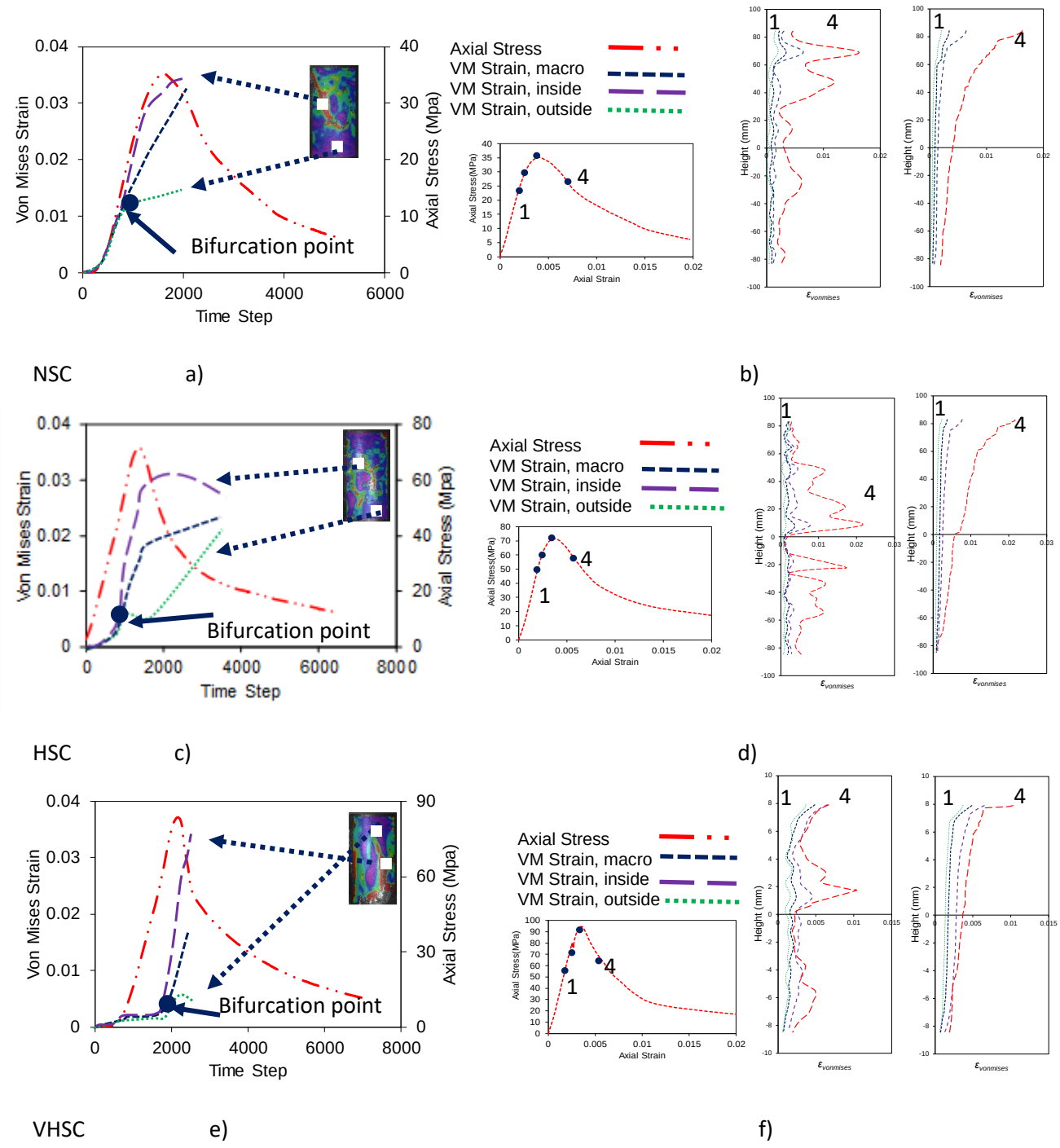

Figure 140-Von Mises strain distribution evolution of unconfined specimens obtained results by DIC

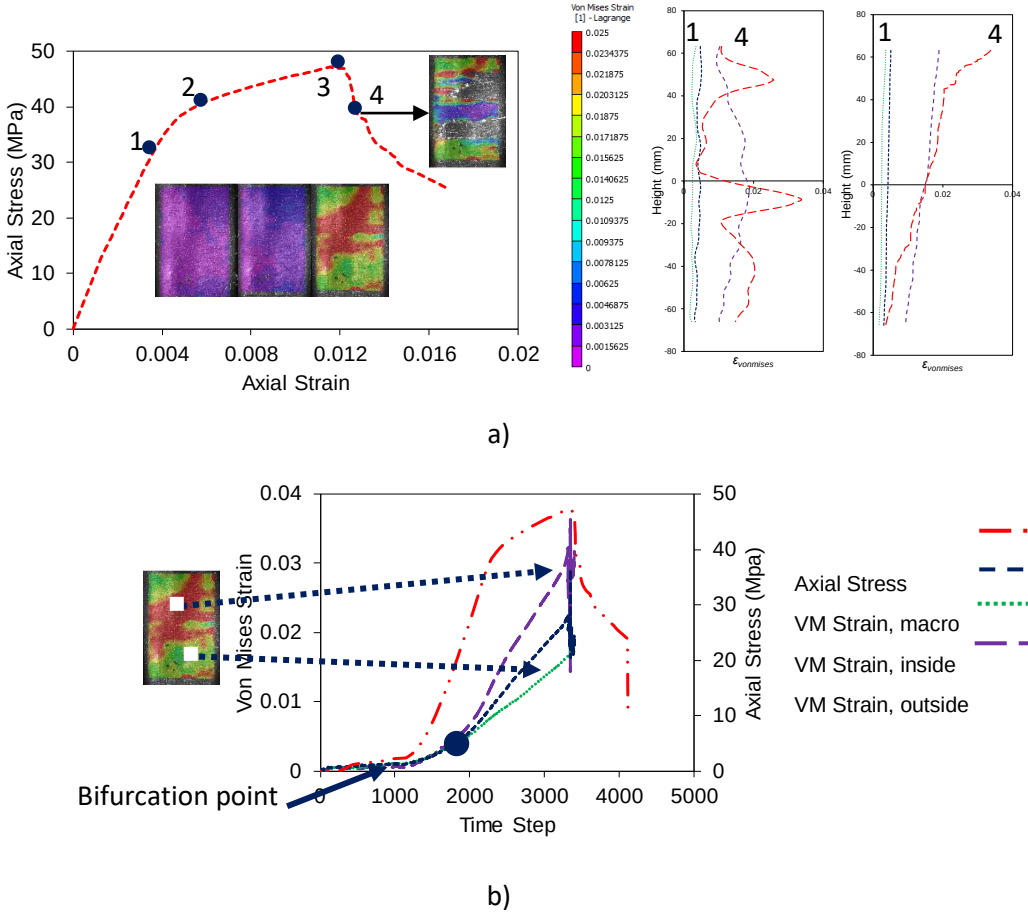

Figure 141- Von Mises strain distribution evolution of BFRP-2 layers (NSC) specimen obtained results by DIC

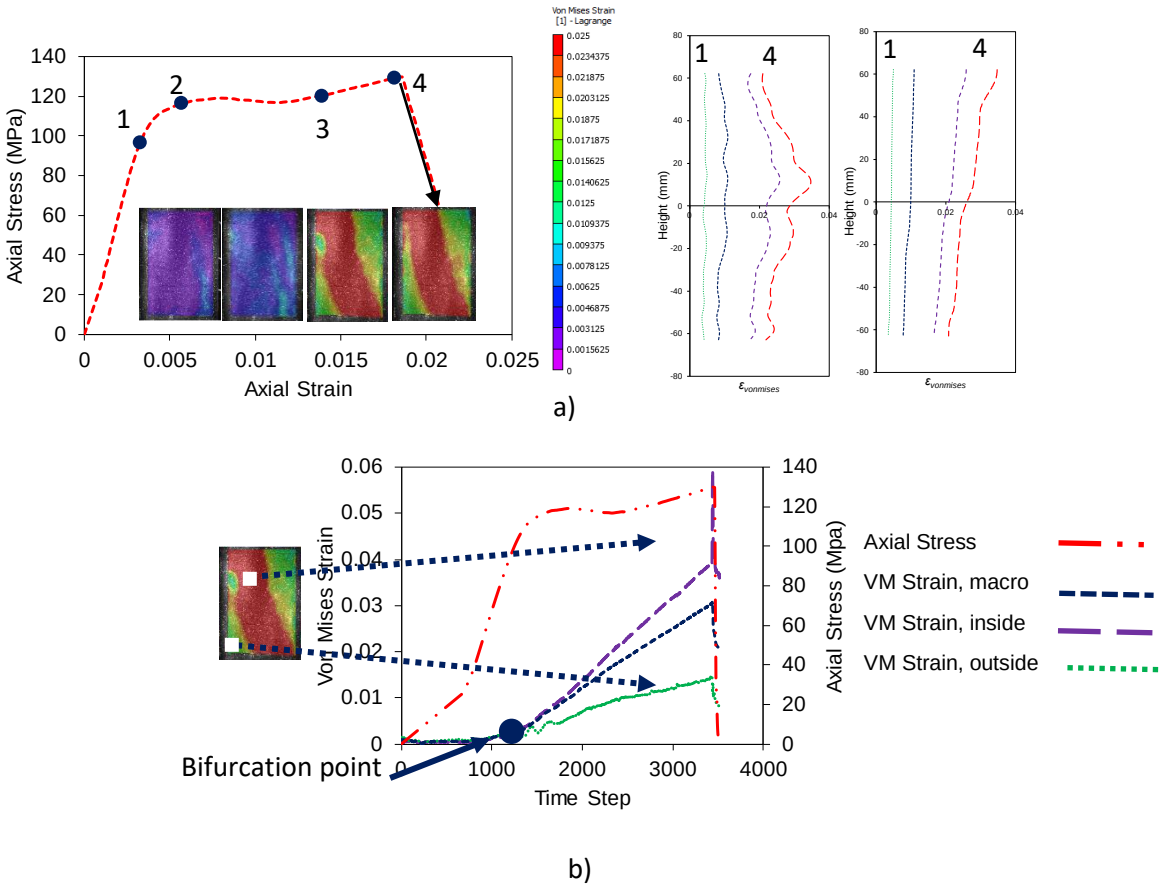

Figure 142- Von Mises strain distribution evolution of BFRP-9 layers (VHSC) specimen obtained results by DIC

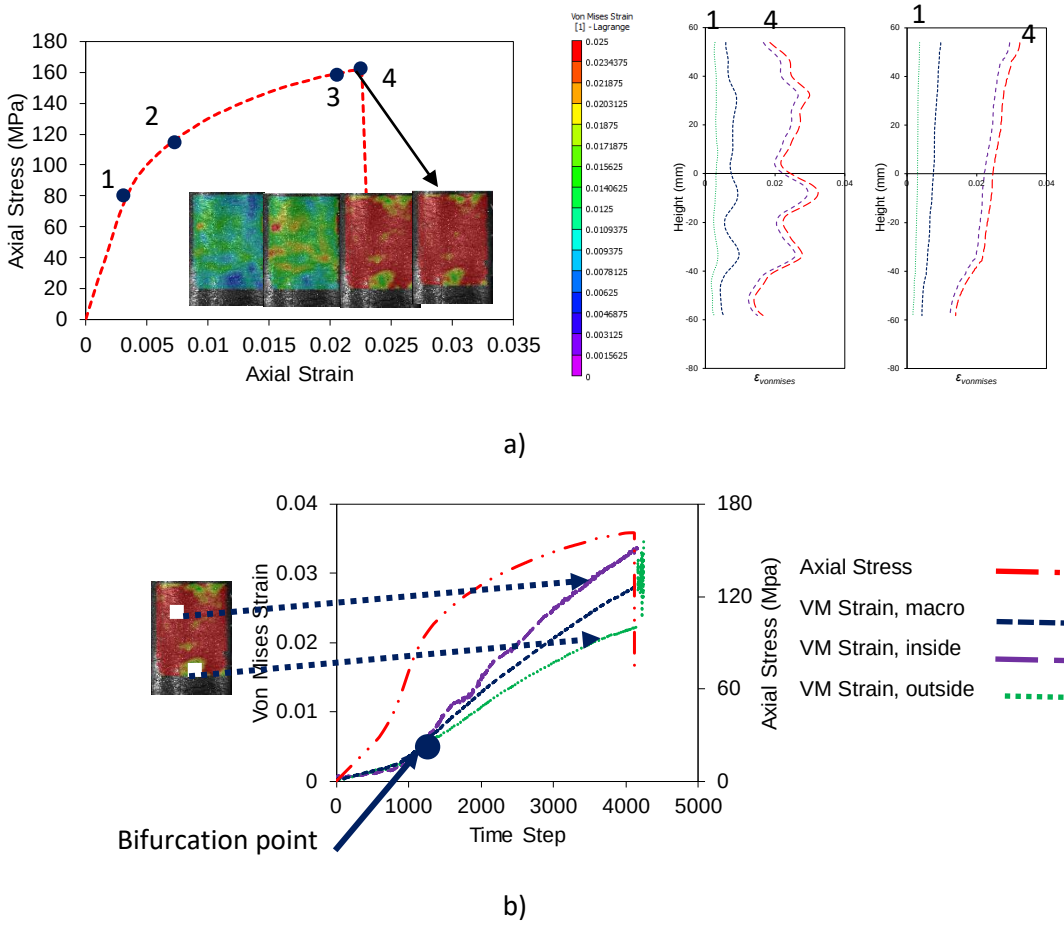

Figure 143- Von Mises strain distribution evolution of CFRP-2 layers (HSC) specimen obtained results by DIC

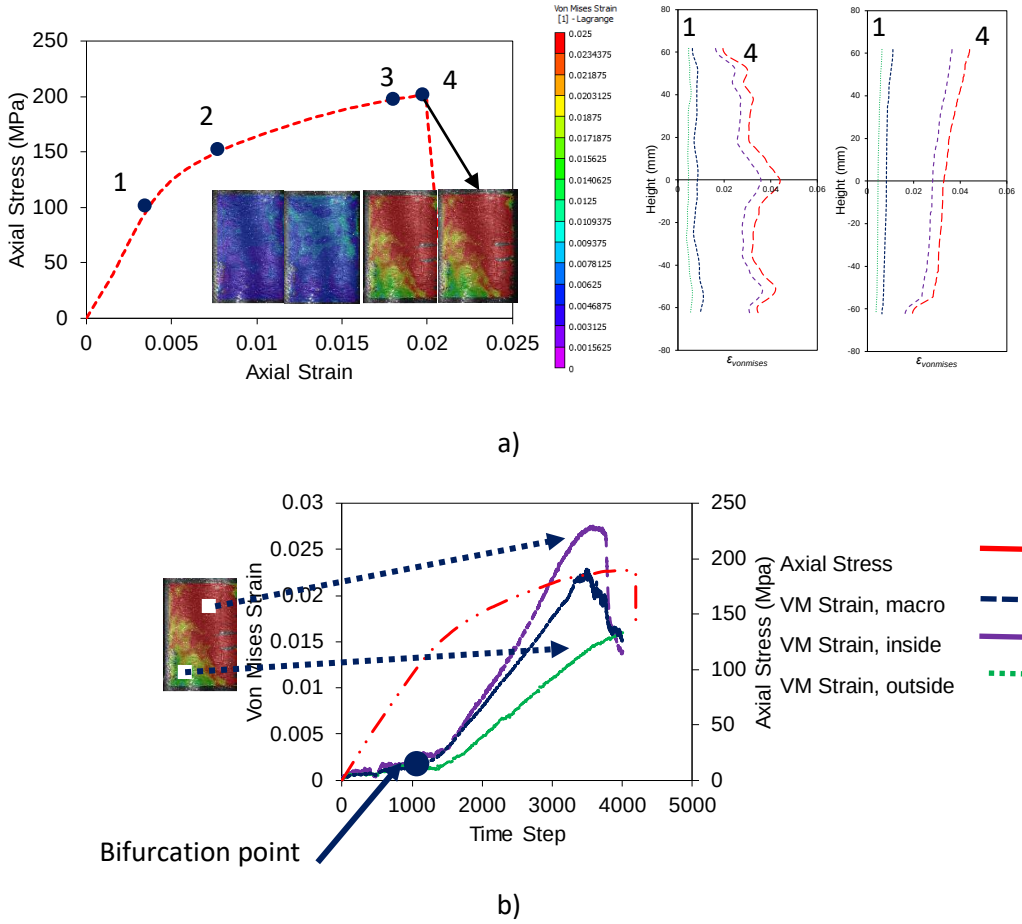

Figure 144- Von Mises strain distribution evolution of CFRP-3 layers (VHSC) specimen obtained results by DIC

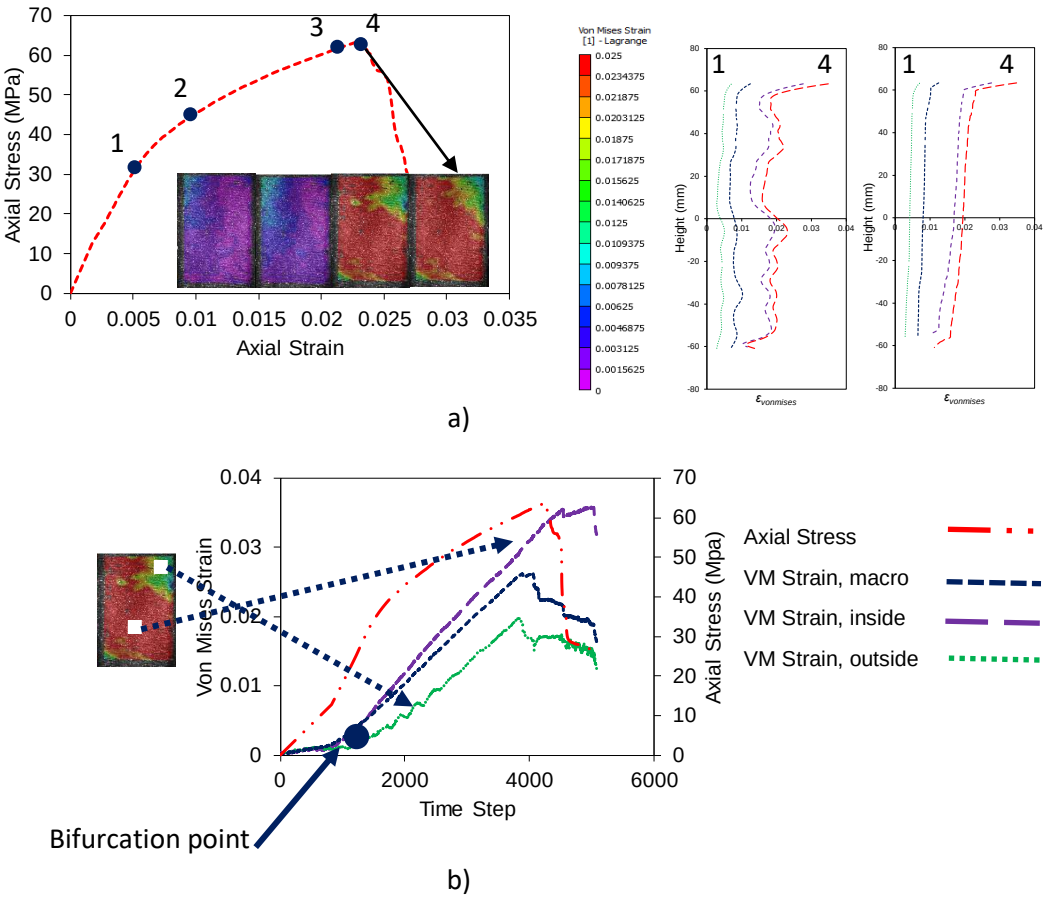

Figure 145- Von Mises strain distribution evolution of GFRP-1 layer (NSC) specimen obtained results by DIC

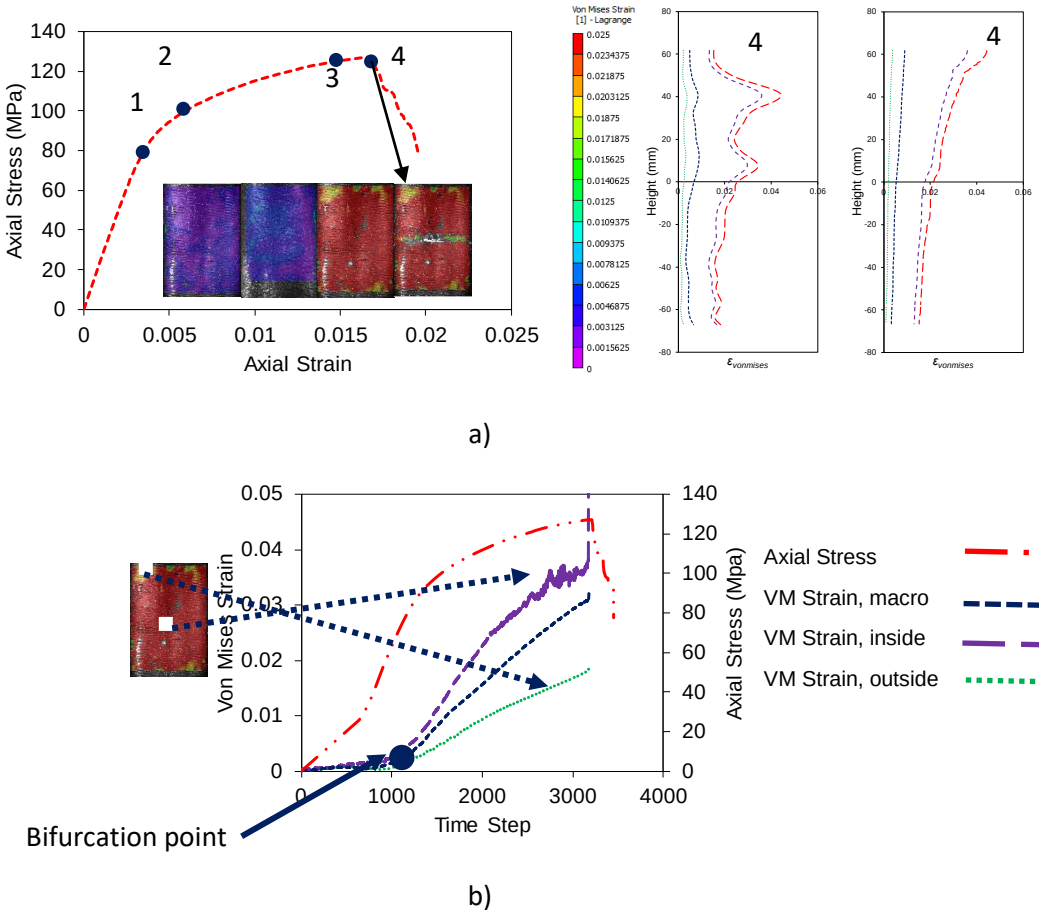

Figure 146- Von Mises strain distribution evolution of GFRP-2 layers (HSC) specimen obtained results by DIC

10.4.2 Shear zone expansion

As explained before, although using the evolution of profiles over specimens' surface can offer approximately accurate localization characteristics, this makes this method as time consuming and difficult technique. To address this problem, Ref. [202] suggested a method and they used the whole obtained Von Mises strain over specimens surface while they condense these data to make them easy to work. Figure 147 shows the shear zone evolution during axial compressive loading for UHSSFRC and UHSSFR-CFFT specimens prepared by suggested method in Ref. [202]. As it is discussed in detail previously [202], the average of obtained Von Mises strain over the specimen surface at each height firstly was calculated. Afterward, these averaged Von Mises strains were sorted in descending order from top to bottom of specimens. Nguyen and Bui [168] and Verma et al. [186] discussed that although this is still not a perfect way to condense the rich DIC data, its usefulness in interpreting and analysing micro-scale structural

data, makes this method attractive in practice. As can be seen in Fig. 147, the evolution of Von Mises strain during the test procedure for both unconfined and FRP-confined specimens can be categorized into two groups. The first group represents steady development of $\varepsilon_{von\ mises}$ during axial compression prior to pre-peak stage along the height of specimens, which can be seen in UHSSFR-CFFTs. Conversely, there is a second group of specimens, i.e. UHSSFRC, which displayed more localized behavior after yielding followed by a strong increase of non-homogeneity during and after specimen failure. Additionally, the shear failure zone for first group expanded gradually during testing whereas the second group showed a rapid transition from homogenous to localized behavior.

Comparing Fig. 147 with obtained results in previous work [202] and section 7 shows that the UHSSFRC outcome had different localization evolution pattern compared to unconfined plain concrete behavior. This different pattern can be explained by the presence of steel fiber in concrete wet mix which changes strongly localized behavior of unconfined plain concrete to more ductile behavior of UHSSFRC. As can be seen in the figures, the well FRP-confined concrete specimens for both plain and UHSSFR-CFFT specimens showed similar behavior (e.g. GFRP, CFRP, BFRP-3, 6 (HSC) and 9 layers) and both set of specimens showed gradual expansion of localization. However, the insufficient confined UHSSFR-CFFT specimens (i.e. BFRP-2 layers, BFRP-4 layers and BFRP-6 layers (VHSC)) displayed approximately similar outcome same as well confined UHSSFR-CFFT specimens opposite to the insufficient FRP-confined plain concrete. This again illustrates the influence of presence of steel fibers in concrete wet mix of the insufficient FRP-confined specimens. Finally, it should be noted that the figures illustrate the unloading procedure after failure point which this unloading behavior varied for different specimens. As explained in previous sections, the speckle patterns were lost partially over the covered area by DIC after failure point. As a consequence, the obtained results after the failure point by DIC cannot be used for any comparison.

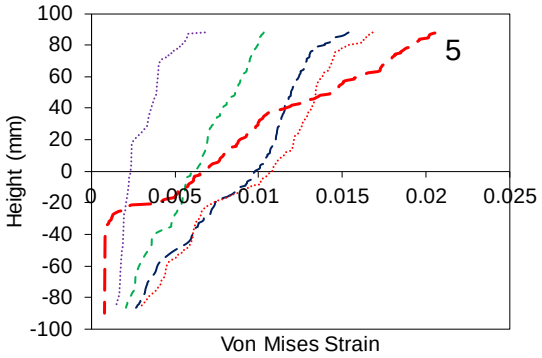

a) NSC

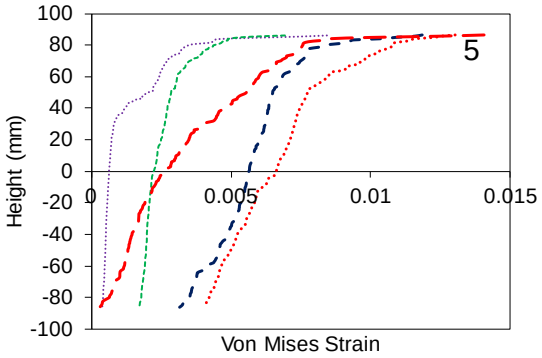

b) HSC

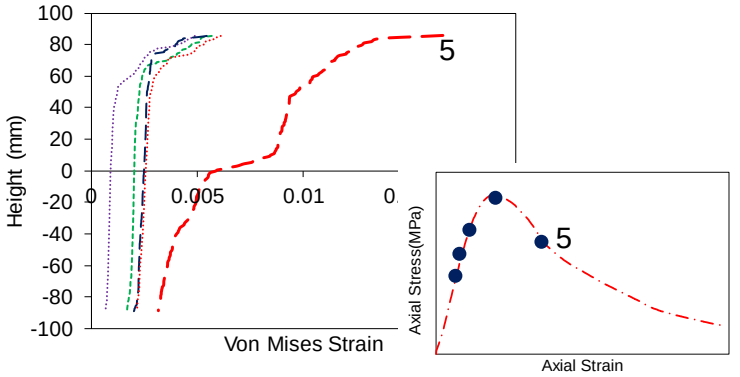

c) VHSC

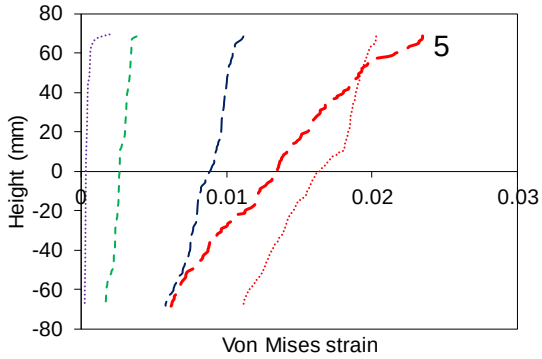

d) BFRP-2 layers NSC

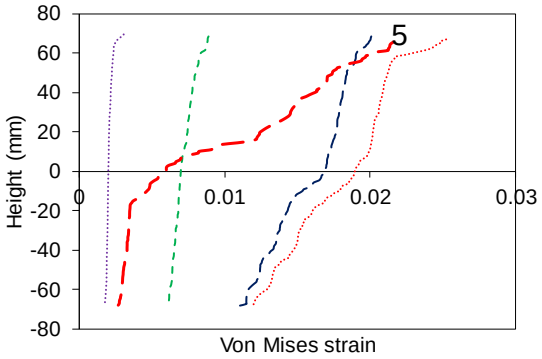

e) BFRP-4 layers HSC

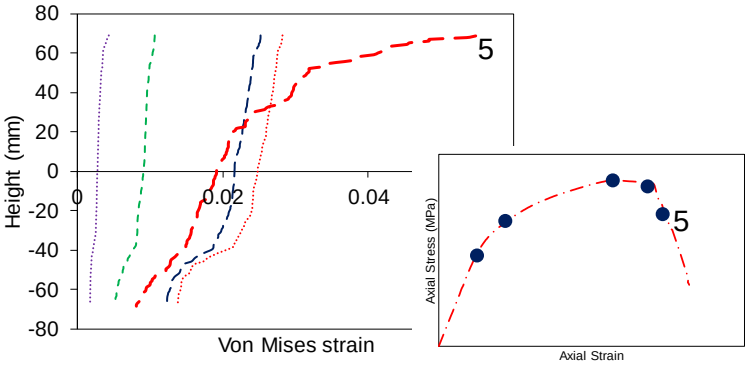

f) BFRP-6 layers VHSC

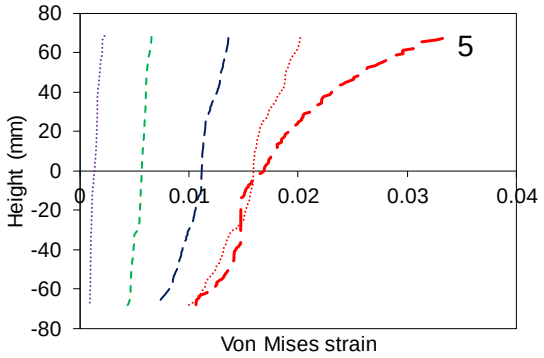

g) BFRP-3 layers NSC

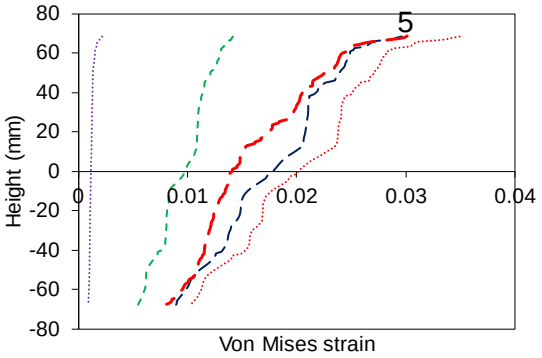

h) BFRP-6 layers HSC

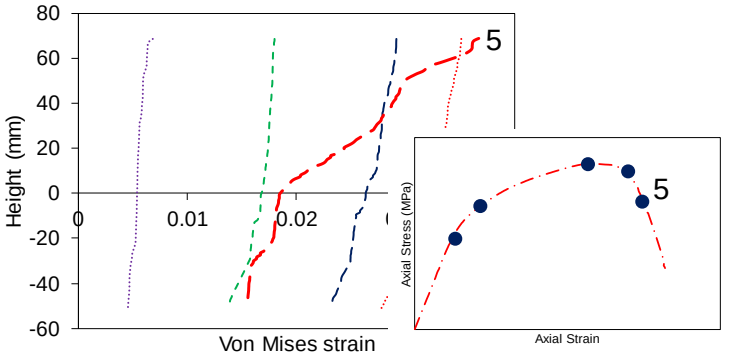

i) BFRP-9 layers VHSC

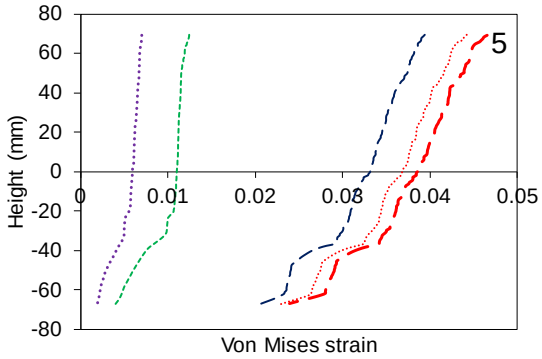

j) CFRP-1 layer NSC

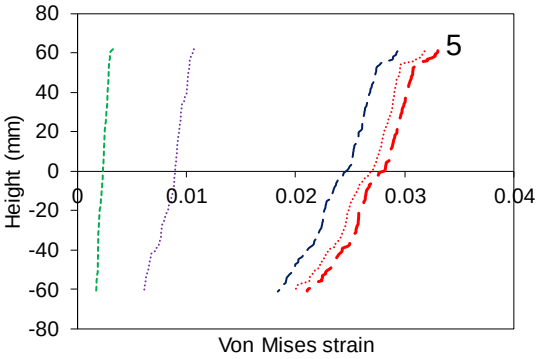

k) CFRP-2 layers HSC

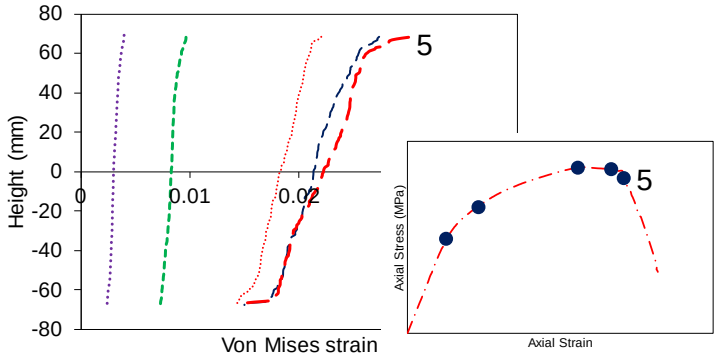

l) CFRP-3 layers VHSC

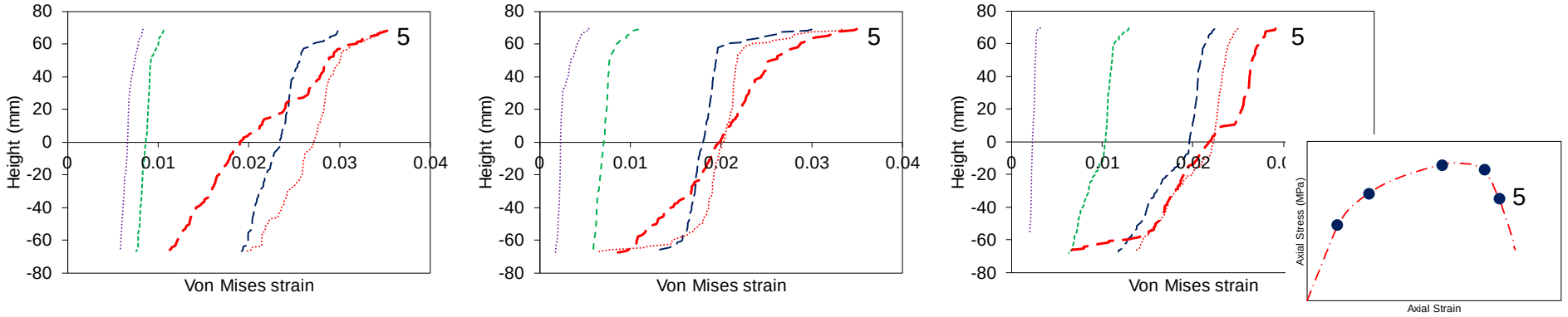

m) GFRP-1 layer NSC n) GFRP-2 layers HSC o) GFRP-3 layers VHSC

Figure 147- Expansion of shear zone along specimens' height

10.5 A new approach to analyze DIC data

As discussed previously, although the suggested technique in section 5 is able to determine accurately the initiation and evolution of localization, these methods cannot correlate these localization characteristics to mechanical response of tested specimens. To provide the mentioned correlation, a new approach was developed in section 6. This method helps to quantify the localization evolution which is an essential element to develop a constitutive model as explained by [156, 168, 169]. The last section of this study will discuss on a potential approach to make all obtained DIC data applicable for mentioned purpose.

10.5.1 Statistical analysis of DIC result

As shown in Nguyen and Bui [168], the raw micro-mechanical data should be analysed and condensed to make them useful in developing and/or validating a constitutive model. To condense the raw obtained data by DIC, a statistical approach was used in this study where this approach was discussed in detail in previous sections, sections 6 and 7. To perform this analysis, the Probability Density Function (PDF) was used to determine the Von Mises strain distribution over the specimen surface as explained in details in section 6. Figs. 148-151 show the experimental distribution of Von Mises strain over the surface of specimens for unconfined and FRP-confined specimens. As can be seen in these figures, the experimental distribution of Von Mises strain over the surface of all specimens kept a similar shape and this shape was similar to PDFs' accumulative curve. As it is discussed previously, the Beta PDF can be used to model the Von Mises strain distribution at each step of the test due to existence of three parameters in this expression. It should be said again that the detail of using Beta-distribution function was presented and discussed in-depth in section 6. Figs. 152-155 show the results of using Beta expression to model the shape of Von Mises strain distribution at different steps of tests. To prepare these figures, three exiting coefficients in Beta expression (i.e. p, q and ξ) were determined experimentally. It can be seen in these figures that there is approximately a good agreement between obtained experimental and theoretical distribution curves. This

approach is able to condense all obtained results by DIC over specimens' surface and use them in the validation or development of a constitutive model. It should be noted that this pattern was observed in this study and more detailed study is needed to generalize this finding. Moreover, it should be said that the similarity between the experimental and theoretical shape of distribution was lost after failure point, although the shape of distribution still can be modelled with a combination of two Beta functions with different parameters. As a last step, the obtained experimental coefficients in Beta distribution expression (i.e. p, q and ξ) should be correlated to mechanical characteristics of tested materials or structural system as performed in section 6. In this study, this indicates that the experimental p, q and ξ should be correlated to f'_{co}, ε_{co}, K_l, K_l/f'_{co} and other mechanical characteristics of structural system such as t_f and aspect ratio similar to section 6. However, this correlation is not performed in this section due to existing various numbers of mechanical characteristics such as f'_{co}, ε_{co}, K_l, K_l/f'_{co}, f_{lu}/f'_{co} and hoop rupture strain ($\varepsilon_{h,rup}$) and few experimental datasets in this study. To conduct this correlation, more experimental data with focusing on variation of influential parameters is essential.

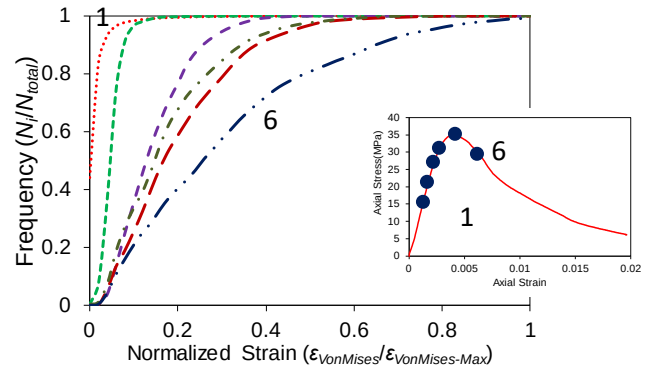

a) NSC

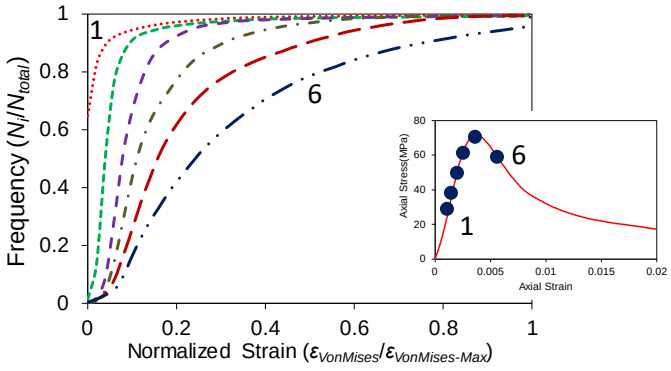

b) HSC

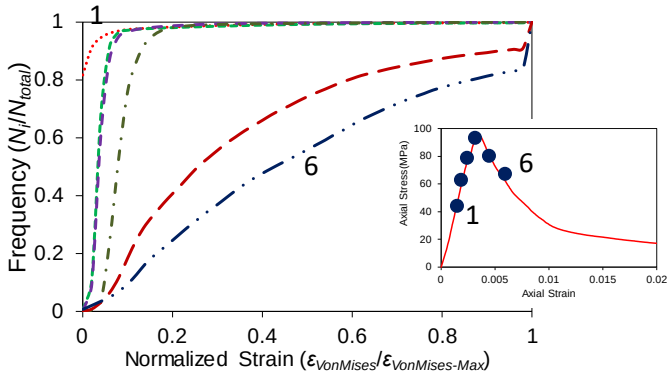

c) VHSC

Figure 148- Experimental accumulative Von Mises strain distribution curve over specimen surface for unconfined specimens

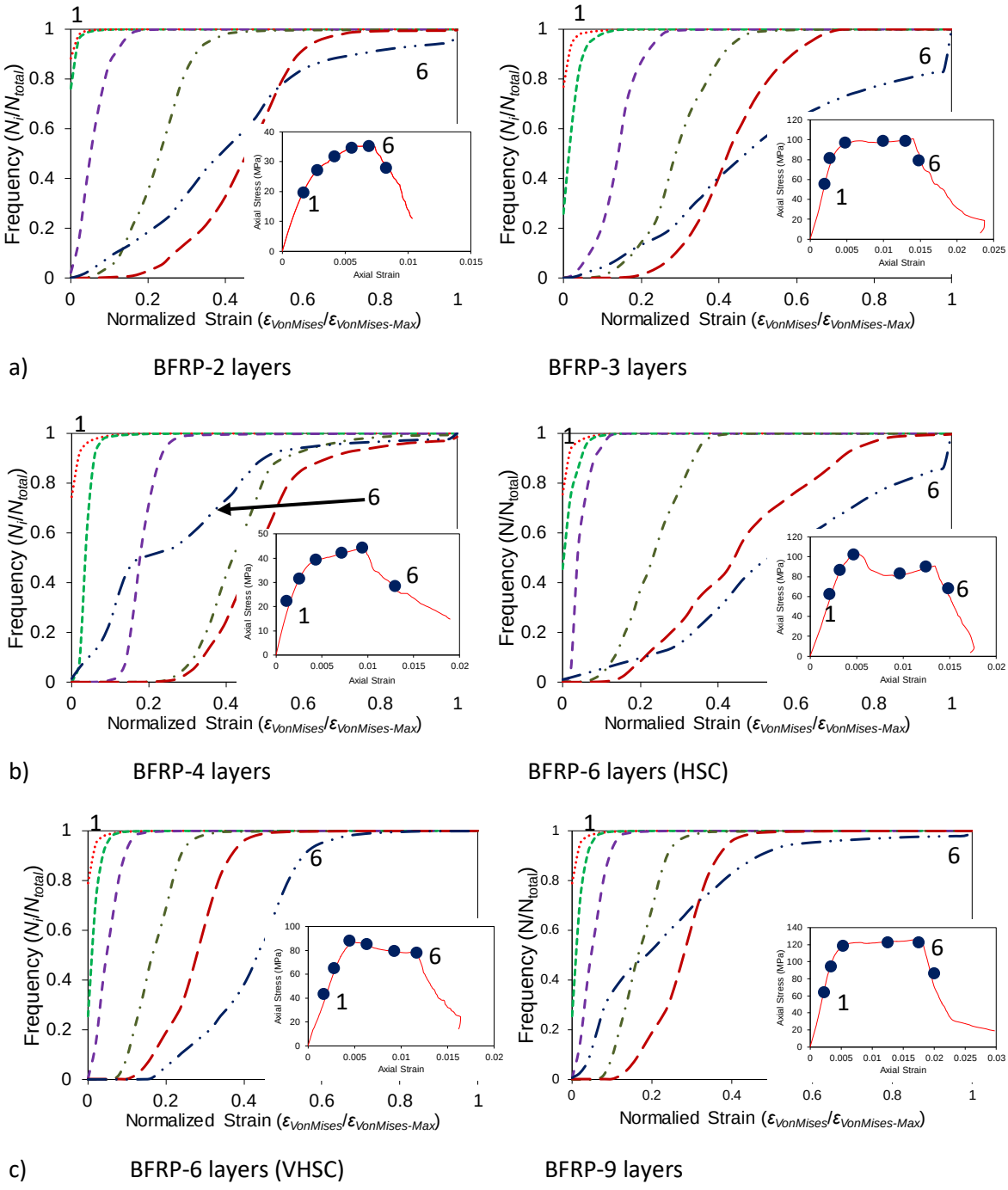

Figure 149- Experimental accumulative Von Mises strain distribution curve over specimen surface for BFRP-confined specimens

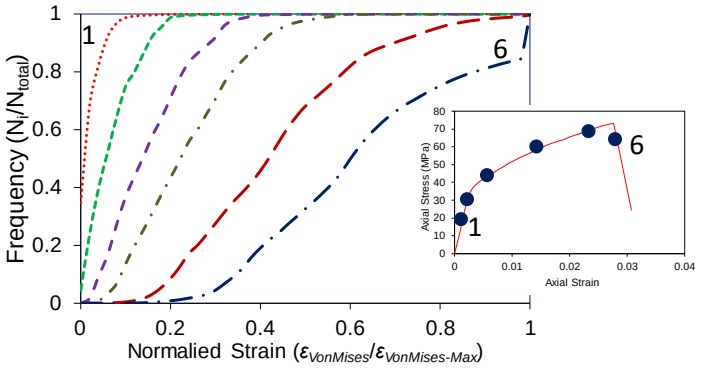

a) CFRP-1 layer

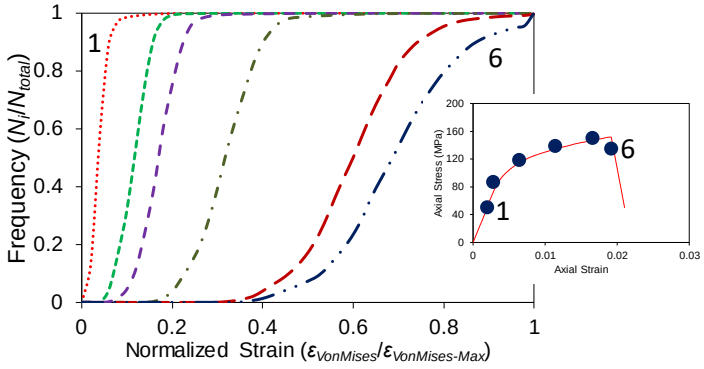

b) CFRP-2 layers

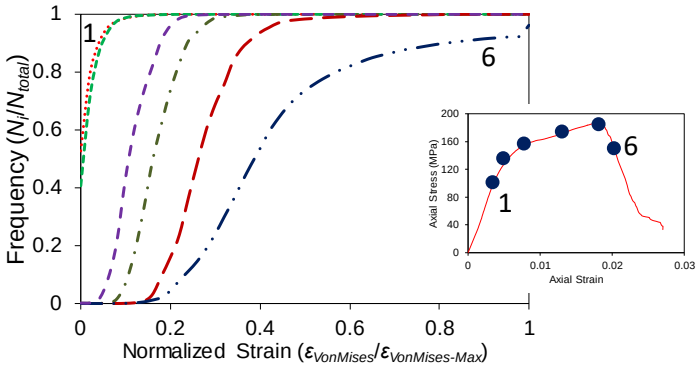

c)

Figure 150-Experimental accumulative Von Mises strain distribution curve over specimen surface for CFRP-confined specimens

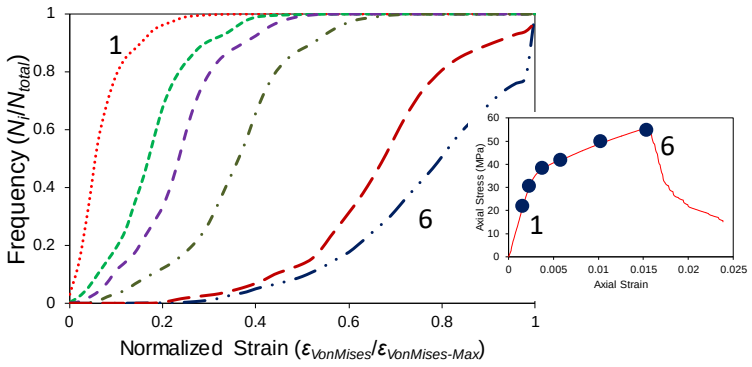

a) GFRP-layer

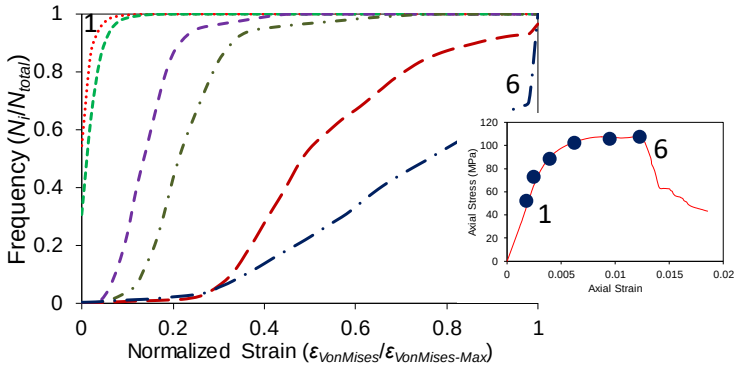

b) GFRP-2 layers

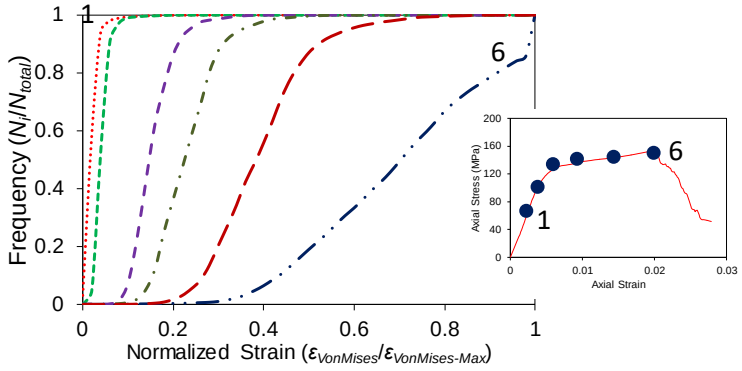

c) GFRP-3 layers

Figure 151-Experimental accumulative Von Mises strain distribution curve over specimen surface for GFRP-confined specimens

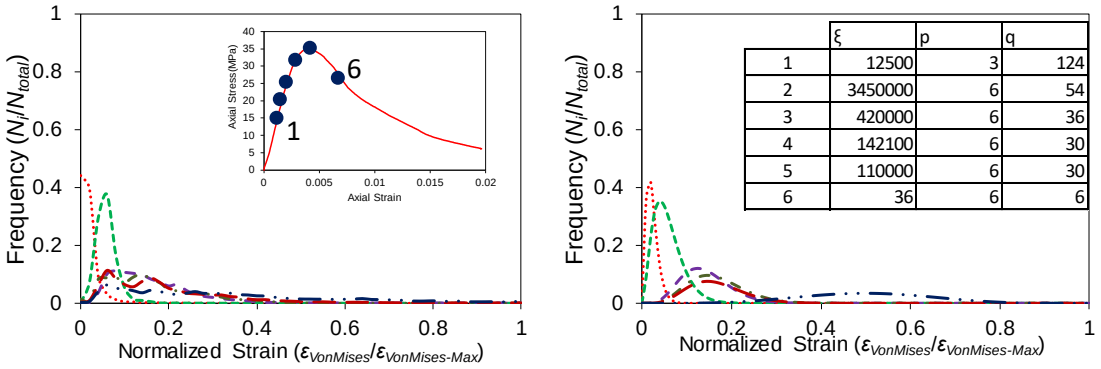

	ξ	p	q
1	12500	3	124
2	3450000	6	54
3	420000	6	36
4	142100	6	30
5	110000	6	30
6	36	6	6

a) NSC

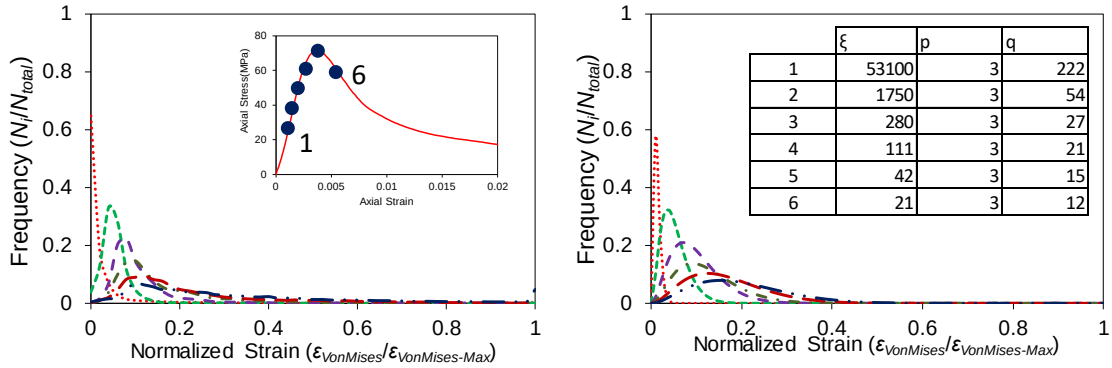

	ξ	p	q
1	53100	3	222
2	1750	3	54
3	280	3	27
4	111	3	21
5	42	3	15
6	21	3	12

b) HSC

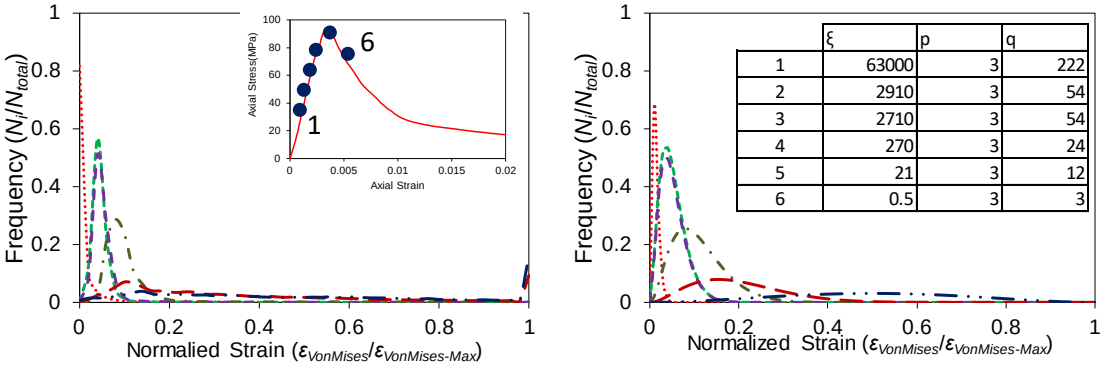

	ξ	p	q
1	63000	3	222
2	2910	3	54
3	2710	3	54
4	270	3	24
5	21	3	12
6	0.5	3	3

b) VHSC

Figure 152- Experimental Von Mises strain distribution over specimen surface for unconfined specimens

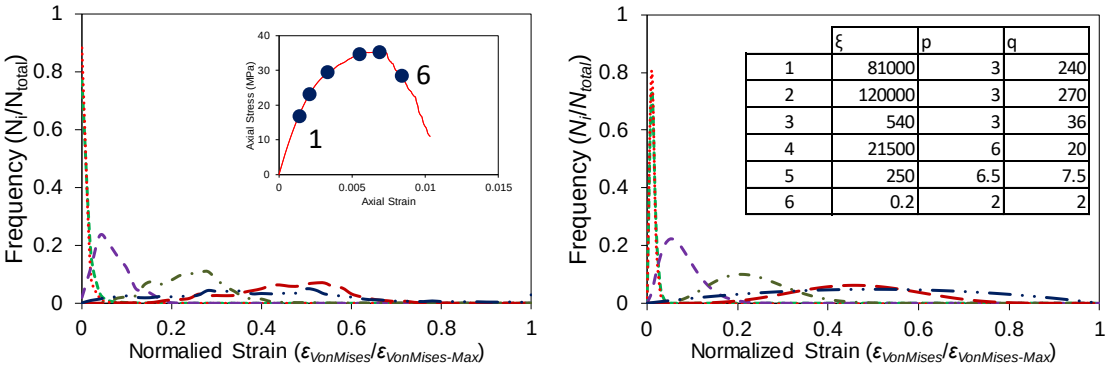

	ξ	p	q
1	81000	3	240
2	120000	3	270
3	540	3	36
4	21500	6	20
5	250	6.5	7.5
6	0.2	2	2

a) BFRP-2 layers

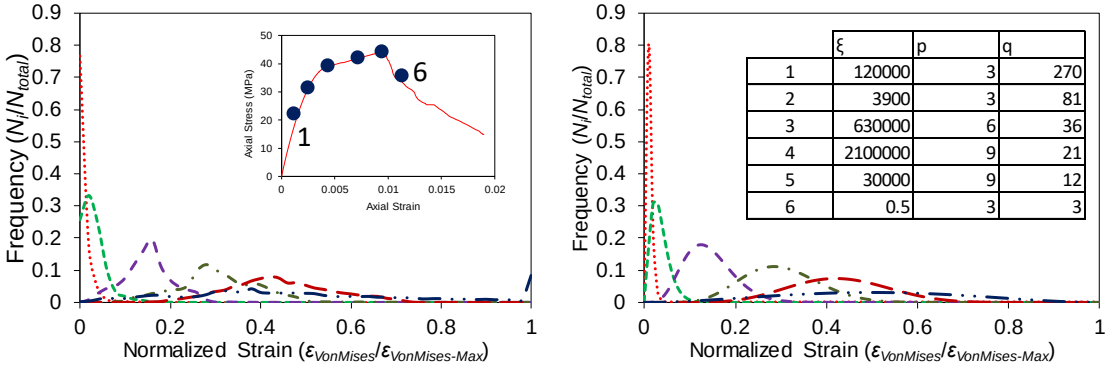

	ξ	p	q
1	120000	3	270
2	3900	3	81
3	630000	6	36
4	2100000	9	21
5	30000	9	12
6	0.5	3	3

b) BFRP-3 layers

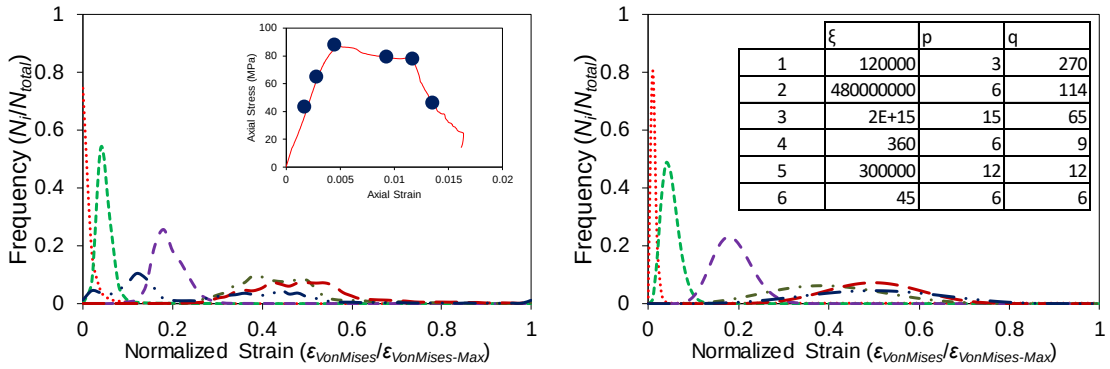

	ξ	p	q
1	120000	3	270
2	480000000	6	114
3	2E+15	15	65
4	360	6	9
5	300000	12	12
6	45	6	6

c) BFRP-4 layers

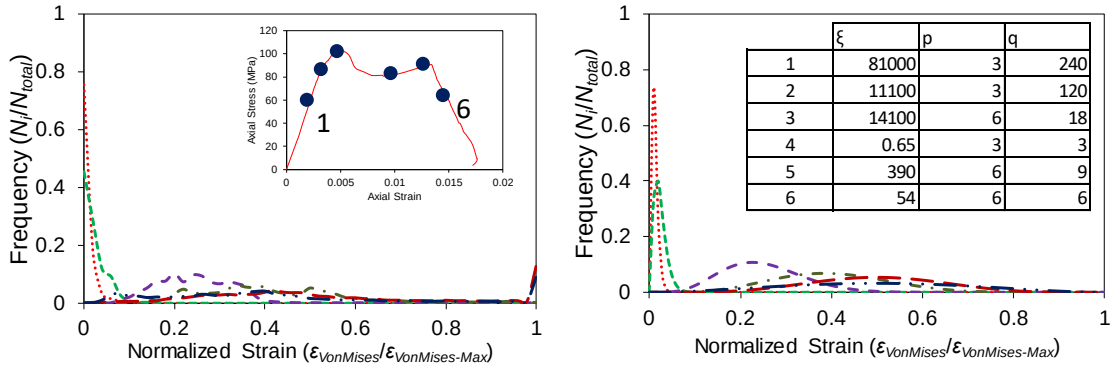

	ξ	p	q
1	81000	3	240
2	11100	3	120
3	14100	6	18
4	0.65	3	3
5	390	6	9
6	54	6	6

d) BFRP-6 layers (HSC)

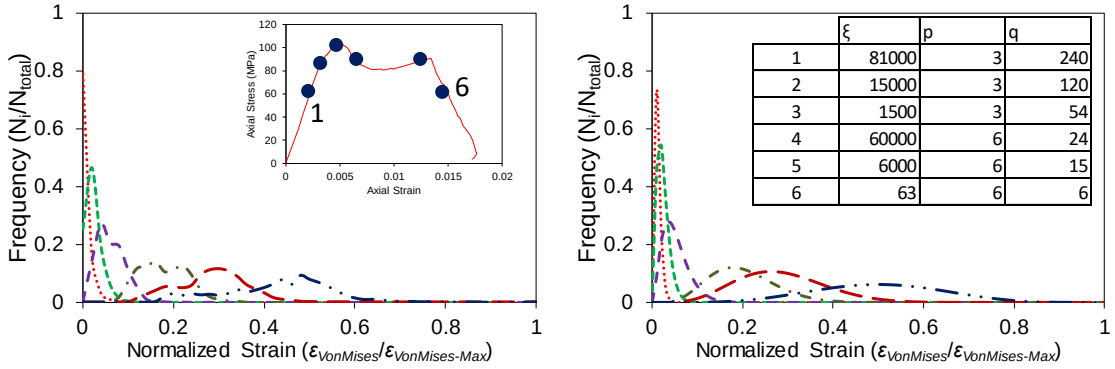

	ξ	p	q
1	81000	3	240
2	15000	3	120
3	1500	3	54
4	60000	6	24
5	6000	6	15
6	63	6	6

e) BFRP-6 layers (VHSC)

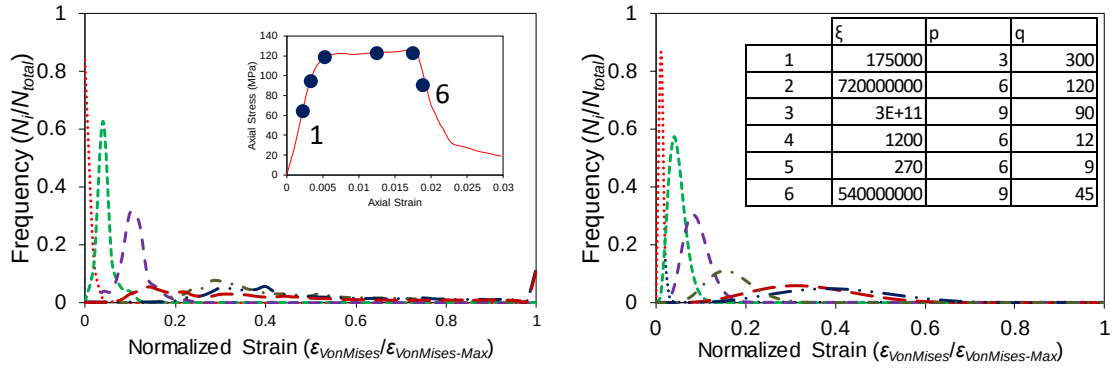

	ξ	p	q
1	175000	3	300
2	720000000	6	120
3	3E+11	9	90
4	1200	6	12
5	270	6	9
6	540000000	9	45

f) BFRP-9 layers

Figure 153-Von Mises strain distribution evolution of BFRP specimens obtained results by DIC

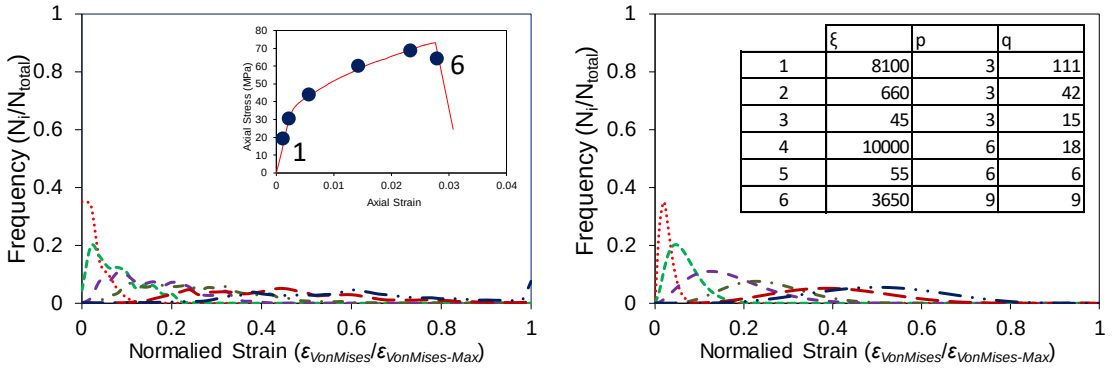

	ξ	p	q
1	8100	3	111
2	660	3	42
3	45	3	15
4	10000	6	18
5	55	6	6
6	3650	9	9

a) CFRP-1 layer

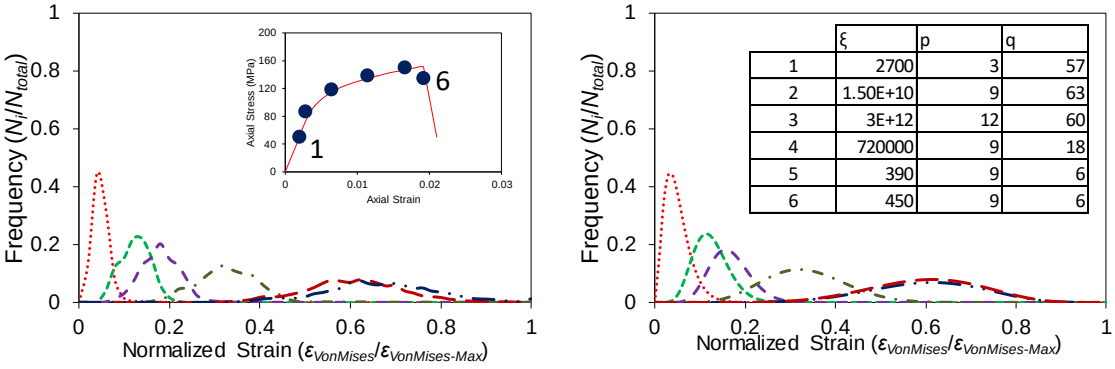

	ξ	p	q
1	2700	3	57
2	1.50E+10	9	63
3	3E+12	12	60
4	720000	9	18
5	390	9	6
6	450	9	6

b) CFRP-2 layers

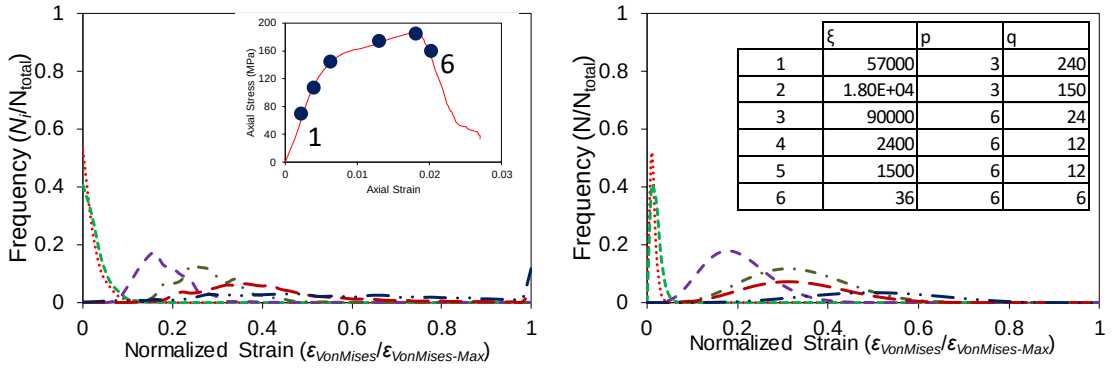

	ξ	p	q
1	57000	3	240
2	1.80E+04	3	150
3	90000	6	24
4	2400	6	12
5	1500	6	12
6	36	6	6

c) GFRP-3 layers

Figure 154-Von Mises strain distribution evolution of CFRP specimens obtained results by DIC

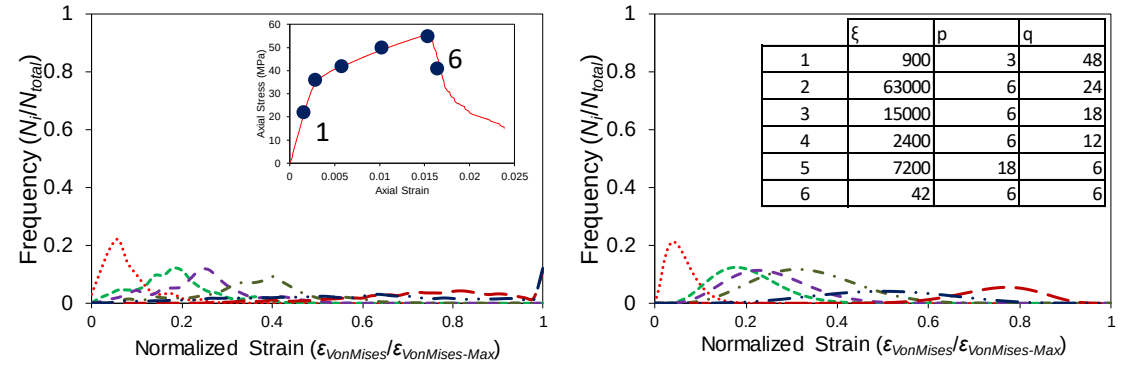

	ξ	p	q
1	900	3	48
2	63000	6	24
3	15000	6	18
4	2400	6	12
5	7200	18	6
6	42	6	6

a) GFRP-1 layer

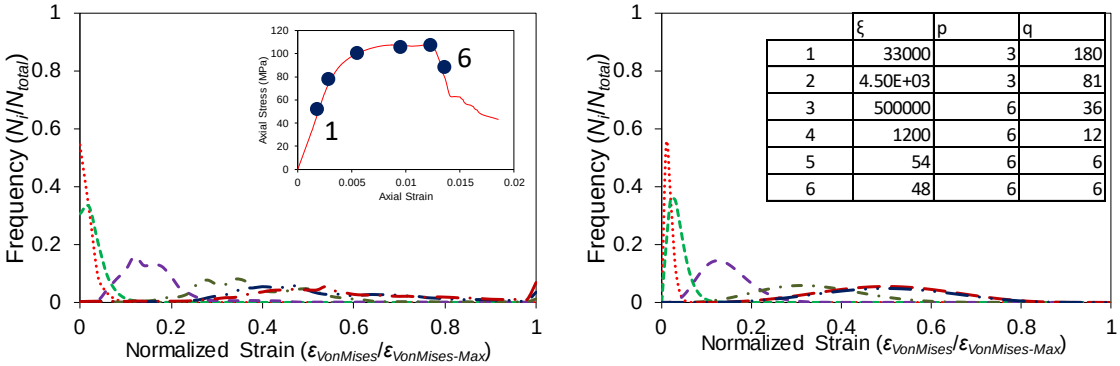

	ξ	p	q
1	33000	3	180
2	4.50E+03	3	81
3	500000	6	36
4	1200	6	12
5	54	6	6
6	48	6	6

b) GFRP-2 layers

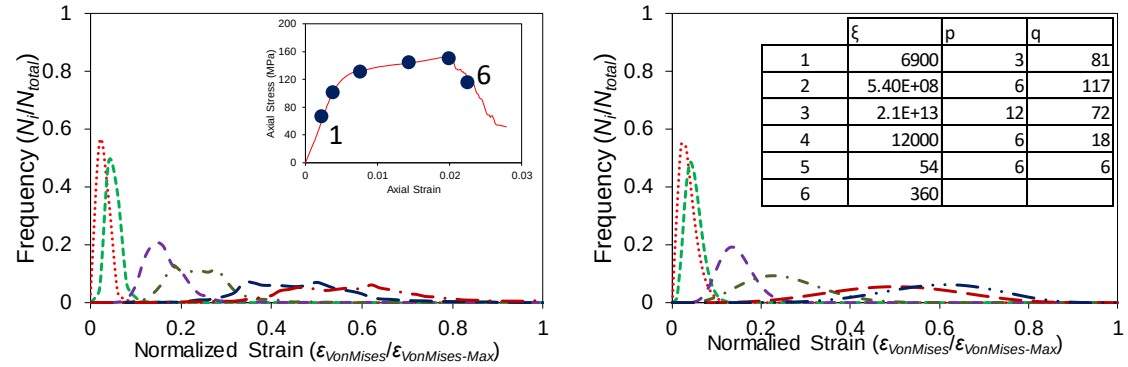

	ξ	p	q
1	6900	3	81
2	5.40E+08	6	117
3	2.1E+13	12	72
4	12000	6	18
5	54	6	6
6	360		

c) GFRP-3 layers

Figure 155-Von Mises strain distribution evolution of GFRP specimens obtained results by DIC

10.6 Conclusions

This section presents the results of an experimental study on the strain localization of UHSSFRC and UHSSFR-CFFT specimens with circular cross-sections under compression. The axial stress-strain curves were obtained and synchronized with captured outcome by DIC system. Based on the results presented in this study, the following conclusions can be drawn:

1-The steel fibers by formation of bridging phenomenon change the crack distribution in UHSSFRC specimens compared to plain unconfined concrete and cracks in UHSSFRCs are distributed all over the surface of specimens. It should be noted that the distribution of steel fiber inside the wet concrete mix and their orientation are significant parameters which influence the crack distribution in unconfined specimens.

2-The thickness of the shear zone in UHSSFR-CFFT specimens increased significantly compared to FRP-confined plain concrete specimens and more homogenous distribution of cracks were observed for CFFT-SFRCs specimens. This can be attributed to the creation of bridges by steel fibers across the cracks and changing behavior of specimens to more ductile behavior.

3-The steel fiber bridging phenomenon started by initiating of localization zone and the steel fibers started to form bridges across this zone. This followed by creating a new strain localized zone approximately perpendicular to the direction of the first localized zone orientation. Due to bridging occurrence, two sets of localization are observed which these two sets are perpendicular together.

4-The unconfined NSC and HSC and VHSC outcome shows a different localization pattern compared to unconfined plain concrete behavior. This different pattern can be explained by the presence of steel fiber in concrete wet mix which changes the strongly localized behavior of unconfined plain concrete to more ductile behavior of UHSSFRC.

5-The NSC, HSC and VHSC specimens showed similar Von Mises strain behavior for inside and outside of the shear zone before bifurcation point. However, the separation point, namely bifurcation point, for VHSC occurs later compared to NSC and HSC where this separation can be seen at about 60-70 per cent of f'_{co}. Moreover, the VHSC specimens show rapid expansion of shear band compared to the other two types of concrete (NSC, HSC).

6-The distribution of Von Mises strain over specimens' surface can be modelled by Beta PDF expression. This technique condense the obtained data by DIC and make these data usable in developing or validating a constitutive model.

Chapter 11: Conclusions and Future work

11.1 Summary

11.1.1 FRP-confined concrete column

This study presents a detailed study on mechanical behavior of FRP-confined high strength concrete (HSC), steel fiber reinforced-CFFTs and PVA fiber reinforced-CFFT. Despite numerous studies on FRP-confined concrete, a detailed studies which show the strain localization characteristics of this structural system and correlate these characteristics to mechanical behavior, does not exist. This study shows the effects of influential parameters on existing stress-strain model for FRP-confined HSC. The influential parameters include both mechanical characteristics of material such as f'_{co} and strain localization and other type of parameters such as measurement methods.

The obtained results from examining existing experimental data show that the measurement method can influence the obtained experimental axial stress-strain curves. The outcome displays that using two different measurement methods, namely Full-height LVDT and Mid-height LVDT, exhibits similar axial stress-strain curve for FRP-confined NSC. However, the outcome shows inconsistency in obtained axial stress-strain curve for FRP-confined HSC using mentioned measurement methods. This inconsistency is due to brittle behavior of HSC and this indicates that both local and overall deformation of specimens should be used when performing an experiment to determine axial stress-strain behaviour. The needs of an advanced measurement method which can provide both local and overall deformation, is essential.

11.1.2 Existing models for prediction of FRP-confined concrete behavior and influential parameters on prediction

The investigation on performance of existing models to predict the mechanical behavior of FRP-confined concrete under compression illustrates that two influential parameters govern the accuracy of the prediction in existing models. These two parameters are unconfined compressive strength of concrete (f'_{co}) and hoop rupture strain ($\varepsilon_{h,rup}$). It is well known that the

brittleness of concrete increases by increasing f'_{co}. This indicates that the mechanical response of FRP-confined concrete under compressive loading varies by change of f'_{co}. Additionally, it is well established that hoop rupture strain is affected by lateral deformation and confinement mechanism of FRP-confined concrete column. However, in the literature hoop rupture strain is usually measured by strain gauges. It is well known that strain gauges record the deformation on a few isolated points over the specimen's surface and hence, they are not able to provide accurate overall lateral deformation of the specimens.

11.1.3 FRP-confined concrete column in real load condition

The confinement mechanism is an influential parameters in determining the mechanical response of FRP-confined concrete. This mechanism is investigated in this study by using two different loading types, namely concentric and eccentric. This investigation shows that the confinement mechanism is influenced significantly by loading types (i.e. concentric and eccentric). The outcome illustrates that the increasing eccentricity causes a decrease in ultimate axial load and axial stress and an increase in ultimate axial strain at loading point, as expected. It should be said that loading point is the location of applied load over specimens which is different in the case of eccentric load compared to concentric load. Furthermore, the variation of lateral strain around the specimens' perimeter due to eccentricity is displayed in this research in addition to increasing curvature by an increase in eccentricity. Finally, cross-section analysis was used to evaluate the mechanical behavior of specimens under eccentric load and it is found that the load-displacement curves cannot be modelled accurately using axial stress-strain curve provided by concentric load.

11.1.4 High strength concrete and its intrinsically brittle behavior

As explained in 11.1.1, to determine the mechanical behavior of a brittle material more sophisticated measurement method and a more comprehensive approach is needed. The obtained outcome in this study shows the need of new method to analyse DIC data and make

a correlation between strain localization and mechanical performance of specimens. Moreover, it is exhibited that the existing methods to analyse DIC data sometimes are not able to capture accurately localization characteristics. Consequently, a new method to analyse the obtained DIC data to determine the onset and evolution of localization is developed. This approach is firstly applied on unconfined NSC and FRP-confined NSC then it is used for unconfined HSC and FRP-confined HSC specimens.

The obtained results for FRP-confined NSC showed the influence of lateral stiffness (K_l) on mechanical behavior of FRP-confined NSC where more homogenous behavior along specimen's height was obtained for higher K_l. The obtained results also show that the localization initiated at 50-60% of f'_{co} for NSC. Afterwards, it is illustrated the existence of two types of localization evolution whereas unconfined and insufficiently FRP-confined NSC specimens have abrupt localization evolution behavior opposite to well confined NSC specimens with more gradual behavior.

The new approach was further used and developed to analyze unconfined HSC specimens and FRP-confined HSC. A bifurcation phenomenon analysis was added to this approach to accurately mark initiation of localization. Additionally, a probability density function (PDF) is used to quantify localization characterization and correlate mechanical characteristics of specimens to localization. By using developed approach in this study on unconfined and FRP-confined HSC, approximately similar results to NSC are obtained and two different evolutions of localization pattern with same characteristic as NSC is observed. In addition, later localization initiation for unconfined HSC and FRP-confined HSC compared to NSC is observed. It is also demonstrated that the strain distribution over both unconfined and FRP-confined HSC specimens' surface can be captured using a PDF. Beta PDF was used in this

study to model the strain distribution over specimens' surface. The outcome indicates that this condensed DIC data is helpful in order to be used in developing/validating a constitutive model.

As explained, the brittle behavior of HSC causes some unfavourable behavior in unconfined HSC and FRP-confined HSC. In this study, the presence of two fibers, namely ultra-high strength steel fibers (UHSSF) and poly vinyl alcohol (PVA) fiber, in concrete wet mix is investigated. These two fiber types are used in this research to control the unfavourable mechanical response of FRP-confined HSC as previously discussed in various researches. To perform mentioned investigation, the same developed approach as explained for plain concrete is applied on fiber reinforced concrete specimens. Afterward, FRP jacket is used to confine concrete columns and these mega performance structural system are studied in the same way. The results exhibit that adding fibers in concrete wet mix leads to more ductile behavior of fiber reinforced concrete and fiber reinforced concrete -filled FRP tubes (CFFT) and the disadvantages due to brittleness of plain HSC significantly reduced. Additionally, a more homogenous crack distribution and localization evolution are observed for both unconfined and FRP-confined fiber reinforced concrete specimens, although the localization characteristics remained similar to those observed in unconfined and FRP-confined plain concrete. The accurate initiation of bridging and how fibers are able to transfer the load to all part of specimens is discussed and illustrated in this research. Although many researchers investigated previously bridging phenomenon in fiber reinforced concrete, no studies exist on correlation of bridging to mechanical response of fiber reinforced concrete. The obtained results show the existing of two sets of deformation localized zone in fiber reinforced concrete due to existence of fibers. In particular, the bridging did not start before initiation of localization and the fibers improve the ductility of FRP-confined HSC specimens by disappearance of temporary loss of strength after transition zone in their axial stress-strain curve. The outcome in this research also shows that lateral deformation of UHSSFR-CFFT and PVAR-CFFT are

approximately similar to FRP-confined concrete, although small differences can be observed. Finally, the outcome showed that the distribution of strain over specimens surface can be modelled by probability density function same as plain concrete. As indicated previously, this helps in developing a more accurate constitutive model for studied structural systems.

11.2 Future work

As explained in section 11.1, the behavior of circular specimens, i.e. FRP-confined concrete, under compression with aspect ratio equals to two were investigated in this study. This signifies that to generalize obtained results in this study, i.e. developed approach to determine localization characteristics which correlate the localization characteristics to mechanical behavior of specimens, more experiments and an in-depth study is essential. All influential parameters on mechanical response of FRP-confined concrete under various loading types should be examined. These parameters are geometry including shape and aspect ratio, structural element types such as FRP-confined concrete or fiber reinforced concrete, FRP shell types namely FRP wrap or FRP tube, variation of f'_{co} and K_l, the influence of ingredient including type and shapes of gravels in concrete mix and others factors such as workmanship. A comprehensive experimental program which is able to cover and investigate all mentioned parameters should be designed. In this experiment, a sophisticated measurement methods which is able to record both local and overall deformation must be provided. This new study should be aimed to correlate the localization characteristics to mechanical response of under studied structural element. The results of these all-inclusive study lead to develop an accurate constitutive model which is validated appropriately by experimental data. These type of constitutive models, in turn, results in safer and more economic designing procedure which is main concern of engineering science.

References

[1] Almusallam TH. Behavior of normal and high-strength concrete cylinders confined with E-glass/epoxy composite laminates. Composites Part B-Engineering. 2007;38:629-39.
[2] Berthet JF, Ferrier E, Hamelin P. Compressive behavior of concrete externally confined by composite jackets - Part B: modeling. Construction and Building Materials. 2006;20:338-47.
[3] Cui C, Sheikh SA. Experimental Study of Normal- and High-Strength Concrete Confined with Fiber-Reinforced Polymers. Journal of Composites for Construction. 2010;14:553-61.
[4] Eid R, Roy N, Paultre P. Normal- and High-Strength Concrete Circular Elements Wrapped with FRP Composites. Journal of Composites for Construction. 2009;13:113-24.
[5] Mandal S, Hoskin A, Fam A. Influence of concrete strength on confinement effectiveness of fiber-reinforced polymer circular jackets. Aci Structural Journal. 2005;102:383-92.
[6] Pham TM, Hadi MNS. Confinement model for FRP confined normal- and high-strength concrete circular columns. Construction and Building Materials. 2014;69:83-90.
[7] Wu HL, Wang YF, Yu L, Li XR. Experimental and Computational Studies on High-Strength Concrete Circular Columns Confined by Aramid Fiber-Reinforced Polymer Sheets. Journal of Composites for Construction. 2009;13:125-34.
[8] Xiao QG, Teng JG, Yu T. Behavior and Modeling of Confined High-Strength Concrete. Journal of Composites for Construction. 2010;14:249-59.
[9] Zohrevand P, Mirmiran A. Behavior of Ultrahigh-Performance Concrete Confined by Fiber-Reinforced Polymers. Journal of Materials in Civil Engineering. 2011;23:1727-34.
[10] Fallah Pour A, Ozbakkaloglu T, Vincent T. Simplified design-oriented axial stress-strain model for FRP-confined normal- and high-strength concrete. Engineering Structures. 2018;175:501-16.
[11] Idris Y, Ozbakkaloglu T. Seismic Behavior of High-Strength Concrete-Filled FRP Tube Columns. Journal of Composites for Construction. 2013;17:04013013.
[12] Lim JC, Ozbakkaloglu T. Influence of silica fume on stress-strain behavior of FRP-confined HSC. Construction and Building Materials. 2014;63:11-24.
[13] Ozbakkaloglu T. Behavior of square and rectangular ultra high-strength concrete-filled FRP tubes under axial compression. Composites Part B: Engineering. 2013;54:97-111.
[14] Ozbakkaloglu T, Lim JC. Axial compressive behavior of FRP-confined concrete: Experimental test database and a new design-oriented model. Composites Part B-Engineering. 2013;55:607-34.
[15] Vincent T, Ozbakkaloglu T. Influence of concrete strength and confinement method on axial compressive behavior of FRP confined high- and ultra high-strength concrete. Composites Part B-Engineering. 2013;50:413-28.
[16] Ozbakkaloglu T, Lim JC, Vincent T. FRP-confined concrete in circular sections: Review and assessment of stress-strain models. Engineering Structures. 2013;49:1068-88.
[17] Lim JC, Ozbakkaloglu T. Confinement Model for FRP-Confined High-Strength Concrete. Journal of Composites for Construction. 2014;18:04013058.
[18] Lim JC, Karakus M, Ozbakkaloglu T. Evaluation of ultimate conditions of FRP-confined concrete columns using genetic programming. Computers & Structures. 2016;162:28-37.
[19] Binici B. Design of FRPs in circular bridge column retrofits for ductility enhancement. Engineering Structures. 2008;30:766-76.
[20] Teng JG, Jiang T, Lam L, Luo YZ. Refinement of a Design-Oriented Stress-Strain Model for FRP-Confined Concrete. Journal of Composites for Construction. 2009;13:269-78.
[21] De Lorenzis L, Tepfers R. Comparative Study of Models on Confinement of Concrete Cylinders with Fiber-Reinforced Polymer Composites. Journal of Composites for Construction. 2003;7:219-37.
[22] Fahmy MFM, Wu ZS. Evaluating and proposing models of circular concrete columns confined with different FRP composites. Composites Part B-Engineering. 2010;41:199-213.
[23] Lim JC, Ozbakkaloglu T. Unified Stress-Strain Model for FRP and Actively Confined Normal-Strength and High-Strength Concrete. Journal of Composites for Construction. 2015;19.

[24] Binici B. An analytical model for stress-strain behavior of confined concrete. Engineering Structures. 2005;27:1040-51.
[25] Karabinis AI, Rousakis TC. Concrete confined by FRP material: a plasticity approach. Engineering Structures. 2002;24:923-32.
[26] Rousakis TC, Karabinis AI, Kiousis PD, Tepfers R. Analytical modelling of plastic behaviour of uniformly FRP confined concrete members. Composites Part B: Engineering. 2008;39:1104-13.
[27] Bisby LA, Take WA. Strain localisations in FRP-confined concrete: new insights. Proceedings of the Institution of Civil Engineers-Structures and Buildings. 2009;162:301-9.
[28] Lam L, Teng JG. Hoop rupture strains of FRP jackets in FRP confined concrete. Proc. 6th Int Symp of Fibre-Reinforcement Polymer Reinforcement for Concrete Structures, Dept of Civil Engineering, National Univ of Singapore, Singapore. 2003;1:601–12.
[29] Lim J, Ozbakkaloglu T. Hoop strains in FRP-confined concrete columns: experimental observations. Materials and Structures. 2015;48:2839-54.
[30] Tabbara M, Karam G. Numerical investigation of failure localisation and stress concentrations in FRP wrapped concrete cylinders. 5th international conference on Advanced composite Materials in Bridges and Structures, Winnipeg. 2008.
[31] Jiang T, Teng JG. Analysis-oriented stress-strain models for FRP-confined concrete. Engineering Structures. 2007;29:2968-86.
[32] Albanesi T, Nuti C, Vanzi I. Closed form constitutive relationship for concrete filled FRP tubes under compression. Construction and Building Materials. 2007;21:409-27.
[33] Chun SS, Park HC. Load carrying capacity and ductility of RC columns confined by carbon fiber reinforced polymer. 3rd Int Conf on Composites in Infrastructure, Univ of Arizona, Tucson, AZ. 2002.
[34] Fam AZ, Rizkalla SH. Confinement Model for Axially Loaded Concrete Confined by Circular Fiber-Reinforced Polymer Tubes. Structural Journal. 2001;98:451-61.
[35] Marques SPC, Marques DCSC, da Silva JL, Cavalcante MAA. Model for analysis of short columns of concrete confined by fiber-reinforced polymer. Journal of Composites for Construction. 2004;8:332-40.
[36] Spoelstra MR, Monti G. FRP-Confined Concrete Model. Journal of Composites for Construction. 1999;3:143-50.
[37] Harries KA, Carey SA. Shape and “gap” effects on the behavior of variably confined concrete. Cement and Concrete Research. 2003;33:881-90.
[38] Mirmiran A, Shahawy M. Dilation characteristics of confined concrete. Mechanics of Cohesive-Frictional Materials. 1997;2:237-49.
[39] Teng JG, Yu T, Wong YL, Dong SL. Hybrid FRP–concrete–steel tubular columns: Concept and behavior. Construction and Building Materials. 2007;21:846-54.
[40] Li J, Hadi MNS. Behaviour of externally confined high-strength concrete columns under eccentric loading. Composite Structures. 2003;62:145-53.
[41] Hadi MNS. Behaviour of FRP wrapped normal strength concrete columns under eccentric loading. Composite Structures. 2006;72:503-11.
[42] Hadi MNS. Comparative study of eccentrically loaded FRP wrapped columns. Composite Structures. 2006;74:127-35.
[43] Hadi MNS. Behaviour of FRP strengthened concrete columns under eccentric compression loading. Composite Structures. 2007;77:92-6.
[44] Hadi MNS. The behaviour of FRP wrapped HSC columns under different eccentric loads. Composite Structures. 2007;78:560-6.
[45] Hadi MNS. Behaviour of eccentric loading of FRP confined fibre steel reinforced concrete columns. Construction and Building Materials. 2009;23:1102-8.
[46] Bisby L, Ranger M. Axial-flexural interaction in circular FRP-confined reinforced concrete columns. Construction and Building Materials. 2010;24:1672-81.
[47] Shaheen E, Shrive NG. Sprayed glass fibre reinforced polymer masonry columns under concentric and eccentric loading. Canadian Journal of Civil Engineering. 2007;34:1495-505.

[48] El Maaddawy T. Behavior of corrosion-damaged RC columns wrapped with FRP under combined flexural and axial loading. Cement & Concrete Composites. 2008;30:524-34.
[49] El Maaddawy T. Post-repair performance of eccentrically loaded RC columns wrapped with CFRP composites. Cement & Concrete Composites. 2008;30:822-30.
[50] El Maaddawy T. Strengthening of Eccentrically Loaded Reinforced Concrete Columns with Fiber-Reinforced Polymer Wrapping System: Experimental Investigation and Analytical Modeling. Journal of Composites for Construction. 2009;13:13-24.
[51] Hajsadeghi M, Alaee FJ. Numerical analysis of rectangular reinforced concrete columns confined with FRP jacket under eccentric loading. In Proc of the 5th International Conference on FRP Composites in Civil Engineering (CICE), Beijing, China. 2010:27-9.
[52] Sadeghian P, Rahai AR, Ehsani MR. Experimental Study of Rectangular RC Columns Strengthened with CFRP Composites under Eccentric Loading. Journal of Composites for Construction. 2010;14:443-50.
[53] Elwan SK, Rashed AS. Experimental behavior of eccentrically loaded RC short columns strengthened using GFRP wrapping. Structural Engineering and Mechanics. 2011;39:207-21.
[54] Quiertant M, Clement JL. Behavior of RC columns strengthened with different CFRP systems under eccentric loading. Construction and Building Materials. 2011;25:452-60.
[55] Csuka B, Kollar LP. FRP-confined circular columns subjected to eccentric loading. Journal of Reinforced Plastics and Composites. 2011;30:1167-78.
[56] Csuka B, Kollar LP. Analysis of FRP confined columns under eccentric loading. Composite Structures. 2012;94:1106-16.
[57] Fam A, Flisak B, Rizkalla S. Experimental and analytical modeling of concrete-filled FRP tubes subjected to combined bending and axial loads. ACI Struct J. 2003;100:499-509.
[58] Wu YF, Jiang C. Effect of load eccentricity on the stress-strain relationship of FRP-confined concrete columns. Composite Structures. 2013;98:228-41.
[59] Bencardino F, Rizzuti L, Spadea G, Swamy RN. Stress-strain behavior of steel fiber-reinforced concrete in compression. Journal of Materials in Civil Engineering. 2008;20:255-63.
[60] Bhargava P, Sharma UK, Kaushik SK. Compressive Stress-Strain Behavior of Small Scale Steel Fibre Reinforced High Strength Concrete Cylinders. Journal of Advanced Concrete Technology. 2006;4:109-21.
[61] Nataraja MC, Dhang N, Gupta AP. Stress–strain curves for steel-fiber reinforced concrete under compression. Cement and Concrete Composites. 1999;21:383-90.
[62] Paultre P, Eid R, Langlois Y, Levesque Y. Behavior of Steel Fiber-Reinforced High-Strength Concrete Columns under Uniaxial Compression. Journal of Structural Engineering-Asce. 2010;136:1225-35.
[63] Soroushian P, Bayasi Z. Fiber Type Effects on the Performance of Steel Fiber Reinforced Concrete. Aci Materials Journal.88:129-34.
[64] Ezeldin AS, Balaguru PN. Normal- and High-Strength Fiber-Reinforced Concrete under Compression. Journal of Materials in Civil Engineering. 1992;4:415-29.
[65] Ding Y, Kusterle W. Compressive stress–strain relationship of steel fibre-reinforced concrete at early age. Cement and Concrete Research. 2000;30:1573-9.
[66] Kholmyansky MM. Mechanical Resistance of Steel Fiber Reinforced Concrete to Axial Load. Journal of Materials in Civil Engineering. 2002;14:311-9.
[67] Ramesh K, Seshu DR, Prabhakar M. Constitutive behaviour of confined fibre reinforced concrete under axial compression. Cement and Concrete Composites. 2003;25:343-50.
[68] Sukontasukkul P, Mindess S, Banthia N. Properties of confined fibre-reinforced concrete under uniaxial compressive impact. Cement and Concrete Research. 2005;35:11-8.
[69] Thomas J, Ramaswamy A. Mechanical Properties of Steel Fiber-Reinforced Concrete. Journal of Materials in Civil Engineering. 2007;19:385-92.
[70] Holschemacher K, Mueller T, Ribakov Y. Effect of steel fibres on mechanical properties of high-strength concrete. Materials & Design (1980-2015). 2010;31:2604-15.

[71] Ayan E, Saatçioğlu Ö, Turanli L. Parameter optimization on compressive strength of steel fiber reinforced high strength concrete. Construction and Building Materials. 2011;25:2837-44.
[72] Ou Y-C, Tsai M-S, Liu K-Y, Chang K-C. Compressive Behavior of Steel-Fiber-Reinforced Concrete with a High Reinforcing Index. Journal of Materials in Civil Engineering. 2012;24:207-15.
[73] Hassan AMT, Jones SW, Mahmud GH. Experimental test methods to determine the uniaxial tensile and compressive behaviour of ultra high performance fibre reinforced concrete (UHPFRC). Construction and Building Materials. 2012;37:874-82.
[74] Tokgoz S, Dundar C. Tests of eccentrically loaded L-shaped section steel fibre high strength reinforced concrete and composite columns. Engineering Structures. 2012;38:134-41.
[75] Wang S, Zhang M-H, Quek ST. Mechanical behavior of fiber-reinforced high-strength concrete subjected to high strain-rate compressive loading. Construction and Building Materials. 2012;31:1-11.
[76] Caballero-Morrison KE, Bonet JL, Navarro-Gregori J, Serna-Ros P. An experimental study of steel fiber-reinforced high-strength concrete slender columns under cyclic loading. Engineering Structures. 2013;57:565-77.
[77] Xie TY, Ozbakkaloglu T. Behavior of steel fiber-reinforced high-strength concrete-filled FRP tube columns under axial compression. Engineering Structures. 2015;90:158-71.
[78] Gholampour A, Ozbakkaloglu T. Behavior of steel fiber-reinforced concrete-filled FRP tube columns: Experimental results and a finite element model. Composite Structures. 2018;194:252-62.
[79] Ghorbi E, Soltani M, Maekawa K. Development of a compressive constitutive model for FRP-confined concrete elements. Composites Part B-Engineering. 2013;45:504-17.
[80] Teng JG, Lin G, Yu T. Analysis-Oriented Stress-Strain Model for Concrete under Combined FRP-Steel Confinement. Journal of Composites for Construction. 2015;19.
[81] Cascardi A, Micelli F, Aiello MA. Unified model for hollow columns externally confined by FRP. Engineering Structures. 2016;111:119-30.
[82] Keshtegar B, Ozbakkaloglu T, Gholampour A. Modeling the behavior of FRP-confined concrete using dynamic harmony search algorithm. Engineering with Computers. 2017;33:415-30.
[83] Al-Rousan RZ, Issa MA. Stress-strain model and design guidelines for CFRP-confined circular reinforced concrete columns. Polymer Composites. 2016.
[84] Zhou YW, Wu YF. General model for constitutive relationships of concrete and its composite structures. Composite Structures. 2012;94:580-92.
[85] Lim JC, Ozbakkaloglu T. Design model for FRP-confined normal- and high-strength concrete square and rectangular columns. Magazine of Concrete Research. 2014;66:1020-35.
[86] Ozbakkaloglu T, Gholampour A, Lim JC. Damage-Plasticity Model for FRP-Confined Normal-Strength and High-Strength Concrete. Journal of Composites for Construction. 2016;20.
[87] Ozbakkaloglu T, Vincent T. Axial Compressive Behavior of Circular High-Strength Concrete-Filled FRP Tubes. Journal of Composites for Construction. 2014;18:04013037.
[88] Ilki A, Peker O, Karamuk E, Demir C, Kumbasar N. FRP retrofit of low and medium strength circular and rectangular reinforced concrete columns. Journal of Materials in Civil Engineering. 2008;20:169-88.
[89] Rousakis TC, Karabinis AI. Adequately FRP confined reinforced concrete columns under axial compressive monotonic or cyclic loading. Materials and Structures. 2012;45:957-75.
[90] Dai J-G, Bai Y-L, Teng JG. Behavior and Modeling of Concrete Confined with FRP Composites of Large Deformability. Journal of Composites for Construction. 2011;15:963-73.
[91] Dundar C, Erturkmen D, Tokgoz S. Studies on carbon fiber polymer confined slender plain and steel fiber reinforced concrete columns. Engineering Structures. 2015;102:31-9.
[92] Vincent T, Ozbakkaloglu T. Axial compressive behaviour of FRP-confined concrete columns: investigation of less-understood influences. Concrete of Australia. 2015;40.
[93] Lam L, Teng JG. Design-oriented stress–strain model for FRP-confined concrete. Constr Build Mater. 2003;17:471–89.

[94] Cascardi A, Micelli F, Aiello MA. An Artificial Neural Networks model for the prediction of the compressive strength of FRP-confined concrete circular columns. Engineering Structures. 2017;140:199-208.
[95] Mozumder RA, Roy B, Laskar AI. Support Vector Regression Approach to Predict the Strength of FRP Confined Concrete. Arabian Journal for Science and Engineering. 2017;42:1129-46.
[96] Wu Y-F, Jiang J-F. Effective strain of FRP for confined circular concrete columns. Composite Structures. 2013;95:479-91.
[97] Fam AZ, Rizkalla SH. Behavior of axially loaded concrete-filled circular fiber-reinforced polymer tubes. Aci Structural Journal. 2001;98:280-9.
[98] Smith ST, Kim SJ, Zhang HW. Behavior and Effectiveness of FRP Wrap in the Confinement of Large Concrete Cylinders. Journal of Composites for Construction. 2010;14:573-82.
[99] Berthet JF, Ferrier E, Hamelin P. Compressive behavior of concrete externally confined by composite jackets. Part A: experimental study. Construction and Building Materials. 2005;19:223-32.
[100] Cui C. Behaviour of normal and high strength concrete confined with fibre reinforced polymers (FRP). MSc Thesis, University of Toronto. 2009:1-376.
[101] Lam L, Teng JG, Cheung CH, Xiao Y. FRP-confined concrete under axial cyclic compression. Cement & Concrete Composites. 2006;28:949-58.
[102] Wang LM, Wu YF. Effect of corner radius on the performance of CFRP-confined square concrete columns: Test. Engineering Structures. 2008;30:493-505.
[103] Shahawy M, Mirmiran A, Beitelman T. Tests and modeling of carbon-wrapped concrete columns. Composites Part B-Engineering. 2000;31:471-80.
[104] Vincent T, Ozbakkaloglu T. Influence of fiber orientation and specimen end condition on axial' compressive behavior of FRP-confined concrete. Construction and Building Materials. 2013;47:814-26.
[105] Vincent T, Ozbakkaloglu T. Influence of overlap configuration on compressive behavior of CFRP-confined normal- and high-strength concrete. Materials and Structures. 2016;49:1245-68.
[106] Lim JC, Ozbakkaloglu T. Influence of concrete age on stress-strain behavior of FRP-confined normal- and high-strength concrete. Construction and Building Materials. 2015;82:61-70.
[107] Vincent T, Ozbakkaloglu T. Influence of shrinkage on compressive behavior of concrete-filled FRP tubes: An experimental study on interface gap effect. Construction and Building Materials. 2015;75:144-56.
[108] Vincent T, Ozbakkaloglu T. Compressive Behavior of Prestressed High-Strength Concrete-Filled Aramid FRP Tube Columns: Experimental Observations. J Compos Constr. 2015:04015003.
[109] Vincent T, Ozbakkaloglu T. Influence of Slenderness on Stress-Strain Behavior of Concrete-Filled FRP Tubes: Experimental Study. Journal of Composites for Construction. 2015;19.
[110] Pham TM, Hadi MNS, Youssef J. Optimized FRP Wrapping Schemes for Circular Concrete Columns under Axial Compression. Journal of Composites for Construction. 2015;19:04015015.
[111] Ozbakkaloglu T, Akin E. Behavior of FRP-Confined Normal- and High-Strength Concrete under Cyclic Axial Compression. Journal of Composites for Construction. 2012;16:451-63.
[112] Ozbakkaloglu T. Compressive behavior of concrete-filled FRP tube columns: Assessment of critical column parameters. Engineering Structures. 2013;51:188-99.
[113] Lim JC, Ozbakkaloglu T. Lateral Strain-to-Axial Strain Relationship of Confined Concrete. Journal of Structural Engineering. 2015;141.
[114] Lim JC, Ozbakkaloglu T. Investigation of the Influence of the Application Path of Confining Pressure: Tests on Actively Confined and FRP-Confined Concretes. Journal of Structural Engineering. 2015;141.
[115] Saafi M, Toutanji HA, Li ZJ. Behavior of concrete columns confined with fiber reinforced polymer tubes. Aci Materials Journal. 1999;96:500-9.
[116] Toutanji HA. Stress-strain characteristics of concrete columns externally confined with advanced fiber composite sheets. Aci Materials Journal. 1999;96:397-404.

[117] Youssef M, Feng M, Mosallam A. Stress–strain model for concrete confined by FRP composites. Composites Part B-Engineering. 2007;38:614-28.
[118] Cui C, Sheikh SA. Analytical Model for Circular Normal- and High-Strength Concrete Columns Confined with FRP. Journal of Composites for Construction2010. p. 562-72.
[119] Miyauchi K. IS, Kuroda T., Kobayashi A. Strengthening effects with carbon fiber sheet for concrete column. Proc Japan concr inst. 1999;21:1453-8.
[120] Mansouri I, Ozbakkaloglu T, Kisi O, Xie TY. Predicting behavior of FRP-confined concrete using neuro fuzzy, neural network, multivariate adaptive regression splines and M5 model tree techniques. Materials and Structures. 2016;49:4319-34.
[121] Ilki A, Kumbasar N. Compressive behaviour of carbon fibre composite jacketed concrete with circular and non-circular cross-sections. Journal of Earthquake Engineering. 2003;7:381-406.
[122] Lim JC, Ozbakkaloglu T. Influence of Size and Slenderness on Compressive Strain Softening of Confined and Unconfined Concrete. Journal of Materials in Civil Engineering. 2016;28.
[123] Aire C, Gettu R, Casas JR, Marques S, Marques D. Estudio experimental y modelo teórico del hormigón confinado lateralmente con polímeros reforzados con fibras (FRP). Materiales de Construcción. 2010;60:19-31.
[124] Benzaid R, Mesbah H, Chikh NE. FRP-confined Concrete Cylinders: Axial Compression Experiments and Strength Model. Journal of Reinforced Plastics and Composites. 2010;29:2469-88.
[125] Ozbakkaloglu T, Fanggi BAL, Zheng JA. Confinement model for concrete in circular and square FRP-concrete-steel double-skin composite columns. Materials & Design. 2016;96:458-69.
[126] Richart FE, Brandtzaeg A, R.L. B. study of failure of concrete under combined compressive stresses. Engineering Experimental Station, Urbana, IL, Bulletin. 1928;185.
[127] Tamuzs V, Tepfers R, Zile E, Ladnova O. Behavior of concrete cylinders confined by a carbon composite - 3. Deformability and the ultimate axial strain. Mechanics of Composite Materials. 2006;42:303-14.
[128] Popovics S. A numerical approach to the complete stress-strain curve of concrete. Cement and Concrete Research. 1973;3:583-99.
[129] Carreira DJ, Chu KH. Stress-Strain Relationship for Plain Concrete in Compression. Journal of the American Concrete Institute. 1985;82:797-804.
[130] Bisby LA, Dent AJS, Green MF. Comparison of confinement models for fiber-reinforced polymer-wrapped concrete. Aci Structural Journal. 2005;102:62-72.
[131] Lam L, Teng JG. Ultimate condition of fiber reinforced polymer-confined concrete. Journal of Composites for Construction. 2004;8:539-48.
[132] Fanggi BAL, Ozbakkaloglu T. Square FRP-HSC-steel composite columns: Behavior under axial compression. Engineering Structures. 2015;92:156-71.
[133] Ozbakkaloglu T, Xie TY. Geopolymer concrete-filled FRP tubes: Behavior of circular and square columns under axial compression. Composites Part B-Engineering. 2016;96:215-30.
[134] Ozbakkaloglu T. A novel FRP-dual-grade concrete-steel composite column system. Thin-Walled Structures. 2015;96:295-306.
[135] Ozbakkaloglu T. Behavior of square and rectangular ultra high-strength concrete-filled FRP tubes under axial compression. Composites Part B-Engineering. 2013;54:97-111.
[136] Ozbakkaloglu T, Fanggi BL. Axial Compressive Behavior of FRP-Concrete- Steel Double-Skin Tubular Columns Made of Normal- and High-Strength Concrete. Journal of Composites for Construction. 2014;18.
[137] Ozbakkaloglu T, Saatcioglu M. Seismic behavior of high-strength concrete columns confined by fiber-reinforced polymer tubes. Journal of Composites for Construction. 2006;10:538-49.
[138] Vincent T, Ozbakkaloglu T. Influence of fiber orientation and specimen end condition on axial compressive behavior of FRP-confined concrete. Construction and Building Materials. 2013;47:814-26.
[139] ASTM D3039/D3039M-08. Standard Test Method for Tensile Properties of Polymer Matrix Composite Materials. 2008.

[140] Pour AF, Gholampour A, Ozbakkaloglu T. Influence of the Measurement Method on Axial Strains of FRP-Confined Concrete under Compression. Composite Structures. 2018.
[141] Lam L, Teng JG. Design-oriented stress-strain model for FRP-confined concrete in rectangular columns. Journal of Reinforced Plastics and Composites. 2003;22:1149-86.
[142] Li PD, Wu YF, Gravina R. Cyclic response of FRP-confined concrete with post-peak strain softening behavior. Construction and Building Materials. 2016;123:814-28.
[143] Li PD, Wu YF, Zhou YW, Xing F. Stress-strain model for FRP-confined concrete subject to arbitrary load path. Composites Part B-Engineering. 2019;163:9-25.
[144] Wu YF, Jiang JF. Effective strain of FRP for confined circular concrete columns. Composite Structures. 2013;95:479-91.
[145] Skarżyński Ł, Kozicki J, Tejchman J. Application of DIC Technique to Concrete—Study on Objectivity of Measured Surface Displacements. Experimental Mechanics. 2013;53:1545-59.
[146] Shah SG, Chandra Kishen JM. Fracture Properties of Concrete–Concrete Interfaces Using Digital Image Correlation. Experimental Mechanics. 2010;51:303-13.
[147] Skarzynski L, Tejchman J. Experimental Investigations of Fracture Process Using DIC in Plain and Reinforced Concrete Beams under Bending. Strain. 2013;49:521-43.
[148] Choi S, Shah SP. Measurement of deformations on concrete subjected to compression using image correlation. Experimental Mechanics. 1997;37:307-13.
[149] Lawler JS, Keane DT, Shah SP. Measuring three-dimensional damage in concrete under compression. Aci Materials Journal. 2001;98:465-75.
[150] Xiao JZ, Li WG, Sun ZH, Shah SP. Crack Propagation in Recycled Aggregate Concrete under Uniaxial Compressive Loading. Aci Materials Journal. 2012;109:451-61.
[151] Li WG, Xiao JZ, Sun ZH, Shah SP. Failure processes of modeled recycled aggregate concrete under uniaxial compression. Cement & Concrete Composites. 2012;34:1149-58.
[152] Mirmiran A. SM, Samaan M., El chary H., Mastrapa JC., Pico O. Effect of Column Parameters on FRP-Confined Concrete. J Compos Constr. 1998;2:175-85.
[153] Xiao Y, Wu H. Compressive Behavior of Concrete Confined by Carbon Fiber Composite Jackets. Journal of Materials in Civil Engineering. 2000;12:139-46.
[154] Fallah Pour A, Gholampour A, Ozbakkaloglu T. Influence of the measurement method on axial strains of FRP-confined concrete under compression. Composite Structures. 2018;188:415-24.
[155] Bisby L, Sinclair D, Webster M, Stratford T, Take W. Effects of Aspect Ratio on the Observed Hoop Strain Variation in FRP Confined Concrete Cylinders. Advanced Composites in Construction (ACIC) 2009 Conference Proceedings. 2009: 570-81.
[156] Nguyen GD, Nguyen CT, Nguyen VP. Modelling Localisation and Spatial Scaling of Constitutive Behaviour: a Kinematically Enriched Continuum Approach. Proceedings of the International Congress (APCF/SIF-2014), Asian-Pacific Conference on Fracture and Strength 2014, Sydney, Australia. 2014.
[157] Mollema PN, Antonellini MA. Compaction bands: A structural analog for anti-mode I cracks in aeolian sandstone. Tectonophysics. 1996;267:209-28.
[158] Baud P, Klein E, Wong TF. Compaction localization in porous sandstones: spatial evolution of damage and acoustic emission activity. Journal of Structural Geology. 2004;26:603-24.
[159] Alshibli KA, Hasan A. Spatial variation of void ratio and shear band thickness in sand using X-ray computed tomography. Geotechnique. 2008;58:249-57.
[160] Ando E, Hall SA, Viggiani G, Desrues J, Besuelle P. Grain-scale experimental investigation of localised deformation in sand: a discrete particle tracking approach. Acta Geotechnica. 2012;7:1-13.
[161] Charalampidou EM, Hall SA, Stanchits S, Viggiani G, Lewis H. Shear-enhanced compaction band identification at the laboratory scale using acoustic and full-field methods. International Journal of Rock Mechanics and Mining Sciences. 2014;67:240-52.
[162] Thakur V, Nordal S, Viggiani G, Charrier P. Shear bands in undrained plane strain compression of Norwegian quick clays. Canadian Geotechnical Journal. 2018;55:45-56.

[163] Guo MH, Alam SY, Bendimerad AZ, Grondin F, Roziere E, Loukili A. Fracture process zone characteristics and identification of the micro-fracture phases in recycled concrete. Engineering Fracture Mechanics. 2017;181:101-15.
[164] Okubo S, Nishimatsu Y. Uniaxial Compression Testing Using a Linear Combination of Stress and Strain as the Control Variable. International Journal of Rock Mechanics and Mining Sciences. 1985;22:323-30.
[165] Labuz JF, Biolzi L. Class-I Vs Class-Ii Stability - a Demonstration of Size Effect. International Journal of Rock Mechanics and Mining Sciences & Geomechanics Abstracts. 1991;28:199-205.
[166] Riedel JJ, Labuz JF. Propagation of a shear band in sandstone. International Journal for Numerical and Analytical Methods in Geomechanics. 2007;31:1281-99.
[167] Shimizu H, Koyama T, Ishida T, Chijimatsu M, Fujita T, Nakama S. Distinct element analysis for Class II behavior of rocks under uniaxial compression. International Journal of Rock Mechanics and Mining Sciences. 2010;47:323-33.
[168] Nguyen GD, Bui HH. A thermodynamics- and mechanism-based framework for constitutive models with evolving thickness of localisation band. International Journal of Solids and Structures. 2020;187:100-20.
[169] Nguyen GD, Houlsby GT. Non-local damage modelling of concrete: a procedure for the determination of model parameters. International Journal for Numerical and Analytical Methods in Geomechanics. 2007;31:867-91.
[170] Nguyen GD, Korsunsky AM. Development of an approach to constitutive modelling of concrete: Isotropic damage coupled with plasticity. International Journal of Solids and Structures. 2008;45:5483-501.
[171] Wang YN, Bui HH, Nguyen GD, Ranjith PG. A new SPH-based continuum framework with an embedded fracture process zone for modelling rock fracture. International Journal of Solids and Structures. 2019;159:40-57.
[172] Pietruszczak S, Haghighat E. Modeling of deformation and localized failure in anisotropic rocks. International Journal of Solids and Structures. 2015;67-68:93-101.
[173] Pietruszczak S, Mroz Z. On failure criteria for anisotropic cohesive-frictional materials. International Journal for Numerical and Analytical Methods in Geomechanics. 2001;25:509-24.
[174] Pietruszczak S, Xu G. Brittle Response of Concrete as a Localization Problem. International Journal of Solids and Structures. 1995;32:1517-33.
[175] du Plessis A, Olawuyi BJ, Boshoff WP, le Roux SG. Simple and fast porosity analysis of concrete using X-ray computed tomography. Materials and Structures. 2016;49:553-62.
[176] Huang YJ, Yan DM, Yang ZJ, Liu GH. 2D and 3D homogenization and fracture analysis of concrete based on in-situ X-ray Computed Tomography images and Monte Carlo simulations. Engineering Fracture Mechanics. 2016;163:37-54.
[177] Huang YJ, Yang ZJ, Ren WY, Liu GH, Zhang CZ. 3D meso-scale fracture modelling and validation of concrete based on in-situ X-ray Computed Tomography images using damage plasticity model. International Journal of Solids and Structures. 2015;67-68:340-52.
[178] Poinard C, Piotrowska E, Malecot Y, Daudeville L, Landis EN. Compression triaxial behavior of concrete: the role of the mesostructure by analysis of X-ray tomographic images. European Journal of Environmental and Civil Engineering. 2012;16:s115-s36.
[179] You ZP, Adhikari S, Kutay ME. Dynamic modulus simulation of the asphalt concrete using the X-ray computed tomography images. Materials and Structures. 2009;42:617-30.
[180] Mahal M, Blanksvard T, Taljsten B, Sas G. Using digital image correlation to evaluate fatigue behavior of strengthened reinforced concrete beams. Engineering Structures. 2015;105:277-88.
[181] Rimkus A, Podviezko A, Gribniak V. Processing digital images for crack localization in reinforced concrete members. Innovative Solutions in Construction Engineering and Management: Flexible Approach. 2015;122:239-43.
[182] Viggiani G, Besuelle P, Desrues J. X-ray micro tomography as a tool for studying localized damage/deformation in clay rock. 2013.

[183] Landis EN, Keane DT. X-ray microtomography. Materials Characterization. 2010;61:1305-16.
[184] Landis EN, Nagy EN, Keane DT. Microstructure and fracture in three dimensions. Engineering Fracture Mechanics. 2003;70:911-25.
[185] Landis EN, Nagy EN, Keane DT, Nagy G. Technique to measure 3D work-of-fracture of concrete in compression. Journal of Engineering Mechanics-Asce. 1999;125:599-605.
[186] Verma RK, Fallah Pour A, Dawidowski P, Nguyen GD, Bui HH, Karakus M, et al. Analyzing localization behavior of rocks using Digital Image Correlation technique. ICM-13 2019, 13th International Conference on the Mechanics Behavior of Material, RMIT University, Melbourne, Australia2019.
[187] Yu Y, Li Q, Zhou CQ, Zhou P, Yan HJ. Investigation of droplet evaporation on heterogeneous surfaces using a three-dimensional thermal multiphase lattice Boltzmann model. Applied Thermal Engineering. 2017;127:1346-54.
[188] Yang D, Bornert M, Gharbi H, Valli P, Wang LL. Optimized optical setup for DIC in rock mechanics. EPJ Web of Conferences. 2010;6:22019.
[189] Lenoir N, Bornert M, Desrues J, Bésuelle P, Viggiani G. Volumetric Digital Image Correlation Applied to X-ray Microtomography Images from Triaxial Compression Tests on Argillaceous Rock. Strain. 2007;43:193-205.
[190] Kemeny J, Post R. Estimating three-dimensional rock discontinuity orientation from digital images of fracture traces. Computers & Geosciences. 2003;29:65-77.
[191] Bisby L, Take W, Caspary A. Quantifying strain variation FRP confined using digital image correlation: proof-of-concept and initial results. Asia–Pacific conference on FRP in structures. 2007.
[192] Chen S, Yue ZQ, Tham LG. Digital image-based numerical modeling method for prediction of inhomogeneous rock failure. International Journal of Rock Mechanics and Mining Sciences. 2004;41:939-57.
[193] Nguyen TL, Hall SA, Vacher P, Viggiani G. Fracture mechanisms in soft rock: Identification and quantification of evolving displacement discontinuities by extended digital image correlation. Tectonophysics. 2011;503:117-28.
[194] Bobet A, Fakhimi A, Johnson S, Morris J, Tonon F, Yeung MR. Numerical models in discontinuous media: review of advances for rock mechanics applications. Journal of Geotechnical and Geoenvironmental Engineering. 2009;135:1547-61.
[195] He W, Hayatdavoudi A. A comprehensive analysis of fracture initiation and propagation in sandstones based on micro-level observation and digital imaging correlation. Journal of Petroleum Science and Engineering. 2018;164:75-86.
[196] He WH, Hayatdavoudi A. A comprehensive analysis of fracture initiation and propagation in sandstones based on micro-level observation and digital imaging correlation. Journal of Petroleum Science and Engineering. 2018;164:75-86.
[197] Lingga BA, Apel DB, Sepehri M, Pu Y. Assessment of digital image correlation method in determining large scale cemented rockfill strains. International Journal of Mining Science and Technology. 2019;29:771-6.
[198] Munoz H, Taheri A. Specimen aspect ratio and progressive field strain development of sandstone under uniaxial compression by three-dimensional digital image correlation. Journal of Rock Mechanics and Geotechnical Engineering. 2017;9:599-610.
[199] Cao RH, Lin H, Cao P. Strength and failure characteristics of brittle jointed rock-like specimens under uniaxial compression: Digital speckle technology and a particle mechanics approach. International Journal of Mining Science and Technology. 2018;28:669-77.
[200] Sharafisafa M, Shen LM, Xu QF. Characterisation of mechanical behaviour of 3D printed rock-like material with digital image correlation. International Journal of Rock Mechanics and Mining Sciences. 2018;112:122-38.
[201] Xing HZ, Zhang QB, Ruan D, Dehkhoda S, Lu GX, Zhao J. Full-field measurement and fracture characterisations of rocks under dynamic loads using high-speed three-dimensional digital image correlation. International Journal of Impact Engineering. 2018;113:61-72.

[202] Fallah Pour A, Nguyen GD, Vincent T, Ozbakkaloglu T. Investigation of the compressive behavior and failure modes of unconfined and FRP-confined concrete using digital image correlation. Composite Structures. 2020:112642.
[203] Afroughsabet V, Biolzi L, Ozbakkaloglu T. High-performance fiber-reinforced concrete: a review. Journal of Materials Science. 2016;51:6517-51.
[204] Afroughsabet V, Ozbakkaloglu T. Mechanical and durability properties of high-strength concrete containing steel and polypropylene fibers. Construction and Building Materials. 2015;94:73-82.
[205] Afroughsabet V, Biolzi L, Ozbakkaloglu T. Influence of double hooked-end steel fibers and slag on mechanical and durability properties of high performance recycled aggregate concrete. Composite Structures. 2017;181:273-84.
[206] Lee SC, Oh JH, Cho JY. Compressive Behavior of Fiber-Reinforced Concrete with End-Hooked Steel Fibers. Materials (Basel). 2015;8:1442-58.
[207] Kazmi SMS, Munir MJ, Wu Y-F, Patnaikuni I, Zhou Y, Xing F. Axial stress-strain behavior of macro-synthetic fiber reinforced recycled aggregate concrete. Cement and Concrete Composites. 2019;97:341-56.
[208] Tadepalli PR, Mo YL, Hsu TTC. Mechanical properties of steel fibre concrete. Magazine of Concrete Research. 2013;65:462-74.
[209] Fanella DA, Naaman AE. Stress-Strain Properties of Fiber Reinforced Mortar in Compression. ACI Journal Proceedings. 1985;82.
[210] Rangan SPS, Rangan BV. Fiber Reinforced Concrete Properties. ACI Journal Proceedings. 1971;68.
[211] Khaloo AR, Kim N. Influence of concrete and fiber characteristics on behavior of steel fiber reinforced concrete under direct shear. Aci Materials Journal. 1997;94:592-601.
[212] Lu X, Hsu C-TT. Behavior of high strength concrete with and without steel fiber reinforcement in triaxial compression. Cement and Concrete Research. 2006;36:1679-85.
[213] Deng Z-c, Qu J-l. The Experimental Studies on Behavior of Ultrahigh-Performance Concrete Confined by Hybrid Fiber-Reinforced Polymer Tubes. Advances in Materials Science and Engineering. 2015;2015:1-18.
[214] Usman M, Farooq SH, Umair M, Hanif A. Axial compressive behavior of confined steel fiber reinforced high strength concrete. Construction and Building Materials. 2020;230:117043.
[215] Dai JG, Bai YL, Teng JG. Behavior and Modeling of Concrete Confined with FRP Composites of Large Deformability. Journal of Composites for Construction. 2011;15:963-73.
[216] Kusumawardaningsih Y, Hadi MNS. Comparative behaviour of hollow columns confined with FRP composites. Composite Structures. 2010;93:198-205.
[217] Wang ZY, Wang DY, Smith ST, Lu DG. CFRP-Confined Square RC Columns. I: Experimental Investigation. Journal of Composites for Construction. 2012;16:150-60.
[218] Wu Y-F, Wei Y-Y. Effect of cross-sectional aspect ratio on the strength of CFRP-confined rectangular concrete columns. Engineering Structures. 2010;32:32-45.
[219] Fam A, Schnerch D, Rizkalla S. Rectangular filament-wound glass fiber reinforced polymer tubes filled with concrete under flexural and axial loading: Experimental investigation. Journal of Composites for Construction. 2005;9:25-33.
[220] Li G. Experimental study of FRP confined concrete cylinders. Engineering Structures. 2006;28:1001-8.
[221] Park JH, Jo BW, Yoon SJ, Park SK. Experimental investigation on the structural behavior of concrete filled FRP tubes with/without steel Re-bar. Ksce Journal of Civil Engineering. 2011;15:337-45.
[222] Noushini A, Samali B, Vessalas K. Flexural toughness and ductility characteristics of polyvinyl-alcohol fibre reinforced concrete (PVA-FRC). 8th International conference on fracture mechanics of concrete and concrete structures, FraMCoS-8 Toledo, Spain. 2013:1110-21.
[223] Yan L, Jenkins CH, Pendleton RL. Polyolefin fiber-reinforced concrete composites - Part I. Damping and frequency characteristics. Cement and Concrete Research. 2000;30:391-401.
[224] Arisoy B. Development and fracture evaluation of high performance fiber reinforced lightweight concrete. Wayne State University. 2002.

[225] Noushini A, Vessalas K, Ghosni N, Samali B. Effect of polyvinyl alcohol fibre and fly ash on flexural tensile properties of concrete. 22nd Australasian conference on the mechanics of structures and materials, ACMSM 2012 Sydney, NSW; Australia;. 2013:1165-70.
[226] Feldman D. Polymeric building materials. London: Elsevier Applied Science, 1989.
[227] Toutanji H, Xu B, Gilbert J, Lavin T. Properties of poly(vinyl alcohol) fiber reinforced high-performance organic aggregate cementitious material: Converting brittle to plastic. Construction and Building Materials. 2010;24:1-10.
[228] Li VC, Wang SX, Wu C. Tensile strain-hardening behavior of polyvinyl alcohol engineered cementitious composite (PVA-ECC). Aci Materials Journal. 2001;98:483-92.
[229] Noushini A, Samali B, Vessalas K. Effect of polyvinyl alcohol (PVA) fibre on dynamic and material properties of fibre reinforced concrete. Construction and Building Materials. 2013;49:374-83.
[230] Zhou JJ, Pan JL, Leung CKY. Mechanical Behavior of Fiber-Reinforced Engineered Cementitious Composites in Uniaxial Compression. Journal of Materials in Civil Engineering. 2015;27.
[231] Hannawi K, Bian H, Prince-Agbodjan W, Raghavan B. Effect of different types of fibers on the microstructure and the mechanical behavior of Ultra-High Performance Fiber-Reinforced Concretes. Composites Part B-Engineering. 2016;86:214-20.
[232] Shao YX, Shah SP. Mechanical properties of PVA fiber reinforced cement composites fabricated by extrusion processing. Aci Materials Journal. 1997;94:555-64.
[233] Otter DE, Naaman AE. Properties of steel fiber reinforced concrete under cyclic load. Materials Journal. 1988;85:254-61.
[234] Hsu LS, Hsu CT. Stress-strain behavior of steel-fiber high-strength concrete under compression. Structural Journal. 1994;91:448-57.
[235] Mansur M, Chin M, Wee T. Stress-strain relationship of high-strength fiber concrete in compression. Journal of Materials in Civil Engineering. 1999;11:21-9.
[236] Dhonde HB, Mo Y, Hsu TT, Vogel J. Fresh and hardened properties of self-consolidating fiber-reinforced concrete. Aci Materials Journal. 2007;104:491.
[237] Grzybowski M, Shah SG. Shrinkage Cracking of Fiber Reinforced Concrete. Aci Materials Journal. 1990;87.
[238] Fanella DA, Naaman AE. Stress-Strain Properties of Fiber Reinforced Mortar in Compression. Journal of the American Concrete Institute. 1985;82:475-83.
[239] Wang P, Sang Y, Shao L, Guo X. Measurement of the deformation of sand in a plane strain compression experiment using incremental digital image correlation. Acta Geotechnica. 2018;14:547-57.

Appendix A

Table 1. Summary of test results used in the current study

Study	f'_{co} (MPa)	FRP TYPE	E_f (GPa)	t_f (mm)	K_l (MPa)	K_l/f'_{co}	$\varepsilon_{cu,FH}$ (%)	$\varepsilon_{cu,MH}$ (%)	$\varepsilon_{cu,MH}/\varepsilon_{cu,FH}$
Vincent and Ozbakkaloglu [104]	49.4	A	120.0	0.6	941.1	19.05	3.15	3.17	1.01
	49.4	A	120.0	0.6	941.1	19.05	3.55	3.73	1.05
	49.4	A	120.0	0.6	941.1	19.05	3.47	3.50	1.01
	49.4	A	120.0	0.6	941.1	19.05	3.01	3.32	1.10
	49.4	A	120.0	0.6	941.1	19.05	3.18	3.52	1.11
	49.4	A	120.0	0.6	941.1	19.05	2.98	3.02	1.01
	49.4	A	120.0	0.6	941.1	19.05	3.73	3.65	0.98
	49.4	A	120.0	0.6	941.1	19.05	3.40	3.67	1.08
	49.4	A	120.0	0.6	941.1	19.05	3.37	3.24	0.96
	49.4	A	120.0	0.6	941.1	19.05	3.41	3.55	1.04
	49.4	A	120.0	0.6	941.1	19.05	3.22	3.32	1.03
	49.4	A	120.0	0.6	941.1	19.05	3.48	3.60	1.03
	103.4	A	120.0	1.2	1882.3	18.20	2.89	2.03	0.70
	103.4	A	120.0	1.2	1882.3	18.20	2.53	1.51	0.60
	103.4	A	120.0	1.2	1882.3	18.20	2.89	1.59	0.55
Vincent and Ozbakkaloglu [105]	52.0	C	230.0	0.333	1001.1	19.25	2.31	2.51	1.09
	52.0	C	230.0	0.333	1001.1	19.25	2.22	2.14	0.96
	52.0	C	230.0	0.333	1001.1	19.25	2.14	2.17	1.01
	52.0	C	230.0	0.333	1001.1	19.25	2.48	2.61	1.05
	52.0	C	230.0	0.333	1001.1	19.25	2.25	2.25	1.00
	52.0	C	230.0	0.333	1001.1	19.25	2.19	2.27	1.04
	52.0	C	230.0	0.333	1001.1	19.25	2.20	2.42	1.10
	52.0	C	230.0	0.333	1001.1	19.25	2.12	2.41	1.14
	52.0	C	230.0	0.333	1001.1	19.25	2.14	2.32	1.08
	52.0	C	230.0	0.333	1001.1	19.25	2.36	2.48	1.05
	84.7	C	230.0	0.666	2002.3	23.64	1.66	1.02	0.61*
	84.7	C	230.0	0.666	2002.3	23.64	1.80	1.37	0.76
	84.7	C	230.0	0.666	2002.3	23.64	1.95	1.40	0.72
Lim and Ozbakkaloglu [106]	34.7	G	86.9	0.4	454.4	13.09	3.39	3.50	1.03
	34.7	G	86.9	0.4	454.4	13.09	3.63	3.74	1.03
	34.7	G	86.9	0.4	454.4	13.09	3.23	3.33	1.03
	74.1	G	86.9	0.8	908.8	12.26	2.69	1.40	0.52
	74.1	G	86.9	0.8	908.8	12.26	2.74	1.42	0.52
	74.1	G	86.9	0.8	908.8	12.26	2.61	1.35	0.52
	74.9	A	118.2	0.8	1236.1	16.50	1.88	1.14	0.61
	74.9	A	118.2	0.8	1236.1	16.50	1.69	1.02	0.60
	74.9	A	118.2	0.8	1236.1	16.50	2.14	1.29	0.60
Vincent and Ozbakkaloglu [107]	44.8	A	118.2	0.4	618.0	13.80	2.15	1.95	0.91
	44.8	A	118.2	0.4	618.0	13.80	1.78	1.50	0.84
	44.8	A	118.2	0.4	618.0	13.80	1.77	1.72	0.97
	83.2	A	118.2	0.8	1236.0	14.86	1.77	0.94	0.53
	83.2	A	118.2	0.8	1236.0	14.86	1.72	0.89	0.52
	83.2	A	118.2	0.8	1236.0	14.86	1.93	0.91	0.47

Study	f'_{co} (MPa)	FRP TYPE	E_f (GPa)	t_f (mm)	K_l (MPa)	K_l/f'_{co}	$\varepsilon_{cu,FH}$ (%)	$\varepsilon_{cu,MH}$ (%)	$\varepsilon_{cu,MH}/\varepsilon_{cu,FH}$
Lim and	29.6	A	118.2	0.2	309.0	10.44	2.12	2.10	0.99
Ozbakkaloglu [29]	29.6	A	118.2	0.2	309.0	10.44	1.95	1.80	0.92
	29.6	A	118.2	0.2	309.0	10.44	2.01	1.83	0.91
	29.6	C	240.0	0.167	523.9	17.70	1.90	1.98	1.04
	29.6	C	240.0	0.167	523.9	17.70	2.03	2.10	1.03
	29.6	C	240.0	0.167	523.9	17.70	2.23	2.34	1.05
	29.6	G	86.9	0.2	227.1	7.68	1.82	1.66	0.91**
	29.6	G	86.9	0.2	227.1	7.68	1.51	1.42	0.94
	29.6	G	86.9	0.2	227.1	7.68	2.02	1.84	0.91
	49.6	A	118.2	0.4	618.0	12.46	2.60	1.79	0.69
	49.6	A	118.2	0.4	618.0	12.46	2.32	2.09	0.90
	49.6	A	118.2	0.4	618.0	12.46	2.75	2.24	0.81
	49.6	C	240.0	0.334	1047.8	21.13	2.48	2.06	0.83
	49.6	C	240.0	0.334	1047.8	21.13	2.17	1.98	0.91
	49.6	C	240.0	0.334	1047.8	21.13	2.07	2.07	1.00
	49.6	G	86.9	0.4	454.3	9.16	1.82	1.32	0.73
	49.6	G	86.9	0.4	454.3	9.16	1.85	1.32	0.71
	49.6	G	86.9	0.4	454.3	9.16	1.42	1.00	0.70
	74.1	A	118.2	0.6	927.1	12.51	2.28	1.44	0.63
	74.1	A	118.2	0.6	927.1	12.51	2.52	1.61	0.64
	74.1	A	118.2	0.6	927.1	12.51	2.09	1.11	0.53
	74.1	C	240.0	0.501	1571.7	21.21	1.47	1.20	0.82
	74.1	C	240.0	0.501	1571.7	21.21	1.71	1.16	0.68
	74.1	G	86.9	0.6	681.5	9.20	0.54	0.30	0.56*
	74.1	G	86.9	0.6	681.5	9.20	1.22	0.50	0.41*
	74.1	G	86.9	0.6	681.5	9.20	1.21	0.70	0.58*
	94.1	A	118.2	0.8	1236.1	13.14	2.06	0.99	0.48
	94.1	A	118.2	0.8	1236.1	13.14	1.73	1.18	0.68
	94.1	A	118.2	0.8	1236.1	13.14	2.39	1.03	0.43**
	94.1	C	240.0	0.668	2095.6	22.27	2.16	1.24	0.57
	94.1	C	240.0	0.668	2095.6	22.27	2.03	1.34	0.66
	94.1	C	240.0	0.668	2095.6	22.27	2.20	1.70	0.77
	94.1	G	86.9	0.8	908.7	9.66	2.29	1.00	0.44
	94.1	G	86.9	0.8	908.7	9.66	2.80	1.57	0.56
	94.1	G	86.9	0.8	908.7	9.66	2.40	1.25	0.52
Lim and	85.7	A	118.2	1.2	1854.1	21.63	2.09	1.16	0.56
Ozbakkaloglu [12]	85.7	A	118.2	1.2	1854.1	21.63	2.18	1.18	0.54
	85.7	A	118.2	1.2	1854.1	21.63	2.02	1.23	0.61
	112.4	A	118.2	1.2	1854.1	16.50	1.94	0.85	0.44
	112.4	A	118.2	1.2	1854.1	16.50	1.75	0.82	0.47
	112.4	A	118.2	1.2	1854.1	16.50	2.04	0.74	0.36
	112.4	A	118.2	1.2	1854.1	16.50	1.87	1.12	0.60
	112.4	A	118.2	1.2	1854.1	16.50	1.74	0.82	0.47
	112.4	A	118.2	1.2	1854.1	16.50	1.97	0.97	0.49
	113.4	A	118.2	1.2	1854.1	16.35	1.78	1.02	0.57
	113.4	A	118.2	1.2	1854.1	16.35	1.76	0.88	0.50
	113.4	A	118.2	1.2	1854.1	16.35	1.77	1.09	0.62
Vincent and	110.3	A	118.2	0.8	1236.0	11.21	1.68	0.91	0.54
Ozbakkaloglu [108]	110.3	A	118.2	0.8	1236.0	11.21	1.75	0.88	0.50

Study	f'_{co} (MPa)	FRP TYPE	E_f (GPa)	t_f (mm)	K_l (MPa)	K_l/f'_{co}	$\varepsilon_{cu,FH}$ (%)	$\varepsilon_{cu,MH}$ (%)	$\varepsilon_{cu,MH}/\varepsilon_{cu,FH}$
	110.3	A	118.2	0.8	1236.0	11.21	2.11	0.96	0.48
	110.3	A	118.2	1.2	1854.1	16.81	1.91	0.95	0.50
	110.3	A	118.2	1.2	1854.1	16.81	1.82	0.60	0.37
	110.3	A	118.2	1.2	1854.1	16.81	1.96	0.78	0.40
Vincent and	55.2	A	118.2	0.2	309.0	5.60	1.06	0.57	0.54*
Ozbakkaloglu [109]	55.2	A	118.2	0.2	309.0	5.60	1.11	0.89	0.80
	57.5	A	118.2	0.2	309.0	5.37	1.17	0.89	0.76
	55.2	A	118.2	0.4	618.0	11.20	1.97	1.63	0.83
	55.2	A	118.2	0.4	618.0	11.20	2.09	1.69	0.81
	55.2	A	118.2	0.4	618.0	11.20	2.20	1.97	0.90
	110.2	A	118.2	0.6	927.0	8.41	1.58	0.67	0.42
	110.2	A	118.2	0.6	927.0	8.41	1.56	0.80	0.51
	114.7	A	118.2	0.6	927.0	8.08	1.45	0.68	0.47
	110.2	A	118.2	1.2	1854.1	16.83	1.96	1.03	0.53*
	119.3	A	118.2	1.2	1854.1	15.54	1.89	0.80	0.42
	119.3	A	118.2	1.2	1854.1	15.54	1.96	0.91	0.46

* Excluded from calculations due to a problem encountered during testing

** Excluded from calculations due a problem with displacements recorded by MLVDTs

K_l: lateral stiffness of the FRP jacket

$\varepsilon_{cu,FH}$: ultimate axial strain measured by full-height LVDTs; $\varepsilon_{cu,MH}$: ultimate axial strain measured by mid-height LVDTs

A, C, and G stand for AFRP, CFRP, and GFRP, respectively

Appendix B

Table 2- Database prepared for axial stress and strain at transition point

Paper	*D (mm)*	*H (mm)*	*Ef (GPa)*	*ff (MPa)*	*tf (mm)*	*f'co (MPa)*	*f'c1 (MPa)*	*εc1 (%)*
Aire et al. [123]	150	300	240	3900	0.117	42.0	42.4	0.351
	150	300	240	3900	0.351	42.0	46.4	0.511
	150	300	240	3900	0.702	42.0	50.9	0.520
	150	300	240	3900	0.351	69.0	91.0	0.443
	150	300	240	3900	0.702	69.0	110.0	0.470
	150	300	240	3900	1.053	69.0	122.3	0.522
	150	300	240	3900	1.404	69.0	133.7	0.533
	150	300	65	3000	0.447	42.0	41.6	0.351
	150	300	65	3000	0.894	42.0	47.1	0.466
	150	300	65	3000	0.894	69.0	98.3	0.405
	150	300	65	3000	1.341	69.0	107.4	0.451
	150	300	65	3000	1.788	69.0	114.9	0.440
Benzaid et al. [124]	160	320	238	4300	0.13	26	31.7	0.260
	160	320	238	4300	0.39	26	39.5	0.332
	160	320	238	4300	0.39	50	66.2	0.304
	160	320	238	4300	0.39	62	78.9	0.511
Cui and Sheikh [100]	152	305	241	3639	0.11	85.6	95.4	0.281
	152	305	241	3639	0.11	85.6	89.8	0.285
	152	305	241	3639	0.22	85.6	96.0	0.312
	152	305	241	3639	0.22	85.6	94.5	0.301
	152	305	241	3639	0.44	85.6	100.8	0.368
	152	305	241	3639	0.44	85.6	100.1	0.395
	152	305	241	3639	0.22	111.8	134.1	0.301
	152	305	241	3639	0.22	111.8	135.7	0.303

Paper	*D (mm)*	*H (mm)*	*Ef (GPa)*	*ff (MPa)*	*tf (mm)*	*f'co (MPa)*	*f'c1 (MPa)*	*εc1 (%)*
	152	305	241	3639	0.55	111.8	145.5	0.334
	152	305	241	3639	0.55	111.8	153.3	0.365
	152	305	436	3314	0.16	85.6	97.1	0.335
	152	305	436	3314	0.16	85.6	99.7	0.36
	152	305	436	3314	0.33	111.8	151.7	0.364
	152	305	436	3314	0.33	111.8	148.9	0.326
	152	305	436	3314	0.82	111.8	183.2	0.470
Lam and Teng [93]	152	305	230	3420	0.165	35.9	37.8	0.315
	152	305	230	3420	0.165	35.9	37.8	0.312
	152	305	230	3420	0.165	35.9	38.3	0.321
	152	305	230	3420	0.330	35.9	43.5	0.353
	152	305	230	3420	0.330	35.9	42.6	0.367
	152	305	230	3420	0.330	35.9	43.0	0.372
	152	305	230	3420	0.495	35.9	44.8	0.375
	152	305	230	3420	0.495	35.9	45.7	0.373
	152	305	230	3420	0.495	35.9	43.9	0.381
	152	305	22.5	450	1.27	35.9	44.1	0.362
	152	305	22.5	450	1.27	35.9	42.1	0.375
	152	305	22.5	450	2.45	35.9	48.8	0.414
	152	305	22.5	450	2.45	35.9	46.8	0.478
	152	305	22.5	450	2.45	35.9	46.8	0.471
Mandal and Fam [5]	100	200	26.1	575	1.3	80.6	100.4	0.445
	100	200	26.1	575	1.3	80.6	96.3	0.302
	100	200	26.1	575	1.3	80.6	111.5	0.371
	100	200	26.1	575	1.3	67.0	86.7	0.313
	100	200	26.1	575	1.3	67.0	81.3	0.294
	100	200	26.1	575	1.3	67.0	92.4	0.347
	100	200	26.1	575	2.6	80.6	98.3	0.361

Paper	*D (mm)*	*H (mm)*	*Ef (GPa)*	*ff (MPa)*	*tf (mm)*	*f'co (MPa)*	*f'c1 (MPa)*	*εc1 (%)*
	100	200	26.1	575	2.6	80.6	95.8	0.375
	100	200	26.1	575	2.6	80.6	101.0	0.321
	100	200	26.1	575	2.6	67.0	97.5	0.323
	100	200	26.1	575	2.6	67.0	97.6	0.365
	100	200	26.1	575	2.6	67.0	89.9	0.455
Ozbakkaloglu and Vincent [92]	100	200	118	2930	0.4	85.9	107.7	0.581
	100	200	118	2930	0.4	83.0	105.9	0.672
	100	200	118	2930	0.4	85.9	106.8	0.592
	100	200	120	2900	0.4	85.9	91.1	0.378
	100	200	120	2900	0.4	82.4	87.2	0.386
	100	200	120	2900	0.4	82.4	86.8	0.333
	100	200	120	2900	0.6	85.9	112.9	0.632
	100	200	120	2900	0.6	85.9	118.4	0.466
	100	200	120	2900	0.6	85.9	106.3	0.578
	100	200	120	2900	0.6	110.1	121.9	0.605
	100	200	120	2900	0.6	110.1	120.3	0.516
	100	200	120	2900	0.6	110.1	120.1	0.557
	100	200	120	2900	0.8	110.1	122.9	0.502
	100	200	120	2900	0.8	110.1	130.3	0.612
	152	305	120	2900	0.6	79.6	87.3	0.476
	152	305	120	2900	0.6	77.2	85.2	0.456
	152	305	120	2900	0.6	77.2	81.1	0.357
	152	305	120	2900	1.2	104.5	119.4	0.523
	152	305	120	2900	1.2	104.5	132	0.731
	152	305	120	2900	1.2	104.5	128.1	0.664
	152	305	120	2900	0.8	100	112.4	0.348
	152	305	120	2900	0.8	102.2	110.6	0.363
	152	305	120	2900	1.2	106.0	121.2	0.424

Paper	*D (mm)*	*H (mm)*	*Ef (GPa)*	*ff (MPa)*	*tf (mm)*	*f'co (MPa)*	*f'c1 (MPa)*	*εc1 (%)*
	152	305	120	2900	1.2	106.0	119.3	0.425
	100	200	118	2930	0.6	110.1	130.4	0.662
	100	200	118	2930	0.6	110.1	133.5	0.641
	100	200	118	2930	0.6	110.1	129.6	0.683
	74	150	240	3800	0.234	55.0	68.9	0.411
	74	150	240	3800	0.117	55.0	62.0	0.429
	74	150	240	3800	0.117	49.7	53.6	0.327
	74	150	240	3800	0.234	50.3	56.8	0.356
	74	150	240	3800	0.234	50.3	60.8	0.434
	74	150	240	3800	0.117	75.0	76.1	0.342
	74	150	240	3800	0.234	83.1	86.3	0.314
	74	150	240	3800	0.117	66.6	71.4	0.323
	74	150	240	3800	0.117	83.1	84.6	0.357
	74	150	240	3800	0.117	77.0	78.0	0.331
	74	150	240	3800	0.117	62.0	67.3	0.279
	74	150	240	3800	0.234	83.1	84.2	0.317
	74	150	240	3800	0.234	66.6	71.2	0.284
	74	150	240	3800	0.351	93.8	105.7	0.443
	74	150	240	3800	0.351	77.0	87.1	0.376
	74	150	240	3800	0.351	82.5	92.0	0.401
	74	150	240	3800	0.351	118.9	112.2	0.478
	74	150	240	3800	0.117	43.0	51.5	0.434
	74	150	240	3800	0.117	43.0	51.1	0.375
	74	150	240	3800	0.117	43.0	50.5	0.362
	302	600	240	3800	0.468	36.3	44.2	0.403
	302	600	240	3800	0.234	36.1	38.0	0.355
	152	305	640	2650	0.38	59.0	62.4	0.279
	152	305	640	2650	0.38	59.0	62.5	0.266
	152	305	640	2650	0.19	59.0	60.2	0.279

Paper	D (mm)	H (mm)	Ef (GPa)	ff (MPa)	tf (mm)	f'co (MPa)	f'c1 (MPa)	εc1 (%)
	152	305	640	2650	0.19	55.6	60.2	0.313
	152	305	640	2650	0.19	59.0	61.3	0.287
	152	305	640	2650	0.38	55.6	60.7	0.305
	152	305	640	2650	0.57	98.9	118.9	0.338
	152	305	640	2650	0.19	36.1	43.4	0.237
	152	305	640	2650	0.19	36.1	40.3	0.212
	152	305	640	2650	0.19	36.1	41.0	0.215
	152	305	120	2900	0.4	38.9	44.8	0.427
	152	305	120	2900	0.4	38.9	44.6	0.380
	152	305	120	2900	0.6	38.9	47.3	0.419
	152	305	120	2900	0.6	38.9	45.8	0.353
	100	200	120	2900	0.2	37.0	44.1	0.347
	100	200	120	2900	0.2	35.5	41.3	0.310
	100	200	120	2900	0.2	34.0	39.1	0.309
	100	200	118	2930	0.3	37.2	45.2	0.402
	100	200	118	2930	0.3	37.2	43.1	0.294
	100	200	118	2930	0.3	35.4	42.3	0.349
	74	150	240	3800	0.117	52.2	58.0	0.271
	74	150	240	3800	0.117	52.2	57.0	0.296
	152	305	240	3800	0.351	65.0	68.7	0.425
	152	305	240	3800	0.351	59.0	64.1	0.482
	152	305	240	3800	0.468	59.0	71.4	0.575
	100	200	118	2930	0.6	70.0	95.7	0.384
	100	200	118	2930	0.6	79.5	90.0	0.345
	100	200	118	2930	0.6	85.5	92.3	0.352
	100	200	118	2930	0.6	80.5	74.5	0.315
	100	200	118	2930	0.6	78.0	79.1	0.331
	100	200	118	2930	0.6	74.0	80.4	0.334
	100	200	118	2930	0.6	83.0	85.4	0.323

Paper	*D (mm)*	*H (mm)*	*Ef (GPa)*	*ff (MPa)*	*tf (mm)*	*f'co (MPa)*	*f'c1 (MPa)*	*εc1 (%)*
	100	200	118	2930	0.6	83.0	92.0	0.387
	100	200	118	2930	0.6	85.9	70.3	0.363
Saafi et al. [115]	152.4	435	32	450	0.8	38.0	45.7	0.411
	152.4	435	34	505	1.6	38.0	48.7	0.432
	152.4	435	36	560	2.4	38.0	54.2	0.481
	152.4	435	367	3300	0.11	38.0	40.9	0.442
	152.4	435	390	3550	0.23	38.0	45.4	0.473
	152.4	435	415	3700	0.55	38.0	47.5	0.472
Shahawy et al. [103]	152.5	305	207	3645	0.5	20.7	21.5	0.314
	152.5	305	207	3645	1.0	20.7	23.9	0.321
	152.5	305	207	3645	1.5	20.7	24.9	0.342
	152.5	305	207	3645	2.0	20.7	27.8	0.390
	152.5	305	207	3645	2.5	20.7	22.9	0.414
	152.5	305	207	3645	0.5	41.4	59.2	0.382
	152.5	305	207	3645	1.0	41.4	60.1	0.404
	152.5	305	207	3645	1.5	41.4	60.1	0.417
	152.5	305	207	3645	2.0	41.4	62.3	0.418
Vincent and Ozbakkaloglu [15]	152	305	240	3800	0.117	59.0	58.8	0.377
	152	305	240	3800	0.234	59.0	60.8	0.377
	152	305	240	3800	0.234	59.0	62.3	0.323
	152	305	240	3800	0.351	59.0	61.4	0.377
	152	305	240	3800	0.468	59.0	65.8	0.512
	152	305	240	3800	0.468	59.0	64.6	0.411
	152	305	240	3800	0.117	64.5	65.7	0.212
	152	305	240	3800	0.234	64.5	68.9	0.345
	152	305	240	3800	0.234	62.4	65.3	0.341
	152	305	240	3800	0.234	64.2	69.6	0.321

Paper	D (mm)	H (mm)	Ef (GPa)	ff (MPa)	tf (mm)	f'co (MPa)	f'c1 (MPa)	εc1 (%)
	152	305	240	3800	0.351	64.5	74.1	0.410
	152	305	240	3800	0.351	64.5	73.2	0.370
	152	305	240	3800	0.468	64.5	77.5	0.426
	152	305	240	3800	0.468	62.4	78.3	0.490
	152	305	240	3800	0.468	65.8	79.4	0.397
	152	305	240	3800	0.117	64.5	68.8	0.292
	152	305	240	3800	0.117	62.9	66.5	0.289
	152	305	240	3800	0.117	59.0	60.1	0.279
	152	305	240	3800	0.117	59.0	57.3	0.280
	152	305	240	3800	0.234	62.0	65.9	0.287
	152	305	240	3800	0.468	95.0	97.7	0.428
	152	305	240	3800	0.702	118.0	103.0	0.428
	152	305	240	3800	0.117	92.0	95.4	0.338
	152	305	240	3800	0.117	85.6	91.0	0.306
	152	305	240	3800	0.117	94.7	96.0	0.333
	152	305	240	3800	0.234	93.1	97.9	0.327
	152	305	240	3800	0.234	83.1	93.0	0.450
	152	305	240	3800	0.351	92.7	101.5	0.359
	152	305	240	3800	0.351	94.7	103.5	0.350
	152	305	240	3800	0.351	90.1	96.1	0.338
	152	305	240	3800	0.468	100.0	108.0	0.415
	152	305	240	3800	0.468	118.0	107.1	0.507
	152	305	240	3800	0.468	108.0	117.4	0.361
	152	305	240	3800	0.585	89.0	101.3	0.345
	152	305	240	3800	0.585	87.0	109.9	0.633
	152	305	240	3800	0.585	102.5	109	0.433
	152	305	240	3800	0.585	102.5	108.8	0.416
	152	305	240	3800	0.702	89.0	103.6	0.580
	152	305	240	3800	0.702	89.0	107.5	0.389

Paper	*D (mm)*	*H (mm)*	*Ef (GPa)*	*ff (MPa)*	*tf (mm)*	*f'co (MPa)*	*f'c1 (MPa)*	*εc1 (%)*
	152	305	240	3800	0.117	34.6	37.5	0.208
	152	305	240	3800	0.117	37.3	40.9	0.230
	152	305	240	3800	0.234	30.0	35.5	0.288
	152	305	240	3800	0.234	35.5	41.7	0.293
	152	305	240	3800	0.234	36.3	42.7	0.294
	152	305	240	3800	0.234	37.3	42.8	0.276
	152	305	240	3800	0.117	35.5	38.6	0.298
	152	305	240	3800	0.117	35.5	38.7	0.306
	152	305	240	3800	0.117	35.5	38.4	0.294
	152	305	240	3800	0.234	38.0	42.3	0.307
	152	305	240	3800	0.234	38.0	43.2	0.364
	152	305	240	3800	0.234	36.1	43.1	0.386
	152	305	240	3800	0.234	10.9	27.4	2.318
	152	305	240	3800	0.234	10.9	49.2	4.478
	152	305	240	3800	0.234	37.3	43.6	0.373
Vincent and Ozbakkaloglu [92]	152	305	118	2900	0.8	110.3	127.6	0.360
	152	305	118	2900	0.8	110.3	128.2	0.300
	152	305	118	2900	0.8	110.3	123.5	0.310
	152	305	118	2900	1.2	110.3	128.4	0.631
	152	305	118	2900	1.2	110.3	129.5	0.987
	152	305	118	2900	1.2	110.3	126.0	0.440
Vincent and Ozbakkaloglu [105]	152	305	230	4370	0.333	52.0	55.8	0.352
	152	305	230	4370	0.333	52.0	58.4	0.413
	152	305	230	4370	0.333	52.0	56.5	0.327
	152	305	230	4370	0.333	52.0	58.0	0.291
	152	305	230	4370	0.333	52.0	57.3	0.360
	152	305	230	4370	0.333	52.0	57.9	0.327

Paper	*D (mm)*	*H (mm)*	*Ef (GPa)*	*ff (MPa)*	*tf (mm)*	*f'co (MPa)*	*f'c1 (MPa)*	*εc1 (%)*
	152	305	230	4370	0.333	52.0	62.1	0.370
	152	305	230	4370	0.333	52.0	62.9	0.447
	152	305	230	4370	0.333	52.0	67.8	0.367
	152	305	230	4370	0.333	52.0	57.9	0.378
	152	305	230	4370	0.333	52.0	54.3	0.288
	152	305	230	4370	0.333	52.0	55.8	0.307
	152	305	230	4370	0.666	84.7	115.6	0.482
	152	305	230	4370	0.666	84.7	116.6	0.472
	152	305	230	4370	0.666	84.7	124.6	0.537
Vincent and Ozbakkaloglu [104]	152	305	120	2900	0.6	49.4	60.4	0.477
	152	305	120	2900	0.6	49.4	59.0	0.509
	152	305	120	2900	0.6	49.4	56.4	0.348
	152	305	120	2900	0.6	49.4	62.9	0.531
	152	305	120	2900	0.6	49.4	63.4	0.561
	152	305	120	2900	0.6	49.4	65.5	0.531
	152	305	120	2900	0.6	49.4	58.7	0.553
	152	305	120	2900	0.6	49.4	57.0	0.488
	152	305	120	2900	0.6	49.4	60.3	0.517
	152	305	120	2900	0.6	49.4	60.4	0.534
	152	305	120	2900	0.6	49.4	60.0	0.543
	152	305	120	2900	0.6	49.4	61.3	0.492
	152	305	120	2900	1.2	103.4	122.1	0.451
	152	305	120	2900	1.2	103.4	121.1	0.472
	152	305	120	2900	1.2	103.4	121.3	0.492
Vincent and Ozbakkaloglu [109]	152	153	118	2900	1.2	119.3	144.5	0.931
	152	153	118	2900	1.2	114.7	144.5	0.921
	152	153	118	2900	1.2	110.2	129.4	0.940

Paper	*D (mm)*	*H (mm)*	*Ef (GPa)*	*ff (MPa)*	*tf (mm)*	*f'co (MPa)*	*f'c1 (MPa)*	*εc1 (%)*
	152	305	118	2900	1.2	110.2	102.9	0.971
	152	305	118	2900	1.2	119.3	130.6	1.273
	152	305	118	2900	1.2	119.3	136.6	0.497
	152	305	118	2900	0.6	110.2	110.5	0.921
	152	305	118	2900	0.6	110.2	108.5	0.809
	152	305	118	2900	0.6	114.7	126.4	0.411
	152	153	118	2900	0.4	57.5	68.1	0.412
	152	153	118	2900	0.4	57.5	64.2	0.410
	152	153	118	2900	0.4	57.5	70.1	0.376
	152	305	118	2900	0.4	55.2	55.1	0.266
	152	305	118	2900	0.4	55.2	59.2	0.305
	152	305	118	2900	0.4	55.2	58.7	0.300
	152	305	118	2900	0.2	57.5	59.2	0.284
	152	305	118	2900	0.2	55.2	56.5	0.291
Vincent and Ozbakkaloglu [107]	152	305	118	2900	0.4	44.0	53.9	0.319
	152	305	118	2900	0.4	44.0	55.1	0.363
	152	305	118	2900	0.4	44.0	54.4	0.260
	152	305	118	2900	0.8	74.5	100.0	0.364
	152	305	118	2900	0.8	74.5	107.0	0.442
	152	305	118	2900	0.8	74.5	108.3	0.573

Appendix C

In this study, Beta distribution expression was used to predict the shape of experimental curves due to the existence of parameters in this distribution expression, which governs the shape of this distribution. The Eq. (1) shows the expression related to Beta distribution:

$$f(x) = \frac{(x-a)^{(p-1)}(b-x)^{(q-1)}}{B(p,q)(b-a)^{(p+q-1)}} \quad a \le x \le b; (p,q) > 0 \qquad (1)$$

By assuming a equals 0, b equals 1 and B (p, q) as a constant value (ξ), Eq. (1) can be modified to Eq.(2):

$$f(x) = \xi x^{(p-1)}(1-x)^{(q-1)} \qquad (2)$$

By using Eq.2 and determination of ξ, p, and q for different stages of the test procedure, the shape of Von Mises strain distribution was predicted for different specimens in this study.

Appendix D (Statement of Authorship -Section 2)

Statement of Authorship

Title of Paper	Influence of the Measurement Method on Axial Strains of FRP-Confined Concrete under Compression
Publication Status	☑ Published ☐ Accepted for Publication ☐ Submitted for Publication ☐ Unpublished and Unsubmitted work written in manuscript style
Publication Details	Ali Fallah Pour, Aliakbar Gholampour, Togay Ozbakkaloglu. Composite Structures, https://doi.org/10.1016/j.compstruct.2018.01.017

Principal Author

Name of Principal Author (Candidate)	Ali Fallah Pour		
Contribution to the Paper	Conceptualization, Methodology, Formal analysis, Writing - Original Draft.		
Overall percentage (%)	60		
Certification:	This paper reports on original research I conducted during the period of my Higher Degree by Research candidature and is not subject to any obligations or contractual agreements with a third party that would constrain its inclusion in this thesis. I am the primary author of this paper.		
Signature		Date	13/08/2020

Co-Author Contributions

By signing the Statement of Authorship, each author certifies that:

i. the candidate's stated contribution to the publication is accurate (as detailed above);
ii. permission is granted for the candidate in include the publication in the thesis; and
iii. the sum of all co-author contributions is equal to 100% less the candidate's stated contribution.

Name of Co-Author	Aliakbar Gholampour		
Contribution to the Paper	Validation, Visualization, Writing - Review & Editing		
Signature		Date	13/08/2020

Name of Co-Author	Togay Ozbakkaloglu
Contribution to the Paper	Supervision, Conceptualization, Methodology, Writing - Review & Editing

Signature		Date	11/11/20

Please cut and paste additional co-author panels here as required.

Appendix E (Statement of Authorship –Section 3)

Statement of Authorship

Title of Paper	Simplified Design-Oriented Axial Stress-Strain Model for FRP-Confined Normal- and High-Strength Concrete
Publication Status	☑ Published ☐ Accepted for Publication ☐ Submitted for Publication ☐ Unpublished and Unsubmitted work written in manuscript style
Publication Details	Ali Fallah Pour, Togay Ozbakkaloglu, Thomas Vincent, Engineering Structures, https://doi.org/10.1016/j.engstruct.2018.07.099

Principal Author

Name of Principal Author (Candidate)	Ali Fallah Pour		
Contribution to the Paper	Conceptualization, Methodology, Formal analysis, Writing - Original Draft		
Overall percentage (%)	60		
Certification:	This paper reports on original research I conducted during the period of my Higher Degree by Research candidature and is not subject to any obligations or contractual agreements with a third party that would constrain its inclusion in this thesis. I am the primary author of this paper.		
Signature		Date	13/08/2020

Co-Author Contributions

By signing the Statement of Authorship, each author certifies that:

i. the candidate's stated contribution to the publication is accurate (as detailed above);
ii. permission is granted for the candidate in include the publication in the thesis; and
iii. the sum of all co-author contributions is equal to 100% less the candidate's stated contribution.

Name of Co-Author	Togay Ozbakkaloglu		
Contribution to the Paper	Supervision, Conceptualization, Methodology, Writing - Review & Editing.		
Signature		Date	11/11/20

Name of Co-Author	Thomas Vincent
Contribution to the Paper	Validation, Visualization, Writing - Review & Editing

Signature		Date	13.8.2020

Please cut and paste additional co-author panels here as required.

Appendix F (Statement of Authorship –Section 4)

Statement of Authorship

Title of Paper	Behavior of FRP-Confined High-Strength Concrete under Eccentric Compression: Tests on Concrete-Filled FRP Tube Columns
Publication Status	☑ Published ☐ Accepted for Publication ☐ Submitted for Publication ☐ Unpublished and Unsubmitted work written in manuscript style
Publication Details	Ali Fallah Pour, Aliakbar Gholampour, Junai Zheng, Togay Ozbakkaloglu, Composite Structures, https://doi.org/10.1016/j.compstruct.2019.03.031

Principal Author

Name of Principal Author (Candidate)	Ali Fallah Pour		
Contribution to the Paper	Conceptualization, Methodology, Formal analysis, Writing - Original Draft		
Overall percentage (%)	55		
Certification:	This paper reports on original research I conducted during the period of my Higher Degree by Research candidature and is not subject to any obligations or contractual agreements with a third party that would constrain its inclusion in this thesis. I am the primary author of this paper.		
Signature		Date	12/08/2020

Co-Author Contributions

By signing the Statement of Authorship, each author certifies that:

i. the candidate's stated contribution to the publication is accurate (as detailed above);
ii. permission is granted for the candidate in include the publication in the thesis; and
iii. the sum of all co-author contributions is equal to 100% less the candidate's stated contribution.

Name of Co-Author	Aliakbar Gholampour		
Contribution to the Paper	Validation, Visualization, Writing - Review & Editing		
Signature		Date	13/08/2020

Name of Co-Author	Junai Zheng
Contribution to the Paper	First conceptualization and methodology, Initial analysis, Writing - Original Draft

Signature		Date	13/08/2020

Name of Co-Author	Togay Ozbakkaloglu		
Contribution to the Paper	Supervision, Conceptualization, Methodology, Writing - Review & Editing.		
Signature		Date	11/11/20

Please cut and paste additional co-author panels here as required.

Appendix G (Statement of Authorship –Section 5)

Statement of Authorship

Title of Paper	Investigation of the compressive behavior and failure modes of unconfined and FRP-confined concrete using digital image correlation
Publication Status	☑ Published ☐ Accepted for Publication ☐ Submitted for Publication ☐ Unpublished and Unsubmitted work written in manuscript style
Publication Details	Ali Fallah Pour, Giang D. Nguyen, Thomas Vincent, Togay Ozbakkaloglu, Composite Structures, https://doi.org/10.1016/j.compstruct.2020.112642.

Principal Author

Name of Principal Author (Candidate)	Ali Fallah Pour		
Contribution to the Paper	Conceptualization, Methodology, Formal analysis, Writing - Original Draft.		
Overall percentage (%)	60		
Certification:	This paper reports on original research I conducted during the period of my Higher Degree by Research candidature and is not subject to any obligations or contractual agreements with a third party that would constrain its inclusion in this thesis. I am the primary author of this paper.		
Signature		Date	13/08/2020

Co-Author Contributions

By signing the Statement of Authorship, each author certifies that:

i. the candidate's stated contribution to the publication is accurate (as detailed above);

ii. permission is granted for the candidate in include the publication in the thesis; and

iii. the sum of all co-author contributions is equal to 100% less the candidate's stated contribution.

Name of Co-Author	Giang D. Nguyen		
Contribution to the Paper	Supervision, Conceptualization, Methodology, Writing - Review & Editing.		
Signature		Date	24 Nov 2020

Name of Co-Author	Thomas Vincent
Contribution to the Paper	Validation, Visualization, Writing - Review & Editing

Signature		Date	13.8.2020

Name of Co-Author	Togay Ozbakkaloglu		
Contribution to the Paper	Supervision, Conceptualization, Methodology, Writing - Review & Editing.		
Signature		Date	11/11/20

Please cut and paste additional co-author panels here as required.

Appendix H (Statement of Authorship –Section 6)

Statement of Authorship

Title of Paper	Analysis of mechanical behavior and localization of deformation in rock and concrete using Digital Image Correlation
Publication Status	☐ Published ☐ Accepted for Publication ☐ Submitted for Publication ☑ Unpublished and Unsubmitted work written in manuscript style
Publication Details	Ali Fallah Pour,

Principal Author

Name of Principal Author (Candidate)	Ali Fallah Pour		
Contribution to the Paper	Conceptualization, Methodology, Formal analysis, Writing - Original Draft.		
Overall percentage (%)	60		
Certification:	This paper reports on original research I conducted during the period of my Higher Degree by Research candidature and is not subject to any obligations or contractual agreements with a third party that would constrain its inclusion in this thesis. I am the primary author of this paper.		
Signature		Date	18/11/2020

Co-Author Contributions

By signing the Statement of Authorship, each author certifies that:

i. the candidate's stated contribution to the publication is accurate (as detailed above);
ii. permission is granted for the candidate in include the publication in the thesis; and
iii. the sum of all co-author contributions is equal to 100% less the candidate's stated contribution.

Name of Co-Author	Rupesh Kumar Verma		
Contribution to the Paper	Validation, Visualization, Writing - Review & Editing		
Signature		Date	18/11/2020

Name of Co-Author	Giang D. Nguyen
Contribution to the Paper	Supervision, Conceptualization, Methodology, Review & Editing

Signature		Date	18 Nov 2020
Name of Co-Author	Ha Bui		
Contribution to the Paper	Conceptualization, Methodology, Review & Editing		
Signature		Date	30 Nov 2020

Please cut and paste additional co-author panels here as required.

Appendix I (Statement of Authorship –Section 7)

Statement of Authorship

Title of Paper	Examination of deformation in FRP-confined high-strength concrete using digital image correlation
Publication Status	☐ Published ☐ Accepted for Publication ☐ Submitted for Publication ☑ Unpublished and Unsubmitted work written in manuscript style
Publication Details	Ali Fallah Pour, Giang D Nguyen

Principal Author

Name of Principal Author (Candidate)	Ali Fallah Pour		
Contribution to the Paper	Conceptualization, Methodology, Formal analysis, Writing - Original Draft.		
Overall percentage (%)	70		
Certification:	This paper reports on original research I conducted during the period of my Higher Degree by Research candidature and is not subject to any obligations or contractual agreements with a third party that would constrain its inclusion in this thesis. I am the primary author of this paper.		
Signature		Date	23/11/2020

Co-Author Contributions

By signing the Statement of Authorship, each author certifies that:

i. the candidate's stated contribution to the publication is accurate (as detailed above);
ii. permission is granted for the candidate in include the publication in the thesis; and
iii. the sum of all co-author contributions is equal to 100% less the candidate's stated contribution.

Name of Co-Author	Giang D Nguyen		
Contribution to the Paper	Supervision, Conceptualization, Methodology, Review & Editing		
Signature		Date	24 Nov 2020

Please cut and paste additional co-author panels here as required.

Appendix J (Statement of Authorship –Section 8)

Statement of Authorship

Title of Paper	**Axial compressive behavior of ultra-high-strength steel fiber-reinforced concrete-filled FRP tube columns**
Publication Status	☐ Published ☐ Accepted for Publication ☑ Submitted for Publication ☐ Unpublished and Unsubmitted work written in manuscript style
Publication Details	Ali Fallah Pour, Togay Ozbakkaloglu, Thomas Vincent,

Principal Author

Name of Principal Author (Candidate)	Ali Fallah Pour		
Contribution to the Paper	Conceptualization, Methodology, Formal analysis, Writing - Original Draft		
Overall percentage (%)	60		
Certification:	This paper reports on original research I conducted during the period of my Higher Degree by Research candidature and is not subject to any obligations or contractual agreements with a third party that would constrain its inclusion in this thesis. I am the primary author of this paper.		
Signature		Date	13/08/2020

Co-Author Contributions

By signing the Statement of Authorship, each author certifies that:

i. the candidate's stated contribution to the publication is accurate (as detailed above);
ii. permission is granted for the candidate in include the publication in the thesis; and
iii. the sum of all co-author contributions is equal to 100% less the candidate's stated contribution.

Name of Co-Author	Togay Ozbakkaloglu		
Contribution to the Paper	Supervision, Conceptualization, Methodology, Writing - Review & Editing		
Signature		Date	11/11/20

Name of Co-Author	Thomas Vincent		
Contribution to the Paper	Validation, Methodology, Review & Editing.		
Signature		Date	26/08/2020

Please cut and paste additional co-author panels here as required.

Appendix K (Statement of Authorship –Section 9)

Statement of Authorship

Title of Paper	Axial compressive behavior of POLYVINYL ALCOHOL fiber-reinforced concrete-filled FRP tube columns
Publication Status	☐ Published ☐ Accepted for Publication ☐ Submitted for Publication ☑ Unpublished and Unsubmitted work written in manuscript style
Publication Details	Ali Fallah Pour, Togay Ozbakkaloglu, Thomas Vincent, Engineering Structures, https://doi.org/10.1016/j.engstruct.2018.07.099

Principal Author

Name of Principal Author (Candidate)	Ali Fallah Pour		
Contribution to the Paper	Conceptualization, Methodology, Formal analysis, Writing - Original Draft		
Overall percentage (%)	60		
Certification:	This paper reports on original research I conducted during the period of my Higher Degree by Research candidature and is not subject to any obligations or contractual agreements with a third party that would constrain its inclusion in this thesis. I am the primary author of this paper.		
Signature		Date	

Co-Author Contributions

By signing the Statement of Authorship, each author certifies that:

i. the candidate's stated contribution to the publication is accurate (as detailed above);
ii. permission is granted for the candidate in include the publication in the thesis; and
iii. the sum of all co-author contributions is equal to 100% less the candidate's stated contribution.

Name of Co-Author	Togay Ozbakkaloglu		
Contribution to the Paper	Supervision, Conceptualization, Methodology, Writing - Review & Editing.		
Signature		Date	11/11/20

Name of Co-Author	Thomas Vincent
Contribution to the Paper	Validation, Visualization, Writing - Review & Editing

Signature		Date	17.11.2020

Please cut and paste additional co-author panels here as required.

Appendix L (Statement of Authorship –Section 10)

Statement of Authorship

Title of Paper	Evaluation of ultra-high-strength steel fiber-reinforced concrete-filled FRP tubes and unconfined concrete columns under compression: an analysis using Digital Image Correlation
Publication Status	☐ Published ☐ Accepted for Publication ☐ Submitted for Publication ☑ Unpublished and Unsubmitted work written in manuscript style
Publication Details	Ali Fallah Pour, Giang D Nguyen

Principal Author

Name of Principal Author (Candidate)	Ali Fallah Pour		
Contribution to the Paper	Conceptualization, Methodology, Formal analysis, Writing - Original Draft.		
Overall percentage (%)	70		
Certification:	This paper reports on original research I conducted during the period of my Higher Degree by Research candidature and is not subject to any obligations or contractual agreements with a third party that would constrain its inclusion in this thesis. I am the primary author of this paper.		
Signature		Date	23/11/2020

Co-Author Contributions

By signing the Statement of Authorship, each author certifies that:

i. the candidate's stated contribution to the publication is accurate (as detailed above);
ii. permission is granted for the candidate in include the publication in the thesis; and
iii. the sum of all co-author contributions is equal to 100% less the candidate's stated contribution.

Name of Co-Author	Giang D Nguyen		
Contribution to the Paper	Supervision, Conceptualization, Methodology, Review & Editing		
Signature		Date	24 Nov 2020

Please cut and paste additional co-author panels here as required.